Exploring Spectral Unmixing Algorithms for Applications to Estimating Asteroid Surface Compositions



Eloïse Céline Brown

St. Cross College

University of Oxford

A thesis submitted for the degree of

Doctor of Philosophy

Hilary Term 2023

This thesis is dedicated to
Phoebe F. Brown
for her inspiring courage and resilience in the darkest of times

Acknowledgements

I would like to thank: RedBull (not sponsored)

So it turns out doing a PhD is pretty hard (who knew?!). Luckily I've had the support from amazing people (and energy drinks...) to help keep me going and actually reach this point of submitting my thesis (wow).

Firstly, my deepest thanks and gratitude go to my supervisory team. To Professor Neil Bowles for his continued generosity and support, particularly when I've faced difficulties and taken sick leave, and for always offering to help and being on my side. He has also created a fantastic research group that I feel so proud to have been a part of – we've collectively been 'livin' the dream' in the 'fun zone', and I'll miss it dearly (even the long group meeting intros with techno music). I've also always felt encouraged to just experiment and give my scientific ideas a go thanks to Neil's enthusiasm and excitement at just the prospect of there being a graph. To Professor Kerri Donaldson Hanna for introducing and welcoming me to the planetary science community, and keeping me inspired to continue on this career path. I wouldn't have been able to make it this far without her easy to follow explanations of the fundamentals behind this project and lab guidance (and of course the endless data she has provided!) To Dr. Katherine Shirley for her increased involvement towards the end of my PhD, helping keep me (and Neil) on track and providing valuable mentorship and advice (and also providing data!) To Dr. Tris Warren for being there right from the start of my PhD as my office buddy, and remaining a much needed calming presence in the group. My thanks also extend to research group members past and present (Team NK: including Rory, Helena, Rowan, Burtie, Nick, Henry, Imi, Jordan, Aria, Bea and Keith, to name just a few), and fellow AOPeePs, for making the department such an enjoyable place to be; which also wouldn't have been possible without the excellent admin support from Lucy and Andrea. Many thanks also go to my college advisor, Professor Dave Waters; to all the other scientists who have shown interest and encouragement in my research; and to new friends made at conferences.

This thesis also wouldn't have been possible without the endless love and support from my family, The Brownies, most of all Mum and Dad (and Mum's office – thanks Vinci Terrassement for letting me use a desk here whilst writing up!) Special shout-out also to my wonderful friends, including some of the best flatmates I've had – Kit and Nathan – who kept me sane and made the pandemic and lockdowns much easier to cope with.

Thank u everyone :)))

Abstract

Understanding asteroid composition is key to better understanding a variety of specific fields within planetary science. Thermal infrared (TIR; $5 - 25\mu$m) spectroscopy is a valuable method for estimating modal mineralogy due to its non-destructive nature, and utility in laboratories on Earth and in spacecraft instrumentation to provide remote sensing observations. The current most widely used forward model (i.e., mathematical expression to describe phenomena), and algorithm (i.e., computational technique to estimate parameters of interest) are linear mixing and a linear least squares, respectively. Whilst this method for spectral interpretation is accurate for whole rock/coarse grained samples, and applications for which we have a wealth of contextual information (e.g., Mars), this combination of model and algorithm becomes unsuitable where fine grains ($< 50\mu$m) dominate, and when there is little additional information about the measurement target. The simplicity behind the linear mixing model and linear least squares algorithm raises the question whether a more complex model is required, or can linear mixing still be used effectively within more sophisticated algorithms?

As the linear mixing model has advantages over others, this project has investigated linear mixing within a selection of increasingly sophisticated spectral unmixing algorithms, whilst adopting a Bayesian approach. Issues of degeneracy and the use of implicit *a priori* information, that are intrinsic to current methods, have also been tackled. Results from this investigation (as presented within this thesis) showed that an alternative model is required; thus, also presented, is preliminary work towards a novel method of parameterising linear mixing via empirical studies of quantitative spectral morphology changes with decreasing grain size. Initial results show promise, but refinement through more in depth future spectral morphology studies is required.

This work has demonstrated the unsuitability of linear mixing with linear least squares for fine-grained mixture composition estimates, and begun laying foundations for improved spectral interpretation tools.

Contents

Acronyms & Glossary **vii**

1 Introduction **1**
1.1 Asteroids . . . 2
1.2 Meteorites . . . 3
1.3 Returned Samples . . . 5
1.4 Space Missions . . . 7
1.5 This Research . . . 10

2 Theory: Spectroscopy and Linear Mixing **14**
2.1 Infrared Spectroscopy . . . 15
2.2 The Linear Spectral Mixing Model . . . 21
2.2.1 Setting Up the Mathematics of Linear Mixing . . . 22
2.2.2 Scattering . . . 23
2.2.3 Potential Degeneracy . . . 25

3 Theory: Computational Techniques for Spectral Unmixing **27**
3.1 Review of Current Spectral Unmixing Algorithms . . . 28
3.1.1 The Linear Least Squares . . . 28
3.1.2 The Non-Negative Linear Least Squares . . . 30
3.1.3 The Partial Least Squares . . . 31
3.1.4 Continued Challenges . . . 33
3.2 Frequentist vs Bayesian Inference . . . 34
3.3 Non-Algorithmic Methods to Enhance Analysis . . . 38
3.3.1 Principal Component Analysis (PCA) . . . 38
3.3.2 Covariance and Correlation Matrices . . . 42
3.3.3 Retrieval Quality Metrics . . . 43

4 Method: Data and Algorithms Used **48**
4.1 Spectral Library . . . 49
4.2 Mixtures for Unmixing . . . 52
4.2.1 Bruce . . . 54
4.2.2 Glenn . . . 58
4.2.3 Qualitative Comparisons to Bennu . . . 63
4.3 Exploration and Development of Spectral Unmixing Algorithms . . . 64
4.3.1 Trialling Existing Python Packages for Spectral Unmixing . . . 65
4.3.2 Developing Bespoke Spectral Unmixing Algorithms . . . 66
4.3.3 Renormalising for Blackbody Abundance . . . 75

5 Results and Discussion: Pre-Unmixing and Frequentist Inference 78
5.1 Pre-Unmixing: *real* vs *math* . . . 79
5.1.1 Bruce . . . 79
5.1.2 Glenn . . . 81
5.2 Pre-Unmixing: Spectral Library PCA . . . 84
5.2.1 *minimal* . . . 85
5.2.2 *expanded* . . . 87
5.2.3 *extensive* . . . 89
5.2.4 Overall Spectral Library PCA Discussion and Summary . . . 92
5.3 Weighted Least Squares . . . 92
5.3.1 Bruce . . . 93
5.3.2 Glenn . . . 106
5.3.3 Overall `WLS_ASC_ILR()` Unmixings Discussion . . . 109

6 Results and Discussion: A Bayesian Approach and Algorithm Comparisons 113
6.1 Optimal Estimation . . . 115
6.1.1 Bruce . . . 115
6.1.2 Glenn . . . 132
6.1.3 Overall `OptEst_ASC_ILR()` Unmixings Discussion . . . 145
6.2 Markov Chain Monte Carlo . . . 149
6.2.1 Bruce . . . 150
6.2.2 Glenn . . . 177
6.2.3 Overall `MCMC()` Unmixings Discussion . . . 195
6.3 Spectral Unmixing Algorithm Comparisons and Overall Conclusions 199

7 Towards A New Spectral Mixing Model 203
7.1 Justification and Overview . . . 204
7.2 Proposed Method . . . 206
7.2.1 Previous Studies of Spectral Changes with Grain Size . . . 206
7.2.2 My Spectral Morphology Study . . . 210
7.3 Preliminary Results . . . 225
7.3.1 Data Used . . . 225
7.3.2 Spectral Morphology Study Results . . . 227
7.3.3 Pre-Unmixing: *brucerealmod* and its Coarse Spectral Libraries 232
7.3.4 `WLS_ASC_ILR()` . . . 238
7.3.5 `OptEst_ASC_ILR()` . . . 241
7.3.6 `MCMC()` . . . 246
7.3.7 Discussion . . . 252

8 Summary, Conclusions and Future Work **254**
8.1 Overview: The Bigger Picture 254
8.2 Overview: This Project 256
8.3 Avenues for Future Research 259

Bibliography **262**

Appendices

A Additional Figures to Accompany Chapters 5, 6 and 7 **268**

B Additional Results Tables to Accompany Chapters 5, 6 and 7 **299**

C Additional Correlation Matrices to Accompany Chapters 5, 6 and 7 **411**

Acronyms & Glossary

TIR . . . . . Thermal Infrared ($5 - 25\mu$m)

WLS . . . . . Weighted least squares

OptEst . . . . . Optimal estimation

ASC . . . . . Abundance sum constraint

ILR . . . . . Iterative library reduction

MCMC . . . . . Markov Chain Monte Carlo

RMS . . . . . Root mean square

BB . . . . . Blackbody (end-member)

CF . . . . . Christiansen Feature

TF . . . . . Transparency Feature

RB . . . . . Reststrahlen Bands

pdf . . . . . Probability density function

Model: a.k.a, the forward model. The mathematical expression used to describe what is observed. Here, the (forward) model used is linear spectral mixing, other examples would include more complete radiative transfer models (e.g., Hapke) that take in relevant information (such as phase function or other scattering parameters) from additional models e.g., Mie or T-matrix.

Algorithm: a.k.a, the retrieval algorithm. The computational technique for estimating/retrieving parameters of the model to best match the data. e.g., weighted least squares, optimal estimation, MCMC. Other examples include Levenberg-Marquardt, non-negative least squares, machine learning etc.

***A priori*:** Any information known before analysis of a measurement. In this work, *a priori* information is further categorised as '**bounds**'/'**constraints**' and '**priors**', based on the specific nature and application of such *a priori* information.

Priors: Probabilistic *a priori* information specifically regarding the quantified value of the solution, usually based on previous research (e.g., the meteorite record). In this work, the priors are in the form of end-member abundances and their uncertainties. It is important to distinguish that these predicted values are used to loosely restrict the parameter space searched for that particular parameter (i.e., end-member abundance), rather than acting as an 'initial guess' for the starting point of the algorithm.

Bounds/Constraints: *A priori* information regarding what would be physically meaningful for the solution. Bounds/constraints firmly restrict the searchable parameter space more generally to ensure no unphysical results. In this application of determining modal mineralogy, it would be unphysical for retrieved abundances to be negative or sum to either less than or greater than one, thus the constraints here are the non-negativity constraint and sum-to-one constraint (a.k.a, abundance sum constraint, ASC).

Retrieval/Unmixing: General reference to specific results from using inverse methods (i.e., obtaining model parameters given data) in the algorithms. Different fields of research often use different terminology, such as 'retrieval': referring to the act of retrieving parameter estimates from the data via a model. In this work, the inversion/retrieval is applied to the problem of 'unmixing' a spectrum composed of a mixture of minerals; thus 'retrieval' and 'unmixing' are used interchangeably throughout.

End-member: Individual mineral component that may be a constituent of a mixture, so is often included in the spectral library.

Frequentist inference: [1]Statistical inference based on frequency of outcomes in a large sample – data vary and parameters are fixed. **Priors** (see above) cannot be set, but it is possible to apply **bounds/constraints** (see above) to the parameter space of the solution with some techniques.

Bayesian inference: [1]Statistical inference based on probability distributions for parameters given ***a priori*** (see above) information, following Bayes' rule - data are fixed and parameters vary. **Priors** are a requirement for all Bayesian methods and so must be set.

Spectral morphology: General term used here to refer to the overall shape of a spectrum over the spectral range, encompassing positions of spectral features and spectral contrast.

[1]Frequentist and Bayesian inference are also defined in Section 3.2, and are included here for easier reference.

Chapter 1

Introduction

Contents

1.1 Asteroids **2**
1.2 Meteorites **3**
1.3 Returned Samples **5**
1.4 Space Missions **7**
1.5 This Research **10**

Asteroids are rocky fragments that exist in a range of shapes and sizes orbiting the Sun and are widely thought of as the remaining material that did not coalesce to form planets during the primordial stages of Solar System formation, making them time capsules holding the secrets to its birth. Occasionally, pieces of these asteroids arrive on Earth as meteorites, and their analyses indicate that some asteroids contain the very first materials to exist within our Solar System (Anders 1971; Connolly Jr. and Jones 2016), so returned samples from asteroids can provide vital context to the origins of meteorites. Recent and current sample return missions, Hayabusa2 (Tachibana et al. 2014; Tsuda et al. 2013) and the Origins, Spectral Interpretation, Resource Identification, Security - Regolith Explorer (OSIRIS-REx; Lauretta, Balram-Knutson, et al. 2017), have already revolutionised the study of asteroids in situ with their data collected so far; and with more returned samples received and planned than their predecessors, they are expected to bring greater detail to compositional information.

1.1 Asteroids

Since asteroids are the remnants of planetary formation, studying them allows us to further understand the formation and evolutionary history of the Solar System. For example, observations of changes in brightness/flux with time produce lightcurves, which can then be interpreted to determine information on properties such as shape, size, and rotational period, which in turn tell us of the likely history of that object.

Asteroid shapes illustrate the dynamical conditions of the Solar System; for example, an elongated dog-bone-like shape may be indicative of a slow collision between two initially separate bodies. The distribution of how many asteroids occur in certain size ranges tells us of their collisional evolution, where the largest asteroids are likely to have been largely unaltered by collisions, making them primordial objects (e.g., Davis et al. 2002). The rotational period of an asteroid can provide hints as to whether it may be a rubble pile or not, and observations have shown many binary near-Earth asteroids to be rubble piles, suggesting a parent body may have undergone the spin up YORP[1] effect that led to its separation into a binary system (e.g., Ostro et al. 2006; Walsh, Richardson, et al. 2008).

Shortly following planetary formation, the recent presence of Jupiter along with other planetary embryos are thought to have caused gravitational perturbations with the asteroid Main Belt, resulting in the dynamical depletion of Main Belt material, leading to the structures and total mass observed today (e.g., Petit et al. 2002). Compositions of asteroids can indicate the distance from the proto-Sun at which they formed within the protoplanetary disk due to the presence of different elements and minerals being feasible within certain formation conditions/environments, as governed by location in the protoplanetary disk. For example, temperatures

[1]The YORP (Yarkovsky-O'Keefe-Radzievskii-Paddack) effect describes how a change in albedo across the surface of a small body, such as an asteroid, can alter its rotation rate due to the combined effects of the body's own thermal emission and the albedo-dependent scattering of solar radiation.

sunward of the water snow-line[2] were generally too hot for volatiles to condense, so observations of volatile-rich asteroids within this range today implies that some form of planetary migration occurred during the Solar System's history (e.g., Walsh, Morbidelli, et al. 2012). So, comparing observed compositions of asteroids with their current positions may aid in determining the dynamical history of the Solar System by placing constraints on planetary migration models.

The variety of properties observed amongst asteroids has led to attempts to categorise them, resulting in a variety of asteroid taxonomy systems; from the Tholen system established in 1984, to the Bus-DeMeo system from 2009, each of which are summarised in Figure 1.1.

Improved knowledge on the orbits and various properties of asteroids not only tells us of our Solar System's past, but can also aid in predicting potential collisions with Earth, which is vital for preparing appropriate mitigation strategies.

1.2 Meteorites

Although there are meteorites from the Moon and Mars, the vast majority are thought to have originated from asteroids (e.g., Yoshikawa, Kawaguchi, et al. 2021). Thus, detailed laboratory studies of meteorites can strengthen or weaken theories based on telescopic observations, and have even led to discoveries that would not have been possible without them. For example, chondrules are spherical igneous silicate droplets at the millimeter scale, that form a key component in chondritic meteorites, giving them their name. Chondrites are the most common type of meteorite, making chondrules one of the most abundant components seen in the meteorite record, however their existence could not have been predicted from models and observations of protoplanetary systems (Connolly Jr. and Jones 2016). Their analyses, however, tell us that they formed from pre-existing condensed material that had later been heated (e.g., Desch et al. 2005; Russell 2007).

[2]The water snow-line marks the heliocentric distance in the protoplanetary disk where the conditions allowed for water ice condensation, and is estimated to be $1.8 - 2.7$AU (Lecar et al. 2006).

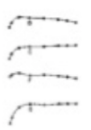
Taxonomic System:	Tholen (1984)	Gaffey (1993)	Bus (2002)	Bus-DeMeo (2009)	Taxonomy Notes	Relevant minerals possible meteorite analogs (for more details see Burbine et al., Asteroids III)
Wavelength Range:	0.33-1.1 um	0.35-2.50 um	0.45-0.90 um	0.45-2.45 um		
S-Complex	 S	SI SII SIII SIV SV SVI SVII	S Sa Sq Sr Sk Sl	 S  Sa  Sq  Sr  Sv	**Tholen:** Defined only S. **Gaffey:** 7 mineralogic classes based on Band I center & Band II / Band I area ratio. Primarily separates olivine to orthopyroxene ratio. **Bus:** Separates based on strength of 0.9um drop, indicative of 1um band. **B-D:** Definition largely preserved from Bus. Now includes full 1um feature and 2 um feature in near-ir. Sl & Sk are removed, Sv is added.	**Minerals:** olivine,pyroxene **Meteorites:** S(I): Pallasites?, R chondrites, Brachinites, S(IV): many are ordinary chondrite-like, S(V): Primitive achondrites?, S(VII): Basaltic Achondrites
C-Complex	 B C F G		B C Cb Cg Cgh Ch	 B C Cb Cg Cgh Ch	**Tholen:** Primarily distinguished by the 0.3-0.5um UV dropoff region. Bus & B-D do not cover this region, thus do not make these distinctions **Bus:** Defined by UV dropoff and/ or by 0.7um Cgh, Ch feature. **B-D:** Definition largely preserved from Bus. Near-infrared is largely degenerate.	**Minerals:** opaques, carbon, phyllosilicates, some have weak features indicating olivine, pyroxene **Meteorites:** carbonaceous chondrites (except CV) , possibly impact melts from ordinary chondrites and HEDs?
X-Complex	E M P		X Xc Xe Xk	 X Xc Xe Xk	**Tholen:** EMP are spectrally degenerate. Distinguished by high (E), med (M) and low (P) albedo. **Bus:** X class defined by shape of curve and/or 0.49um Xe feature. **B-D:** Definition largely preserved from Bus. Near-infrared is largely degenerate.	**Minerals:** M,P: opaques, carbon, low-Fe pyroxene. E: enstatite, oldhamite **Meteorites:** M,P: carbonaceous chondrites (not CV). M w/high radar albedo: irons, CB condrites, Silicate rich irons. E: enstatites
Other: End Members, Outliers	 T D O R V A		T D Q O R V A K L	 T D Q O R V A K L	Definitions for each of these classes are relatively consistent among taxonomies as they are each spectrally distinct.	D opaques, organics Q mostly LL OCs O pyroxene, olivine R olivine, pyroxene V HEDs, pyroxene, plagioclase feldspar A pallasite, brachinite, R chondrites, olivine. K CO,CV. olivine L CAI-rich, spinel-rich

Figure 1.1: Chart from DeMeo et al. 2015 (Tab. 1) summarising the different asteroid taxonomy systems.

Another component of meteorites that have brought us a wealth of information are calcium-aluminium-rich inclusions (CAIs; MacPherson 2003). Their ages have been found through isotopic dating, estimated to be $\sim 4567.3 \pm 0.16$Ma – the oldest material measured and therefore taken to be the age of the Solar System (e.g., Amelin, Kaltenbach, et al. 2010; Amelin, Krot, et al. 2002; Connelly et al. 2012). Thus, CAIs are considered the first solids to have condensed from the protoplanetary disk during Solar System formation, and their range of textures are suggestive of some of them having been directly condensed from gas, and others

crystallised from a melt (e.g., Beckett et al. 2006).

As with asteroids, the studies of a variety of meteorites have led to their classification, following the system shown in Figure 1.2. The main defining factor of which broad class a meteorite falls into is the presence or absence of chondrules. Achondrite meteorites (including irons, stony-irons and stones) have no chondrules present, indicating their parent bodies had undergone a substantial amount of processing via melting and differentiation. Chondrite meteorites, however, display characteristics suggesting their parent bodies underwent a much lesser degree of processing, experiencing little to no modification via melting and/or differentiation. This means that some chondrites contain primordial material from the early stages of Solar System formation, making them particularly insightful for learning about the formation of the Solar System.

Within the chondrite classification (e.g., Figure 1.2), those described as 'carbonaceous' contain carbon compounds, such as amino acids, known to be an essential building block of life. Carbonaceous chondrites further classified as CM type are Mighei-like, indicating similarities to the Mighei meteorite: the type specimen for this classification. Within the chondrite classification, meteorites can also be ascribed a petrologic type describing the degree of aqueous or thermal alteration. Petrologic types of: 1/2⇒aqueous alteration, 3⇒unaltered, 4/5/6⇒thermal metamorphism, where 2 specifically indicates moderate aqueous alteration but with some primary/unaltered mineral phases still present (Weisberg et al. 2006). The Murchison meteorite is classed as a CM2, a sample of which was used in this work (see Section 4.2.2).

1.3 Returned Samples

No matter how quickly a meteorite is retrieved or how primitive it is (as indicated by its classification), all meteorites have undergone some processing simply by travelling through the Earth's atmosphere. Additionally, there is naturally some bias to what is possible to exist within the meteorite record, based on what properties are required

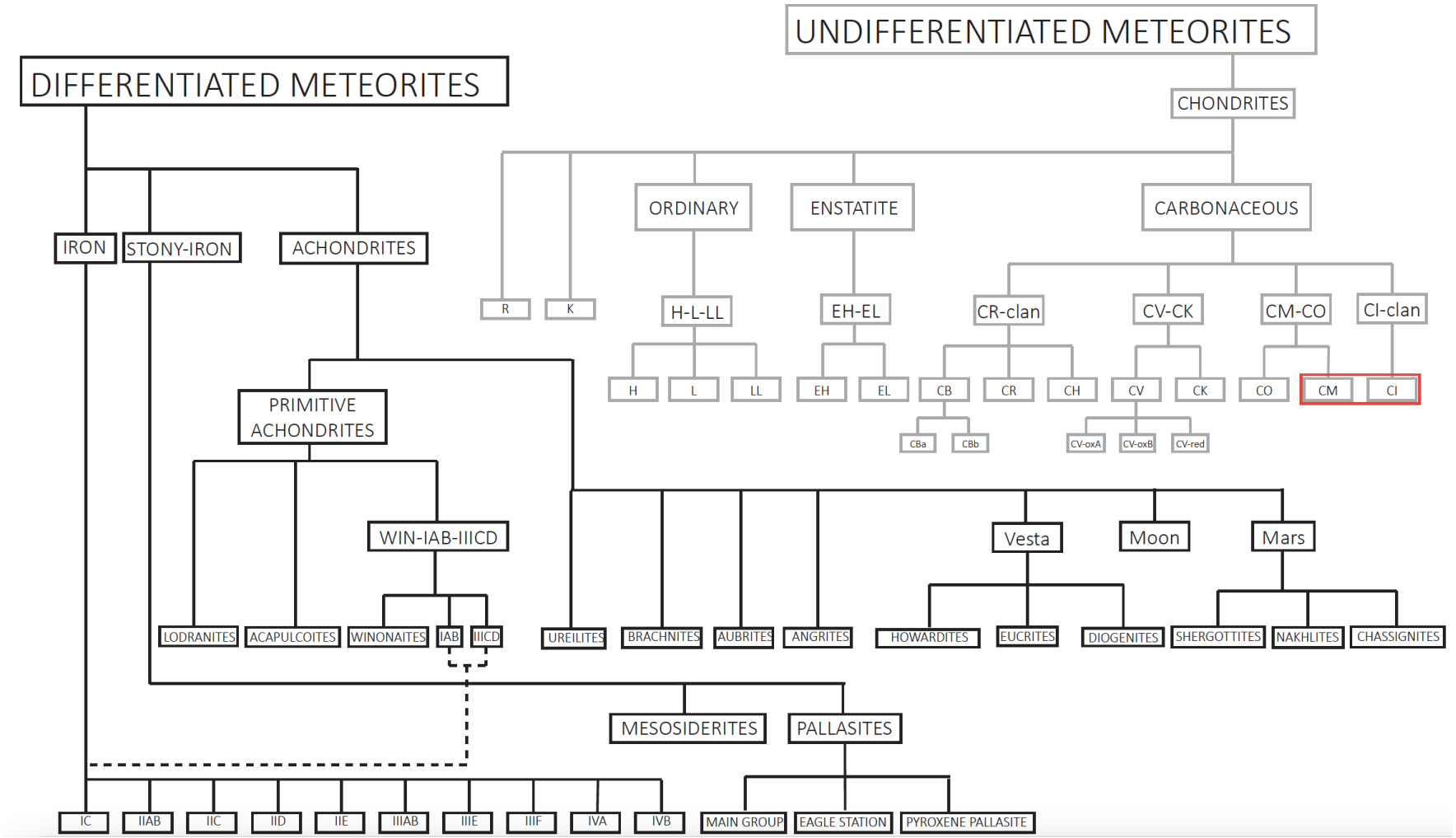


Figure 1.2: Current meteorite classification system taken from Bates 2020 (Fig. 1.4), which was adapted from Weisberg et al. 2006.

of the meteorite in order to actually survive entry through the atmosphere. So, although meteorites bring with them a huge wealth of information, some of which we could never have imagined, they cannot provide the full picture.

Returned samples, on the other hand, allow us to study samples that may never otherwise reach Earth, and do so in immense detail. Prior to the return of an asteroid sample, its parent body will have been studied extensively via telescopic and remote sensing observations, thus providing vital context to laboratory measurements. This therefore strengthens links between laboratory and remote sensing observations, such as which meteorite classifications originate from which asteroid complexes and/or asteroid families, thus providing a ground truth to telescopic and remote sensing observations.

JAXA's Hayabusa mission was the first to return an asteroid sample to Earth, bringing back approximately 100μg from the surface of near-Earth S-type asteroid (25143) Itokawa in June 2010 (Yoshikawa, Kawaguchi, et al. 2021). Ground-based telescopic observations of Itokawa suggested it may have similar composition to LL ordinary chondrites that had undergone thermal alteration (i.e., LL5-6), which was confirmed on analysis of the returned sample, thus verifying the connection between S-type asteroids and ordinary chondrites (Yoshikawa, Kawaguchi, et al. 2021). Much more recently, JAXA's Hayabusa2 mission returned 5.424 ± 0.217g of sample from C-type asteroid (162173) Ryugu in December 2020 (Yada et al. 2022). Preliminary analysis has shown the Ryugu samples to have a lower bulk density than is seen in meteorites which indicates greater microporosity. Additionally, spectral analysis suggests carbonaceous composition, having greatest resemblance to CI chondrites but with some key differences, such as the higher porosity (Yada et al. 2022).

1.4 Space Missions

Although returned samples are invaluable for the depth of knowledge they bring, often it is not feasible to collect a sample to bring back for analysis on Earth. Fortunately, it is still possible to learn about the compositions of planetary bodies

via remote sensing observations; where a spacecraft visits an object and takes measurements at a distance, often from orbit.

Remote sensing from specialised missions allow for a much greater depth of information to be discovered, whilst complementing observations made by ground- and space-based telescopes. The Near Earth Asteroid Rendezvous (*NEAR Shoemaker*) mission to S-type asteroid (433) Eros conducted the first orbit and landing of an asteroid, completing its mission in February 2001 (Cheng 2002). Results from the *NEAR* mission showed that Eros had a mineral composition closely resembling that of ordinary chondrite meteorites, with the exception of a depletion of certain elements (e.g., sulphur and iron) in Eros' surface compared to ordinary chondrites (Cheng 2002).

With many questions answered by *NEAR*, but even more arising from its results, this led to a variety of further space missions dedicated to asteroid science, including Hayabusa (Yoshikawa, Fujiwara, et al. 2006) and Hayabusa2 (Tachibana et al. 2014; Tsuda et al. 2013) as discussed in Section 1.3. OSIRIS-REx is another sample return mission; its sample capsule due to arrive on Earth in September 2023 (Lauretta, Balram-Knutson, et al. 2017). Prior to collecting the sample in October 2020, OSIRIS-REx conducted extensive and detailed surveys of B-type near-Earth asteroid (101955) Bennu to provide as much context as possible for the future laboratory measurements of the returned sample. During these phases of characterising Bennu, OSIRIS-REx spacecraft observations matched those from previous telescopic observations for global properties, such as shape, size, rotation and mass, however, unexpected results included albedo variation, surface roughness and boulder coverage (Lauretta, Enos, et al. 2021; Lauretta, DellaGiustina, et al. 2019).

Each successive space mission follows in the footsteps of those that came previously, and paves the way for exciting current and future missions. Some examples include:

- **DART and Hera** – NASA's Double Asteroid Redirection Test to conduct the kinetic impactor planetary defence technique. On impact in September 2022, DART successfully altered the orbit of asteroid Dimorphos, and measurements are to be followed up by ESA's Hera mission, which aims to launch in 2024 and complete a more comprehensive study of the (65803) Dimorphos-Didymos binary system (Rivkin and Cheng 2023).

- **Lucy** – beginning its 12-year mission on launch in October 2021, the NASA mission Lucy will be the first to conduct several flybys of the Jupiter Trojan asteroids, visiting at least one from each known asteroid taxonomic type/complex (Levison 2016).

- **MMX** – the JAXA Martian Moons eXploration mission, set for launch in 2024 to return samples from Phobos, Mars' largest moon, in 2029 (Kuramoto et al. 2018).

Space missions that conduct a variety of extensive remote sensing surveys of the objects they collect samples from are particularly valuable, as they are able to provide the greatest context to what is eventually measured in the laboratory. Missions with instruments that can take measurements similar to those from Earth-based laboratories (such as infrared spectroscopy) further allow for the strengthening of how remote sensing and laboratory observations may relate to each other, thus improving interpretations of observations of objects from which we do not have a sample. Of the missions mentioned, *NEAR shoemaker* carried a near-infrared spectrometer (NIS), Hayabusa and Hayabusa2 also had near-infrared spectrometers (NIRS and NIRS3, resepctively), whilst the OSIRIS-REx instrument suite included three separate spectrometers covering the visible and near-infrared (OVIRS), thermal infrared (OTES) and X-ray imaging (REXIS). Lucy also carries a thermal emission spectrometer (L'TES), and MMX plans include a near-infrared spectrometer (MIRS).

1.5 This Research

As discussed, knowing and understanding the surface compositions of asteroids is a key part in research across many aspects of planetary physics and astronomy; from constraining planetary dynamics and migration models (e.g., Morbidelli, Walsh, et al. 2015; Walsh, Morbidelli, et al. 2012), to finding the origin of water and organics on Earth (e.g., Morbidelli, Chambers, et al. 2000).

Remote sensing observations and laboratory measurements in the thermal infrared (TIR; $5 - 25\mu$m) are particularly valuable in finding asteroid compositions due to the rich diagnostic information in this region. Here, the vibrational bending and stretching modes between atoms within a crystal lattice cause characteristic absorption features in TIR spectra of relevant rock forming minerals. A way to interpret such spectra is with the linear mixing assumption, under which these spectral features from the individual minerals sum together linearly (weighted by their abundances) to form the spectrum of their mixture (Lyon 1964; Ramsey and Christensen 1998). The principle behind this is that at TIR wavelengths, a photon will only interact with one grain due to strong absorption in this region, and so will only carry information about that particular grain upon detection (Lyon 1964; Ramsey and Christensen 1998). However, this assumption begins to break down as the grain size of the material decreases and approaches the scale of the photon wavelength, leading to an increase in volume scattering.

Despite the known issues of this model for fine grains ($< 50\mu$m), linear mixing is still the model of choice most widely used in the community, due to its success for whole rock and coarse grained ($\geq 60\mu$m) samples (Ramsey and Christensen 1998). Similarly, the preferred spectral unmixing algorithm remains as a traditional linear least squares method, as it works well for situations with good background knowledge that can lead to implicit inclusion of *a priori*/contextual information, particularly within the spectral library. For example, if trying to retrieve mineralogy of a Martian lithology that previous measurements have shown to have a low albedo,

thus indicating a basaltic composition (e.g., Rogers and Aharonson 2008), then the spectral library could be tailored to include only basaltic mineral phases, such as plagioclase, pyroxene and olivine (e.g., Hamilton, Christensen, et al. 1997).

Therefore, the focus of my thesis is to investigate spectral unmixing algorithms, finding a way to improve on current Frequentist techniques (e.g., linear least squares) by adopting a Bayesian approach (e.g., optimal estimation, MCMC).

Frequentist techniques use statistical inference based on frequency of outcomes in an infinitely large sample, whereas Bayesian methods are based on probability distributions for parameters given *a priori* information (following Bayes' rule). A major difference between Frequentist and Bayesian inference is the use and integration of *a priori* information, some of which can relate to what is necessary for a physical solution (e.g., abundances must be non-negative and sum to one), and can be enforced as **bounds/constraints** in the algorithm. Other *a priori* information can come from previous research that specifies what we expect the results to be (e.g., based on the meteorite record, we may expect a mixture to have a specific mineralogy), and these can be set as **priors**. These priors are probabilistic in nature, with some probability density function (pdf) defined, and so cannot be set within Frequentist methods. On the other hand, they are intrinsic to Bayesian methods as the explicit quantification of priors is at the very core of Bayesian inference. (Further details on how I define 'priors', 'constraints', and other terms that may be ambiguous can be found in the Acronyms & Glossary before this chapter, pages vii-viii).

This thesis aims to provide a comprehensive evaluation of spectral unmixing algorithms, and to lay the foundations for alternative spectral interpretation methods that would be more widely applicable and flexible. Thus the main questions my work strived to answer were: "**what are the limits of using the linear mixing model with thermal infrared observations to determine asteroid composition; can these be improved by adopting a Bayesian approach; and, if not, what might a suitable alternative to linear mixing be?**" These questions led to two main objectives (also illustrated in Figure 1.3):

1. To constrain confidence in retrieved mineral abundances from a selection of unmixing algorithms (including Frequentist and Bayesian methods) using the linear mixing model, and

2. To begin work towards alternative spectral interpretation methods for asteroid composition estimates, based on the findings from Objective 1.

From my work presented within this thesis, I have shown that the limitations of the linear mixing model cannot be compensated for by using increasingly sophisticated algorithms (Chapters 5 and 6), and so, I have begun setting the path towards a more suitable model that may be used effectively in the spectral unmixing algorithms developed for Objective 1. Whilst other researchers gain insight through machine learning in its various forms, my work for Objective 2 aspires to find a hybrid solution that captures more detailed physics in the spectral mixing model, whilst retaining the computational ease (and thus accessibility and reproducibility) of more traditional methods. My starting point for this has been investigating quantitative changes in spectral morphology with decreasing grain size (Chapter 7), as the different scattering regime for fine grains is what causes the invalidation of linear mixing for such applications.

To provide the required background knowledge on the topics within this thesis, Chapter 2 covers the theory behind spectroscopy and the linear mixing model; and Chapter 3 outlines the relevant analytical and computational techniques used in my project. Chapter 4 provides details on the data used and algorithms developed, leading into Chapters 5 and 6 presenting the main results and discussions for Objective 1. The work for Objective 2 is detailed in Chapter 7, and an overall summary and conclusions, along with potential future research that may build on this thesis, are presented in Chapter 8.

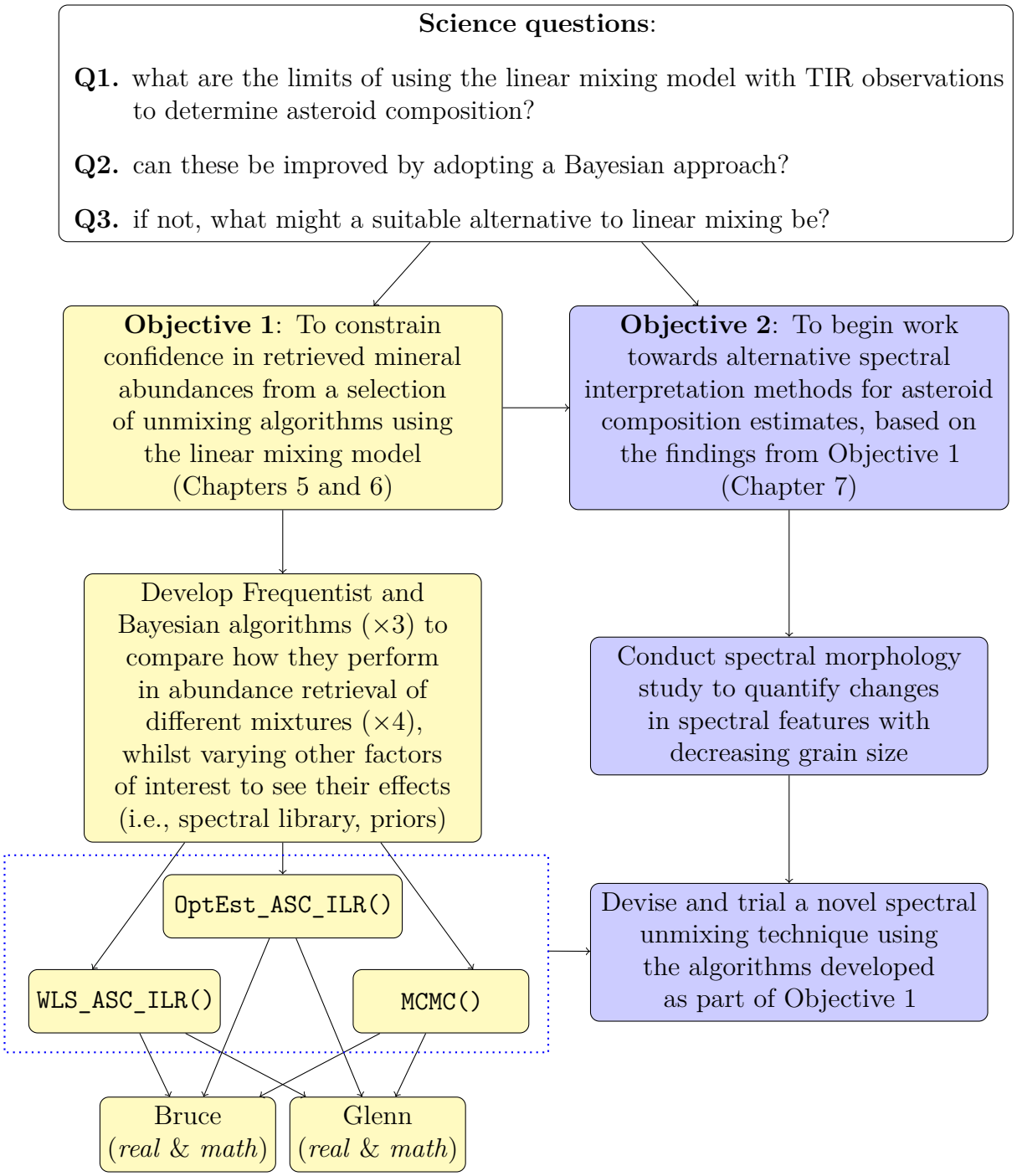


Figure 1.3: Flowchart illustrating the skeleton of my project rooting from my main science questions and objectives. The main bulk of my thesis work is for Objective 1 (highlighted in yellow), with much of this leading into the work for Objective 2 (highlighted in blue).

Chapter 2

Theory: Spectroscopy and Linear Mixing

Contents

2.1 Infrared Spectroscopy 15
2.2 The Linear Spectral Mixing Model 21
2.2.1 Setting Up the Mathematics of Linear Mixing 22
2.2.2 Scattering 23
2.2.3 Potential Degeneracy 25

Spectroscopy is the study of light-matter interaction, encapsulating how matter absorbs, emits and reflects electromagnetic radiation. Spectroscopic experimental techniques are often non-destructive, making spectroscopy a valuable tool that allows other measurements to be made on the same sample – this is particularly important for rare samples such as meteorites or those returned from asteroids. Spectroscopy focusing on different regions of the electromagnetic spectrum can provide insights into the nature of matter at different scales and energies; for example gamma ray spectroscopy is used to characterise gamma emitters from a source, which is particularly useful in nuclear physics and astrophysics, whereas infrared spectroscopy tells us about the molecular scale, allowing for identification of various properties such as chemical composition.

2.1 Infrared Spectroscopy

Spectroscopy in the infrared (IR; $\sim$ 700nm $-$ 1mm) observes and interprets the changes in energy as a result of different types of relative movements between the atoms of a molecule, known as vibrational bending and stretching modes. These modes occur at different frequencies, governed by the mass of the atoms and strength of the bond between them, only absorbing radiation at quantised resonant frequencies that match those of the atomic movements (more details of the relevant quantum mechanics may be found in e.g., Eisberg and Resnick 1985). The different relative vibrations of atoms can be categorised into bending modes, in which the vibrations involve a change in bond angle (deformation, rocking, wagging and twisting) and stretching modes, where there is a change in bond length (symmetric and asymmetric), as illustrated in Figure 2.1 and summarised in Stuart 2004. There are other types of molecular vibrational modes, such as rotational, however these often do not give rise to observable IR absorptions due to a lack of change in electric dipole moment during the motion – this is known as the selection rule; and is also the reason why symmetric stretching modes often lead to weaker features than asymmetric modes (which tend to cause larger changes in dipole moment and thus lead to more intense absorption bands; e.g., Stuart 2004).

An infrared spectrum is essentially a measurement of changes in energy across the wavelength range of the IR region as a result of atomic vibrations within molecules (illustrated in Figure 2.1); and one way to obtain this is through Fourier Transform Infrared (FTIR) spectroscopy. This works by measuring the interference between radiation from two beams in the form of an interferogram, where the distance and frequency domains can be converted into each other through a Fourier transformation (Stuart 2004). FTIR is often conducted using a Michelson interferometer, consisting of a stationary and a moving mirror, each positioned within the perpendicular paths traversed by the two beams output from the beam splitter (shown in Figure 2.2). The moving mirror causes the distance travelled by one beam to be different from the other, giving rise to a path difference between the two that can lead to

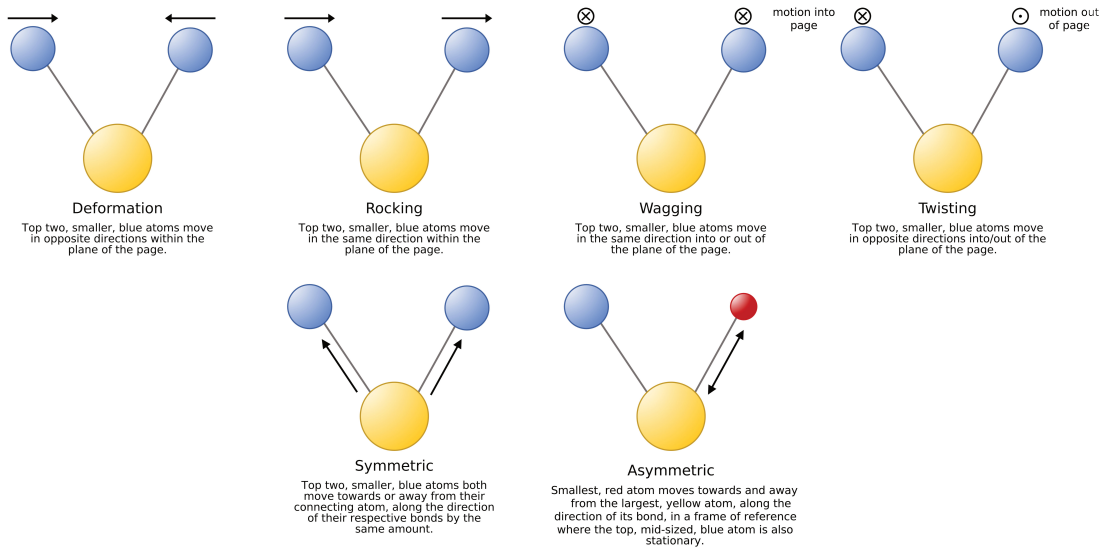


Figure 2.1: Diagrams of molecular bending modes (deformation, rocking, wagging, twisting) and stretching modes (symmetric, asymmetric); all are in a frame of reference where the large yellow atom on the bottom is stationary. These molecular vibrations are usually part of a much larger crystal lattice.

constructive or destructive interference when they reflect from the mirrors and later recombine back at the beam splitter. The interferogram recorded at the detector is a measure of light intensity of the recombined beam vs path difference, varying between constructive and destructive interference. The sample being measured absorbs/reflects particular wavelengths based on its structure and composition, and these absorptions modulate the detected interferogram, later translating as spectral features upon Fourier transformation. Calibrating the measurements from the sample to some standard measured under the same conditions (e.g., gold) produces a reflectance spectrum representative of the sample, ready for interpretation.

The underlying chemical compositions, molecular geometries and bonds in different minerals not only result in their characteristic properties (e.g., colour, hardness, shape), but also lead to their unique spectra. As resonant frequencies (and therefore wavelength positions of spectral features) are dependent on atom mass and bond strength, this means they are also dependent on chemical and structural composition, and so can be used in the identification of materials. Even within the infrared region, subsections of this (i.e., far infrared, mid/thermal infrared and

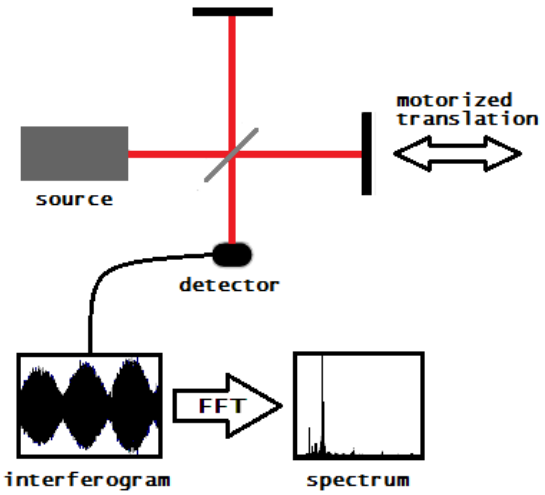


Figure 2.2: Schematic of a Fourier Transform spectrometer (Image credit: Stigmatella aurantiaca at English Wikipedia, CC BY-SA 3.0 <https://creativecommons.org/licenses/by-sa/3.0>, via Wikimedia Commons).

visible/near infrared) bring to light slightly different information about the material in question. The section of the electromagnetic spectrum considered in this thesis is the thermal infrared (TIR; $5 - 25\mu$m, where the fundamental vibrational modes occur) as many rock forming minerals relevant to extraterrestrial materials (e.g., silicates) have distinct features within this region (e.g., Figure 2.3), making it rich in diagnostic information for compositional analysis.

Some of these distinct, characteristic features are caused by the same underlying physics and so are observed across many different minerals, with their own unique variations (such as exact feature position) depending on their underlying chemistry, making these particularly useful in mineral identification. The main features/regions of note in the TIR are the Christiansen Feature(s), Reststrahlen Bands, and the Transparency Feature(s):

Christiansen Feature(s): The Christiansen Feature (CF) is an emissivity maximum (reflectance minimum) occurring at the wavelength where the real part of the refractive index, $n = 1$ (i.e., equal to that of the surrounding medium: air, or vacuum if in space), and the imaginary part, k, is at a minimum (Bishop et al. 2019; Mustard and Hays 1997). An emissivity maximum occurs

here because having the real part of the refractive index of the material, n, equalling that of the surrounding medium means that radiation is able to pass freely through the material without reflection or scattering at grain boundaries; and from Kirchhoff's law relating emissivity, E, and reflectivity, R, as $E = 1 - R$, a lack of reflection manifests as a trough in reflectivity and therefore a peak in emissivity. The CF may also be considered as the emissivity maxima resulting from the transition from volume to surface light-particle scattering, which may occur at a slightly different wavelength compared to where $n = 1$ and k is small (Mustard and Hays 1997). The exact positioning of the CF is indicative of silicate composition, with mafic compositions (magnesium and iron rich silicates; e.g., olivine, pyroxene) giving rise to CFs towards lower wavenumbers (longer wavelengths), shifting to higher wavenumbers (shorter wavelengths) as compositions become more felsic (silicates rich in lighter elements such as silicon and oxygen; e.g., Bishop et al. 2019). For example, the TIR spectrum of olivine, such as the one shown in Figure 2.3, displays a 'principal CF' at $\sim 1100\text{cm}^{-1}$ (9.0μm), and a 'secondary CF' at $\sim 700\text{cm}^{-1}$ (14μm), but these positions are different for different minerals. Spectral morphology in the TIR is known to be sensitive to differences in e.g., surface roughness, sample packing/porosity and grain size, but the positions of the features remain largely unchanged; so, with the principal CF being easy to locate for many minerals, this makes the CF a particularly useful indicator of composition (Mustard and Hays 1997). A more in depth discussion of CF morphology changes with grain size can be found in Chapter 7.

Reststrahlen Bands: The Reststrahlen Bands (RB) are emissivity minima (reflectance maxima) in strongly absorbing regions where k is large (>0.1) – this prevents most of the energy from propagating through grain boundaries, thus leading to surface scattering, i.e., specular reflection, displayed as peaks in reflectance and troughs in emissivity (e.g., Bishop et al. 2019;

Mustard and Hays 1997). Features in the RB arise from molecular vibrational modes (as shown in Figure 2.1), which for silicates usually occur between $1250 - 400\text{cm}^{-1}$ ($8 - 25\mu\text{m}$). Here, features due to stretching modes (particularly asymmetric stretching of the oxygen atom in SiO) occur between $1176 - 833\text{cm}^{-1}$ ($8.5 - 12\mu\text{m}$), and those arising from bending modes appear between $600 - 400\text{cm}^{-1}$ ($16.6 - 25\mu\text{m}$; Salisbury et al. 1987). Specific molecular configurations lead to additional features at corresponding frequencies; for example, a broad feature at 1630cm^{-1} ($6.1\mu\text{m}$) is indicative of H_2O bending vibrations of hydrogen bonded water molecules (Salisbury et al. 1987). Surface scattering from strong absorption in the RB becomes dominated by volume scattering as grain size decreases and grains become optically thin. Although many features remain unchanged (particularly their positions), the transition in dominant scattering regime from surface to volumetric can cause significant changes in spectral morphology, i.e., overall spectral contrast (band depth/intensity), appearance of some features, and may result in new features (e.g., Transparency Features; see below). Effects of porosity and sample packing bring further complexities to interpreting the RB – compared to a whole rock sample, fine particulates naturally have increased porosity, leading to 'photon traps' in the space between grains. These photon traps allow photons to travel further into the sample, whilst also increasing the difficulty for their escape, thus resulting in increased emissivity. However, even for a fine grained sample, the porosity can be reduced by preparing the sample in such a way to increase packing – this can be done by pressing down the surface, for example, which effectively lightly compacts the sample. A more densely packed fine grained sample has a reduced porosity, leading to fewer photon traps and thus preventing deep penetration of photons into the sample. Consequently, this leads to increased surface scattering, and the spectrum appearing more as it would for a whole rock/coarse particulate sample (Salisbury et al. 1987).

Transparency Feature(s): The Transparency Feature (TF) is an emissivity minimum (reflectance maximum) located between Reststrahlen Bands (e.g., $\sim 850 - 600\text{cm}^{-1}$ for silicates), occurring in samples for which the mean grain diameter is of the order of the mean optical path length; i.e., when grain size approaches the wavelength of interacting light, thus acting as a signature of the presence of fine grains, in the TIR. Here, k is small and the absorption coefficient is low enough for the grains to be optically thin allowing a greater proportion of photons to pass through more than one grain and undergo volume scattering (Bishop et al. 2019; Salisbury et al. 1987). The TF occurring typically $\sim 800\text{cm}^{-1}$ is not present for all minerals, with its prominence being partly down to the degree in which the adjacent RB diminish with decreasing grain size. However, the distinctive nature of the TF in the minerals that do display it, and its consistent position for different grain sizes makes the TF an additional indicator of composition, particularly at the finest size fractions (Salisbury et al. 1987). Transparency also presents as a steep decline in emissivity from the principal CF towards higher frequencies (Bishop et al. 2019), which becomes increasingly steep as grain size reduces. This is referred to as the 'CF roll-off' within this thesis, and is discussed further in Chapter 7. The presence of transparency signatures in spectra therefore not only aids with mineralogy estimates, but may also provide an initial indication to the grain size fractions that may dominate a sample, which could possibly serve as useful *a priori* information, albeit relatively vague.

Each of the above spectral features are annotated in Figure 2.3. Exact positions of any CFs and TFs present can be key indicators of composition, as can additional features in the RB corresponding to particular molecular vibrational modes. Spectra are results of a complex interplay between factors such as optical constants (including refractive index and absorption coefficient), grain size, and sample packing; making it particularly challenging to interpret spectra of particulate mixtures containing a variety of mineral species, such as those from asteroid regolith.

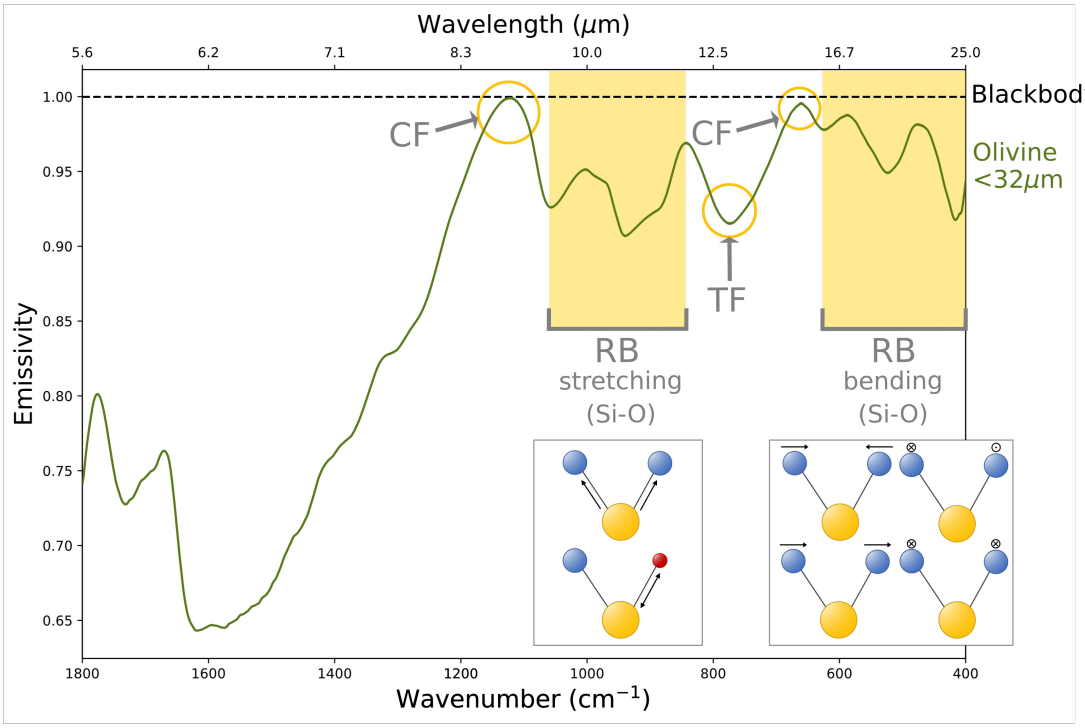


Figure 2.3: Fine grained ($< 32\mu$m) olivine spectrum from Shirley and Glotch 2019 with key features labelled: CF=Christiansen Feature, TF=Transparency Feature, RB=Reststrahlen Bands. The CF and TF are results of scattering, and the RB of molecular vibrational modes, which are also indicated for the relevant regions.

2.2 The Linear Spectral Mixing Model

With a spectrum obtained and in need of interpretation, one approach is to consider how the overall spectrum of a mixture of constituent minerals (e.g., meteorites, asteroid regolith etc.) relates to the spectra of its individual components. Many physical phenomena may be simplified into mathematical expressions – i.e., models – to describe the physics at play; and in the case of light scattering in the TIR, the linear mixing model is most commonly used.

Linear mixing is based on the assumption that spectral features from individual minerals sum together linearly (weighted by their abundances) to form the spectrum of their mixture (e.g., Lyon 1964; Ramsey and Christensen 1998; see also Section 2.2.1). This is currently the underlying model most widely used due to its physical accuracy in many applications (e.g., whole rock and coarse particulate samples),

and its mathematical simplicity owing to a basis on a relatively straightforward set of assumptions. Linear mixing works for such situations involving coarse particulate or whole rock samples as the fundamental assumption made about light scattering from grains holds true, however these scattering assumptions become invalid as grain size decreases leading to a change in scattering regime from predominantly surface scattering to volume scattering (see Section 2.2.2).

The straightforward approach of linear mixing lends itself well to linear least squares and similar algorithms to solve the inverse problem of 'unmixing' a spectrum to retrieve its composition (i.e., which minerals are present, and in what abundances). For this to work effectively, it is assumed that the individual components (known as end-members) have unique spectra that can only combine in one way to form the spectrum of their mixture. Whilst technically it is true that end-member spectra are unique (due to differing chemical compositions leading to differences in exact spectral morphology), many display sufficient similarities such that there could be more than one reasonable solution – this introduces potential degeneracy to the problem, which is often not accounted for nor acknowledged in literature, and is discussed further in Section 2.2.3.

2.2.1 Setting Up the Mathematics of Linear Mixing

As previously mentioned, the linear mixing model states that spectra of independent mineral components (a.k.a., end-members) may be considered to sum together linearly in proportion to their abundances to produce the the overall spectrum of their mixture – this can be translated into a mathematical expression, following Ramsey and Christensen 1998 (Equation 2.1):

$$y(\lambda) = x_1 k(\lambda)_1 + x_2 k(\lambda)_2 + x_3 k(\lambda)_3 + ... + x_n k(\lambda)_n, \tag{2.1}$$

where $y(\lambda)$ is the modelled emissivity spectrum of the mixture and is a function of wavelength, λ; x_1, x_2, x_3 and x_n are the abundances of the first, second, third and n^{th} end-members, respectively; $k(\lambda)_1$, $k(\lambda)_2$, $k(\lambda)_3$ and $k(\lambda)_n$ are the emissivity spectra of the first, second, third and n^{th} end-members, respectively; and n is

the number of end-members. This can be further simplified into summation form (Equation 2.2), and translated into matrix form (Equation 2.3):

$$\vec{y} = \sum_{i=1}^{n} x_i \vec{k_i}, \tag{2.2}$$

$$[y]_{(\nu,1)} = [k]_{(\nu,n)}.[x]_{(n,1)}, \tag{2.3}$$

where ν is the number of wavenumber channels (i.e., number of data points in the spectrum). Having the linear mixing model in matrix form allows the end-member abundances, $[x]$, to be estimated for a spectrum of unknown composition, $[y]$, given a set of end-member spectra as a spectral library, $[k]$, via inverse methods (e.g., Section 4.3).

2.2.2 Scattering

Equations 2.1 to 2.3 above are based on the principle that, at TIR wavelengths, a photon will only interact with one grain due to the strong absorption in this region, and will therefore only carry information about that particular grain upon detection, with the total energy measured being a function of the abundance of each grain type/end-member (e.g., Lyon 1964; Ramsey and Christensen 1998). Generally, the combined effect of minerals having high absorption coefficients but small optical path lengths in the TIR (compared to the visible/near-IR) leads to the photon-matter interaction in this spectral region to be dominated by surface scattering/specular reflection. This effect is seen in whole rock and coarse particulate samples, where a photon is either detected following a single-grain interaction or is absorbed, thus making the linear mixing model valid and effective in these scenarios.

However, the single grain interaction assumption begins to break down as grain size decreases and approaches the scale of the photon wavelength, leading to an increase in volume scattering where a photon may experience multi-grain interactions before being detected. If a photon interacts with more than one grain (thus gaining information about each of them within a single photon), the total energy detected can no longer be considered as coming from a photon per grain, and can therefore

no longer be represented as a linear sum of contributions from each grain. This transition in scattering regime as a result of changing grain size is illustrated in Figure 2.4. A conclusion from Ramsey and Christensen 1998 was that linear mixing may be used effectively for modal mineralogy estimates down to grain sizes of $\sim 60\mu$m, but that this threshold decreases to $10-20\mu$m when appropriately sized end-member samples (also $10-20\mu$m) are used in the spectral library.

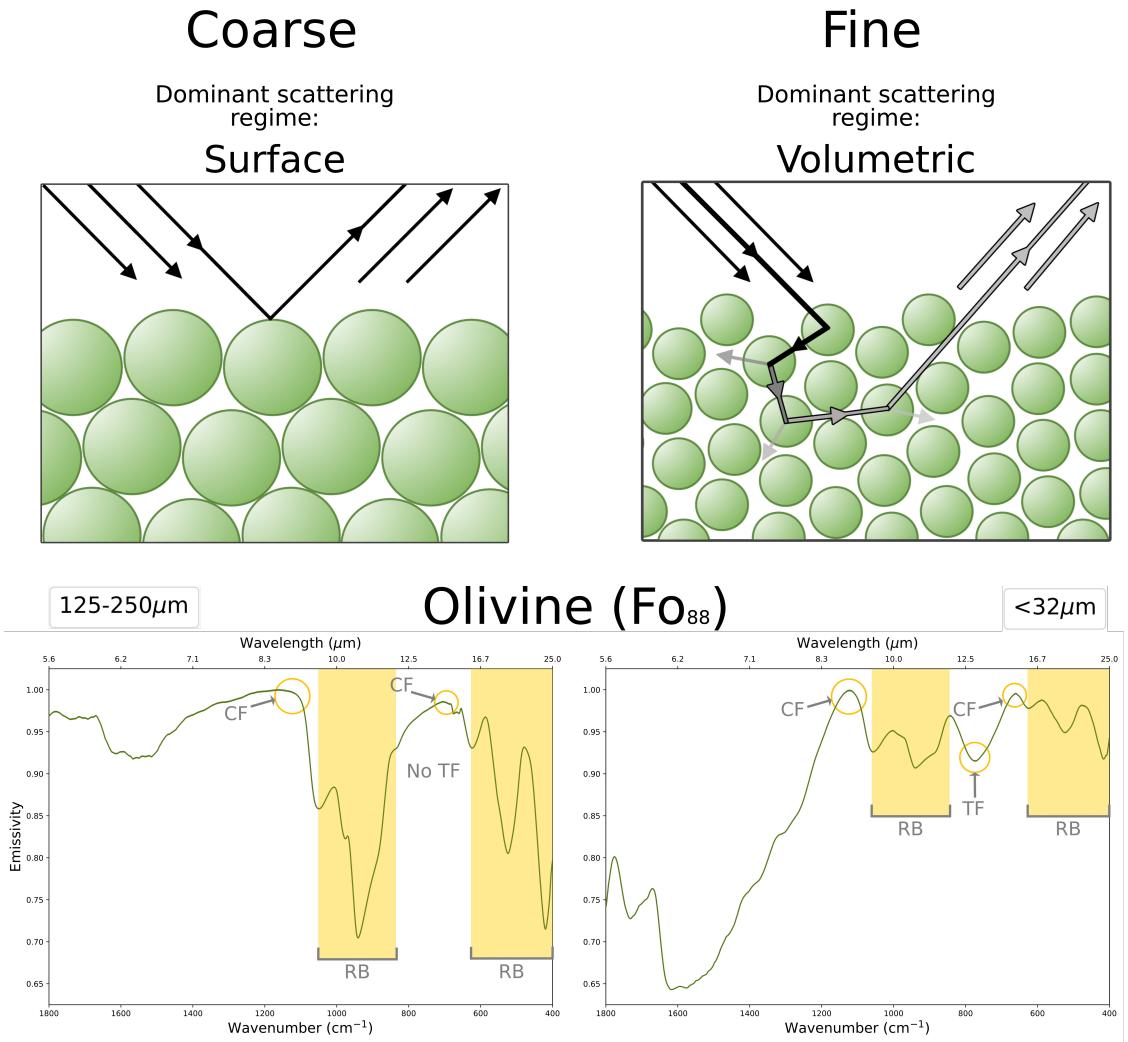


Figure 2.4: Schematic showing the difference between olivine spectra when surface scattering dominates for large grains, and volumetric scattering dominates for fine grains, with the gradual lightening of the arrows from black to grey in the volumetric scattering diagram representing the loss of energy with each interaction, also illustrated by the translucent arrows ending in the spaces between grains. The coarse ($125-250\mu$m) and fine grained ($< 32\mu$m) olivine spectra were from Shirley and Glotch 2019 with key features labelled: CF=Christiansen Feature, TF=Transparency Feature, RB=Reststrahlen Bands.

2.2.3 Potential Degeneracy

Issues surrounding use of the linear mixing model when there is a substantial presence of fine grains is widely known; with active research aiming to further understand the behaviour of light-matter interaction in such cases (e.g., Shirley and Glotch 2019). However, an important caveat lesser discussed is the potential degree of degeneracy intrinsic to a simple model – linear mixing – which works under the assumption that the end-members are spectrally independent. Although it is true that each end-member spectrum is unique, there may still be a large number of possible combinations of these spectra and their abundances that could produce very similar mixture spectra; especially when a large spectral library is involved. This therefore leads to the degenerate nature of the linear spectral mixing problem.

This degeneracy comes from the fact that different end-members can occur at varying points of the same solid solution series; for example, albite and anorthite are at opposite ends of the plagioclase series which has the general formula (Na,Ca)[(Si,Al)$AlSi_2$]O_8, where albite is the sodium-rich end-member ($NaAlSi_3O_8$), and anorthite the calcium-rich end-member ($CaAl_2Si_2O_8$). Similarly, the olivine series follows the general chemical formula X_2SiO_4; where forsterite is Mg_2SiO_4, fayalite is Fe_2SiO_4, and the solid solution series has varying contributions from Mg and Fe (or different elements) in between. Minerals falling within the same solid solution series will therefore naturally have similar compositions, and hence share common spectral features. This is illustrated in Hamilton 2010 which showed how spectra change with varying composition between forsterite (Mg-rich) and fayalite (Fe-rich) – the opposite ends of the olivine series (Figure 2.5; Fig. 9 of Hamilton 2010). When comparing forsterite (top spectrum) and fayalite (bottom spectrum) within Figure 2.5, the differences between them may seem clear. However, if these two were incorporated in a spectral library with a variety of other mineral species, their differences could become somewhat more challenging to distinguish within the context of the entire spectral library. This challenge could be further amplified

if, for example, intermediate spectra from Figure 2.5 were included in the spectral library, rather than using the opposite ends of the solid solution series.

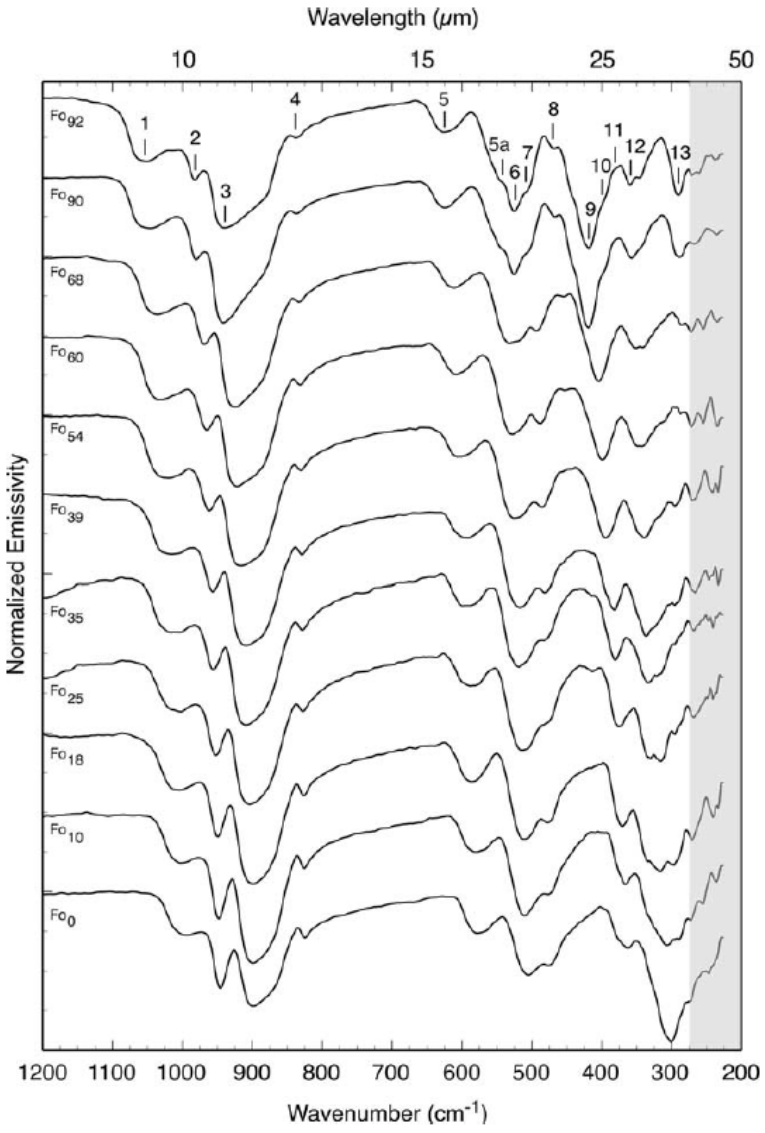


Figure 2.5: Hamilton 2010 Fig. 9 - Emissivity spectra of 11 coarse grained ($> 125\mu$m) natural Mg-Fe series olivines.

One way of investigating the variation within a dataset (in this case how similar the end-member spectra are) is with principal component analysis (PCA), as discussed further in Section 3.3.1. With such analytical tools providing further insight, the question arises whether it is possible for a more sophisticated algorithm to get around the known limits of the linear mixing model; and could this issue of degeneracy be addressed with a quantitative treatment of prior information?

Chapter 3

Theory: Computational Techniques for Spectral Unmixing

Contents

3.1 Review of Current Spectral Unmixing Algorithms . . 28
3.1.1 The Linear Least Squares 28
3.1.2 The Non-Negative Linear Least Squares 30
3.1.3 The Partial Least Squares 31
3.1.4 Continued Challenges 33
3.2 Frequentist vs Bayesian Inference 34
3.3 Non-Algorithmic Methods to Enhance Analysis 38
3.3.1 Principal Component Analysis (PCA) 38
3.3.2 Covariance and Correlation Matrices 42
3.3.3 Retrieval Quality Metrics 43

With a model in place to describe the physics of light scattering in relation to composition (i.e., linear mixing; see Section 2.2), this model can then be used with a variety of numerical and analytical techniques to solve for parameters of interest. The continuing and rapid advancement of computing technology has naturally led to a vast array of computational techniques that may be used to solve a wide variety of problems; from somewhat crude brute force trial and error type calculations, to highly advanced machine learning methods. A number of different algorithms have been applied to the spectral mixing problem with varying levels of success, all with significant pros as well as their substantial cons.

3.1 Review of Current Spectral Unmixing Algorithms

3.1.1 The Linear Least Squares

In Hamilton, Christensen, et al. 1997, a linear least squares deconvolution algorithm was used on laboratory thermal infrared emission spectra of four Martian meteorite samples (ALH77005, Nakhla, Zagami and EET79001) to determine their mineralogies and lithologies. Here they were able to estimate the modal mineralogies to within $2-19\%$ for ALH77005, Nakhla and Zagami; whilst, although correct end-members were identified from those available for Zagami and EET79001, their modelled spectra mismatched their measured spectra, and was attributed to the lack of a key end-member in the library (pigeonite), and/or shock effects present in the meteorites.

Later, Ramsey and Christensen 1998 published their work on "quantitative deconvolution of thermal emission spectra" to estimate mineral abundances; focusing more on the validity of the linear mixing model and the algorithmic side of the spectral mixing problem. In this work, they studied various aspects, including the effects of noise addition, reproducibility of laboratory measurements, changes in grain size of the samples, and complexity of mixtures (i.e., how many minerals they were composed of).

From this they found that the addition of noise to spectra can lead to an additional deviation of 2.4%, but the variability from spectrometer reproducibility was greater than this, with an average uncertainty of 4%. One of their most influential conclusions was that the linear mixing model is valid (i.e., abundances predicted to within 5% on average with residual errors $< 0.1\%$ total emissivity) down to $\sim 60\mu$m when the library end-members are in the $250-500\mu$m size fraction, but that their spectral deconvolution algorithm failed when the grain size of the mixture fell below $\sim 60\mu$m. However, when the spectral library contained end-members also sized $< 60\mu$m, linear mixing remained valid, and the algorithm

effective, down to the $10 - 20\mu$m size fraction. In addition to this, they also demonstrated that their spectral deconvolution algorithm was effective in mineral detection for mixtures containing 15 end-members, which is much greater than is likely to be found in natural geology.

Based on this success, the algorithm presented in Ramsey and Christensen 1998 would go on to become the most widely used for mineralogical analysis of thermal infrared spectra, serving as what may be considered the 'default' algorithm choice.

Building on this foundation, Feely and Christensen 1999 investigated the application of the linear least squares deconvolution algorithm for TIR spectra of igneous and metamorphic rocks, to quantitatively find the mineralogy of these samples; and showed that this algorithm and linear mixing model within were applicable to laboratory samples, and in situ field analysis. To reach this conclusion, Feely and Christensen 1999 unmixed their igneous and metamorphic samples against a diverse spectral library containing 36 common rock-forming and accessory minerals.

By comparing their results to abundances derived via petrographic techniques, they found that the unmixed abundances from TIR spectra agreed with the petrographic estimates to within $\pm 7 - 17\%$, depending on mineral species. Overall, the the determinations of rock type, main mineralogy and reproduction of spectral features were more accurate for the igneous rock samples compared to the metamorphic samples; and additional work into streamlining the spectral library based on initial rock type estimates improved the unmixings by only a few percent.

These successes placed great confidence in the linear mixing model with linear least squares algorithm, indicating that a simple model (compared to those of e.g., a full radiative transfer 'forward model') and simple algorithm may be used to effectively estimate composition for large grain sizes ($> 60\mu$m).

3.1.2 The Non-Negative Linear Least Squares

Although Ramsey and Christensen 1998 provided a significant contribution towards developing a way to determine mineral abundances, it was shown in Rogers and Aharonson 2008 that the algorithm employed in Ramsey and Christensen 1998 may incorrectly discard a correct end-member, thus ultimately giving an incorrect solution. This error occurs as a result of implementing the non-negativity constraint – a negative abundance is not physically meaningful, and so is regarded as indicating a lack of presence of that mineral within the mixture. To incorporate this in the algorithm, Ramsey and Christensen 1998 adopted **iterative library reduction** (ILR), where an end-member with a negative abundance would be removed from the spectral library, and the linear least squares calculated again with the reduced spectral library. The algorithm would then iterate until all abundances were positive, giving the final solution. A significant disadvantage of this is that an end-member actually present in the unknown mixture may be prematurely removed.

To combat this, Rogers and Aharonson 2008 used the more specialised, non-negative least squares (NNLS) approach to find mineralogy of sands in Meridiani Planum (on Mars) from data collected by the Mars Exploration Rover Opportunity Miniature Thermal Emission Spectrometer (Mini-TES). In this work, they used a modified non-negative (MNN) least squares algorithm, and compared it to the original ILR technique of Ramsey and Christensen 1998. They found MNN to be more reliable than ILR, and although both algorithms could retrieve an incorrect end-member, it was likely to be in low enough abundance to be below the detection limit and so may be dismissed. Rogers and Aharonson 2008 also confirmed that in the case of a spectral library containing a large number of end-member spectra compared to the number of spectral channels (i.e., data points forming a spectrum), it was more likely that the ILR algorithm would prematurely discard a correct end-member. For example, the Mini-TES instrument has 167 channels, whereas THEMIS (the Thermal Emission Imaging System on the Mars Odyssey spacecraft; Christensen, Jakosky, et al. 2004) only has 10; so a large spectral library of e.g.,

30 end-members used to unmix THEMIS data would be more likely to incorrectly remove an end-member in comparison to Mini-TES.

3.1.3 The Partial Least Squares

With the disadvantages of the Ramsey and Christensen 1998 type of algorithm becoming increasingly evident, efforts to build upon this basic linear least squares with ILR algorithm were explored. One of the new algorithms tried was a standard regression method: partial least squares (PLS) – a technique where, in the application to spectral unmixing, the spectral bands have eigenvectors that are used in such a way to allow their corresponding scores (the latent variables) to display a strong correlation with the mineral abundances (the response variables), as well as be able to explain the variance between the spectral channels (the independent variables; e.g., Li et al. 2012).

Pan et al. 2015 studied the TIR spectral properties of fine-grained mineral mixtures to asses the linearity of the mixtures using NNLS (non-negative least squares) and PLS (partial least squares). In this work, they found that NNLS performed poorly compared to PLS, attributing this to the fine particulates; thus implying that PLS may be more appropriate to use for modal mineralogy estimates.

As PLS is purely linear and had not been tested with non-linear applications, Li et al. 2012 investigated the hybridisation of PLS with neural network models for the application to lunar mineralogy. In this they compared the standard PLS and GA-PLS (genetic algorithm - partial least squares) algorithms with their developed PLS-BPNN (partial least squares - back propagation neural network) for use with visible-near IR reflectance spectra of the lunar surface:

- The genetic algorithm - partial least squares (GA-PLS) uses a simplified PLS model for the minimisation within a GA (genetic algorithm); using the principal of natural selection in evolution to, in this case, select the spectral channels most sensitive to compositional differences. To train the GA-PLS, user-defined criteria (such as a fit within ±5% of measurements) helped

determine the selected subset of spectral channels by the end of the process, which were then used as inputs to the PLS, along with the known abundances corresponding to each reflectance spectrum within the training set. From this, the trained GA-PLS algorithm only used the determined subset of spectral channels found by the GA to unmix new spectra with PLS (e.g., Li et al. 2012).

- With the partial least squares - back propagation neural network (PLS-BPNN), here the BPNN (back propagation neural network) algorithm is based on the human brain, by learning and storing knowledge through idealised node layers; which allowed redundant spectral bands to still be included, but with a lower 'weight'. The appropriate weights for the nodes were determined via the training process, after which BPNN could interpret new spectra, with input parameters coming from the PLS-derived latent variables (Li et al. 2012).

The conclusions reached were that PLS-BPNN performed the best, based on providing better estimations of the dominant minerals on the lunar surface, that it could surpass the limitations of PLS and GA-PLS (such as the treatment of redundant spectral bands and inability to account for non-linear mixing, as is relevant for fine particulates), and that PLS-BPNN could even accommodate for the change in spectral morphology caused by variations in grain size.

From these conclusions in may seem that PLS-BPNN would be the ideal algorithm as it overcomes the limitations of many others, however, this does not mean that it is without downfalls of its own. As PLS-BPNN is a machine learning technique, this means that a training set is required, and so the most accurate results are achieved when measurements are most similar to this training set, thus losing reliability for measurements that deviate from the training set (Li et al. 2012). This reliance on an appropriate training set spanning a wide range of e.g., mineral species and grain sizes for each of these, in order to obtain reliable and accurate results remains a major limitation of the machine learning approach.

3.1.4 Continued Challenges

Although a range of techniques have been explored, there is still much work to do in order to develop a reliable and robust spectral unmixing algorithm. Whilst current methods, including those discussed in Sections 3.1.1 to 3.1.3, work well for applications with good prior knowledge, such as research targeted at understanding thermal emission data from Mars (e.g., Hamilton, Christensen, et al. 1997), they are less applicable to datasets for which there is not a high level of detailed knowledge, such as individual asteroids, comets etc., that may have limited measurements available. As we explore more and more Solar System objects previously unreachable to us, the need for improved statistical analysis grows.

Additionally, a particular issue intrinsic to the spectral mixing problem is the effect of grain size on spectral morphology (as mentioned in Section 2.2.2). So far, the focus of spectral unmixing algorithms has mostly been their application to coarse particulate and whole rock samples where the linear mixing model holds and works well; and studies including fine size fractions often highlight the difficulties in retrieving reliable results (e.g., Hamilton, Christensen, et al. 1997; Li et al. 2012; Pan et al. 2015; Ramsey and Christensen 1998). However, finer grain sizes ($< 60\mu$m) appear to dominate planetary surfaces (Mustard and Hays 1997), making it vital to find a way to reliably estimate composition of fine particulate material.

The current combination of such a simple model within such a simple algorithm (despite the known issues) creates an opportunity to explore other model-algorithm combinations that have not already been tried, particularly with a focus on applications to fine particulate samples. Advancements in computing power and efficiency since Ramsey and Christensen 1998 introduce the idea that a more sophisticated and statistically complete algorithm could overcome the hurdle of using linear mixing for fine grains; as has been the case so far with NNLS improving on linear least squares, PLS improving on NNLS, and PLS-BPNN improving on PLS (however each of these progressions has still had substantial drawbacks). Going back to the roots of how to construct an effective algorithm (different from NNLS,

PLS, PLS-BPNN etc.) with full treatment of statistics is a good starting point when striving to improve on current techniques, and begins with considering the fundamentals of statistical inference.

3.2 Frequentist vs Bayesian Inference

Statistical inference is a key component to any and all scientific research, and using different viewpoints and techniques can lead to differing conclusions. The two major types are Frequentist and Bayesian inference, where their key difference is in their interpretation and handling of parameters in relation to observations.

Frequentist: Statistical inference based on frequency of outcomes in a large sample – data vary and parameters are fixed. Priors (i.e., probabilistic quantification of believed solution based on previous research) cannot be set, but it is possible to apply bounds/constraints to the parameter space of the solution with some techniques (e.g., the answer must lie between 0 and 1)[1].

Bayesian: Statistical inference based on probability distributions for parameters given *a priori* information, following Bayes' rule (Equation 3.1) – data are fixed and parameters vary. Priors are a requirement for all Bayesian methods and so must be set[1].

In Frequentist inference, the particular data collected at any moment in time are just one of the infinite number of possible outcomes from exact repeats of the same experiment. In this framework, events giving rise to those particular data occur with some probability, defined by the frequency of which data within some range of those exact data would be collected from an infinite set of repeat experiments. The key viewpoint here is that this probability is fixed with a defined distribution from which the data are randomly sampled; therefore the data vary and the parameters are fixed (Lambert 2018). Many classical methods (e.g., linear least squares, Levenberg-Marquardt etc.) are rooted in Frequentist inference, and work

[1]See Acronyms & Glossary preceding Chapter 1 for more detailed definitions of terms used throughout this thesis, such as 'prior' and 'bound/constraint' that may be ambiguous.

towards maximising the likelihood of obtaining the observed data. In the linear least squares (such as that used in Ramsey and Christensen 1998), maximising the likelihood is mathematically equivalent to minimising the residual of the sum of the squares; i.e., minimise $\sum_i (y_i - f_i)^2$ for each y_i data point of the measurement, where f_i is the corresponding modelled data point. This is done by differentiating the function to be minimised, setting to zero, and then solving for the parameters of interest (e.g., mineral abundances).

In Bayesian inference, the probability ascribed to a particular outcome is a quantification of the pre-held belief that this outcome will occur. In this sense, probabilities are used to indicate our level of certainty/uncertainty in whether the outcome will happen. This means that the unavoidable subjective nature of statistical inference is acknowledged and represented. Here, the data are fixed and the parameters vary in a way that they may be continually updated based on pre-known (i.e., *a priori*) information, such as observations and conclusions from previous experiments (Lambert 2018). This *a priori* knowledge is incorporated into Bayes' rule (Equation 3.1, illustrated in Figure 3.1), which requires its explicit statement and allows it to be updated when new information comes to light.

$$p(\theta|data) = \frac{p(data|\theta) \times p(\theta)}{p(data)}, \tag{3.1}$$

where θ is the set of parameters to be estimated, $p(\theta|data)$ is the **posterior** probability distribution (i.e., the probability of the retrieved parameters being correct, given the data), $p(data|\theta)$ is the **likelihood** (i.e., probability of obtaining the data measured given this set of parameters), $p(\theta)$ is the **prior**, and $p(data)$ is the **denominator** (i.e., a normalising factor to satisfy conditions of a valid probability density).

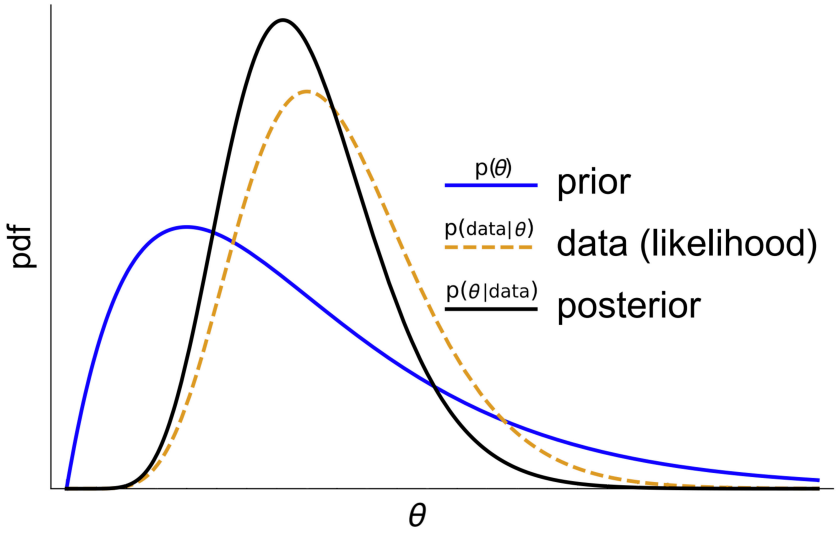


Figure 3.1: Schematic illustrating Bayes' rule (Equation 3.1), taken from Lambert 2019 (see also Lambert 2018).

Bayes' Rule serves as the foundations to many machine learning techniques, however, within the fundamental Bayesian framework, priors are often user-defined probabilistic quantifications of what the parameter solution may be. For example, if an asteroid has been classed as a C-type, we may turn to the meteorite record to set known mineralogy of relevant meteorite classes (e.g, CM, CI etc.[2]) as the priors for the asteroid mineralogy; thus naturally requiring more input and specialist knowledge from the analyst. Machine learning goes a step further by requiring a variety of datasets (e.g., many meteorite spectra and their known mineralogies) in order to train a model that can estimate mineralogy of an uncharacterised spectrum (e.g., an asteroid), often with minimal to no input from the analyst.

Some examples of methods within the fundamental Bayesian framework include optimal estimation and Markov Chain Monte Carlo (MCMC). Optimal estimation (e.g., Rodgers 2000) may be considered as a bridge between Frequentist and Bayesian techniques, as its form follows very closely to that of linear least squares, yet still incorporates *a priori* information (see Equation 4.4 in Section 4.3.2.2); indeed, in the absence of priors, the linear optimal estimation expression simply collapses to

[2]More details on relevant meteorite classifications may be found in e.g., Bates 2020.

the linear least squares form. MCMC is a fully Bayesian technique that samples from probability density functions (which are a core part of Bayesian inference not present in Frequentism), and give solutions in the form of probability density functions which are more versatile to interpretation and can provide insights not available with a singular numeric solution. Further details of optimal estimation and MCMC are covered in Chapter 4.

A fundamental difference between Frequentist and Bayesian inference is the use and integration of *a priori* information, some of which can be regarding what is necessary for a physical solution (e.g., for this application, abundances must be non-negative and sum to one), and can be enforced as **bounds/constraints** in the algorithm (which may be included in some Frequentist techniques). Other *a priori* information can come from previous research that specifies what we expect the results to be (e.g., based on the meteorite record, we may expect a mixture to have a specific mineralogy), and these can be set as **priors**. These priors are probabilistic in nature, with some probability density function defined, and so cannot be set within Frequentist methods. Priors are intrinsic to Bayesian methods as their explicit quantification is at the very core of Bayesian inference. For more detailed definitions of terms like **bounds**, **constraints** and **priors**, and how they are different, please see Acronyms & Glossary preceding Chapter 1.

Frequentist techniques are often chosen based on the belief that they are completely objective, however, it can be argued that *all* statistical inference is tinged with some degree of subjectivity. For example, in the Ramsey and Christensen 1998 algorithm (and similar), the choice of end-members used in the spectral library is inherently subjective, even for a vast spectral library, as it is unfeasible to include every single TIR spectral dataset; therefore the spectral library is often curated to the context of the mixture or target of observations (e.g., interpretation of Mars remote sensing data takes the context of local topography as *a priori* information). A benefit of many Frequentist techniques is that they are not computationally expensive and can be very quick to obtain a solution. However, the lack of quantitative

treatment of *a priori* information can leave many gaps in the analysis and as such, conclusions may be more poorly constrained. The requirement to explicitly and quantitatively include *a priori* information in Bayesian inference brings transparency to the subjectivity, which is vital when estimating composition of small solar system bodies for which we may not have obvious context.

Current methods (e.g., spectral unmixing following the Ramsey and Christensen 1998 method) are riddled with implicit *a priori* information due to the use of Frequentist inference, making it somewhat challenging to make fair comparisons between Frequentist and Bayesian algorithms. To address this, I used a variety of other statistical techniques which allow for more complete cross-comparison of the algorithms themselves.

3.3 Non-Algorithmic Methods to Enhance Analysis

Additional to the main algorithms that were used to retrieve estimates of parameters of interest, complementary techniques independent from the algorithms were key to providing greater context and meaning to the retrieved solution. Such additional techniques are described in Sections 3.3.1 to 3.3.3 below.

3.3.1 Principal Component Analysis (PCA)

The linear mixing model works under the assumption that the end-members are spectrally independent (i.e., each spectrum is totally unique), and so can be thought of as being orthogonal. A way of looking into whether this mathematically is the case is through principal component analysis (PCA), which investigates the degree of variation within a dataset (and is often used for dimensionality reduction and in machine learning).

Using singular value decomposition, PCA works by looking at the averages of the samples in each 'dimension'. Here, the dimensions are the wavenumber channels that the emissivity measurements are taken over (i.e., the x-coordinate of

a spectrum), and so the number of dimensions corresponds to spectral resolution. The raw data is then shifted to place the projected average from each dimension in the data space to be at the origin. From here, a straight line of best fit through the origin is found by maximising the sum of the squared distances between the origin and the projected data points on this line. The best fit line found is known as 'principal component 1' (PC1), and its equation is scaled to have a unit vector (the eigenvector). This process is repeated for principal component 2 (PC2), and so on, where all principal components are perpendicular to each other, and the total number of principal components in this application is the number of end-members within the spectral library. A PCA plot (usually PC1 vs PC2) can then be made by using the projected points on PC1 and PC2 to plot the samples in PC1 vs PC2 space (where PC1 is on the x-axis and PC2 on the y-axis). How well the entire dataset is represented by the first two principal components is described by the sum of their explained variance ratios, where this sums to 100% for all principal components, so this value is important to keep in mind when interpreting the PCA plot. The steps taken by PCA are illustrated in Figure 3.2.

Similarities between samples (e.g., end-member spectra) are indicated by clustering in the PCA plot, so by performing PCA on the various versions of the spectral library used in this study (*minimal*, *expanded*, *extensive* - see Section 4.1), any clustering apparent in the PC1 vs PC2 plots can provide valuable insight to the similarities between end-members, and thus the validity of the assumption that the end-members are independent, as required by linear mixing.

At its core, PCA is a method that explores the degree of variation within a dataset. By doing PCA on the spectral library, this tells us of spectral similarities between end-members, thus illustrating the degeneracy of the spectral unmixing problem. This can therefore highlight the consequential impact of spectral library selection, which is often overlooked in the literature. The choice of end-members within the spectral library has a major impact on this degeneracy, so performing PCA on the spectral library can help highlight this before doing the unmixing/retrieval, making

it a useful tool that is independent to the algorithm used. Incorporating PCA into the overall assessment of different algorithms also allows us to see the influence the inclusion of priors may have when adopting a Bayesian approach as opposed to a Frequentist one. This leads to the question: can a quantitative treatment of *a priori* information reduce the degeneracy? Thus working towards **Q2** from Figure 1.3.

Similarly to PCA, factor analysis and target transformation techniques together extract variability from a dataset into independently variable components (e.g., Bandfield et al. 2000). This has been used to recover independent end-member spectra of e.g., atmospheric dust, water ice cloud, basaltic sand, outcrops etc. from a selection of measurements of a region e.g. on Mars (Bandfield et al. 2000; Glotch and Bandfield 2006). Based on this research, it may be possible to take the use of PCA further by unmixing against a library of the principal components accounting for e.g., 90% of the variation amongst the end-members. However, it is important to note that the eigenvectors/principal components are not representative of the true spectral end-members (Bandfield et al. 2000), and are not directly comparable to them due to their complex combinations to derive the principal components. Therefore it is unclear whether it is possible to then extract compositional information from the retrieved 'abundances' of the principal components, or how useful this information would be if it is possible (i.e., if, for example, retrieved principal component (PC) 'abundances' were PC1=0.5, PC2=0.2, PC3=0.3, where PC1, PC2 and PC3 account for 90% of the variability, we may not be able to go from this to modal mineralogy as the only information available is the relative influence of each spectral end-member on each PC which is not directly quantifiable into spectral end-member abundances). Thus, this is beyond the scope of my thesis but could be an interesting avenue to explore in future research (see Chapter 8).

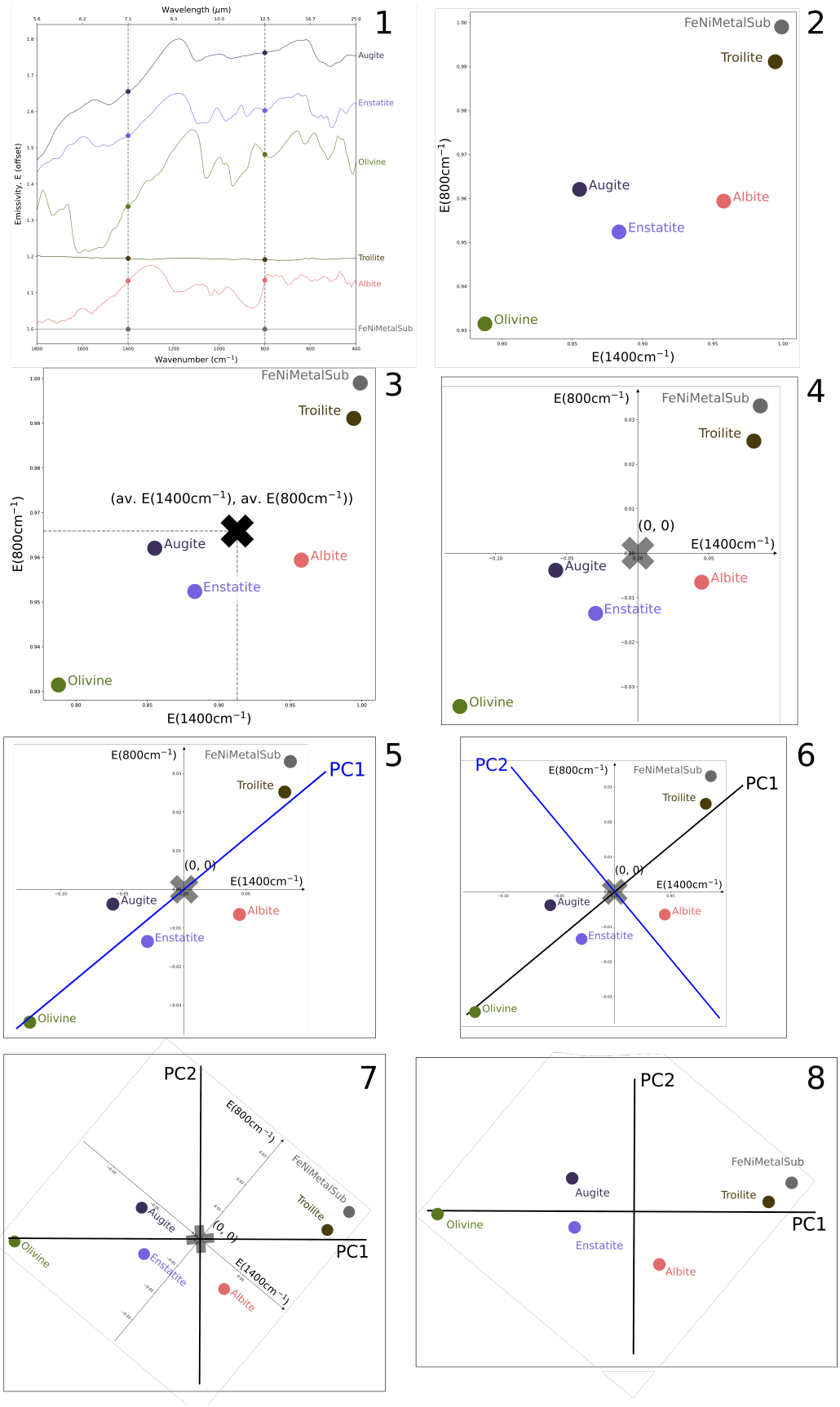


Figure 3.2: Schematic showing the process of PCA, illustrated as steps 1 to 8. For ease of visualisation, in this example only two dimensions are considered: wavenumbers 1400 and 800cm^{-1}.

3.3.2 Covariance and Correlation Matrices

Whilst PCA provides a visual, albeit somewhat abstract, way to examine variance within the spectral library (before unmixing), this can be followed up with consideration of the error covariance matrix (after unmixing) which quantifies how retrieved parameters may vary based on each other. As the diagonal of a covariance matrix is simply the covariance of a parameter with itself (i.e., the variance), it is also possible to find the uncertainty on each retrieved parameter by taking the square root of their variance; making the covariance matrix a valuable part of analysis. The covariance matrix may be found as part of the matrix inversion involved in finding the solution, or with inbuilt python functions such as `numpy.cov()`; details on how the covariance matrix is found for each algorithm is covered in Chapter 4.

Within a covariance matrix, if the parameters are truly independent then the off-diagonal elements should be very small. However, it is not necessarily clear what constitutes a 'small' or 'large' covariance, so it is perhaps more intuitive to consider a correlation matrix, which has a clear scale between 0 and ±1. Here, 0 indicates no correlation, and ±1 indicates the strongest possible correlation, thus the diagonal elements of a correlation matrix should all be 1 since this is the correlation of a parameter with itself. Conversion of a covariance matrix into a correlation matrix is done via Equation 3.2:

$$[S_x^{\text{corr.}}]_{i,j} = \frac{[S_x]_{i,j}}{\sqrt{[S_x]_{i,i}} \times \sqrt{[S_x]_{j,j}}}, \tag{3.2}$$

where $[S_x^{\text{corr.}}]_{i,j}$ is the $(i,j)th$ element in the correlation matrix, and $[S_x]_{i,j}$, $[S_x]_{i,i}$ and $[S_x]_{j,j}$ are the $(i,j)th$, $(i,i)th$ and $(j,j)th$ elements in the error covariance matrix of the retrieved parameters, respectively.

Thus, within the correlation matrix, the off-diagonal elements should be zero in the case of truly independent parameters, with any non-zero values indicating some degree of correlation, and therefore a dependence of parameters on each other to retrieve the final solution. A high degree of strong correlation would suggest

that the key underlying assumption of independence between end-members for the linear mixing model does not hold, therefore invalidating linear mixing. For the results presented from Chapter 5 onwards, I flag values $> |0.6|$ as being notably 'strong' correlations, with the choice of 0.6 being somewhat arbitrary and loosely based on conventions for rounding off numbers.

Upon completion of unmixing/retrieval, correlation matrices and corner plots[3] (where applicable) are complementary to the spectral library PCA in that they provide information on the correlation and dependencies of end-members with each other. This means they can be considered together in overall analysis to provide useful context to the validity of assumptions in linear mixing that is currently missing in literature.

3.3.3 Retrieval Quality Metrics

In order to draw useful comparisons between algorithms, it is useful to calculate quantitative metrics that describe the quality of the retrieval, which may be considered in two different ways: goodness of fit and, in the context of this work, goodness of abundance.

Goodness of fit is widely used to assess the quality of a model by quantifying how closely the modelled version matches what is observed; which in this case considers how similar the modelled spectrum using retrieved abundances in the linear mixing model is to the laboratory measured spectrum. Fit quality is often represented by the root mean square (RMS) error, found via Equation 3.3. The RMS is a singular value that essentially summarises the residuals (i.e., the modelled spectrum subtracted from the measured spectrum) across the entire wavelength range, where the smaller the RMS the better the fit. However, it is not always clear if a value is small enough to indicate a 'good' fit for that particular application, so, following the convention of Ramsey and Christensen 1998, RMS values of the

[3]Corner plots are a way of displaying both singular and joint probability density functions (pdfs) for parameters of interest, and are particularly useful for MCMC techniques (e.g., see Section 4.3.2.3).

order 10^{-3} are considered to indicate that the measured spectrum is well-captured by the modelled spectrum (i.e., a good fit).

$$\text{RMS} = \sqrt{\frac{\sum_{i=1}^{\nu} (y(\lambda)_i - y_{\text{model}}(\lambda)_i)^2}{\nu}}, \tag{3.3}$$

where $y(\lambda)$ is the measured mixture spectrum, $y_{\text{model}}(\lambda)$ is the modelled emissivity spectrum, and ν is the number of wavenumber channels.

Another goodness of fit metric is the reduced chi squared/chi squared per degrees of freedom, $\chi^2_{d.o.f}$, which is also a way of summarising the residuals into a singular numeric value, but takes into account other factors such as the degrees of freedom (discussed further in Section 4.1) etc., via Equation 3.4. The $\chi^2_{d.o.f}$ has a target value of 1 to indicate a perfect fit, where values < 1 are overconstrained, and those > 1 represent a poor fit of the model to the measurements. The additional nuance captured in the $\chi^2_{d.o.f}$ (compared to the RMS error) comes with the caveat that, because uncertainties are taken into account, if a modelled spectrum has a poor fit but large uncertainty envelope that overlaps with the measured spectrum, then this can give a deceptively good $\chi^2_{d.o.f}$ (i.e., a value close to 1).

$$\chi^2_{d.o.f} = \frac{(y - kx)^T S_y^{-1} (y - kx)}{\nu - 1 - n}, \tag{3.4}$$

where y is the measured mixture spectrum, k is the spectral library, x is the solution (i.e., end-member abundances; see Chapter 4), S_y is the measurement error covariance matrix, ν is the number of wavenumber channels, n is the number of end-members, and $\nu - 1 - n$ is the number of degrees of freedom

Having both an RMS error and $\chi^2_{d.o.f}$ can give a more complete picture of how well the model actually resembles the data, with each of these having their own nuances. In order to account for and try to balance out these nuances, I derived an overall fit quality metric that incorporates both the RMS and $\chi^2_{d.o.f}$ into a single value via Equation 3.5:

$$\text{Fit Quality} = (1 - \chi^2_{d.o.f}) \times \text{RMS}. \tag{3.5}$$

For this, the closer to zero, the better the fit, based on 1 being the ideal $\chi^2_{d.o.f}$ value and that RMS should be as small as possible. A negative value is therefore indicative of a poor fit, and a positive value represents a good but overconstrained fit.

It is common in published literature using the Ramsey and Christensen 1998 type algorithm to conclude that a good fit, represented by an appropriately small RMS error ($\leq 10^{-3}$), implies a broadly correct solution. Fit quality metrics are useful when there is only one possible solution, however these do not take into account potential degeneracies within a system; where degeneracy means that a 'good' fit can be separate from the 'correct' solution. In linear least squares, only one solution with the 'best' fit (i.e., lowest RMS) is chosen, but there could be other solutions with similarly good fits and low RMS values that are not considered: for example, with linear mixing it is possible that the configuration of end-members and their abundances which is most accurate to the correct solution is different from the end-member and abundance configuration with the lowest RMS error, which would be selected as the single solution.

For the main thesis work of algorithm development, the true answer must be known, meaning it is then possible to evaluate the quality of the unmixing/retrieval by comparing the estimated abundances found by the algorithm with the true values. Such comparisons can be considered in terms of **precision** and **accuracy**, visualised in Figure 3.3. Here, precision is considered to be a measure of certainty in the estimated value, relative to the estimated value itself (Equation 3.6); i.e., it is the uncertainty expressed as a percentage (e.g., $0.4 \pm 0.2 \equiv 0.4 \pm 50\%$), where Equation 3.6 is simply multiplied by 100 to obtain the precision in percentage format.

$$\text{Precision} = \frac{\sigma(x)}{x}, \tag{3.6}$$

where x and $\sigma(x)$ are the retrieved abundance and its uncertainty, respectively. Accuracy is how many 'sigma', σ (i.e., quanta of uncertainty), away the estimated value is from the true value (Equation 3.7; e.g., $0.4 \pm 0.2(50\%)$ is within 1σ of 0.3).

$$\text{Accuracy} = \frac{x_{\text{true}} - x}{\sigma(x)}, \tag{3.7}$$

where x_{true} is the true abundance. In the results tables presented in Chapters 5 to 7, accuracy is quoted to a number of σ, where a positive value indicates an underestimation, and a negative value an overestimation.

It is important to account for both precision and accuracy when determining whether a retrieved value matches that of the true answer, as a value could appear very accurate (i.e., within 1σ), but this could be due to poor precision (e.g., $\pm 90\%$); likewise, a highly precise value could have very poor accuracy (Figure 3.3).

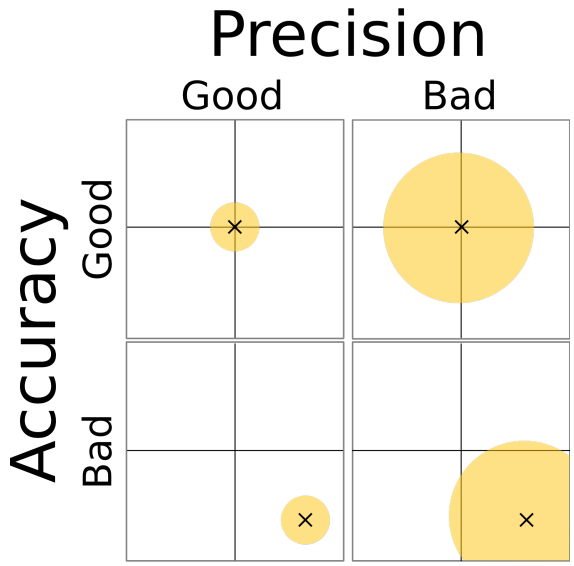


Figure 3.3: Basic schematic to illustrate the difference between accuracy and precision, where the shaded yellow region represents the uncertainty on the position of the X, and the centre of the crosshairs is the true solution/target value.

To take both precision and accuracy into consideration for determining the quality of retrieved abundances, I devised a 'goodness of abundance' metric (Equation 3.8):

$$\text{Abundance Quality} = \text{Precision} \times |\text{Accuracy}|, \tag{3.8}$$

where the precision value should be kept in decimal form, as calculated directly from Equation 3.6. Since fit quality is quantified with one value per unmixing, to complement this, a singular abundance quality value representative of each unmixing is found by using the mean of precisions across all end-members as the 'Precision' value in Equation 3.8, and the mean of the accuracy magnitudes (i.e., $|\sigma|$) across

all end-members as the '|Accuracy|' value in Equation 3.8. As with the fit quality metric (Equation 3.5), the smaller/closer to zero, the better the quality.

As with all analysis techniques, these newly derived retrieval quality metrics are not perfect as they cannot accommodate for all the possible nuances each individual unmixing may have, but it is useful to have a quantitative and consistent metric per unmixing to allow for easier and more efficient comparisons.

Chapter 4

Method: Data and Algorithms Used

Contents

4.1 Spectral Library 49
4.2 Mixtures for Unmixing 52
4.2.1 Bruce 54
4.2.2 Glenn 58
4.2.3 Qualitative Comparisons to Bennu 63
4.3 Exploration and Development of Spectral Unmixing Algorithms 64
4.3.1 Trialling Existing Python Packages for Spectral Unmixing 65
4.3.2 Developing Bespoke Spectral Unmixing Algorithms . . . 66
4.3.2.1 Algorithm 1: `WLS_ASC_ILR()` 67
4.3.2.2 Algorithm 2: `OptEst_ASC_ILR()` 68
4.3.2.3 Algorithm 3: `MCMC()` 69
4.3.3 Renormalising for Blackbody Abundance 75

The main objective of this thesis is to explore and evaluate spectral unmixing algorithms in order to build an improved alternative to the linear least squares approach currently most widely used. To do this, a core dataset was used to trial a variety of different algorithms, which are introduced and discussed within this chapter.

The majority of the laboratory data came from the OSIRIS-REx Blind Test Study of Donaldson Hanna et al. 2019, provided by co-supervisor Prof. Kerri Donaldson Hanna. The Blind Test data suite contained spectra of fine-grained ($< 38\mu$m) end-member minerals, selected based on being the most suitable analogues for mineral phases detected within carbonaceous chondrite meteorites of varying degrees of

aqueous alteration. These end-members were combined in the laboratory in a variety of different configurations (i.e., end-members and their abundances), to form physical simulant mixtures representing different petrologic types of carbonaceous chondrites[1]; displaying their complex compositions of minerals, organic matter, metals etc., and progressing from unaltered (type 3) to highly aqueously altered (type 1), and their spectra measured. In addition to these simulant mixtures, the Blind Test suite included spectral data for a selection of fine grained chondrite meteorite samples, also covering a range of the degree of aqueous alteration. The particular focus on carbonaceous chondrites was due to previous studies suggesting that the composition of OSIRIS-REx target asteroid, Bennu, could be most closely related to this classification of meteorite (e.g., Clark et al. 2011).

In order to preserve the blind nature of the study, each sample, whether an anhydrous/hydrated simulant mixture or meteorite, was given an obscure code name. The intention of the Blind Test Study was to have consistent measurements of individual components and their mixtures, ensuring well-characterised composition, thus making this the ideal dataset for use in spectral analysis developments. However, due to the blind nature of the study, sample preparation and spectroscopic measurements were carried out separately by different people. Misunderstandings/miscommunication between groups resulted in limited quantities of some of the samples, and consequently a few of the end-members did not have their individual measurements as part of the Blind Test suite. Therefore, it was necessary to compile substitute data from alternative sources for those missing. Details of the Blind Test and substitute end-members are outlined in Table 4.1, with further information covered in Section 4.1 below.

4.1 Spectral Library

A vital part of spectral unmixing methods is the choice of end-members for the spectral library to unmix against; which can be thought of as implicit *a priori*

[1]Carbonaceous chondrites and the petrologic scale are discussed briefly in Section 4.2.2, but further details of meteorite classification can be found in e.g., Bates 2020.

information whose influence is often not quantitaively discussed, particularly in linear least squares fitting. To demonstrate this issue, my work used three different versions of the spectral library:

- *minimal* – only end-members we knew or believed to be in the mixture,
- *expanded* – the *minimal* library plus randomly selected extra end-members from the *extensive* library (up to some maximum library size e.g., 10 end-members) to see how the number of degrees of freedom would effect the fit, and
- *extensive* – all end-members available (i.e., Table 4.1).

Note: The number of end-members, n, (i.e., the number of parameters to be found) in relation to the number of wavenumber channels (i.e., number of data points in each spectrum), ν, determined the number of degrees of freedom (used in this work as: $d.o.f = \nu - 1 - n$); and defined whether the system could be described as the critical case, over-, or under-determined. In this application, the critical case would be when $n = \nu$, over-determined when $n < \nu$, and under-determined when $n > \nu$. The linear least squares adopted by Ramsey and Christensen 1998 assumed the over-determined case as there were usually a few unknowns (i.e., end-member abundances), and hundreds of equations (i.e., instrument measurement channels). For the analyses presented in Chapters 5 and 6, the *minimal*, *expanded*, and *extensive* spectral libraries all contained much fewer end-members than there were number of wavenumber channels (i.e., $n < \nu$), so all were over-determined in this sense.

The motivation behind using these different versions of spectral library was to highlight the implicit *a priori* information contained within the spectral library. Differences across unmixings/retrievals against the *minimal*, *expanded* and *extensive* spectral libraries for the same mixture spectrum would illustrate that even the basic selection of end-members can influence the results. In scientific practice it is unavoidable to use some form of *a priori* information, whether this is conscious, subconscious, relatively informative or 'uninformative'/'diffuse'. Therefore it is

important to not only acknowledge this, but to also be explicit in how the *a priori* information is used and applied, incorporating the context it provides into the overall analysis. This conscious and explicit acknowledgment and use of priors is at the heart of Bayesian inference.

As well as the discussed implicit *a priori* information tied into the curation of the spectral library, if these library end-members were spectrally similar, this could lead to potential 'degeneracy' in the unmixing; whereby, theoretically, there could be several solutions (i.e., combinations of end-members and their abundances) that provide similarly 'good' fits (i.e., small residuals between measured and modelled spectra). In linear least squares, however, the degenerate nature of the problem is not taken into account as it returns only the single 'best' solution (as defined by the lowest residual error), regardless of feasibility based on physical or geological context. This degeneracy comes from the fact that different end-members can occur at varying points of the same solid solution series (e.g., albite and anorthite are at opposite ends of the plagioclase series), so will naturally have similar compositions and thus share common spectral features (as discussed in Section 2.2.3 and illustrated in Figure 2.5, originally from Hamilton 2010).

As described in Chapter 3, principal component analysis (PCA) is a useful tool, which was used to investigate the potential degeneracy within the spectral library due to spectral similarities across end-members – any clustering in the PCA plot would indicate similarity between the clustered end-members. In this work, PCA was done using Python library `scikit-learn` (Pedregosa et al. 2011), which has a number of tools for use in a variety of machine learning methods. PCA could provide context and explanation to the retrieved solutions that may otherwise be speculative or simply missing, and so the results and interpretation of PCA on the spectral libraries were included in the analysis, covered in Chapters 5 and 6.

The exploration of PCA was a valuable additional tool, independent from and complementary to my main work of developing and evaluating Frequentist and Bayesian unmixing algorithms to retrieve mineral abundances using the linear

mixing model. The majority of my work was in the development of these algorithms, as described in Section 4.3. In order to develop and investigate these algorithms, a set of 'mixtures' had to be 'unmixed', which are described in Section 4.2 below.

4.2 Mixtures for Unmixing

During the development stage for these algorithms it was important to first use a sample (i.e., 'mixture') that already had a well-characterised composition – knowing what the answers should be was a key part in testing and improving the algorithms. Therefore, I used the 'Bruce' mixture from the anhydrous group of the Blind Test suite (Donaldson Hanna et al. 2019), with composition outlined in Table 4.2. Of all the possible simulant mixtures from the Blind Test Study, Bruce was chosen as it was the sample with the most complete knowledge on its end-members (i.e., most of the spectra for each end-member actually used to create Bruce were available as part of the Blind Test suite).

However, as the Blind Test Study used fine grained samples and a major caveat with the linear mixing model is its breakdown as grain size decreases, it would have been hard to see whether the algorithm worked if the underlying model itself does not. So, to ensure my codes worked as expected during algorithm development, I unmixed an idealised case – a mathematical (i.e., theoretical) mixture. Here I define a 'mathematical' mixture as being the spectrum generated from user defined abundances of the *minimal* spectral library end-members using the linear mixing model. In contrast to this, I define 'real' (i.e., physical) mixtures as being the actual samples measured in the laboratory (such as meteorite samples or simulant mixtures, as in the Blind Test suite from Donaldson Hanna et al. 2019). By unmixing a mathematical mixture, I was able to better identify and solve any coding errors as they occurred during algorithm development, as well as highlight issues due to the unmixing algorithm rather than the model.

Incorporating mathematical versions of mixtures into the investigation had the added benefit of showcasing potential accuracies and deficiencies in the linear mixing

Table 4.1: Sample information on end-members used for the spectral unmixing algorithm investigation.

Mineral Grouping	End-member	Full Sample Name (and ID)	Measurement Mode (e.g., reflectance or emissivity)	Grain Size	Notes	Source of Data (and reference)
Pyroxene	Augite	Kakanui augite (NMNH 122142)	Emissivity (University of Oxford Planetary Spectroscopy Facility)	$< 38\mu$m	Ambient measurements at $\sim$ 1000mbar with chamber at 300K and sample heated from below to 353K	Blind Test suite (Donaldson Hanna et al. 2019)
	Enstatite	Johnstown orthopyroxene (USNM 6633, USNM 7418)		$< 38\mu$m; $38-105\mu$m		
Olivine	Olivine (forsterite)	San Carlos olivine (NMNH 170992)				
Calcite	Calcite	New Mexico calcite (NMNH 143299-18)		$< 38\mu$m		
Phyllosilicate	Saponite	Mono Lake saponite (NMNH 154326)				
	Cronstedtite	Unknown		$< 90\mu$m	Provided with Blind Test data	Kerri Donaldson Hanna
	Lizardite	Unknown	Emissivity (Moonbox)	$< 45\mu$m	Substitute for Morris County Lizardite (NMNH 47656) in Blind Test suite	Kerri Donaldson Hanna (private correspondence)
Spinel	Magnetite	Minas Gerais magnetite (NMNH 114111)	Emissivity (University of Oxford Planetary Spectroscopy Facility)	$< 38\mu$m	Ambient measurements at $\sim$ 1000mbar with chamber at 300K and sample heated from below to 353K	Blind Test suite (see reference above)
	Spinel	Unknown		$< 45\mu$m	Provided with Blind Test data	Kerri Donaldson Hanna
Pyrrhotite	Troilite	Mundrabilla troilite (USNM 5914)		$< 38\mu$m	Ambient measurements at $\sim$ 1000mbar with chamber at 300K and sample heated from below to 353K	Blind Test suite (see reference above)
	Pyrrhotite	Unknown		$< 90\mu$m	Provided with Blind Test data	Kerri Donaldson Hanna
Feldspar/ Plagioclase	Albite	Unknown	Emissivity (Moonbox)	$< 25\mu$m	Substitute for Amelia albite (NMNH CS390-26) in Blind Test suite	Kerri Donaldson Hanna (private correspondence)
	Anorthite	Miyake Jima anorthite	Emissivity (PASCALE)	Unknown		
Gypsum	Gypsum	Gypsum (HS333.3B Selenite NIC4aaa)	Biconical reflectance (RREF with Nicolet FTIR Spectrometer)	$75-250\mu$m	Reflectance measurements converted to emissivity with E=1-R	USGS (Kokaly et al. 2017)
Other	Amorphous Mg	Unknown	Emissivity (Moonbox)	Unknown	Used as the amorphous silicates end-member	Kerri Donaldson Hanna (private correspondence)
	Amorphous Fe	Unknown				
	Murchison IOM	Murchison IOM (OG-CMA-003_ BKR1OG003)	Reflectance (BD-VNIR + BCF-FTIR2)	$90-106\mu$m	Substitute for synthetic IOM in Blind Test suite. "High purity organic residue"	RELAB Spectral Database (Copyright 2014, Brown University, Providence, RI.; All Rights Reserved)
	FeNiMetalSub	N/A	Straight line at $E = 0.999$	N/A	Substitute for Fe, Ni-metal in Blind Test suite	N/A
Normalisation factor	BB		Straight line at $E = 1.0$		Renormalised out (Equation 4.6)	

model through comparison with their real counterparts, before any unmixing had taken place. This therefore provided an independent element of insight, leading to more robust conclusions.

As a further test, I also completed unmixings of 'Glenn' from the Blind Test suite, which was a fine grained sample of the Murchison meteorite, and thus a more complicated mixture than Bruce. For a full investigation, it would have been preferable to unmix more than these two samples and their mathematical versions, however, due to time constraints it was unfeasible to do so. Therefore, unmixing a relatively basic mixture (Bruce) and a more complex one (Glenn/Murchison) was deemed to be as representative as possible of the options from the Blind Test study.

Further details of the Bruce and Glenn samples are outlined in the following subsections.

4.2.1 Bruce

As previously mentioned, Bruce was a simulant mixture created to have anyhdrous composition in line with type 3 carbonaceous chondrites (outlined in Table 4.2; Donaldson Hanna et al. 2019). Bruce had the fewest number of constituent end-members, requiring only two substitutes to supplement the rest from the Blind Test suite, thus making it fairly straightforward to construct its mathematical counterpart. The unavailable end-members requiring substitutes were Amelia albite (NMNH C5390-26) and Fe powder (stock # 39813, Lot# JO2M27 from Alfa Aesar), as outlined in Table 4.2.

The spectrum for the Fe,Ni-metal end-member was likely to have been featureless, making an artificial blackbody (i.e., a continuum at constant emissivity across the spectral range), named as 'FeNiMetalSub', a reasonable substitute. For the albite end-member, a substitute was provided by supervisor Dr. Kerri Donaldson Hanna, who had conducted the original Blind Test study. Making substitutions had the potential to introduce an unavoidable source of discrepancy that would need to be taken into account when comparing the real and mathematical spectra.

The only major potentially incorrect end-member (forming 10% of the mixture) was albite, so I investigated whether the albite provided was a suitable substitute for the original Amelia albite sample used in the mixture. To do this I first obtained more details about the substitute albite: the sample came from the Arizona State University (ASU) spectral library (Christensen, Bandfield, et al. 2000) and was crushed and sieved to $< 25\mu$m, but the locality was unknown. The online ASU spectral library contains spectra for coarse samples of albite originating from Amelia County Virginia, Pala California, and Keystone South Dakota. Spectra of albite samples from Amelia County Virginia and South Dakota were also available from the USGS online library (Kokaly et al. 2017), so these were compared to the corresponding sample spectra from ASU, and the provided substitute albite spectrum. Additionally, these were also compared to the spectrum of the $0 - 74\mu$m size fraction NMNH C5390 Amelia albite sample (used in the Blind Test), presented as a figure in Salisbury et al. 1987. These comparisons demonstrated that the substitute albite was likely to have been Amelia albite after all, and so was appropriate to use (illustrated in Figure 4.1). This therefore indicated that any differences between the real and mathematical spectra were most likely due to inaccuracies of the linear mixing model (or other factors such as packing effects in the samples), and not incorrect/missing end-members.

The spectra for the real and mathematical Bruce mixtures (denoted respectively as '*brucereal*' and '*brucemath*' from here on) are shown together in Figure 4.2 along with the relevant end-member spectra to show likely origins of certain features. Figure 4.2 showed that the *brucereal* and *brucemath* spectra were largely similar, with perhaps the most noticeable difference being the spectral contrast. For full discussion and analysis of *brucereal* vs *brucemath* see Section 5.1.1.

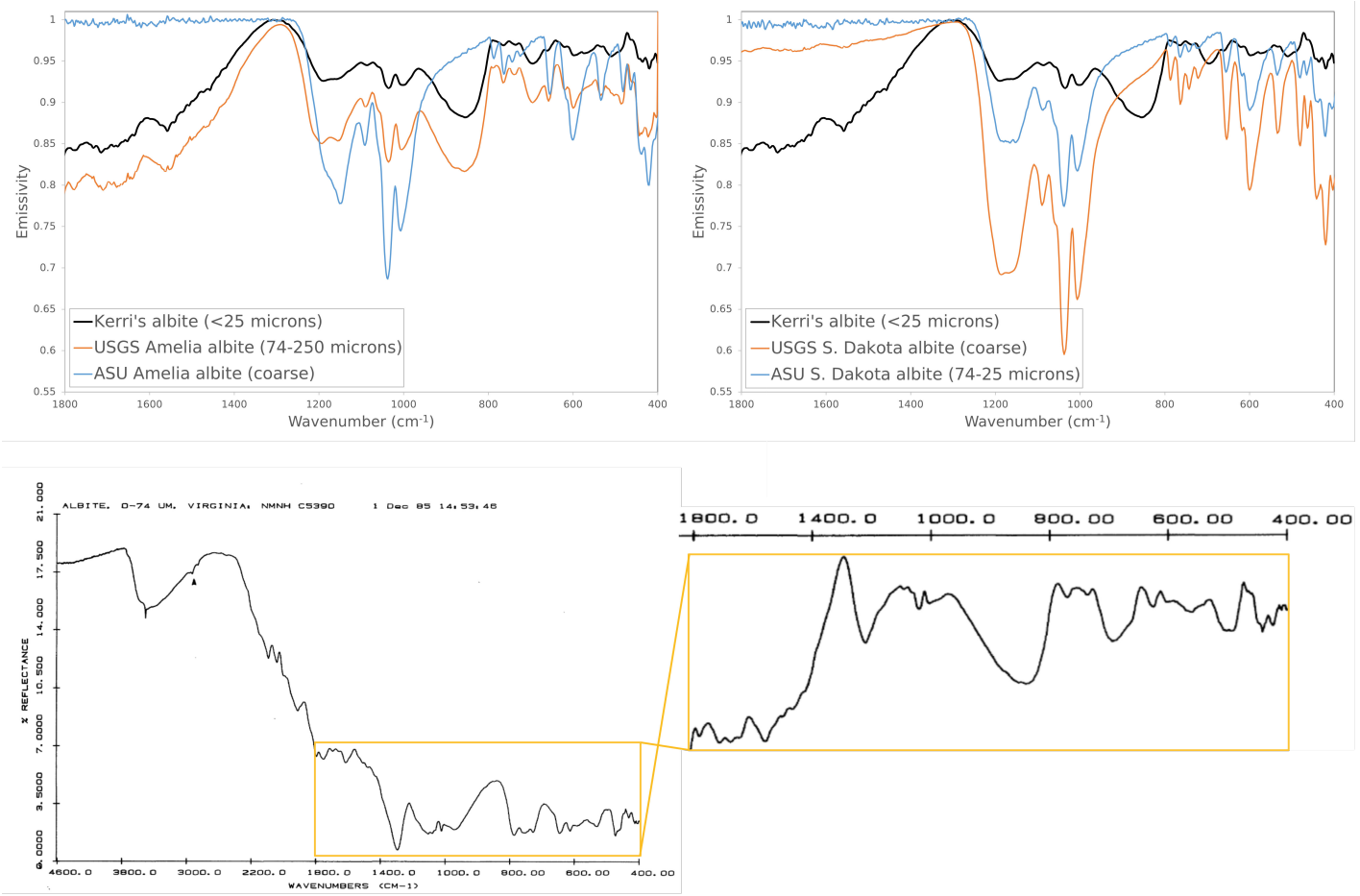


Figure 4.1: Comparing spectra of different albite samples to help identify whether the Amelia albite substitute provided was appropriate. In the top panel, both spectra from USGS were of samples sized $74-250\mu$m (Kokaly et al. 2017), and both spectra from ASU were of coarse particulate samples, with no further specification of size fraction (Christensen, Bandfield, et al. 2000). The bottom panel shows the Amelia albite NMNH C5390 sample used in the Blind Test, at the $0-74\mu$m size fraction from a previous study by Salisbury et al. 1987.

Table 4.2: Compositional information of the real Bruce mixture (*brucereal*; Donaldson Hanna et al. 2019) and the input abundances for the mathematical Bruce (*brucemath*). For full details on each end-member please refer to Table 4.1. *HCP=high calcium pyroxene; LCP=low calcium pyroxene.

Full Sample Name	**End-member**	**Grain Size**	**Abundance (wt.%)** ***brucereal***	**Input Abundance (%)** ***brucemath***
Kakanui augite (NMNH 122142) *HCP - 15% of pyroxene total	Augite	$< 38\mu$m	1.50	1.50
Johnstown orthopyroxene (USNM 6633 and USNM 7418) *LCP - 85% of pyroxene total	Enstatite	$< 38\mu$m	8.50	8.50
San Carlos olivine (NMNH 170992)	Olivine (85% fine 15% coarse)	$< 38\mu$m (fine) $38 - 105\mu$m (coarse)	70.00	70.00
Mundrabilla troilite (USNM 5914)	Troilite	$< 38\mu$m	5.00	5.00
Amelia albite (NMNH C5390-26)	Albite	$< 38\mu$m	10.00	Unavailable
Albite data from Kerri (Amelia albite substitute)		$< 25\mu$m	N/A	10.00
Fe powder from Alfa Aesar ([stock# 39813, Lot# JO2M27], reduced 98%[metal basis], 44 μm)	Fe,Ni-metal	$< 38\mu$m	5.00	Unavailable
Blackbody at emissivity=0.999 (Fe,Ni-metal substitute)	FeNiMetalSub	N/A	N/A	5.00

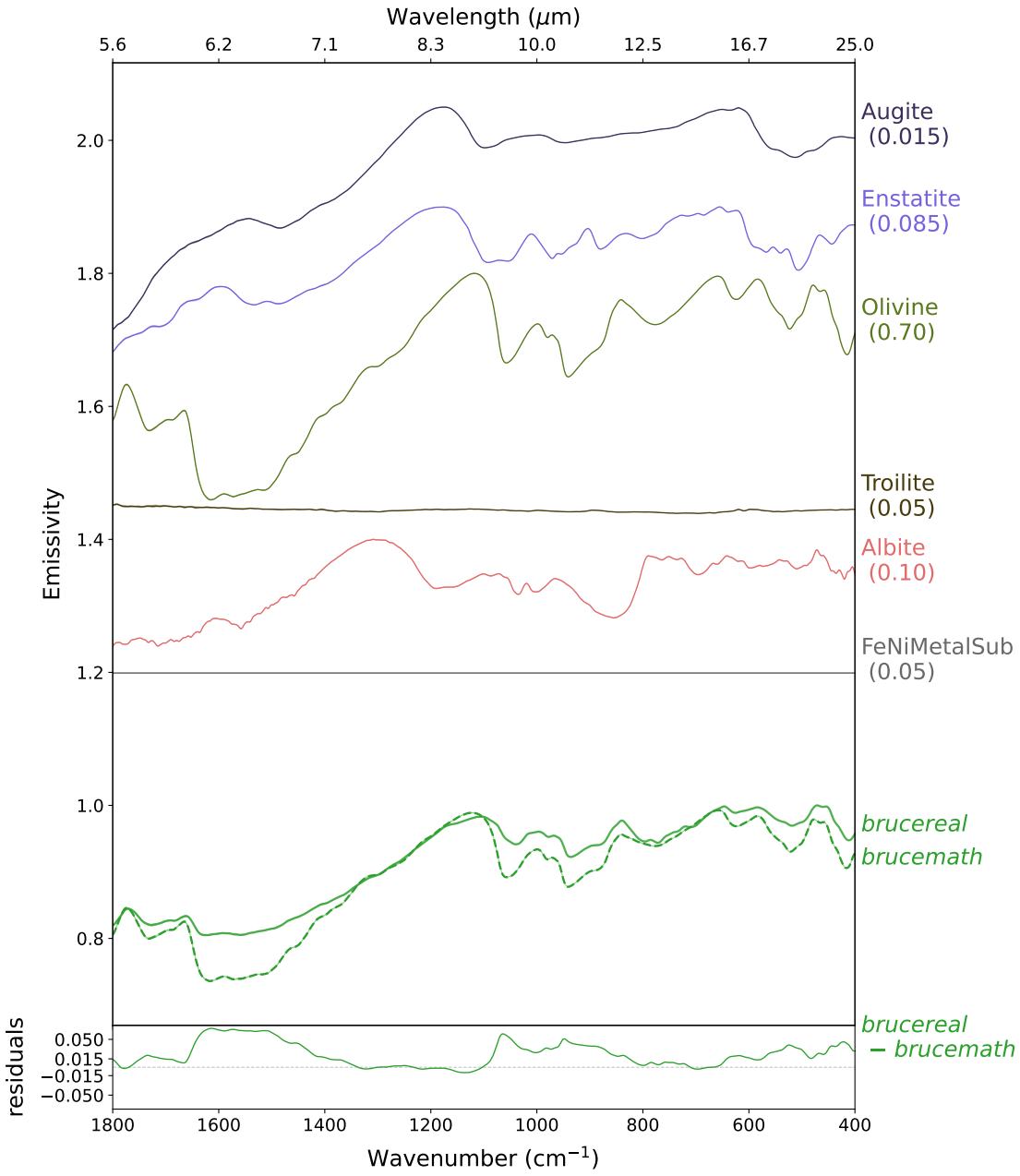


Figure 4.2: Spectra of *brucereal*, *brucemath*, and their end-members (offset for clarity), with the true abundance of each end-member indicated in parentheses.

4.2.2 Glenn

Glenn was the code name for the predominantly fine-grained Murchison sample (USNM5376-1) used in the Blind Test Study (Donaldson Hanna et al. 2019), and had the composition outlined in Table 4.3. Each of the meteorite samples in Donaldson Hanna et al. 2019 were crushed and sieved into three different size fractions, each

combined with different mass distributions to form the final sample; these were: 67wt.% at $< 38\mu$m, 22wt.% at $38-105\mu$m, and $\sim$ 11wt.% at $105-150\mu$m. Murchison is a widely studied and well-characterised CM2 type carbonaceous chondrite meteorite ("Meteoritical Bulletin, No. 36-48" 1970; see Section 1.2 for further details about meteorite classifications), making it a natural step up from Bruce to introduce a more complex mixture into the algorithm and model assessment.

It is hypothesised that Bennu may be related to CM or CI carbonaceous chondrite type meteorites (e.g., Clark et al. 2011), meaning Murchison could serve as a potential analogue for Bennu. Therefore using Murchison for the unmixing test case could aid in future work to verify links between asteroid classes and meteorite types through compositional analysis.

As part of the Blind Test Study, the modal mineralogy of the samples were estimated using position-sensitive-detector X-ray diffraction (PSD-XRD) and digital point counting (conducted at The Natural History Museum, London), the results of which were shown in Tables 4 and 5 of Donaldson Hanna et al. 2019. The 'true' composition of Glenn was taken to be that from Table 5 of Donaldson Hanna et al. 2019, and is summarised here in Table 4.3, along with information on the mathematical version of Glenn. This indicated that the mineral species present in Glenn were olivine, pyroxene, Ca-carbonate, phyllosilicate, Fe-Oxide (magnetite + rust), sulphide + sulphate, and gypsum.

However, as there were multiple mineral phases for some of these (i.e., augite and enstatite are pyroxenes, and saponite, cronstedtite and lizardite are phyllosilicates - see Table 4.1), the abundances for these specific end-members first needed to be determined in order to construct the mathematical version of Glenn. In Murchison, the phyllosilicates present are from the solid solution series between the Fe and Mg end-members of serpentines, where cronstedtite is the Fe end-member and lizardite the Mg end-member, and in reality are likely to have a more intermediate composition (e.g., Zolensky et al. 1993). Howard et al. 2015 provided the break-down of their 72.5% phyllosilicate abundances in Murchison as 50.3% cronstedtite and

22.2% Mg-serpentine (lizardite), so these were scaled to the measured phyllosilicate abundance of Glenn (76.2%; Table 5 of Donaldson Hanna et al. 2019), to give the final abundances used in mathematical Glenn shown in Table 4.3. For Murchison, it is probably more accurate to model enstatite as contributing to the full pyroxene abundance, as Fe-rich pyroxenes (e.g., augite) are among the first to be altered on interaction with fluid (e.g., Suttle et al. 2021).

The spectra for the real and mathematical Glenn mixtures (denoted respectively as '*glennreal*' and '*glennmath*' from here on) are shown together in Figure 4.3, along with their end-member spectra to display the likely origins of certain features. This showed that there were significant differences between the *glennreal* and *glennmath* spectra, with spectral contrast being one of them; as was the case for the Bruce mixture. For full discussion and analysis of *glennreal* vs *glennmath* please see Section 5.1.2.

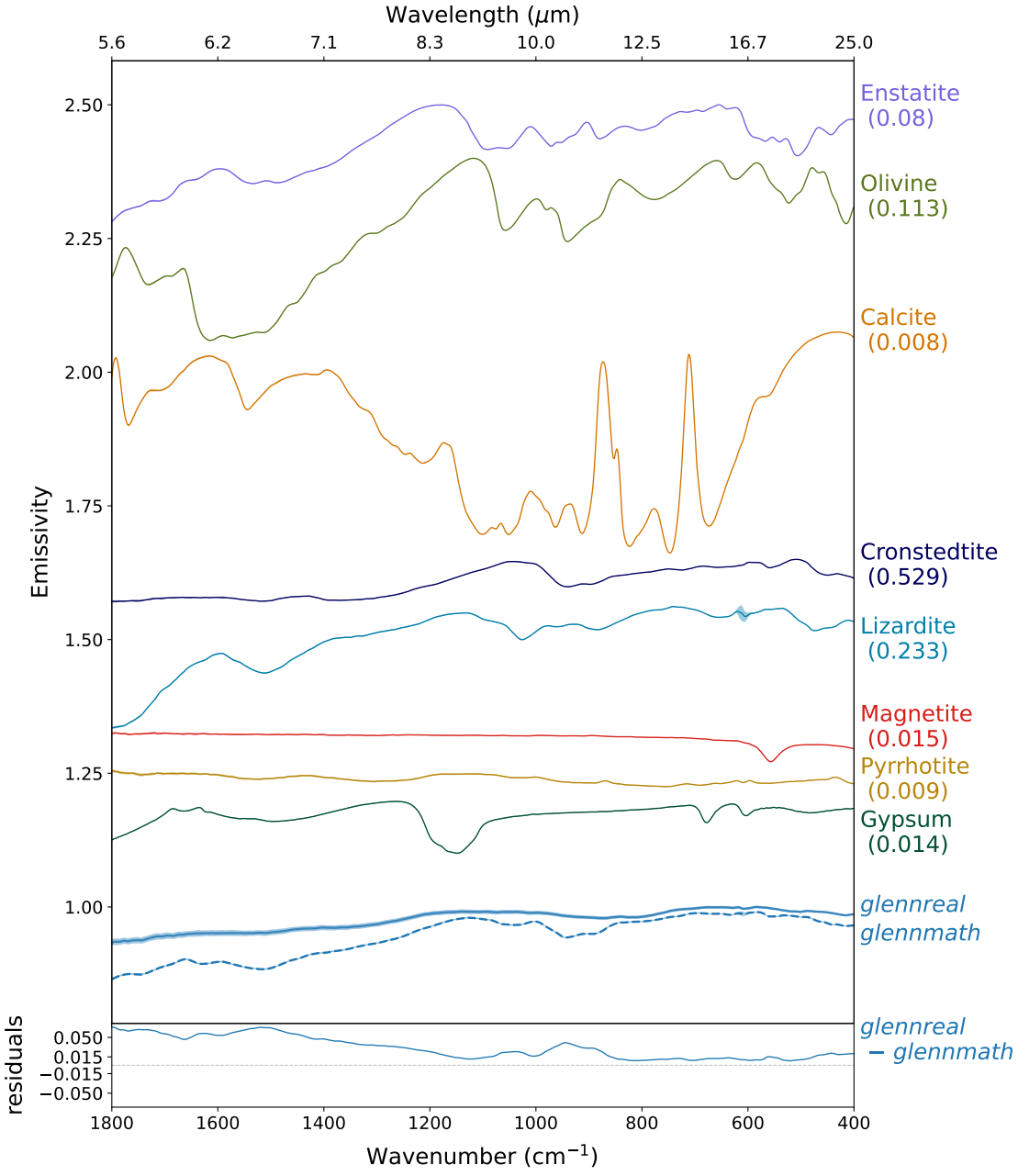


Figure 4.3: Spectra of *glennreal*, *glennmath*, and their end-members (offset for clarity), with the 'true' abundance of each end-member indicated in parentheses.

Table 4.3: Compositional information of the Blind Test Glenn/Murchison sample (*glennreal*; Donaldson Hanna et al. 2019) and the input abundances for the mathematical Glenn (*glennmath*). For full details on each end-member please refer to Table 4.1.

Mineral **(Group)**	**Abundance (vol.%)** ***glennreal***	**End-member** **(sample ID)**	**Grain Size**	**Input Abundance (%)** ***glennmath***
Pyroxene (Silicates)	8.0	Enstatite (USNM 6633, USNM 7418)	$< 38\mu$m	8.0
Olivine (Silicates)	11.3	Olivine (NMNH 170992)	$< 38\mu$m (fine) $38 - 105\mu$m (coarse)	11.3
Ca-carbonate (Opaques)	0.8	Calcite (NMNH 143299-18)	$< 38\mu$m	0.8
Pyllosilicate (Phyllosilicates)	76.2	Cronstedtite (unknown)	$< 90\mu$m	52.9
		Lizardite (from Kerri)	$< 45\mu$m	23.3
Fe-Oxide: magnetite + rust (Opaques)	1.5	Magnetite (NMNH 114111)	$< 38\mu$m	1.5
Sulfide + Sulfate (Opaques)	0.9	Pyrrhotite (unknown)	$< 90\mu$m	0.9
Gypsum (Opaques)	1.4	Gypsum (HS333.3B Selenite NIC4aaa)	$75 - 250\mu$m	1.4

4.2.3 Qualitative Comparisons to Bennu

Since the Blind Test study of Donaldson Hanna et al. 2019 was part of the OSIRIS-REx mission, it was interesting to take a quick, qualitative look at how the Bruce and Glenn spectra compare to the average OSIRIS-REx Thermal Emission Spectrometer (OTES) spectrum of Bennu (taken from Fig. 3 of Hamilton, Simon, et al. 2019), as shown in Figure 4.4. The primary and secondary CFs of Bennu are indicated, along with two major minima, and projected down to the Bruce and Glenn spectra to see if these align with any features. The Bennu primary CF seemed roughly aligned with the Bruce primary CF, and potentially also with the Glenn primary CF, although its position was difficult to define (see Section 5.1.2 for further discussion). Bennu's secondary CF appeared broad across the same general region as the Bruce and Glenn secondary CFs, and the trough at $\sim 950\text{cm}^{-1}$ was also roughly aligned with troughs in Bruce and *glennmath* (but not *glennreal*). The approximate alignments of some features across Bennu, Bruce and Glenn could be indicative of some common end-members across all three. The general TF region for Bruce and Glenn was also highlighted, and projected up to the Bennu spectrum, which did not appear to have any clear indication of a TF. For these quick comparisons, it is important to keep in mind that a more robust comparison to this OTES Bennu spectrum

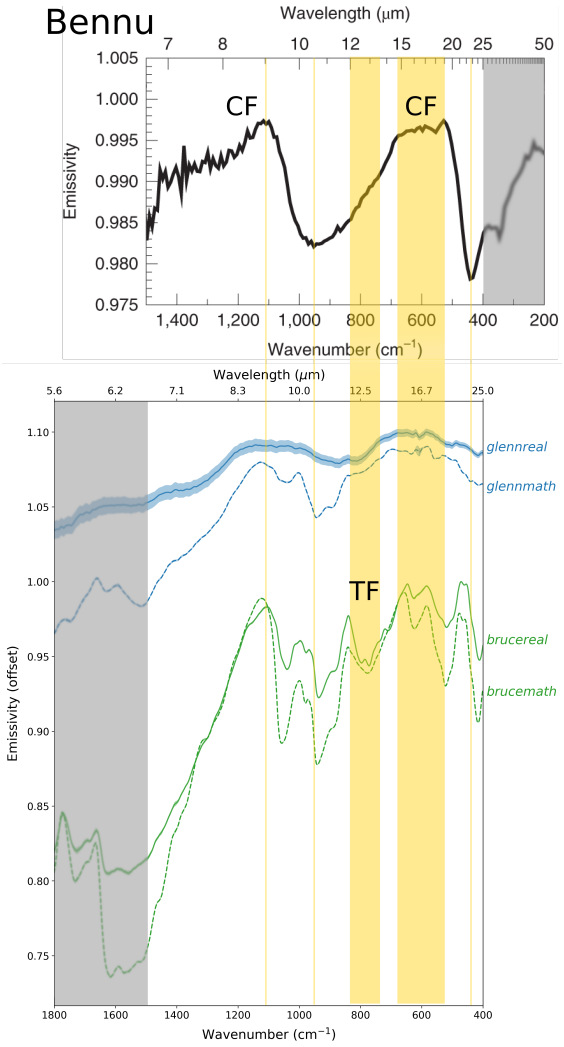


Figure 4.4: Spectra of *brucemath*, *brucereal*, *glennmath* and *glennreal* with the average OTES spectrum of Bennu, taken from Fig. 3 of Hamilton, Simon, et al. 2019.

would be with Bruce and Glenn spectra measured under a simulated asteroid environment (SAE), but their spectra presented in Figure 4.4 (and throughout this thesis) were measured under ambient conditions, thus making it somewhat redundant to comment further on any resemblances (or lack of).

4.3 Exploration and Development of Spectral Unmixing Algorithms

To meet the primary aim of my doctoral research (to investigate and improve spectral unmixing algorithms), several existing packages from publicly available Python libraries[2] were trialled and assessed, using the Blind Test data described in Sections 4.1 and 4.2. This ultimately led to the development of my custom spectral unmixing algorithms (Section 4.3.2).

When considering how to improve on current methods, this raises the question: do we need a new/different spectral mixing model, or just a new/different unmixing algorithm? Although studying real vs mathematical versions of mixtures and complementary techniques such as PCA indicated that the underlying model was unsuitable (see Sections 5.1 and 5.2), the current use of a basic linear least squares as the algorithm leaves space open to explore whether it is possible to accommodate the shortcomings of the linear mixing model by using more sophisticated (i.e., Bayesian) algorithms. As the linear mixing model is mathematically simple and upgrading it would require the addition of significantly more complex physics (which may be intractable with current computing resources), it is arguably easier to improve the algorithm rather than the model – thus this formed the first step and main bulk of my work (i.e., Objective 1 in Figure 1.3).

[2]The existing algorithms used are available in several other programming languages, with Python being the language of choice for this work.

4.3.1 Trialling Existing Python Packages for Spectral Unmixing

Based on the original linear least squares fitting approach used in Ramsey and Christensen 1998, and subsequent developments such as NNLS (non-negative least squares, e.g., Rogers and Aharonson 2008; discussed in Chapter 3), a number of similar packages, and those with increasing complexity, available in Python were trialled:

`scipy.optimize.nnls()`: To follow Rogers and Aharonson 2008, a non-negative least squares (NNLS) package in Python, based on the original Fortran code outlined in Lawson and Hanson 1995, was trialled. The abundance sum constraint was conducted post-retrieval using two different methods: basic normalisation such that the output abundances were rescaled to sum to one; and passing the `nnls()` solution through another Python package, `scipy.optimize.minimize()` (Virtanen et al. 2020, Jones et al. 2001). The results overall were very poor regardless of which abundance sum constraint method was used (RMS values of the order 16, where values of the order 10^{-3} would be considered 'good', following Ramsey and Christensen 1998 – see Section 3.3.3).

`scipy.optimize.minimize()`: An optimisation tool in itself, `minimize()` (Virtanen et al. 2020, Jones et al. 2001) was tested, using an array of equal abundances as the required initial guess for the parameters, rather than using values derived from `nnls()`. The non-negativity constraint was implemented using `minimize()`'s ability to include bounds (which were set to ≥ 0). Although using `minimize()` alone showed some improvement, with RMS values of the order 0.02, these were not sufficient to go forward with developing a spectral unmixing algorithm using `minimize()`.

`LMFIT()`: Inspired by colleagues within the department (Atmospheric, Oceanic and Planetary Physics), the Levenberg-Marquardt technique (as used in similar problems to retrieve atmospheric parameters, e.g., NEMESIS; Irwin et al. 2008) was also tested. Levenberg-Marquardt is a commonly used non-linear

least squares routine (e.g., Gavin 2017, Levenberg 1944, Marquardt 1963), using the Gauss-Newton and steepest descent methods, varying smoothly between them as it iterates towards a solution. These iterations are guided by a parameter (often denoted as λ) that keeps track of changes to the χ^2 as it is minimised, and is adjusted accordingly (Press et al. 1992). Applying constraints required for spectral unmixing (abundances must sum to one and be non-negative) meant that the unmixing algorithm would require iteration, hence trialling the Levenberg-Marquardt method. To do this, Python package `LMFIT()` (Newville et al. 2021) was used, as it would allow the non-negative and abundance sum constraints to be imposed simultaneously, rather than sequentially. However, as the forward model being used here (linear spectral mixing) was already linear, the advantage of using Levenberg-Marquardt to linearise a non-linear forward model became redundant, giving no real benefit to using this technique. This became clear when working with `LMFIT()`, as it showed no real improvements (RMS values also of the order 0.02), nor had any particular advantages over `nnls()` or `minimize()`, thus making it unsuitable for my project.

The unsatisfactory performance of the above, increasingly complex, Python packages was perhaps the first indication that improving the algorithm is unable to solve the problems of linear mixing for fine grains. However, it was unclear if this could simply be due to limitations intrinsic to using a pre-developed code that is difficult to customise. Therefore, to introduce more consistency in algorithm testing, I decided to develop my own bespoke algorithms for spectral unmixing.

4.3.2 Developing Bespoke Spectral Unmixing Algorithms

Starting with my own version of the Ramsey and Christensen 1998 iterative library reduction (ILR) linear least squares algorithm, coding my own version of the 'default' unmixing algorithm meant that I would have a baseline algorithm to draw comparisons against with more sophisticated Bayesian algorithms, and ultimately determine whether these are indeed an improvement on current techniques. Adopting

a fully Bayesian approach, I also developed a Markov Chain Monte Carlo algorithm, using Python's `emcee`, for use in spectral unmixing. Additionally, to serve as meeting point between Frequentist and Bayesian techniques, I developed a spectral unmixing algorithm that used optimal estimation – a Bayesian method that is mathematically very similar to a linear least squares. Each of these algorithms are described in more detail below.

4.3.2.1 Algorithm 1: `WLS_ASC_ILR()`

The **Weighted Least Squares** with **Abundance Sum Constraint** and **Iterative Library Reduction**, `WLS_ASC_ILR()`, algorithm was based on the traditional linear least squares with iterative library reduction technique of Ramsey and Christensen 1998 – a classical Frequentist method of linear regression, widely used within the community for spectral unmixing. By using the community standard as a baseline, it was then possible to evaluate whether more sophisticated algorithms could get around the limits of linear mixing as the underlying model, and would be an overall improvement, as was one of the aims of my project (see Figure 1.3).

The starting point for development was to use the simplest form of the weighted least squares (Equation 4.1; providing a small step up from the basic linear least squares, which is Equation 4.1 without the $[S_y]^{-1}$), later adding in the abundance sum constraint (from Eqns. 8 and 9 of Heinz and Chang 2001), modified to the weighted least squares form, giving Equation 4.2. In `WLS_ASC_ILR()`, the solution to Equation 4.2 would be checked for values < 0, and corresponding end-members with negative abundance removed from the spectral library. Equation 4.2 would then be recalculated with the reduced library, and the process repeated until all retrieved abundances are ≥ 0. This is the iterative library reduction (ILR), following the method of Ramsey and Christensen 1998, on the basis that a negative abundance implies the corresponding mineral is not present in the mixture.

$$[x]_{(n,1)} = \left([k]^T_{(n,\nu)} [S_y]^{-1}_{(\nu,\nu)} [k]_{(\nu,n)} \right)^{-1} [k]^T_{(n,\nu)} [S_y]^{-1}_{(\nu,\nu)} [y]_{(\nu,1)}, \tag{4.1}$$

$$x = \left(I - (k^T S_y^{-1} k)^{-1} 1[1^T (k^T S_y^{-1} k)^{-1} 1]^{-1} 1^T\right)\left((k^T S_y^{-1} k)^{-1} k^T S_y^{-1} y\right) + (k^T S_y^{-1} k)^{-1} 1[1^T (k^T S_y^{-1} k)^{-1} 1]^{-1}, \quad (4.2)$$

where $[x]_{(n,1)}$ is the solution vector containing n retrieved abundances, $[k]_{(\nu,n)}$ is the spectral library containing n end-member spectra each with ν wavenumber channels, $[S_y]_{(\nu,\nu)}$ is the covariance matrix containing uncertainty on the mixture spectrum, $[y]_{(\nu,1)}$, $[I]_{(n,n)}$ is the identity matrix, and $[1]_{(n,1)}$ is a vector of ones.

The `WLS_ASC_ILR()` algorithm also returned the covariance matrix of the retrieved abundances through Equation 4.3:

$$[S_x]_{(n,n)} = \left([k]^T_{(n,\nu)} [S_y]^{-1}_{(\nu,\nu)} [k]_{(\nu,n)}\right)^{-1}, \quad (4.3)$$

where $[S_x]_{(n,n)}$ is the covariance matrix of solution, $[x]_{(n,1)}$. The covariance matrix would later be translated into a correlation matrix via Equation 3.2 (Section 3.3.2) for more straightforward analysis of the dependence of end-member abundances on each other. Analysis of the correlation matrix could be related back to PCA, as clustering of library end-members in PC1-PC2 space may indicate similarity between them, thus providing a prediction of which end-members may be strongly correlated. The variables output from `WLS_ASC_ILR()` could also be used to find retrieval quality metrics described in Section 3.3.3.

4.3.2.2 Algorithm 2: `OptEst_ASC_ILR()`

As described above, Frequentist inference has commonly been used for spectral unmixing through the linear least squares technique. However, as discussed in Section 3.2, it is not possible to set **priors**[3] with Frequentist methods, where, here, 'priors' are the abundances and their uncertainties expected based on previous studies. Conversely, Bayesian inference requires the inclusion of *a priori* information as quantified priors (as opposed to just having general bounds/constraints, such as abundances summing to one and being non-negative), so the ability to do this with optimal estimation makes it inherently Bayesian. Optimal estimation (e.g., Rodgers 2000) is arguably as close as you can get to a Frequentist method with 'priors', as

[3]See Acronyms & Glossary for disambiguation.

Equations 4.1 and 4.4 for weighted least squares and optimal estimation, respectively, are mathematically similar, following the same form, where the optimal estimation solution collapses to that of linear least squares in the absence of quantitatively defined priors (i.e., without $[S_a]^{-1}$ and $[x_a]$).

So, as a bridge between Frequentist and Bayesian methods, I developed the **Optimal Estimation** with **Abundance Sum Constraint** and **Iterative Library Reduction** algorithm, `OptEst_ASC_ILR()`. This followed the same structure as `WLS_ASC_ILR()`, instead using the optimal estimation form of the matrix expression to find mineral abundances (Equation 4.4), with a modified version of the abundance sum constraint for this (Equation 4.5), iterating until the solution only contains abundances ≥ 0.

$$\begin{aligned}[x]_{(n,1)} = &\left([k]^T_{(n,\nu)}[S_y]^{-1}_{(\nu,\nu)}[k]_{(\nu,n)} + [S_a]^{-1}_{(n,n)}\right)^{-1} \\ &\times\left([k]^T_{(n,\nu)}[S_y]^{-1}_{(\nu,\nu)}[y]_{(\nu)} + [S_a]^{-1}_{(n,n)}[x_a]_{(n,1)}\right),\end{aligned} \tag{4.4}$$

$$\begin{aligned}x = &\left(I - (k^T S_y^{-1} k + S_a^{-1})^{-1} 1[1^T (k^T S_y^{-1} k + S_a^{-1})^{-1} 1]^{-1} 1^T\right) \\ &\times\left(k^T S_y^{-1} k + S_a^{-1}\right)^{-1}\left(k^T S_y^{-1} y + S_a^{-1} x_a\right) \\ &+\left(k^T S_y^{-1} k + S_a^{-1}\right)^{-1} 1\left[1^T (k^T S_y^{-1} k + S_a^{-1})^{-1} 1\right]^{-1}.\end{aligned} \tag{4.5}$$

where $[S_a]_{(n,n)}$ is the covariance matrix containing uncertainties on the a priori abundances, $[x_a]_{(n,1)}$, and the other variables are as defined above.

4.3.2.3 Algorithm 3: `MCMC()`

To investigate a different Bayesian method, I also employed the Markov Chain Monte Carlo (MCMC) technique at the core of my `MCMC()` spectral unmixing algorithm. MCMC is a widely used technique suitable to a range of applications, and allows the parameter space to be fully explored in order to find the most appropriate solution given the explicit and probabilistic *a priori* knowledge provided; whether this is well-defined or somewhat uninformative (e.g., Lambert 2018).

Basics of the MCMC Technique:

Generally, Markov Chain Monte Carlo methods work to estimate parameters of interest by random sampling from a probability distribution, from which they estimate the posterior probability distributions of each parameter that may then be interpreted by the analyst. The random nature comes from the 'Monte Carlo' part of MCMC: Monte Carlo simulations simply generate random numbers on a continual basis, and perform calculations with these in order to estimate the parameter of interest. Markov chains describe a sequence of outcomes, where each outcome is dependent only on the previous step of the sequence, and based on probability.

In an MCMC, a starting point (say, x_0) is required to begin exploration of parameter space to find a value for each parameter of interest; which in my algorithm, `MCMC()`, was a randomly generated value from a Gaussian distribution, between 0 and 1. From this starting point, the MCMC then randomly samples from the estimated posterior distribution to provide another random value (say, x_1') as a candidate for the parameter. Any step taken to form the Markov chain has a 'transition probability' which must satisfy 'detailed balance': the probability of stepping from x_i to x_{i+1} is equal to the probability of stepping from x_{i+1} to x_i; i.e., the probability is the same in both directions.

The proposed value, x_1', is then compared with the starting value, x_0, usually following the Metropolis-Hastings rule, which determines whether the proposed value is accepted or rejected as the next step. In Metropolis-Hastings, the value of x_1' is considered 'better' than x_0, and the step accepted, if x_1' is more likely to explain the data observed, given the prior, than x_0. Thus, the next step taken, $x_1 = x_1'$ is added to the Markov chain and ascribed a probability that describes how much 'better' x_1' is compared to x_0. If, however, x_1' does not better explain the data than x_0, the value of x_1' will not be added to the chain, and the next step will be taken as $x_1 = x_0$. From x_1 the process repeats, with further steps proposed (i.e., x_2') and potentially taken (i.e., $x_2 = x_2'$ or $x_2 = x_1$).

The steps (or 'samples') continue until the number of steps/samples defined by the analyst has been reached. The total number of steps taken is often referred to as the length of the (Markov) chain, and is a key MCMC 'hyperparameter' (i.e., a parameter whose value is chosen by the analyst that shapes the algorithm and may affect its performance). Due to the probabilistic nature of the sampling, the samples/steps tend to eventually converge within a region around the value with the highest probability for the parameter of interest. This convergence takes time, however, with the number of steps required to reach convergence highly dependent on the application. Therefore it is important to set the length of the chain (number of steps taken) to be long enough such that convergence may be reached, preferably much before the end of the chain. Although longer chains often lead to more accurate estimations as convergence (or its lack of) becomes clearer, taking more steps/samples is more time consuming and computationally expensive; thus the choice of chain length by the analyst is a balance between what is sufficient to meet convergence criteria and that will be completed within an appropriate time frame.

The first few steps of the chain often explore the entire parameter space before convergence is reached, and may still have residual influence from the starting point, x_0, and so these steps are not considered representative of the posterior probability distribution for the parameter of interest. Therefore, another hyperparameter set in MCMC is the number of 'burn-in' steps, which is how many steps from the beginning of the chain that should be discarded before statistical analysis. Additionally, if the chain is sufficiently large that it may compromise computing efficiency, the chain may be 'thinned' by some 'thinning' factor, e.g., `thin`; whereby only every `thin` steps are taken from the full sampling chain.

From the chain of samples (whether full, burnt-in or thinned, as desired), any statistics of choice may be conducted (e.g., finding the mode, median or mean); and is particularly useful visualised as a histogram. When solving for multiple parameters, it is often useful to plot 'joint probability density functions' (pdfs), between two parameters at a time. Joint pdfs display the values sampled for each

parameter against each other, and so can be a way to visualise any dependencies between parameters; e.g., diagonal trends indicate correlation between parameters, whereas a more circular form shows they are independent.

To avoid samples becoming stuck in local probability maxima, which may not be representative of the global probability distribution function, often several 'walkers' are used to explore the parameter space separately. These walkers essentially represent the individual chains for which sampling is conducted for each parameter. The number of walkers (i.e., number of chains) per parameter of interest is another MCMC hyperparameter that must be set by the analyst, and should be considered in combination with the number of steps/length of each chain to ensure appropriate sampling of the parameter space. The value adopted per step of the chain may be plotted as a walkers (or 'trace') plot, which can be a useful visualisation to help assess convergence (and is therefore included in the analysis of Chapter 6).

Development of the `MCMC()` Spectral Unmixing Algorithm:

From the MCMC basis described above, there are many variations that have since been developed. For my `MCMC()` algorithm, I used `emcee` (Foreman-Mackey et al. 2013): "an MIT licensed pure-Python implementation of the Goodman and Weare 2010 'Affine Invariant MCMC Ensemble Sampler'". In this affine invariant MCMC, the Markov chains evolve by considering one walker at a time, where each walker position is dependent on those of the other walkers. The 'affine invariance' refers to the property of this method that its performance is independent to the qualities of distributions (e.g., the aspect ratio of a highly anisotropic distribution; Goodman and Weare 2010). The details of this affine invariance are beyond the scope of this thesis, but it generally refers to surfaces being considered equal during affine transformations, whereby points, straight lines and planes are preserved during the transformation.

The development of `MCMC()` first involved running extensive trial and error tests to check functionality for use in spectral unmixing. A particular advantage of MCMC is the flexibility to customise the probability distributions for the prior,

likelihood and posterior; and so this formed an important part of the development process, and algorithm comparison.

The default and most 'uninformative' (or 'diffuse') distribution often used for the priors in MCMC is the Uniform distribution (i.e., equal probability between defined bounds; e.g., 0 and 1), and so it was used as one of the prior versions in the `MCMC()` unmixings presented in Chapter 6. As the Gaussian distribution is intrinsic to optimal estimation, to allow for more robust comparisons between `MCMC()` and `OptEst_ASC_ILR()`, the Gaussian distribution was also used for the priors, likelihood and posteriors in `MCMC()`. The priors were defined in four different ways, *P1*→*P4*, as outlined in Table 4.4; where the same definitions *P1*→*P4* were also used in `OptEst_ASC_ILR()`. Full results and discussion of the unmixings using the different versions of priors can be found in Chapter 6.

Table 4.4: Different versions of priors used for `OptEst_ASC_ILR()` and `MCMC()` runs. *P4* represented perhaps a more realistic situation, whereby upon presentation of an unknown mixture spectrum with no other information, the analyst would then use their expertise and judgement to define the priors and confidence in them by comparing the mixture spectrum with a spectral library.

Version		**Description**
Uniform	*U*	The Uniform distribution which gives equal probability to all possible solutions between the bounds (0, 1).
Gaussian (a.k.a., Normal distribution) $\mathcal{N}(\mu, \sigma^2) = \frac{1}{\sigma\sqrt{2\pi}} exp(-\frac{1}{2}(\frac{x-\mu}{\sigma})^2)$ where μ = mean, σ^2 = variance	*P1*	Gaussian distribution with randomly generated μ (between 0 and 1) and $\sigma = 0.001\mu$ for each end-member, to simulate incorrect random priors with high confidence.
	P2	As above (P1) but with $\sigma = 1.001\mu$ to simulate low confidence in the priors.
	P3	'Perfect' priors where μ is the 'true' abundance used in the mathematical version (or 0.001 for incorrect end-members), and $\sigma = 0.001\mu$ for correct end-members and $\sigma = 1.001\mu$ for incorrect ones.
	P4	Manually selected μ and σ based on comparing the mixture and spectral library used, to simulate 'realistic' priors.

A large part of the credibility of MCMC solutions is drawn from convergence criteria – in `emcee` (Foreman-Mackey et al. 2013), this is implemented by imposing that the length of the sampler chain must be larger than 50× the integrated autocorrelation time for each parameter being estimated. The integrated autocorrelation time is the number of steps the sampler requires for the starting point, x_0, to no longer have any influence on further steps taken – this is an important measure for interpreting convergence as the steps of the sampler are not independent (Foreman-Mackey et al. 2013).

Following the `emcee` documentation, I set the burn-in (number of steps to be removed from the beginning) and thinning (only use every `thin` steps from the chain) parameters to be the integers of 3× and 0.5× the mean integrated autocorrelation time across all the parameters, respectively.

During preliminary work, I ran many trial and error `MCMC()` runs to try and find an appropriate number of walkers (number of samplers exploring the parameter space for each end-member) and steps/samples (chain length for each walker) to satisfy the default convergence requirement mentioned above, that would be applicable to all runs. Based on this work and guidelines from the `emcee` documentation (Foreman-Mackey et al. 2013), I decided to use 500 walkers each taking 1000 samples, making sure to include observations of the walkers (a.k.a., trace) plots, for the final investigation.

From the repeated issues to meet `emcee`'s convergence criteria in this preliminary work, I hypothesised that there may be a link between the integrated autocorrelation time (i.e., ability to converge) and the degree of internal variability within the spectral library (as explored through PCA), and that the way the priors are set could influence the convergence of the MCMC chains. Unfortunately there was not sufficient time to explore this in more depth, and so is discussed as a future research avenue in Chapter 8.

4.3.3 Renormalising for Blackbody Abundance

Due to scattering effects from packing of a sample, there will naturally be differences between a spectrum of a single mixture sample vs spectra of separate end-member samples later added together mathematically. This is because of the difference in overall surface area of each end-member when in a mixture vs on its own; where there is a larger proportion of exposed surfaces for each end-member when taking spectra of them separately in comparison to their combination in a physical mixture. These packing effects are therefore propagated through the forward model and amplified when mathematically summing them together, and so needs to be addressed.

It is standard practice in spectral unmixing to include an artificial blackbody component (labelled in this work as BB – a straight line at emissivity=1.0) as an end-member in the spectral library to decrease spectral contrast when unmixing, which is later renormalised out (Hamilton, Christensen, et al. 1997). So an important addition to my work was to incorporate this blackbody renormalisation, redistributing the BB retrieved abundance across the real end-members, ensuring the bounds and constraints were still met (Equation 4.6), and error propagation properly followed through (Equation 4.7).

$$x'_n = \frac{x_n}{(\sum \vec{x}) - x_{BB}}, \tag{4.6}$$

$$\begin{aligned} \sigma(x'_n) &= x'_n \sqrt{\left(\frac{\sigma(x_n)}{x_n}\right)^2 + \left(\frac{\sigma\Big((\sum \vec{x}) - x_{BB}\Big)}{(\sum \vec{x}) - x_{BB}}\right)^2} \\ &= x'_n \sqrt{\left(\frac{\sigma(x_n)}{x_n}\right)^2 + \left(\frac{\sqrt{(\sum \sigma(\vec{x})^2) + \sigma(x_{BB})^2}}{(\sum \vec{x}) - x_{BB}}\right)^2}, \end{aligned} \tag{4.7}$$

where x'_n is the blackbody renormalised abundance for end-member n, x_n is the retrieved abundance of end-member n, x_{BB} is the retrieved abundance for the artificial blackbody component, and $\sum \vec{x}$ should $= 1$. In published literature, it is common for the blackbody renormalised abundances to be what is quoted as the retrieved solution, but accompanied with a plot of the pre-BB-normalised model spectrum (e.g., Hamilton, Christensen, et al. 1997). For completeness, I

include all pre- and post-BB-normalisation information in my results tables and figures, where legible and feasible.

With the final set of unmixing algorithms developed and tested, the next step was to conduct a full investigation in order to evaluate the performance of each algorithm for estimating mineralogy. To do this I ran each algorithm on the same datasets (i.e., mixtures: Bruce and Glenn) and other consistent factors (e.g., spectral library) to judge how they perform relative to each other. To see what effects different factors have, I repeated the unmixings with just the factor of interest changed and everything else remaining unchanged – using different versions of the spectral library to highlight problems of implicit *a priori* information/bias from end-member selection, whilst using different prior values (where applicable) to highlight the importance of being able to explicitly set priors to see their influence. The various retrieval quality metrics and other contextual information were then used to compare the different algorithms, with full analysis outlined in Chapters 5 and 6.

The Bruce and Glenn samples each had the real and mathematical versions of their spectra analysed and unmixed, giving four mixtures (i.e., test cases) in total. These were each unmixed a total of 30 times through the different combinations of algorithm (`WLS_ASC_ILR()`, `OptEst_ASC_ILR()`, `MCMC()`), spectral library (*minimal*, *expanded*, *extensive*), and prior (*U*, *P1*, *P2*, *P3*, *P4* – where applicable), as summarised in Table 4.5.

Table 4.5: Summary of the unmixings/retrievals completed, with cross-references to the relevant sections for each.

			Bruce		Glenn	
			brucemath	*brucereal*	*glennmath*	*glennreal*
`WLS_ASC_ILR()`	*minimal*		§5.3.1.1	§5.3.1.1	§5.3.2.1	§5.3.2.1
	expanded		§5.3.1.2	§5.3.1.2	§5.3.2.2	§5.3.2.2
	extensive		§5.3.1.3	§5.3.1.3	§5.3.2.2	§5.3.2.2
`OptEst_ASC_ILR()`	*min*	*P1*	§6.1.1.1	§6.1.1.2	§6.1.2.1	§6.1.2.2
		P2	§6.1.1.5	§6.1.1.2	§6.1.2.1	§6.1.2.2
		P3	§6.1.1.5	§6.1.1.2	§6.1.2.1	§6.1.2.2
		P4	§6.1.1.5	§6.1.1.2	§6.1.2.1	§6.1.2.2
	exp	*P1*	§6.1.1.3	§6.1.1.4	§6.1.2.3	§6.1.2.4
		P2	§6.1.1.3	§6.1.1.4	§6.1.2.3	§6.1.2.4
		P3	§6.1.1.3	§6.1.1.4	§6.1.2.3	§6.1.2.4
		P4	§6.1.1.3	§6.1.1.4	§6.1.2.3	§6.1.2.4
	ext	*P1*	§6.1.1.5	§6.1.1.6	§6.1.2.5	§6.1.2.6
		P2	§6.1.1.5	§6.1.1.6	§6.1.2.5	§6.1.2.6
		P3	§6.1.1.5	§6.1.1.6	§6.1.2.5	§6.1.2.6
		P4	§6.1.1.5	§6.1.1.6	§6.1.2.5	§6.1.2.6
`MCMC()`	*min*	*U*	§6.2.1.1	§6.2.1.2	§6.2.2.1	§6.2.2.2
		P1	§6.2.1.1	§6.2.1.2	§6.2.2.1	§6.2.2.2
		P2	§6.2.1.1	§6.2.1.2	§6.2.2.1	§6.2.2.2
		P3	§6.2.1.1	§6.2.1.2	§6.2.2.1	§6.2.2.2
		P4	§6.2.1.1	§6.2.1.2	§6.2.2.1	§6.2.2.2
	exp	*U*	§6.2.1.3	§6.2.1.4	§6.2.2.3	§6.2.2.4
		P1	§6.2.1.3	§6.2.1.4	§6.2.2.3	§6.2.2.4
		P2	§6.2.1.3	§6.2.1.4	§6.2.2.3	§6.2.2.4
		P3	§6.2.1.3	§6.2.1.4	§6.2.2.3	§6.2.2.4
		P4	§6.2.1.3	§6.2.1.4	§6.2.2.3	§6.2.2.4
	ext	*U*	§6.2.1.5	§6.2.1.6	§6.2.2.5	§6.2.2.6
		P1	§6.2.1.5	§6.2.1.6	§6.2.2.5	§6.2.2.6
		P2	§6.2.1.5	§6.2.1.6	§6.2.2.5	§6.2.2.6
		P3	§6.2.1.5	§6.2.1.6	§6.2.2.5	§6.2.2.6
		P4	§6.2.1.5	§6.2.1.6	§6.2.2.5	§6.2.2.6

Chapter 5

Results and Discussion: Pre-Unmixing and Frequentist Inference

Contents

5.1 Pre-Unmixing: *real* vs *math* 79
5.1.1 Bruce 79
5.1.2 Glenn 81
5.2 Pre-Unmixing: Spectral Library PCA 84
5.2.1 *minimal* 85
5.2.1.1 Bruce 85
5.2.1.2 Glenn 87
5.2.2 *expanded* 87
5.2.2.1 Bruce 87
5.2.2.2 Glenn 88
5.2.3 *extensive* 89
5.2.4 Overall Spectral Library PCA Discussion and Summary 92
5.3 Weighted Least Squares 92
5.3.1 Bruce 93
5.3.1.1 *brucemathmin* and *brucerealmin* Unmixings . . 94
5.3.1.2 *brucemathexp* and *brucerealexp* Unmixings . . 98
5.3.1.3 *brucemathext* and *brucerealext* Unmixings . . . 102
5.3.1.4 Summary of Bruce `WLS_ASC_ILR()` Unmixings 105
5.3.2 Glenn 106
5.3.2.1 *glennmathmin* and *glennrealmin* Unmixings . . 106
5.3.2.2 *glennmathexp*, *glennrealexp*, *glennmathext* and *glennrealext* Unmixings 109
5.3.3 Overall `WLS_ASC_ILR()` Unmixings Discussion 109

Pre-unmixing analysis can help provide a fuller picture of how the algorithms work, and how these could be improved. Comparing the mathematically derived

version of a mixture spectrum to its real spectrum as measured in the laboratory can provide initial insight into the accuracy and validity of linear mixing as a model. Additionally, principal component analysis (PCA) on the different versions of the spectral library may also provide context to the degree of degeneracy within the problem as it is a way of examining the internal variability of a dataset, thus also giving indication to the validity of linear mixing. These analyses and results using current techniques (i.e., linear least squares) can then pave the way for development of improved methods (i.e., adopting a Bayesian approach).

5.1 Pre-Unmixing: *real* vs *math*

5.1.1 Bruce

The composition of the real and mathematical versions of the Bruce mixture (*brucereal* and *brucemath* respectively) are outlined in Table 4.2, along with an initial plot of the two together with their end-member spectra (Figure 4.2). The *brucereal* and *brucemath* spectra were largely similar, with the main difference being the spectral contrast, emphasising the need for the artificial blackbody (BB) in the spectral library to be later renormalised out (as discussed in Section 4.3.3).

To illustrate this further, Figure 5.1 demonstrated how the addition of BB reduced the spectral contrast of *brucemath* to more closely match *brucereal*. Here, BB was included with an abundance of 0.25, where the input abundances of Table 4.2 were rescaled to allow the addition of BB but keep the sum of all abundances equal to one. The value for BB abundance (0.25) was selected via manual trial and error to find a value that matched the spectra as closely as possible at their minimum and maximum points, and giving them both a similar magnitude of spectral contrast by eye[1].

[1]I acknowledge that there are more quantitative ways to do this, however this was intended as a qualitative first look to demonstrate the concept and provide a starting point for later work, so judging by eye here was sufficient.

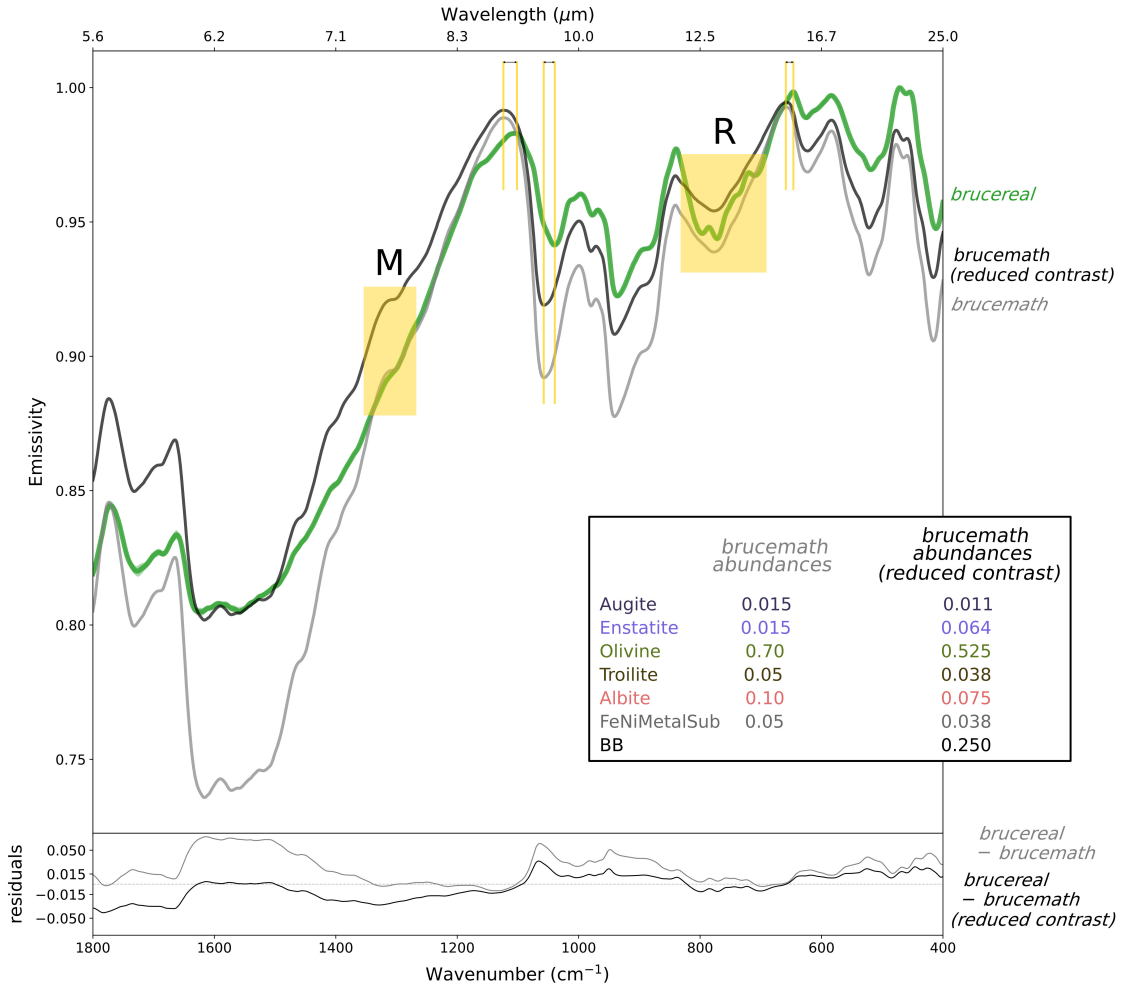


Figure 5.1: Spectra of *brucereal*, *brucemath*, and a reduced spectral contrast version of *brucemath*. M denotes highlighted features only present in *brucemath*, and R denotes highlighted features only present in *brucereal*.

With the spectra matching more closely in spectral contrast, it became easier to see the more subtle differences between the mathematically derived and laboratory measured Bruce spectra. It was clear that even with this modification, the *brucereal* and *brucemath* spectra had significant differences in morphology, which could provide insight into the physics not being fully captured by the linear model. On closer inspection it could be seen that some features were misaligned, with *brucemath*'s generally being towards higher wavenumbers by about $3 - 20\text{cm}^{-1}$. There were also some features present only in *brucereal* and some only in *brucemath*, as highlighted in Figure 5.1.

A particularly interesting difference was the small peak ($\sim 780\text{cm}^{-1}$) within the

Transparency Feature (between $\sim 840 - 630\text{cm}^{-1}$), present only in the *brucereal* spectrum. As the TF is known to be strongly influenced by the grain size (see Section 2.1 and Chapter 7), it is possible that this could be a grain size scattering effect not well captured by the linear mixing model; which could potentially have also been a cause of the differences highlighted in the Christiansen Feature (CF) roll-off zone (between $\sim 1560 - 1100\text{cm}^{-1}$) – also a transparency effect.

The *brucereal* principal CF also did not have a perfectly smooth single peak, but actually appeared as though it could be two CFs superimposed together; with the higher wavenumber minor peak ($\sim 1170\text{cm}^{-1}$) aligning with the augite and enstatite principal CFs. The lower wavenumber major *brucereal* CF peak ($\sim 1110\text{cm}^{-1}$), however, was shifted from the olivine CF by approximately 11cm^{-1} towards lower wavenumbers, but was very closely aligned with the first major Reststrahlen Band (RB) trough (low wavenumber side of the CF) for both augite and enstatite, as well as a minor peaked RB feature in albite.

As discussed in Section 4.2.1, even though there were two substitute end-members used in *brucemath*, these were deemed to be appropriate and so the differences between *brucereal* and *brucemath* were most likely due to the inaccuracies of linear mixing rather than incorrect/missing end-members. This analysis therefore provided an initial insight that we need a new model, but did not answer the question of whether we can compensate for the limitations of the linear mixing model by using more sophisticated unmixing algorithms.

5.1.2 Glenn

The composition of *glennreal* is outlined in Table 4.3, along with the end-members and abundances used to create *glennmath*. The spectra of *glennreal*, *glennmath* and the appropriate end-members are shown in Figure 4.3.

Overall, *glennmath* showed very little resemblance to *glennreal*. Although there were some vague similarities in overall morphology (such as the location of the primary and secondary CF peaks, located approximately between $1190 - 930\text{cm}^{-1}$

and $800 - 440\text{cm}^{-1}$, respectively), many features appeared misaligned and generally broader in *glennreal* compared to *glennmath* – it is almost as though *glennreal* was a stretched out version of *glennmath*, with the ends of the spectrum having been lightly drawn apart.

The region containing the CF roll-off zone and the highest wavenumber end of the spectral range ($\sim 1130 - 1800\text{cm}^{-1}$) was poorly captured in *glennmath*, as the main peaks and troughs seemed grossly exaggerated in *glennmath* compared to those corresponding features for *glennreal*. The major trough in this region (i.e., the end-point of the CF roll-off zone) for *glennmath* ($\sim 1510\text{cm}^{-1}$) was roughly aligned with the CF roll-off zone end-point in olivine, a small peak within a trough in enstatite, a shallow but wide trough in cronstedtite, and a similarly shaped major trough in lizardite. The major peak on the larger wavenumber side of the CF roll-off zone in *glennmath* ($\sim 1600\text{cm}^{-1}$) was aligned with the first major peak on the high wavenumber side of the CF roll-off zone in olivine.

The primary CF for *glennreal* was very broad, thus making it difficult to determine its exact position initially by eye, however, it appeared roughly aligned with the enstatite CF ($\sim 1150\text{cm}^{-1}$) but could also encapsulate the olivine, lizardite and cronstedtite CFs ($\sim$ 1100, 1130 and 1000cm^{-1}, respectively) as it almost appeared smeared across the region where all of these are located. On the other hand, the *glennmath* CF could be considered as appearing bimodal with two distinct peaks present within the width of the principal *glennreal* CF. The right hand side (minor) peak ($\sim 1000\text{cm}^{-1}$) of the bimodal *glennmath* principal CF appeared to be aligned with the cronstedtite CF and the first peak on the lower wavenumber side of the CF in olivine and enstatite; whilst the left hand side (major) peak had a similar appearance to the Bruce CF (Figure 5.1), as though two CFs had been superimposed. The highest point of the major peak ($\sim 1120\text{cm}^{-1}$) was better aligned with the lizardite CF, and the small bump on this peak ($\sim 1100\text{cm}^{-1}$) aligned with the olivine CF.

The morphology indicative of CF superposition from strongly featured and/or high abundance end-member spectra seen in the CFs of both Bruce and Glenn could be a sign that the linear mixing model is unable to accurately capture the physics occurring at the CF (described in Section 2.1).

Interestingly, the residuals of the *glennmath* spectrum subtracted from *glennreal* looked almost like a reflection of *glennmath* about a plane at some constant value on the y-axis. This was possibly due to the fact that the *glennreal* spectrum was so much flatter, further emphasising the difference in spectral contrast between the two.

Following the same method to reduce spectral contrast of the mathematical mixture as for Bruce, BB in an abundance of 0.6 was added to *glennmath* (Figure 5.2). The addition of BB reduced the spectral contrast of *glennmath* very effectively, giving a generally similar magnitude of spectral contrast when compared qualitatively to *glennreal*.

Figure 5.2 demonstrated the misalignment of features and poor replication of the CF in *glennmath*, although the residuals appeared relatively flat, which alone would indicate a good likeness. The bimodal nature of the *glennmath* CF was also much clearer in Figure 5.2; as was a similarly bimodal peak in *glennmath* between $\sim 1730 - 1560\text{cm}^{-1}$, where the feature was much broader in *glennreal*, which also became more apparent in the reduced contrast *glennmath* spectrum (as highlighted in Figure 5.2). It was difficult to decipher which features correspond to each other in *glennreal* and *glennmath* due to their differing morphologies (particularly the apparent bimodality of some features in *glennmath* compared to their *glennreal* counterparts), however some that could be identified are indicated on Figure 5.2, showing the shift in position between the *glennreal* and *glennmath* spectra.

Overall, it was clear that *glennmath* and *glennreal* did not look alike, which could provide further evidence into the inaccuracy of linear mixing as the underlying model. However, the differences in crystalline structure and grain size present within an extraterrestrial sample like Murchison may be significantly different to those

of the terrestrial samples used for the individual end-members (e.g., Vaccaro et al. 2023; Zanetta et al. 2022). This factor, along with the possible impurities and small quantities of organics in *glennreal*, could therefore be a cause (or a contribution to the cause) of the large discrepancies between *glennreal* and *glennmath*.

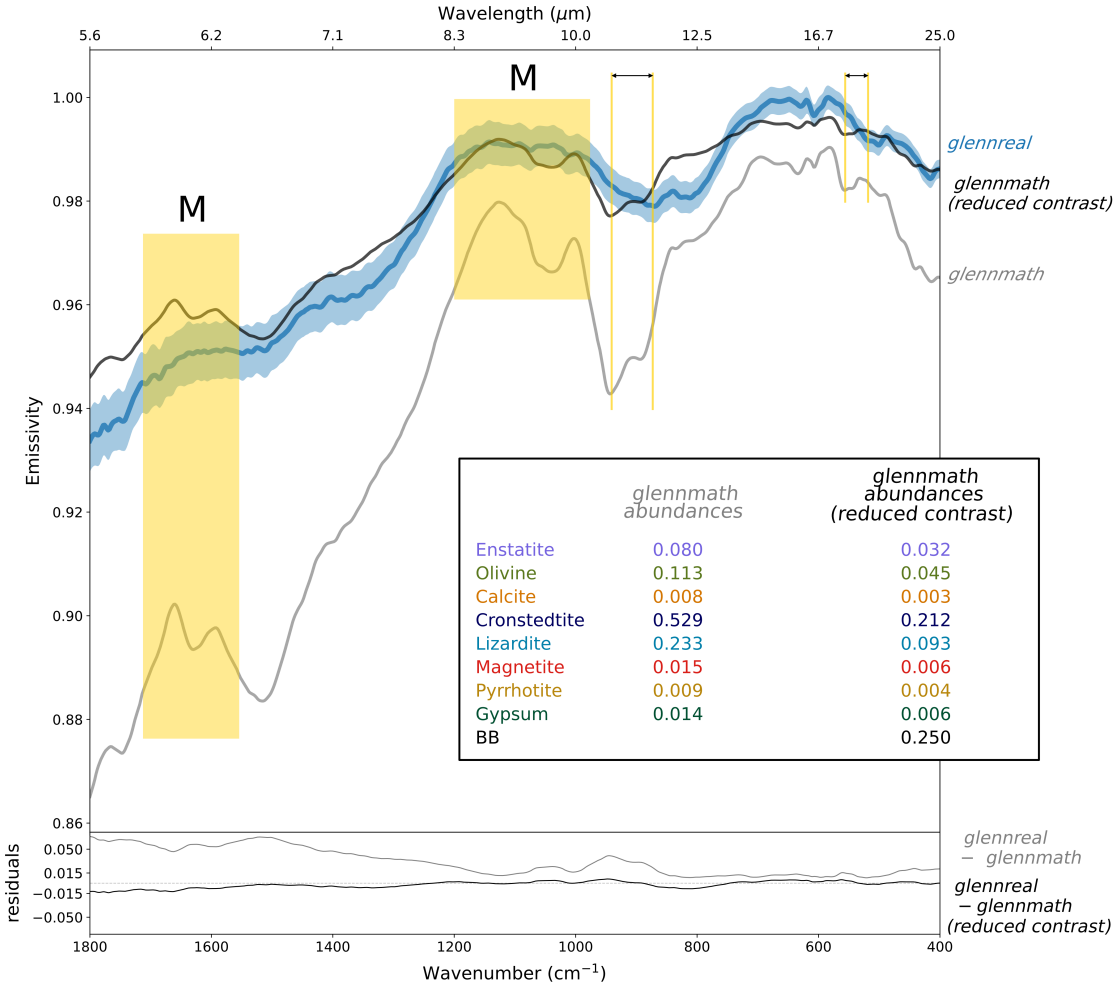


Figure 5.2: Spectra of *glennreal*, *glennmath*, and a reduced spectral contrast version of *glennmath*. M denotes highlighted features that appear bimodal in *glennmath* but as a single, broad peak in *glennreal*.

5.2 Pre-Unmixing: Spectral Library PCA

Insight independent from both the mixtures and the algorithms can come from PCA of the different spectral libraries used (e.g., Section 3.3.1). The *minimal*, *expanded*, and *extensive* spectral libraries used to unmix the Bruce and Glenn

mixtures are shown, along with their principal component PC1 vs PC2 plots, in the following sections accompanying their discussions.

A key part of PCA is the principal component plot which shows the first principal component, PC1 (x-axis), plotted against the second principal component, PC2 (y-axis), where the total number of principal components is equal to the number of end-members in the spectral library. In these PCA plots, clustering of points indicates spectral similarities between end-members within the context of the entire spectral library, therefore providing insight to the degree of degeneracy and potential correlation between the estimated end-member abundances. This clustering could also explain why the retrieval of any particular end-member would preferred by the algorithm, and/or why any may be incorrectly discarded during the iterative library reduction (e.g., for two end-members in close proximity on the PCA plot, the algorithm may struggle to distinguish them and only identify one of these to retain in the retrieval, which could be an incorrect end-member, and the correct one discarded).

The PC1+PC2 explained variance ratio is the amount of variance contained within the first two principal components. A high value for PC1+PC2 explained variance ratio indicates that the variance in the dataset is well captured within just the first two principal components, whereas a lower value for this means that more principal components are needed to describe the variability, which should be kept in mind when interpreting the PC1 vs PC2 plots that accompany the spectral libraries.

5.2.1 *minimal*

5.2.1.1 Bruce

The PCA plot for the Bruce *minimal* spectral library (Figure 5.3) – containing augite, enstatite, olivine, troilite, albite and FeNiMetalSub – mostly showed the expected trends. Troilite and FeNiMetalSub were close together, which is likely due to the relatively featureless nature of both spectra, especially in relation to the other end-members. Enstatite and augite were also close to each other as they

are both pyroxenes, with enstatite being an orthopyroxene (i.e., a pyroxene with orthorhombic crystal system) and augite a clinopyroxene (i.e., a pyroxene with monoclinic crystal stystem). Olivine and FeNiMetalSub being furthest apart on the PCA plot indicated that there was little to no similarity between the two, which was confirmed on visual inspection, as olivine had the greatest spectral contrast amongst the *minimal* Bruce spectral library, and FeNiMetalSub the least.

The PC1+PC2 explained variance ratio of 85.3% indicated that the variance across end-members in the *minimal* library was well described by just the first two principal components, and so interpretations based on proximity in PC1-PC2 space were reasonable.

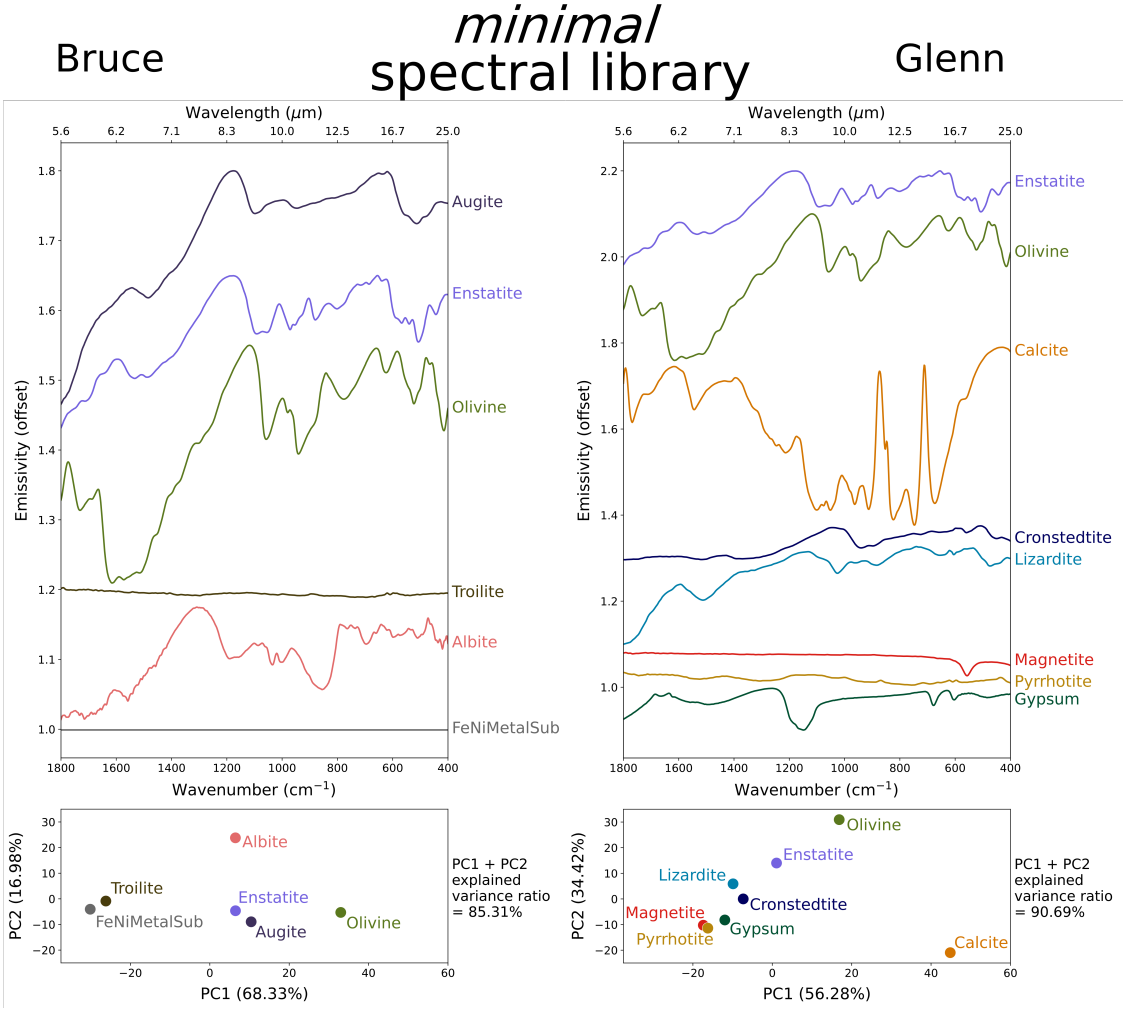


Figure 5.3: The *minimal* spectral libraries used for Bruce (left) and Glenn (right).

5.2.1.2 Glenn

The *minimal* spectral library for Glenn (Figure 5.3) was different to that for Bruce as the *minimal* version is designed to reflect the expected end-members (Section 4.1), which for Glenn were enstatite, olivine, calcite, cronstedtite, lizardite, magnetite, pyrrhotite and gypsum. On the PCA plot, magnetite and pyrrhotite were clustered, probably as they were the most featureless spectra across the spectral range within the library. Lizardite and cronstedtite were also very close together and is likely because they are both phyllosilicates. As was seen for the Bruce *minimal* spectral library, here the end-members with the largest difference in spectral contrast – calcite and magnetite/pyrrhotite – were located furthest apart on the PCA plot.

The high explained variance ratio of 90.7% indicated these were well-backed interpretations.

5.2.2 *expanded*

5.2.2.1 Bruce

For Bruce, the *expanded* spectral library (Figure 5.4) was designed to choose random extra end-members from all of those available in the *extensive* library (Table 4.1), up to a maximum library size of 10, with the addition of BB if not already selected, to expand on the foundations of the *minimal* spectral library. The construction of *expanded* was done only once in the early stages of investigation, and saved such that the same library was used for the all Bruce unmixings, allowing for fairer comparisons to be made between the algorithms. For Bruce, the additional end-members randomly selected were calcite, lizardite, gypsum and amorphous Fe, with BB also included manually.

Again, the PCA plot for Bruce's *expanded* spectral library followed prediction, with the relatively featureless spectra (BB, FeNiMetalSub and troilite) forming a cluster. Enstatite and augite were close together, with albite also in relatively close proximity, particularly on the PC1 axis. Looking at the albite spectrum in the context of the others in *expanded*, its morphology and spectral contrast

qualitatively more closely resemble those of enstatite and augite, and also arguably olivine, in comparison with the other end-members. Similarly, where olivine and FeNiMetalSub were the furthest apart due to their large difference in spectral contrast in Bruce's *minimal* library (Figure 5.3), in the *expanded* PCA plot, calcite and BB are furthest apart for the same reason of their extreme difference in spectral contrast within the context of the other spectra.

A high PC1+PC2 explained variance ratio of 84.9% supported these observations.

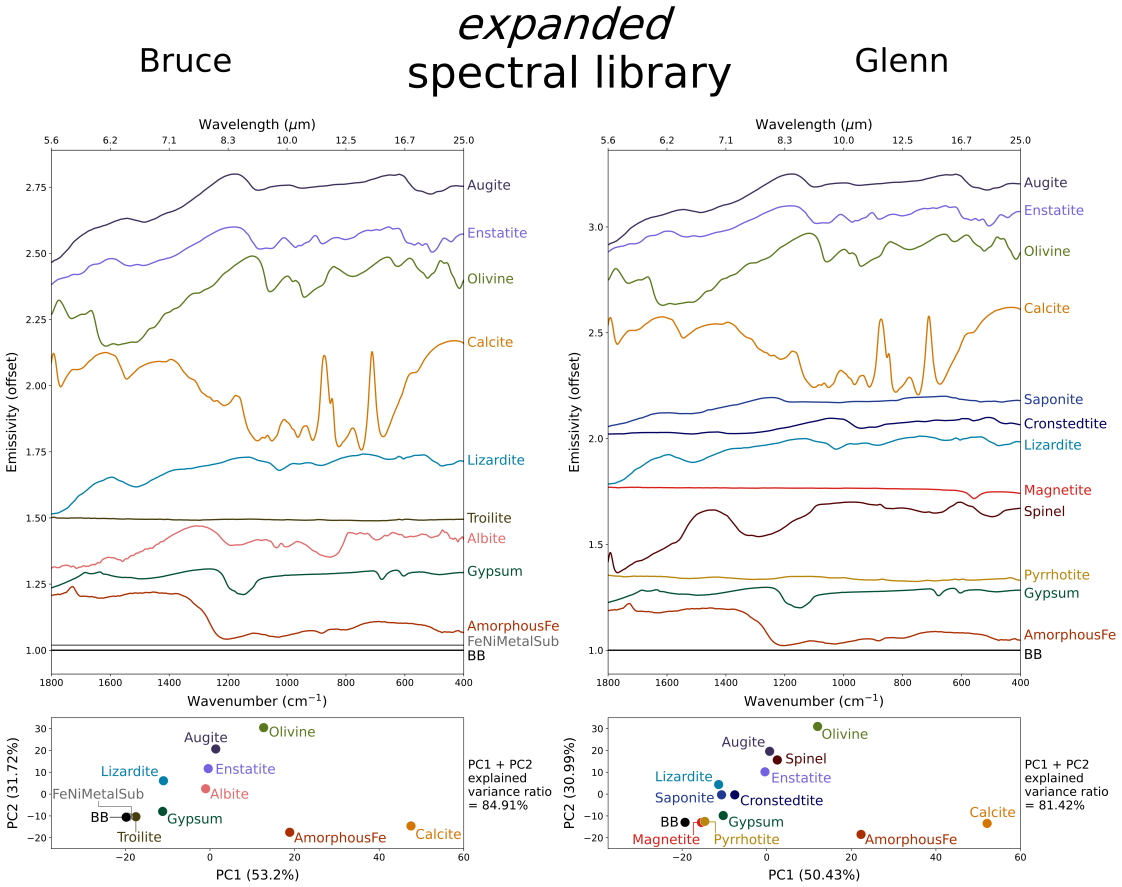


Figure 5.4: The *expanded* spectral libraries used for Bruce (left) and Glenn (right).

5.2.2.2 Glenn

For Glenn, the *expanded* spectral library (Figure 5.4) had a set maximum size of 12 to give the same difference in degrees of freedom between *min* and *exp* as for Bruce, and was also kept consistent for every Glenn unmixing against the *expanded*

library using each algorithm. The randomly selected extras were augite, saponite, spinel and amorphous Fe, and BB also added in manually.

Similarly to the Glenn *minimal* PCA plot (Figure 5.3), pyrrhotite and magnetite were clustered, with gypsum and BB nearby – these were all relatively flat/featureless and generally horizontal (i.e., very shallow to no overall slope across the entire spectral range). Lizardite, saponite and cronstedtite appeared in a cluster, also with gypsum nearby. As lizardite, saponite and cronstedtite are all phyllosilicates, it was expected that these would form a cluster in PC1-PC2 space. They were also relatively featureless with low spectral contrast when compared to some of the other end-member spectra such as olivine, calcite etc.

Augite and spinel could be considered a cluster, with enstatite a tenuous additional member. As augite and enstatite are both pyroxenes, we would expect them to be in close proximity on the PCA plot. Spinel being close to them as well could be due to its seemingly similar overall slope magnitude to augite and enstatite, and all three display a trough at $\sim 400 - 600\text{cm}^{-1}$ and peak at $\sim 600\text{cm}^{-1}$. As seen with the other PCA plots, BB and calcite, as the two end-members with the greatest difference in spectral contrast, were located on opposite sides. Again, the high explained variance ratio of 81.4% backed up these analyses.

5.2.3 *extensive*

Finally, the *extensive* spectral library (Figure 5.5) containing all 19 end-members from Table 4.1 was the same for both Bruce and Glenn, and displayed some interesting behaviour in PC1-PC2 space.

Again, the relatively featureless spectra (BB, FeNiMetalSub, magnetite, pyrrhotite and Murchison IOM) were very close together, appearing almost as a straight horizontal line. Perpendicular to the 'featureless' group, forming an almost straight vertical line was a cluster containing lizardite, saponite, cronstedtite and AmorphousMg – Lizardite, saponite and cronstedtite are all phyllosilicates, and looking at the whole *extensive* spectral library together, AmorphousMg could be considered to have a

similar scale of relatively low spectral contrast whilst still having identifiable features, as the phyllosilicates. Interestingly, gypsum was located at the corner/intersection of these perpendicular groupings and so could be considered a distant member of both. As gypsum was closer to the lizardite et al. cluster on the PC1 axis than it was to the BB et al. cluster, this may suggest that gypsum shared more similarities with the phyllosilicate end-members than the more featureless end-members. This interpretation was strengthened on visual inspection of the gypsum spectrum, as it had some notable, deep features (e.g., $\sim$ 1150, 780, 600cm^{-1}), similar to those seen in the lizardite et al. cluster spectra, but in between these (e.g., $\sim 1620-1220,\ 1080-700,\ 580-400$cm^{-1}) the spectrum was very flat/featureless, and the overall shape generally horizontal/very shallow sloped, as seen in the BB et al. cluster spectra.

Meanwhile, augite, anorthite, spinel and enstatite could be considered as a somewhat tenuous cluster – augite and enstatite are both pyroxenes (and also appeared in close proximity to each other in all the *minimal* and *expanded* libraries; Figures 5.3 and 5.4), and these with anorthite and spinel could be considered as displaying similarly steep CF roll-off gradients compared to the other spectra (e.g., Section 2.1 and Chapter 7). As with the *expanded* PCA plots, BB and calcite sat furthest apart, likely due to their extreme differences in spectral contrast across the entire range. Another high PC1+PC2 explained variance ratio of 81.8% implied these were reasonable interpretations.

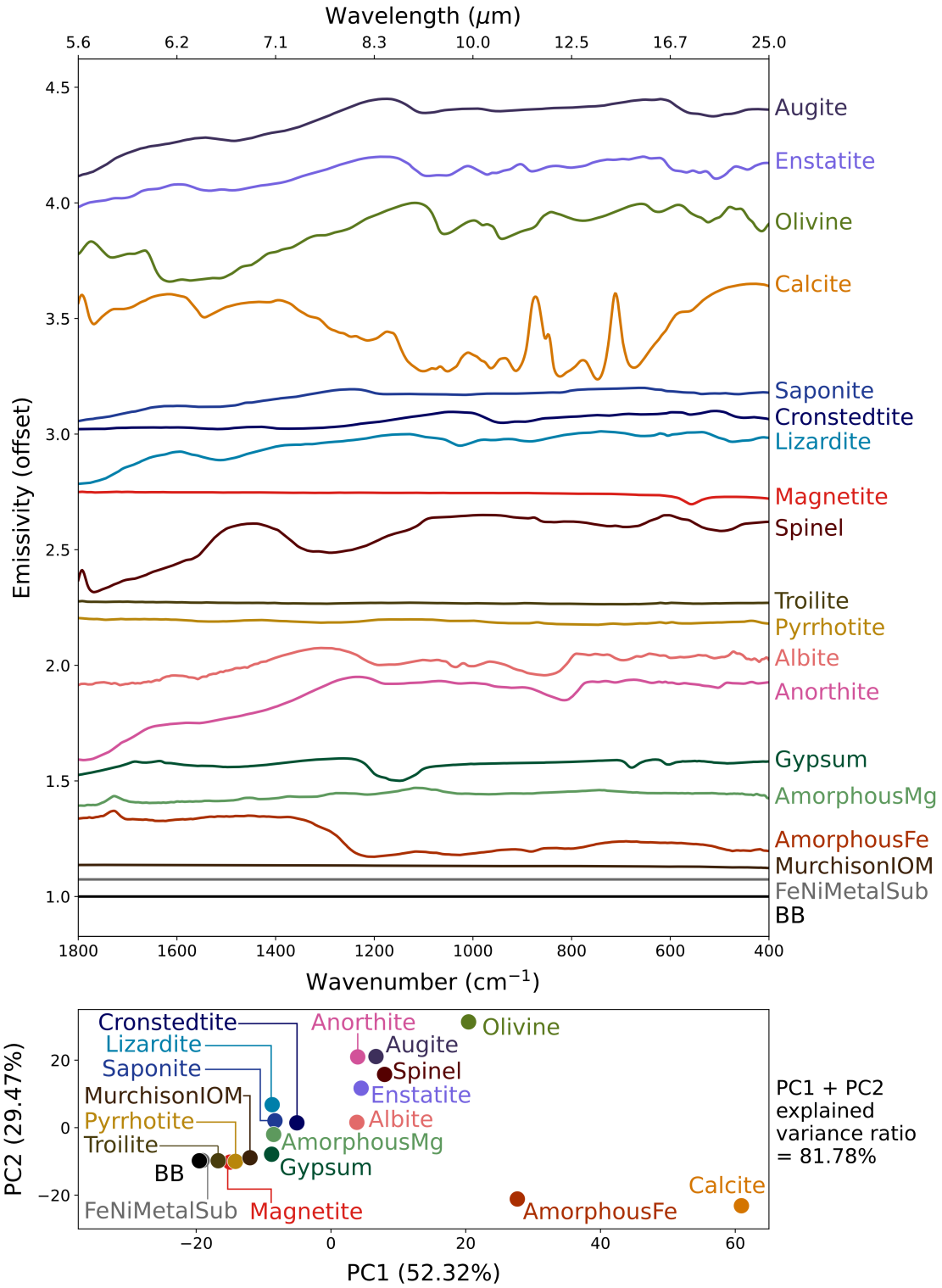


Figure 5.5: The *extensive* spectral library containing all end-members available (Table 4.1), used for both Bruce and Glenn unmixings.

5.2.4 Overall Spectral Library PCA Discussion and Summary

Overall, the PCA plots of Bruce and Glenn's *minimal*, *expanded* and *extensive* spectral libraries displayed some clustering between end-members of the same mineral grouping and/or general spectral morphology, as predicted, thus providing evidence of the degenerate nature of the spectral unmixing problem. This degeneracy means that there could be more than one configuration of end-members and their abundances that provide a good model fit, however, commonly used methods such as the linear least squares will only return the single 'best' solution (i.e., lowest residuals), which may not be correct.

Based on the application of PCA to the different spectral libraries, it was predicted that the Frequentist algorithm, `WLS_ASC_ILR()`, would perform increasingly poorly as more end-members were introduced in the spectral library (i.e., for the *expanded* and *extensive* unmixings), but that improvements would be seen with the addition of quantitative, explicit priors by taking a Bayesian approach with `OptEst_ASC_ILR()` and `MCMC()`.

5.3 Weighted Least Squares

The weighted least squares with abundance sum constraint and iterative library reduction, `WLS_ASC_ILR()`, was a Frequentist algorithm developed and used here for spectral unmixing. It followed the convention of Ramsey and Christensen 1998, forming a baseline representative of current techniques in order to allow for evaluation of improvements (if any) when adopting a Bayesian approach. More details on the `WLS_ASC_ILR()` algorithm can be found in Section 4.3.2.1.

Each mixture (*brucemath*, *brucereal*, *glennmath*, *glennreal*; discussed in Section 5.1) was unmixed against their *minimal*, *expanded* and *extensive* spectral libraries (discussed Section 5.2), resulting in three retrievals per mixture (12 in total for `WLS_ASC_ILR()`). The results and analysis of these are presented in the subsections below, where each unmixing follows the nomenclature of e.g., *brucemathmin*, which

refers to the mathematical Bruce spectrum being unmixed against the Bruce *minimal* spectral library.

5.3.1 Bruce

The idealised case (as used for initial algorithm development and testing) was captured in the mathematical Bruce unmixing against the *minimal* spectral library (*brucemathmin*).

In some preliminary work[2], unmixing *brucemathmin* with `WLS_ASC_ILR()` retrieved the exact correct abundances, as expected, and gave a perfect fit as indicated by the very low RMS (of the order 10^{-11}) and $\chi^2_{d.o.f}$ (of order 10^{-15}). Although the smaller the RMS, the better the fit, this very small $\chi^2_{d.o.f}$ showed that the model was 'over-fitting' the data, as it was $<< 1$ (where $\chi^2_{d.o.f} = 1$ indicates a perfect fit, and is the desired outcome; Section 3.3.3). These results were somewhat reassuring as they should (and did) show that the algorithm functions correctly, by simply returning what was put in. However, the $\chi^2_{d.o.f}$ was unrealistically small – we know that for a 'perfect' fit, $\chi^2_{dof} = 1$, and that the *brucemathmin* unmixing should give a perfect fit, so its $\chi^2_{d.o.f}$ should equal 1. As this was not the case, it would therefore make it difficult to compare this metric across other unmixings, and comment on their quality.

This problem of a very small $\chi^2_{d.o.f}$ was likely due to the small scale of uncertainties on the *brucemath* spectrum ($\sim 0.06\%$). The *brucemath* uncertainties were derived from full error propagation of the end-member spectra measurement uncertainties through the linear mixing equation (Equation 2.1), assuming no errors on the 'true' abundances. This resulted in the *brucemath* uncertainties being very small due to the propagation of small measurement uncertainties from the end-member spectra ($\sim 0.1 - 0.2\%$). Thus, to address the problem, randomly generated Gaussian distributed noise was added to both the signal and

[2]The preliminary work was intended to help determine how the final unmixings should be run; e.g., exact wavenumber range to be used, and how different versions of the priors would eventually be defined (Table 4.4). Therefore this preliminary work had some minor differences to what was adopted for the final unmixings analysed for this thesis.

uncertainty for *brucemath*; where the signal for *brucemath* was the spectrum itself, generated using the linear mixing model with the end-members and abundances specified in Table 4.2. When adding noise, both the signal and uncertainty were used for the μ value of their Gaussian distributions, and both took the OTES Noise Equivalent Delta Emissivity for the standard deviation of their Gaussian distributions, $\sigma = 0.003125$ (Christensen, Hamilton, et al. 2018). When unmixing this noisy version of *brucemath* against the *minimal* library with `WLS_ASC_ILR()`, this returned $\chi^2_{dof} = 47.0$ – a much more realistic value (compared to χ^2_{dof} of the order 10^{-15}) and clearly indicative of a poor model (as it was > 1).

To see what effect the addition of priors would have, and whether they may improve the fit, this noise addition test was repeated with the `OptEst_ASC_ILR()` algorithm using different versions of prior. These gave values of similar order of magnitude (i.e., $\chi^2_{d.o.f} \sim 30 - 50$), so as none of these were giving $\chi^2_{d.o.f} = 1$ (or close to it), I decided to revert back to using the measurement derived uncertainties for the full investigation as these are what would be used in future applications.

5.3.1.1 *brucemathmin* and *brucerealmin* Unmixings

***brucemathmin*: (Figure 5.6, Table 5.1)**

As with the preliminary tests discussed above, the *brucemathmin* unmixing with `WLS_ASC_ILR()` retrieved all the true abundances exactly; i.e., agreeing to within 0σ for all end-members (Table 5.1), and had a perfect fit (indicated by residuals at zero across the entire spectral range; Figure 5.6). This reinforced that the algorithm functions correctly, as it simply returned the input, therefore confirming validity for the remaining `WLS_ASC_ILR()` unmixings analyses. Similar to the preliminary work again, the RMS (5.84×10^{-12}) and $\chi^2_{d.o.f}$ (3.31×10^{-16}) were incredibly small, indicating an overconstrained fit.

The most precise retrieved abundances for the *brucemathmin* `WLS_ASC_ILR()` unmixing (Table 5.1) were for olivine (0.04%) and albite (0.48%), which were relatively distant from each other and the other clusters on the PCA plot (Figure

5.6). Here the connection between retrieved uncertainties and PCA could be made: olivine and albite being distant from the other end-members indicated that they were spectrally distinct, and so it would be likely for the algorithm to be able to estimate their abundances to high precision.

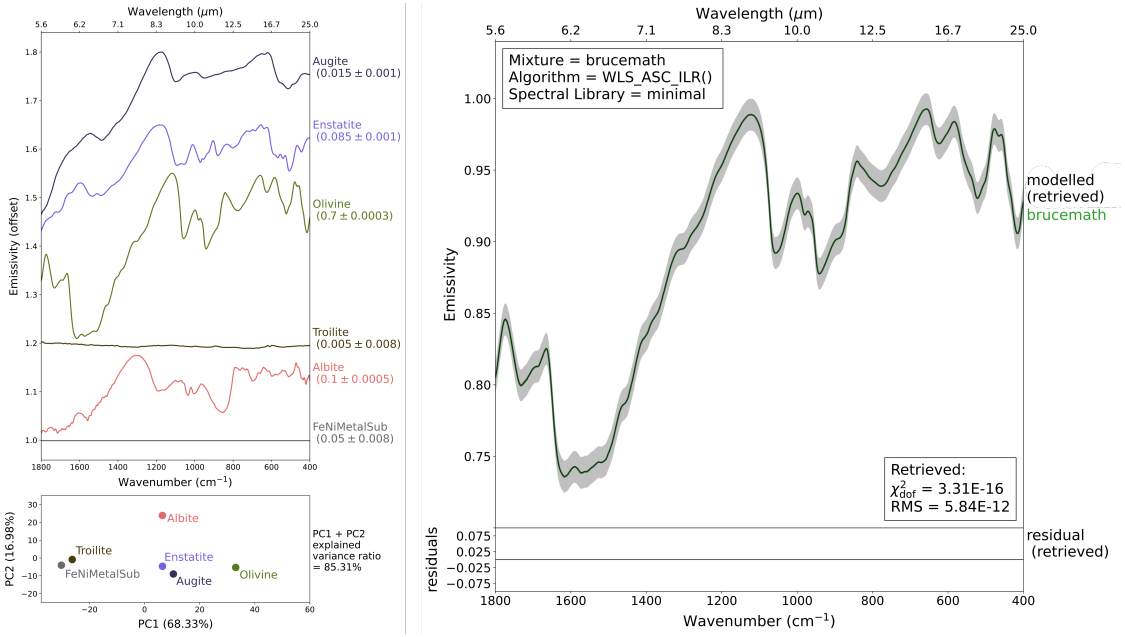


Figure 5.6: *brucemathmin* `WLS_ASC_ILR()` unmixing reduced spectral library with model fit. As this unmixing did not remove any end-members, the reduced spectral library was the same as the original Bruce *minimal* spectral library (Figure 5.3).

Table 5.1: *brucemathmin* `WLS_ASC_ILR()` unmixing results. Precision and accuracy were calculated via Equations 3.6 and 3.7 respectively. The unit for accuracy, σ, represents the retrieved abundance uncertainty.

End-member	**'True' Abundance**	**Retrieved Abundance**	**Uncertainty**	**Precision %**	**Accuracy σ**
Augite	0.015	0.015	0.000813	5.42	0
Enstatite	0.085	0.085	0.000877	1.03	0
Olivine	0.700	0.700	0.000305	0.04	0
Troilite	0.050	0.050	0.007695	15.39	0
Albite	0.100	0.100	0.000484	0.48	0
FeNiMetalSub	0.050	0.050	0.007937	15.87	0
RMS error	$\mathbf{5.84 \times 10^{-12}}$				
$\chi^2_{\text{d.o.f}}$	$\mathbf{3.31 \times 10^{-16}}$				

Augite and enstatite, however, were clustered on the PCA plot (Figure 5.6) indicating their similarity, which was reflected in the similar absolute values for their

retrieved abundance uncertainties (±0.00081 and ±0.00088, respectively; Table 5.1). The estimated augite and enstatite abundances were also strongly correlated (-0.79; Table 5.2), where the negative correlation was expected based on their clustering in the PCA plot (Figure 5.6) – due to their similarity and the sum to one constraint, the more of one there is, the less of the other there must be in order to compensate.

Table 5.2: *brucemathmin* `WLS_ASC_ILR()` unmixing correlation matrix. Notably 'strong' correlations ($> |0.6|$) are indicated in bold.

	Au	**En**	**Ol**	**Tr**	**Al**	**FeNi**
Augite (Au)	1.000	**-0.791**	-0.496	0.211	0.098	-0.205
Enstatite (En)	**-0.791**	1.000	0.097	0.053	-0.139	-0.075
Olivine (Ol)	-0.496	0.097	1.000	-0.061	-0.232	0.075
Troilite (Tr)	0.211	0.053	-0.061	1.000	0.192	**-0.998**
Albite (Al)	0.098	-0.139	-0.232	0.192	1.000	-0.229
FeNiMetalSub (FeNi)	-0.205	-0.075	0.075	**-0.998**	-0.229	1.000

Finally, troilite and FeNiMetalSub had similar uncertainties to each other (±0.0077 and ±0.0079, respectively), but were much larger than the other uncertainties by approximately an order of magnitude (Table 5.1), and were the least precise (of order 15%). This could also be attributed to their clustering on the PCA plot (Figure 5.6), their very strong correlation (-0.998; Table 5.2), and possibly also the fact that they were relatively featureless so did not have strong features that would be useful in fitting.

***brucerealmin*: (Figure 5.7, Table 5.3)**

For the *brucerealmin* unmixing using `WLS_ASC_ILR()`, the iterative library reduction procedure removed enstatite, troilite and albite. As enstatite and troilite were members of distinct clusters on the original Bruce *minimal* PCA plot (enstatite with augite, and troilite with FeNiMetalSub; Figure 5.3), it is possible that the algorithm struggled to identify their contributions as being separate from augite and FeNiMetalSub, respectively, which could highlight the significance of the difference between *brucereal* and *brucemath*.

The residuals for the *brucerealmin* `WLS_ASC_ILR()` unmixing (Figure 5.7), qualitatively looked almost identical (in morphology and scale) to the difference

between the *brucereal* and reduced contrast *brucemath* spectra (Figure 5.1), despite having half the number of end-members as *brucemath* to form the modelled spectrum from the *brucerealmin* unmixing. This demonstrated the issues of degeneracy within the spectral unmixing: different combinations of end-members and their abundances used in linear mixing gave very similar model fits.

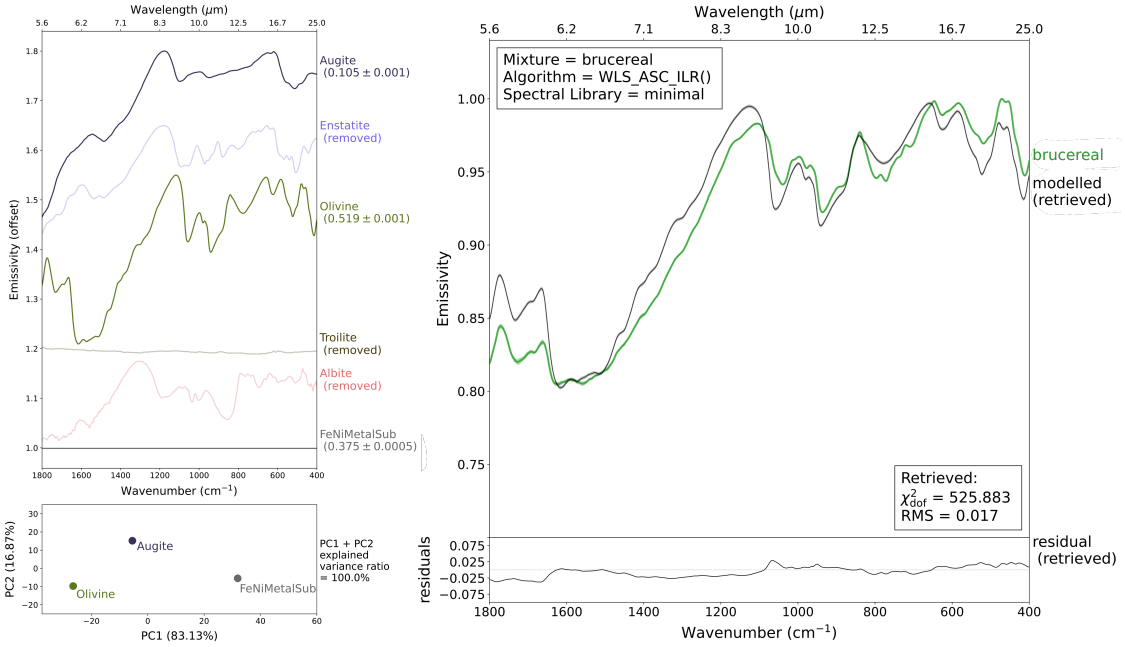


Figure 5.7: *brucerealmin* `WLS_ASC_ILR()` unmixing reduced spectral library with model fit.

Table 5.3: *brucerealmin* `WLS_ASC_ILR()` unmixing results. The unit for accuracy, σ, represents the retrieved abundance uncertainty, and a negative value here corresponds to an overestimation, whereas a positive value shows an underestimation. rm = removed.

End-member	**'True' Abundance**	**Retrieved Abundance**	**Uncertainty**	**Precision %**	**Accuracy σ**
Augite	0.015	0.105	0.000785	0.75	-116
Enstatite	0.085	rm			
Olivine	0.700	0.519	0.000530	0.10	340
Troilite	0.050	rm			
Albite	0.100	rm			
FeNiMetalSub	0.050	0.375	0.000484	0.13	-673
RMS error	**0.017**				
$\chi^2_{\mathbf{d.o.f}}$	**525.9**				

The reduced library PCA plot (Figure 5.7) showed the remaining three end-members (augite, olivine and FeNiMetalSub) well spread across the axes, providing

context as to why their retrieved abundance uncertainties were all so precise ($\leq 0.75\%$; Table 5.3) – more spectrally distinct end-members would be easier to identify and thus more likely to have their abundances estimated to high precision. Perhaps counter-intuitive to this was the high degree of correlation between the retrieved end-members (augite/olivine: -0.77, augite/FeNiMetalSub: -0.76); Table 5.4), however, it is useful to keep in mind here that with so few end-members and the abundance sum constraint, it was natural for there to be strong correlation. The high precision of the retrieved abundances, however, was almost cancelled out by the very poor accuracy ($\geq |116|\sigma$ – all far beyond the $|1|\sigma$ threshold often used in physics; Table 5.3).

Table 5.4: *brucerealmin* `WLS_ASC_ILR()` unmixing correlation matrix. Notably 'strong' correlations ($> |0.6|$) are indicated in bold.

	Au	**Ol**	**FeNi**
Augite (Au)	1.000	**-0.767**	**-0.759**
Olivine (Ol)	**-0.767**	1.000	0.166
FeNiMetalSub (FeNi)	**-0.759**	0.166	1.000

5.3.1.2 *brucemathexp* and *brucerealexp* Unmixings

***brucemathexp*: (Figure 5.8, Table 5.5)**

In the *brucemathexp* `WLS_ASC_ILR()` unmixing, augite was incorrectly removed, gypsum incorrectly kept, and BB also removed, meaning it was not possible to do the BB renormalisation step. The retrieved abundances had a wide range of precisions ($0.04 - 484.3\%$) and accuracies ($|0.3| - |25|\sigma$), as shown in Table 5.5. The high precisions of albite (0.52%), enstatite (0.55%) and olivine (0.04%), and the lower precisions of troilite (23.7%) and FeNiMetalSub (13.75%), were be explained by the reduced library PCA plot (Figure 5.8) and correlation matrix (Table 5.6): troilite and FeNiMetalSub were clustered in PC1-PC2 space, and had a very strong correlation of -0.996, thus leading to lower precisions.

The RMS (0.00042) and $\chi^2_{d.o.f}$ (0.498), along with visual inspection of the model, indicated another perfect fit with indiscernible residuals (Figure 5.8), as was the case with *brucemathmin* (Figure 5.6). This fit therefore provided further evidence

for the degenerate nature of the current state of spectral unmixing, and showed that even with only a few extra end-members in the spectral library, the linear mixing model in a weighted least squares algorithm was unable to retrieve the correct result for a spectrum created mathematically using the linear mixing model itself.

Table 5.5: *brucemathexp* `WLS_ASC_ILR()` unmixing results. The unit for accuracy, σ, represents the retrieved abundance uncertainty, and a negative value here corresponds to an overestimation, whereas a positive value shows an underestimation. rm = removed.

End-member	**'True' Abundance**	**Retrieved Abundance**	**Uncertainty**	**Precision %**	**Accuracy σ**
Augite	0.015	rm			
Enstatite	0.085	0.098	0.000538	0.55	-25
Olivine	0.700	0.703	0.000275	0.04	-11
Calcite	0.000	rm			
Lizardite	0.000	rm			
Troilite	0.050	0.035	0.008253	23.73	1.9
Albite	0.100	0.099	0.000515	0.52	1.1
Gypsum	0.000	0.0002	0.001	484.32	-0.3
Amorphous Fe	0.000	rm			
FeNiMetalSub	0.050	0.064	0.008860	13.75	-1.7
BB	n/a	rm			
RMS error	**0.00042**				
$\chi^2_{\text{d.o.f}}$	**0.498**				

Table 5.6: *brucemathexp* `WLS_ASC_ILR()` unmixing correlation matrix. Notably 'strong' correlations ($> |0.6|$) are indicated in bold.

	En	**Ol**	**Tr**	**Al**	**FeNi**	**Gy**
Enstatite (En)	1.000	-0.511	0.371	-0.126	-0.389	0.089
Olivine (Ol)	-0.511	1.000	0.155	-0.286	-0.155	0.267
Troilite (Tr)	0.371	0.155	1.000	0.003	**-0.996**	0.412
Albite (Al)	-0.126	-0.286	0.003	1.000	-0.005	-0.355
FeNiMetalSub (FeNi)	-0.389	-0.155	**-0.996**	-0.005	1.000	-0.481
Gypsum (Gy)	0.089	0.267	0.412	-0.355	-0.481	1.000

***brucerealexp*: (Figure 5.9, Table B.1)**

The *brucerealexp* unmixing using `WLS_ASC_ILR()` incorrectly removed augite, enstatite, troilite and albite (as well as BB), whilst incorrectly keeping lizardite and calcite; meaning that the only correct end-members retrieved were olivine and FeNiMetalSub. This therefore highlighted a major issue with this algorithm: the possibility to prematurely remove correct end-members.

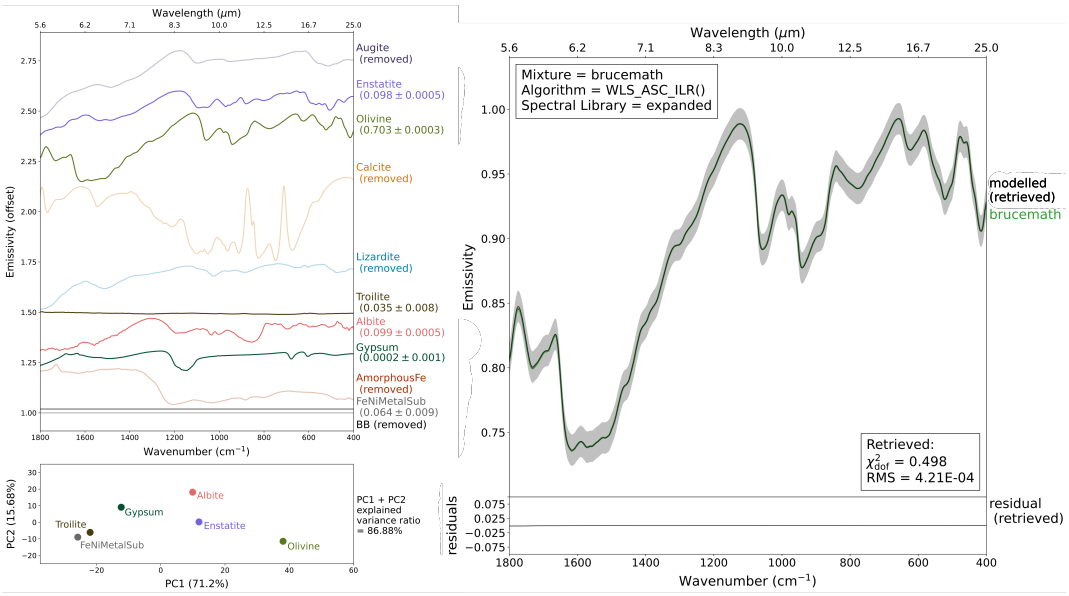


Figure 5.8: *brucemathexp* `WLS_ASC_ILR()` unmixing reduced spectral library with model fit.

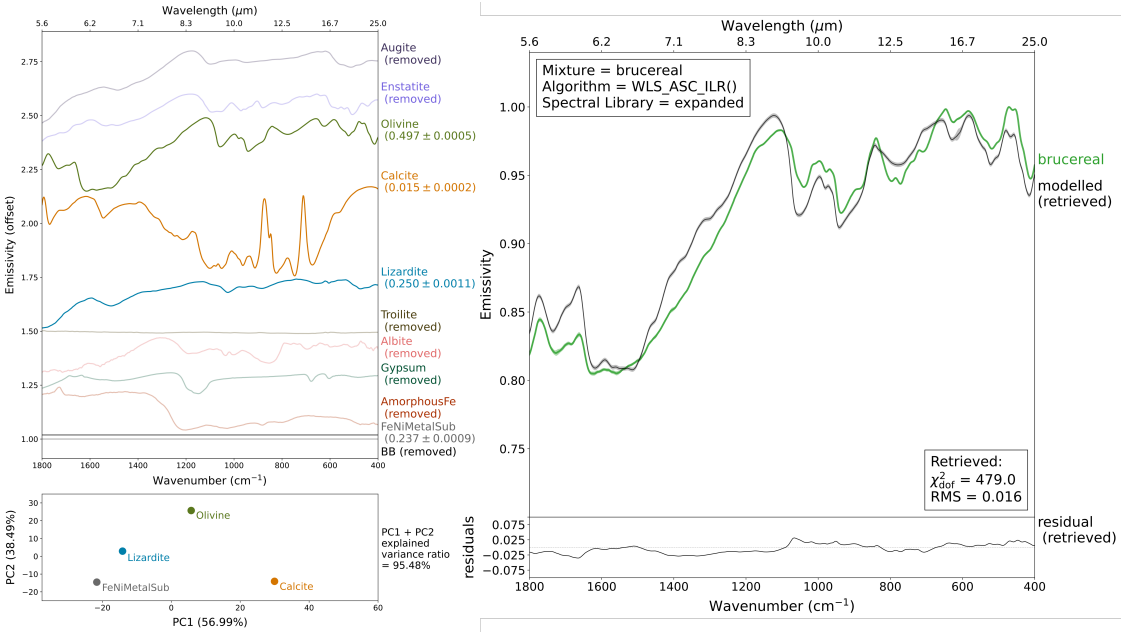


Figure 5.9: *brucerealexp* `WLS_ASC_ILR()` unmixing reduced spectral library with model fit.

Comparing this `WLS_ASC_ILR()` *brucerealexp* unmixing (Figure 5.9, Table B.1) to the *brucemathexp* unmixing (Figure 5.8, Table 5.5), in both cases augite, amorphous Fe and BB were removed; however, the additional removals for *brucemathexp* were lizardite and calcite (neither are in Bruce), but were enstatite, troilite, albite (all

are in Bruce), and gypsum (not in Bruce) for *brucerealexp*. Based on original Bruce *expanded* PCA plot (Figure 5.4), it looks like the *brucerealexp* `WLS_ASC_ILR()` unmixing removed any end-members that formed any kind of cluster, with the exception of keeping FeNiMetalSub, which was in a cluster with BB and troilite (and almost gypsum).

The impact of spectral library curation was evident when comparing the `WLS_ASC_ILR()` unmixings of *brucerealexp* and *brucerealmin* (Section 5.3.1.1). Augite (a correct end-member) was kept for the *brucerealmin* unmixing, but removed for the *brucerealexp* unmixing – this could perhaps be attributed to the larger number of degrees of freedom that comes with a larger spectral library, leading to a greater number of possible combinations of end-members for the solution, one of which retrieved a negative abundance of augite, resulting in its removal during one of the iterations. The very large $\chi^2_{d.o.f} = 479$ indicated a very poor fit, but slightly better (i.e., closer to 1) than *brucerealmin*'s $\chi^2_{d.o.f} = 526$, suggesting an improvement in fit with extra degrees of freedom, as brought by a larger spectral library.

There was also strong correlation between lizardite and olivine (-0.7; Table C.1), and very strong correlation between lizardite and FeNiMetalSub (-0.9). Although not especially close on the reduced PCA plot (Figure 5.9), lizardite was in between olivine and FeNiMetalSub and was probably slightly closer to either of these than any of them were to calcite; but again with so few end-members and a constraint to sum to one, there was bound to be some degree of correlation.

Generally, the unmixing of *brucerealexp* was very different to that of *brucemathexp*, with the only end-members kept by both unmixings being olivine and FeNiMetalSub. Uncertainty on the modelled spectrum for *brucerealexp* (Figure 5.9) was very narrow (about the width of the line), whereas it was much thicker for *brucemathexp* (Figure 5.8), and similarly to *brucerealmin*, the retrieved abundances had very high precision paired with very poor accuracy (Tables B.1 and 5.3).

5.3.1.3 *brucemathext* and *brucerealext* Unmixings

***brucemathext*: (Figure 5.10, Table B.2)**

The `WLS_ASC_ILR()` unmixing for *brucemathext* removed almost all of the end-members, keeping only enstatite and albite, and could be explained by the grouping patterns seen in the original *extensive* PCA plot (Figure 5.5). The large degree of clustering shows that the end-member spectra within the *extensive* spectral library are largely similar to one another, making them difficult to distinguish and difficult for their potential individual contributions to be identified during the unmixing process. Within the iterative library reduction (ILR) procedure, it is likely that similar end-members may have had opposing positive and negative abundances retrieved in order to satisfy the sum to one constraint; but in doing so, the negative end-member was removed and the inversion calculated again, finding another end-member with negative abundance to give the 'best' fit. This would have continued until there was a solution with only positive abundances, which in this case for *brucemathext*, was only able to retain enstatite and albite throughout the ILR procedure.

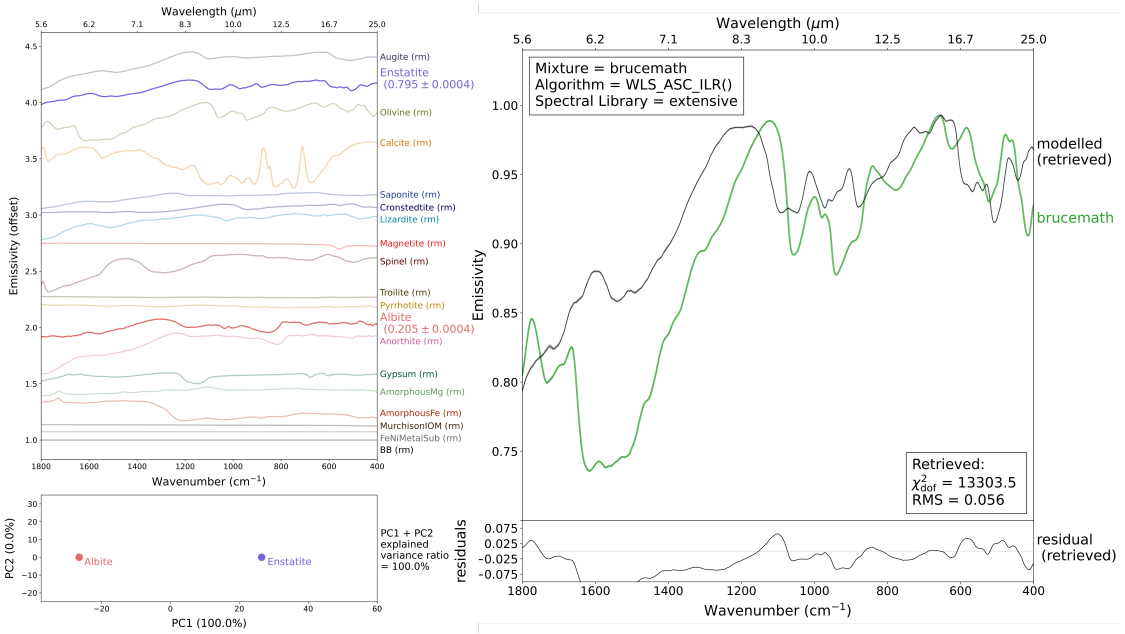


Figure 5.10: *brucemathext* `WLS_ASC_ILR()` reduced spectral library with model fit. rm=removed.

It came as quite a surprise to see the removal of olivine from the spectral library since it was the dominant end-member in Bruce, and relatively isolated on the original *extensive* PCA plot (Figure 5.5). It is possible that with the wide range of end-member options in early iterations, there may have been some combination that led to olivine having a negative abundance and therefore being removed, thus further highlighting this disadvantage of the `WLS_ASC_ILR()` algorithm.

Based on the final fit (Figure 5.10) and results (Table B.2), it appeared as though `WLS_ASC_ILR()` struggled to find a solution with the remaining end-members (enstatite and albite), leading to a very poor fit (reflected in the $\chi^2_{d.o.f} = 13303$) and very inaccurate abundances ($\geq |297|\sigma$). The residuals looked almost spectral-like (Figure 5.10), indicating missing end-members, of which we know were many. To avoid this issue of correct end-members missing, it is likely that an additional requirement of `WLS_ASC_ILR()` could have been to force the retention of the correct end-members (e.g., olivine in this case), but would be another form of including implicit *a priori* information. Within a Bayesian framework, however, it would be possible to set the explicit priors in such a way that certain end-members (like olivine) would be more likely to be kept.

***brucerealext*: (Figure 5.11, Table 5.7)**

Finally, the *brucerealext* `WLS_ASC_ILR()` unmixing removed most of the end-members; including correct end-members augite, enstatite, troilite, albite and FeNiMetalSub. Unlike with *brucemathext* (discussed above), here, olivine was kept, along with cronstedtite, spinel, anorthite and BB. Based on the original *extensive* PCA plot (Figure 5.5), anorthite, augite and spinel were clustered, so it is possible that `WLS_ASC_ILR()` picked out anorthite and spinel instead of augite (located between anorthite and spinel).

In this *brucerealext* `WLS_ASC_ILR()` unmixing, BB was kept, and so the BB renormalisation step took place, leading to two solutions (both of which are shown in Figure 5.11 and Table 5.7).

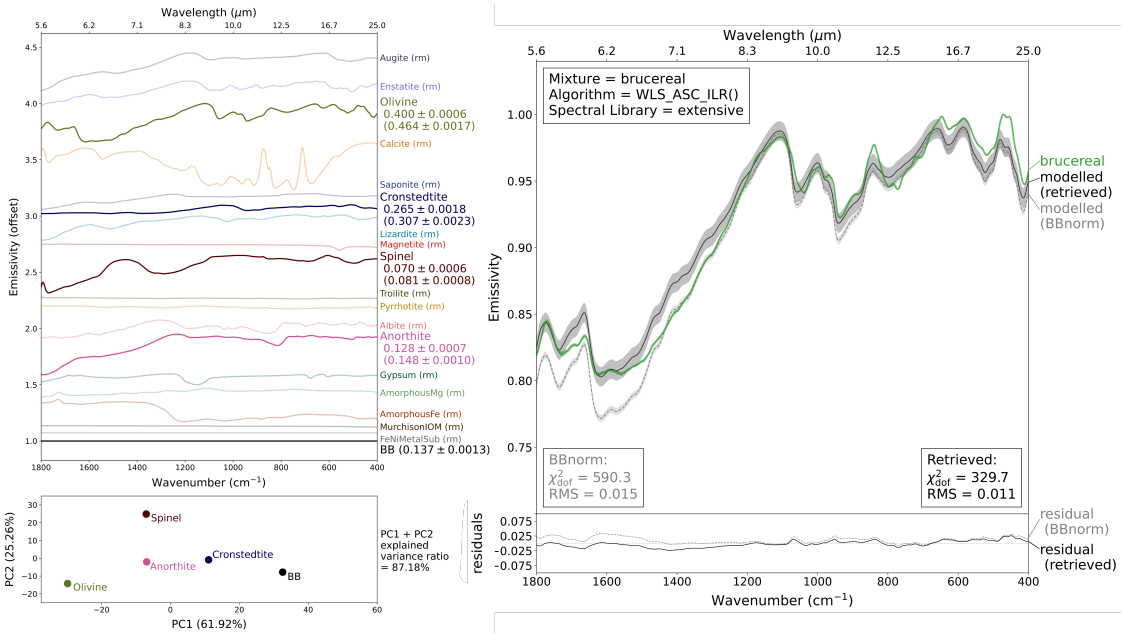


Figure 5.11: *brucerealext* `WLS_ASC_ILR()` reduced spectral library with model fit. rm=removed

The RMS and $\chi^2_{d.o.f}$ (0.0109 and 329.7, respectively) from the retrieved abundances model fit were smaller than those from the BB normalised abundances model fit (0.0151 and 590.3, respectively), indicating that the BB normalised abundances gave a worse fit (as expected – they were not the values retrieved based on a solution that minimises the residuals). This was also apparent in Figure 5.11, which showed the residuals from the BB normalised model being consistently further from zero across the entire spectral range, than the residuals from the retrieved abundance model.

Although the retrieved abundances gave a model with a better spectral fit, the BB normalised abundances were more accurate, as indicated by these abundances being within fewer σ to the true abundances than the retrieved values were (Table 5.7). However, both the retrieved and BB normalised solutions were poor, especially as most of the end-members kept were not actually part of the Bruce mixture, all abundances had accuracies $\geq |107|\sigma$, and $\chi^2_{d.o.f} >> 1$.

The very different results here for *brucerealext* compared to *brucemathext* could be considered as further evidence of the significant difference between the real and

mathematical versions of a mixture, thus demonstrating the limitations of the linear mixing model.

Table 5.7: *brucerealext* `WLS_ASC_ILR()` unmixing results. The unit for accuracy, σ, represents the retrieved abundance uncertainty, and a negative value here corresponds to an overestimation, whereas a positive value shows an underestimation. Values within square brackets are corresponding values from blackbody renormalisation (BBnorm; Equation 4.6). rm=removed.

End-member	**'True' Abundance**	**Retrieved Abundance [BBnorm]**	**Uncertainty [BBnorm]**	**Precision % [BBnorm]**	**Accuracy σ [BBnorm]**
Augite	0.015	rm			
Enstatite	0.085	rm			
Olivine	0.700	0.400 [0.464]	0.000060 [0.00169]	0.15 [0.36]	501 [141]
Calcite	0.000	rm			
Saponite	0.000	rm			
Cronstedtite	0.000	0.265 [0.307]	0.00060 [0.00169]	0.69 [0.76]	-146 [132]
Lizardite	0.000	rm			
Magnetite	0.000	rm			
Spinel	0.000	0.070 [0.081]	0.00061 [0.00076]	0.88 [0.94]	-115 [-107]
Troilite	0.050	rm			
Pyrrhotite	0.000	rm			
Albite	0.100	rm			
Anorthite	0.000	0.128 [0.148]	0.00073 [0.00098]	0.57 [0.66]	-176 [-153]
Gypsum	0.000	rm			
Amorphous Mg	0.000	rm			
Amorphous Fe	0.000	rm			
MurchisonIOM	0.000	rm			
FeNiMetalSub	0.050	rm			
BB	n/a	0.137	0.00134	0.98	n/a
RMS error	**0.0109** [**0.0151**]				
$\chi^2_{\mathbf{d.o.f}}$	**329.7** [**590.3**]				

5.3.1.4 Summary of Bruce `WLS_ASC_ILR()` Unmixings

Across all the Bruce unmixings with `WLS_ASC_ILR()`, the clear differences between the results for *brucemath* and *brucereal* could indicate not only that the algorithm

was insufficient, but that linear mixing as the underlying model was also insufficient.

Discrepancies between which end-members were kept/removed for the same mixture spectrum (i.e., *brucemath* or *brucereal*) with different spectral libraries (*min*, *exp* and *ext*) showed the implicit bias introduced in spectral library selection; particularly for *brucerealexp* (Section 5.3.1.2) vs *brucerealext* (Section 5.3.1.3). Additionally, the very different selection of end-members for *brucemath* vs *brucereal* using the same spectral library could indicate the unsuitability of linear mixing as the underlying model – the model and observation were sufficiently mismatched such that different end-members were kept/removed during the iterative library reduction (ILR) process. However, the core issue of which end-members were kept/removed in `WLS_ASC_ILR()` made it somewhat unclear if a better algorithm, in which it is possible to set priors (i.e., Bayesian), could solve this problem.

Overall, many of the disadvantages of the classical Frequentist linear least squares algorithm were demonstrated in the Bruce `WLS_ASC_ILR()` unmixings: i.e., implicit priors/bias from the spectral library, degenerate nature of the problem not taken into account, and the premature removal of correct end-members. Therefore these unmixings showed that `WLS_ASC_ILR()` with linear mixing is unsuitable where fine grains dominate, thus justifying the need to work towards an improvement.

Although this is a clear conclusion from these experiments, these were still only considering one sample (Bruce), so in order to consolidate these findings, the investigation was repeated for another sample, Murchison (a.k.a., Glenn), as shown below.

5.3.2 Glenn

5.3.2.1 *glennmathmin* and *glennrealmin* Unmixings

***glennmathmin*: (Figure A.1, Table 5.8)**

Despite Glenn being a naturally more complex mixture than Bruce (Section 4.2.2), unmixing *glennmathmin* may be considered an idealised case for which we would expect another 'perfect' retrieval, as seen for *brucemathmin* (Section 5.3.1.1).

Indeed, with residuals from the `WLS_ASC_ILR()` unmixing of *glennmathmin* being very close to zero (of the order 10^{-5}), RMS = 0.0003, and $\chi^2_{d.o.f} = 0.57$, these indicated an almost perfect fit. However, this unmixing could not be considered 'correct' as magnetite (a known component of Glenn with abundance = 0.015; Table 4.3) was removed. The remaining end-members were all retrieved with high precision ($< 7\%$; with the majority $< 2\%$) but low accuracy ($> |1|\sigma$), with gypsum and olivine being the most accurate and the only abundances within 3σ of their true values ($|1.6|\sigma$ and $|2.9|\sigma$, respectively; Table 5.8).

Table 5.8: *glennmathmin* `WLS_ASC_ILR()` unmixing results. The unit for accuracy, σ, represents the retrieved abundance uncertainty, and a negative value here corresponds to an overestimation, whereas a positive value shows an underestimation. rm=removed.

End-member	**'True' Abundance**	**Retrieved Abundance**	**Uncertainty**	**Precision** %	**Accuracy** σ
Enstatite	0.080	0.0727	0.0008	1.15	9
Olivine	0.113	0.1117	0.0004	0.40	2.9
Calcite	0.008	0.0055	0.0001	2.58	19
Cronstedtite	0.529	0.5218	0.0013	0.26	6
Lizardite	0.233	0.2421	0.0010	0.42	-9
Magnetite	0.015	rm			
Pyrrhotite	0.009	0.0306	0.0010	3.24	-22
Gypsum	0.014	0.0154	0.0009	6.07	-1.6
RMS error	**0.00029**				
$\boldsymbol{\chi^2_{d.o.f}}$	**0.569**				

The removal of magnetite could be explained by the original *minimal* PCA plot for Glenn (Figure 5.3), as the two end-members closest together were magnetite and pyrrhotite, so the `WLS_ASC_ILR()` algorithm may have had difficulty distinguishing their contributions to *glennmath* as being from individual components. Additionally, the abundance retrieved for pyrrhotite was overestimated ($0.031 \pm 0.001(3.2\%)$ – within 22σ of 'true' abundance 0.009; Table 5.8), possibly to contain the spectral contributions from both magnetite and pyrrhotite. Despite its spectral similarity to pyrrhotite (as indicated by their proximity in Glenn's *minimal* PC1-PC2 space of Figure 5.3), the removal of magnetite could indicate the unsuitability of this algorithm, particularly as it had relatively high abundance in the mixture (0.015: greater than calcite's 0.008, pyrrhotite's 0.009 and gypsum's 0.014; Table 5.8).

***glennrealmin*: (Figure 5.12, Table B.3)**

For *glennrealmin*, the `WLS_ASC_ILR()` algorithm incorrectly removed over half of the end-members, however, it seemed to have been able to identify the two most abundant end-members – cronstedtite ('true' abundance = 0.529) and lizardite ('true' abundance = 0.233) – as individuals, despite their close proximity on the original Glenn *minimal* PCA plot (Figure 5.3).

Upon visual inspection of the *glennrealmin* modelled spectrum in Figure 5.12, it was apparent that the fit was poor, as none of the modelled features aligned with with the *glennreal* spectrum across the entire spectral range (with the exception of $\sim$ 600cm^{-1}, however this region is known to be affected by a fault with the beamsplitter within the spectrometer). Despite the poor recreation of the *glennreal* spectrum with the *glennrealmin* `WLS_ASC_ILR()` derived modelled spectrum, the residuals were of relatively small scale ($\leq \pm 0.015$ across the entire spectral range), and the RMS = 0.007 and $\chi^2_{d.o.f} = 4.6$ were suggestive of a relatively accurate fit. The retrieved abundances themselves had a large range of accuracies ($|15| - |108|\sigma$; all $>> |1|\sigma$), and were generally quite precise ($< 5\%$; Table B.3).

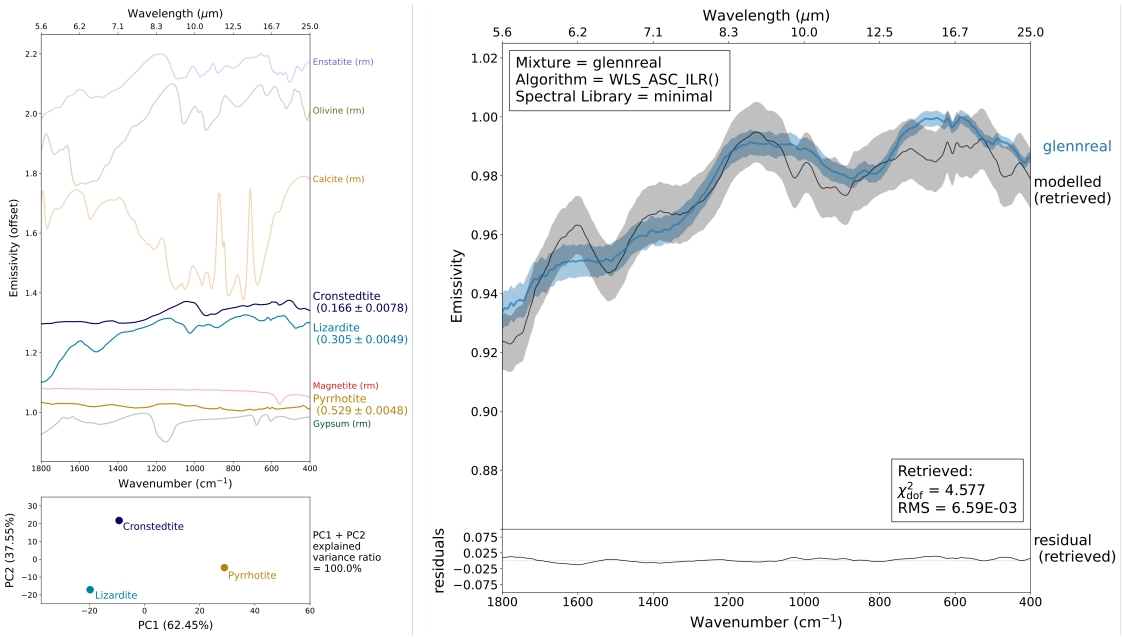


Figure 5.12: *glennrealmin* `WLS_ASC_ILR()` reduced spectral library with model fit. rm=removed.

Overall, these results from unmixing Glenn with `WLS_ASC_ILR()` against its *minimal* spectral library strengthened the argument that current unmixing methods can find good fits (as indicated by small scale of residuals, $\leq \pm 0.015$, and $\chi^2_{d.o.f}$ close to 1), but these did not necessarily represent the correct solution. Additionally, these analyses show that the discrepancy between the *glennmath* and *glennreal* spectra was sufficient to impact their unmixings, which may point to the linear mixing model being insufficient.

5.3.2.2 *glennmathexp*, *glennrealexp*, *glennmathext* and *glennrealext* Unmixings

The main contribution that the *glennmathexp* (Figure A.2), *glennrealexp* (Figure A.3, Table B.4), *glennmathext* (Figure A.4, Table B.5), and *glennrealext* (Figure A.5, Table B.6) `WLS_ASC_ILR()` unmixings gave to the overall analysis was to consolidate previous results that a 'good' fit (as indicated by the scale of residuals across the spectral range, and values for the RMS and $\chi^2_{d.o.f}$) did not always correspond to 'good' abundances (as indicated by the accuracy of estimated abundances from the unmixing). There was again a discrepancy in which end-members were kept/removed from the original Glenn *expanded* spectral library (Figure 5.4) when unmixing *glennreal* vs *glennmath*; further demonstrating the inaccuracy in which the linear mixing model replicates observation.

Overall, the results of unmixing Glenn with `WLS_ASC_ILR()` displayed much of the same issues seen for the Bruce mixture, thus strengthening the case for developing an improved model and algorithm.

5.3.3 Overall `WLS_ASC_ILR()` Unmixings Discussion

Throughout this Section (5.3), the results of unmixing real and mathematical versions of the Bruce and Glenn samples with the `WLS_ASC_ILR()` unmixing algorithm against their *minimal*, *expanded* and *extensive* spectral libraries have demonstrated some of the major issues with current spectral interpretation techniques (i.e., using the linear mixing forward model in a linear least squares unmixing/retrieval algorithm).

Although some of the model fits were 'good', as indicated by the fit quality metric (introduced in Section 3.3.3 and outlined in Table 5.9) and visual inspection of both the modelled spectra and their residuals, many of these gave a completely incorrect solution (i.e., the wrong selection and/or estimated abundances of end-members), as captured quantitatively by the abundance quality metric (Section 3.3.3) per unmixing. The fit and abundance quality metric values for the `WLS_ASC_ILR()` unmixings are summarised in Table 5.9; highlighting the discrepancy between unmixings that gave a 'good' fit, and those that gave 'good' abundance estimates, thus also proving the significance of the degenerate nature of the spectral mixing problem. The analyses presented throughout this Chapter have shown that there are non-unique solutions which can result in fits of similar quality; thus the classical linear least squares approach is not well suited to handle this issue, as it will only give the single 'best' fit without indicating other solutions that may have similarly 'good' fits but could have more accurate results.

The issue of degeneracy is due to similarities between end-member spectra within the spectral library; and, for some of the unmixings, the original PCA plots were indicative of where the algorithm may have struggled to distinguish certain end-members from one another (as presented in these analyses). Further PCA of the reduced spectral libraries (following the iterative library reduction, ILR, procedure), and interpretation of the correlation matrices, have shown that the end-members were not completely independent, with many of the retrieved end-member abundances displaying strong correlations ($>|0.6|$). If the end-member spectra were truly independent, as required by the linear mixing model, their correlations would be zero (or very close to it), which was not the case.

Using different versions of spectral libraries (introduced in Section 4.1) for these `WLS_ASC_ILR()` unmixings has also demonstrated the implicit bias introduced by the selection of end-members for the libraries. Each of the unmixings with different libraries on the same mixture generally gave very different results, particularly in which end-members were retained or discarded in the ILR process. Additionally,

the all-round poor performance of unmixing against the *extensive* spectral library proved that, even if it was not impractical, using a very large spectral library is not a suitable solution to the subjectivity tied to spectral library curation.

Unmixing mathematical versions of samples has highlighted the unsuitability of a weighted least squares, as even for these cases where the spectra were created using the linear mixing model, the algorithm was often unable to retrieve the correct answers; and in fact with the *extensive* library the algorithm failed completely. However, this could have also been rooted in the degeneracy issue, making it unclear whether a new model or just a new algorithm is required.

Overall, these results of unmixing real and mathematical versions of the Bruce and Glenn samples using `WLS_ASC_ILR()` show that the current 'default' method used for spectral unmixing is insufficient for predominantly fine grained mixtures ($\leq 38\mu$m), even if the spectral library contains appropriately sized end-members; contrary to one of the conclusions of Ramsey and Christensen 1998 (Section 3.1.1).

To tackle some of these issues algorithmically, it may help to adopt a Bayesian approach, where it is possible to explicitly set quantitative and probabilistic priors. The next steps were therefore to trial an algorithm similar to least squares, with the only change being the addition of priors – the optimal estimation algorithm – followed by a fully Bayesian technique: Markov Chain Monte Carlo (MCMC). Any similarities/differences in the unmixings could indicate and identify issues rooted in the algorithm vs the model, which could then be the focus for further improvements.

Table 5.9: Retrieval quality metrics summary table for the `WLS_ASC_ILR()` unmixings of Bruce and Glenn. Values in square brackets correspond to metrics derived from the blackbody renormalised abundances (BBnorm). Details on these metrics and how to interpret them are covered in Section 3.3.3, where generally the smaller/closer to zero, the better the quality.

	`WLS_ASC_ILR()`	Fit Quality $(1-\chi^2_{d.o.f})\times$ RMS [BBnorm]	Abundance Quality accuracy $\times$ precision [BBnorm]
Bruce	*brucemathmin*	5.84×10^{-12}	0
	brucemathexp	2.11×10^{-4}	5.68
	brucemathext	-744.9	1.27
	brucerealmin	-8.9	1.13
	brucerealexp	-7.65	1.18
	brucerealext	-3.6	1.33
		[-8.8]	[0.90]
Glenn	*glennmathmin*	1.25×10^{-4}	0.19
	glennmathexp	1.28×10^{-4}	0.34
		[-0.04]	[0.37]
	glennmathext	-35.4	1.41
	glennrealmin	-0.02	1.35
	glennrealexp	-7.27×10^{-4}	2.34
		[-4.7]	[0.25]
	glennrealext	-1.70×10^{-3}	6.41
		[-21.2]	[1.64]

Chapter 6

Results and Discussion: A Bayesian Approach and Algorithm Comparisons

Contents

6.1 Optimal Estimation 115
6.1.1 Bruce 115
6.1.1.1 *brucemathmin* Unmixings 115
6.1.1.2 *brucerealmin* Unmixings 120
6.1.1.3 *brucemathexp* Unmixings 123
6.1.1.4 *brucerealexp* Unmixings 127
6.1.1.5 *brucemathext* Unmixings 127
6.1.1.6 *brucerealext* Unmixings 130
6.1.1.7 Summary of Bruce `OptEst_ASC_ILR()` Unmixings 131
6.1.2 Glenn 132
6.1.2.1 *glennmathmin* Unmixings 132
6.1.2.2 *glennrealmin* Unmixings 136
6.1.2.3 *glennmathexp* Unmixings 139
6.1.2.4 *glennrealexp* Unmixings 139
6.1.2.5 *glennmathext* Unmixings 143
6.1.2.6 *glennrealext* Unmixings 143
6.1.3 Overall `OptEst_ASC_ILR()` Unmixings Discussion . . . 145
6.2 Markov Chain Monte Carlo 149
6.2.1 Bruce 150
6.2.1.1 *brucemathmin* Unmixings 150
6.2.1.2 *brucerealmin* Unmixings 159
6.2.1.3 *brucemathexp* Unmixings 165
6.2.1.4 *brucerealexp* Unmixings 170
6.2.1.5 *brucemathext* Unmixings 170
6.2.1.6 *brucerealext* Unmixings 175
6.2.1.7 Summary of Bruce `MCMC()` Unmixings 176
6.2.2 Glenn 177
6.2.2.1 *glennmathmin* Unmixings 177

6.2.2.2 *glennrealmin* Unmixings 180
6.2.2.3 *glennmathexp* Unmixings 185
6.2.2.4 *glennrealexp* Unmixings 185
6.2.2.5 *glennmathext* Unmixings 188
6.2.2.6 *glennrealext* Unmixings 192
6.2.3 Overall `MCMC()` Unmixings Discussion 195
6.3 Spectral Unmixing Algorithm Comparisons and Overall Conclusions 199

For a fair comparison across spectral unmixing algorithms, the `WLS_ASC_ILR()` *brucereal*, *brucemath*, *glennreal* and *glennmath* unmixings of Chapter 5 were repeated with Bayesian algorithms, `OptEst_ASC_ILR()` and `MCMC()`. For the Bayesian unmixings, the same *minimal*, *expanded* and *extensive* spectral libraries were used (as shown in Figures 5.3, 5.4 and 5.5, respectively), each additionally using different versions of **priors** (Table 4.4).

To simulate a range of possibilities when setting priors, I set up four different versions of these priors, labelled *P1*→*P4*, as defined in Table 4.4. These priors were designed to simulate a range of different situations where there may be differing combinations of 'loose' priors – i.e., low confidence in the given prior value; e.g., 0.3004 ± 0.3007 (100.1%) – and 'tight' priors – i.e., high confidence in the given prior value; e.g., 0.3004 ± 0.0003 (0.1%). Therefore, each mixture (*brucemath*, *brucereal*, *glennmath*, *glennreal*) was unmixed against their *minimal*, *expanded* and *extensive* spectral libraries using the different versions of the priors, *P1*, *P2*, *P3* and *P4* for each library, resulting in twelve retrievals per mixture for `OptEst_ASC_ILR()`. The `MCMC()` algorithm also used *P1*→*P4* as Gaussian priors, as well as the Uniform prior, *U*, to provide the most 'diffuse'/'uninformative' option for the prior distribution, giving fifteen retrievals per mixture. Each Bayesian unmixing followed the naming convention of e.g., *glennmathminP1* (the mathematical version of Glenn being unmixed against its *minimal* spectral library, using the *P1* priors).

6.1 Optimal Estimation

The optimal estimation with abundance sum constraint and iterative library reduction, `OptEst_ASC_ILR()`, algorithm was what may be considered a meeting point between Frequentist and Bayesian techniques, providing a step towards more sophisticated computational methods whilst retaining the ease of a weighted least squares. Without the addition of priors, optimal estimation (Equation 4.4) simply collapses to the linear least squares form (Equation 4.1), and so can be a way to test how the sole addition of priors impacts the unmixing. More details on `OptEst_ASC_ILR()` can be found in Section 4.3.2.2.

6.1.1 Bruce

6.1.1.1 *brucemathmin* Unmixings

As in Section 5.3.1.1, unmixing *brucemathmin* was an idealised case, making it particularly useful to see the impact of different types of priors on the unmixing.

***P1* (Figure 6.1, Table 6.1):**

For the `OptEst_ASC_ILR()` unmixing of *brucemathminP1*, the modelled spectrum and its residuals displayed a slight difference in spectral contrast, as most features were present and aligned; e.g., the primary CF at $\sim 1150\text{cm}^{-1}$, RB between $\sim 1050 - 850\text{cm}^{-1}$, and secondary CF at $\sim 650\text{cm}^{-1}$ (Figure 6.1). However, the RMS $= 0.01$ and $\chi^2_{d.o.f} = 403.8$ were more indicative of a poor fit, and the retrieved abundances were all very inaccurate ($\geq |35|\sigma$) with high precision ($< 0.5\%$; Table 6.1).

Based on their retrieval quality metrics, the *brucemathminP1* `OptEst_ASC_ILR()` unmixing (fit quality $= -4.18$, abundance quality $= 3.26$; Table 6.12) performed much worse than the *brucemathmin* `WLS_ASC_ILR()` unmixing (which was essentially a perfect retrieval: fit quality $= 3.84 \times 10^{-12}$, abundance quality $= 0$; Table 5.9). This instantly showed the impact of priors – here, for *P1*, the priors were defined to all be very 'tight' (i.e., have high confidence/small uncertainties; $\pm 0.1\%$), which

theoretically would make it difficult for the algorithm to consider solutions away from these estimates; however, the retrieved abundances were not simply the same as these priors, thus giving some reassurance that the priors did not dominate over the data for the unmixing.

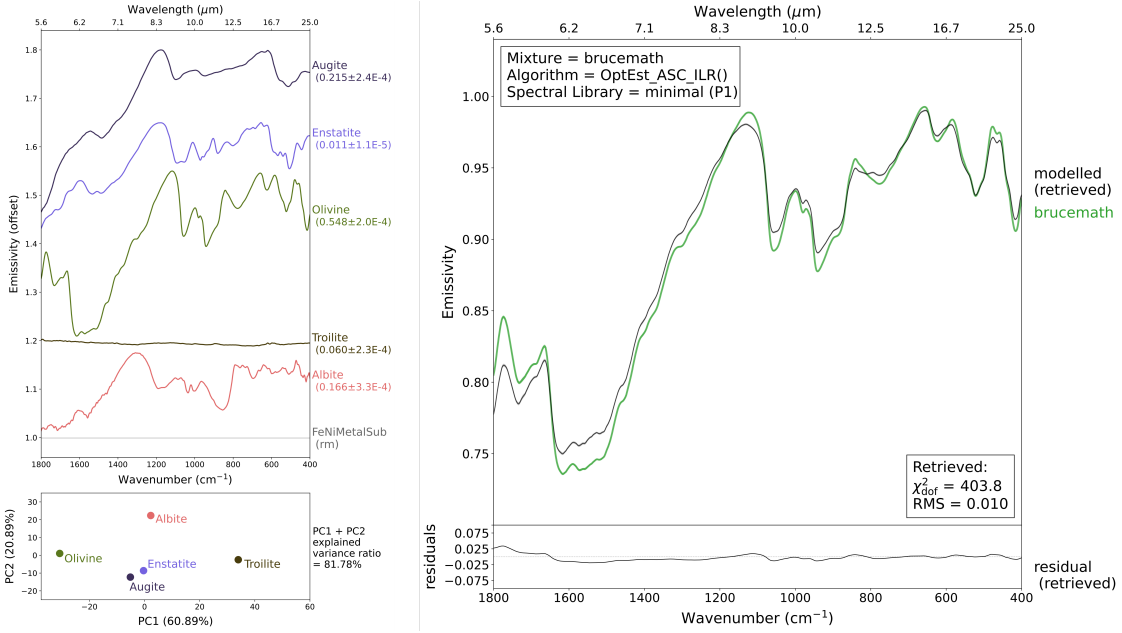


Figure 6.1: *brucemathminP1* `OptEst_ASC_ILR()` reduced spectral library with model fit. rm=removed.

The influence of the addition of priors can additionally be seen via the accuracy of the retrieved abundances in relation to the prior abundances, which were more accurate (mean of modulus of values = $|836|\sigma$) than the accuracies of retrieved abundances to the true answers (mean of modulus of values = $|1714|\sigma$; Table 6.1).

P2 (Figure 6.2, Table 6.2):

The unmixing of *brucemathminP2* with `OptEst_ASC_ILR()`, on the other hand, gave a 'perfect' retrieval, with visually perfect fit (shown by residuals at zero across the entire spectral range; Figure 6.2), small RMS = 8.48×10^{-6} and $\chi^2_{d.o.f} = 0.0004$, and all abundances very accurate to the true abundances ($\leq |0.52|\sigma$; Table 6.2).

The subtle differences between the *brucemathminP2* `OptEst_ASC_ILR()` unmixing and that of *brucemathmin* with `WLS_ASC_ILR()` (Section 5.3.1.1), such as exact

retrieved abundances and scale of errors (compare Tables 6.2 and 5.1), showed that even with the very 'loose' priors (i.e., low confidence/large uncertainties) of *P2*, simply the presence of priors had some effect on the retrieval.

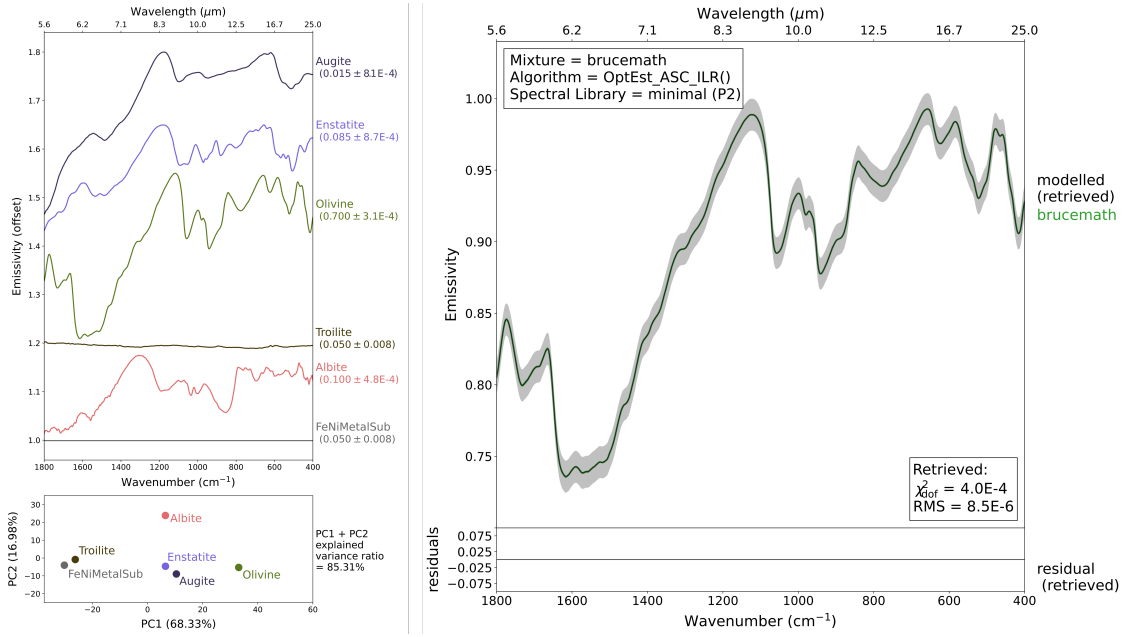


Figure 6.2: *brucemathminP2* `OptEst_ASC_ILR()` reduced spectral library with model fit.

It was expected that with the large uncertainties for *P2* (±100.1%), the optimal estimation algorithm would relax back to the weighted least squares (within rounding errors); as a large uncertainty on the prior can be considered almost like having no prior at all. However, the differences observed between the *brucemathminP2* `OptEst_ASC_ILR()` and *brucemathmin* `WLS_ASC_ILR()` unmixings could indicate that the precisions of the priors need to be poorer (> 100.1%) in order for the optimal estimation with loose priors to become equivalent to a weighted least squares.

P3 (Figure A.6, Table B.7):

Another 'perfect' retrieval came from the `OptEst_ASC_ILR()` unmixing of *brucemathminP3* (Figure A.6, Table B.7), which was to be expected given that the *P3* version of priors was defined to be the 'perfect' priors (i.e., the true abundances with high confidence for correct end-members; see definition in Table 4.4).

Table 6.1: *brucemathminP1* `OptEst_ASC_ILR()` results. The unit for accuracy, σ, represents the retrieved abundance uncertainty, and a negative value here corresponds to an overestimation, whereas a positive value shows an underestimation. rm=removed.

End-member	**'True' Abundance**	**Prior, P1**	**Retrieved Abundance**	**Accuracy to 'True' Abundance** σ	**Accuracy to P1 Abundance** σ
Augite	0.015	0.3004 ± 0.0003 (0.10%)	0.2148 ± 0.0002 (0.11%)	-845.7	362.5
Enstatite	0.085	0.0110 ± 1.10E-5 (0.10%)	0.0109 ± 1.10E-5 (0.10%)	6732.7	10.9
Olivine	0.700	0.3872 ± 0.0004 (0.10%)	0.5482 ± 0.0002 (0.04%)	752.9	-798.6
Troilite	0.050	0.5015 ± 0.0005 (0.10%)	0.0599 ± 0.0003 (0.48%)	-34.6	1550.3
Albite	0.100	0.6452 ± 0.0006 (0.10%)	0.1663 ± 0.0003 (0.20%)	-201.2	1454.6
FeNiMetalSub	0.050	0.8508 ± 0.0009 (0.10%)	rm		
		RMS	0.0104		
		$\chi^2_{\mathbf{d.o.f}}$	403.8		

Table 6.2: *brucemathminP2* `OptEst_ASC_ILR()` results. The unit for accuracy, σ, represents the retrieved abundance uncertainty, and a negative value here corresponds to an overestimation, whereas a positive value shows an underestimation.

End-member	**'True' Abundance**	**Prior, P2**	**Retrieved Abundance**	**Accuracy to 'True' Abundance** σ	**Accuracy to P2 Abundance** σ
Augite	0.015	0.3004 ± 0.3007 (100.1%)	0.0154 ± 0.0008 (5.28%)	-0.43	351.51
Enstatite	0.085	0.0110 ± 0.110 (100.1%)	0.0845 ± 0.0009 (1.03%)	0.52	-84.16
Olivine	0.700	0.3872 ± 0.3876 (100.1%)	0.7000 ± 0.0003 (0.04%)	0.05	-1024.15
Troilite	0.050	0.5015 ± 0.5020 (100.1%)	0.0504 ± 0.0077 (15.25%)	-0.06	58.64
Albite	0.100	0.6452 ± 0.6459 (100.1%)	0.1001 ± 0.0005 (0.48%)	-0.11	1127.60
FeNiMetalSub	0.050	0.8508 ± 0.8517 (100.1%)	0.0496 ± 0.0079 (15.99%)	0.05	100.96
		RMS	8.48E-06		
		red. Chi squ.	0.0004		

Tiny values for RMS = 4.91×10^{-15} and $\chi^2_{d.o.f} = 9.43 \times 10^{-23}$ (Table B.7) – even smaller than for *brucemathmin* `WLS_ASC_ILR()` (Table 5.1) – indicated that this retrieval was overconstrained, which was also expected as the priors added another level of constraint. Here, the exact true abundances were retrieved with extremely high precision ($\leq 0.1\%$; Table B.7), making all the abundance estimates much more precise than the `WLS_ASC_ILR()` unmixing ($< 16\%$; Table 5.1), and the `OptEst_ASC_ILR()` unmixings with *P1* ($< 0.5\%$; Table 6.1) and *P2* ($< 16\%$ Table 6.2) discussed above.

There were also no high correlation pairs with *P3* (Table C.2), indicating the high influence of the priors here (compared to other unmixings), as any retrieved abundance appeared to be more dependant on its prior than the other retrieved abundances.

***P4* (Figure 6.3, Table B.8):**

Unmixing *brucemathminP4* with `OptEst_ASC_ILR()` also gave a perfect fit (RMS = 2.72×10^{-5}, $\chi^2_{d.o.f} = 0.0025$, and residuals at zero across entire spectral range; Table B.8, Figure 6.3), with a slightly narrower uncertainty envelope (of scale $\sim \pm 0.008$; Figure 6.3) than the *brucemathmin* `WLS_ASC_ILR()` unmixing uncertainty envelope (of scale $\sim \pm 0.011$; Figure 5.6), indicating slightly greater confidence in the modelled spectrum derived from `OptEst_ASC_ILR()` estimated abundances using *P4*, compared to that from `WLS_ASC_ILR()`.

The retrieved abundances mostly agreed to within 1σ (the only exception being olivine within 1.3σ due to its high precision of 0.04%; Table B.8), and had equal, or higher, precisions than the *brucemathmin* `WLS_ASC_ILR()` unmixing ($< 11\%$ for *brucemathminP4* with `OptEst_ASC_ILR()`, Table B.8, and $< 16\%$ for *brucemathmin* with `WLS_ASC_ILR()`, Table 5.1). The greater precision achieved with `OptEst_ASC_ILR()` may suggest that priors can improve the confidence in the retrieved solution, and could be due to the very definition of what priors are and what they represent: priors encapsulate pre-held beliefs in what the solution may

be (in this case, the abundance of each end-member). Therefore, by including *a priori* information in this way (i.e., quantitatively, probabilistically and explicitly through Bayes' rule; Equation 3.1), this can help confirm or reject a hypothesis (i.e., a particular end-member having a particular abundance), thus naturally leading to greater confidence in the final solution, compared to the omittance of such priors.

The abundances retrieved with `OptEst_ASC_ILR()` for *brucemathminP4* were also more accurate to the correct solution (agreeing to within $0.14 - 1.3\sigma$) than they were to the priors (agreeing to within $4.7 - 328\sigma$; Table B.8), thus further demonstrating that the data had the largest influence in determining the solution, but still with some influence from the priors.

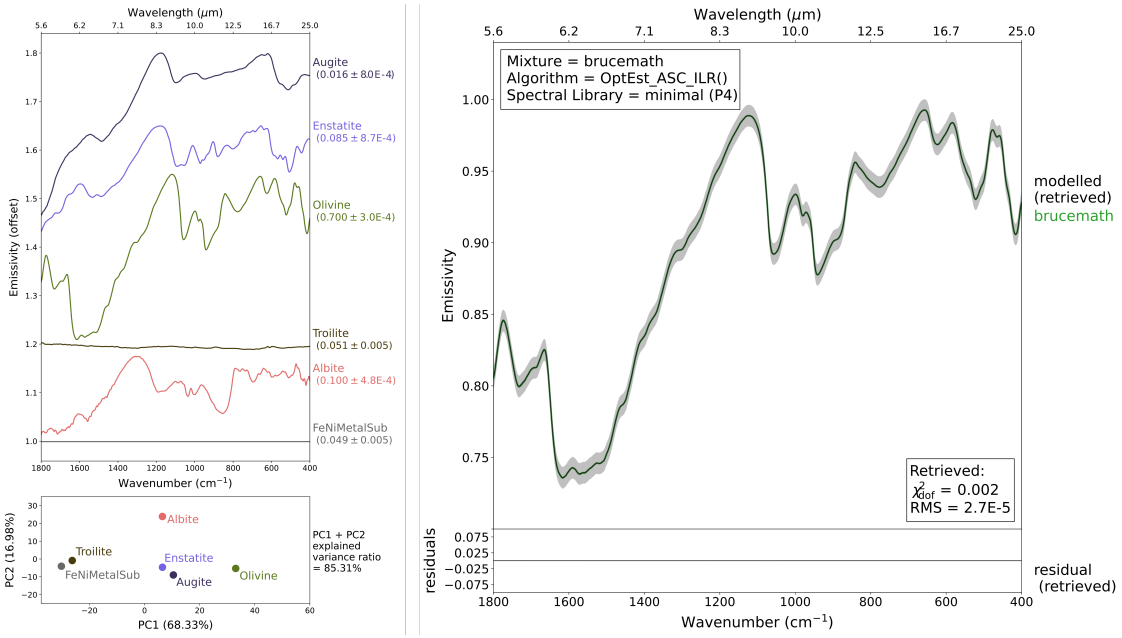


Figure 6.3: *brucemathminP4* `OptEst_ASC_ILR()` reduced spectral library with model fit.

6.1.1.2 *brucerealmin* Unmixings

P1 (Figure 6.4, Table B.9)

In contrast to the *brucemathminP1* `OptEst_ASC_ILR()` unmixing (Figure 6.1, Table 6.1), which removed FeNiMetalSub, the *brucerealminP1* `OptEst_ASC_ILR()` unmixing (Figure 6.4, Table B.9) retained all end-members from the Bruce *minimal*

spectral library. The difference here could highlight the need for a spectrally flat end-member (e.g., BB, FeNiMetalSub) in order for the model spectrum to match the real one (for reasons discussed in Section 4.3.3).

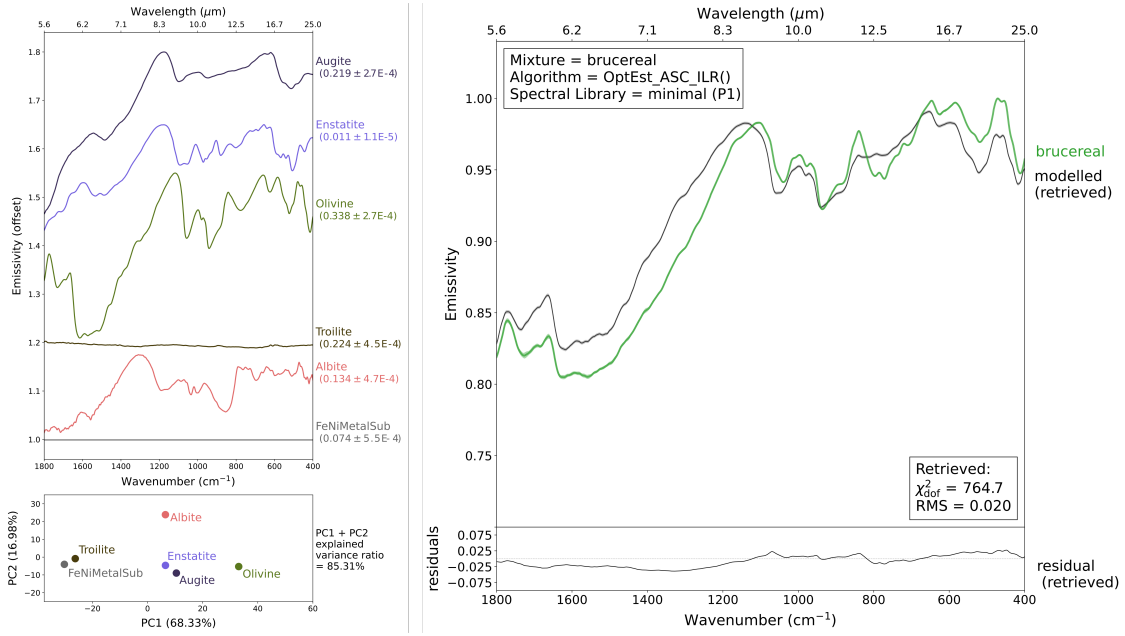


Figure 6.4: *brucerealminP1* `OptEst_ASC_ILR()` reduced spectral library with model fit.

The retrieved abundances were all very precise (between $0.08 - 0.74\%$) but also very inaccurate ($|44| - |6734|\sigma$; Table B.9), and gave a visually poor fit, evidenced by residuals extending beyond ± 0.01 between $1756 - 1218\text{cm}^{-1}$, $1091 - 1037\text{cm}^{-1}$, $861 - 828\text{cm}^{-1}$, $806 - 762\text{cm}^{-1}$, and $587 - 411\text{cm}^{-1}$ (Figure 6.4), and confirmed by the very large $\chi^2_{d.o.f} = 764.7$, and relatively poor RMS $= 0.02$.

P2 (Table B.10)

Unmixing *brucerealminP2* with `OptEst_ASC_ILR()` (Table B.10) removed enstatite, troilite and albite, which was the same as the *brucerealmin* `WLS_ASC_ILR()` unmixing (Section 5.3.1.1). These end-member removals could be understood by considering the original *minimal* PCA plot (Figure 5.3), and the priors (Table B.10). On the PCA plot, troilite and FeNiMetalSub were close together, as were enstatite and augite, so it was more probable that one may be chosen over the other within these pairings, due to the difficulty in distinguishing them from each other.

The overall *brucerealminP2* `OptEst_ASC_ILR()` unmixing (Table B.10) was almost identical to that of *brucerealmin* with `WLS_ASC_ILR()` (Figure 5.7, Table 5.3), confirming that, in this case, loose priors could be considered equivalent to no priors. Additionally, the *brucerealminP2* `OptEst_ASC_ILR()` unmixing (Table B.10) was much more similar to the *brucerealmin* `WLS_ASC_ILR()` unmixing (Figure 5.7, Table 5.3) than to the *brucemathmin* `WLS_ASC_ILR()` unmixing (Figure 5.6, Table 5.1); as indicated by the retrieval quality metrics being -8.9 (fit quality), and 1.13 (abundance quality) for both the *brucerealminP2* `OptEst_ASC_ILR()` (Table 6.12) and *brucerealmin* `WLS_ASC_ILR()` (Table 5.9) unmixings, but were 5.84×10^{-12} (fit quality) and 0 (abundance quality) for the *brucemathmin* `WLS_ASC_ILR()` unmixing (Table 5.9). This could therefore be considered to show that the addition of loose priors cannot compensate for the linear mixing model being incorrect for this application to fine grained samples.

So, although `OptEst_ASC_ILR()` was a more sophisticated algorithm than `WLS_ASC_ILR()`, if the priors were too 'loose' then `OptEst_ASC_ILR()` performed almost equivalently to `WLS_ASC_ILR()`; which could either point to more sophisticated algorithms being unable to get around limitations of linear mixing, or that unmixings are sensitive to the 'tightness' of the priors. Differences between the *brucerealminP1* `OptEst_ASC_ILR()` (tight priors), *brucerealminP2* `OptEst_ASC_ILR()` (loose priors), and *brucerealmin* `WLS_ASC_ILR()` unmixings (as summarised in Tables 5.9 and 6.12) suggested it may be the latter.

P3 (Figure 6.5, Table B.11)

The retrieved abundances for the *brucerealminP3* `OptEst_ASC_ILR()` unmixing had very high precision ($\leq$ 0.1%) with poor accuracy ($> |20|\sigma$; Table B.11). Additionally, this gave a poor fit, evidenced by residuals that closely resembled those between *brucereal* vs *brucemath* (Figure 4.2); extending beyond ± 0.01 between $1740 - 1707\text{cm}^{-1}$, $1652 - 1399\text{cm}^{-1}$, $1081 - 817\text{cm}^{-1}$, and $642 - 400\text{cm}^{-1}$, and even beyond ± 0.05 between $1624 - 1487\text{cm}^{-1}$ and $1075 - 1048\text{cm}^{-1}$ (Figure 6.5), as well as RMS $= 0.027$ and $\chi^2_{d.o.f} = 1703.4$.

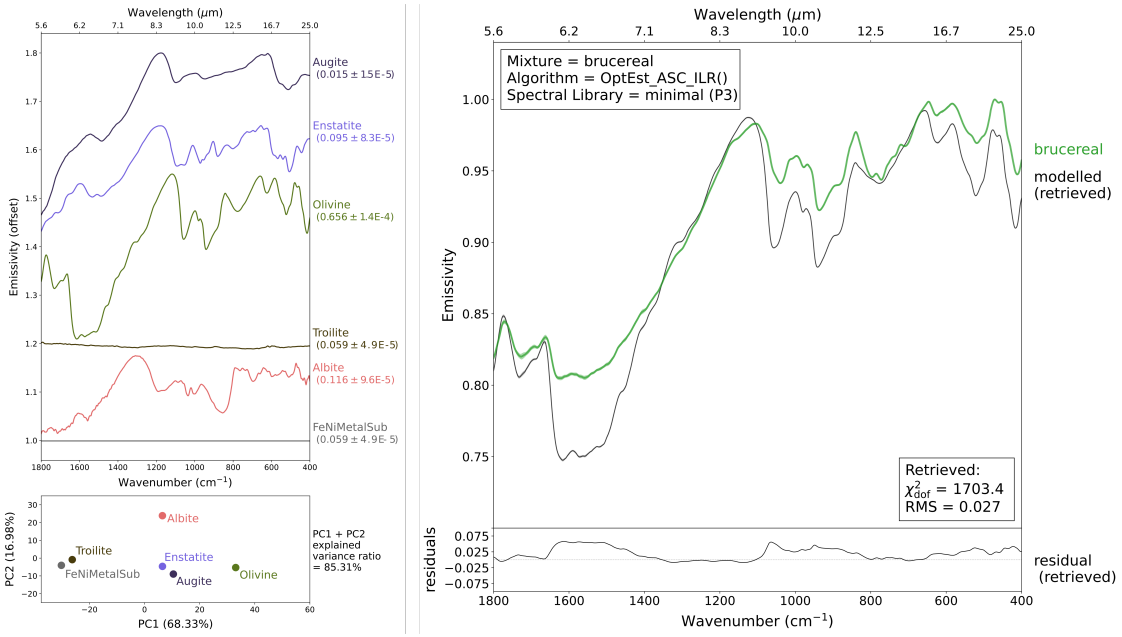


Figure 6.5: *brucerealminP3* `OptEst_ASC_ILR()` reduced spectral library with model fit.

The poor performance of this unmixing despite the 'perfect' priors could highlight problems with the model, as even when the algorithm contained the solution in the priors, a spectrum derived from linear mixing still did not match laboratory observation; thus confirming what was initially seen in the *brucemath* vs *brucereal* discussion of Section 5.1.1.

P4 (Table B.12)

Finally, the *brucerealminP4* unmixing using `OptEst_ASC_ILR()` (Table B.12) was almost identical to that for *brucerealminP2* (Table B.10), with a very slightly reduced scale for correlations (of scale |0.562| for *brucerealminP4* and |0.564| for *brucerealminP2*; Tables C.6 and C.4, respectively).

6.1.1.3 *brucemathexp* Unmixings

P1 (Figure 6.6, Table B.13)

Troilite, FeNiMetalSub and BB were removed from the *brucemathexpP1* unmixing using `OptEst_ASC_ILR()` (Figure 6.6, Table B.13); which was quite different from the *brucemathminP1* `OptEst_ASC_ILR()` unmixing (Figure 6.1, Table 6.1), where only FeNiMetalSub was removed, and troilite kept. The discrepancy here,

where the only change was going from the *minimal* to *expanded* spectral library, demonstrated the issues in spectral library curation, and how different spectral libraries can lead to different solutions even when everything else is kept the same.

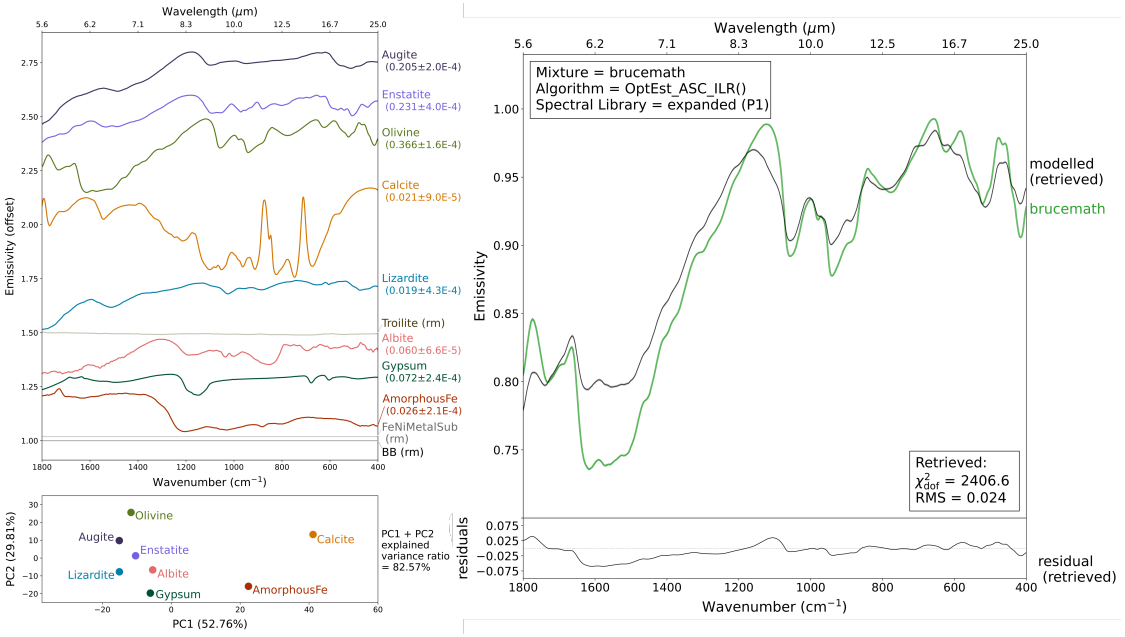


Figure 6.6: *brucemathexpP1* `OptEst_ASC_ILR()` reduced spectral library with model fit. rm=removed.

The fit for the *brucemathexpP1* `OptEst_ASC_ILR()` unmixing was poor (evidenced by $\chi^2_{d.o.f} = 2406.6$, RMS = 0.02, and residuals $> \pm 0.01$ between $1800 - 1740\text{cm}^{-1}$, $1663 - 1191\text{cm}^{-1}$, $1152 - 1031\text{cm}^{-1}$, $960 - 872\text{cm}^{-1}$, $598 - 565\text{cm}^{-1}$, and $499 - 400\text{cm}^{-1}$ in Figure 6.6), but with generally better feature alignment and spectral contrast between $\sim 1050 - 400\text{cm}^{-1}$ (particularly around 1000cm^{-1}). The residuals looked almost spectral-like, with some resemblance to the olivine spectrum (e.g., Figure 6.6), which may suggest missing end-members, or simply that the retrieved abundance for one of the end-members (i.e., olivine) was too low. Generally, the overall locations of peaks and troughs (at e.g., $\sim$ 1100, 1050, 850cm^{-1}) in the residuals here for the *brucemathexpP1* `OptEst_ASC_ILR()` unmixing (Figure 6.6) were similar to those for the *brucemathminP1* `OptEst_ASC_ILR()` unmixing (Figure 6.1); although they clearly had very different magnitudes (average of ± 0.018 across spectral range for *brucemathexpP1*, and ± 0.008 for *brucemathminP1*), which may suggest that incorrect missing/present end-members was not the core problem.

P2 (Figure 6.7, Table B.14)

With the loose priors of *P2*, for the `OptEst_ASC_ILR()` unmixing of *brucemathexpP2* (Figure 6.7, Table B.14), none of the correct end-members were removed, and the only incorrect end-member kept was calcite – possibly due to its independence as represented by relative isolation on the original Bruce *expanded* PCA plot (Figure 5.4).

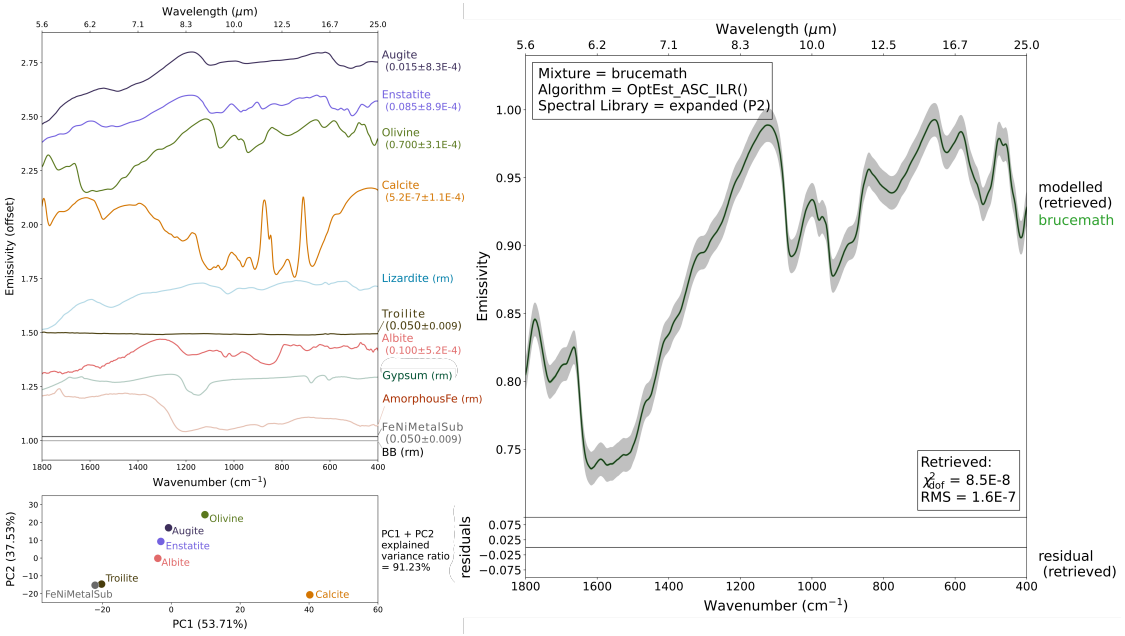


Figure 6.7: *brucemathexpP2* `OptEst_ASC_ILR()` reduced spectral library with model fit. rm=removed.

The retrieved abundances for the *brucemathexpP2* `OptEst_ASC_ILR()` unmixing gave a 'perfect' fit (indicated by RMS $= 1.6 \times 10^{-7}$, $\chi^2_{d.o.f} = 8.5 \times 10^{-8}$ in Table B.14, and residuals at zero across the entire spectral range in Figure 6.7), like the *brucemathexp* `WLS_ASC_ILR()` model fit (Section 5.3.1.2). However, the retrieved abundances themselves from the *brucemathexpP2* `OptEst_ASC_ILR()` (Table B.14) and *brucemathexp* `WLS_ASC_ILR()` (Table 5.5) unmixings were actually quite different; where the *brucemathexpP2* `OptEst_ASC_ILR()` unmixing had generally better precision and accuracy, thus furthering the belief that it is better to have priors with low confidence than none at all.

The differences between the `OptEst_ASC_ILR()` unmixings for *brucemathexpP1* (Figure 6.6, Table B.13) and *brucemathexpP2* (Figure 6.7, Table B.14) particularly highlighted the influence of priors, and that this was driven by their uncertainties.

P3 and *P4* (Figures A.7 and 6.8, Tables 6.3 and B.15)

As expected, the *brucemathexpP3* unmixing with `OptEst_ASC_ILR()` (Figure A.7, Table 6.3) gave a visually perfect fit for both the retrieved and blackbody renormalised (BBnorm) solutions (as seen by zero residuals across the full spectral range in Figure A.7), also indicated quantitatively by the RMS $= 1.84 \times 10^{-5}$ (retrieved), 1.34×10^{-5} (BBnorm), and $\chi^2_{d.o.f} = 1.06 \times 10^{-3}$ (retrieved), 6.69×10^{-4} (BBnorm). Additionally, the retrieved and BBnorm abundances were precise ($\leq 0.1\%$) and accurate (within 0.8σ) for the correct end-members, and imprecise ($\geq 273\%$) for incorrect end-members (Table 6.3); following how the priors were set (Table 4.4).

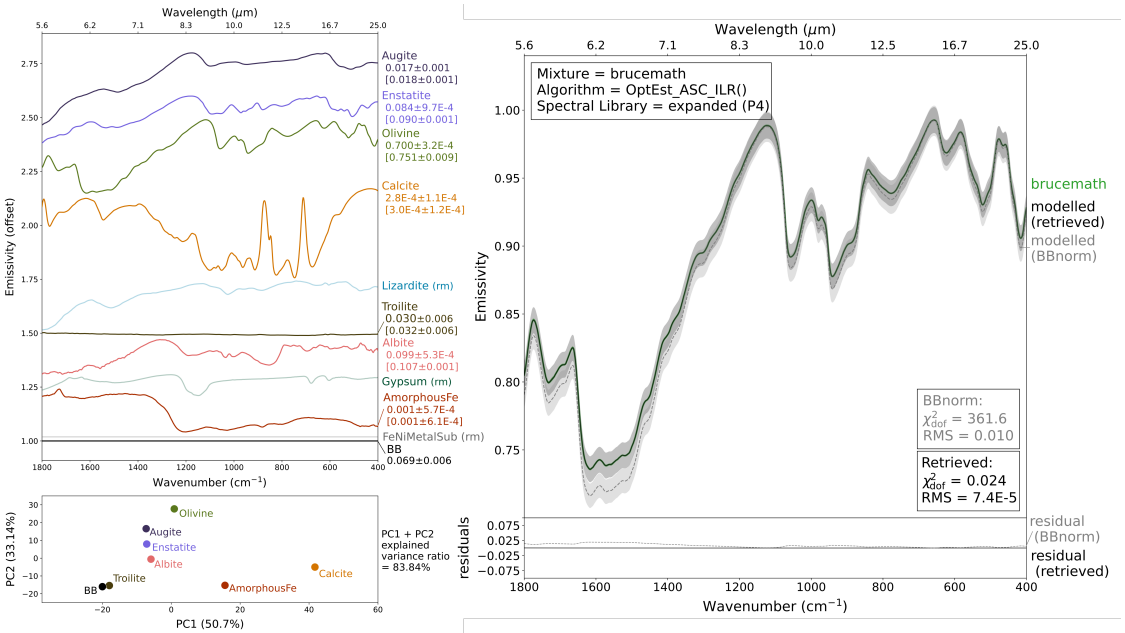


Figure 6.8: *brucemathexpP4* `OptEst_ASC_ILR()` reduced spectral library with model fit. Values in square brackets are the blackbody renormalised (BBnorm) abundances. rm=removed.

Similarly, the *brucemathexpP4* `OptEst_ASC_ILR()` retrieved abundances gave a 'perfect' fit (also zero residuals, Figure 6.8, and RMS $= 7.45 \times 10^{-5}$, $\chi^2_{d.o.f} = 0.02$,

Table B.15). The BBnorm abundances gave a visually good fit, with some slight deviations that were more clearly seen in the residuals, which had an average of ±0.008 across the spectral range, extending slightly beyond ±0.01 (reaching a maximum of ±0.02) between $1800 - 1366\text{cm}^{-1}$; but the RMS = 0.010 and $\chi^2_{d.o.f} = 361.6$ were more indicative of a poor fit.

6.1.1.4 *brucerealexp* Unmixings

In the `OptEst_ASC_ILR()` unmixings of *brucerealexpP1→P4* (Tables B.16, B.17, B.18 and B.19), they all removed at least two end-members, but were quite varied in terms of which end-members were removed/kept – none of them had an identical choice of end-members, and were also very different from their corresponding *brucemathexpP1→P4* unmixings with `OptEst_ASC_ILR()` (Tables B.13, B.14, 6.3 and B.15); thus further highlighting the influence of the priors combined with spectral library curation.

As seen across the `WLS_ASC_ILR()` unmixings presented in Section 5.3, these `OptEst_ASC_ILR()` unmixings of *brucerealexpP1→P4* provided further evidence of the discrepancy between best fit (i.e., fit quality metric closest to zero) and best abundances (i.e., abundance quality metric closest to zero), as here the *brucerealexpP3* blackbody renormalised (BBnorm) solution provided the worst fit (fit quality = −33.9) but the best abundances (abundance quality = 0.29); where the retrieval quality metrics (introduced in Section 3.3.3) for all `OptEst_ASC_ILR()` unmixings are summarised in Table 6.12.

6.1.1.5 *brucemathext* Unmixings

P1 (Table B.20)

The incorrect removal of troilite and FeNiMetalSub, and incorrect retention of calcite, saponite, gypsum and amourphous Mg for the *brucemathextP1* unmixing using `OptEst_ASC_ILR()` (Table B.20) could be explained by the original *extensive* PCA plot (Figure 5.5). Here, troilite, FeNiMetalSub, BB, pyrrhotite, magnetite, Murchison IOM, and arguably gypsum, formed a cluster – the only end-members

Table 6.3: *brucemathexpP3* `OptEst_ASC_ILR()` results. The unit for accuracy, σ, represents the retrieved abundance uncertainty: a negative value here ⇒ overestimation, a positive value ⇒ underestimation. Values in square brackets are from the blackbody renormalisation.

End-member	**'True' Abundance**	**Prior, P3**	**Retrieved Abundance [BBnorm]**	**Accuracy to 'True' Abundance σ [BBnorm]**	**Accuracy to P3 Abundance σ [BBnorm]**
Augite	0.015	0.015 ± 1.5E-5 (0.10%)	0.0150 ± 1.50E-5 (0.10%) [0.015 ± 1.57E-5 (0.10%)]	0.04 [-0.01]	0.04 [-0.01]
Enstatite	0.085	0.085 ± 8.5E-5 (0.10%)	0.0850 ± 8.22E-5 (0.10%) [0.0850 ±8.62E-5 (0.10%)]	0.27 [0.22]	0.27 [0.22]
Olivine	0.700	0.700 ± 7.0E-4 (0.10%)	0.6999 ± 1.58E-4 (0.02%) [0.6999 ± 2.66E-4 (0.04%)]	0.79 [0.35]	0.79 [0.35]
Calcite	0.000	0.0001 ± 1.001E-4 (100.1%)	2.39E-5 ± 6.50E-5 (272.47%) [2.39E-5 ± 6.50E-5 (272.47%)]	-0.37 [-0.37]	1.17 [1.17]
Lizardite	0.000	0.0001 ± 1.001E-4 (100.1%)	6.12E-5 ± 9.59E-5 (156.81%) [6.12E-5 ± 9.59E-5 (156.81%)]	-0.64 [-0.64]	0.40 [0.40]
Troilite	0.050	0.050 ± 5.0E-5 (0.10%)	0.0500 ± 4.92E-5 (0.10%) [0.0500 ± 5.16E-5 (0.10%)]	0.28 [0.22]	0.28 [0.22]
Albite	0.100	0.100 ± 1.0E-4 (0.10%)	0.1000 ± 9.49E-5 (0.09%) [0.1000 ± 9.97E-5 (0.10%)]	0.43 [0.37]	0.43 [0.37]
Gypsum	0.000	0.0001 ± 1.001E-4 (100.1%)	4.64E-5 ± 9.39E-5 (202.53%) [4.64E-5 ± 9.39E-5 (202.53%)]	-0.49 [-0.49]	0.57 [0.57]
Amorphous Fe	0.000	0.0001 ± 1.001E-4 (100.1%)	3.99E-5 ± 8.87E-5 (222.15%) [3.99E-5 ± 8.87E-5 (222.15%)]	-0.45 [-0.45]	0.68 [0.68]
FeNiMetalSub	0.050	0.050 ± 5.0E-5 (0.10%)	0.0500 ± 4.93E-5 (0.10%) [0.0500 ± 5.16E-5 (0.10%)]	0.28 [0.22]	0.28 [0.22]
BB	n/a	0.0001 ± 1.001E-4 (100.1%)	4.52E-5 ± 9.40E-5 (207.85%)	n/a	n/a
		RMS error $\chi^2_{d.o.f}$	1.84E-5 [1.34E-5] 0.0011 [0.0007]		

kept from this cluster were BB and gypsum, which were at the opposite ends, and so could have been selected as a representatives of the whole cluster. The retention of only BB and gypsum from that cluster may have also been due to the other members of this cluster being too difficult to distinguish from one another (especially BB and FeNiMetalSub as they were simply straight horizontal lines across the spectral range).

Saponite and amorphous Mg were very close together on the original *extensive* PCA plot (Figure 5.5), and were also in close proximity to gypsum; so it may seem odd that they were all kept, given the `OptEst_ASC_ILR()` algorithm's apparent struggle to distinguish other end-members clustered together and ultimately removing them. This serves a useful reminder that, although the PCA can provide context, it may not always provide the full picture, as some amount of explained variance is lost when only considering PC1 vs PC2 (particularly when there are more than two end-members, and therefore more than two principal components).

The unintuitive choice of end-member retention/removal based on spectral library PCA could be indicative of the dominance of priors over variations in the spectral library (represented via PCA) to explain end-member choices, particularly when the priors have high confidence. This is to be expected because tight priors represent high confidence in these values being the solution, which may be considered as an insistence to retrieve a solution at, or close to, these prior values. Thus the tighter the priors, the greater the tendency for the solution to relax back to the prior; effectively breaking the link to PCA as the tight priors dominate over variance in end-member spectral morphology when finding the solution.

This *brucemathextP1* `OptEst_ASC_ILR()` unmixing provides a good example of how adding priors (i.e., going from `WLS_ASC_ILR()` to `OptEst_ASC_ILR()`) can massively change which end-members are kept/removed. The expectation is that end-members with tight priors would be more likely to be retained than those with loose (or no) priors – so, for the tight priors of *P1* we would expect

the *brucemathextP1* `OptEst_ASC_ILR()` unmixing to retain more end-members than that of *brucemathext* with `WLS_ASC_ILR()`, which was the case. For the *brucemathextP1* `OptEst_ASC_ILR()` unmixing (Table B.20), enstatite and albite were kept in addition to calcite, augite, olivine, saponite, gypsum, amorphous Mg and BB; but for the *brucemathext* `WLS_ASC_ILR()` unmixing (Section 5.3.1.3), only enstatite and albite were kept. As the only difference between the *brucemathextP1* `OptEst_ASC_ILR()` and *brucemathext* `WLS_ASC_ILR()` unmixings was the addition of (tight) priors, the only explanation must be the influence of priors, governed by the confidence in these priors.

P2→P4 (Tables B.21, B.22, B.23)

Building from the conclusions drawn for *brucemathextP1* above, the difference in end-member selection between the remaining *brucemathextP2→P4* `OptEst_ASC_ILR()` unmixings (Tables B.21, B.22, B.23), the *brucemathextP1* `OptEst_ASC_ILR()` (Table B.20), and *brucemathext* `WLS_ASC_ILR()` (Figure 5.10, Table B.2) unmixings demonstrated the sensitivity of influence from priors to their confidence.

6.1.1.6 *brucerealext* Unmixings

Lastly, the `OptEst_ASC_ILR()` unmixings of *brucerealextP1→P4* (Tables B.24, B.25, B.26 and B.27) demonstrated, through the abundance quality metric (Table 6.12), that there was no significant improvement with the most basic addition of priors; unless they provided the correct solution (which is an unrealistic scenario in real-world applications).

The similarities between some of the `OptEst_ASC_ILR()` *brucerealextP1→P4* unmixings and the `WLS_ASC_ILR()` unmixing for *brucerealext* (Section 5.3.1.3) further point to the conclusion that just adding in priors is not enough to get around the limits of linear mixing as the underlying model, and it is perhaps worth trialling another Bayesian algorithm, but one that takes a different approach to finding a solution, such as MCMC.

6.1.1.7 Summary of Bruce `OptEst_ASC_ILR()` Unmixings

Throughout the Bruce unmixings using `OptEst_ASC_ILR()`, the RMS values across *P1→P4* were generally very similar (e.g., the RMS values ranged between 0.0170 − 0.0273 for *brucerealminP1→P4*), whereas there was larger variation in $\chi^2_{d.o.f}$ (e.g., range of 525.9 − 1703.4 for *brucerealminP1→P4*), highlighting that considering only the RMS as a fit quality metric is insufficient.

A common theme seen when comparing the *P1→P4* `OptEst_ASC_ILR()` unmixings for *brucemath* and *brucereal* was that the addition of priors could massively change the retrieval, even when all the priors were very 'loose', and any influence from the priors was governed by the scale of their uncertainties (i.e., the confidence in the priors).

A major noticeable difference between the *P1→P4* `OptEst_ASC_ILR()` and `WLS_ASC_ILR()` unmixings for the same mixture was the choice of end-members kept/removed. For example, the *brucemathext* `WLS_ASC_ILR()` unmixing only kept enstatite and albite, whereas enstatite and albite were kept for all *brucemathextP1→P4* `OptEst_ASC_ILR()` unmixings, along with other combinations of additional end-members. This could therefore be attributed to how the priors were set.

Based on the abundance quality metric, both the retrieved and blackbody renormalised (BBnorm) abundances for the *P2* unmixings were better than their respective *P4* values (i.e., abundance quality values for the unmixings with *P2* were consistently smaller than those for *P4*; Table 6.12), which would suggest that having loose priors was key to retrieving better abundances, even if the priors themselves were random rather than educated guesses. Loose priors leading to better abundances (i.e., abundance quality metric closest to zero) was further shown as the retrieved *P2* abundances were better than the retrieved *P3*s for the *brucemathexp*, and *brucemathext* `OptEst_ASC_ILR()` unmixings (Table 6.12) – even though *P3* represented the 'perfect' priors, the presence of tight priors seemed to be a disadvantage compared to having them all loose, as for *P2*.

Across the *P1→P4* `OptEst_ASC_ILR()` unmixings for *brucemath* and *brucereal*, there was a clear relation between the degree of correlation between retrieved abundances (as shown in the correlation matrices, Appendix C), and the confidence of the priors: tighter priors (i.e., high confidence/low uncertainties) led to weaker correlations ($<|0.6|$). So although the best abundance estimations (i.e., abundance quality metric closest to zero) came from the loosest priors, these also gave the strongest correlations (i.e., greater proportion of correlations $>|0.6|$), thus introducing a trade-off between abundance quality and strength of correlation that must be considered when setting priors.

In the case of unmixing a mathematical mixture created using linear mixing, we know that linear mixing is the correct model, and so abundance quality may have higher importance when evaluating algorithm performance (i.e., when considering just the performance of the algorithm separately from the correctness of the model, the unmixing that retrieves the 'best' abundance – abundance quality metric value closest to zero – would be considered to have performed the 'best'). However, when the validity of the model comes into question (as was the case for *brucereal*), the correlation aspect may be more important: a potentially unsuitable model comes with more nuances when evaluating algorithm performance; i.e., the fit may be good, and the retrieved abundances accurate (which would indicate a correct model), but strong correlation between retrieved abundances would invalidate linear mixing due to its assumption of spectrally independent end-members.

6.1.2 Glenn

Repeating the `OptEst_ASC_ILR()` unmixings for Glenn was vital for verifying conclusions made from the Bruce unmixings, ensuring that these were not sample-specific.

6.1.2.1 *glennmathmin* Unmixings

The *glennmathmin* `OptEst_ASC_ILR()` unmixings across *P1→P4* (Figures A.8, A.9, 6.9, 6.10, Tables B.28, B.29, 6.4, 6.5) again showed that the best fit did not necessarily mean the best abundance estimations; as, for example, *glennmathminP4*

(Figure 6.10, Table 6.5) had the best fit (indicated by fit quality metric value of 0.000121, Table 6.12) but *glennmathminP3* (Figure 6.9, Table 6.4) had the best abundance estimates (indicated by abundance quality metric value of 0.004; Table 6.12). These also further showed that tighter priors tend to lead to weaker correlation (greater proportion of values $< |0.6|$ in correlation matrices; Tables C.7 to C.10), with the unexpected exception of *P3* which only gave one highly correlated pair (-0.84 between cronstedtite and lizardite, the strongest correlation of all seen in this *P1*→*P4* set; Table C.9).

Of the *glennmathminP1*→*P4* `OptEst_ASC_ILR()` unmixings, the worst results came from the unmixing using *P1* (fit quality $= -4.52$, abundance quality $= 4.54$; Table 6.12), which were much worse than the `WLS_ASC_ILR()` *glennmathmin* unmixing (fit quality $= 0.0001252$, abundance quality $= 0.194$; Table 5.9); however, the *glennmathminP2* unmixing with `OptEst_ASC_ILR()` was marginally better (fit quality $= 0.0001246$, abundance quality $= 0.193$; Table 6.12) than the `WLS_ASC_ILR()` equivalent (Table 5.9). This therefore strengthened the conclusion drawn from Bruce analysis (Section 6.1.1) that using inaccurate priors with high confidence (i.e., *P1*) gave worse retrieval quality metrics than no priors at all (i.e., `WLS_ASC_ILR()`), as indicated by larger values for fit and abundance qualities; but that using the same inaccurate priors with low confidence (i.e., *P2*) gave better retrieval quality metrics (values closer to zero) than no priors. Thus implying that priors should be used, and in a truly blind case, these should all be given low confidence.

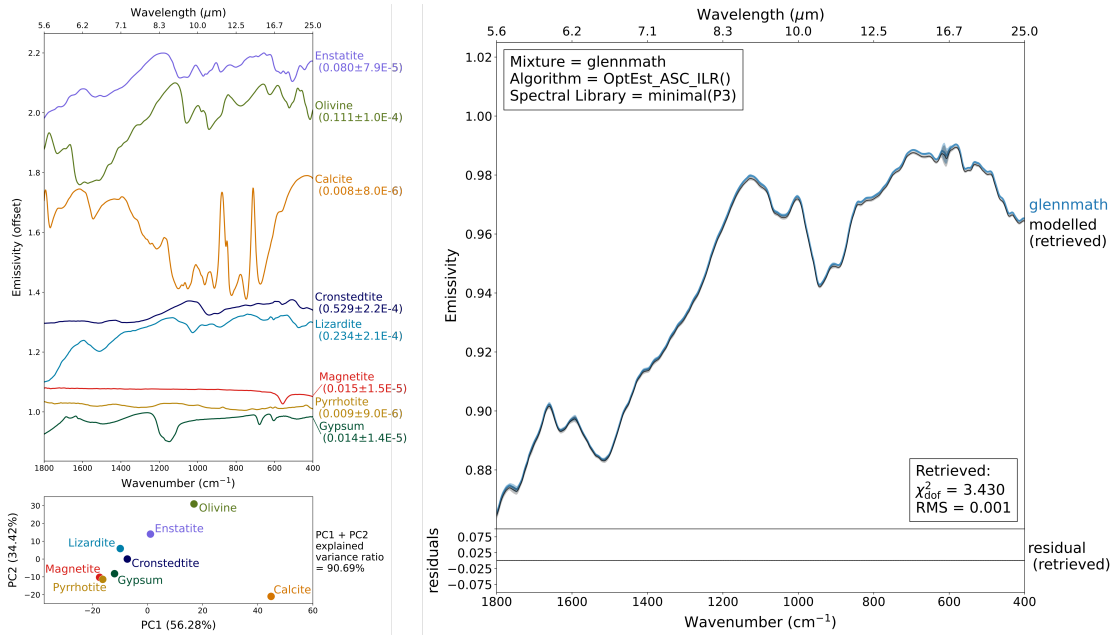


Figure 6.9: *glennmathminP3* `OptEst_ASC_ILR()` reduced spectral library with model fit.

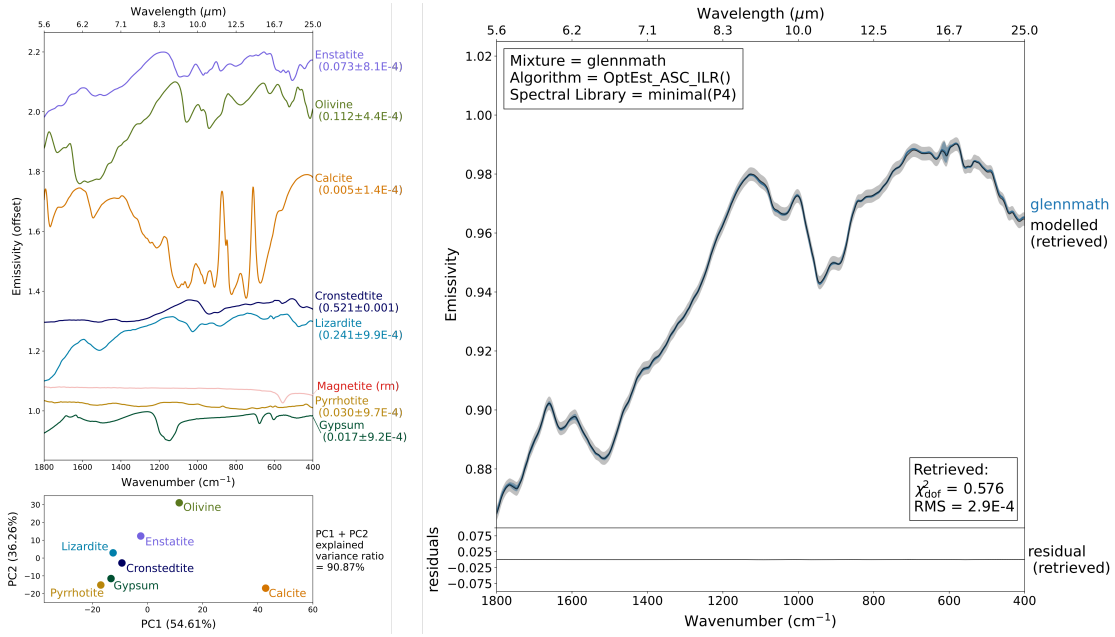


Figure 6.10: *glennmathminP4* `OptEst_ASC_ILR()` reduced spectral library with model fit. rm=removed.

Table 6.4: *glennmathminP3* `OptEst_ASC_ILR()` results. The unit for accuracy, σ, represents the retrieved abundance uncertainty: a negative value here ⇒ overestimation, a positive value ⇒ underestimation.

End-member	**'True' Abundance**	**Prior, P3**	**Retrieved Abundance**	**Accuracy to 'True' Abundance** σ	**Accuracy to P3 Abundance** σ
Enstatite	0.0800	0.0800 ± 8.00e-05 (0.10%)	0.0796 ± 7.85e-05 (0.10%)	5.44	5.44
Olivine	0.1130	0.1130 ± 1.13e-04 (0.10%)	0.1111 ± 1.02e-04 (0.09%)	18.72	18.72
Calcite	0.0080	0.0080 ± 8.00e-06 (0.10%)	0.0080 ± 7.98e-06 (0.10%)	3.65	3.65
Cronstedtite	0.5290	0.5290 ± 5.29e-04 (0.10%)	0.5291 ± 2.23e-04 (0.04%)	-0.67	-0.67
Lizardite	0.2330	0.2330 ± 2.33e-04 (0.10%)	0.2342 ± 2.05e-04 (0.09%)	-5.82	-5.82
Magnetite	0.0150	0.0150 ± 1.50e-05 (0.10%)	0.0150 ± 1.50e-05 (0.10%)	-0.72	-0.72
Pyrrhotite	0.0090	0.0090 ± 9.00e-06 (0.10%)	0.0090 ± 9.00e-06 (0.10%)	-0.41	-0.41
Gypsum	0.0140	0.0140 ± 1.40e-05 (0.10%)	0.0140 ± 1.40e-05 (0.10%)	-0.19	-0.19
			RMS error	7.90E-04	
			$\chi^2_{d.o.f}$	3.43	

Table 6.5: *glennmathminP4* `OptEst_ASC_ILR()` results. The unit for accuracy, σ, represents the retrieved abundance uncertainty: a negative value here ⇒ overestimation, a positive value ⇒ underestimation. rm=removed.

End-member	**'True' Abundance**	**Prior, P4**	**Retrieved Abundance**	**Accuracy to 'True' Abundance** σ	**Accuracy to P4 Abundance** σ
Enstatite	0.08	0.1000 ± 0.0050 (5.00%)	0.0733 ± 8.10e-04 (1.11%)	8.3	32.99
Olivine	0.113	0.1000 ± 0.0050 (5.00%)	0.1119 ± 4.35e-04 (0.39%)	2.47	-27.39
Calcite	0.008	0.0100 ± 0.0100 (100.00%)	0.0053 ± 1.41e-04 (2.64%)	19.07	33.3
Cronstedtite	0.529	0.5000 ± 0.0050 (1.00%)	0.5213 ± 0.0013 (0.24%)	6.08	-16.73
Lizardite	0.233	0.2000 ± 0.0050 (2.50%)	0.2408 ± 0.0010 (0.41%)	-7.9	-41.15
Magnetite	0.015	0.0100 ± 0.0100 (100.00%)	rm		
Pyrrhotite	0.009	0.0200 ± 0.0100 (50.00%)	0.0304 ± 0.0010 (3.18%)	-22.12	-10.77
Gypsum	0.014	0.0500 ± 0.0050 (10.00%)	0.0169 ± 0.0009 (5.41%)	-3.19	36.12
			RMS error	2.86E-04	
			$\chi^2_{d.o.f}$	0.576	

6.1.2.2 *glennrealmin* Unmixings

From the *glennrealminP1→P4* `OptEst_ASC_ILR()` unmixings (Tables B.30, 6.6, 6.7, B.31; correlation matrices C.11, C.12, C.13, C.14), it became clearer that the degree of correlation between retrieved end-member abundances was governed by the tightness of the priors; which dominated over any spectral similarity (as usually implied by clustering of end-members in PC1-PC2 space), and strong correlations often due to few end-members being constrained to sum to one. However, the priors did not have such an overwhelming influence as to lead the retrieval into returning the priors themselves as the solution.

Comparing the `OptEst_ASC_ILR()` unmixings of *glennrealminP3* (Figure 6.12, Table 6.7) and *glennrealminP2* (Figure 6.11, Table 6.6) highlighted the disparity between best fit (i.e., fit quality metric closest to zero, given by the *glennrealminP2* unmixing with a fit quality of -0.023, Table 6.12) and best abundances (i.e., abundance quality metric closest to zero; given by the *glennrealminP3* unmixing with an abundance quality of 0.00029, Table 6.12); however this could also have been due to missing phases in spectral library to represent the amorphous and imperfect nature of end-members in meteorites (as discussed in Section 5.1.2).

The *glennrealminP3* and *glennmathminP3* `OptESt_ASC_ILR()` unmixings had the same high correlation pair (cronstedtite and lizardite), where for *glennrealminP3* the correlation observed was weaker (-0.74, Table C.13) than for *glennmathminP3* (-0.84, Table C.9). This could suggest higher dependence on priors attributable to the mismatch between model and observation – if the model is sufficiently inaccurate to measurements, the retrieval may rely more on the priors than the data.

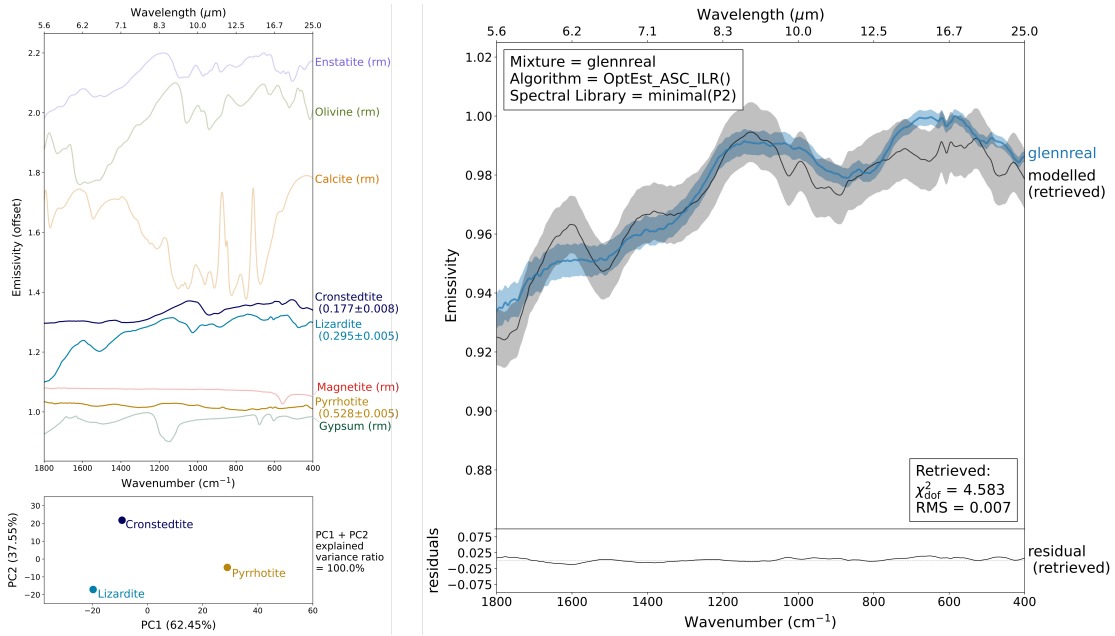


Figure 6.11: *glennrealminP2* `OptEst_ASC_ILR()` reduced spectral library with model fit. rm=removed.

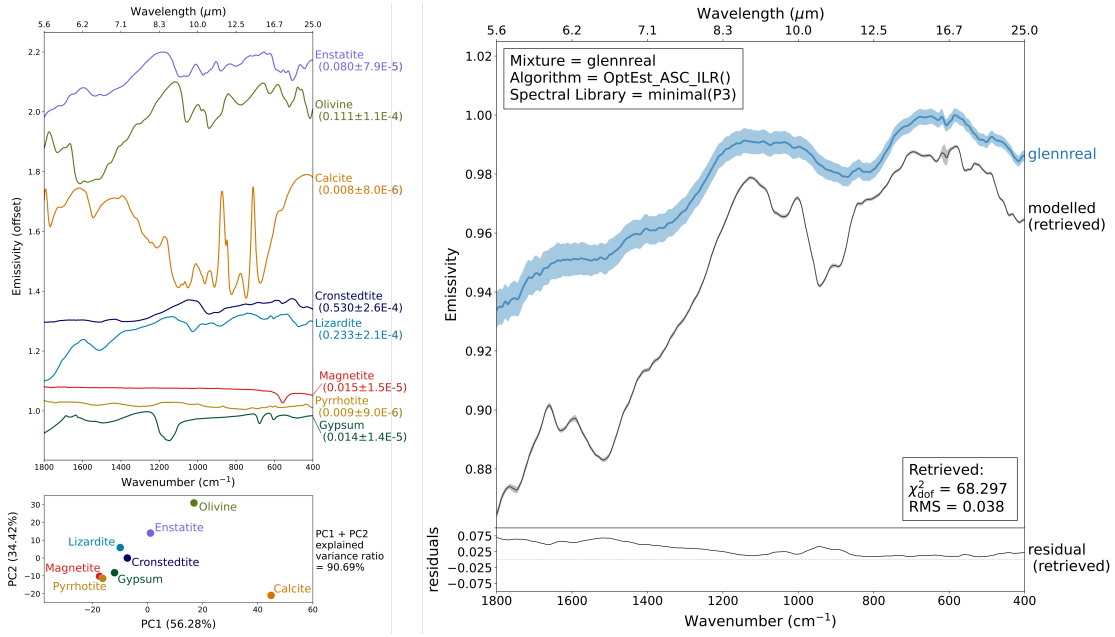


Figure 6.12: *glennrealminP3* `OptEst_ASC_ILR()` reduced spectral library with model fit.

Table 6.6: *glennrealminP2* `OptEst_ASC_ILR()` results. The unit for accuracy, σ, represents the retrieved abundance uncertainty: a negative value here ⇒ overestimation, a positive value ⇒ underestimation.

End-member	**'True' Abundance**	**Prior, P2**	**Retrieved Abundance**	**Accuracy to 'True' Abundance** σ	**Accuracy to P2 Abundance** σ
Enstatite	0.080	0.8513 ± 0.8522 (100.10%)	rm		
Olivine	0.113	0.6683 ± 0.6690 (100.10%)	rm		
Calcite	0.008	0.6946 ± 0.6953 (100.10%)	rm		
Cronstedtite	0.529	0.8687 ± 0.8696 (100.10%)	0.1768 ± 0.0077 (4.33%)	45.99	90.35
Lizardite	0.233	0.3065 ± 0.3068 (100.10%)	0.2950 ± 0.0048 (1.63%)	-12.89	2.38
Magnetite	0.015	0.6813 ± 0.6819 (100.10%)	rm		
Pyrrhotite	0.009	0.2281 ± 0.2284 (100.10%)	0.5282 ± 0.0048 (0.91%)	-107.74	-62.26
Gypsum	0.014	0.7782 ± 0.7790 (100.10%)	rm		
		RMS error	**0.007**		
		$\chi^2_{d.o.f}$	**4.58**		

Table 6.7: *glennrealminP3* `OptEst_ASC_ILR()` results. The unit for accuracy, σ, represents the retrieved abundance uncertainty: a negative value here ⇒ overestimation, a positive value ⇒ underestimation.

End-member	**'True' Abundance**	**Prior, P3**	**Retrieved Abundance**	**Accuracy to 'True' Abundance** σ	**Accuracy to P3 Abundance** σ
Enstatite	0.080	0.0800 ± 8.00E-05 (0.10%)	0.0797 ± 7.93E-05 (0.10%)	3.61	3.61
Olivine	0.113	0.1130 ± 1.13E-04 (0.10%)	0.1114 ± 1.11E-04 (0.10%)	14.77	14.77
Calcite	0.008	0.0080 ± 8.00E-06 (0.10%)	0.0080 ± 8.00E-06 (0.10%)	1.31	1.31
Cronstedtite	0.529	0.5290 ± 5.29E-04 (0.10%)	0.5299 ± 2.60E-04 (0.05%)	-3.56	-3.56
Lizardite	0.233	0.2330 ± 2.33E-04 (0.10%)	0.2330 ± 2.15E-04 (0.09%)	0.04	0.04
Magnetite	0.015	0.0150 ± 1.50E-05 (0.10%)	0.0150 ± 1.50E-05 (0.10%)	-0.77	-0.77
Pyrrhotite	0.009	0.0090 ± 9.00E-06 (0.10%)	0.0090 ± 9.00E-06 (0.10%)	-0.44	-0.44
Gypsum	0.014	0.0140 ± 1.40E-05 (0.10%)	0.0140 ± 1.40E-05 (0.10%)	-0.39	-0.39
		RMS error	**0.0375**		
		$\chi^2_{d.o.f}$	**68.30**		

6.1.2.3 *glennmathexp* Unmixings

Some deviations from the conclusions reached so far were shown in the unmixings of *glennmathexpP1→P4* with `OptEst_ASC_ILR()`, particularly when comparing the *P2* (Figure A.10, Table 6.8) and *P4* (Figure A.11, Table 6.9) results; although it was difficult to compare them thoroughly due to their different end-member selections. Here, *P2* generally performed better than *P4* (based on retrieval quality metrics in Table 6.12) and had lower correlations (although both were still very similar; *P2* average correlation $\sim |0.321|$, Table C.15, and *P4* average correlation $\sim |0.318|$, Table C.16). It was possible that the extra end-member (augite, which was not in *glennmath*) kept in *P4* compared to *P2* was sufficient to cause this difference in the general behaviour seen thus far, therefore highlighting that care needs to be taken when setting priors.

Based on retrieval quality metrics summarised in Tables 5.9 and 6.12, the `WLS_ASC_ILR()` unmixing for *glennmathexp* performed similarly or better than many of the unmixings of *glennmathexpP1→P4* with `OptEst_ASC_ILR()`; further demonstrating a lack of significant improvement with this more sophisticated algorithm, optimal estimation, compared with the a weighted least squares.

6.1.2.4 *glennrealexp* Unmixings

The *glennrealexpP1* `OptEst_ASC_ILR()` unmixing (Figure 6.13, Table B.32) showed that if an end-member had particularly strong features, like calcite, then these features could have a strong influence on the modelled spectrum, even if present in low abundance (as evidenced particularly clearly by calcite's $\sim 900\text{cm}^{-1}$ and $\sim 720\text{cm}^{-1}$ features being apparent in the *glennrealexpP1* retrieved and BBnorm modelled spectra; Figure 6.13). Additionally, in this unmixing, even when there was clustering apparent on the PCA plot (Figure 6.13), if the priors were tight enough then the correlations were low (i.e., $< |0.6|$; Table C.17).

The `OptEst_ASC_ILR()` unmixings of *glennrealexpP3* (Table B.33) and *glennmathexpP3* had the same selection of retained end-members (enstatite, olivine,

Table 6.8: *glennmathexpP2* `OptEst_ASC_ILR()` results. The unit for accuracy, σ, represents the retrieved abundance uncertainty: a negative value here ⇒ overestimation, a positive value ⇒ underestimation. Values in square brackets are from the blackbody renormalisation. rm=removed.

End-member	**'True' Abundance**	**Prior, P2**	**Retrieved Abundance [BBnorm]**	**Accuracy to 'True' Abundance σ [BBnorm]**	**Accuracy to P2 Abundance σ [BBnorm]**
Augite	0.000	0.7976 ± 0.7984 (100.10%)	rm		
Enstatite	0.080	0.0915 ± 0.0915 (100.10%)	0.0763 ± 0.0011 (1.43%) [0.0791 ± 0.0012 (1.51%)]	3.39 [0.75]	13.91 [10.35]
Olivine	0.113	0.6376 ± 0.6383 (100.10%)	0.1125 ± 4.69E-04 (0.42%) [0.1167 ± 7.52E-04 (0.65%)]	0.97 [-4.86]	1118.40 [692.36]
Calcite	0.008	0.0846 ± 0.0847 (100.10%)	0.0070 ± 1.45E-04 (2.07%) [0.0072 ± 1.54E-04 (2.13%)]	7.00 [4.92]	535.95 [501.44]
Saponite	0.000	0.4432 ± 0.4437 (100.10%)	0.0071 ± 0.0033 (46.03%) [0.0074 ± 0.0034 (46.03%)]	-2.17 [-2.17]	132.70 [127.94]
Cronstedtite	0.529	0.0716 ± 0.0717 (100.10%)	0.5234 ± 0.0014 (0.26%) [0.5426 ± 0.0030 (0.56%)]	4.07 [-4.49]	-330.74 [-155.87]
Lizardite	0.233	0.7173 ± 0.7180 (100.10%)	0.2314 ± 0.0015 (0.65%) [0.2399 ± 0.0020 (0.82%)]	1.04 [-3.52]	321.46 [243.39]
Magnetite	0.000	0.7075 ± 0.7082 (100.10%)	rm		
Spinel	0.000	0.9608 ± 0.9617 (100.10%)	rm		
Pyrrhotite	0.000	0.9220 ± 0.9229 (100.10%)	rm		
Gypsum	0.014	0.1268 ± 0.1269 (100.10%)	0.0069 ± 0.0014 (19.96%) [0.0071 ± 0.0014 (19.96%)]	5.19 [4.82]	87.35 [84.06]
AmorphousFe	0.000	0.5804 ± 0.5810 (100.10%)	rm		
BB	0.000	0.9208 ± 0.9218 (100.10%)	0.0353 ± 0.0015 (4.14%)		
		RMS error	**1.46E-4** **[0.0025]**		
		$\chi^2_{d.o.f}$	**0.12** **[17.55]**		

Table 6.9: *glennmathexpP4* `OptEst_ASC_ILR()` results. The unit for accuracy, σ, represents the retrieved abundance uncertainty: a negative value here ⇒ overestimation, a positive value ⇒ underestimation. Values in square brackets are from the blackbody renormalisation. rm=removed.

End-member	**'True' Abundance**	**Prior, P4**	**Retrieved Abundance [BBnorm]**	**Accuracy to 'True' Abundance σ [BBnorm]**	**Accuracy to P4 Abundance σ [BBnorm]**
Augite	0.000	0.1000 ± 0.5000 (500.00%)	0.0024 ± 0.0015 (64.78%) [0.0025 ± 0.0016 (64.78%)]	-1.54 [-1.54]	63.69 [61.17]
Enstatite	0.080	0.1000 ± 0.0050 (5.00%)	0.0761 ± 0.0013 (1.73%) [0.0792 ± 0.0014 (1.82%)]	2.96 [0.58]	18.20 [14.46]
Olivine	0.113	0.1000 ± 0.0050 (5.00%)	0.1133 ± 4.62E-04 (0.41%) [0.1178 ± 8.39E-04 (0.71%)]	-0.64 [-5.77]	-28.76 [-21.26]
Calcite	0.008	0.0100 ± 0.0100 (100.00%)	0.0069 ± 1.46E-04 (2.12%) [0.0071 ± 1.57E-04 (2.20%)]	7.75 [5.43]	21.48 [18.15]
Saponite	0.000	0.2540 ± 0.5000 (196.85%)	0.0000 ± 0.0038 (49873.32%) [0.0000 ± 0.0039 (49873.32%)]	-0.00 [-0.00]	67.45 [64.85]
Cronstedtite	0.529	0.5000 ± 0.0050 (1.00%)	0.5207 ± 0.0014 (0.27%) [0.5416 ± 0.0035 (0.64%)]	5.83 [-3.62]	-14.65 [-11.94]
Lizardite	0.233	0.2000 ± 0.0050 (2.50%)	0.2317 ± 0.0014 (0.62%) [0.2410 ± 0.0020 (0.85%)]	0.88 [-3.92]	-22.18 [-20.03]
Magnetite	0.000	0.0100 ± 0.0100 (100.00%)	rm		
Spinel	0.000	0.0050 ± 0.0500 (1000.00%)	rm		
Pyrrhotite	0.000	0.0200 ± 0.0100 (50.00%)	rm		
Gypsum	0.014	0.0500 ± 0.0050 (10.00%)	0.0103 ± 0.0015 (14.25%) [0.0107 ± 0.0015 (14.26%)]	2.50 [2.13]	26.97 [25.64]
AmorphousFe	0.000	0.0100 ± 0.1000 (1000.00%)	rm		
BB	0.000	0.6000 ± 0.0300 (5.00%)	0.0385 ± 0.0018 (4.78%)		
		RMS error	**1.51E-4** **[0.0027]**		
		$\chi^2_{d.o.f}$	**0.14** **[20.97]**		

calcite, saponite, cronstedtite, lizardite, magnetite, pyrrhotite, gypsum and BB), which could indicate that with perfect priors (i.e., *P3*; Table 4.4), `OptEst_ASC_ILR()` had the potential to overcome the differences in linear mixing model vs observation, or at least saw these spectra as similar enough to choose the same end-members. More likely though, was that *glennrealexpP3* had a greater reliance on these priors than *glennmathexpP3*, as indicated by the same high correlation pairing given by both (cronstedtite and lizardite), but with a slightly weaker magnitude (-0.65; Table C.18), and hence greater dependence on priors, for *glennrealexpP3* than for *glennmathexpP3* (-0.70).

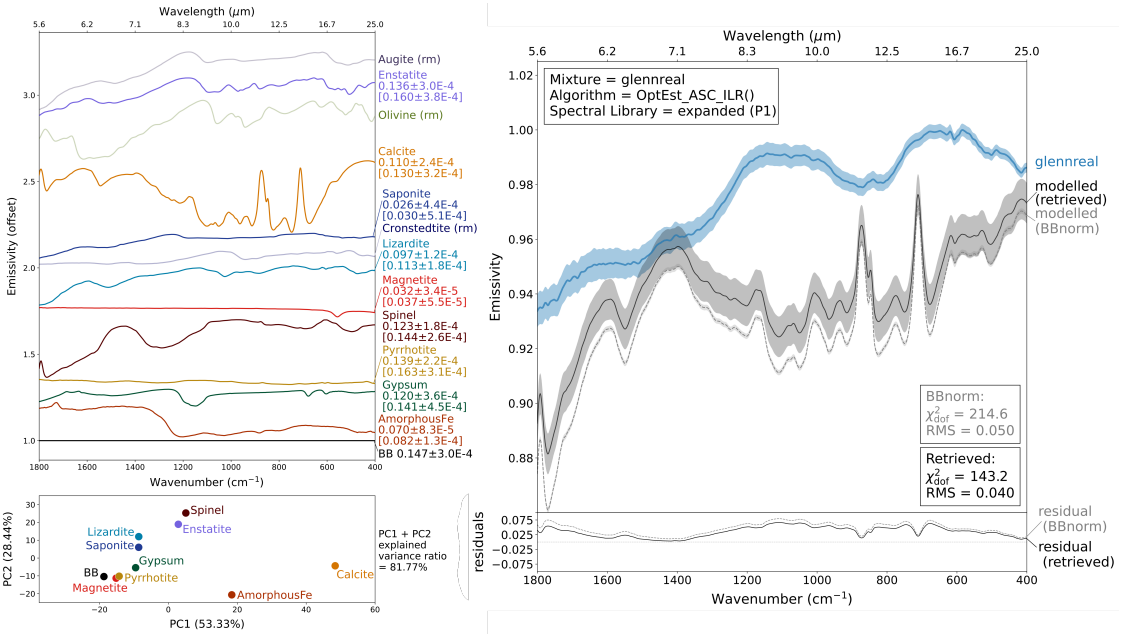


Figure 6.13: *glennrealexpP1* `OptEst_ASC_ILR()` reduced spectral library with model fit. Values in square brackets are from the blackbody renormalisation. rm=removed.

The best abundances of the *glennrealexpP1→P4* set of unmixings, as indicated by the abundance quality metric (Table 6.12), came from *glennrealexpP3* (abundance quality = 0.19 for retrieved values, and 0.18 for BBnorm values), but the corresponding `WLS_ASC_ILR()` BBnorm abundances were better (abundance quality = 0.25; Table 5.9) than both retrieved and BBnorm abundances from *P1* (retrieved = 1.79, BBnorm = 1.52), *P2* (retrieved = 1.90, BBnorm = 0.32) and *P4* (retrieved = 1.24, BBnorm = 0.38; Table 6.12), thus strengthening the

argument that there was not much improvement with this more sophisticated algorithm; unless the priors represented the correct solution (which is unrealistic for applications outside of algorithm development).

6.1.2.5 *glennmathext* Unmixings

The inference that tight priors were more important in the determination of correlation than spectral similarity (implied by PCA clustering), was again shown with the *glennmathextP1→P4* `OptEst_ASC_ILR()` unmixings. These also demonstrated that generally tighter priors lead to weaker correlation (e.g., compare Tables 6.10 and 6.11, where *P1* only had one strongly correlated pair, whereas *P2* had five, all of which were stronger).

The best fit for the *glennmathextP1→P4* `OptEst_ASC_ILR()` unmixing set was from the retrieved *P2* abundances (fit quality of 0.000128; Table 6.12), but the best abundances were those retrieved with *P4* (abundance quality of 0.084; Table 6.12), which may show that the best fit required more 'wiggle room' as provided by looser priors, but that more guidance from the priors was needed to retrieve better quality abundances.

The *glennmathextP2* `OptEst_ASC_ILR()` unmixing (Figure A.12) retained the same end-members as the *glennmathexpP2* `OptESt_ASC_ILR()` unmixing (Figure A.10) – enstatite, olivine, calcite, saponite, cronstedtite, lizardite, gypsum and BB – which may be interpreted as the addition of priors having the ability to counteract the bias introduced in spectral library curation (to some degree).

6.1.2.6 *glennrealext* Unmixings

Unmixing *glennrealextP3* with `OptEst_ASC_ILR()` retained the same end-members as the `OptEst_ASC_ILR()` unmixing for *glennmathextP3* (enstatite, olivine, calcite, saponite, cronstedtite, lizardite, magnetite, troilite, pyrrhotite, gypsum, amorphous Mg, MurchisonIOM, FeNiMetalSub, and BB), with similar correlation matrix values that were generally slightly weaker for *glennrealextP3* (average correlation |0.039|; Table C.19) than *glennmathextP3* (average correlation |0.044|). Thus further

Table 6.10: Correlation matrix for retrieved abundances from the *glennmathextP1* `OptEst_ASC_ILR()` unmixing. Strong correlations ($> |0.6|$) are indicated in bold.

glennmathextP1	Au	En	Ol	Sa	Cr	Li	Sp	Tr	Py	Gy	AmFe
Augite (Au)	1.0000	-0.3033	-0.4086	-0.0125	-0.0519	-0.2299	-0.3364	-0.0088	0.0002	-0.0154	0.0216
Enstatite (En)	-0.3033	1.0000	-0.0817	-0.0072	-0.0762	-0.0883	0.0302	-0.1175	-0.0071	-0.0496	-0.0083
Olivine (Ol)	-0.4086	-0.0817	1.0000	0.0000	-0.2687	-0.0822	0.0247	0.2404	0.0158	0.1133	0.0451
Saponite (Sa)	-0.0125	-0.0072	0.0000	1.0000	-0.0158	-0.0084	-0.0030	-0.0136	-0.0008	-0.0071	-0.0014
Cronstedtite (Cr)	-0.0519	-0.0762	-0.2687	-0.0158	1.0000	-0.2325	-0.2899	**-0.6077**	-0.0394	-0.2346	-0.0434
Lizardite (Li)	-0.2299	-0.0883	-0.0822	-0.0084	-0.2325	1.0000	-0.1129	-0.1112	-0.0062	-0.0648	-0.0110
Spinel (Sp)	-0.3364	0.0302	0.0247	-0.0030	-0.2899	-0.1129	1.0000	0.0541	0.0050	0.0037	0.0175
Troilite (Tr)	-0.0088	-0.1175	0.2404	-0.0136	**-0.6077**	-0.1112	0.0541	1.0000	-0.0374	-0.1836	-0.0515
Pyrrhotite (Py)	0.0002	-0.0071	0.0158	-0.0008	-0.0394	-0.0062	0.0050	-0.0374	1.0000	-0.0105	-0.0032
Gypsum (Gy)	-0.0154	-0.0496	0.1133	-0.0071	-0.2346	-0.0648	0.0037	-0.1836	-0.0105	1.0000	-0.0216
Amorphous Fe (AmFe)	0.0216	-0.0083	0.0451	-0.0014	-0.0434	-0.0110	0.0175	-0.0515	-0.0032	-0.0216	1.0000

Table 6.11: Correlation matrix for retrieved abundances from the *glennmathextP2* `OptEst_ASC_ILR()` unmixing. Strong correlations ($> |0.6|$) are indicated in bold.

glennmathextP2	Ca	En	Ol	Sa	Cr	Li	Gy	BB
Calcite (Ca)	1.0000	0.0059	-0.1489	0.2622	0.0554	-0.1673	-0.3454	-0.1780
Enstatite (En)	0.0059	1.0000	-0.1939	**-0.6317**	0.2350	0.1551	0.3606	0.0313
Olivine (Ol)	-0.1489	-0.1939	1.0000	-0.2924	**-0.6446**	0.1867	0.3775	0.5445
Saponite (Sa)	0.2622	**-0.6317**	-0.2924	1.0000	0.1536	**-0.7394**	**-0.6546**	-0.4667
Cronstedtite (Cr)	0.0554	0.2350	**-0.6446**	0.1536	1.0000	-0.4051	-0.1946	**-0.6367**
Lizardite (Li)	-0.1673	0.1551	0.1867	**-0.7394**	-0.4051	1.0000	0.3915	0.4632
Gypsum (Gy)	-0.3454	0.3606	0.3775	**-0.6546**	-0.1946	0.3915	1.0000	-0.0423
BB	-0.1780	0.0313	0.5445	-0.4667	**-0.6367**	0.4632	-0.0423	1.0000

suggesting a greater reliance on priors for *glennreal* because the theoretical and measured mixture spectra were different enough to require more guidance from the priors when the model was potentially incorrect.

Similarly, the *glennrealextP4* `OptEst_ASC_ILR()` unmixing (Table B.39) had the same end-member retention as that for *glennrealexpP4* (Table B.34) – enstatite, cronstedtite, lizardite and BB – which could suggest that quantitative, explicit priors can somewhat counteract the implicit priors/bias of spectral library curation.

6.1.3 Overall `OptEst_ASC_ILR()` Unmixings Discussion

The choice of end-members in the spectral library introduces implicit bias, the effects of which are often not considered in published literature, so the aim of adding explicitly set quantitative priors (as made possible by adopting a Bayesian approach) was to understand and quantify this influence.

From all the unmixings of Bruce and Glenn with `OptEst_ASC_ILR()`, a very clear effect resulting from the addition of priors was the reduction in correlation, following the general trend that the 'tighter' (i.e., more confident) the priors, the weaker the correlation (as expected). A reduced scale of correlation implies a reduced degree of degeneracy, thus suggesting that having priors could improve the validity of the linear mixing model when used within `OptEst_ASC_ILR()` compared to `WLS_ASC_ILR()`. However, there did not seem to be a sufficient enough difference to say definitively that linear mixing was valid within an optimal estimation algorithm; just that if the linear mixing model was to be used as the forward model, then the unmixing/retrieval algorithm used should take the optimal estimation form, rather than the weighted least squares form, given the choice between the two.

Additionally, throughout the `OptEst_ASC_ILR()` unmixings, it was evident that the strong correlation (i.e., $>|0.6|$), often caused by spectral similarity between end-members (as indicated by clustering in PC1-PC2 space), could be counteracted with appropriately set priors; which could also counteract the general tendency of fewer end-members leading to higher correlations (usually resulting from the

sum to one constraint). These effects were governed by the confidence ascribed to the priors, where priors with high confidence led to weaker correlations, even for end-members in close proximity in PC1-PC2 space.

An interpretation of the Glenn unmixing results was that that common high correlation pairs between equivalent *glennmath* and *glennreal* `OptEst_ASC_ILR()` unmixings generally displayed slightly weaker correlations for *glennreal*, which was likely due to greater reliance on priors for the retrieval, as caused by the mismatch between model and observation. However, this was only seen with Glenn as the Bruce unmixings did not have any common high correlation pairs between corresponding *brucemath* and *brucereal* unmixings; but the 'strong' correlations (if present) for *brucereal* were generally weaker, or had fewer pairings, than their *brucemath* counterparts.

It was also evident from the similarities in the retrievals across different priors, especially between *P2* and *P4*, that regardless of how tight the priors were, the unmixings were still most strongly guided by the data, as none of the retrievals relaxed back to their priors; thus dispelling any reservations that may be had about using Bayesian techniques, and their requirement for explicitly defined *a priori* information. However, the few minor deviations from overall conclusions (e.g., *glennmathminP3* having a strongly correlated pair; Section 6.1.2.1, and the differences between the *glennmathexpP2* and *glennmathexpP4* unmixings, Section 6.1.2.3) could be down to how priors were set, thus emphasising the care that needs to be taken when setting priors.

Dependant on how priors were set was the potential for better retrievals compared with no priors (as determined by retrieval quality metrics outlined in Table 6.12). An important conclusion was that inaccurate, tight priors (i.e., *P1*) were worse than none (i.e., `WLS_ASC_ILR()`), but the same inaccurate priors with lower confidence (looser priors; i.e., *P2*) were better than no priors; suggesting that in a truly blind case, it would be more suitable to have even a random guess for the priors as long as they are very 'loose'. However, the improvements seen (if any) were minimal

and did not counteract the issues that remained unresolved (such as incorrect end-member retention/removal), thus implying that `OptEst_ASC_ILR()` was not a satisfactory improvement on `WLS_ASC_ILR()`.

Priors, and the way in which they were set, clearly impacted the end-member choices, as indicated by the differences across *P1→P4* for each version of the spectral library; but, there was still the possibility of prematurely removing correct end-members, and retaining incorrect ones (as with `WLS_ASC_ILR()`). A promising result, however, was that using `OptEst_ASC_ILR()` to unmix *glennrealP4* gave the same end-member selections when unmixing against the *expanded* and *extensive* spectral libraries; possibly suggesting that quantitative, explicit priors can counteract the implicit priors/bias tied to spectral library curation (to a degree).

Shown several times across the Bruce and Glenn `OptEst_ASC_ILR()` unmixings was the disparity between unmixings that gave the best fit vs those that gave the best abundances (as indicated by the fit quality and abundance quality metrics summarised in Table 6.12). This could indicate that methods of finding the solution via minimising the residuals are not suitable for linear mixing, regardless of whether they are Frequentist or Bayesian; which is likely due to the degenerate nature of the problem, whereby many combinations of end-members and their abundances may give similar quality fits.

Although the inclusion of priors made `OptEst_ASC_ILR()` somewhat more sophisticated than `WLS_ASC_ILR()`, it still only returned the single 'best' solution (i.e., what gave the smallest residual), with no indication of other solutions that may come close. This justifies the need for trialling an MCMC-based algorithm, as showing the posterior probability density functions (pdfs) allows for investigation of other possible abundances based on e.g., multiple peaks, using the mode/median/mean etc. Additionally, there were issues in end-member removal/retention from `WLS_ASC_ILR()` that remained in `OptEst_ASC_ILR()`, which may be resolved by an alternative Bayesian algorithm that strays a little further from the methods of linear least squares and optimal estimation (e.g., MCMC).

Table 6.12: Retrieval quality metrics summary table for the `OptEst_ASC_ILR()` unmixings of Bruce and Glenn. Values in square brackets correspond to metrics derived from the blackbody renormalised abundances (BBnorm). Details on these metrics and how to interpret them are covered in Section 3.3.3, where generally the smaller/closer to zero, the better the quality.

OptEst_ASC_ILR()		Fit Quality				Abundance Quality			
		P1	P2	P3	P4	P1	P2	P3	P4
Bruce	brucemathmin	-4.18	8.48E-06	4.91E-15	2.71E-05	3.26	0.016	0	0.023
	brucemathexp	-58.3	1.50E-07	1.8E-5 [1.3E-5]	7.3E-5 [-3.5]	3.13	0.097	0.37 [0.32]	0.29 [0.59]
	brucemathext	-2.7 [-0.96]	3.1E-6 [-0.94]	2.4E-5 [2.2E-5]	7.05E-5 [-4.0]	6.7 [5.3]	0.5 [2.5]	1.0 [1.0]	1.7 [3.0]
	brucerealmin	-15.6	-8.9	-46.4	-8.9	4.04	1.13	0.12	1.13
	brucerealexp	-33.4	-7.4	-26.8 [-33.9]	-7.6	5.81	3.15	0.31 [0.29]	1.44
	brucerealext	-21.9 [-15.5]	-3.6	-17.0 [-19.4]	-3.6 [-10.3]	1.49 [1.18]	1.33	0.73 [0.68]	66.2 [37.0]
Glenn	glennmathmin	-4.52	1.25E-04	-1.92E-03	1.21E-04	4.54	0.192	0.004	0.189
	glennmathexp	-5.71 [-12.8]	1.28E-4 [-0.041]	-1.72E-3 [-2.02E-3]	1.31E-4 [-0.054]	1.94 [1.63]	0.344 [0.373]	0.224 [0.202]	172.6 [179.5]
	glennmathext	-3.49	1.28E-4 [-0.040]	-1.51E-3 [-1.73E-3]	1.35E-4 [-0.048]	4.22	0.340 [0.367]	0.733 [0.666]	0.084 [0.131]
	glennrealmin	-0.53	-0.02	-2.5	-0.04	11.85	1.27	0.003	1.96
	glennrealexp	-5.62 [-10.6]	2.51E-4 [-3.7]	-2.52 [-2.53]	-2.95E-3 [-0.78]	1.79 [1.52]	1.90 [0.32]	0.19 [0.18]	1.24 [0.38]
	glennrealext	-3.03	8.44E-4 [-4.66]	-2.52 [-2.53]	-2.95E-3 [-0.78]	1.39	2.44 [0.53]	0.55 [0.50]	1.24 [0.38]

So by trialling an additional Bayesian algorithm (i.e., MCMC), any similar or additional issues seen between optimal estimation and MCMC may be indicative that it is indeed a new model that is required.

6.2 Markov Chain Monte Carlo

Markov Chain Monte Carlo (used here in the `MCMC()` algorithm for spectral umixing) is a popular Bayesian tool for parameter estimation, based on sampling from probability distributions in the parameter space, thus providing an alternative method to `WLS_ASC_ILR()` and `OptEst_ASC_ILR()`. For more details on the `MCMC()` algorithm, see Section 4.3.2.3.

For the `MCMC()` unmixings of Bruce and Glenn, two different distributions were used for the priors: Uniform and Gaussian. The Uniform prior served as the most 'uninformative' or 'diffuse' option as this simply constrained the abundance retrieval to be between 0 and 1 (giving equal probability to all values in between), and so could be considered almost as an equivalent to `WLS_ASC_ILR()` in relation to *P1→P4* for `OptEst_ASC_ILR()`. The Gaussian (or 'Normal') distribution was also chosen as this is the distribution intrinsic to the priors in optimal estimation, thus allowing more direct comparison between `MCMC()` and `OptEst_ASC_ILR()`. The Gaussian distribution is also commonly found throughout sampling/population applications in nature (as per the Central Limit Theorem[1]), making it a reasonable first choice alternative to the Uniform distribution when a more accurate distribution is unknown (as is the case for the error distribution of abundances).

In the Gaussian distribution, μ corresponds to the 50^{th}percentile (i.e., the median[2]), and 68% of the samples lie within one standard deviation (1σ) of μ; which, for the symmetrical Gaussian distribution, is equivalent to the $16^{\text{th}}$and 84^{th}percentiles. Based on this, and following the `emcee` documentation (Foreman-Mackey et al. 2013),

[1]The Central Limit Theorem states that as sample size increases, the probability distribution tends towards the Normal distribution, providing an exact fit with infinite samples.

[2]In the Gaussian (or 'Normal') distribution, μ is often labelled as the mean, but as the Gaussian is symmetrical, the mean is equivalent to the median (and the mode).

the values quoted for each end-member were their 50$^{\text{th}}$percentile, with the largest out of the 16$^{\text{th}}$and 84$^{\text{th}}$percentiles used as the uncertainty. For consistency in comparisons across algorithms, only one out of the 16$^{\text{th}}$and 84$^{\text{th}}$percentiles was chosen to be quoted because `WLS_ASC_ILR()` and `OptEst_ASC_ILR()` only had a single value for the uncertainty on each abundance estimate (the standard deviation as derived from the covariance matrix); and the largest of the two chosen, as per standard statistical practice (it is better to overestimate an error than to underestimate it).

However, as a product of the MCMC process was the collection of samples for each parameter, these allowed for more versatile analyses. Comparing the quoted median value with the mean of the distribution provided a quick look into how considering different statistical properties of a sample could lead to differing interpretations; and as such, these comparisons are included in some of the analysis presented within this section.

The same priors used in the `OptEst_ASC_ILR()` unmixings were also used for the `MCMC()` unmixings (see Table 4.4 for how *P1*→*P4* were defined). With the inclusion of Uniform priors, each mixture had fifteen `MCMC()` retrievals/unmixings, again following the same nomenclature previously defined (e.g., *glennmathminP1*, *brucerealexpU*, etc.). As introduced in Section 4.3.2.3, 500 walkers, each taking 1000 steps/samples, were used for all `MCMC()` unmixings.

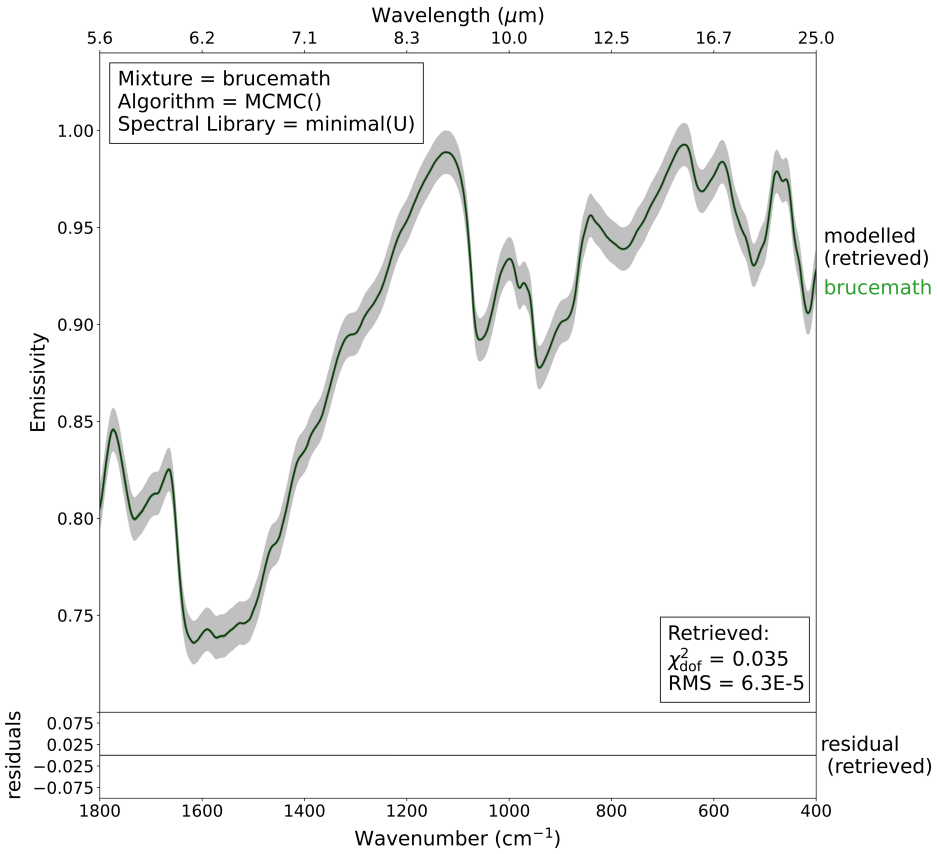
6.2.1 Bruce

6.2.1.1 *brucemathmin* Unmixings

_U_ (Figure 6.14, Table 6.14):

The *brucemathminU* `MCMC()` unmixing gave a 'perfect' fit with residuals at zero, RMS $= 6.26 \times 10^{-5}$, $\chi^2_{d.o.f} = 0.035$, and narrow uncertainty envelope (Figure 6.14a), thus providing some confidence to `MCMC()`, as it gave the result expected in this idealised case. The addition of corner plots in Figure 6.14b, showing singular and joint posterior probability density functions (pdfs) for each end-member abundance

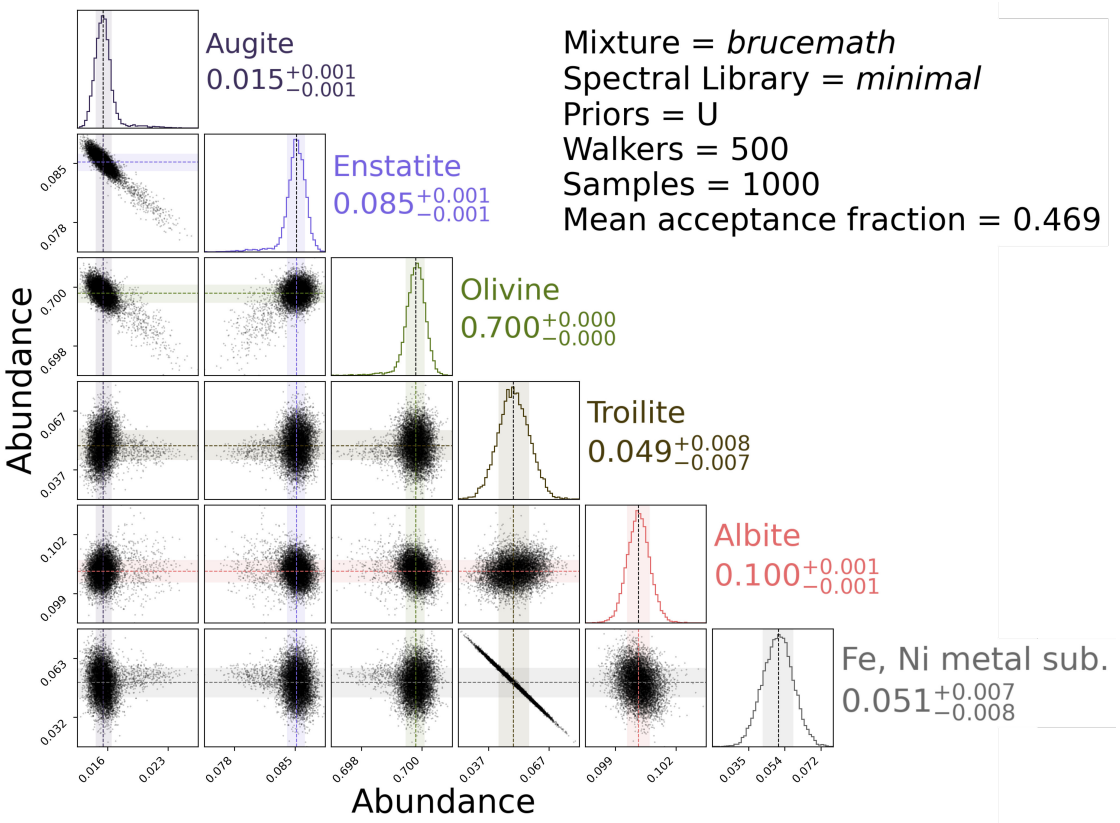
was particularly useful for providing further information that would be otherwise unavailable (e.g., range of possible solutions, bimodality etc).



(a) *brucemathminU* `MCMC()` model fit.

Figure 6.14: *brucemathminU* `MCMC()` (a) model fit with (b) corner and (c) walkers plots. For clarity, each subfigure here is shown larger than in the proceeding similar figures, with guidance on how to interpret each in the subcaptions. In general, the important thing to takeaway from the corner and walkers plots are the general shapes displayed, since important quantitative information from the axes etc. are presented in the relevant tables.

For the *brucemathminU* unmixing with `MCMC()`, the posterior pdfs appeared as narrow Gaussian peaks (Figure 6.14b), with those for troilite and FeNiMetalSub being slightly wider. The forms of these posterior pdfs were reflected quantitatively in the precisions, where troilite and FeNiMetalSub were slightly less precise (15.5% and 15.8%, respectively) than the others ($0.05 - 6.5\%$; Table 6.14). The retrieved abundances were also very accurate, with all of them being well within 1σ (even the least accurate were within 0.2σ; Table 6.14).



(b) *brucemathminU* `MCMC()` corner plot. In corner plots, the axes along the diagonal show the posterior pdfs for the end-members, as labelled to the right. The key property shown here are the shapes of the pdfs, as quantitative interpretation of the pdfs to estimate abundances and their uncertainties are presented in the relevant tables. Any pdfs of particularly notable shape (e.g., bimodal) are shown separately as appropriate later in this thesis. The inner axes show the joint pdfs for the relevant end-members according to column and row position. Again, the shape of these is of greatest importance for interpretation – more circular distributions indicate low to no correlation (e.g., between enstatite and albite here), whereas diagonal trends show moderate to strong correlation (e.g., between troilite and FeNiMetalSub here).

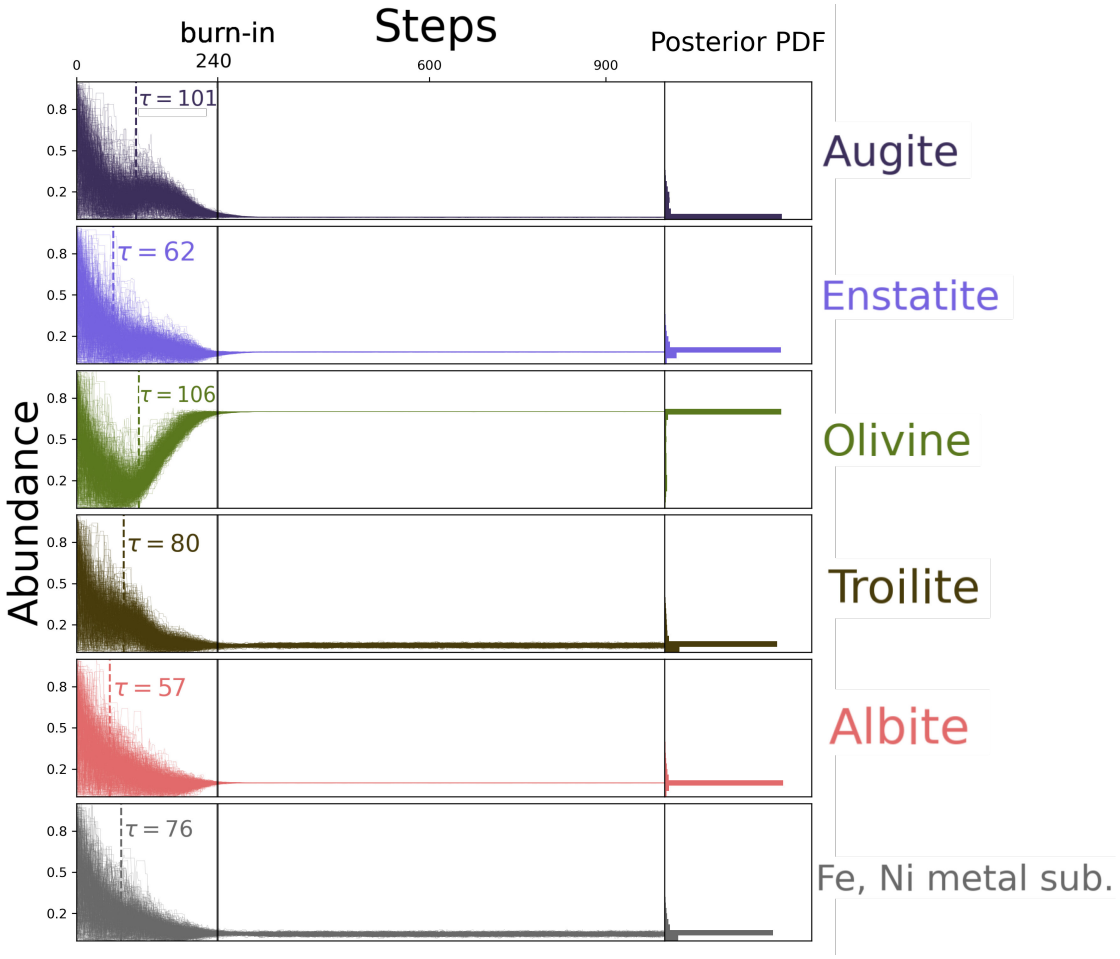
Figure 6.14: (cont.) *brucemathminU* `MCMC()` model fit, corner and walkers plots.

A quick comparison of the 50$^{\text{th}}$percentile (i.e., the median) to the mean for each end-member showed that they were very much the same for this *brucemathminU* `MCMC()` unmixing; with the means summing to slightly less than 1 (0.999987) and the medians summing to slightly more than 1 (1.000057), serving as a good reminder of a flaw with the `MCMC()` algorithm: that it does not implement the abundance sum constraint. In this case, the abundances not summing to exactly 1 was probably due to a rounding error, however the issue of the lack of sum to one constraint became more apparent with the larger spectral libraries (e.g., Section 6.2.1.3).

The strong correlations (>|0.6|) indicated by the correlation matrix (Table 6.13) were also apparent in the joint pdfs (Figure 6.14b). Particularly clear was the strong negative correlation between troilite and FeNiMetalSub, which also had the strongest correlation of -0.996 within the correlation matrix (Table 6.13). Context for this was provided by the *minimal* spectral library PCA plot (Figure 5.3), where troilite and FeNiMetalSub were clustered. Their lower precisions (15.5% and 15.8%, respectively) compared to the other end-members ($0.05 - 6.5\%$; Table 6.14) could be explained by their strong correlation.

The same was true for augite and enstatite, which were also clustered on the PCA plot and had a strong correlation of -0.94 (Table 6.13); but were not in as close proximity as troilite and FeNiMetalSub were to each other (e.g., Figure 5.3), hence the slightly weaker correlation between augite and enstatite (-0.94) compared to troilite and FeNiMetalSub (-0.996; Table 6.13). The correlation between augite and enstatite being weaker than that between troilite and FeNiMetalSub, but stronger than the other end-member pairings (Table 6.13), explained the precisions being better for augite and enstatite (6.5% and 1.3%, respectively), compared to troilite (15.5%) and FeNiMetalSub (15.8%), but worse than the others: albite 0.5%, olivine 0.05%.

As discussed in Section 4.3.2.3, a key aspect of MCMC analyses in general is convergence, which can be assessed from the walkers plots showing the path taken by each walker at each step of the chain. For the *brucemathminU* unmixing with `MCMC()`, the walkers plots (Figure 6.14c) showed that all chains were clearly converged from the burn-in mark (240 steps in); therefore the sampled posterior pdfs were considered to be accurate.



(c) *brucemathminU* `MCMC()` walkers plot. When interpreting the walkers plots, the key aspect to notice is whether convergence has been achieved post-burn-in – by the end of the chain, which was 1000 steps in this case, there should be no overall gradient/trend in the abundance value with progressive step numbers. The frequency of abundances for each end-member, as selected by each walker at each step, is mapped as a histogram displaying the posterior pdf on the right hand side, and is rotated 90° clockwise to how they are usually viewed, such as in the corner plots.

Figure 6.14: (cont.) *brucemathminU* `MCMC()` model fit, corner and walkers plots.

Table 6.13: Correlation matrix for retrieved abundances from the *brucemathminU* `MCMC()` unmixing. Strong correlations ($> |0.6|$) are indicated in bold.

brucemathminU	Au	En	Ol	Tr	Al	FeNi
Augite (Au)	1.000	**-0.936**	**-0.885**	-0.032	-0.083	0.072
Enstatite (En)	**-0.936**	1.000	**0.717**	0.104	0.004	-0.153
Olivine (Ol)	**-0.885**	**0.717**	1.000	0.062	0.052	-0.089
Troilite (Tr)	-0.032	0.104	0.062	1.000	0.110	**-0.996**
Albite (Al)	-0.083	0.004	0.052	0.110	1.000	-0.168
FeNiMetalSub (FeNi)	0.072	-0.153	-0.089	**-0.996**	-0.168	1.000

Table 6.14: *brucemathminU* `MCMC()` results. The unit for accuracy, σ, represents the retrieved abundance uncertainty: a negative value here ⇒ overestimation, a positive value ⇒ underestimation.

End-member	**'True' Abundance**	**Prior, U**	**Retrieved Abundance**	**Accuracy to 'True' Abundance** σ	**Accuracy to U Abundance** σ
Augite	0.0150	n/a	0.0151 ± 0.0010 (6.53%)	-0.12	n/a
Enstatite	0.0850	n/a	0.0849 ± 0.0011 (1.25%)	0.14	n/a
Olivine	0.7000	n/a	0.7000 ± 3.62E-04 (0.05%)	0.07	n/a
Troilite	0.0500	n/a	0.0495 ± 0.0077 (15.51%)	0.07	n/a
Albite	0.1000	n/a	0.1000 ± 5.10E-04 (0.51%)	-0.02	n/a
FeNiMetalSub	0.0500	n/a	0.0506 ± 0.0080 (15.76%)	-0.08	n/a
		RMS error	6.26E-05		
		$\chi^2_{d.o.f}$	0.0345		

Table 6.15: *brucemathminP1* `MCMC()` results. The unit for accuracy, σ, represents the retrieved abundance uncertainty: a negative value here ⇒ overestimation, a positive value ⇒ underestimation.

End-member	**'True' Abundance**	**Prior, P1**	**Retrieved Abundance**	**Accuracy to 'True' Abundance** σ	**Accuracy to P1 Abundance** σ
Augite	0.0150	0.3004 ± 3.00E-04 (0.10%)	0.2132 ± 2.83E-04 (0.13%)	-701.19	308.68
Enstatite	0.0850	0.0110 ± 1.10E-05 (0.10%)	0.0109 ± 1.37E-05 (0.13%)	5406.76	9.54
Olivine	0.7000	0.3872 ± 3.87E-04 (0.10%)	0.5346 ± 2.43E-04 (0.05%)	680.28	-606.43
Troilite	0.0500	0.5015 ± 5.02E-04 (0.10%)	0.1028 ± 4.30E-04 (0.42%)	-122.93	927.77
Albite	0.1000	0.6452 ± 6.45E-04 (0.10%)	0.1339 ± 5.51E-04 (0.41%)	-61.53	927.59
FeNiMetalSub	0.0500	0.8508 ± 8.51E-04 (0.10%)	2.46E-06 ± 9.71E-06 (394.26%)	5149.58	87631.39
		RMS error	0.0106		
		$\chi^2_{d.o.f}$	462.64		

***P1* (Figure 6.15, Table 6.15):**

The *brucemathminP1* `MCMC()` unmixing fit had an indiscernible uncertainty envelope (indicating high confidence in the modelled spectrum), with all the features well-aligned across the entire spectral range. However, there were some discrepancies in spectral contrast, seen clearly in the residuals particularly in the regions between $1645 - 1429\text{cm}^{-1}$, $1136 - 1097\text{cm}^{-1}$, $1070 - 1047\text{cm}^{-1}$, and $956 - 926\text{cm}^{-1}$ where they extended beyond ± 0.01 (Figure 6.15).

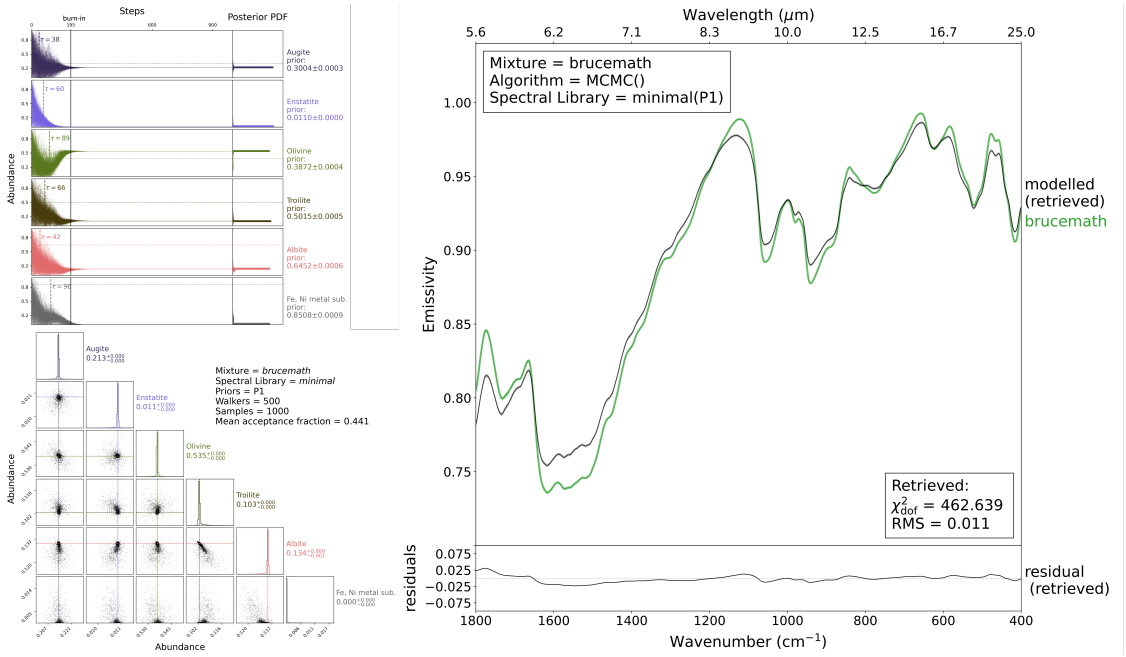


Figure 6.15: *brucemathminP1* `MCMC()` walkers and corner plots with model fit.

The influence of priors was evident here, particularly in the retrieval for the FeNiMetalSub end-member, which had a posterior pdf with a very narrow peak hugging the zero bound (Figure 6.15), and a poor precision of 395% (Table 6.15) – a vast contrast to the very high precisions of the other end-members ($< 0.5\%$). Another unique trait to the retrieval of FeNiMetalSub compared to the other end-members was the large discrepancy between its median (2.46×10^{-6}) and mean (0.0006) abundance values, whereas all the other end-members had almost identical values for their mean and median. Common to the other abundance estimates, however, was the accuracy, which was very poor across all the end-members ($\geq |61.6|\sigma$; Table 6.15).

The walkers plots for the *brucemathminP1* `MCMC()` unmixing (Figure 6.15) again showed that convergence was achieved by, or shortly after, the burn-in mark (195 steps in), and none simply converged on the priors (as shown by poor accuracy of retrieved abundances in relation to prior values; Table 6.15), which indicated that the data were still the driving force in the retrieval, despite the very tight priors of *P1*.

***P2* (Figure A.14, Table B.40):**

Unmixing *brucemathminP2* with `MCMC()` (Figure A.14, Table B.40) gave results almost identical to those for *brucemathminU* (Figure 6.14, Table 6.14), confirming that the very loose priors of *P2* were almost equivalent to no, or very diffuse, priors. The slight differences between the *brucemathminP2* and *brucemathminU* `MCMC()` unmixings, however, highlighted that even loose Gaussian priors can lead to a sufficiently different retrieval compared to Uniform priors; as evidenced by the $\chi^2_{d.o.f}$ for *brucemathminP2* (0.004) being an order of magnitude smaller that for *brucemathminU* (0.03). Even with large uncertainty, a Gaussian distribution will still be more constrained than the Uniform distribution, which was reflected here with the $\chi^2_{d.o.f}$ for *brucemathminU* and *brucemathminP2* being < 1 for both, but smaller for *brucemathminP2* as it was more over-constrained.

Table 6.16: Correlation matrix for retrieved abundances from the *brucemathminP2* `MCMC()` unmixing. Strong correlations ($> |0.6|$) are indicated in bold.

brucemathminP2	Au	En	Ol	Tr	Al	FeNi
Augite (Au)	1.000	**-0.882**	**-0.890**	0.050	-0.466	-0.010
Enstatite (En)	**-0.882**	1.000	**0.642**	0.043	0.303	-0.094
Olivine (Ol)	**-0.890**	**0.642**	1.000	0.001	0.408	-0.030
Troilite (Tr)	0.050	0.043	0.001	1.000	0.106	**-0.995**
Albite (Al)	-0.466	0.303	0.408	0.106	1.000	-0.174
FeNiMetalSub (FeNi)	-0.010	-0.094	-0.030	**-0.995**	-0.174	1.000

The `MCMC()` unmixings for *brucemathminU* and *brucemathminP2* had the same high correlation pairs: augite with enstatite, augite with olivine, enstatite with olivine, and troilite with FeNiMetalSub (Tables 6.13 for *U* and 6.16 for *P2*). The correlations were the same or weaker for *brucemathminP2* compared to *brucemathminU*; e.g., the correlation between augite and enstatite was -0.94 for

brucemathminU (Table 6.13), but was -0.88 for *brucemathminP2* (Table 6.16). This effect of priors acting to reduce correlation (and therefore degree of degeneracy) was also seen with the `OptEst_ASC_ILR()` unmixings (Section 6.1).

P3 (Figure A.15, Table 6.19):

As expected, the *brucemathminP3* `MCMC()` unmixing gave a perfect fit with indiscernible uncertainty envelope, residuals at zero (Figure A.15), RMS = 1.97×10^{-6}, and $\chi^2_{d.o.f} = 2.45 \times 10^{-5}$ (Table 6.19). The retrieved abundances were highly precise ($\leq 0.1\%$) and accurate (within 0.1σ; Table 6.19), with negligible difference between their median and mean values. Interestingly, there were a few strong correlation pairings here – enstatite with olivine (-0.89), enstatite with albite (0.66), olivine with albite (-0.88), and olivine with FeNiMetalSub (-0.70; Table 6.17) – which was not the case for the equivalent (*brucemathminP3*) unmixing with `OptEst_ASC_ILR()` (Section 6.1.1.1), and there were no obvious hints from the Bruce *minimal* library PCA plot (e.g., Figure 5.3) as to why this may be.

Table 6.17: Correlation matrix for retrieved abundances from the *brucemathminP3* `MCMC()` unmixing. Strong correlations ($> |0.6|$) are indicated in bold.

brucemathminP3	Au	En	Ol	Tr	Al	FeNi
Augite (Au)	1.000	-0.394	0.376	0.253	-0.370	-0.341
Enstatite (En)	-0.394	1.000	**-0.888**	-0.413	**0.660**	0.543
Olivine (Ol)	0.376	**-0.888**	1.000	0.343	**-0.884**	**-0.699**
Troilite (Tr)	0.253	-0.413	0.343	1.000	-0.446	-0.416
Albite (Al)	-0.370	**0.660**	**-0.884**	-0.446	1.000	0.541
FeNiMetalSub (FeNi)	-0.341	0.543	**-0.699**	-0.416	0.541	1.000

P4 (Figure A.16, Table B.41):

The *brucemathminP4* unmixing with `MCMC()` (Figure A.16, Table B.41) was largely similar to those using *U* (Figure 6.14 Table 6.14) and *P2* (Figure A.14, Table B.40), particularly in the model fit, as it displayed a 'perfect' fit with indiscernible residuals (zero across entire spectral range; Figure A.16), RMS = 3.33×10^{-5} and $\chi^2_{d.o.f} = 0.005$ (Table B.41). However, with unexpectedly strong correlation pairs – augite with enstatite (-0.78), augite with olivine (-0.85), augite with albite (-0.77), olivine with albite (0.71), and troilite with FeNiMetalSub (-0.98;

Table 6.18) – the *brucemathminP4* `MCMC()` unmixing was more similar to the *brucemathminP3* `MCMC()` unmixing in this aspect.

Table 6.18: Correlation matrix for retrieved abundances from the *brucemathminP4* `MCMC()` unmixing. Strong correlations ($> |0.6|$) are indicated in bold.

brucemathminP4	Au	En	Ol	Tr	Al	FeNi
Augite (Au)	1.000	**-0.784**	**-0.846**	-0.214	**-0.766**	0.346
Enstatite (En)	**-0.784**	1.000	0.422	0.200	0.408	-0.309
Olivine (Ol)	**-0.846**	0.422	1.000	0.191	**0.707**	-0.297
Troilite (Tr)	-0.214	0.200	0.191	1.000	0.305	**-0.980**
Albite (Al)	**-0.766**	0.408	**0.707**	0.305	1.000	-0.467
FeNiMetalSub (FeNi)	0.346	-0.309	-0.297	**-0.980**	-0.467	1.000

6.2.1.2 *brucerealmin* Unmixings

***U* (Figure 6.16, Table 6.20):**

The *brucerealminU* `MCMC()` unmixing gave a poor fit (Figure 6.16), with RMS = 0.016, $\chi^2_{d.o.f} = 484.1$ (Table 6.20), and overall residual morphology similar to those for the reduced spectral contrast *brucemath* spectrum subtracted from the *brucereal* spectrum across the entire spectral range (Figure 5.1), again mostly indicating offsets in spectral contrast as the majority of features were well aligned.

The retrieved abundances had a mix of low and high precision, with the worst precision for enstatite and FeNiMetalSub (254.5% and 255.0%, respectively), and the best for olivine (0.11%; Table 6.20). The low precision for enstatite and FeNiMetalSub was also apparent in their posterior pdfs (Figure 6.16), appearing as the right half of a Gaussian distribution due to being peaked at the lower bound of 0.

Table 6.19: *brucemathminP3* `MCMC()` results. The unit for accuracy, σ, represents the retrieved abundance uncertainty: a negative value here ⇒ overestimation, a positive value ⇒ underestimation.

End-member	**'True' Abundance**	**Prior, P3**	**Retrieved Abundance**	**Accuracy to 'True' Abundance** σ	**Accuracy to P3 Abundance** σ
Augite	0.015	0.0150 ± 1.50E-05 (0.10%)	0.0150 ± 1.64E-05 (0.11%)	0.08	0.08
Enstatite	0.085	0.0850 ± 8.50E-05 (0.10%)	0.0850 ± 9.26E-05 (0.11%)	-0.07	-0.07
Olivine	0.7	0.7000 ± 7.00E-04 (0.10%)	0.7000 ± 1.48E-04 (0.02%)	0.07	0.07
Troilite	0.05	0.0500 ± 5.00E-05 (0.10%)	0.0500 ± 5.46E-05 (0.11%)	0.1	0.1
Albite	0.1	0.1000 ± 1.00E-04 (0.10%)	0.1000 ± 1.03E-04 (0.10%)	-0.07	-0.07
FeNiMetalSub	0.05	0.0500 ± 5.00E-05 (0.10%)	0.0500 ± 5.45E-05 (0.11%)	-0.08	-0.08
		RMS error	1.97E-06		
		$\chi^2_{d.o.f}$	2.46E-05		

Table 6.20: *brucerealminU* `MCMC()` results. The unit for accuracy, σ, represents the retrieved abundance uncertainty: a negative value here ⇒ overestimation, a positive value ⇒ underestimation.

End-member	**'True' Abundance**	**Prior, U**	**Retrieved Abundance**	**Accuracy to 'True' Abundance** σ	**Accuracy to U Abundance** σ
Augite	0.0150	n/a	0.1376 ± 0.0009 (0.67%)	-132.39	n/a
Enstatite	0.0850	n/a	6.24E-06 ± 1.59E-05 (254.48%)	5351.27	n/a
Olivine	0.7000	n/a	0.5373 ± 6.11E-04 (0.11%)	266.09	n/a
Troilite	0.0500	n/a	0.3012 ± 0.0009 (0.31%)	-265.44	n/a
Albite	0.1000	n/a	0.0328 ± 0.0010 (2.91%)	70.34	n/a
Fe, Ni metal sub.	0.0500	n/a	1.10E-04 ± 2.79E-04 (255.01%)	178.6	n/a
		RMS error	0.0158		
		$\chi^2_{d.o.f}$	484.11		

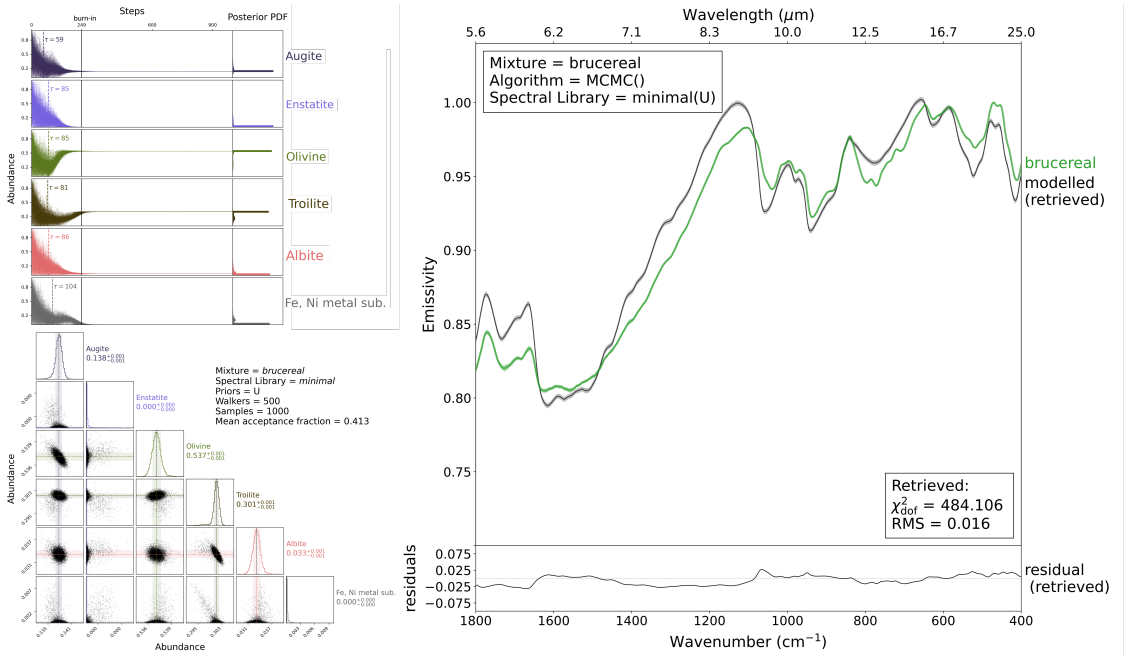


Figure 6.16: *brucerealminU* `MCMC()` walkers and corner plots with model fit.

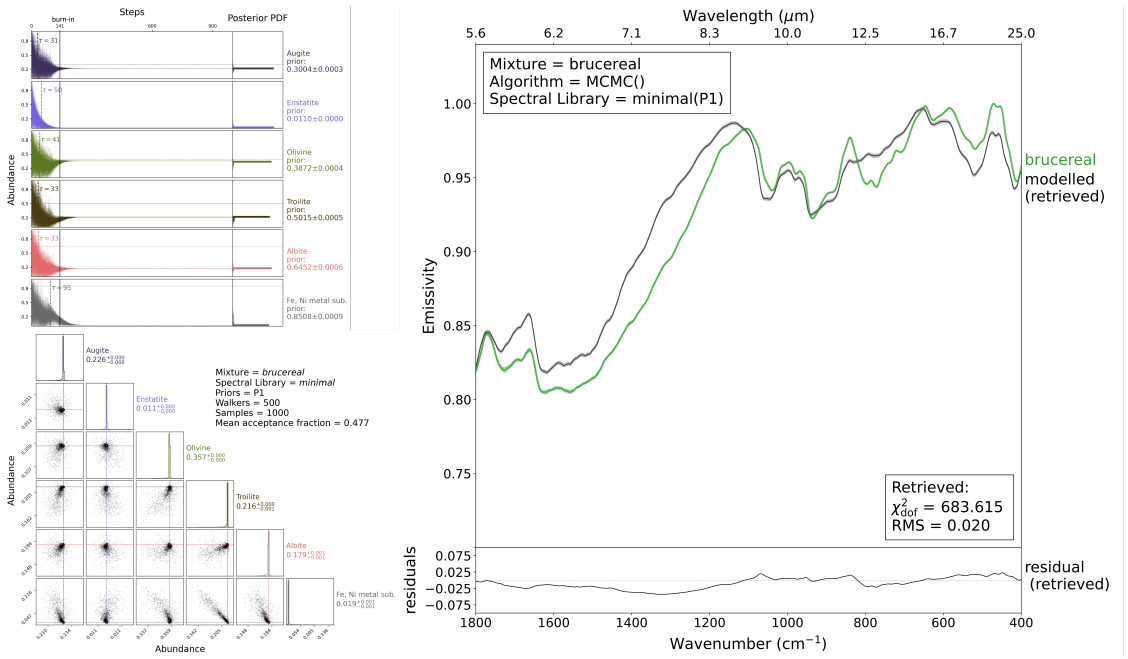


Figure 6.17: *brucerealminP1* `MCMC()` walkers and corner plots with model fit.

P1 (Figure 6.17, Table B.42):

The `MCMC()` unmixing of *brucerealminP1* displayed a poor fit (i.e., RMS = 0.020, $\chi^2_{d.o.f}$ = 683.6; Figure 6.17, Table B.42), with residuals resembling those for the `OptEst_ASC_ILR()` unmixing of *brucerealminP1* (Figure 6.4, Section 6.1.1.2).

The poor accuracies ($|1270|\sigma$ on average) but high precisions (0.90% on average) of the *brucerealminP1* `MCMC()` derived abundances were well captured in the posterior pdfs, which all appeared as very narrow single peaks centred around abundances distant from the correct values (Figure 6.17).

Contrary to the previously seen trend that tighter priors led to weaker correlation, there were several strongly correlated pairs – augite with troilite (0.66), augite with FeNiMetalSub (-0.74), olivine with troilite (0.73), olivine with FeNiMetalSub (-0.80), troilite with albite (0.66), troilite with FeNiMetalSub (-0.96), and albite with FeNiMetalSub (-0.78; Table 6.21) – which was vastly different from the *brucerealminP1* unmixing with `OptEst_ASC_ILR()` (Section 6.1.1.2); so this could be an initial indication into how the optimal estimation and MCMC algorithms use priors differently.

Table 6.21: Correlation matrix for retrieved abundances from the *brucerealminP1* `MCMC()` unmixing. Strong correlations ($> |0.6|$) are indicated in bold.

brucerealminP1	Au	En	Ol	Tr	Al	FeNi
Augite (Au)	1.000	-0.371	0.520	**0.659**	0.476	**-0.739**
Enstatite (En)	-0.371	1.000	-0.513	-0.430	-0.299	0.470
Olivine (Ol)	0.520	-0.513	1.000	**0.734**	0.455	**-0.802**
Troilite (Tr)	**0.659**	-0.430	**0.734**	1.000	**0.659**	**-0.963**
Albite (Al)	0.476	-0.299	0.455	**0.659**	1.000	**-0.778**
FeNiMetalSub (FeNi)	**-0.739**	0.470	**-0.802**	**-0.963**	**-0.778**	1.000

***P2* (Figure A.17, Table B.43):**

The *brucerealminP2* `MCMC()` unmixing also had a similar fit (RMS = 0.016, $\chi^2_{d.o.f} = 484.1$) to its `OptEst_ASC_ILR()` counterpart (RMS = 0.017, $\chi^2_{d.o.f} = 525.9$), but displayed a greater degree of strong correlation in comparison – four strongly correlated pairs for unmixing *brucerealminP2* with `MCMC()` (Table 6.22), vs two pairs with `OptEst_ASC_ILR()` (Table C.4). Overall, this `MCMC()` unmixing of *brucerealmin* with the *P2* version of the priors was very similar to that using the U priors.

Table 6.22: Correlation matrix for retrieved abundances from the *brucerealminP2* `MCMC()` unmixing. Strong correlations (> |0.6|) are indicated in bold.

brucerealminP2	Au	En	Ol	Tr	Al	FeNi
Augite (Au)	1.000	-0.323	**-0.690**	0.203	-0.274	-0.308
Enstatite (En)	-0.323	1.000	0.142	**-0.740**	0.365	**0.742**
Olivine (Ol)	**-0.690**	0.142	1.000	-0.039	-0.173	0.123
Troilite (Tr)	0.203	**-0.740**	-0.039	1.000	-0.569	**-0.949**
Albite (Al)	-0.274	0.365	-0.173	-0.569	1.000	0.359
FeNiMetalSub (FeNi)	-0.308	**0.742**	0.123	**-0.949**	0.359	1.000

P3 (Figure 6.18):

The walkers plots for the `MCMC()` unmixing of *brucerealminP3* converged tightly around the priors before the burn-in mark (i.e., before 222 steps in; Figure 6.18); which could be an indication that convergence is related to how priors are set, with convergence being achieved more quickly when the priors represent the correct solution. Again here, there was generally a stronger degree of correlation observed between the retrieved end-member abundances for the *brucerealminP3* `MCMC()` unmixing (average correlation |0.37|; Table 6.23) than seen for the *brucerealminP3* `OptEst_ASC_ILR()` unmixing (average correlation |0.14|; Section 6.1.1.2, Table C.5).

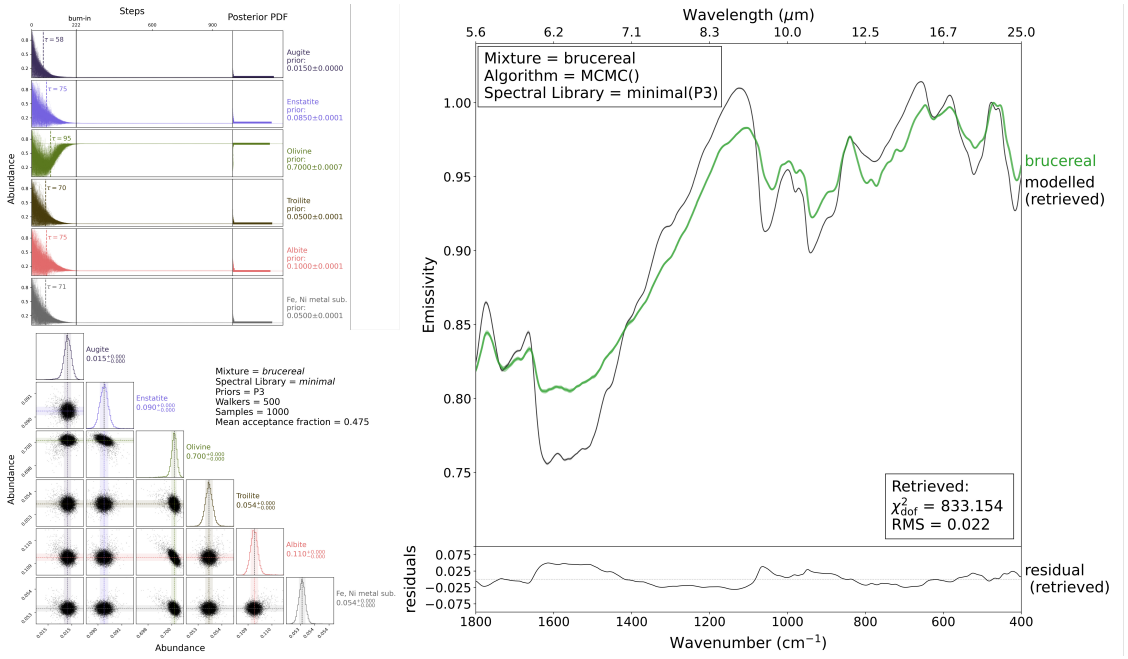


Figure 6.18: *brucerealminP3* `MCMC()` walkers and corner plots with model fit.

Table 6.23: Correlation matrix for retrieved abundances from the *brucerealminP3* `MCMC()` unmixing. Strong correlations ($> |0.6|$) are indicated in bold.

brucerealminP3	Au	En	Ol	Tr	Al	FeNi
Augite (Au)	1.000	-0.156	0.381	-0.176	-0.351	-0.331
Enstatite (En)	-0.156	1.000	-0.537	0.145	0.192	0.215
Olivine (Ol)	0.381	-0.537	1.000	-0.521	**-0.824**	**-0.727**
Troilite (Tr)	-0.176	0.145	-0.521	1.000	0.274	0.288
Albite (Al)	-0.351	0.192	**-0.824**	0.274	1.000	0.484
FeNiMetalSub (FeNi)	-0.331	0.215	**-0.727**	0.288	0.484	1.000

***P4* (Figure 6.19):**

The *brucerealminP4* `MCMC()` unmixing (Figure 6.19) had an almost identical model fit to the *brucerealminU* and *brucerealminP2* `MCMC()` unmixings (Figures 6.16 and A.17, respectively); with indiscernible uncertainty envelope, residuals extending beyond ± 0.01 between $1800 - 1651\text{cm}^{-1}$, $1440 - 1103\text{cm}^{-1}$, $1081 - 1044\text{cm}^{-1}$, $962 - 942\text{cm}^{-1}$, $823 - 765\text{cm}^{-1}$, $721 - 666\text{cm}^{-1}$, $566 - 502\text{cm}^{-1}$, and $477 - 411\text{cm}^{-1}$ (e.g., Figure 6.19), RMS = 0.015755, 0.015773, and 0.015771, and $\chi^2_{d.o.f} = 484.1539$, 484.1063, and 484.1083, for *P4*, *U* and *P2*, respectively. Unmixing *brucerealminP4* with `MCMC()` also gave the same set of strongly correlated pairs as *brucerealminU* and *brucerealminP2*, with some of them showing slightly weaker correlation and some slightly stronger:

- augite and olivine: -0.63 (*P4*), -0.74 (*U*), -0.69 (*P2*)
- enstatite and troilite: -0.73 (*P4*), -0.72 (*U*), -0.74 (*P2*)
- enstatite and FeNiMetalSub: 0.75 (*P4*), 0.73 (*U*), 0.74 (*P2*)
- troilite and FeNiMetalSub: -0.97 (*P4*), -0.95 (*U*), -0.95 (*P2*)

Table 6.24: Correlation matrix for retrieved abundances from the *brucerealminP4* `MCMC()` unmixing. Strong correlations ($> |0.6|$) are indicated in bold.

brucerealminP4	Au	En	Ol	Tr	Al	FeNi
Augite (Au)	1.000	-0.321	**-0.634**	0.251	-0.237	-0.333
Enstatite (En)	-0.321	1.000	-0.022	**-0.731**	0.186	**0.752**
Olivine (Ol)	**-0.634**	-0.022	1.000	0.099	-0.214	-0.043
Troilite (Tr)	0.251	**-0.731**	0.099	1.000	-0.385	**-0.973**
Albite (Al)	-0.237	0.186	-0.214	-0.385	1.000	0.216
FeNiMetalSub (FeNi)	-0.333	**0.752**	-0.043	**-0.973**	0.216	1.000

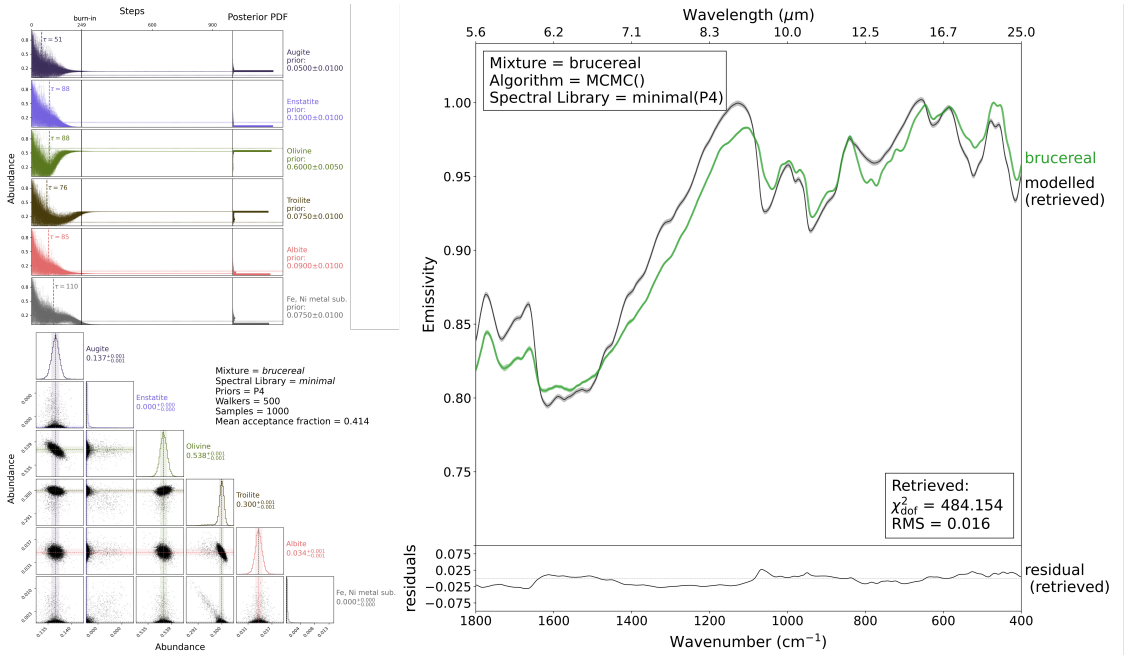


Figure 6.19: *brucerealminP4* `MCMC()` walkers and corner plots with model fit.

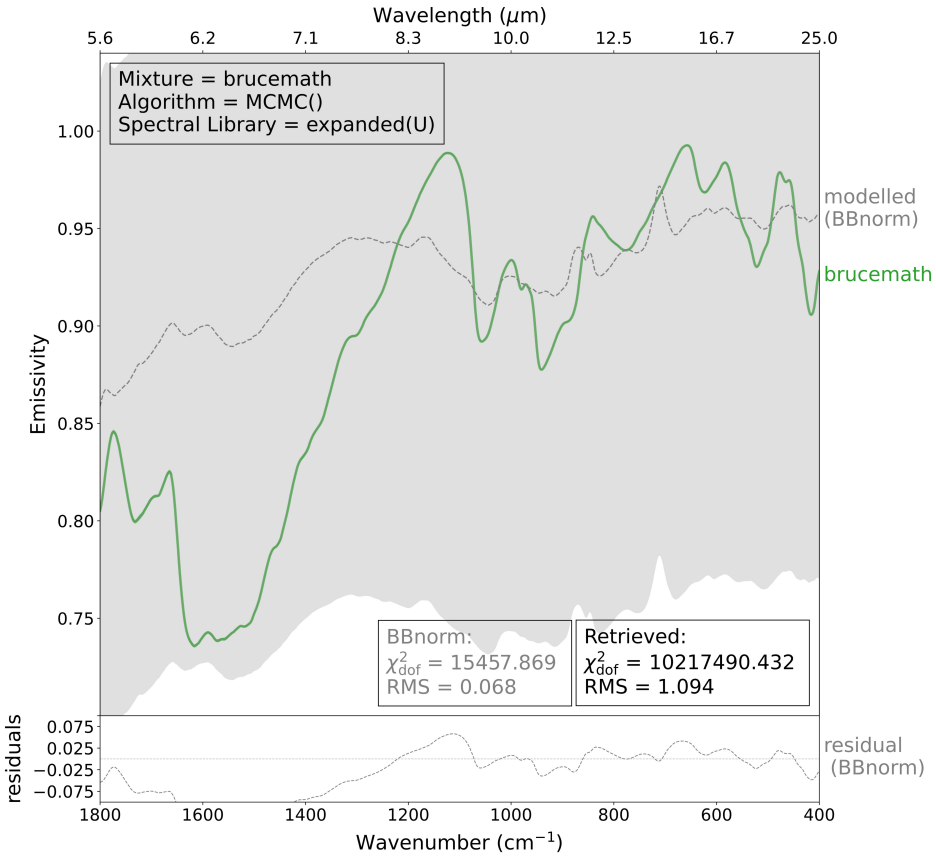
6.2.1.3 *brucemathexp* Unmixings

The `MCMC()` Bruce unmixings using the *expanded* spectral library showed the first indications of issues with `MCMC()` not incorporating an abundance sum constraint – the retrieved abundances throughout $U{\rightarrow}P4$ did not sum to one (usually > 1), and so their modelled spectra often went off the useful axes scale for model fit visualisation. With the blackbody renormalisation (BBnorm) step, however, the BBnorm abundances did sum to one, and so the BBnorm modelled spectra were more appropriate for considering fit quality (as considered in the following analyses); hence figures for any Bruce unmixing against the *expanded* spectral library with `MCMC()` presented in this thesis show only the BBnorm modelled spectra where it is not practical to also show the retrieved modelled spectra.

U (Figure 6.20, Table B.44):

The `MMC()` unmixing of *brucemathexpU* gave a very poor fit (BBnorm: RMS = 0.068 and $\chi^2_{d.o.f} = 15457.9$; Table B.44), showing almost no common features with *brucemath* across the entire spectral range (Figure 6.20a), and a very wide uncertainty envelope (± 0.18 on average across the spectral range). In fact, morphologically,

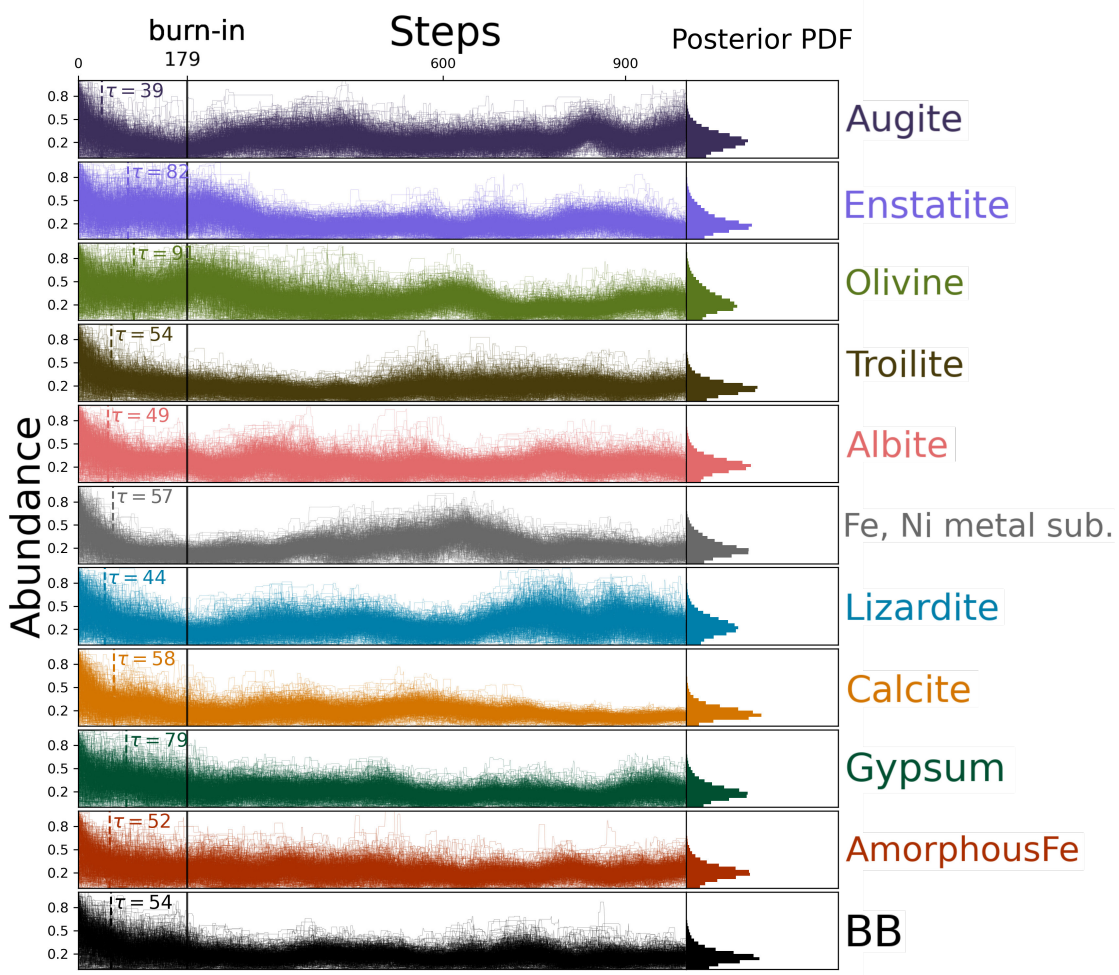
the residuals more closely resembled the *brucemath* spectrum than the BBnorm modelled spectrum did, thus emphasising the poor performance of this retrieval.



(a) *brucemathexpU* `MCMC()` model fit.

Figure 6.20: *brucemathexpU* `MCMC()` (a) model fit with (b) walkers and (c) corner plots. For clarity, each subfigure here is shown larger than in similar figures, with guidance on how to interpret each in the subcaptions. In general, the important thing to takeaway from the corner and walkers plots are the general shapes displayed, since important quantitative information from the axes etc. are presented in the relevant tables.

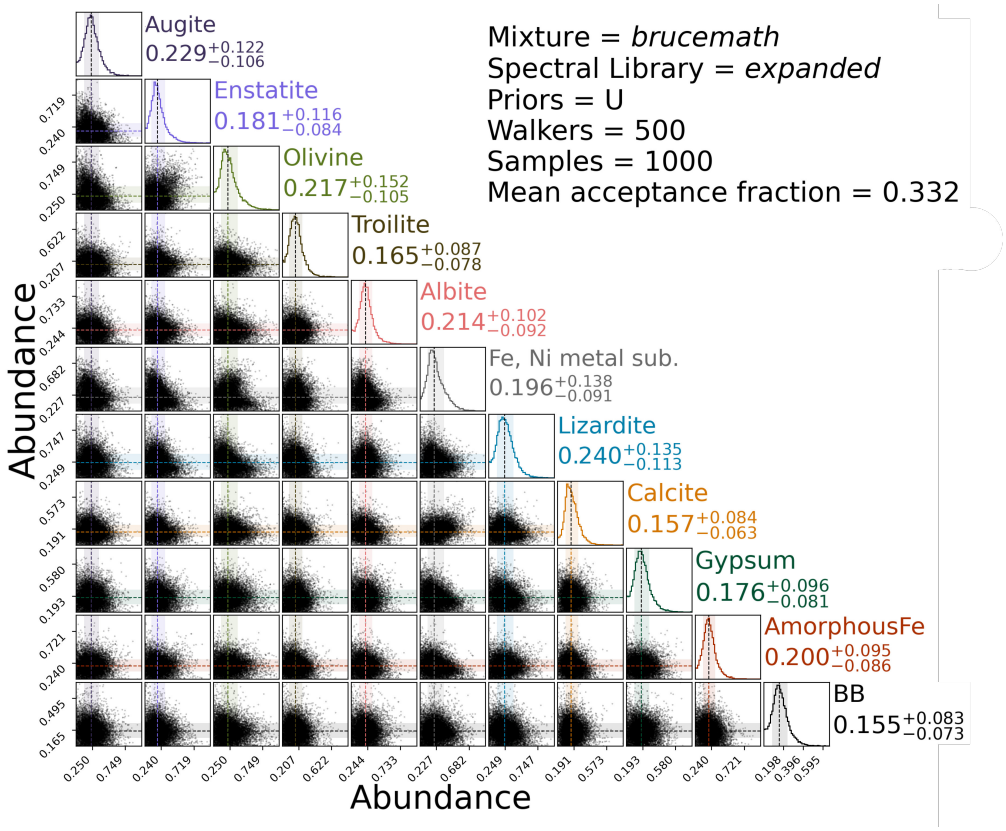
The walkers plots all appeared converged, but with a wide spread about the modal values (average walkers range of 0.89 post-burn-in across all end-members; Figure 6.20b), as reflected by the poor retrieved accuracies of $47-70\%$ (Table B.44).



(b) *brucemathexpU* `MCMC()` walkers plot. When interpreting the walkers plots, the key aspect to notice is whether convergence has been achieved post-burn-in – by the end of the chain, which was 1000 steps in this case, there should be no overall gradient/trend in the abundance value with progressive step numbers. The frequency of abundances for each end-member, as selected by each walker at each step, is mapped as a histogram displaying the posterior pdf on the right hand side, and is rotated 90° clockwise to how they are usually viewed, such as in the corner plots.

Figure 6.20: (cont.) *brucemathexpU* `MCMC()` model fit, walkers and corner plots.

Most of the posterior pdfs appeared Gaussian (Figure 6.20c) with perhaps a slight tail towards larger abundances, and their peaks generally well-aligned with their median values. The only slight deviation from this was the olivine pdf, which could be considered slightly bimodal with the median value lying in between the two 'peaks' (Figure 6.21).



(c) *brucemathexpU* `MCMC()` corner plot. Axes along the diagonal show the posterior pdfs for the end-members (labelled on their right). The key property shown here are the shapes of the pdfs (quantitative interpretation of the pdfs for abundances and uncertainties are presented in the relevant tables). Any pdfs of particularly notable shape are shown separately (e.g., olivine in Figure 6.21). Inner axes show the joint pdfs for the end-members indicated by column and row position. Again, the shape of these is of greatest importance for interpretation – more circular distributions indicate low to no correlation, whereas diagonal trends show moderate to strong correlation.

Figure 6.20: (cont.) *brucemathexpU* `MCMC()` model fit, walkers and corner plots.

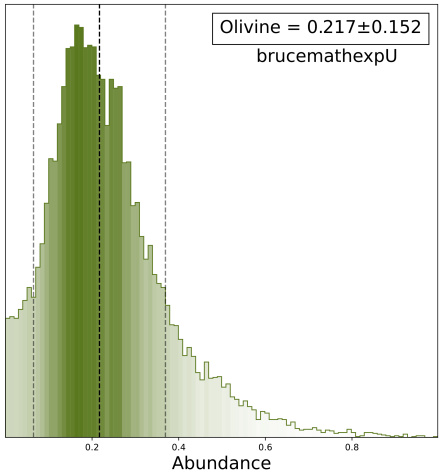


Figure 6.21: *brucemathexpU* `MCMC()` olivine posterior pdf.

***P1→P4* (Figures A.18, A.19, A.20, A.21, Tables B.45, B.46, B.47, B.48):**

The *brucemathexpP1* `MCMC()` unmixing (Figure A.18, Table B.45) gave very much the same results as *brucemathexpU* (Figure 6.20, Table B.44), with a minor difference being that the olivine posterior pdf appeared slightly less bimodal (Figure A.18). Unmixing with *P2* for *brucemathexp* in `MCMC()` (Figure A.19, Table B.46) again gave very similar results to those for *brucemathexpU* and *brucemathexpP1*, but the *brucemathexpP2* posterior pdfs for troilite, lizardite and BB had slightly more prominent tails, and the amorphous Fe posterior pdf appeared very slightly bimodal (Figure 6.22). Virtually the same results were seen again for the *brucemathexpP3* (Figure A.20, Table B.47) and *brucemathexpP4* (Figure A.21, Table B.48) `MCMC()` unmixings, with minor variations in exact shape of each end-member's posterior pdf.

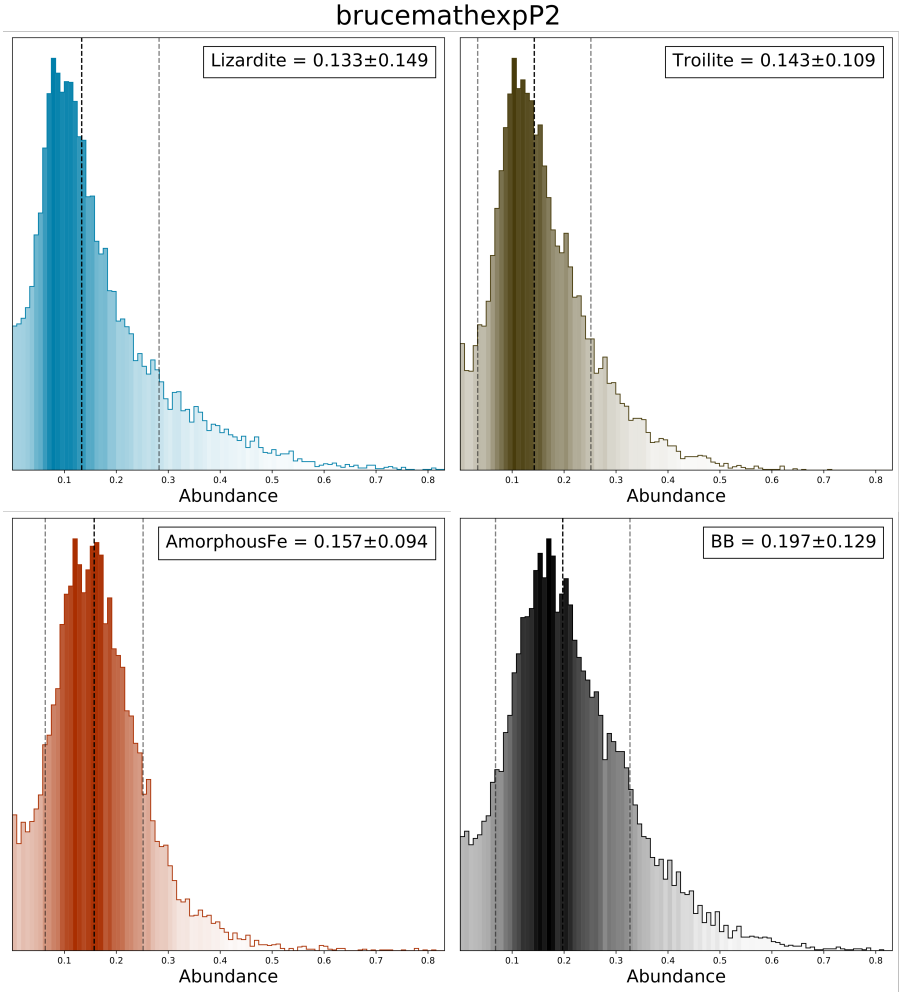


Figure 6.22: *brucemathexpP2* `MCMC()` lizardite, troilite, amorphous Fe and BB posterior pdfs.

6.2.1.4 *brucerealexp* Unmixings

The *brucerealexpU→P4* `MCMC()` unmixings (Tables B.49, B.50, B.51, B.52, B.53) were much the same as those for *brucemathexpU→P4* (Section 6.2.1.3), with these all retrieving very similar abundances, of order $0.1 - 0.2$, for each end-member (Tables B.44 to B.53).

Comparing the abundance quality metric for the *brucerealexpU→P4* `MCMC()` unmixings (between $0.99 - 1.43$, 1.16 on average including retrieved and BBnorm abundances; Table 6.29) with those from `WLS_ASC_ILR()` (1.18; Table 5.9) and `OptEst_ASC_ILR()` (between $0.29 - 5.81$, 2.20 on average including retrieved and BBnorm values; Table 6.12), the performance of `MCMC()` unmixing *brucereal* against the Bruce *expanded* spectral library was similar to that for the *brucerealexp* `WLS_ASC_ILR()` unmixing; implying a lack of improvement in performance from a basic linear least squares to a sophisticated MCMC.

6.2.1.5 *brucemathext* Unmixings

Issues with the lack of abundance sum constraint within `MCMC()` were further exaggerated in the `MCMC()` unmixings against the *extensive* spectral library, so, as for the unmixings against the *expanded* library, discussions of fit refer to the modelled spectrum using the blackbody renormalised (BBnorm) abundances, unless specified otherwise.

***U* (Figure 6.23, Table B.54):**

The *brucemathextU* `MCMC()` unmixing gave a terrible fit (BBnorm RMS = 0.079, $\chi^2_{d.o.f} = 21308.3$; Figure 6.23, Table B.54), and although most of the posterior pdfs appeared as single peaked Gaussians (with some potentially more log-normal or Poisson due to slight tails; Figure 6.23), those for saponite, amorphous Fe and FeNiMetalSub were notably slightly different. The saponite pdf had a slight bump on the tail (around 0.522), and the amorphous Fe and FeNiMetalSub both appeared almost bimodal (or could be seen as having a wide peak with internal variation; Figure 6.24).

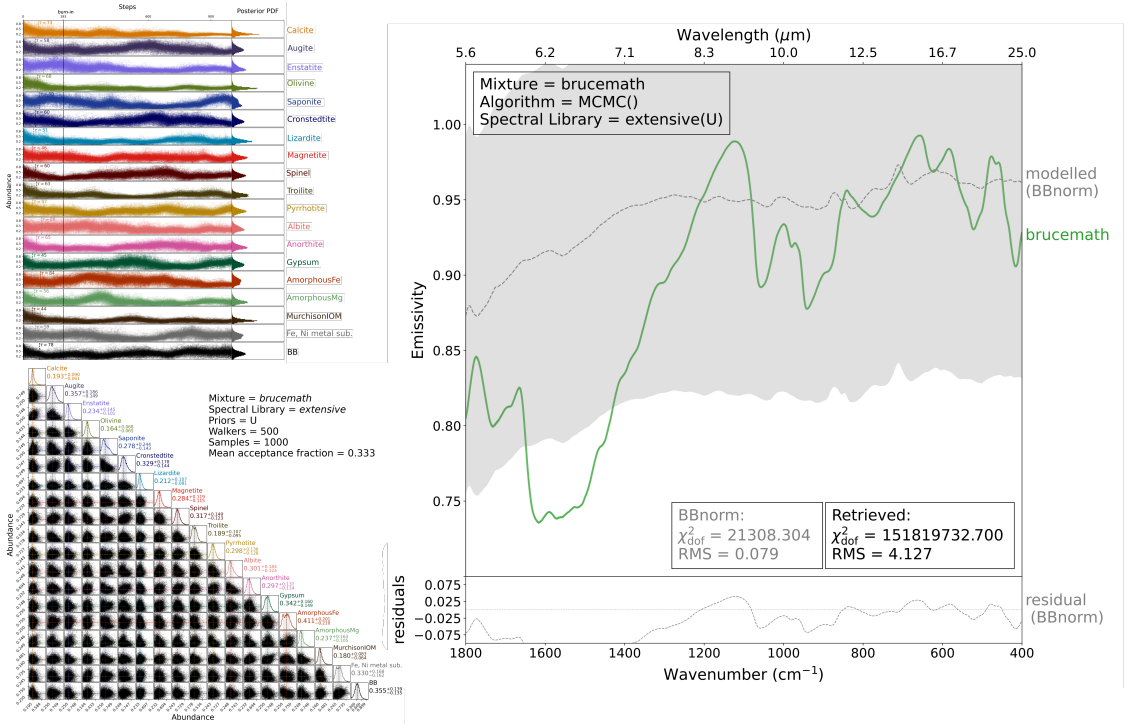


Figure 6.23: *brucemathextU* `MCMC()` walkers and corner plots with model fit.

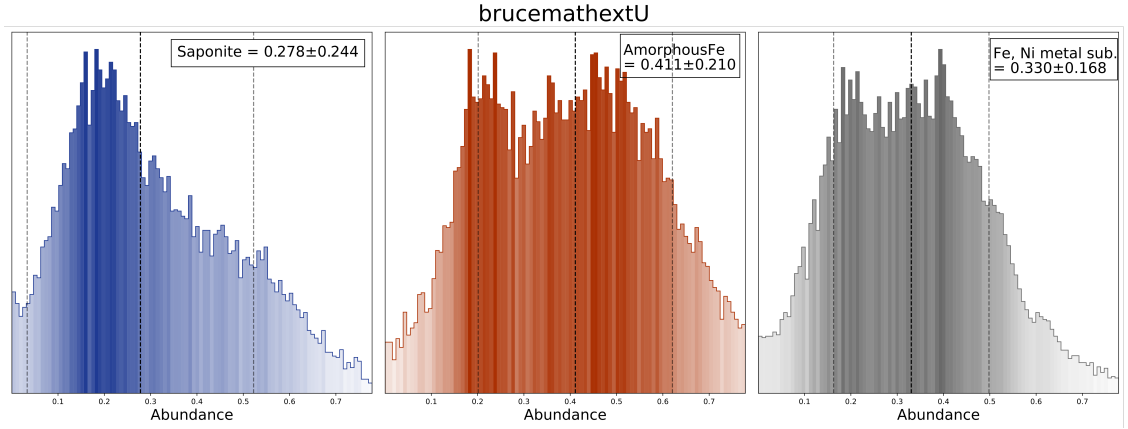


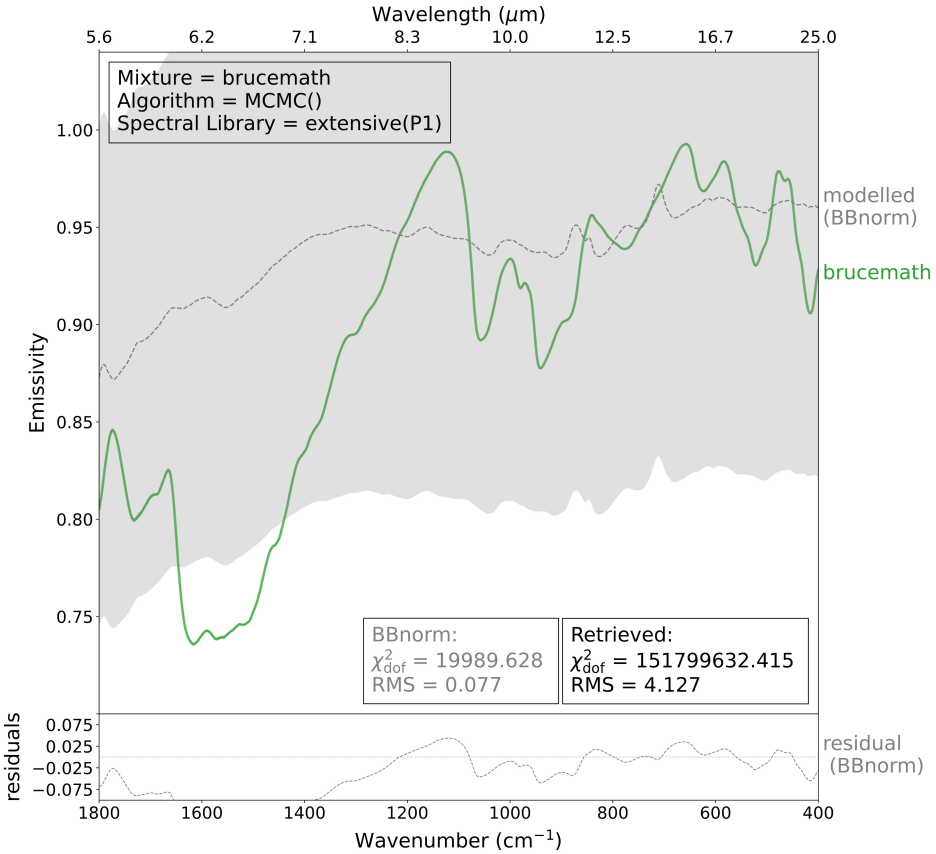
Figure 6.24: *brucemathextU* `MCMC()` saponite, amorphous Fe and FeNiMetalSub posterior pdfs.

Similarly to the *brucemathexp* `MCMC()` unmixings (Section 6.2.1.3), the retrieved abundances for the *brucemathextU* `MCMC()` unmixing were generally very similar, but covering a slightly larger range, of the order $0.2-0.4$ (Table B.54), and displayed generally weak correlations ($|0.15|$ on average; Table C.20).

P1 (Figure 6.25):

The `MCMC()` derived model fit for *brucemathextP1* (Figure 6.25a) was almost

identical to that for *brucemathextU* unmixed with `MCMC()` (Figure 6.23), but for *brucemathextP1*, there was a high correlation pair – saponite and amorphous Fe, with a correlation of 0.63 (Table C.21). The cause of this correlation was unclear, but referring back to the *extensive* PCA plot (e.g., Figure 5.5), saponite and amorphous Fe were relatively distant from each other, signifying substantial spectral differences, and so more of one may require more of the other to balance out; hence the positive correlation.

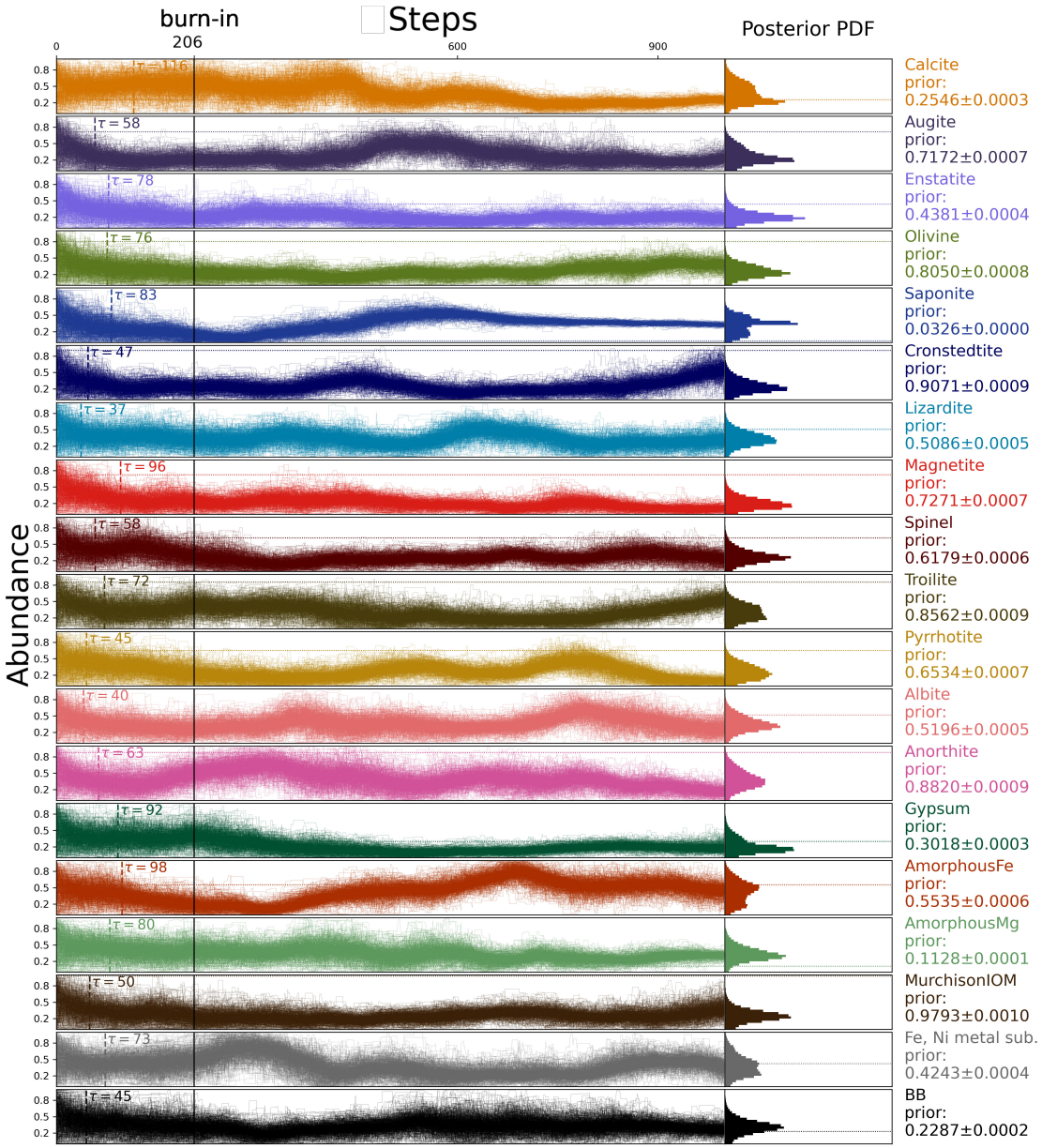


(a) *brucemathextP1* `MCMC()` model fit.

Figure 6.25: *brucemathextP1* `MCMC()` (a) model fit with (b) walkers and (c) corner plots. For clarity, each subfigure here is shown larger than in similar figures, with guidance on how to interpret each in the subcaptions. In general, the important thing to takeaway from the corner and walkers plots are the general shapes displayed, since important quantitative information from the axes etc. are presented in the relevant tables.

Convergence of some end-members for the *brucemathextP1* unmixing with `MCMC()` was hard to judge from the walkers plots (Figure 6.25b), as these did not appear to be completely settled by the end of the chain – i.e., general trend of walkers

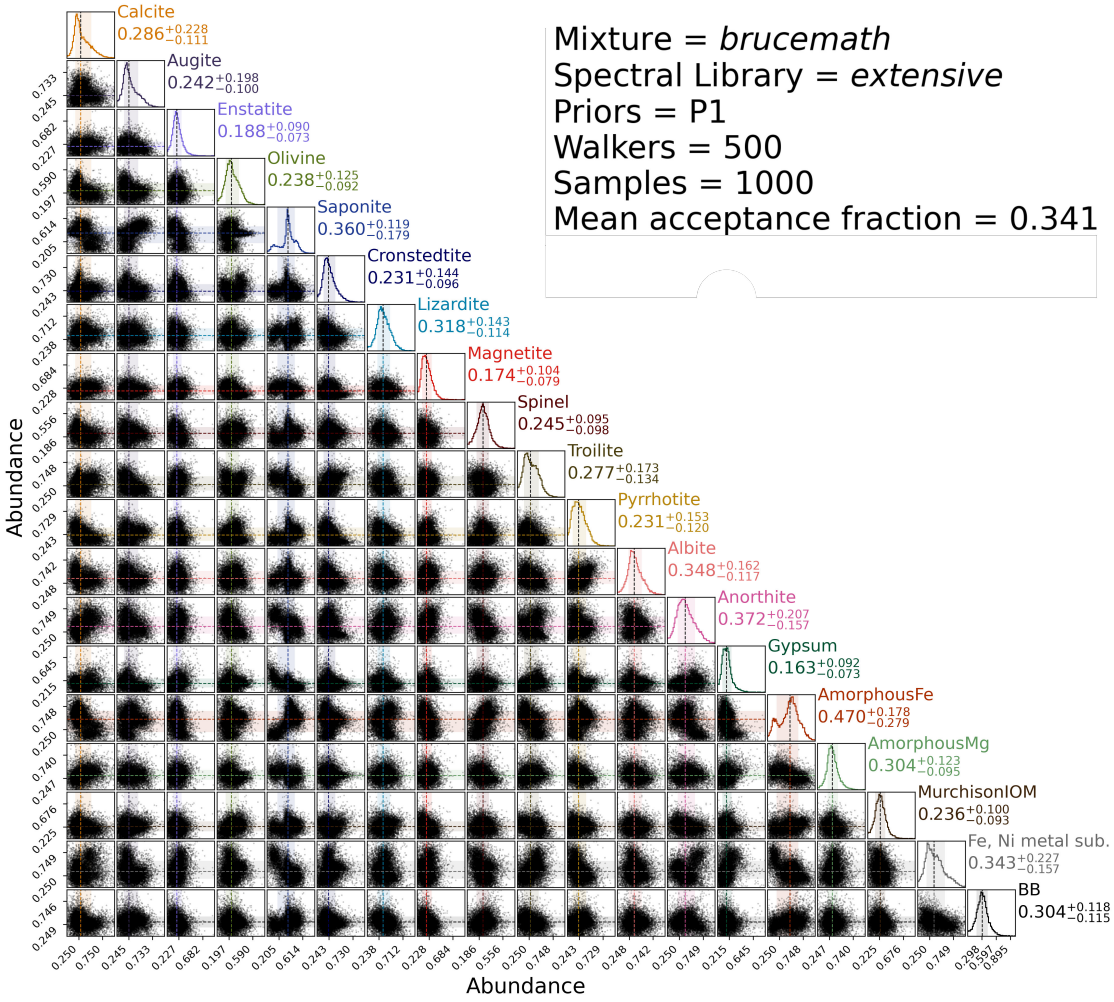
had non-zero gradient within the last ~ 50 steps of the chain; particularly evident for cronstedtite and troilite, but also seen more subtly in augite, MurchisonIOM, and FeNiMetalSub (Figure 6.25b).



(b) *brucemathextP1* `MCMC()` walkers plot. When interpreting the walkers plots, the key aspect to notice is whether convergence has been achieved post-burn-in – by the end of the chain, which was 1000 steps in this case, there should be no overall gradient/trend in the abundance value with progressive step numbers. The frequency of abundances for each end-member, as selected by each walker at each step, is mapped as a histogram displaying the posterior pdf on the right hand side, and is rotated 90° clockwise to how they are usually viewed, such as in the corner plots. The value of the *P1* prior for each end-member is also indicated here, so it is possible to see whether the walkers converged on the priors or not.

Figure 6.25: (cont.) *brucemathextP1* `MCMC()` model fit, walkers and corner plots.

Some of the posterior pdfs from the *brucemathextP1* `MCMC()` unmixing strayed away from the Gaussian distribution, displaying a range of shapes such as tails (particularly clear for e.g., calcite, augite; Figure 6.25c), bumps/tenuous bimodality (e.g., troilite, FeNiMetalSub; Figure 6.26) and clear bimodality (e.g., saponite, amorphous Fe; Figure 6.26). Much the same was also observed for the `MCMC()` unmixings of *brucemathextP2→P4*.



(c) *brucemathextP1* `MCMC()` corner plot. Axes along the diagonal show the posterior pdfs for the end-members (labelled on their right). The key property shown here are the shapes of the pdfs (quantitative interpretation of the pdfs for abundances and uncertainties are presented in the relevant tables). Any pdfs of particularly notable shape are shown separately (e.g., saponite, troilite, amorphousFe and FeNiMetalSub in Figure 6.26). Inner axes show the joint pdfs for the end-members indicated by column and row position. Again, the shape of these is of greatest importance for interpretation – more circular distributions indicate low to no correlation, whereas diagonal trends show moderate to strong correlation.

Figure 6.25: (cont.) *brucemathextP1* `MCMC()` model fit, walkers and corner plots.

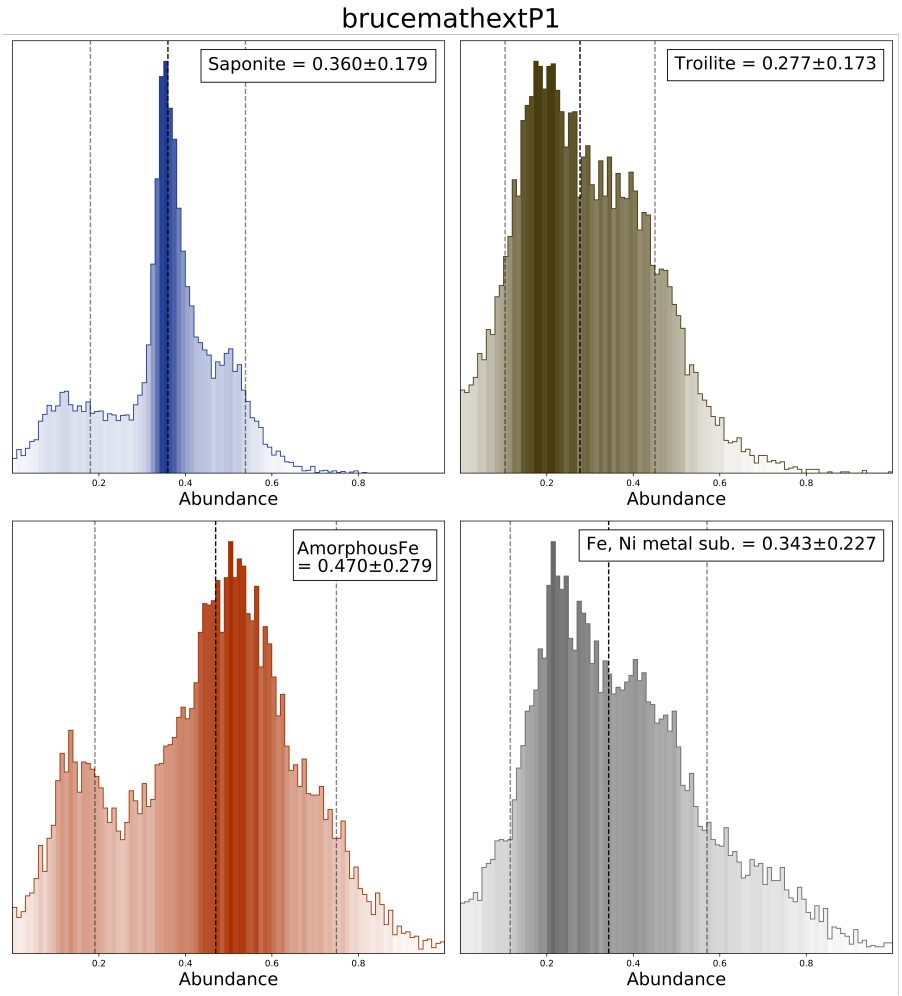


Figure 6.26: *brucemathextP1* `MCMC()` saponite, troilite, amorphous Fe and FeNiMetalSub posterior pdfs.

6.2.1.6 *brucerealext* Unmixings

Generally, the *brucerealextU→P4* `MCMC()` unmixings (Figures A.22, A.23, A.24, A.25, A.26, Tables B.55, B.56, B.57, B.58, B.59) showed the same results as those seen for *brucemathextU→P4* (Section 6.2.1.5), but this time with perhaps a greater diversity of posterior pdf morphologies (Figures A.22 to A.26). More of the end-member posterior pdfs from the *brucerealextU→P4* `MCMC()` unmixings displayed a variety of tails (e.g., amorphous Fe for *U*, olivine for *P1*, augite, enstatite for *P3*, and calcite, cronstedtite for *P4*), bumps (e.g., troilite, anorthite, amorphous Mg for *P1*, lizardite for *P2*, saponite, and albite for *P3*), and bimodality (e.g., calcite and augite for *U*, saponite for *P1*, calcite for *P2*, calcite, and cronstedtite, spinel,

pyrrhotite, gypsum, FeNiMetalSub for *P3*; Figures A.22 to A.26). Another common result was the small range of abundance qualities across *U→P4* ($0.98 - 2.06$; Table 6.29), suggesting little influence from the priors during the abundance estimation.

6.2.1.7 Summary of Bruce `MCMC()` Unmixings

The Bruce unmixings with the `MCMC()` algorithm have generally displayed a higher degree of strong correlations, providing a stark difference to a major conclusion from `OptEst_ASC_ILR()`: that priors can act to reduce correlation. Results from the *brucerealminU→P4* `MCMC()` unmixings further disagreed with the conclusion from the `OptEst_ASC_ILR()` unmixings that inaccurate priors with high confidence are worse than none/diffuse priors; therefore this conclusion was not applicable to the `MCMC()` algorithm.

Abundances for the *brucemathexpU→P4* `MCMC()` unmixings were more similar across the different versions of priors than they were when using `OptEst_ASC_ILR()` to unmix *brucemathexpP1→P4*, which could suggest that priors have a smaller influence within `MCMC()` compared to `OptEst_ASC_ILR()`.

The mean acceptance fraction (i.e., the mean of the fraction of proposed steps that were accepted, taken over all end-members) should be between $0.2 - 0.5$ (Foreman-Mackey et al. 2013), which was the case for all the Bruce `MCMC()` unmixings, indicating that there were no issues with the quality of sampling; thus interpretations of these `MCMC()` unmixings were unaffected by faulty sampling.

On the whole, the `MCMC()` algorithm performed very poorly for these Bruce unmixings, especially with the *expanded* and *extensive* spectral libraries. The only exception to this was that the *minimal* spectral library unmixings performed well, with nice clear convergences in particular; and the fact these performed so well gave more confidence to the interpretation of the other unmixings.

6.2.2 Glenn

Finally, to complete the full investigation of spectral unmixing algorithms, the `MCMC()` $U{\rightarrow}P4$ unmixings against the *minimal*, *expanded* and *extensive* spectral libraries were repeated for Glenn.

6.2.2.1 *glennmathmin* Unmixings

***U* (Figure 6.27):**

The *glennmathminU* `MCMC()` unmixing gave an almost perfect fit, as demonstrated by completely flat/featureless residuals and RMS = 0.0039, although the $\chi^2_{d.o.f} = 75.0$ was more indicative of a poor fit (Figure 6.27) – the only imperfection here was that the modelled spectrum sat slightly above the *glennmath* spectrum, giving residuals of the order 0.004 across the entire spectral range. However, with the very wide uncertainty envelope ($\pm$0.33 on average across the spectral range), this contained the entirety of *glennmath*.

In contrast to the *brucemathminU* `MCMC()` unmixing, where the posterior pdfs appeared as symmetrical Gaussians, with only slight asymmetry for a couple of end-members (e.g., augite and enstatite; Section 6.2.1.1), the *glennmathminU* `MCMC()` unmixing posteriors displayed a wider variety of different forms, where most had a narrow peak at the median with varying degrees of tails, and bumps on these tails (Figure 6.27). Cronstedtite in particular appeared bimodal with a very narrow primary peak at 0.527, and a low, broad secondary peak at $\sim$ 0.15 (Figure 6.27).

Another contrast to the `MCMC()` unmixing of *brucemathminU* (Section 6.2.1.1), was that for *glennmathminU* there were many more high correlation pairs (24 pairs for *glennmathminU*, Table 6.25, compared to 4 for *brucemathminU*, Table 6.13), with only a few possible pairings not meeting the arbitrary criteria of being $> |0.6|$ to be considered 'strongly' correlated (these pairings being: enstatite with olivine, enstatite with magnetite, enstatite with pyrrhotite, and enstatite with gypsum; Table 6.25). In fact, the few 'non-strongly' correlated pairs for the *glennmathminU* `MCMC()` unmixing were only slightly $< |0.6|$, with the lowest being 0.39 between

enstatite and olivine, going up to 0.54 between enstatite and pyrrhotite. This large degree of correlation between all the end-members was well represented in the joint pdfs (Figure 6.27), however, there was no obvious explanation for these provided by the Glenn *minimal* PCA plot (e.g., Figure 5.3).

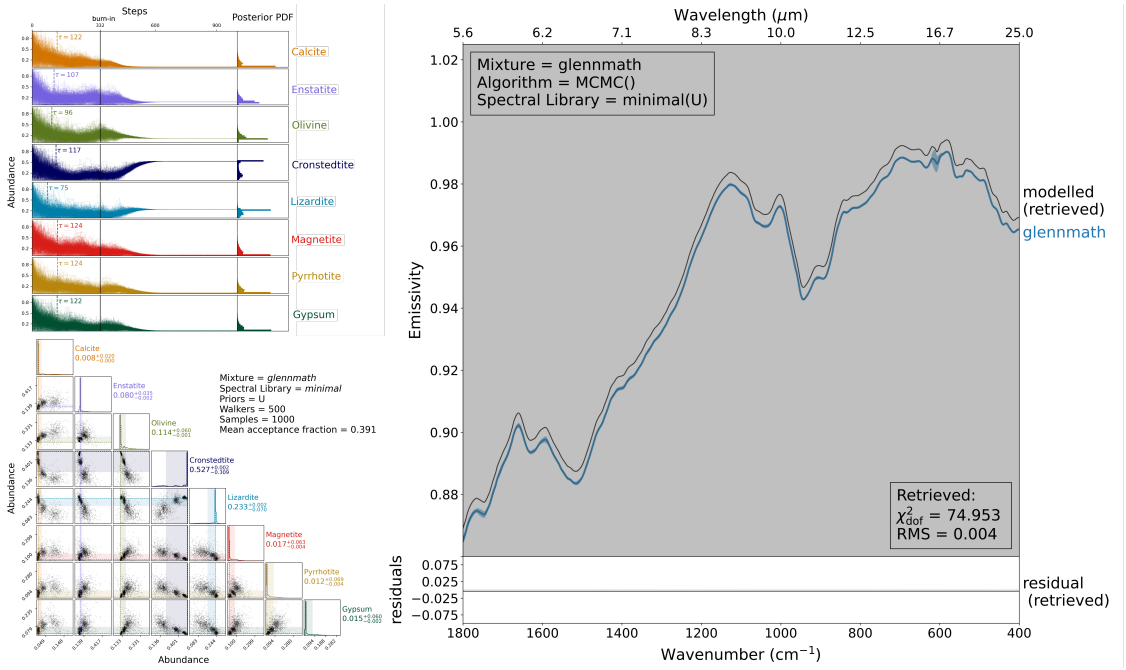


Figure 6.27: *glennmathminU* `MCMC()` walkers and corner plots with model fit.

Table 6.25: Correlation matrix for retrieved abundances from the *glennmathminU* `MCMC()` unmixing. Strong correlations ($> |0.6|$) are indicated in bold.

glennmathminU	Ca	En	Ol	Cr	Li	Ma	Py	Gy
Calcite (Ca)	1.000	**0.619**	**0.759**	**-0.804**	**-0.797**	**0.651**	**0.621**	**0.640**
Enstatite (En)	**0.619**	1.000	0.386	**-0.670**	**-0.703**	0.460	0.538	0.510
Olivine (Ol)	**0.759**	0.386	1.000	**-0.827**	**-0.733**	**0.691**	**0.650**	**0.655**
Cronstedtite (Cr)	**-0.804**	**-0.670**	**-0.827**	1.000	**0.823**	**-0.840**	**-0.859**	**-0.858**
Lizardite (Li)	**-0.797**	**-0.703**	**-0.733**	**0.823**	1.000	**-0.731**	**-0.738**	**-0.769**
Magnetite (Ma)	**0.651**	0.460	**0.691**	**-0.840**	**-0.731**	1.000	**0.613**	**0.702**
Pyrrhotite (Py)	**0.621**	0.538	**0.650**	**-0.859**	**-0.738**	**0.613**	1.000	**0.723**
Gypsum (Gy)	**0.640**	0.510	**0.655**	**-0.858**	**-0.769**	**0.702**	**0.723**	1.000

P1 (Figure 6.28):

Unmixing *glennmathminP1* with `MCMC()` gave a poor fit, seen quantitatively by the RMS (0.011) and $\chi^2_{d.o.f}$ (341.1), and qualitatively from visual inspection of the fit (Figure 6.28); where the residuals extended beyond ± 0.01 between $1800 - 1656 \text{cm}^{-1}$,

$1368 - 1153\text{cm}^{-1}$, $1078 - 1042\text{cm}^{-1}$, $566 - 494\text{cm}^{-1}$ and $483 - 444\text{cm}^{-1}$. The uncertainty envelope was relatively narrow (± 0.016 on average across the spectral range), and almost entirely contained the *glennmath* spectrum, only diverging at the high wavenumber end (between $\sim 1800 - 1695\text{cm}^{-1}$).

For the *glennmathminP1* `MCMC()` unmixing, the majority of the posterior pdfs displayed tight single peaks around their median values, but still with low and long tails where there were still a significant number of samples (Figure 6.28).

Similar to the contrast between the `MCMC()` unnmixings of *glennmathminU* and *brucemathminU* (Section 6.2.1.1), there were many more strongly correlated pairs for the *glennmathminP1* `MCMC()` unmixing (8 pairs with correlations ranging from -0.61 to -0.75; Table 6.26) than there were for *brucemathminP1* (one pair: albite and FeNiMetalSub with correlation of -0.76; Section 6.2.1.1). However, there were fewer pairs for this *glennmathminP1* `MCMC()` unmixing than for the *glennmathminU* `MCMC()` unmixing (24 pairs, as discussed above; Table 6.25).

The walkers plots for the *glennmathminP1* `MCMC()` unmixing also all appeared well converged (Figure 6.28), reaching convergence after the burn-in mark (roughly 300 steps in), but earlier than for *U* (which were converged by roughly 550 steps in; Figure 6.27), which could be considered an indication that the priors can have an impact on convergence.

Table 6.26: Correlation matrix for retrieved abundances from the *glennmathminP1* `MCMC()` unmixing. Strong correlations ($> |0.6|$) are indicated in bold.

glennmathminP1	Ca	En	Ol	Cr	Li	Ma	Py	Gy
Calcite (Ca)	1.000	-0.523	**-0.698**	**-0.749**	**0.732**	0.248	-0.169	**0.627**
Enstatite (En)	-0.523	1.000	0.268	0.461	-0.390	-0.122	-0.037	**-0.638**
Olivine (Ol)	**-0.698**	0.268	1.000	0.597	**-0.611**	-0.264	-0.028	**-0.650**
Cronstedtite (Cr)	**-0.749**	0.461	0.597	1.000	-0.580	-0.245	-0.124	**-0.673**
Lizardite (Li)	**0.732**	-0.390	**-0.611**	-0.580	1.000	0.244	-0.126	0.490
Magnetite (Ma)	0.248	-0.122	-0.264	-0.245	0.244	1.000	-0.143	-0.052
Pyrrhotite (Py)	-0.169	-0.037	-0.028	-0.124	-0.126	-0.143	1.000	-0.253
Gypsum (Gy)	**0.627**	**-0.638**	**-0.650**	**-0.673**	0.490	-0.052	-0.253	1.000

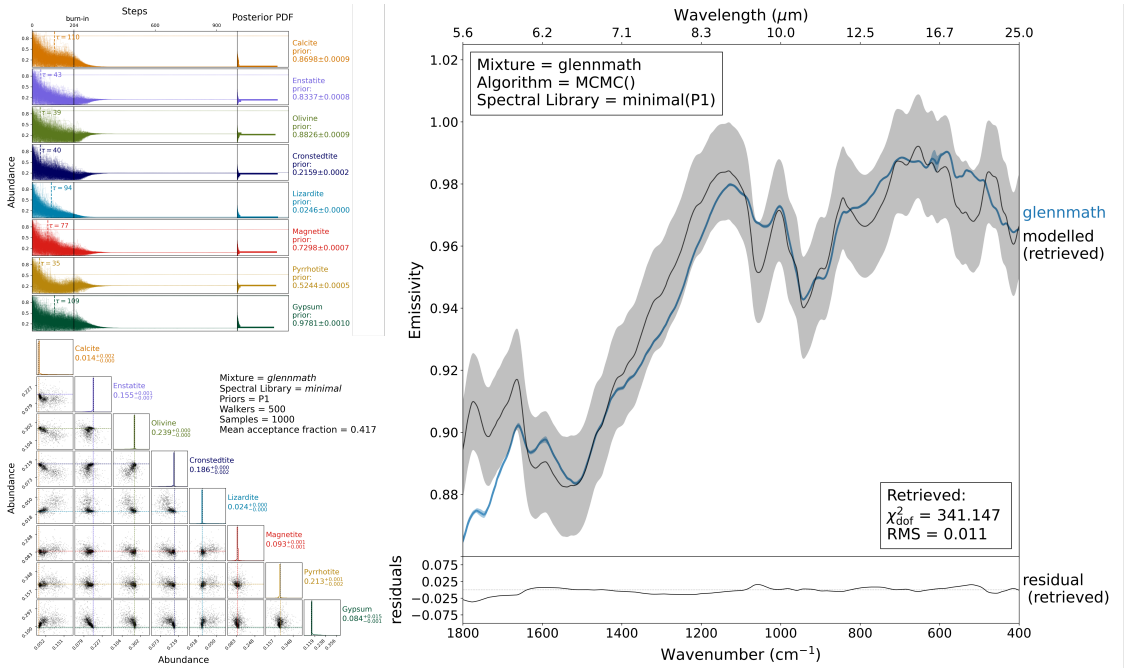


Figure 6.28: *glennmathminP1* `MCMC()` walkers and corner plots with model fit.

Overall, across *U*→*P4*, the *glennmathmin* `MCMC()` fits were perfect, with only slight offsets from *glennmath* and varying widths of uncertainty envelope (Figures 6.27, 6.28, A.27, A.28, A.29); the only exception was *P1* (Figure 6.28), which had a visibly poorer fit than those for *U*, *P2*, *P3* and *P4* (Figures 6.27, A.27, A.28, A.29). The posterior pdfs all generally displayed a single narrow peak, where some had a tail of some description, with some of these having a bump on their tails that appeared as bimodality (e.g., Figures 6.27 and 6.28).

6.2.2.2 *glennrealmin* Unmixings

***U* (Figure 6.29, Table B.60):**

The fit for the *glennrealminU* `MCMC()` unmixing had a relatively narrow uncertainty envelope (±0.022 on average across the full spectral range), containing the entire *glennreal* spectrum (Figure 6.29). The residuals were mostly within ±0.01 of the zero line across the full spectral range, only extending beyond ±0.01 between $936 - 958\text{cm}^{-1}$, reaching a maximum of 0.0114 at 948cm^{-1} (Figure 6.29). This qualitative assessment of a 'good' fit was strengthened with the quantitative contribution from $\chi^2_{d.o.f} = 1.3$ and RMS= 0.004 (Table B.60).

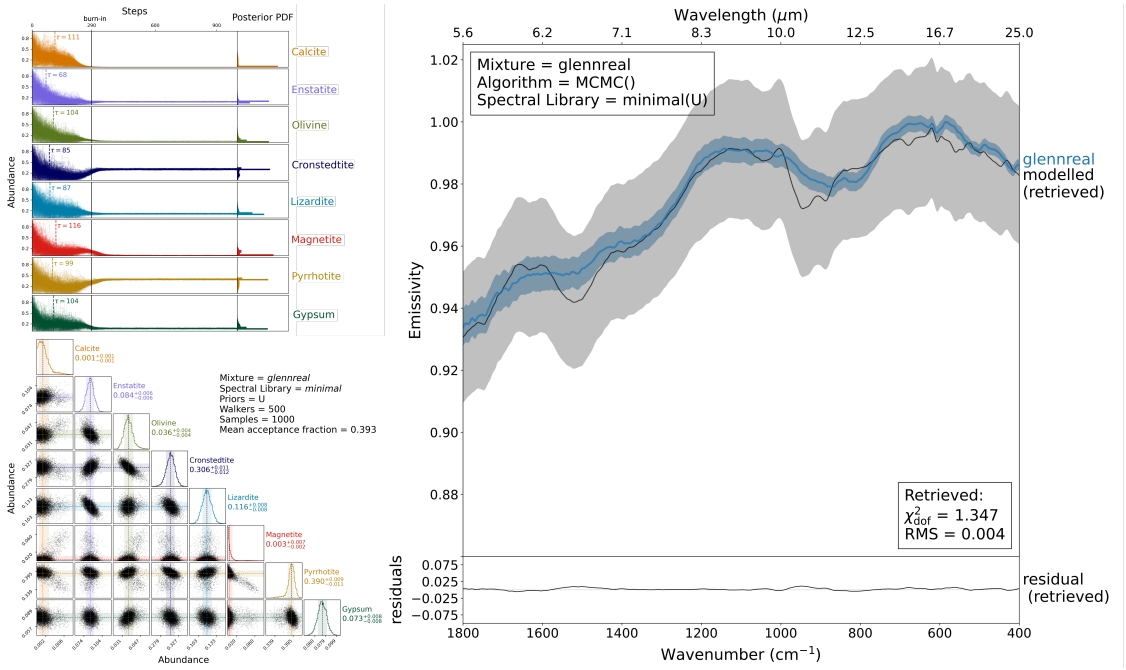


Figure 6.29: *glennrealminU* `MCMC()` walkers and corner plots with model fit.

Similarly to the *glennmathminU→P4* `MCMC()` unmixings (Section 6.2.2.1), the posterior pdfs for *glennrealminU* were largely singular peaks with varying widths and tails (Figure 6.29). The *glennrealminU* `MCMC()` joint pdfs displayed some strong correlation (Figure 6.29), also evidenced by the many high correlation pairs found from the correlation matrix (8 pairs with correlations ranging from −0.65 between cronstedtite and magnetite, to −0.91 between magnetite and pyrrhotite; Table 6.27); but again the strong correlations observed were not obvious from considering the Glenn *minimal* PCA plot (Figure 5.3).

Table 6.27: Correlation matrix for retrieved abundances from the *glennrealminU* `MCMC()` unmixing. Strong correlations ($> |0.6|$) are indicated in bold.

glennrealminU	Ca	En	Ol	Cr	Li	Ma	Py	Gy
Calcite (Ca)	1.000	-0.201	**0.680**	-0.599	0.141	**0.861**	**-0.803**	0.265
Enstatite (En)	-0.201	1.000	-0.526	0.487	**-0.657**	-0.332	0.166	-0.239
Olivine (Ol)	**0.680**	-0.526	1.000	**-0.841**	0.151	**0.770**	-0.597	0.526
Cronstedtite (Cr)	-0.599	0.487	**-0.841**	1.000	-0.441	**-0.649**	0.415	-0.510
Lizardite (Li)	0.141	**-0.657**	0.151	-0.441	1.000	0.142	0.014	-0.107
Magnetite (Ma)	**0.861**	-0.332	**0.770**	**-0.649**	0.142	1.000	**-0.915**	0.341
Pyrrhotite (Py)	**-0.803**	0.166	-0.597	0.415	0.014	**-0.915**	1.000	-0.452
Gypsum (Gy)	0.265	-0.239	0.526	-0.510	-0.107	0.341	-0.452	1.000

***P1* (Figure 6.30):**

The unmixing for *glennrealminP1* with `MCMC()` gave a poor fit, with RMS = 0.019, $\chi^2_{d.o.f} = 47.2$, and residuals extending beyond ± 0.01 between $1800-1578\text{cm}^{-1}$, $1467-1133\text{cm}^{-1}$, $1078-1033\text{cm}^{-1}$, $983-906\text{cm}^{-1}$, $883-839\text{cm}^{-1}$, $758-739\text{cm}^{-1}$, $722-694\text{cm}^{-1}$, $611-567\text{cm}^{-1}$, and $539-400\text{cm}^{-1}$ (Figure 6.30). The modelled spectrum was clearly heavily influenced by calcite, displaying features in many of the same locations (e.g., $\sim$ 1175, 1020, 875, 850, and 725cm^{-1}), despite calcite being retrieved in an abundance of 0.126 ($<$ 0.156, 0.140, 0.169, 0.188, and 0.243 retrieved for enstatite, olivine, cronstedtite, magnetite, and pyrrhotite, respectively). This confirmed an earlier observation that even in low abundances, an end-member with strong features (i.e., large spectral contrast) can have significant impact on the modelled mixture spectrum (Section 6.1.2.4).

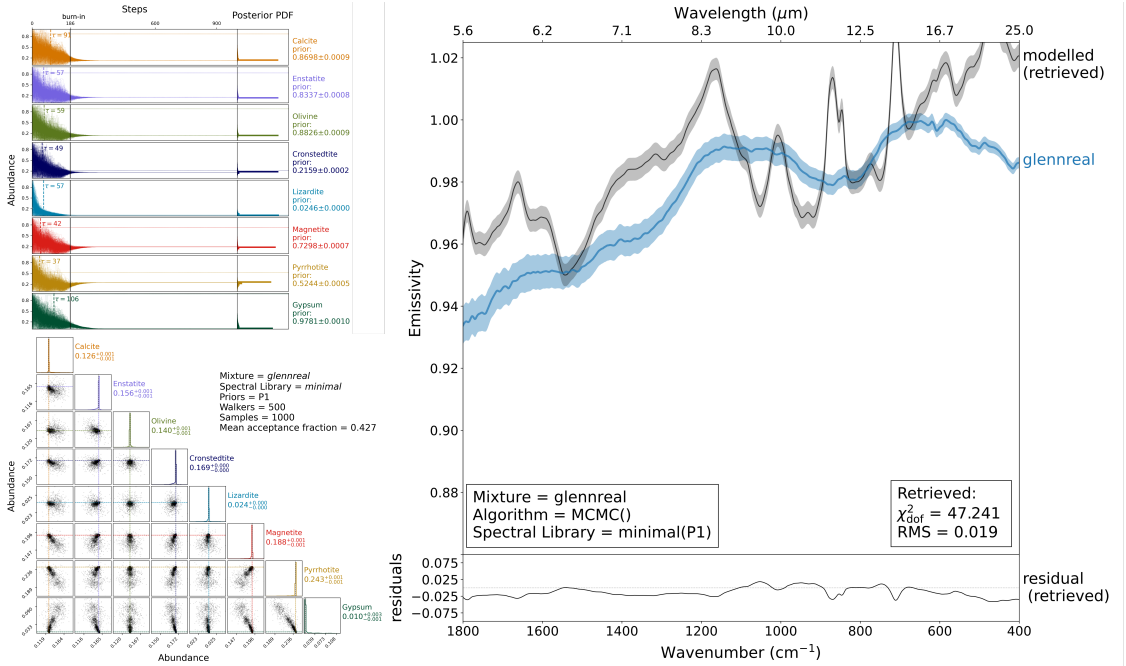


Figure 6.30: *glennrealminP1* `MCMC()` walkers and corner plots with model fit.

The *glennrealminP1* posterior pdfs again appeared as narrow single peaks, and the joint pdfs showed some degree of correlation for some (e.g., pyrrhotite with calcite, gypsum with calcite, and pyrrhotite with gypsum), whereas others were more circular, signifying a lack of correlation (e.g., enstatite with cronstedtite, and olivine

with lizardite; Figure 6.30). The walkers plots were all well converged (Figure 6.30), showing tighter convergence than the *glennrealminU* `MCMC()` unmixing (Figure 6.29). Most of the *glennrealminP1* `MCMC()` walkers plots reached convergence shortly after burn-in (186 steps in), with the exceptions of lizardite and cronstedtite, which appeared to converge on their priors by the burn-in mark.

***P2* (Figure A.30, Table B.61):**

The *glennrealminP2* `MCMC()` unmixing (Figure A.30, Table B.61) was very similar to that of *glennrealminU* (Figure 6.29, Table B.60), but with twice the number of strong correlation pairings – 16 pairs for *glennrealminP2*, with correlations ranging from 0.61 for magnetite and gypsum, to -0.99 for magnetite and pyrrhotite (Table 6.28), and 8 pairs for *glennrealminU*, with correlations ranging from -0.65 for cronstedtite and magnetite, to -0.91 for magnetite and pyrrhotite (Table 6.27) – which again contrasted the effect seen in the `OptEst_ASC_ILR()` unmixings (Section 6.1): tighter priors acting to suppress correlation.

Table 6.28: Correlation matrix for retrieved abundances from the *glennrealminP2* `MCMC()` unmixing. Strong correlations ($> |0.6|$) are indicated in bold.

glennrealminP2	Ca	En	Ol	Cr	Li	Ma	Py	Gy
Calcite (Ca)	1.000	-0.405	**0.873**	**-0.784**	0.437	**0.908**	**-0.907**	**0.699**
Enstatite (En)	-0.405	1.000	-0.474	0.320	**-0.657**	-0.563	0.533	-0.277
Olivine (Ol)	**0.873**	-0.474	1.000	**-0.893**	0.329	**0.804**	**-0.781**	**0.782**
Cronstedtite (Cr)	**-0.784**	0.320	**-0.893**	1.000	-0.426	**-0.661**	**0.624**	**-0.788**
Lizardite (Li)	0.437	**-0.657**	0.329	-0.426	1.000	0.513	-0.489	0.157
Magnetite (Ma)	**0.908**	-0.563	**0.804**	**-0.661**	0.513	1.000	**-0.991**	**0.608**
Pyrrhotite (Py)	**-0.907**	0.533	**-0.781**	**0.624**	-0.489	**-0.991**	1.000	**-0.642**
Gypsum (Gy)	**0.699**	-0.277	**0.782**	**-0.788**	0.157	**0.608**	**-0.642**	1.000

***P3* (Figure 6.31):**

Unmixing *glennrealminP3* with `MCMC()` gave a poor fit (RMS = 0.023, $\chi^2_{d.o.f} = 23.1$), with residuals closely resembling those of the *glennmath* spectrum subtracted from the *glennreal* spectrum (Figure 5.2); further emphasising the discrepancy between the linear mixing modelled spectrum and observation. The posterior pdfs for the *glennrealminP3* `MCMC()` unmixing had narrow single peaks (Figure 6.31), and a substantial degree of strong correlation was evident through both the

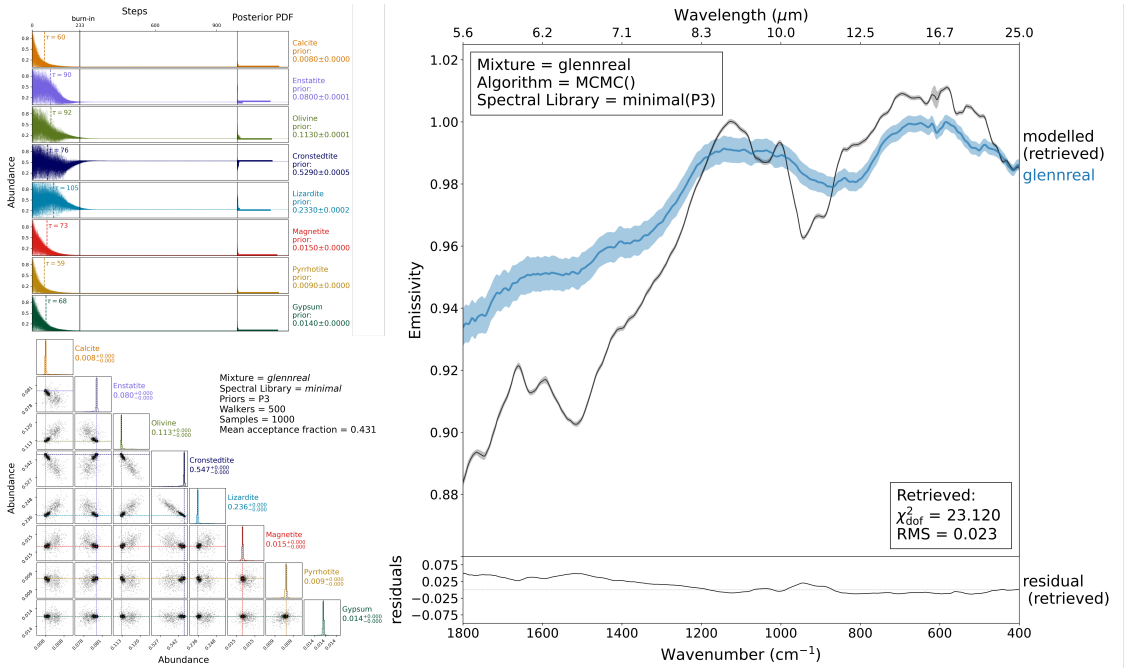


Figure 6.31: *glennrealminP3* `MCMC()` walkers and corner plots with model fit.

joint pdfs (Figure 6.31), and the correlation matrix (14 pairs with correlations ranging from 0.62 between calcite and magnetite, to -0.97 between cronstedtite and lizardite; Table C.22).

P4 (Figure A.31):

The `MCMC()` unmixing for *glennrealmin* with *P4* (Figure A.31) gave a model fit that closely resembled those for *glennrealminU* (Figure 6.29) and *glennrealminP2* (Figure A.30). The model fit uncertainty envelope was ±0.023 on average across the full spectral range for *glennrealminP4*, making it closer in scale to that for *U* (±0.022 on average; Figure 6.29), and narrower than *P2* (±0.053 on average; Figure A.30).

The posterior pdfs for the *glennrealminP4* `MCMC()` unmixing were mostly single peaks again, but with some having more significant tails than others (e.g., olivine, cronstedtite and gypsum); some of which displayed bumps indicative of some level of bimodality that was more clearly seen in the joint pdfs (e.g., enstatite, cronstedtite and gypsum; Figure A.31).

6.2.2.3 *glennmathexp* Unmixings

Similarly to the Bruce `MCMC()` unmixings against the *expanded* and *extensive* spectral libraries, the issues surrounding the lack of abundance sum constraint were evident for the equivalent unmixings of Glenn, where the retrieved modelled spectra sat outside the practical axis range for visualisation, but the blackbody renormalised (BBnorm) spectra were more in line with the relevant *glennmath* or *glennreal* spectrum. Therefore, as with the Bruce `MCMC()` model fit discussions (Section 6.2.1), the `MCMC()` unmixings for Glenn against its *expanded* (Sections 6.2.2.3 and 6.2.2.4) and the *extensive* (Sections 6.2.2.5 and 6.2.2.6) spectral libraries also refer to the BBnorm modelled spectrum, unless stated otherwise.

Abundances retrieved from the *glennmathexpU→P4* `MCMC()` unmixings were generally of the order $0.1 - 0.3$ (Tables B.62, B.63, B.64, B.65, B.66), and displayed weak correlations (all $\leq |0.55|$; Tables C.23, C.24, C.25, C.26, C.27) – a large contrast from what was seen with *glennmathminU→P4* (Section 6.2.2.1) – and it was not obvious why these correlations should be weak based on the Glenn *expanded* PCA plot (e.g., Figure 5.4), since there were some clusters which would ordinarily suggest some degree of correlation. The similar scale of abundances retrieved across *U→P4* implied little influence from the priors.

6.2.2.4 *glennrealexp* Unmixings

The `MCMC()` unmixings of *glennrealexp* with the *U* (Figure A.32, Table B.67), *P1* (Figure A.33, Table B.68), *P2* (Figure A.34, Table B.69) and *P4* (Figure A.35, Table B.71) priors showed similar patterns to their *glennmathexp* counterparts (Section 6.2.2.3). The main noteworthy differences between the *glennrealexpU→P4* and *glennmathexpU→P4* `MCMC()` unixings were in the particular forms of the posterior pdfs:

- For *glennrealexpU* the posterior pdfs were mostly single peaked Gaussians (Figure A.32). Some of the posterior pdfs had tails (e.g., calcite and olivine),

and magnetite had a clear bump around 0.279, indicative of bimodality (Figure 6.32), that could also be seen in the relevant joint pdfs (Figure A.32).

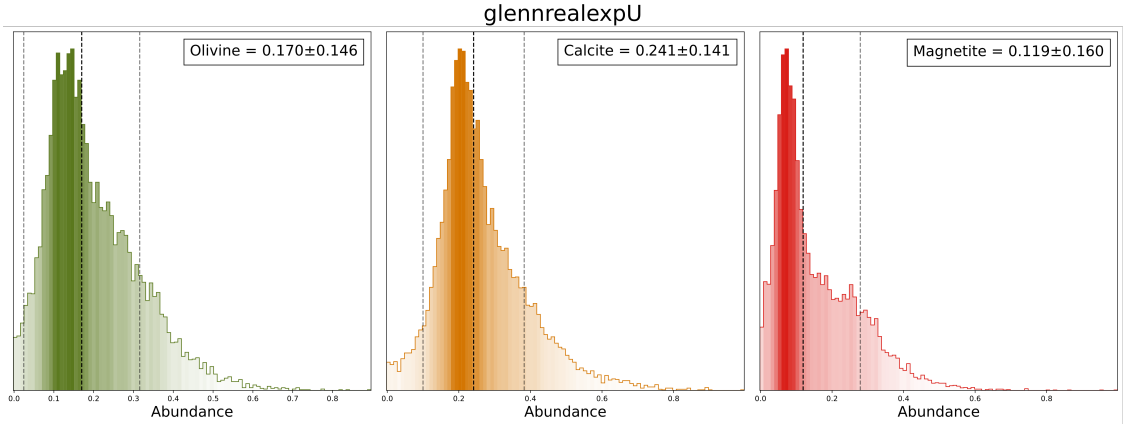


Figure 6.32: *glennrealexpU* `MCMC()` olivine, calcite and magnetite posterior pdfs.

- The *glennrealexpP1* unmixings displayed a greater variety of pdf shapes; cronstedtite, pyrrhotite and spinel had clear bumps at abundances greater than their median values, and the bump on magnetite made it appear more bimodal (Figure 6.33). The joint pdfs were mostly relatively circular, with some indicating bimodality (e.g., calcite, magnetite, and pyrrhotite), and even potentially some multi-modality (e.g., cronstedtite; Figure A.33).

- The posterior pdfs for *glennrealexpP2* were more similar to those for *glennrealexpU*, as most were single peaked Gaussians, with some displaying clear tails (e.g., olivine, cronstedtite, lizardite, spinel, saponite and BB), and gypsum with a bump on its tail located at an abundance around 0.218 (Figure A.34).

- The posterior pdfs for *glennrealexpP4* again looked similar, with the majority being single peaked Gaussians, some of which with a visible tail (e.g., enstatite, pyrrhotite, saponite and BB). The outliers to the general trend of single peaked Gaussian posterior pdfs for the *glennrealexpP4* `MCMC()` unmixing, however, were calcite, which displayed a broad peak, and both gypsum and amorphous Fe appeared bimodal (Figure 6.34).

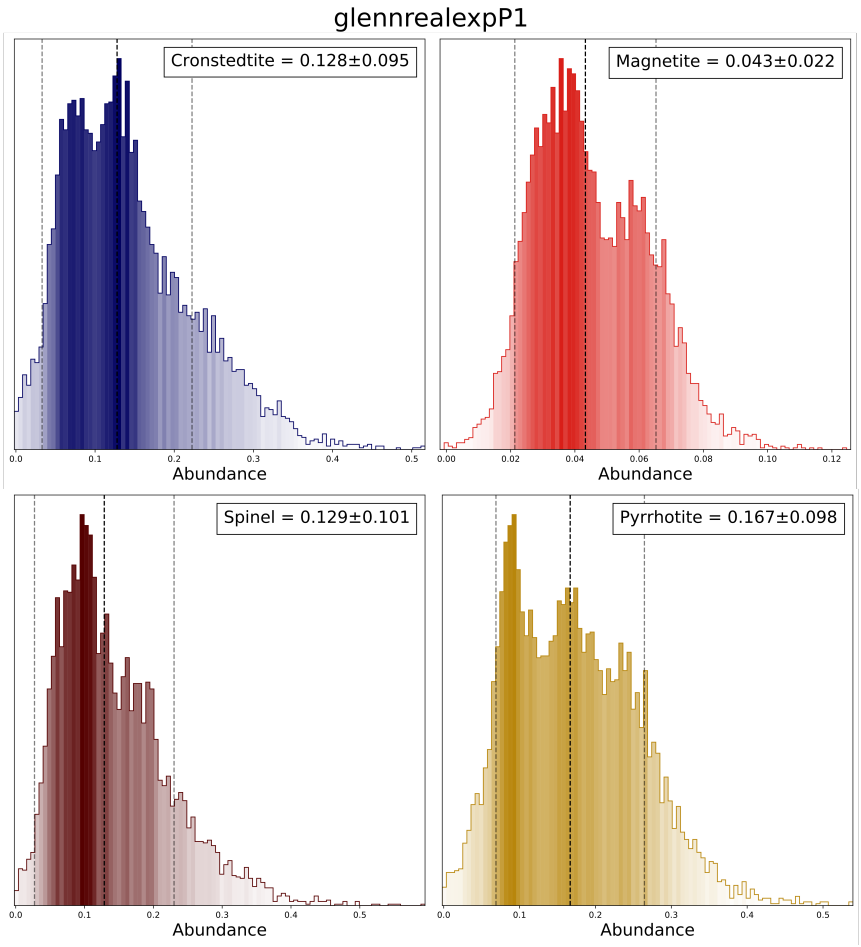


Figure 6.33: *glennrealexpP1* `MCMC()` cronstedtite, magnetite, spinel and pyrrhotite posterior pdfs.

The *glennrealexpP3* `MCMC()` unmixing, however, gave very different results to those seen for *U*, *P1*, *P2* and *P4*. This time, both the retrieved and BB normalised spectra sat level with *glennreal* (Figure 6.35), and almost all of the possible end-member pairings had strong correlation ($> |0.6|$); with most of the exceptions being $\geq |0.5|$, and only olivine with enstatite (0.41), lizardite with enstatite (-0.38) and magnetite with enstatite (0.46) having weaker correlations (Table C.31).

The solutions being largely similar across *U*→*P4*, with the exception of *P3*, further suggested a relative lack of influence from the priors unless they contained the correct solution; and in this case there was an overwhelming amount of correlation which acted to invalidate the linear mixing model.

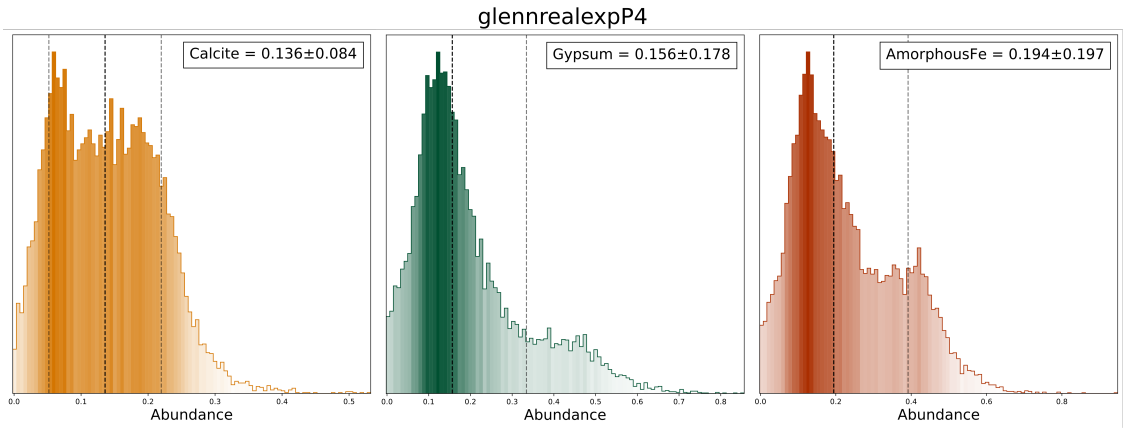


Figure 6.34: *glennrealexpP4* `MCMC()` calcite, gypsum and amorphous Fe posterior pdfs.

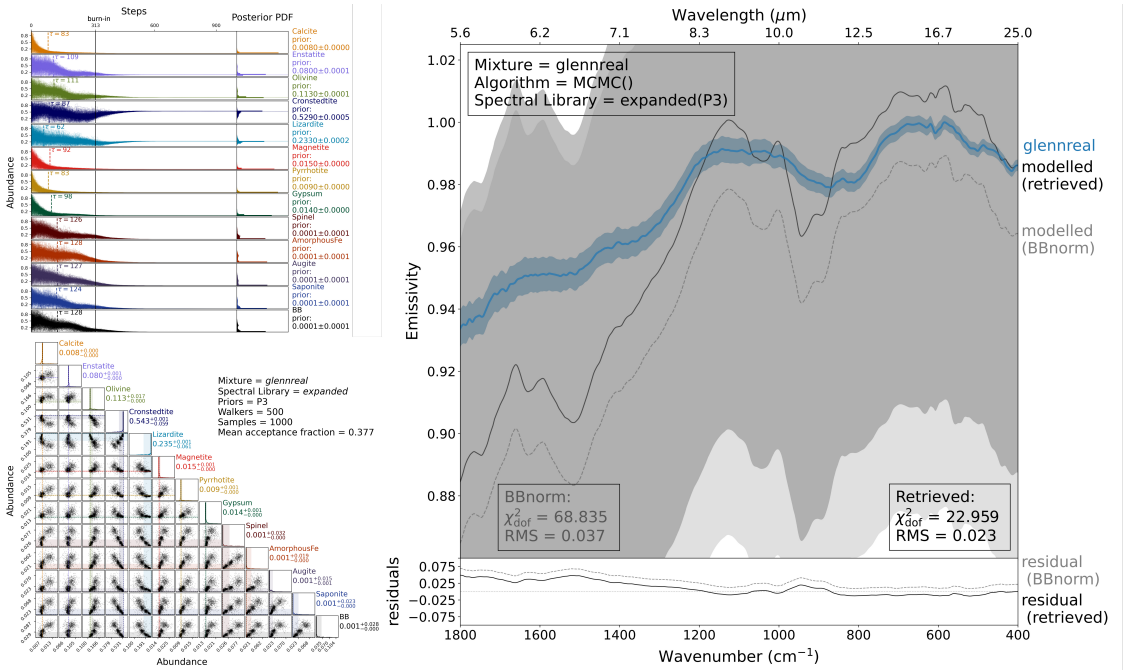


Figure 6.35: *glennrealexpP3* `MCMC()` walkers and corner plots with model fit.

6.2.2.5 *glennmathext* Unmixings

U (Figure A.36, Table B.72):

For the *glennmathextU* `MCMC()` unmixing, most of the posterior pdfs appeared as single peaked Gaussians, with some displaying clear symmetry (e.g., saponite, magnetite, spinel, albite, amorphous Mg and FeNiMetalSub; Figures A.36 and 6.36), and others appearing more asymmetrical with prominent tails (with or without bumps, e.g., calcite, olivine, cronstedtite, and troilite; Figures A.36 and 6.36). Pyrrhotite and gypsum in particular appeared bimodal (Figure 6.36), and there

were no strongly correlated pairs (Table C.33).

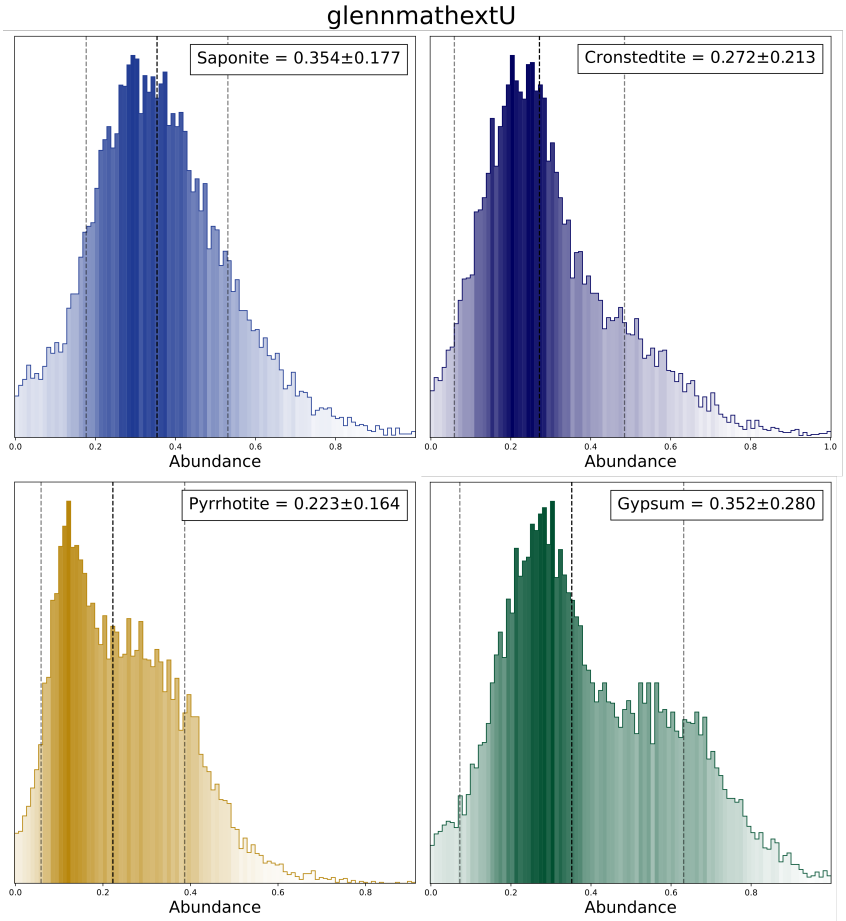


Figure 6.36: *glennmathextU* `MCMC()` saponite, cronstedtite, pyrrhotite and gypsum posterior pdfs.

P1 (Figure A.37, Table B.73):

Results from unmixing *glennmathextP1* with `MCMC()` (Figure A.37, Table B.73) were very similar to those for *glennmathextU* (Figure A.36, Table B.72), also having a lack of strongly correlated pairs; although the general scale of values in the correlation matrix for *glennmathextP1* (|0.14| on average; Table C.34) seemed slightly weaker than for *glennmathextU* (|0.17| on average; Table C.33). For *glennmathextP1*, the notably different posterior pdfs, shown in Figure 6.37, were olivine and saponite (particularly bimodal in appearance), and magnetite (a wide peak with slight bulge on one side at around 0.683).

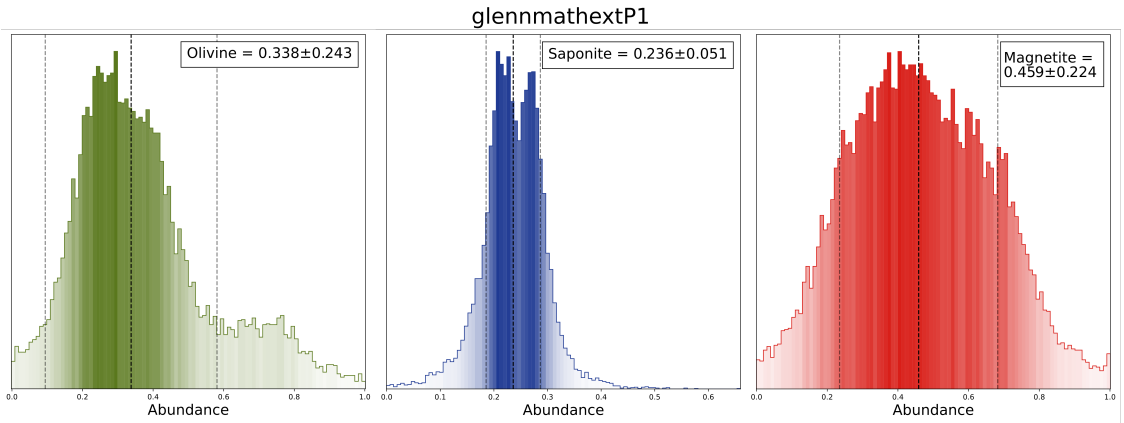


Figure 6.37: *glennmathextP1* `MCMC()` olivine, saponite and magnetite posterior pdfs.

P2 (Figure A.38, Table B.74):

The *glennmathextP2* `MCMC()` unmixing (Figure A.38, Table B.74) was again similar to those for *glennmathextU* (Figure A.36, Table B.72) and *glennmathextP1* (Figure A.37, Table B.73), with subtle differences in residuals morphology, and no correlations $\geq |0.6|$ (Table C.35). A difference with the *glennmathextP2* `MCMC()` unmixing, though, was a greater degree of bimodality observed: the calcite and amorphous Fe posterior pdfs displayed clear bimodal form, and spinel and albite showed more tenuous bimodality (Figure 6.38).

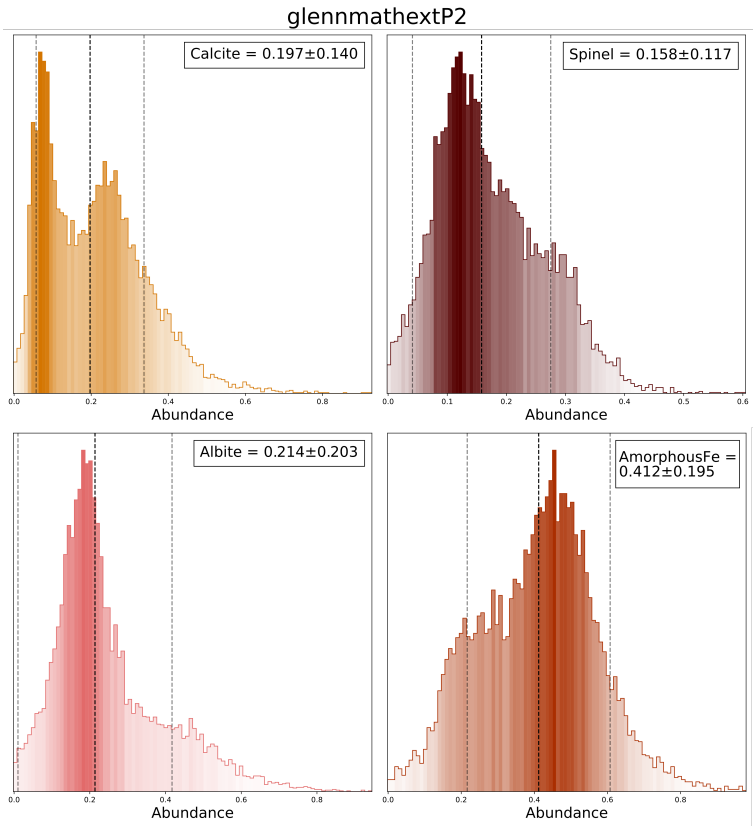


Figure 6.38: *glennmathextP2* `MCMC()` calcite, spinel, albite and amorphous Fe posterior pdfs.

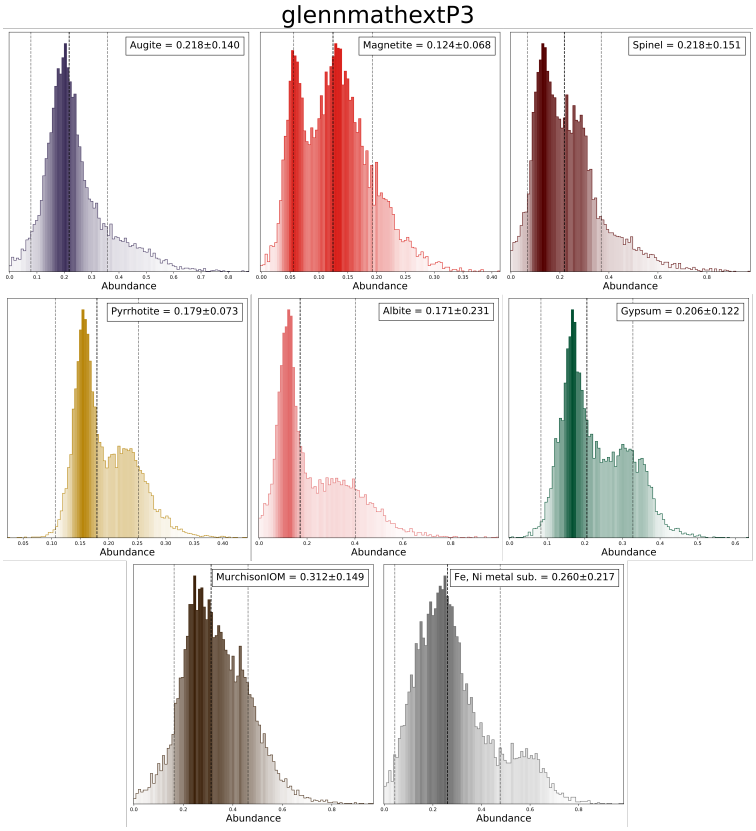


Figure 6.39: *glennmathextP3* `MCMC()` augite, magnetite, spinel, pyrrhotite, albite, gypsum, MurchisonIOM and FeNiMetalSub posterior pdfs.

***P3* (Figure A.39):**

A furthering of bimodal form was seen for the *glennmathextP3* `MCMC()` unmixing (Figure A.39), where the posterior pdfs for augite, magnetite, spinel, pyrrhotite, albite, gypsum, Murchison IOM, and FeNiMetalSub displayed varying degrees of bimodality (Figure 6.39). There were also two strong correlation pairs: augite with FeNiMetalSub (0.62), and pyrrhotite with albite (0.63; Table C.36); confirmed by the joint pdfs (Figure A.39), but would not have been predicted based on the *extensive* library PCA plot (Figure 5.5).

***P4* (Figure A.40):**

The *glennmathextP4* `MCMC()` unmixing (Figure A.40) resembled that of *glennmathextP3* in model fit (Figure A.39), but more closely resembled the *glennmathextU→P2* `MCMC()` unmixings with regards to the lack of high correlation pairs (Table C.37). The posterior pdfs mostly appeared as single peaked Gaussians, with varying widths and levels of asymmetry (Figure A.40). Augite's pdf looked particularly wide, and magnetite and albite's appeared more bimodal (Figure 6.40).

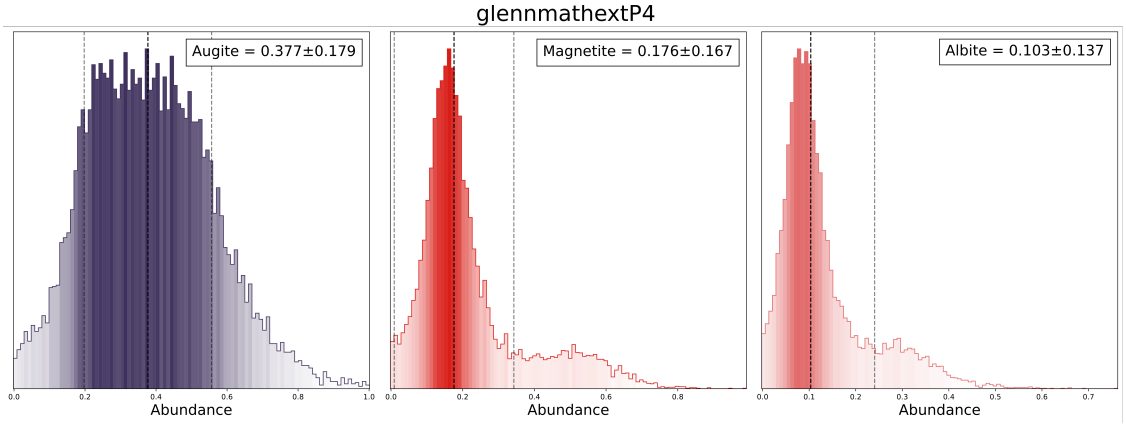


Figure 6.40: *glennmathextP4* `MCMC()` augite, magnetite and albite posterior pdfs.

6.2.2.6 *glennrealext* Unmixings

For the *glennrealextU* `MCMC()` unmixing (Figure 6.41, Table B.75), the fit was poor (BBnorm RMS = 0.038, $\chi^2_{d.o.f}$ = 124.2), with some BBnorm modelled spectrum features clearly aligned with those from calcite (e.g., at ∼ 875 and 725cm^{-1}).

The posterior pdfs showed a range of single peaked Gaussians, to Gaussians with bumpy tails (Figure 6.41; as seen throughout the `MCMC()` analyses), with those for cronstedtite and amorphous Fe appearing particularly bimodal (Figure 6.42).

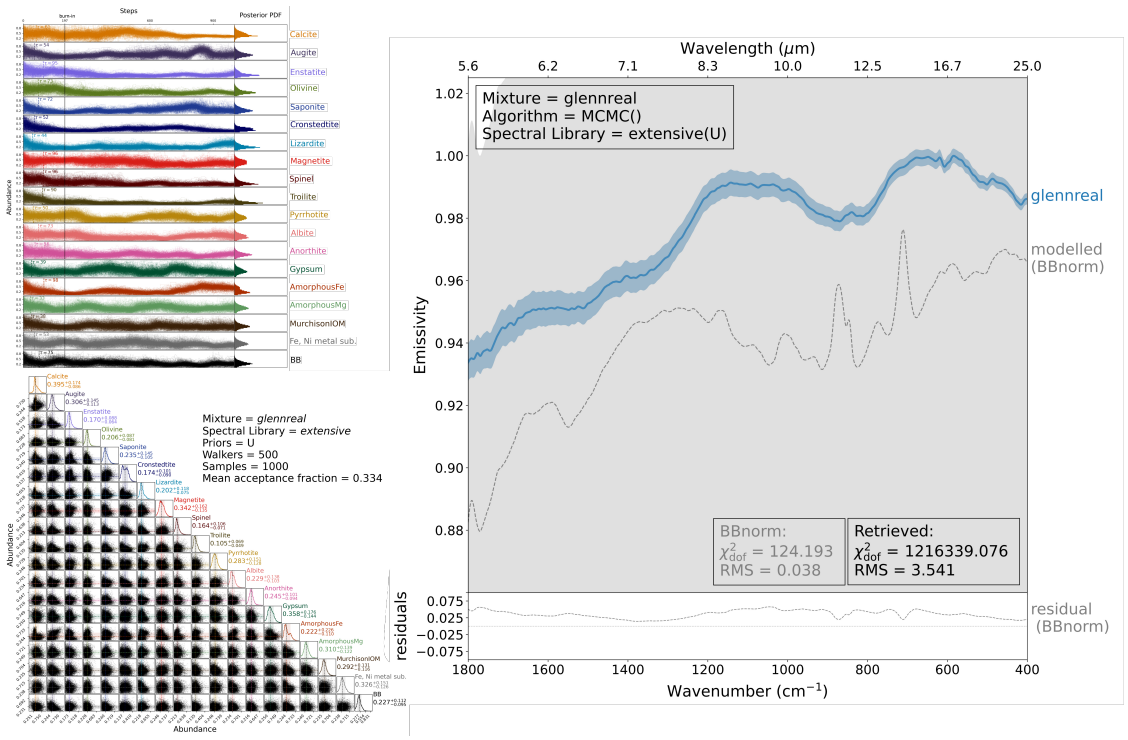


Figure 6.41: *glennrealextU* `MCMC()` walkers and corner plots with model fit.

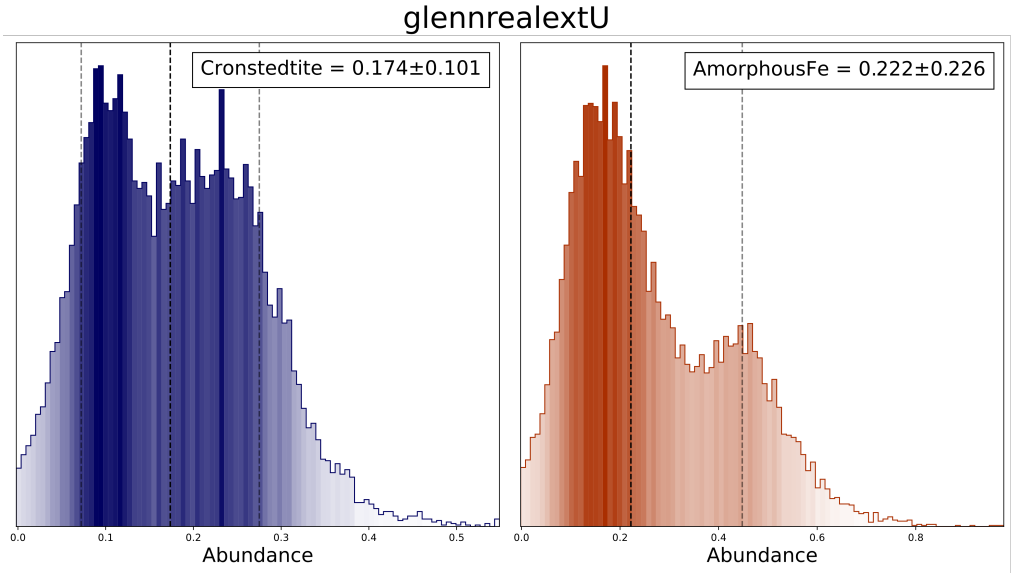


Figure 6.42: *glennrealextU* `MCMC()` cronstedtite and amorphous Fe posterior pdfs.

There were no high correlation pairs for *glennrealextU* (Table C.38), but there were for *glennrealextP1* (Table C.39): saponite and pyrrhotite with a correlation of 0.66, as was also evident from their joint pdf (Figure A.41), but would not have been predicted based on the *extensive* spectral library PCA plot (Figure 5.5). Other than the difference in correlations, the unmixings for *glennrealextU* (Figure 6.41, Table B.75) and *glennrealextP1* (Figure A.41, Table B.76) were largely similar.

The *glennrealextP2* `MCMC()` unmixing was much the same as that of *glennrealextU*, whereas *glennrealextP3*'s `MCMC()` unmixing was quite different: with a very high degree of strong correlation (42 pairs, with the strongest being 0.89 between calcite and magnetite; Table C.40) and a lot of bimodality present in the posterior pdfs (e.g., calcite, augite, saponite, magnetite, albite, gypsum, MurchisonIOM and BB; Figure 6.44). Finally, the *glennrealextP4* unmixing with `MCMC()` was overall very similar to those for *glennrealextU→P2*, and showed clear bimodality for the calcite and pyrrhotite posterior pdfs (Figure 6.43).

For all of the Glenn unmixings using `MCMC()`, the mean acceptance fraction was between the desired range of 0.2-0.5, indicating no issues with the sampling, as was the case for Bruce (Section 6.2.1).

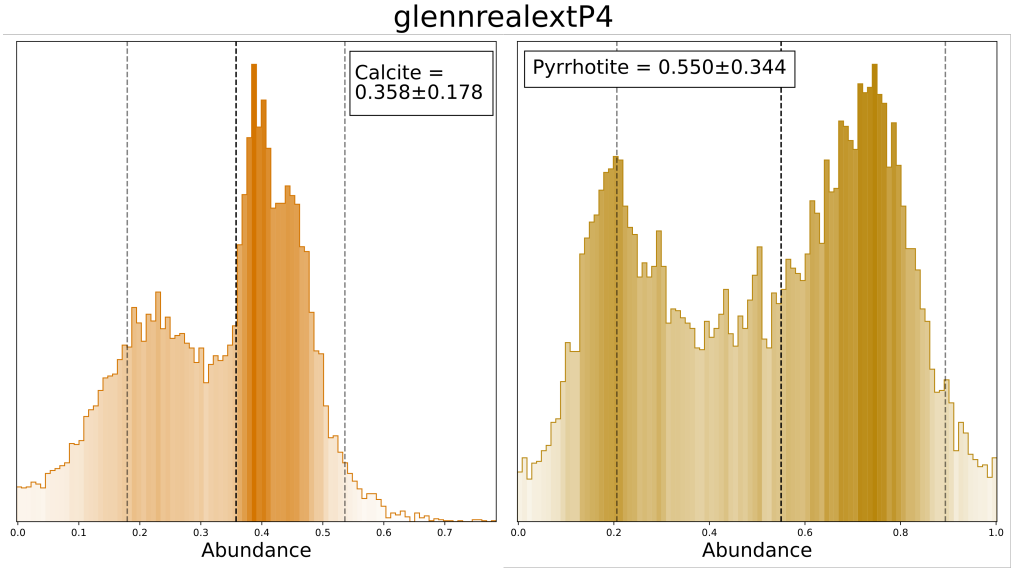


Figure 6.43: *glennrealextP4* `MCMC()` calcite and pyrrhotite posterior pdfs.

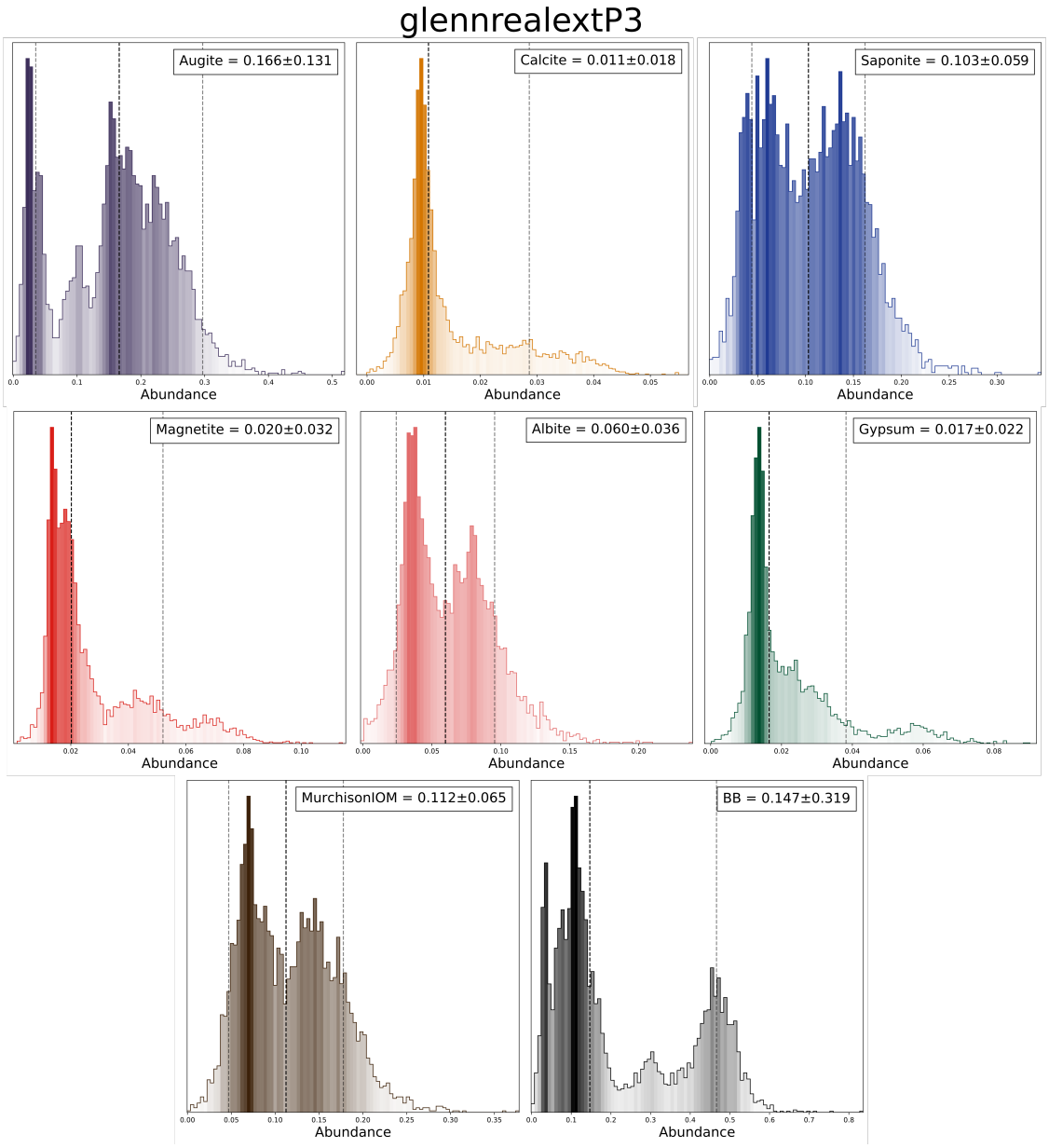


Figure 6.44: *glennrealextP3* `MCMC()` augite, calcite, saponite, magnetite, albite, gypsum, MurchisonIOM and BB posterior pdfs.

6.2.3 Overall `MCMC()` Unmixings Discussion

One of the benefits of the `MCMC()` algorithm was that it output an array of all the samples, which could form the posterior pdf histogram for each end-member, allowing for a wider range of interpretations compared to the single abundance estimates per end-member given by `WLS_ASC_ILR()` and `OptEst_ASC_ILR()`. This therefore provided further context and insight into the problem of degeneracy,

making `MCMC()` a valuable method for exploring spectral unmixing.

Major differences (and potential disadvantages) of the `MCMC()` algorithm compared to `WLS_ASC_ILR()` and `OptEst_ASC_ILR()`, were that all end-members were kept, and there was no abundance sum constraint. From the results presented throughout this section (6.2), the combination of retrieving an abundance for all end-members, but not constraining them to sum to one, proved to be somewhat problematic – most unmixings retrieved the same scale of abundances (usually of the order $0.1 - 0.3$) for all end-members. Even though the blackbody renormalisation (BBnorm) step ensured that the final abundances summed to one, the results overall were still very poor, providing neither good quality fits nor good quality abundances (as summarised in Table 6.29). The sequential steps of retrieval followed by implementing the abundance sum constraint highlighted the requirement for the non-negativity and sum to one constraints to be carried out simultaneously within the retrieval.

For most of the `MCMC()` unmixings, the results were much the same across *U*→*P4*, often with the exception of *P3*, thus implying very little influence from the priors unless they were very accurate to the true answer (which is generally unknown in real-world applications). This could therefore suggest that a more successful retrieval using `MCMC()` would be achieved the closer the priors are to the true answers, with very little range outside of this; thus presenting a very similar issue to one of the main caveats with machine learning techniques: a heavy dependence on their training sets. Having the true answers is unrealistic for genuine scientific studies, and is only applicable to algorithm development, as demonstrated here.

The *P4* version of the priors was intended to represent what may be more realistically set as priors in a semi-blind case, based on educated guesses from comparing the mixture spectrum with spectra of the end-members used in the spectral library, and little additional *a priori* knowledge. However, the `MCMC()` unmixings for both Bruce and Glenn demonstrated that unmixing with *P4* was

no better than a Uniform prior, nor the randomly generated values of *P1* and *P2*, therefore indicating a low tolerance to the inaccuracy of the priors for the retrieval.

Having a visual representation of the solution via posterior pdfs greatly enhanced the analysis, however. Throughout all the unmixings, the posterior pdfs displayed a variety of forms, from tight single peaked symmetrical Gaussians, to clear signs of bimodality that highlighted the degenerate nature of spectral unmixing. The similarities seen in the unmixings across $U \rightarrow P4$ for each mixture indicated that the use of priors had little influence on the `MCMC()` retrievals, and therefore were unable to address the degeneracy issue. Additionally, there were some very strong correlations observed through the correlation matrices and the joint pdfs, particularly for the Glenn *P3* unmixings against each spectral library (*min*, *exp* and *ext*), that could not be obviously explained through contextual information provided by the spectral library PCA plots. The large degree of correlation further demonstrated that the degeneracy issue remained, regardless of priors, and was often actually relatively stronger for the 'perfect' priors of *P3*.

Overall, these Bruce and Glenn unmixings using the `MCMC()` algorithm further demonstrated that linear mixing with fine grains is too large a problem to be compensated for with more complex algorithms, and it is therefore necessary to work towards an alternative model.

Table 6.29: Retrieval quality metrics summary table for the `MCMC()` unmixings of Bruce and Glenn. Values in square brackets correspond to metrics derived from the blackbody renormalised abundances (BBnorm). Details on these metrics and how to interpret them are covered in Section 3.3.3, where generally the smaller/closer to zero, the better the quality.

MCMC()		Fit Quality					Abundance Quality				
		U	*P1*	*P2*	*P3*	*P4*	*U*	*P1*	*P2*	*P3*	*P4*
Bruce	*brucemathmin*	6.04E-05	-4.9	2.12E-05	1.97E-06	3.31E-05	0.0073	1333.7	0.014	0.00007	0.025
	brucemathexp	-11,180,089 [-1056]	-4,195,035 [-1206]	-3,972,987 [-1307]	-3,993,437 [-1547]	-7,630,810 [-1757]	0.96 [1.07]	0.89 [1.04]	1.12 [1.36]	1.03 [1.15]	1.19 [1.46]
	brucemathext	-626523114 [-1679]	-626520660 [-1540]	-654273487 [-1935]	-612393385 [-1444]	-395592330 [-1646]	1.14 [2.25]	1.03 [1.68]	1.15 [2.04]	1.01 [1.41]	0.99 [1.43]
	brucerealmin	-7.62	-13.4	-7.62	-18.3	-7.61	893.5	11.5	929.0	0.043	896.0
	brucerealexp	-1,957,366 [-291]	-973,197 [-259]	-573,962 [-153]	-302,930 [-196]	-630,329 [-230]	1.11 [1.35]	1.12 [1.43]	1.08 [1.19]	0.99 [1.03]	1.06 [1.20]
	brucerealext	-128613955 [-215]	-143390860 [-142]	-159392477 [-214]	-103247084 [-252]	-163659837 [-162]	1.17 [1.92]	0.98 [1.27]	1.14 [2.06]	1.20 [1.91]	1.01 [1.64]
Glenn	*glennmathmin*	-0.289	-3.60	-4.60E-03	1.28E-05	-0.022	0.029	33.4	0.012	2.1E-4	0.132
	glennmathexp	-19,027,795 [-103]	-47,960,808 [-62]	-5,598,023 [-69]	-6,191,943 [-41]	-24,461,169 [-198]	0.961 [1.36]	0.973 [1.42]	0.963 [1.30]	0.878 [1.06]	0.883 [1.40]
	glennmathext	-281,694,548 [-39]	-317,664,413 [-45]	-111,615,956 [-81]	-187,419,953 [-33]	-190,942,626 [-34]	0.945 [1.52]	1.05 [1.69]	0.991 [1.78]	1.08 [1.41]	1.02 [1.95]
	glennrealmin	-1.37E-3	-0.898	-3.57E-4	-0.513	-2.48E-3	5.82	38.8	12.2	0.009	1.27
	glennrealexp	-172,709 [-11.6]	-24,838 [-9.4]	-35,544 [-9.9]	-0.500 [-2.54]	-178,344 [-5.8]	1.02 [1.44]	1.10 [1.37]	1.11 [1.32]	0.754 [0.873]	0.836 [1.28]
	glennrealext	-4,306,956 [-4.7]	-3,145,726 [-4.6]	-5,234,783 [-5.4]	-49,030 [-4.1]	-7,506,199 [-4.1]	0.981 [1.84]	1.07 [1.46]	0.929 [1.53]	0.955 [1.04]	0.960 [1.70]

6.3 Spectral Unmixing Algorithm Comparisons and Overall Conclusions

The `WLS_ASC_ILR()` algorithm was based on the currently most commonly used Ramsey and Christensen 1998 style spectral unmixing algorithm, with minor changes such as using a weighted least squares (as opposed to the ordinary least squares), and modifying this to contain the abundance sum constraint based on that for the ordinary least squares from Heinz and Chang 2001. This provided a baseline for comparison when developing increasingly sophisticated algorithms, which aimed to surpass the physical inaccuracies of the linear mixing model (for fine particulate dominated samples), thus providing an improved spectral unmixing algorithm. The direction taken with this was to adopt a Bayesian approach, leading to the development of spectral unmixing algorithms, `OptEst_ASC_ILR()` and `MCMC()`.

Unmixing the mathematical versions of Bruce and Glenn against their *minimal* spectral libraries using `WLS_ASC_ILR()` generally performed well (based on fit and abundance quality metrics outlined in Table 5.9); as was expected given that the mathematical mixtures were just their *minimal* spectral library end-members combined using the linear mixing model, with their known abundances as defined in Tables 4.2 (for Bruce) and 4.3 (for Glenn).

However, when introducing more end-members through the *expanded* and *extensive* spectral libraries, the `WLS_ASC_ILR()` algorithm began to perform poorly, and highlighted some of the major issues with this technique; particularly that the iterative library reduction process (used to implement the non-negativity constraint) would often remove correct end-members and/or retain incorrect ones. The very different selection of end-members for the mathematical vs real versions of the mixtures with each version of the spectral library could be an indication of how poor the model is; however, this was also a flaw of the algorithm, which was thought could be rectified with a different method. Overall, the analyses outlined in Section 5.3 showed that the linear mixing model used within `WLS_ASC_ILR()` was unreliable

and unsuitable for fine grained mixtures, thus justifying the need for algorithm investigation and development to find an improvement.

A significant advantage to the weighted least squares technique is its computational ease and reproducability. In an effort to retain these attributes whilst adopting a Bayesian approach, the optimal estimation algorithm, `OptEst_ASC_ILR()`, was developed; as optimal estimation is arguably a weighted least squares with the addition of priors. Having these priors did clearly have some effect on the retrieval (as presented throughout Section 6.1), particularly that 'tighter' priors (i.e., more confidence/low percentage uncertainty), could act to reduce the overall scale of correlation, and therefore the degree of degeneracy. This suppression of degeneracy could potentially improve the validity of using linear mixing in this algorithm compared to `WLS_ASC_ILR()`.

However, some of the main issues of `WLS_ASC_ILR()` were still present in `OptEst_ASC_ILR()` – particularly the retention/removal of correct/incorrect end-members during iterative library reduction (ILR) – thus making `OptEst_ASC_ILR()` similarly unreliable to `WLS_ASC_ILR()`. From this, and the insufficient improvement on retrieval quality metrics (as summarised in Tables 5.9 and 6.12), the simple addition of priors via optimal estimation was not considered a viable improvement over the weighted least squares.

`MCMC()` was a completely different type of algorithm, with a key difference being that it retained all end-members, as the non-negativity constraint was taken care of by defining the prior probability density functions (pdfs) such that sampling below zero would not be possible. Performance when unmixing against the *minimal* spectral libraries was generally good for both the mathematical and real versions of Bruce and Glenn. However, when unmixing against the *expanded* and *extensive* spectral libraries, `MCMC()` performed poorly all round (as summarised in Table 6.29), which may have been down to the lack of an intrinsic sum to one constraint enforced for the sampling. Even though the end-member selection problem from

`WLS_ASC_ILR()` and `OptEst_ASC_ILR()` was addressed with `MCMC()`, this did not improve the retrieval.

A potential issue with MCMC techniques in general is convergence – it is possible that with a longer chain, some end-members could have converged better. However, although there were some differences with these final unmixings, in my preliminary work, I experimented using different combinations of number of walkers and steps (e.g., 150 walkers each taking 100,000 steps) which displayed the same level of 'fuzziness' (i.e., uncertainty about the median value) in the walkers plots, suggesting that a significantly longer chain would not have improved convergence. Therefore, for the final unmixings, I followed the advice from the `emcee` documentation (Foreman-Mackey et al. 2013) with regards to setting the number of walkers and samples in such a way that satisfactory convergence could be reached without significantly slowing down the entire process. Additionally, assessment of the walkers plots throughout Section 6.2 suggested that convergence was obtained for all end-member samplings, with only a couple of exceptions that were somewhat dubious.

Despite addressing issues with `WLS_ASC_ILR()` and `OptEst_ASC_ILR()`, the overall poor performance of `MCMC()` indicated that this was also an unsuitable algorithm for use in spectral unmixng.

The overall lack of improvement seen when trialling increasingly sophisticated algorithms (as summarised in Tables 5.9, 6.12 and 6.29), along with initial hints into the inaccuracy of the linear mixing model from comparisons between real and mathematical versions of the Bruce and Glenn mixtures, and PCA of different sizes of spectral library, suggested that **the answer to the question: 'do we need a new model or just a new algorithm?' was that a new model is required**.

The wider implication of this result is that perhaps more caution should be taken when interpreting compositions derived from the linear mixing model, particularly when fine grains dominate; regardless of whether the spectral library end-members are appropriately sized. As such, results from previous literature may need to be

treated more as estimations with a larger degree of uncertainty, and it could even be useful to revisit some of the more definitive/highly cited works to conduct a more rigorous quantitative assessment, especially in cases that had minimal statistical analysis to begin with. Generally, the work presented here so far has shown that what has typically been taken to be 'true' compositions, based on previous linear unmixing analysis, may be less robust/accurate than originally thought, which could then have knock-on effects to further conclusions based on these results (e.g., planetary dynamics constraints, origins of organics etc.). This therefore provides further justification to continue in the improvement of spectral interpretation techniques.

Of course it would be possible to continue trialling continually more complex algorithms, potentially entering the realm of machine learning; however, in the interest of retaining the computational ease of current methods, it is desirable to derive an alternative model. This alternative model should include greater physical accuracy than the linear mixing model, and serve as a mid-point between linear mixing and full radiative transfer models (e.g., the Hapke model; Hapke 2012); ideally being well suited to Bayesian algorithms similar to `OptEst_ASC_ILR()` and `MCMC()`, whilst being accessible and reproducible.

Chapter 7

Towards A New Spectral Mixing Model

Contents

7.1 Justification and Overview 204
7.2 Proposed Method 206
7.2.1 Previous Studies of Spectral Changes with Grain Size . 206
7.2.2 My Spectral Morphology Study 210
7.3 Preliminary Results 225
7.3.1 Data Used 225
7.3.2 Spectral Morphology Study Results 227
7.3.3 Pre-Unmixing: *brucerealmod* and its Coarse Spectral Libraries 232
7.3.3.1 PCA of 'Coarse' Spectral Libraries 233
7.3.4 `WLS_ASC_ILR()` 238
7.3.4.1 *brucerealmodmin* 238
7.3.4.2 *brucerealmodexp* 239
7.3.4.3 *brucerealmodext* 239
7.3.5 `OptEst_ASC_ILR()` 241
7.3.5.1 *brucerealmodminP1→P4* 241
7.3.5.2 *brucerealmodexpP1→P4* 244
7.3.5.3 *brucerealmodextP1→P4* 245
7.3.6 `MCMC()` 246
7.3.6.1 *brucerealmodminU→P4* 246
7.3.6.2 *brucerealmodexpU→P4* 248
7.3.6.3 *brucerealmodextU→P4* 249
7.3.7 Discussion 252

In an effort to derive a more physically complete spectral mixing model that is not computationally expensive, nor requires a significant amount of additional data, I chose to work towards parameterisation of linear mixing, such that the new

model would be usable for a wider range of grain sizes. As it is the dominance of fine grains within this wavelength range ($5 - 25\mu$m; TIR) that invalidates linear mixing, the work outlined in this chapter lays the foundations for an empirical parameterisation of linear mixing via studies of spectral morphology changes with grain size, since the change in scattering regime caused by the change in grain size primarily manifests as changes in spectral morphology (e.g., Figure 7.1).

7.1 Justification and Overview

As discussed in more depth in Chapter 2, the linear mixing model states that the spectrum of a mixture may be considered as the sum of its individual component spectra in proportion to their abundances. This is based on the principle that each detected photon contains information from only a single grain, thus relying on specular reflection in order to be valid. This is a good representation of light scattering from coarse and whole rock samples, however, as grain size decreases and approaches the wavelength of interacting light, a photon may undergo volumetric scattering where it interacts with multiple grains before detection; thus leading to the break down of linear mixing with decreasing grain size. The main bulk of my research has been to answer the question of whether we can get around this issue by using better algorithms, or whether we need a new model; the answer to which I have found is that a new model is necessary (see Section 6.3).

It is important to note that there are models other than linear mixing that describe the relevant light-matter interaction in order to obtain composition. The most physically complete and commonly used are radiative transfer models, such as the Hapke model[1] (e.g., Hapke 2012), that parameterise the combination of radiative transfer and the light scattering phase function to estimate a reflectance spectrum, which is then often converted to emissivity via Kirchhoff's law ($E = 1 - R$; e.g., Section 2.1). However, these models need to be used in conjunction with additional methods such as T-matrix (e.g., Mackowski and Mishchenko 1996, 2011)

[1]Hapke modelling is mostly applicable for shorter wavelengths, with some less complete approximations for use in the TIR (Hapke 2012).

or Mie theory (e.g., Hulst and van de Hulst 1981) to provide the phase function parameters. These methods are often more computationally expensive than linear mixing, and/or additionally require optical constant data, which are not readily available for a number of end-members.

A promising method is T-matrix, which explicitly calculates Maxwell's equations[2] for particulate samples that are densely packed, thus avoiding the assumption of widely separated grains (i.e., 3× the grain radius, as required in Mie theory; Hulst and van de Hulst 1981), which is often inaccurate for planetary surfaces (e.g., Ito et al. 2017). A benefit of the T-matrix method allowing for closely packed grains is that this inherently includes multiple scattering, which the linear mixing model not only assumes, but requires, to not be the case. This multiple scattering is more prevalent for finer grain sizes, and is what causes non-linearity, thus making linear mixing invalid as grain size decreases, and the T-matrix method a potentially more accurate model for use in spectral mixing.

Hybrid T-matrix/radiative transfer models have been investigated and found to be an improvement on Mie/radiative transfer models for application to planetary surfaces; which has been attributed to the multiple scattering for densely packed grains that is intrinsic to the T-matrix method, and absent in Mie theory; as shown in Ito et al. 2017. In this work, Ito et al. 2017 generated emissivity spectra of enstatite grains at 3.3, 32.1, 48.4, and 93.9μm size fractions, using parameters calculated from T-matrix within three different radiative transfer models: Conel 1969, Hapke 1993, and Hapke 1996, and compared these with laboratory measured spectra. From this they found that the T-matrix hybrid models performed better than Mie hybrid models, producing "more consistent emissivity spectra for the finest particle size fraction (3.3μm)", but performed poorly for the larger size fractions.

Despite the improvement seen with T-matrix vs Mie, the poor performance of the T-matrix/radiative transfer hybrid models for larger grain sizes (Ito et al. 2017)

[2]Maxwell's equations are a fundamental set of equations that underpin the physics of electromagnetism.

leaves a space that would be valuable to fill with a semi-empirical, alternative model to linear mixing and radiative transfer. This alternative model would serve as a meeting point between the two – containing the greater physical completeness and accuracy of radiative transfer, whilst retaining the computational ease, accessibility and reproducibility of linear mixing – and would be effective for applications to both fine and coarse grained samples.

7.2 Proposed Method

As discussed throughout this thesis, the prevailing issue with linear mixing is its invalidation for use with fine grained samples, making it unsuitable for application to many planetary surfaces where fine grains dominate. However, it has been previously shown (e.g., Ramsey and Christensen 1998) that linear mixing is highly effective for coarse particulate samples.

Since the unsuitability of linear mixing for fines is caused by the change in scattering regime from specular to volumetric as grain size decreases, which also manifests as alterations in spectral morphology (e.g., Figures 2.4 and 7.1), this raises the question: can linear mixing be used successfully for fine grained samples if their spectra were transformed to appear as equivalent coarse spectra for the same samples, and unmixed against an appropriate 'coarse' spectral library? Manipulating a fine grained spectrum to appear coarse grained requires good knowledge on exactly how spectral morphology changes with grain size. Although other investigations have collected data and studied spectral changes with grain size, these have often been more qualitative in nature, quantified different effects, and/or not taken the findings further e.g., to parameterise spectral mixing models.

7.2.1 Previous Studies of Spectral Changes with Grain Size

Salisbury et al. 1987 presented spectra in both transmittance and reflectance of 78 minerals (mostly silicates), where the reflectance spectra were collected at two different grain size fractions ($0 - 74$ and $74 - 250\mu$m), in order to see how

scattering is effected by grain size. To provide full context to the spectra, each sample was also characterised thoroughly via X-ray diffraction and microprobe analysis. As well as presenting a large suite of spectra and detailed accounts of sample preparation and data collection, Salisbury et al. 1987 also provided a more qualitative discussion of the presented spectra, covering explanations of the major spectral features and the effects of crystallographic orientation, packing, atmospheric gases, impurities and grain size.

In their discussion of the effect of grain size on spectra, Salisbury et al. 1987 mentioned the role of surface and volume scattering, changes in spectral contrast, the Transparency Features (TFs) and Christiansen Features (CFs). Here, they noted that surface or volumetric scattering (e.g., Figure 2.4) being dominant in the detected radiation was governed by the absorption coefficient and grain size. In their presented spectra, they showed that for solid samples, the majority of the spectral range ($4600 - 400\text{cm}^{-1}$) was predominantly surface scattering; displaying strong features corresponding to the strongest molecular vibration bands (also noting that the strong absorption coefficient, at the locations of the strong features, caused a "mirror-like opacity" in these regions). Their spectra also showed that strong troughs in reflectance (i.e., peaks in emissivity) generally indicated regions dominated by volume scattering for finer particulate samples; as here the grains were small enough to allow the complete passage of photons in regions of relatively low absorption coefficient.

Salisbury et al. 1987 also highlighted that spectral contrast (or band intensity/depth) clearly changed with grain size, but that the changes were not consistent; explaining that this was due to how the mean optical path length[3] scaled relative to the grain size. With the spectra presented, they also provided several examples of minerals displaying a TF – a region of high transparency between the main stretching and bending Reststrahlen Bands (RB; e.g., Section 2.1). They also provided an explanation that the appearance of this TF was dependent on how

[3]The mean optical path length is the mean distance into a material traversed by a photon before being absorbed.

decreasing grain size impacted the decreasing spectral contrast of the adjacent RB, and that not all minerals will display a TF. However, if present, the TF was often a prominent, and recognisable, feature for fine particulate samples, and due to the location between fundamental RB, the TF could be a valuable indicator of composition. In Salisbury et al. 1987, they also showed that, although the principal CF was generally present at all grain sizes, it was more easily identified in spectra of fine particulate samples, due to the transparency effects at wavelengths short-ward of the CF (the CF roll-off; e.g., Section 2.1).

Later, in Shirley and Glotch 2019, their work on investigating grain size effects on TIR spectra of lunar analogues, measured under simulated lunar conditions[4] (i.e., pressure of $< 10^{-5}$mbar, samples heated from below to 350 ± 0.5K, with additional heating from above via a quartz halogen lamp, and chamber cooled to $< 150 \pm 2$K), showed various changes to the spectra. These changes included an enhancement of RB and TF spectral contrast, and a shifting in CF position to longer wavelengths – an important observation for relating remote sensing to laboratory measurements in compositional studies, as the CF position is often indicative of composition. To gain these insights, they took measurements of quartz, anorthite (An_{95}), labradorite (An_{49}), albite (An_{24}), augite ($Wo_{50}En_{34}Fs_{16}$), diopside ($Wo_{51}En_{43}Fs_{6}$), enstatite ($Wo_{1}En_{70}Fs_{29}$), forsterite (Fo_{88}) – all silicates observed on the Moon – and ilmenite (also relevant to the Moon). The samples were crushed and sieved to < 32, $32 - 63$, $63 - 90$, $90 - 125$, and $125 - 250\mu$m size fractions (e.g., Figures 7.3 and 7.4 which show the olivine spectra at these size fractions), chosen to represent the size fractions seen in the Apollo soils.

Mustard and Hays 1997 investigated the effects of fine grains on the reflectance spectra ($0.3 - 25\mu$m wavelength range) of olivine and quartz, at < 5, $5 - 10$, $10 - 15$, $15 - 20$ and $20 - 25\mu$m grain size fractions. In this work, they observed several changes in the reflectance spectra as grain size decreased, including: a saturation of

[4]The same measurements were also taken under ambient conditions, defined as a pressure of 1000mbar, chamber temperature of $\sim 300 \pm 1$K, and sample temperature of 350 ± 0.5K, without illumination.

CF, spectral contrast decrease in the RB – where some features displayed variations in shape, though those used for compositional determinations remained largely unaffected – and an increase then decrease in spectral contrast, changes of position of the reflectance peak (emissivity trough), and symmetry alterations, of the TF. In this work they also derived the critical diameter (where the extinction and scattering efficiencies rapidly decline when grain size is roughly equal to wavelength, as predicted by Mie theory) as a function of wavelength; and showed that this qualitatively explained the observed changes in spectra with decreasing grain size. Finally, they modelled the olivine and quartz spectra at each grain size fraction using a Mie/Hapke hybrid model, which included the exact grain size distributions as measured. From this, Mustard and Hays 1997 showed that the model worked well for olivine, but less so for quartz, where the largest discrepancies occurred in the RB and overall spectral contrast.

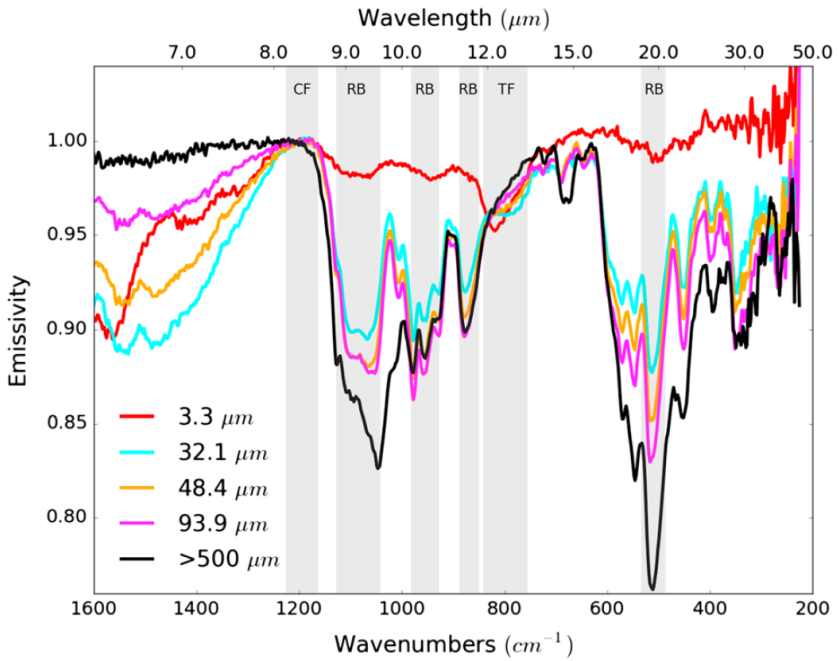


Figure 7.1: Ito et al. 2017 Fig. 3 - Enstatite emissivity spectra at five different grain size fractions measured in the laboratory.

As discussed in Section 7.1, Ito et al. 2017 showed that the T-matrix method was better than Mie theory in capturing the differences in spectral morphology with decreasing grain size, as shown in Figure 7.2 (Fig. 8 of Ito et al. 2017). However, a

significant downside to using T-matrix (or even Mie) models, is the requirement of optical constant data (typically the complex refractive index or scattering albedo), which are currently unavailable for the majority of potential end-member minerals needed for robust planetary surface analysis (discussed during the Sofia Science Series 'Rock, Dust and Ice: Interpreting Planetary Data' 2021 online workshop).

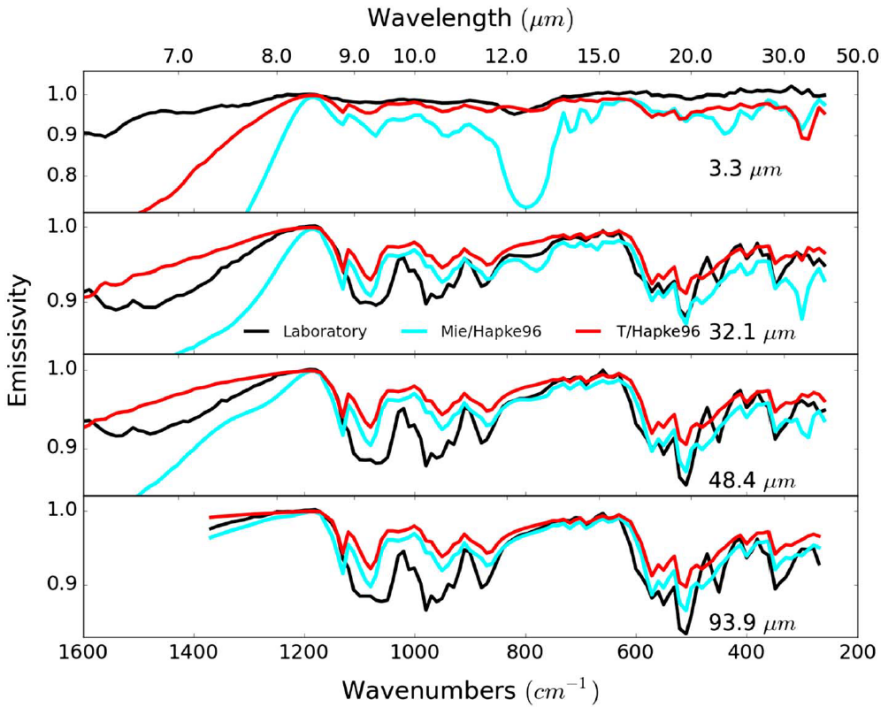


Figure 7.2: Ito et al. 2017 Fig. 8 - Measured and modelled enstatite emissivity spectra at four different grain size fractions for the Mie/Hapke96 and T/Hapke96 hybrid models.

7.2.2 My Spectral Morphology Study

As seen in in Figure 7.1 (enstatite; Fig. 3 of Ito et al. 2017), there are distinct differences in spectral morphology between the coarsest ($> 500\mu$m) and finest (3.3μm) size fractions. The coarse spectrum displays much greater overall spectral contrast, whereas the fine spectrum shows a steeper gradient on the higher frequency (larger wavenumber/shorter wavelength) side of the Christiansen Feature (CF; $\sim 1200\text{cm}^{-1}$), and has the Transparency Feature (TF; $\sim 800\text{cm}^{-1}$) present, which is not there at all for the coarse spectrum.

In previous work (e.g., Salisbury et al. 1987, Mustard and Hays 1997 and Shirley and Glotch 2019), the particularly well described changes in spectral morphology with grain size have been of this gradient on the high frequency side of the CF (defined here as the 'CF roll-off gradient'), and the prominence of the TF (defined here as 'TF depth'), both of which are clearly seen in Figure 7.1, and described in Section 7.2.1. Thus, the starting point for this work quantifies changes in CF roll-off gradient and TF depth as grain size decreases, and non-linearity becomes more dominant, to see whether there are any trends that may aid in the development of a new spectral mixing model.

In order to have consistent quantitative measurements of CF roll-off gradient and TF depth across grain sizes, I devised standardised ways to measure these. The steps to find the CF roll-off gradient are as follows:

1. **Find CF Position:** Crop the spectrum to just the CF region between user-defined bounds, chosen by eye to be roughly the troughs either side of the CF peak (e.g., $1600 - 1050\text{cm}^{-1}$ for olivine; Figure 7.3) for the smallest size fraction available (as this is where the CF is most prominent). Within this section, find the emissivity maximum, and then further crop the spectrum to be within a user defined range of the maximum point; i.e., crop to e.g., $\text{CF}_{\text{max}} \pm 30\text{cm}^{-1}$ (Figure 7.3). Then, following the method of Donaldson Hanna et al. 2012, model this section of the spectrum centered on the CF maximum as a 2^{nd}order polynomial, and find its stationary point (where the derivative is zero; Figure 7.3). The CF position is then defined as the wavenumber coordinate nearest to the stationary point of the modelled quadratic. I chose this method, as opposed to simply selecting the wavenumber coordinate of the data maximum, for consistency with previous datasets and analyses (e.g., Donaldson Hanna et al. 2012), and to allow this method to be more widely applicable to datasets where there may be poorer resolution and/or noise.

2. **Find End Point for CF Gradient:** The opposite end of the CF roll-off zone is defined here as the trough on the high frequency side of the CF peak

(Figure 7.3), and is found by locating the minimum emissivity of the CF region defined in Step 1 (Note: the bounds selected for the CF region should ensure that this trough is easy to identify and is the global minima within these bounds).

3. **Calculate CF Roll-Off Gradient:** Using the locations found in Steps 1 and 2, trim the spectrum again to be just within these two points (the CF roll-off region; Figure 7.3). Fit a 1storder polynomial (i.e., a straight line) to the spectral data in this region, using wavelength rather than wavenumber for the x-axis so that the gradient value is more intuitive with the conventional way of plotting (i.e., a positive gradient; Figure 7.3), thus giving the gradient units of emissivity per micron. The final value of the CF roll-off gradient and its uncertainty are derived from this straight line fit, which in this work was found using Python's `polyfit()`, which returned the coefficients for the equation of the best fit line, and their covariance matrix.

Note: Step 1 should first be done with the finest size fraction in order to more easily select the user-defined parameters by eye (e.g., axis limits for CF region) that will be used for the remaining size fractions. All steps above are illustrated in Figure 7.3

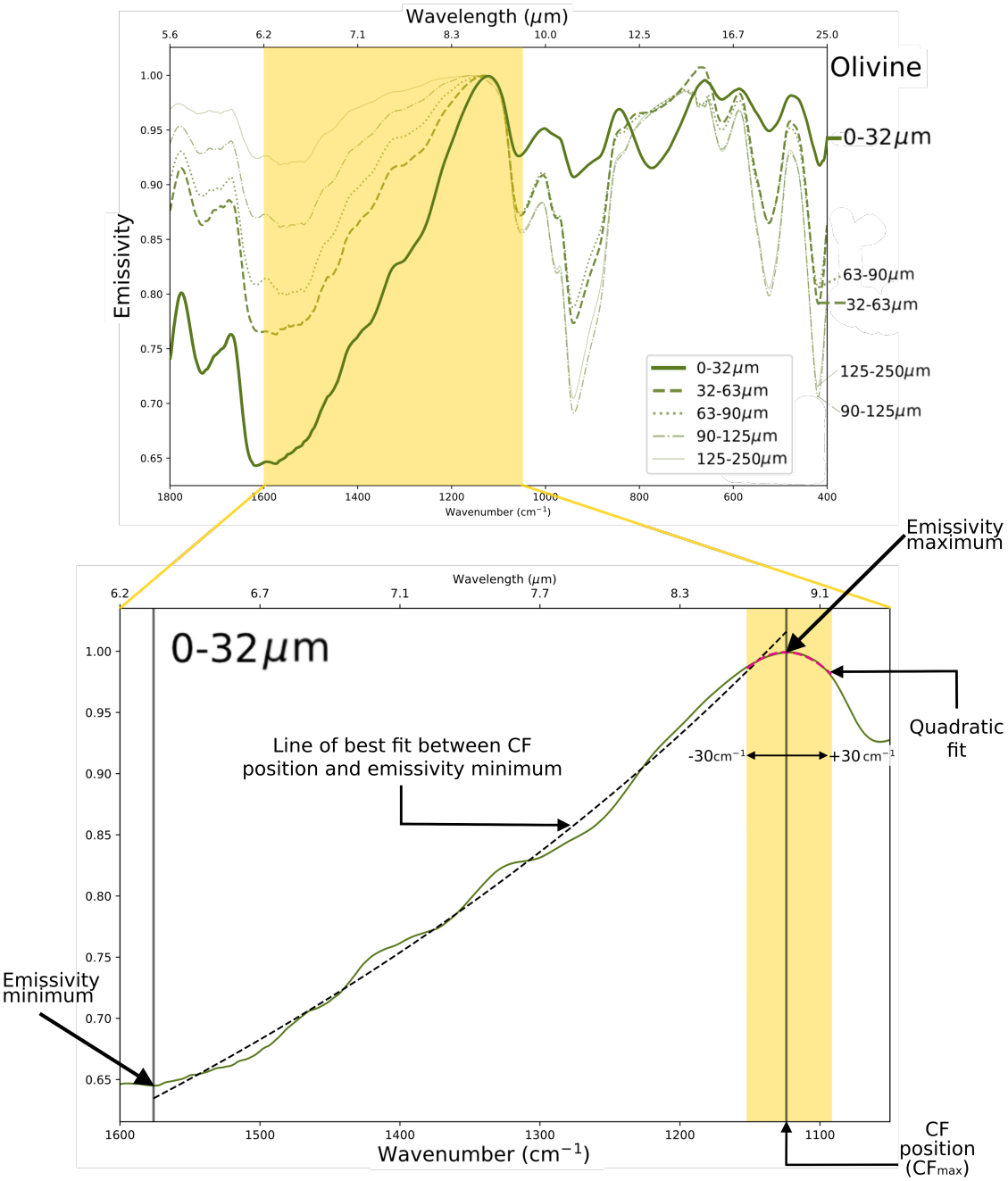


Figure 7.3: Diagram showing how the CF roll-off gradient was found (Olivine data from Shirley and Glotch 2019).

The TF depth is similar to the 'concavity index' of e.g., Glotch, Lucey, et al. 2010, and other standard measures of band depth, with the precise steps used in this work outlined below:

1. **Define the TF Region:** Crop the spectrum to fully contain the TF, bounded by user defined values, chosen by eye, to go beyond the peaks either side of the

TF trough such that these peaks are the local maxima (e.g., $950 - 600\text{cm}^{-1}$ for olivine; Figure 7.4). Find a number of inflection points (e.g., 10, 20, etc., as defined by the user), where the derivative of the spectrum is closest to zero, within the user defined TF region[5]. From this, locate the positions of the peaks either side of the TF, as illustrated in Figure 7.4 – these form the bounds of the TF at all size fractions to find its depth.

2. **Find TF Position:** Further crop the spectrum to be only between the TF adjacent peaks, as located in Step 1 (the TF region; Figure 7.4). Then, following a similar method used to identify the CF position, find the data minimum of the TF region and trim to a user defined region centred about this minimum (e.g., $\text{TF}_{\text{min}} \pm 10\text{cm}^{-1}$), and fit this with a 2^{nd}order polynomial to then find its stationary point. The TF position is then defined as the closest wavenumber coordinate available to this stationary point (i.e., minimum of the modelled quadratic; Figure 7.4).

3. **Calculate TF Depth:** Within the TF region defined in Step 2, fit a continuum across the TF[6]; i.e., a straight line connecting the two data points at either end of the TF region, which should be the peaks either side of the TF trough (Figure 7.4). Find the emissivity value of this line at the TF position, and subtract from it, the emissivity value of the data at the TF position, i.e., $A - B$ as shown on Figure 7.4, to obtain the TF depth and its uncertainty (which is just the measurement error at the TF position).

Note: Steps 1 and 2 should be done for the finest size fraction only, as these set up how positions are defined in order to find consistent measures of TF depth across all size fractions. Only Step 3 should then be repeated for all size fractions available. Calculating the CF roll-off gradient and TF depth for the finest size fractions first follows the method of Shirley and Glotch 2019, as the CF and TF

[5]The number of inflection points chosen here may require some trial and error to ensure the desired inflection points are identifiable from the selection returned.

[6]Again using Python's `polyfit()`.

are much more readily picked out by eye for fine particulate spectra. The steps taken to find the TF depth are illustrated in Figure 7.4.

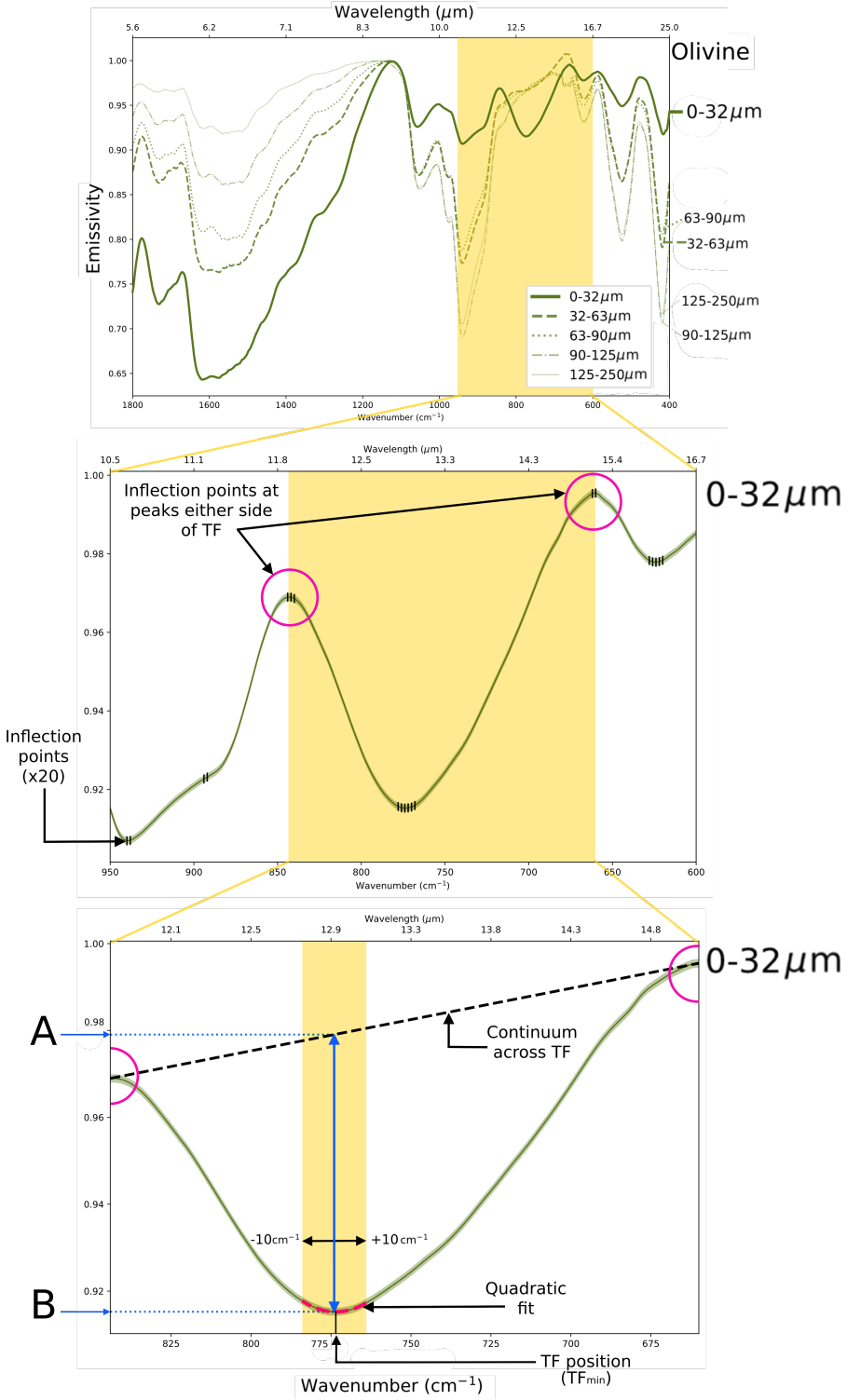


Figure 7.4: Diagram showing how the TF depth was found (Olivine data from Shirley and Glotch 2019).

As previously mentioned, the main changes in spectral morphology seen as grain size decreases are a general decrease in spectral contrast, an increase in CF roll-off gradient, and increase in TF depth. These increases in CF roll-off gradient and TF depth may be considered as increases in spectral contrast for these regions, which decreases for the remainder of the spectrum.

Thus to manipulate a fine spectrum to appear coarse (named here as 'coarsification'), a way of doing this could be to scale the spectral contrast according to region; i.e., decrease the contrast in the CF roll-off and TF regions, and increase it everywhere else. A standard method for taking into account spectral contrast effects is the use of a blackbody component (i.e., BB end-member), as discussed in Section 4.3.3; therefore the approach taken here was to 'add' or 'subtract' an abundance of BB in the appropriate regions of the spectrum. This BB abundance was determined empirically through the spectral morphology study using the methods described above. This coarsification process is outlined as follows:

1. **Section the Spectrum (Figure 7.5):** Divide the spectrum into the different 'zones' that will be treated differently. The high frequency side of the CF up to the CF position (found via CF roll-off gradient steps above) is labelled as the 'CF zone' (Figure 7.5). Between the CF position and the first peak adjacent to the TF (found via TF depth steps above) is labelled as the first Reststrahlen Bands zone, 'RB1 zone' (Figure 7.5). Between this peak and the first peak on the other side of the TF is the 'TF zone' (Figure 7.5). Finally, from this second peak towards lower frequencies for the remainder of the spectral range is the second Reststrahlen Bands zone, 'RB2 zone' (Figure 7.5).

2. **CF Zone Modification (Figure 7.6):** Decrease spectral contrast in the CF zone by 'adding' a BB abundance, determined from empirical spectral morphology studies, via Equation 7.1, propagating uncertainties via Equation 7.2:

$$\epsilon'_{CF} = (1 - x_{BB}^{CF})\epsilon_{CF} + x_{BB}^{CF}\epsilon_{BB} \tag{7.1}$$

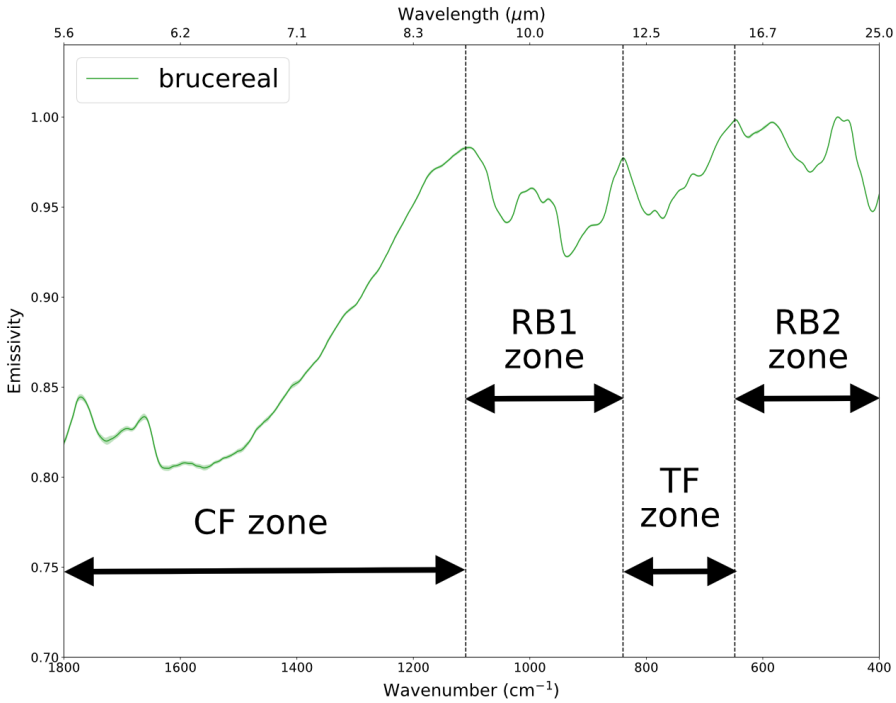


Figure 7.5: Diagram showing step 1 of the coarsification process on *brucereal* (data from Donaldson Hanna et al. 2019).

$$\sigma(\epsilon'_{CF}) = \left[(1-x_{BB}^{CF})^2\epsilon_{CF}^2\left[\left(\frac{\sigma(x_{BB}^{CF})}{1-x_{BB}^{CF}}\right)^2+\left(\frac{\sigma(\epsilon_{CF})}{\epsilon_{CF}}\right)^2\right]\right. \\ \left.+(x_{BB}^{CF}\epsilon_{BB}^{CF})^2\left[\left(\frac{\sigma(x_{BB}^{CF})}{x_{BB}^{CF}}\right)^2+\left(\frac{\sigma(\epsilon_{BB})}{\epsilon_{BB}}\right)^2\right]\right]^{\frac{1}{2}} \tag{7.2}$$

where ϵ'_{CF} is the modified (i.e., decreased spectral contrast) emissivity in the CF zone; x_{BB}^{CF} is the BB abundance for the CF zone (found empirically via spectral morphology studies; e.g., Section 7.3.2); ϵ_{CF} is the measured emissivity data in the CF zone; ϵ_{BB} is the emissivity of the blackbody component (which is 1 across the spectral range); and these variables surrounded by $\sigma()$ denotes their uncertainties. Then shift the entire zone so that the CF of the modified spectrum sits at the same x- and y-coordinates as the original CF (Equation 7.3), propagating uncertainties again in the appropriate manner via Equation 7.4:

$$\epsilon''_{CF} = \epsilon'_{CF} - (\epsilon'_{CF}(\nu_{CF}) - \epsilon(\nu_{CF})) \tag{7.3}$$

$$\sigma(\epsilon''_{CF}) = \sqrt{\sigma(\epsilon'_{CF})^2 + \sigma(\epsilon'_{CF}(\nu_{CF}))^2 + \sigma(\epsilon(\nu_{CF}))^2} \tag{7.4}$$

where ϵ''_{CF} is the modified CF zone emissivity (ϵ'_{CF}) shifted to the appropriate location; $\epsilon'_{CF}(\nu_{CF})$, and $\epsilon(\nu_{CF})$ are the emissivity of the modified CF zone spectrum, and the measurement spectrum, at the CF position, ν_{CF}, respectively. Again, $\sigma()$ around the variables denotes their uncertainties.

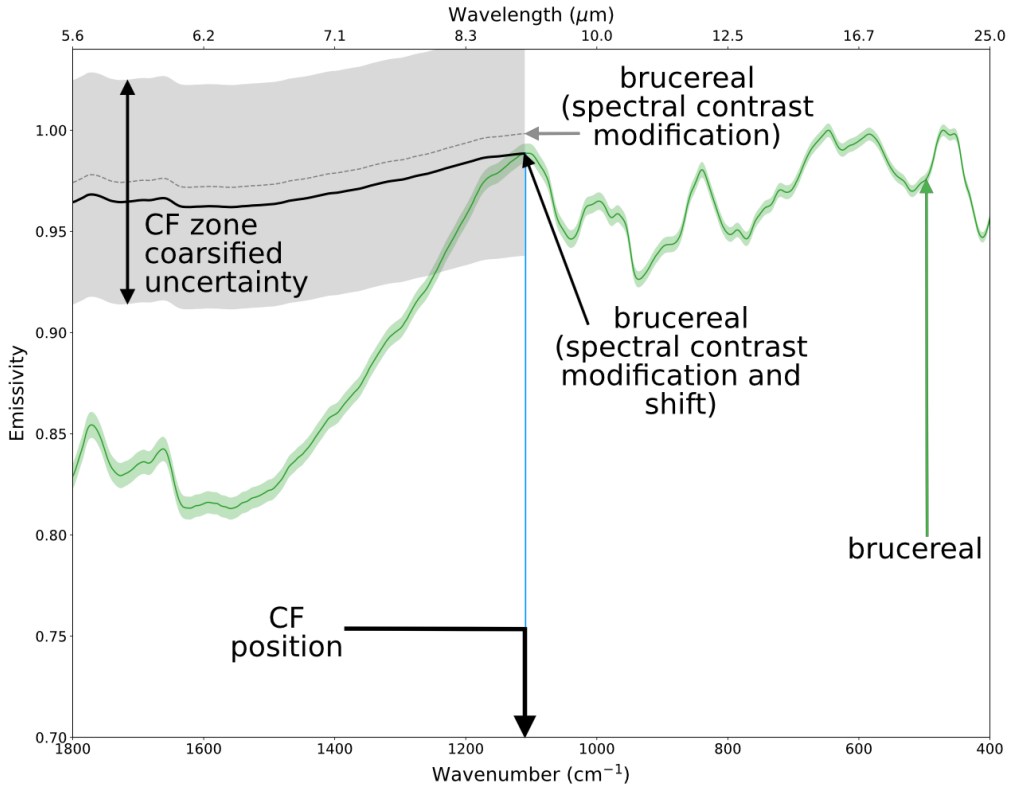


Figure 7.6: Diagram showing step 2 of the coarsification process on *brucereal*. Note: For the example spectrum here (*brucereal*), between Figures 7.5 and 7.6, a continuum correction was applied to the spectrum to ensure either the primary or secondary CF had an emissivity of 1 (as per calibration standards), with errors propagated accordingly; hence the difference in uncertainty scales between Figures 7.5 and 7.6. (Data from Donaldson Hanna et al. 2019).

3. **RB1 Zone Modification (Figure 7.7):** Increase spectral contrast in the RB1 zone by 'removing' a BB component (i.e., BB renormalisation, as introduced in Section 4.3.3) by an amount also determined by empirical studies, as above, via Equation 7.5 with uncertainties propagated via Equation 7.6.

$$\epsilon'_{RB} = \frac{\epsilon_{RB} - x_{BB}^{RB}\epsilon_{BB}}{1 - x_{BB}^{RB}} \tag{7.5}$$

$$\sigma(\epsilon'_{RB}) = \epsilon'_{RB}\left[\frac{\sigma(\epsilon_{RB})^2 + (x_{BB}^{RB}\epsilon_{BB})^2\left[\left(\frac{\sigma(x_{BB}^{RB})}{x_{BB}^{RB}}\right)^2 + \left(\frac{\sigma(\epsilon_{BB})}{\epsilon_{BB}}\right)^2\right]}{(\epsilon_{RB} - x_{BB}^{RB}\epsilon_{RB})^2} + \left(\frac{\sigma(x_{BB}^{RB})}{1 - x_{BB}^{RB}}\right)^2\right]^{\frac{1}{2}} \tag{7.6}$$

where ϵ'_{RB} is the modified (i.e., increased spectral contrast) emissivity in the RB zone; x_{BB}^{RB} is the BB abundance for the RB zones (found empirically via spectral morphology studies; e.g., Section 7.3.2); ϵ_{RB} is the measured emissivity data in the RB zone; ϵ_{BB} is the emissivity of the blackbody component (which is 1 across the spectral range); and these variables surrounded by $\sigma()$ denotes their uncertainties. Shift the RB1 zone to join up with the CF zone at the CF (Equation 7.7), again propagating uncertainties (Equation 7.8).

$$\epsilon''_{RB} = \epsilon'_{RB} - (\epsilon'_{RB}(\nu_{CF}) - \epsilon(\nu_{CF})) \tag{7.7}$$

$$\sigma(\epsilon''_{RB}) = \sqrt{\sigma(\epsilon'_{RB})^2 + \sigma(\epsilon'_{RB}(\nu_{CF}))^2 + \sigma(\epsilon(\nu_{CF}))^2} \tag{7.8}$$

where ϵ''_{RB} is the modified RB zone emissivity (ϵ'_{RB}) shifted to the appropriate location.

4. **TF Zone Modification (Figures 7.8 to 7.10):** Decrease spectral contrast and shift as appropriate in the same manner as for the CF zone, following Equations 7.1 to 7.4 from Step 2 above, using a BB abundance relevant for the TF, x_{BB}^{TF}, and shifting to match to the original spectrum at the boundary between the TF and RB2 zones (which is likely to be the position of the secondary CF). As this will still give the spectrum a somewhat concave shape (curving downwards) for this zone (seen in Figure 7.8), whereas coarse spectra are more convex here (i.e., curving upwards; e.g., the $> 500\mu$m spectrum within the highlighted TF region in Figure 7.1, and the coarse olivine spectrum in Figure 2.4), to achieve a more convex appearance, reflect and rotate the TF zone as appropriate:

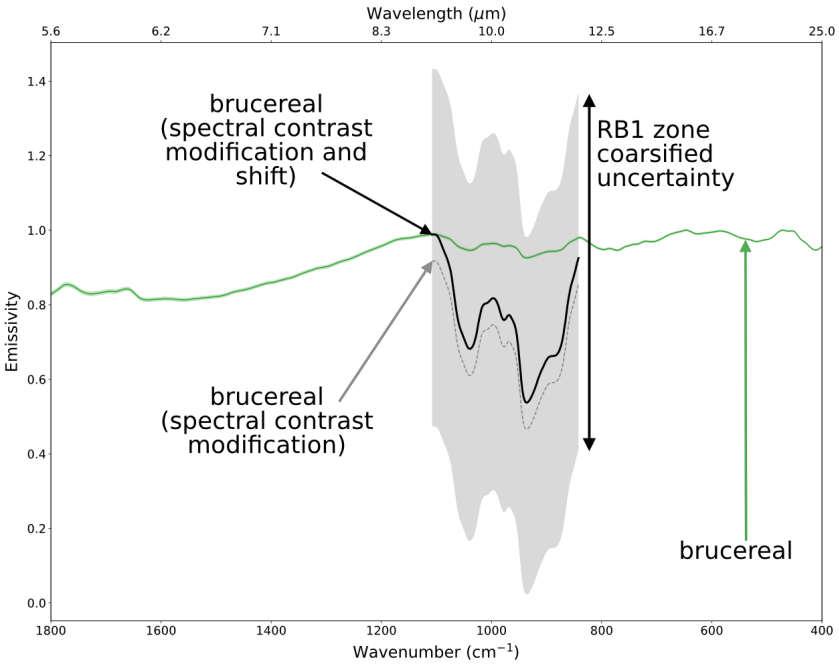


Figure 7.7: Diagram showing step 3 of the coarsification process on *brucereal*. Note: the emissivity axis scale is different here compared to Figures 7.5 and 7.6 in order to show the full scale of the transformed RB1 zone and associated uncertainty. (Data from Donaldson Hanna et al. 2019).

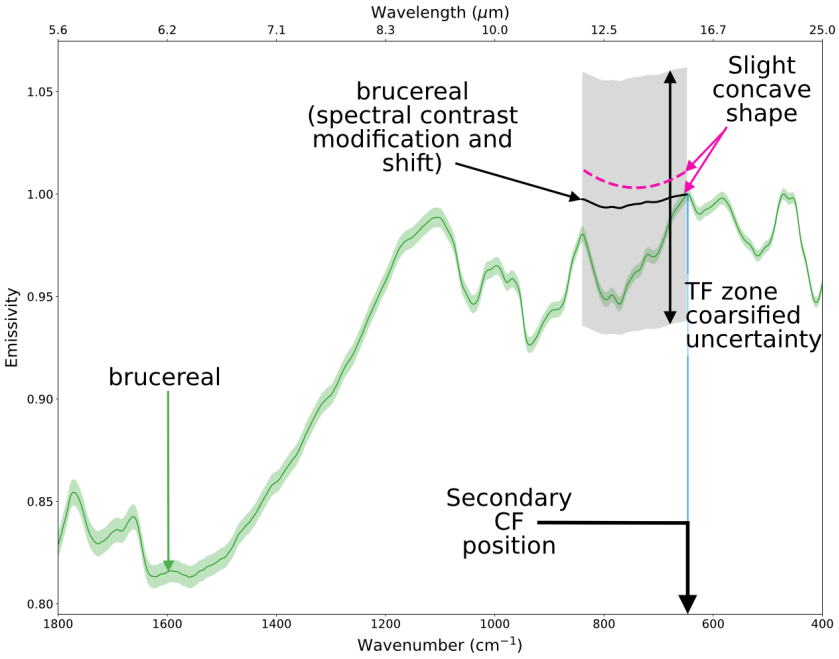


Figure 7.8: Diagram showing the initial stage of step 4 of the coarsification process on *brucereal*, indicating the slight concave shape of the modified TF zone spectral section. Note: the shift occurring here was small, so the section of spectrum from just the spectral contrast modification is not visible here as it was in Figures 7.6 and 7.7. (Data from Donaldson Hanna et al. 2019).

(a) First reflect about a horizontal plane positioned at the spectral coordinate at the low frequency end of the TF zone (i.e., at at the secondary CF, which may be at emissivity=1 depending on how the spectrum has been calibrated; Figure 7.9). This should follow Equation 7.9, with error propagation from Equation 7.10.

$$\epsilon''^{\text{Refl.}}_{TF} = -\epsilon''_{TF} + 2\epsilon(\nu_{CF2}) \tag{7.9}$$

$$\sigma(\epsilon''^{\text{Refl.}}_{TF}) = \sqrt{\sigma(\epsilon''_{TF})^2 + 4\sigma(\epsilon(\nu_{CF2}))^2} \tag{7.10}$$

where $\epsilon''^{\text{Refl.}}_{TF}$ is the reflected emissivity of the modified and shifted TF zone emissivity, ϵ''_{TF} (first stage of Step 4 prior to this step, 4a), and $\epsilon(\nu_{CF2})$ is the original measured emissivity at the secondary CF position, ν_{CF2}.

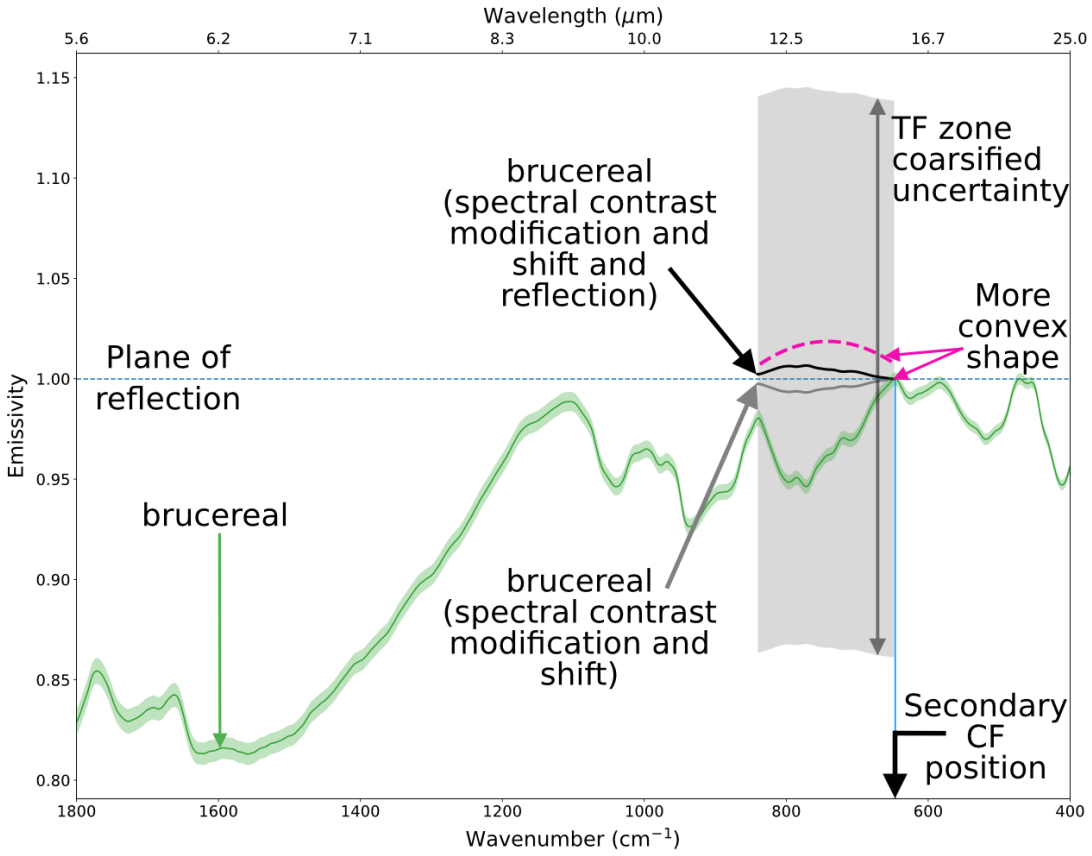


Figure 7.9: Diagram showing step 4a of the coarsification process on *brucereal* – reflecting the TF zone to appear more convex, as observed in coarse spectra. (Data from Donaldson Hanna et al. 2019).

(b) Then rotate the spectral section about the secondary CF such that the higher frequency end of the TF zone matches with the RB1 zone at the appropriate point:

i. First, the TF zone must be shifted (and uncertainties propagated) to place the point of rotation (i.e., the secondary CF) at the origin (Equations 7.11 and 7.12).

$$\epsilon''^{\text{Refl.}}_{TF}(\nu_{CF2\rightarrow 0}) = \epsilon - \epsilon''^{\text{Refl.}}_{TF}(\nu_{CF2}) \tag{7.11}$$

$$\sigma(\epsilon''^{\text{Refl.}}_{TF}(\nu_{CF2\rightarrow 0})) = \sqrt{\sigma(\epsilon)^2 + \sigma(\epsilon''^{\text{Refl.}}_{TF}(\nu_{CF2}))^2} \tag{7.12}$$

where $\epsilon''^{\text{Refl.}}_{TF}(\nu_{CF2\rightarrow 0})$ is the emissivity coordinate on shifting the spectrum to place the secondary CF, CF2, at the origin; ϵ is the emissivity value at any point in the spectrum being shifted; $\epsilon''^{\text{Refl.}}_{TF}(\nu_{CF2})$ is the emissivity found from Equation 7.9 (Step 4a) at CF2; and the wavenumber coordinates are shifted via $\nu_{CF2\rightarrow 0} = \nu - \nu_{CF2}$.

ii. From here, the anticlockwise rotation can occur, giving new spectral coordinates, $(\nu_\theta, \epsilon_\theta)$, via Equation 7.13 about the angle, θ, found from Equation 7.14, with uncertainty propagation through Equations 7.15 to 7.17.

$$\begin{bmatrix} \nu_\theta \\ \epsilon_\theta \end{bmatrix} = \begin{bmatrix} cos(\theta) & sin(\theta) \\ -sin(\theta) & cos(\theta) \end{bmatrix} \cdot \begin{bmatrix} \nu_{CF2\rightarrow 0} \\ \epsilon''^{\text{Refl.}}_{TF}(\nu_{CF2\rightarrow 0}) \end{bmatrix} \tag{7.13}$$

$$\theta = tan^{-1}\left(\frac{\epsilon''^{\text{Refl.}}_{TF}(\nu_{RB1/TF}) - \epsilon''_{RB1}(\nu_{RB1/TF})}{\nu_{RB1/TF} - \nu_{CF2}}\right) \tag{7.14}$$

$$\sigma(\theta) = \frac{\sqrt{\sigma(\epsilon''^{\text{Refl.}}_{TF}(\nu_{RB1/TF}))^2 + \sigma(\epsilon''_{RB1}(\nu_{RB1/TF}))^2}}{\nu_{RB1/TF} - \nu_{CF2}} \times \frac{1}{\left(\frac{\epsilon''^{\text{Refl.}}_{TF}(\nu_{RB1/TF}) - \epsilon''_{RB1}(\nu_{RB1/TF})}{\nu_{RB1/TF} - \nu_{CF2}}\right)^2 + 1} \tag{7.15}$$

$$\sigma(\nu_\theta) = \left[\left(\nu_{CF2\rightarrow 0}\sigma(\theta)sin(\theta)\right)^2 + \left(\epsilon''^{\text{Refl.}}_{TF}sin(\theta)\sqrt{\left(\frac{\sigma(\epsilon''^{\text{Refl.}}_{TF})}{\epsilon''^{\text{Refl.}}_{TF}}\right)^2 + \left(\frac{\sigma(\theta)cos(\theta)}{sin(\theta)}\right)^2}\right)^2\right]^{\frac{1}{2}} \tag{7.16}$$

$$\sigma(\epsilon_\theta) = \left[\left(\nu_{CF2\rightarrow 0}\sigma(\theta)cos(\theta)\right)^2 + \left(\epsilon_{TF}^{\prime\prime\text{Refl.}}cos(\theta)\sqrt{\left(\frac{\sigma(\epsilon_{TF}^{\prime\prime\text{Refl.}})}{\epsilon_{TF}^{\prime\prime\text{Refl.}}}\right)^2 + \left(\frac{\sigma(\theta)sin(\theta)}{cos(\theta)}\right)^2}\right)^2\right]^{\frac{1}{2}} \quad (7.17)$$

where $\nu_{RB1/TF}$ is the wavenumber at the boundary between the RB1 and TF zones; and the other variables are as previously defined.

iii. Finally, this then needs to be shifted back into the appropriate position, and uncertainties propagated once again (Equations 7.18 and 7.19).

$$\epsilon_{TF}^{\prime\prime ReRo}(\nu_{0\rightarrow CF2}) = \epsilon_\theta + \epsilon_{TF}^{\prime\prime\text{Refl.}}(\nu_{CF2}) \quad (7.18)$$

$$\sigma(\epsilon_{TF}^{\prime\prime ReRo}(\nu_{0\rightarrow CF2})) = \sqrt{\sigma(\epsilon_\theta)^2 + \sigma(\epsilon_{TF}^{\prime\prime\text{Refl.}}(\nu_{CF2}))^2} \quad (7.19)$$

where $\epsilon_{TF}^{\prime\prime ReRo}(\nu_{0\rightarrow CF2})$ is the reflected, rotated and shifted emissivity in the TF zone (i.e., the final emissivity coordinate of the coarsified TF zone); and the wavenumber coordinates are shifted via $\nu_{0\rightarrow CF2} = \nu_\theta + \nu_{CF2}$, with uncertainty $\sigma(\nu_{0\rightarrow CF2}) = \sigma(\nu_\theta)$.

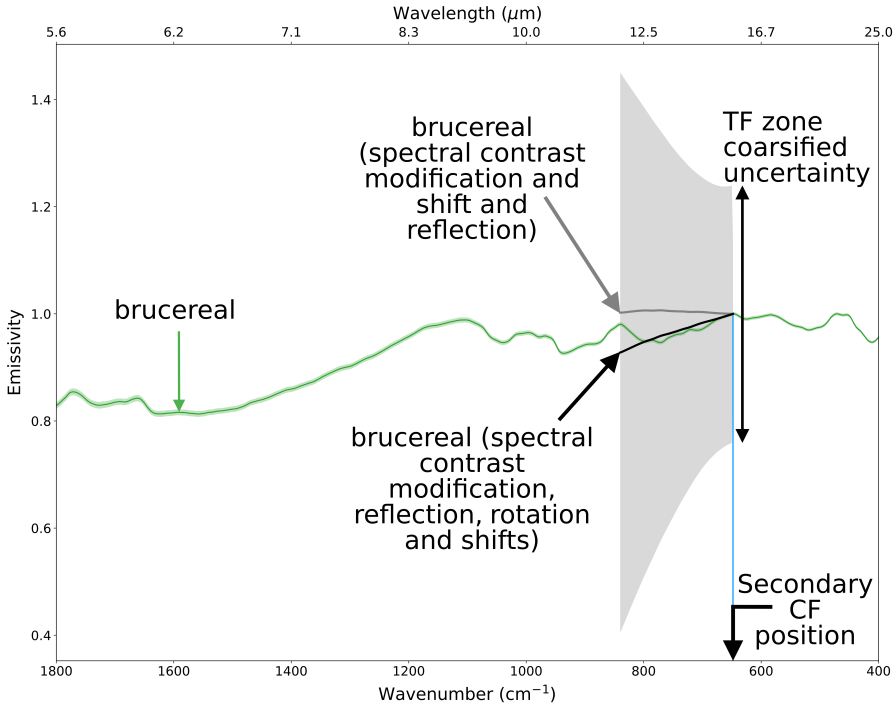


Figure 7.10: Diagram showing the result from step 4b of the coarsification process on *brucereal*. Note: another change in axis scale to contain the extent of the propagated uncertainties. (Data from Donaldson Hanna et al. 2019).

5. **RB2 Zone Modification (Figure 7.11):** Increase spectral contrast and shift in the same manner as for RB1 zone, following Equations 7.5 to 7.8 (Step 3) above.

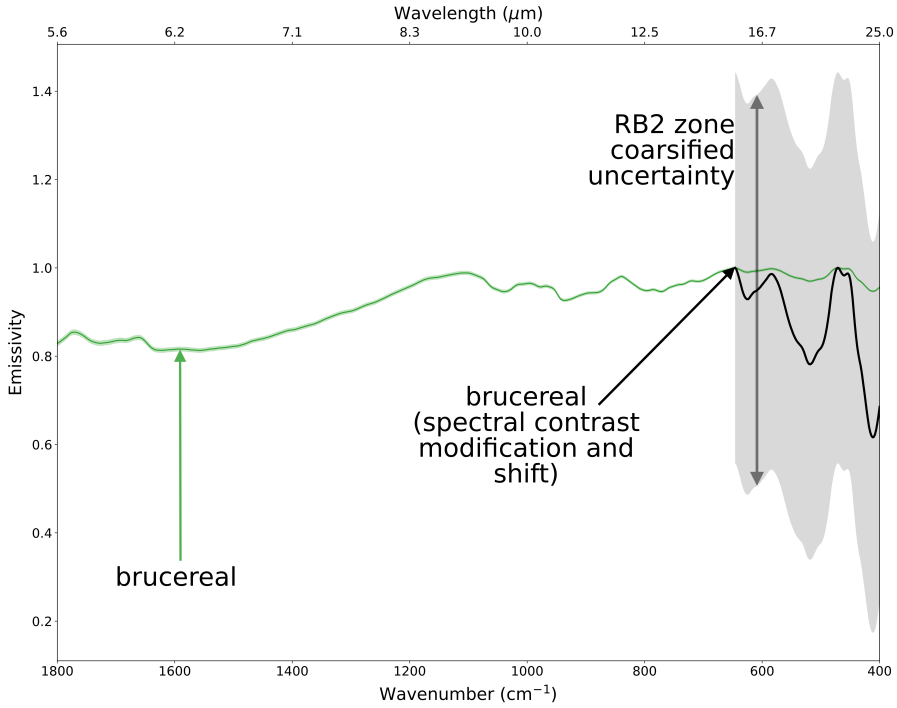


Figure 7.11: Diagram showing step 5 of the coarsification process on *brucereal*. Note: another change in axis scale to contain the extent of the propagated uncertainties. (Data from Donaldson Hanna et al. 2019).

Although somewhat experimental, the concept of transforming a fine grained spectrum to appear as it would coarse grained (named here as coarsification) retains links to the underlying scattering physics as observed via laboratory data. Non-linear scattering effects caused by a decrease in grain size are well known, and clearly observed in spectral morphology changes; whereby spectral contrast changes according to spectral region but the feature positions largely remain unchanged as these are defined by crystal structure etc. The coarsification approach here was a preliminary attempt to parameterise non-linear mixing based on empirical observations of spectral morphology changes with decreasing grain size. To test coarsification, the Bruce mixture was coarsified (as illustrated in Figures 7.5 to 7.11), shown in full in Figure 7.12 (note there are only changes in spectral contrast, with

spectral feature positions unchanged). The coarsified Bruce, *brucerealmod* (meaning the modified *brucereal* spectrum), was unmixed with the linear mixing model using the `WLS_ASC_ILR()`, `OptEst_ASC_ILR()`, and `MCMC()` algorithms (presented in Section 7.3) to see if there were any improvements on the original results outlined in Chapters 5 and 6.

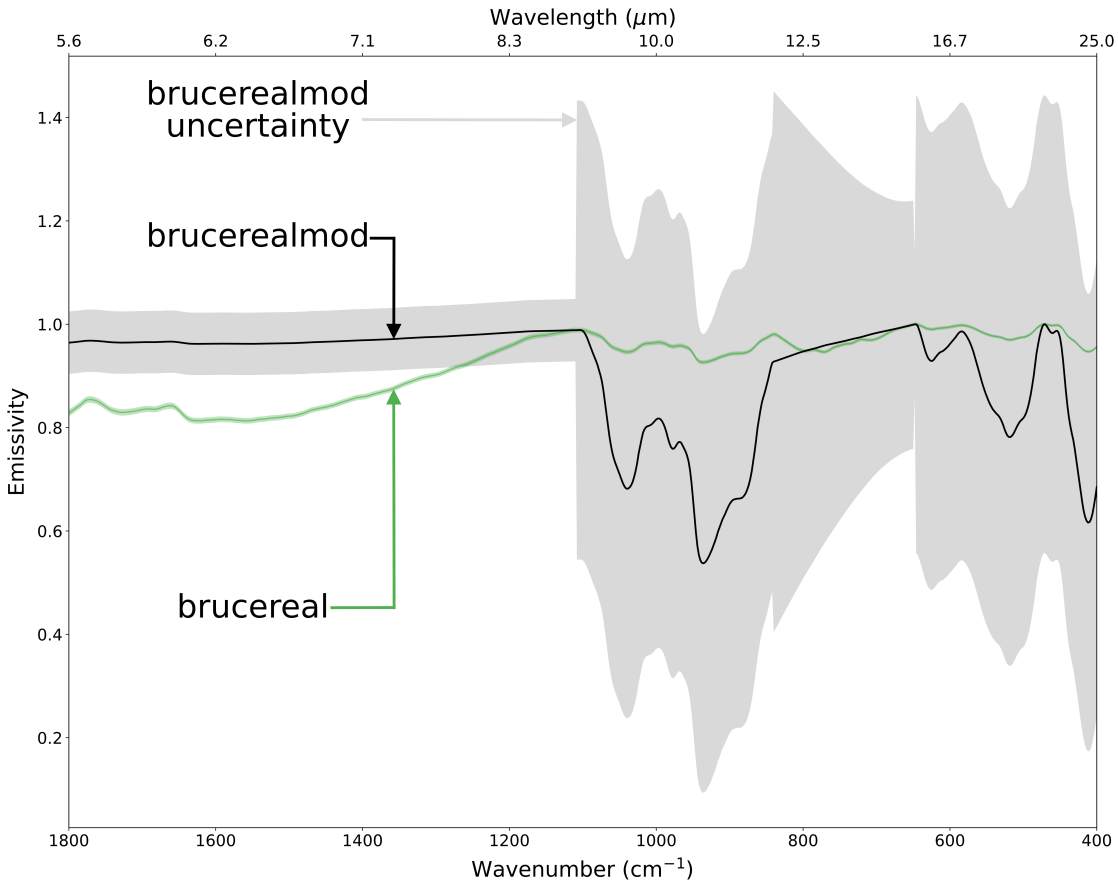


Figure 7.12: Full coarsified Bruce (*brucerealmod*) plotted with the original Bruce (*brucereal*; data from Donaldson Hanna et al. 2019).

7.3 Preliminary Results

7.3.1 Data Used

Following on from the unmixing algorithms investigation (Chapters 4 to 6), Bruce was selected as the sample to be coarsified as it was the mixture with the most complete knowledge, making it ideal for use in the development and testing of novel techniques. However, in order to coarsify Bruce, appropriate BB abundances

to modify spectral contrast appropriately in each spectral zone (as indicated in Figure 7.5) needed to be determined via spectral morphology investigation. For this, measurements of the same end-member samples at a selection of different grain sizes, ranging from coarse to fine, with several size fractions in between, were required. In my review of available data[7], I found suitable datasets difficult to come by, as many studies (where these data originated) only considered a single 'coarse' and single 'fine' size fraction, each of which actually covered a large range of grain sizes; and therefore would give just two data points, which is insufficient for pulling out a meaningful trend. It was also important for the different size fractions to come from the same sample (or very close), as even for an end-member labelled only as an 'olivine', this could be sufficiently different from another 'olivine' mineral from a different point in the same solid solution series, as covered in the degeneracy discussion of Section 2.2.3 (see Figure 2.5).

To ensure the data requirements for the spectral morphology study were met, it would have been ideal to take the relevant measurements myself. However, due to time constraints, and the Covid-19 pandemic limiting access to the laboratory, it was unfeasible to do so, therefore making it necessary to turn to existing data from a variety of sources (detailed in Table 7.1), whilst keeping in mind any caveats associated with this. A potential future investigation to collect an extensive set of data for spectral morphology studies is discussed further in Chapter 8.

In Shirley and Glotch 2019, effects on mid-IR spectra due to grain size were investigated for applications to lunar data (as discussed in Section 7.2.1). For my spectral morphology study, I used data from their work for different size fractions of enstatite, albite, augite and olivine (specifically, forsterite Fo_{88}) – the end-members most relevant to the Bruce and Glenn samples out of those available; full details of these samples are outlined in Table 7.1 along with information on additional olivine samples data collated from USGS (Fo_{89}; Kokaly et al. 2017) and provided by Dr. Kerri Donaldson Hanna and her student Vanessa Lowry (San Carlos

[7]This data search used the same online spectral libraries as mentioned in Chapter 4 (USGS and RELAB), as well as the ASU spectral library (Christensen, Bandfield, et al. 2000).

Olivine, usually $Fo_{\sim 90}$). Olivine was selected as the first mineral to study using additional data to those from Shirley and Glotch 2019, due to its wide availability through online spectral libraries at a variety of size fractions. Olivine is also a common end-member between the Bruce and Glenn samples, with a relatively large abundance in both (70% in Bruce and 11.3% in Glenn/Murchison), and is relevant for studies of meteorites and asteroids.

Although the Shirley and Glotch 2019 data were appropriate (i.e., spectra of the same sample at more than two different size fractions), the level of noise (likely due to atmospheric contamination) for some of the end-members made it difficult to calculate the CF roll-off gradient and TF depth appropriately, as per the methods described in Section 7.2.2. Thus these data required smoothing, which was done via a smoothing function written in Python based on Matlab's default `smooth` function – a standard boxcar average. An example of the raw spectrum (pre-smoothing) and smoothed spectrum for the same data is shown in Figure 7.13.

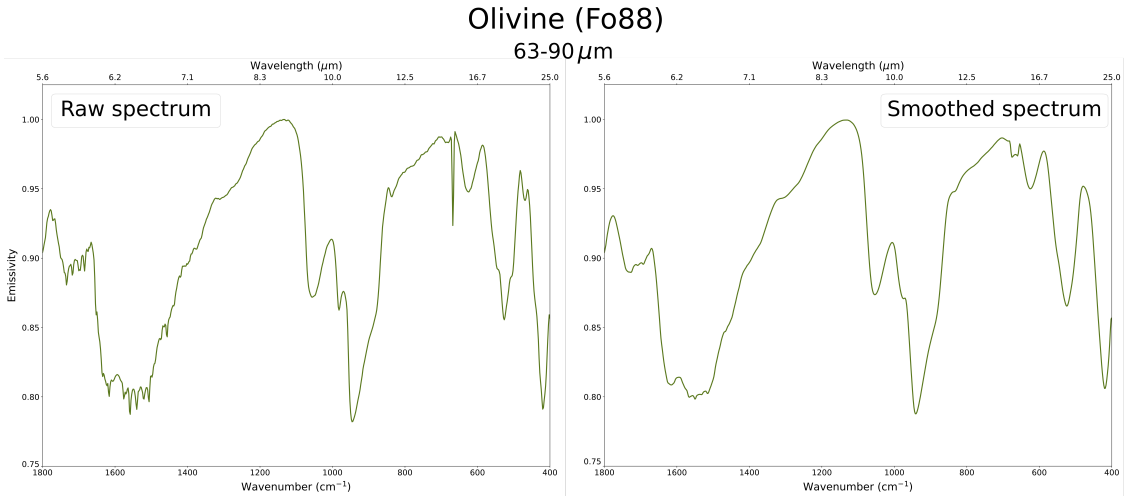


Figure 7.13: Before and after spectral smoothing with a boxcar average for the $63-90\mu$m size fraction of olivine, Fo_{88} (data from Shirley and Glotch 2019).

7.3.2 Spectral Morphology Study Results

The spectral morphology study was first carried out on the enstatite ($Wo_1En_{70}Fs_{29}$), albite (An_{24}), augite ($Wo_{50}En_{34}Fs_{16}$) and olivine (Fo_{88}) data of Shirley and Glotch

Table 7.1: Information on samples used for the spectral morphology study.

Mineral/End-member	**Size Fractions Available (μm)**	**Notes**	**Source of Data**
Augite ($Wo_{50}En_{34}Fs_{16}$)	<32 32-63 63-90 90-125 125-250	Natural terrestrial sample	Shirley and Glotch 2019
Enstatite ($Wo_1En_{70}Fs_{29}$)	<32 32-63 63-90 90-125 125-250 >250	Natural terrestrial sample	Shirley and Glotch 2019
Albite (An_{24})	<32 32-63 63-90 90-125 125-250 >250	Natural terrestrial sample	Shirley and Glotch 2019
Olivine (Fo_{88})	<32 32-63 63-90 90-125 125-250	Natural terrestrial sample	Shirley and Glotch 2019
Olivine (Fo_{89})	<30 <60 60-104 104-150 150-250	Sample name: GDS70.a/b/c/d/eFo89 NIC4bbbRREF Measured in reflectance. GDS70.e = <30μm GDS70.d = <60μm GDS70.c = 60-104μm with median grain size of 70μm GDS70.b = 104-150μm with median grain size of 115μm GDS70.a = 150-250μm with median grain size of 165μm	USGS (Kokaly et al. 2017)
Olivine (San Carlos, usually $Fo_{\sim 90}$)	<25 25-45 25-32 32-45	The sample was only described as being San Carlos olivine (which usually is $Fo_{\sim 90}$)	Kerri Donaldson Hanna and Vanessa Lowry (private correspondence)

2019, the plots of which are shown in Figure 7.14, showing how the CF roll-off gradient and TF depth values changed with grain size. In the absence of grain size distribution information, here the grain size coordinates used were simply the mid-points of each range of sizes, and the x-direction error bars set to span the range (e.g., $47.5 \pm 15.5\mu$m was used for the $32 - 63\mu$m size fraction). There were also error bars in the y-direction (i.e., on the CF roll-off gradient and TF depth coordinates), however these were generally small at this scale.

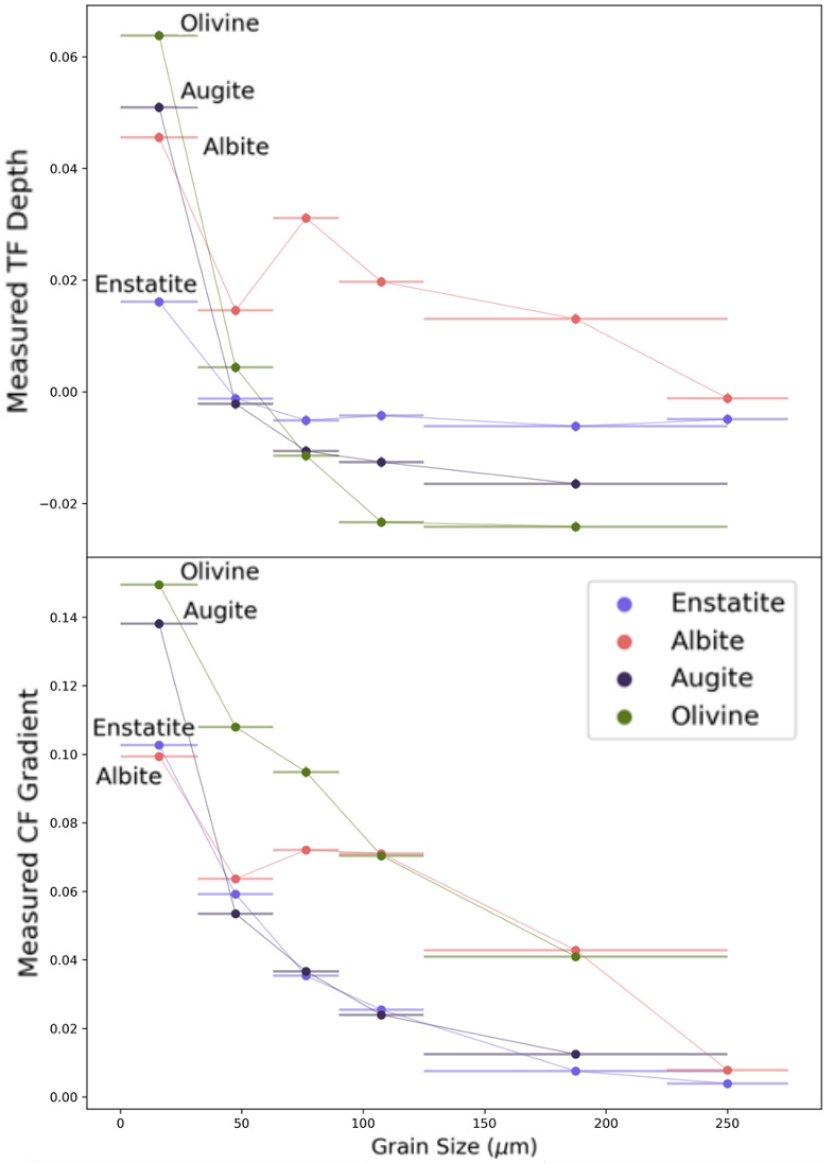


Figure 7.14: Spectral morphology plots of measured TF depth, and measured CF roll-off gradient, vs grain size for enstatite, albite, augite and olivine (data from Shirley and Glotch 2019).

In an attempt to observe a more universal trend across different end-members, Figure 7.14 was also considered in a relative sense; where, for each end-member, the CF roll-off gradient and TF depth were both set to 1 for the smallest size fraction (where the measured values for these were the greatest), and the values for these at the remaining size fractions scaled relative to this (Figure 7.15).

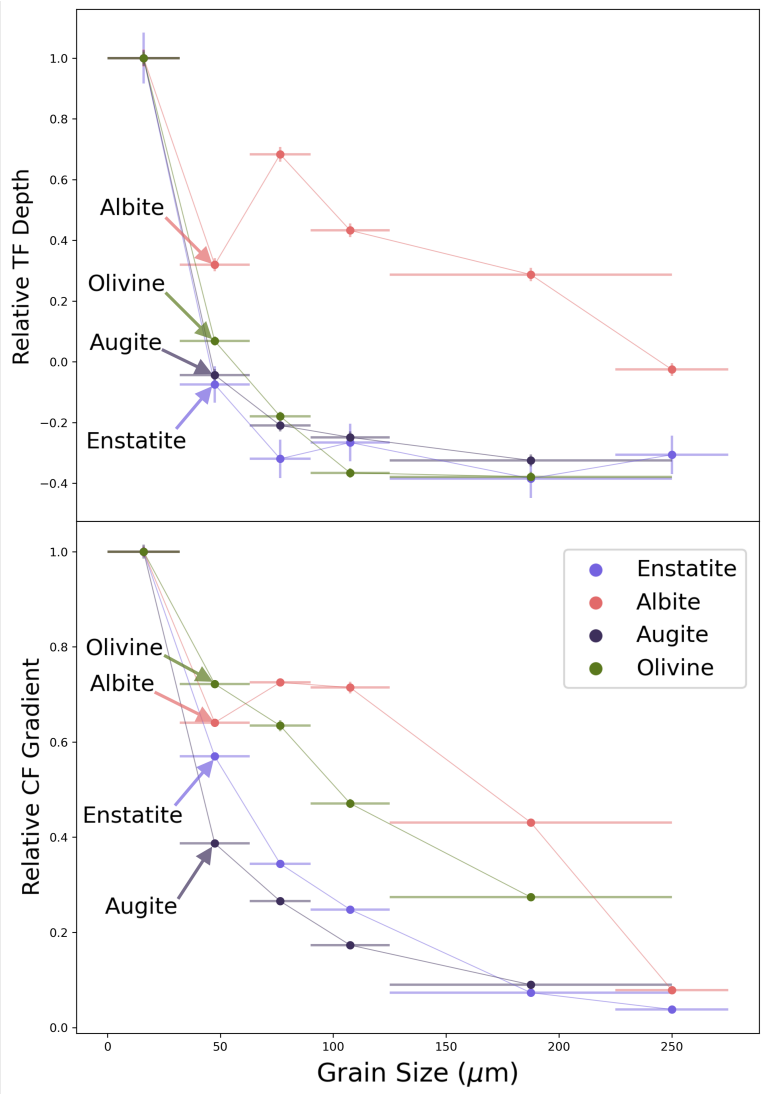


Figure 7.15: Spectral morphology plots of relative TF depth, and relative CF roll-off gradient, vs grain size for enstatite, albite, augite and olivine (data from Shirley and Glotch 2019).

The differences between the absolute and relative versions of these spectral

morphology plots were particularly interesting, where there appeared to be more commonality (i.e., smaller spread) across end-members seen in the relative TF depth (Figure 7.15) and measured CF roll-off gradient (Figure 7.14) plots compared to their counterparts (the measured TF depth, Figure 7.14, and relative CF roll-off gradient, Figure 7.15, respectively). From this discrepancy it was evident that more data were needed to fill in the size fraction gaps in order to see a trend; so focusing first on olivine (as justified in Section 7.3.1), the spectral morphology investigation was repeated using additional olivine data (see Table 7.1), shown in Figure 7.16.

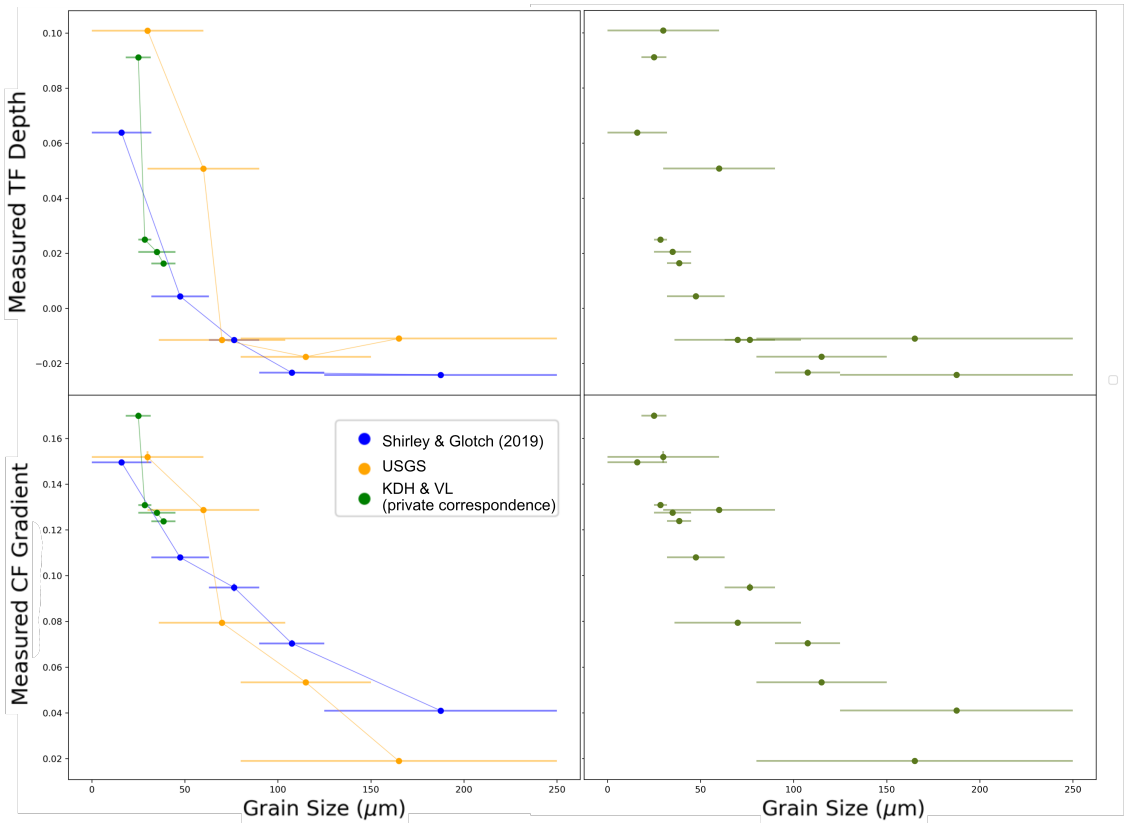


Figure 7.16: Spectral morphology plots of measured TF depth, and measured CF roll-off gradient, vs grain size for the laboratory measured olivines from different sources (sample details in Table 7.1). The left hand side shows them as separate datasets, and the right hand side shows them all together in an effective olivine spectral morphology plot.

From Figure 7.16 there appeared to be some kind of trend emerging between spectral morphology and grain size. However, due to the large scale of uncertainty in the x-axis and still relatively few data points, a number of different functions could potentially fit: such as exponential decay or just a straight line; making

future research necessary to explore this relationship more deeply (as discussed in Chapter 8).

Although an exact trend had not yet been determined, an attempt to test the coarsification method was carried out in order to get an indication of whether this method has potential, whilst noting the many caveats. Thus, the results and discussion of unmixing the coarsified Bruce (*brucerealmod*) using linear mixing in `WLS_ASC_ILR()`, `OptEst_ASC_ILR()` and `MCMC()`, compared to the conclusions from Chapters 5 and 6, are presented in the following subsections.

7.3.3 Pre-Unmixing: *brucerealmod* and its Coarse Spectral Libraries

In the absence of a well-defined trend, there was some trial and error to experiment with appropriate BB abundance values for each zone. These values were derived from the olivine spectral morphology study (Figure 7.16) as Bruce was 70% olivine, so basing the coarsification on olivine values was deemed a suitable estimation at this stage, but was perhaps the first notable caveat. The BB abundance values (x_{BB}) used were simply based on the range of the measured CF roll-off gradients and TF depths, following Equations 7.20 to 7.25:

$$x_{BB}^{CF} = 1 - (\text{CF gradient}_{\max} - \text{CF gradient}_{\min}) \tag{7.20}$$

$$\sigma(x_{BB}^{CF}) = \sqrt{\sigma(\text{CF gradient}_{\max})^2 + \sigma(\text{CF gradient}_{\min})^2} \tag{7.21}$$

$$x_{BB}^{TF} = 1 - (\text{TF depth}_{\max} - \text{TF depth}_{\min}) \tag{7.22}$$

$$\sigma(x_{BB}^{TF}) = \sqrt{\sigma(\text{TF depth}_{\max})^2 + \sigma(\text{TF depth}_{\min})^2} \tag{7.23}$$

$$\begin{aligned} x_{BB}^{RB} &= 1 - \frac{(\text{CF gradient}_{\max} - \text{CF gradient}_{\min}) + (\text{TF depth}_{\max} - \text{TF depth}_{\min})}{2} \\ &= \frac{-x_{BB}^{CF} - x_{BB}^{TF}}{2} \end{aligned} \tag{7.24}$$

$$\sigma(x_{BB}^{RB}) = \frac{1}{2}\sqrt{\sigma(x_{BB}^{CF})^2 + \sigma(x_{BB}^{TF})^2} \tag{7.25}$$

where CF gradient$_{max}$, CF gradient$_{min}$, TF depth$_{max}$ and TF depth$_{min}$ are the maximum and minimum values of the CF roll-off gradient and TF depth found for olivine in Figure 7.16, respectively.

Figures 7.5 to 7.11 show the spectral contrast modifications to *brucereal*, following each of the coarsification steps outlined in Section 7.2.2. Although the *brucerealmod* spectrum in Figure 7.12 did look somewhat convincing as a coarse spectrum, it was clearly not perfect, especially at the CF zone and TF zone boundaries, and so future work could be in refining this further (see Chapter 8).

7.3.3.1 PCA of 'Coarse' Spectral Libraries

With the spectrum modified to appear coarse, suitable spectral libraries containing coarse end-member spectra were required. For this, the same collection of end-members were used as the *minimal*, *expanded* and *extensive* spectral libraries for the main Bruce unmixings (shown in Section 5.2); however, as the Blind Test suite only contained fine particulate samples, it was necessary to search for appropriate coarse data using online spectral libraries, the details of which are outlined in Table 7.2. Another important caveat here was that it was not possible to find appropriate coarse versions of all the fine spectra from the Blind Test suite, and so the same data as those used for the main unmixings of Chapters 5 and 6 were used here (full details are outlined in Table 7.2).

As before (Section 5.2), PCA was conducted on each of the *minimal*, *expanded* and *extensive* coarse spectral libraries (Figures 7.17 to 7.19):

***minimal* spectral library:**

The *minimal* spectral library PCA plot showed no real clustering, with end-members more evenly distributed across the axes than in the original fine grained version (Figure 7.17). The end-members closest together on the PC1 axis were augite with enstatite (both pyroxenes), and troilite with FeNiMetalSub (both had relatively featureless spectra); which was as expected, and were the same pairings as seen for the fine *minimal* PCA plot (Figure 7.17).

Table 7.2: Sample information on end-members used for the coarse spectral libraries.

Mineral Grouping	End-member	Sample ID	Measurement Info.	Grain Size	Notes	Source
Pyroxene	Augite	HS-119.4B, BUR-620, NMNH-119197	Nicolet Nexus 670 FTIR (emission)	Coarse particulate	Overall end-member spectrum is the mean of spectra from each sample listed in Sample ID column	ASU (Christensen, Bandfield, et al. 2000)
	Enstatite	HS-9.4B, DSM-ENS01, NMNH-38833, NMNH-R14440, NMNH-34669, NMNH-82436, WAR-2889				
Olivine	Olivine (forsterite)	AZ-01 (San Carlos)				
Calcite	Calcite	C9, C10, C12, C8, C22, C40, C27, C6, C2		Hand sample	Overall end-member spectrum is the mean of spectra from each sample listed in Sample ID column	
Phyllosilicate	Saponite	Saponite MINUN-29		Coarse particulate Hand sample		
	Cronstedtite	M354 NIC4bb	RREF with Nicolet FTIR Spectrometer (biconical reflectance)	Unknown	Reflectance measurements converted to emissivity with E=1-R	USGS (Kokaly et al. 2017)
	Lizardite	NMNHR4687.b NIC4aa		150-250μm		
Spinel	Magnetite	WAR-0384	Nicolet Nexus 670 FTIR (emiss.)	Coarse particulate		ASU (Christensen, Bandfield, et al. 2000)
	Spinel	Unknown	University of Oxford Planetary Spectroscopy Facility (emission)	<45μm	Same as Table 4.1	Kerri Donaldson Hanna (provided with Blind Test data)
Pyrrhotite	Troilite	USNM 5914 (Mundrabilla)		<38μm		Blind Test suite (Donaldson Hanna et al. 2019)
	Pyrrhotite	HS269.3B NIC4ccu	RREF with Nicolet FTIR Spectrometer (biconical reflectance)	74-250μm	Reflectance measurements converted to emissivity with E=1-R	USGS (Kokaly et al. 2017)
Feldspar/ Plagioclase	Albite	WAR-0235 (Amelia)	Nicolet Nexus 670 FTIR (emission)	Coarse particulate		ASU (Christensen, Bandfield, et al. 2000)
	Anorthite	BUR-340				
Gypsum	Gypsum	HS333.3B Selenite NIC4aaa	RREF with Nicolet FTIR Spectrometer (biconical reflectance)	75-250μm	Same as Table 4.1	USGS (Kokaly et al. 2017)
Other	Amorphous Mg	Unknown	Moonbox (emission)	Unknown		Kerri Donaldson Hanna (private correspondence)
	Amorphous Fe					
	Murchison IOM	OG-CMA-003_BKR1OG003	BD-VNIR + BCF-FTIR2 (refl.)	90-106μm		RELAB (see Table 4.1 for citation)
	FeNiMetalSub	N/A	Straight line at E = 0.999	N/A		N/A
	BB		Straight line at E = 1.0			

Another similarity with the Bruce fine grained *minimal* library (Figure 7.17) was that the most distant end-members were olivine and FeNiMetalSub, due to their large difference in spectral contrast. The explained variance ratio for the coarse grained *minimal* library was 76.56%, suggesting that these interpretations were reasonable, but there may still have been some nuance missing with the absence of more axes.

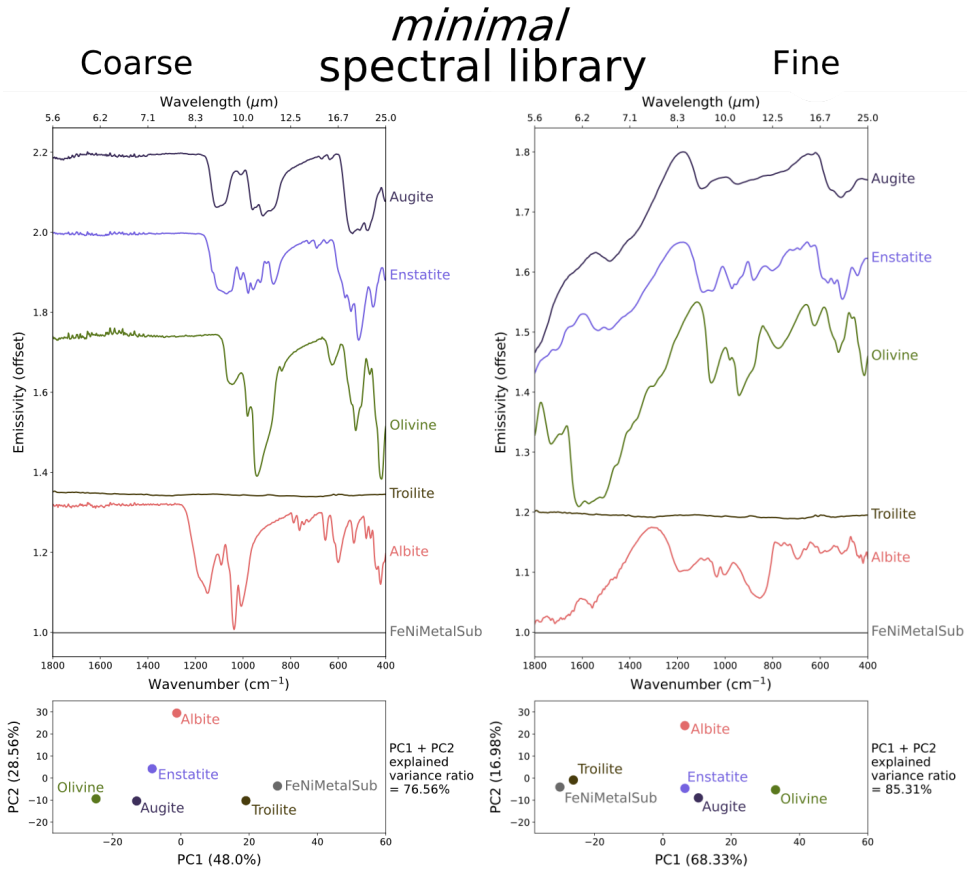


Figure 7.17: *minimal* spectral library with spectra from coarse grained end-members (left), and from fine grained end-members (right; same as from Figure 5.3, repeated here to aid with comparisons).

expanded spectral library:

The Bruce *expanded* spectral library using coarse grained end-members appeared to display more clustering in PC1-PC2 space than was seen with the original fine grained *expanded* spectral library (Figure 7.18). However, similarities were the BB, FeNiMetalSub, troilite cluster, and amorphous Fe and calcite being very distant from the others. Additional clusters seen with the coarse *expanded* library were albite

with olivine, where enstatite and augite were somewhat tenuous additional members, and gypsum with lizardite. However, it was important to note here that the gypsum end-member was the same as used in the original fine spectral libraries due to being $75 - 250\mu$m size fraction. On a retrospective closer inspection, there were some fine grained signatures in the gypsum spectrum (mostly in the CF roll-off; e.g., Figure 7.18), and so the use of this gypsum in the coarse libraries was a potential source of error, linked to the caveat mentioned previously[8] of not having a fully suitable dataset (due to being unable to find relevant coarse grained substitutes).

It was possible that the increased clustering apparent here (due to greater similarities across the coarse spectral library compared to the original fine version) could be due to the major morphological differences observed between fine and coarse spectra – for coarse grained samples, the CF roll-off region was very flat (i.e., horizontal) and featureless, whereas fine grained spectra displayed much more variation in this region (including a clear slope) that led to greater differences across the spectral library.

The explained variance ratio for the coarse *expanded* spectral library at 64.13% similarly implied that the above interpretations were reasonable, but that additional context was lost by only considering PC1 and PC2.

***extensive* spectral library:**

Finally, the PCA plot for the *extensive* coarse spectral library displayed a lot of clustering; but perhaps not quite as much as for the fine *extensive* spectral library (Figure 7.19). Again, gypsum had the same caveat as mentioned above for the *expanded* spectral library, however here this caveat also extended to spinel, amorphous Fe and amorphous Mg, as suitable coarse spectra for these could not be found, and so these were also the same as used in the fine spectral libraries. The explained variance ratio for the coarse grained *extensive* library being 67.83% again suggested that some nuance may be missing.

[8]Gypsum caveat mentioned at the start of Section 7.3.3.1.

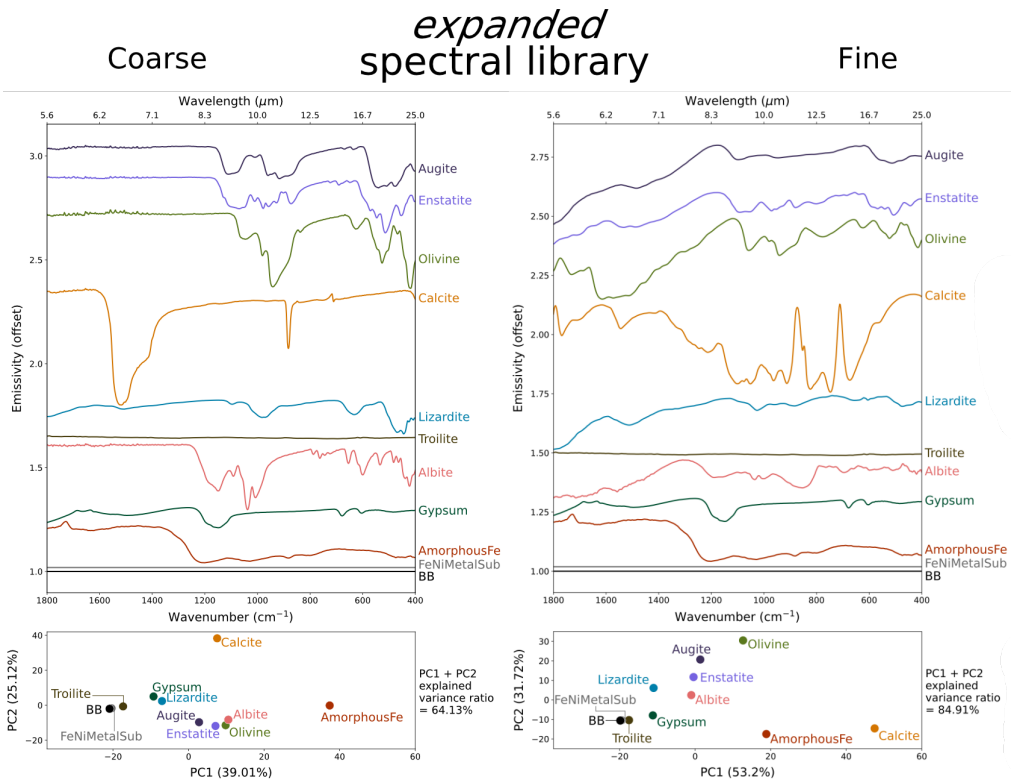


Figure 7.18: *expanded* spectral library with spectra from coarse grained end-members (left), and from fine grained end-members (right; same as from Figure 5.4, repeated here to aid with comparisons).

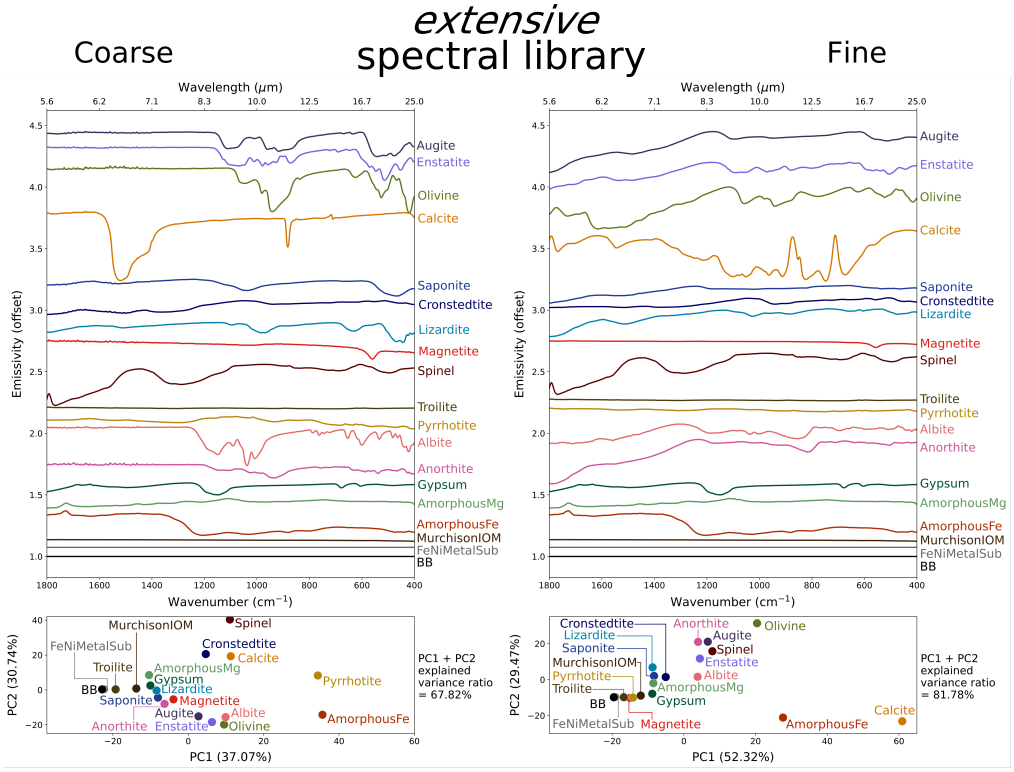


Figure 7.19: *extensive* spectral library with spectra from coarse grained end-members (left), and from fine grained end-members (right; same as from Figure 5.5, repeated here to aid with comparisons).

7.3.4 WLS_ASC_ILR()

7.3.4.1 *brucerealmodmin*

The *brucerealmodmin* WLS_ASC_ILR() unmixing retrieved only augite and olivine, resulting in a poor fit (particularly in the RB1 zone: $1100 - 840\text{cm}^{-1}$; Figure 7.20), with most features present but slightly off-set (by $\sim 9.0\text{cm}^{-1}$) from *brucerealmod*. The residuals appeared close to the zero line (within ± 0.01) around the CF ($\sim 1110\text{cm}^{-1}$) and in the TF zone ($840 - 646\text{cm}^{-1}$), but showed large variations outside of these (reaching a maximum of ± 0.19 at 1038cm^{-1} in the RB1 zone); as captured in the RMS= 0.048 (Table B.77). The $\chi^2_{d.o.f} = 0.084$, however, was closer to 1 than many of the main unmixings (Chapters 5 and 6), however it was important to keep in mind that the reduced chi-squared metric takes measurement uncertainties into account (Section 3.3.3), which were large here for *brucerealmod* (of scale $\sim \pm 0.24$ across the entire spectral range; where the scale was significantly larger, $\sim \pm 0.4$, for the RB1, TF, and RB2 zones, with the CF zone scale being $\sim \pm 0.06$; Figure 7.12).

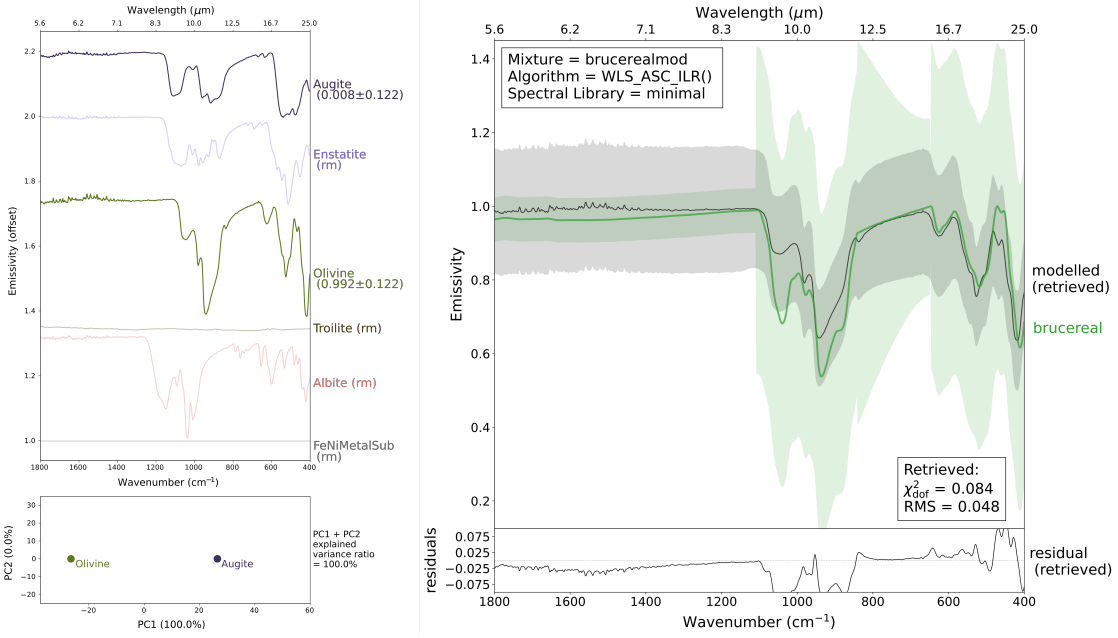


Figure 7.20: *brucerealmodmin* WLS_ASC_ILR() unmixing reduced spectral library with model fit.

7.3.4.2 *brucerealmodexp*

Unmixing *brucerealmodexp* with `WLS_ASC_ILR()` only kept olivine (correctly) and calcite (incorrectly), giving a similar fit with much narrower uncertainty envelope (mean of ±0.02 across the entire spectral range; Figure 7.21) compared to *brucerealmodmin* (mean of ±0.16 across the entire spectral range; Figure 7.20). This was due to them both retrieving a very high abundance of olivine (> 0.9; Table B.78 for *brucerealmodexp* and Table B.77 for *brucerealmodmin*), but even the low abundance of calcite ($0.077 \pm 0.019(24.6\%)$) retrieved for *brucerealmodexp* had clear influence on the modelled spectrum, due to the very strong features present in calcite (e.g., at $\sim$ 1500cm^{-1}; Figure 7.21).

Based on the retrieval quality metrics for the `WLS_ASC_ILR()` algorithm (Table 7.3), the *brucerealmodexp* unmixing had both better abundances (abundance quality = 0.23) and fit (fit quality = 0.05) than the *brucerealexp* unmixing (abundance quality = 1.18, fit quality = −7.65; Table 7.3). Due to the large discrepancy between the scale of measurement uncertainty on the *brucereal* spectrum (mean of ±0.005 across entire spectral range) and the *brucerealmod* spectrum (mean of ±0.24 across entire spectral range), it was difficult to make fair comparisons on their fit qualities, even with the bespoke metric introduced in Section 3.3.3. Therefore, the abundance quality metric perhaps provided a better indication of overall retrieval quality for these comparisons.

7.3.4.3 *brucerealmodext*

The only correct end-member kept by the *brucerealmodext* unmixing was enstatite, whilst lizardite, amorphous Fe and amorphous Mg were incorrectly kept. Overall, the fit was very poor (Figure 7.22), as indicated by the RMS = 0.11 (although the $\chi^2_{d.o.f} = 0.07$ was less suggestive of such a poor fit; Table B.79), and had a very wide uncertainty envelope (mean of ±0.36 across entire spectral range). The spectral features were generally poorly recreated by the model, with the exception of most of the CF roll-off zone where the fit was good, as indicated by residuals close to zero (within ±0.01 between $1754 - 1146$cm^{-1}).

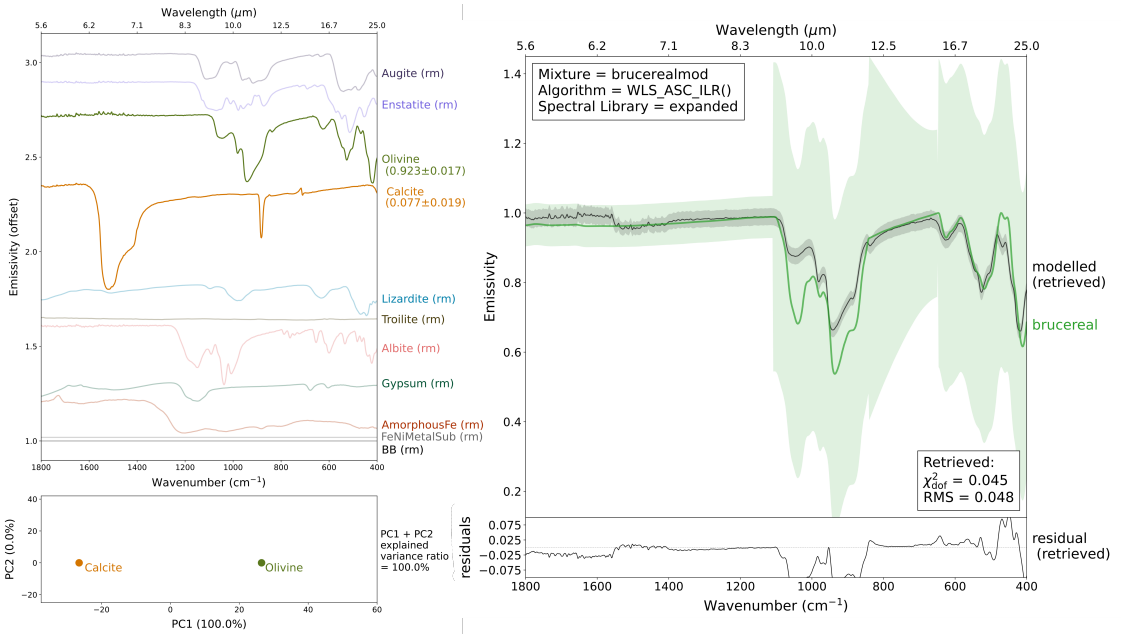


Figure 7.21: *brucerealmodexp* `WLS_ASC_ILR()` unmixing reduced spectral library with model fit.

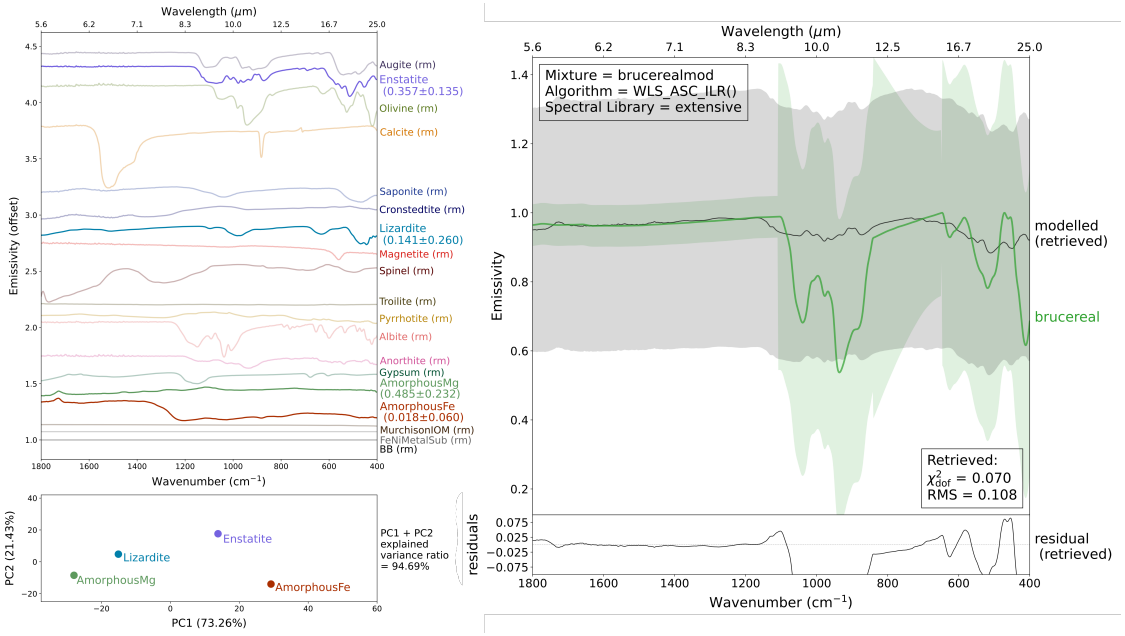


Figure 7.22: *brucerealmodext* `WLS_ASC_ILR()` unmixing reduced spectral library with model fit.

The retrieval quality metrics here (Table 7.3) indicated that the *brucerealmodext* `WLS_ASC_ILR()` unmixing performed better than for *brucerealext*; however the fit quality again had the caveat regarding scales of uncertainty, as the uncertainty envelopes for both the measured and modelled spectra were very narrow for

brucerealext (means across the entire spectral range of ±0.005 for *brucereal*, and ±0.007, ±0.003 for the `WLS_ASC_ILR()` retrieved and BBnorm modelled *brucerealext* spectra, respectively; Figure 5.11), but were very wide for *brucerealmodext* (means of ±0.24 and ±0.36 across the entire spectral range for *brucerealmod* and the `WLS_ASC_ILR()` modelled *brucerealmodext* spectra, respectively; Figure 7.22), thus leading to a numerically 'better' fit (fit quality = 0.10 for *brucerealmodext*, and fit quality = −3.6, −8.8 for *brucerealext* retrieved and BBnorm; Table 7.3).

Table 7.3: Retrieval quality metrics summary table for the `WLS_ASC_ILR()` unmixings of the real and coarsified versions of Bruce (*brucereal* and *brucerealmod*, respectively). Values in square brackets correspond to metrics derived from the blackbody renormalised abundances (BBnorm). Details on these metrics and how to interpret them are covered in Section 3.3.3, where generally the smaller/closer to zero, the better the quality.

	`WLS_ASC_ILR()`	Fit Quality [BBnorm]	Abundance Quality [BBnorm]
Real Bruce	*brucerealmin*	-8.9	1.13
	brucerealexp	-7.65	1.18
	brucerealext	-3.6 [-8.8]	1.33 [0.90]
Coarsified Bruce	*brucerealmodmin*	0.044	3.197
	brucerealmodexp	0.046	0.230
	brucerealmodext	0.101	0.419

Overall, it seemed that with `WLS_ASC_ILR()`, unmixing *brucerealmod* performed marginally better than *brucereal*. But with no clear improvement nor decline, this could further consolidate previous conclusions that the `WLS_ASC_ILR()` algorithm is unsuitable for spectral unmixing. The slight improvement (particularly for abundance quality; Table 7.3), and taking the various caveats into account, however, could suggest that there is potential in coarsification if it can be refined further.

7.3.5 `OptEst_ASC_ILR()`

7.3.5.1 *brucerealmodminP1→P4*

P1 **(Figure 7.23, Table B.80)**:

The *brucerealmodminP1* unmixing using `OptEst_ASC_ILR()` correctly kept all the end-members, but with some retrieved abundances being more accurate to

their prior values (e.g., enstatite was within 12σ of its *P1* prior value, but within 6732σ of its true value; Table B.80) and all having very poor accuracy to their true values ($> |58|\sigma$; Table B.80). The fit generally was also very poor (RMS = 0.09, although again the $\chi^2_{d.o.f} = 0.16$ was less indicative of a poor fit; Table B.80), appearing somewhat better in the TF zone (residuals within ± 0.01 between $767 - 665\text{cm}^{-1}$) in comparison to the RB zones (residuals extending beyond ± 0.05 between $1073 - 847\text{cm}^{-1}$, $551 - 489\text{cm}^{-1}$, and $440 - 400\text{cm}^{-1}$, reaching a maximum of ± 0.33 at 934cm^{-1}; Figure 7.23).

The correlations were all remarkably small ($|0.016|$ on average; Table C.41), with the strongest being -0.047 between albite and FeNiMetalSub. Although the *brucerealminP1* `OptEst_ASC_ILR()` unmixing (Section 6.1.1.2) also had relatively low correlation ($|0.156|$ on average; Table C.3), the significantly weaker scale here for *brucerealmodminP1* could indicate a larger suppressing of correlation (and therefore degeneracy) with apparently coarse spectra, or a greater reliance on priors due to an inaccurate model.

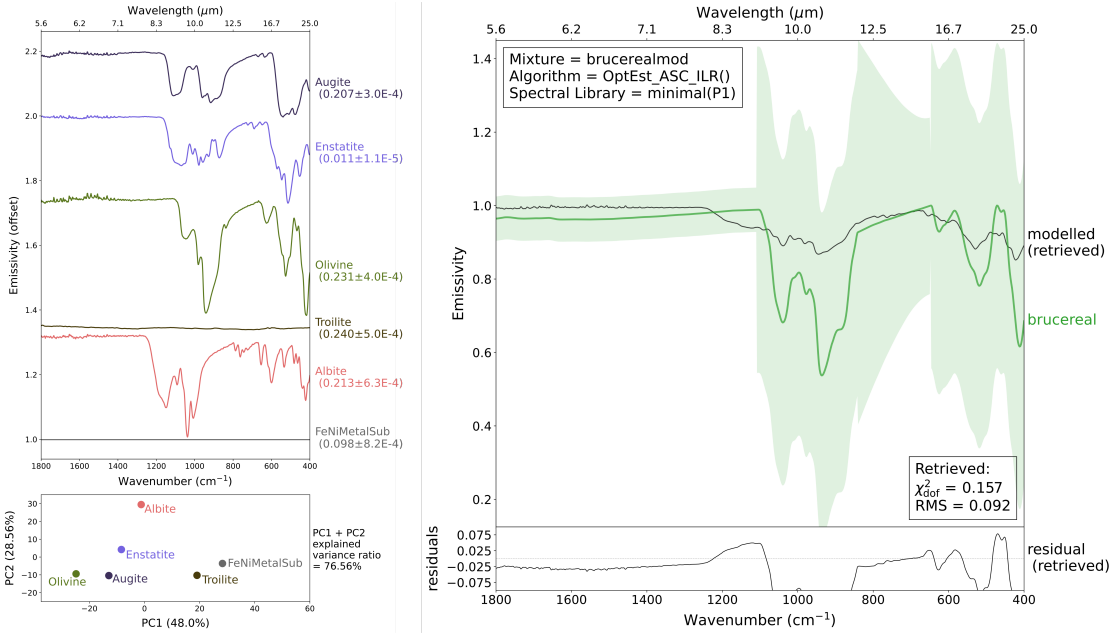


Figure 7.23: *brucerealmodminP1* `OptEst_ASC_ILR()` unmixing reduced spectral library with model fit.

***P2* (Figure 7.24)**:

Unmixing for *brucerealmodminP2* with `OptEst_ASC_ILR()` incorrectly removed troilite, albite and FeNiMetalSub yet gave a decent fit in most regions (i.e., residuals within ± 0.01 between $1234 - 1153\text{cm}^{-1}$, $822 - 665\text{cm}^{-1}$, $632 - 589\text{cm}^{-1}$, and $521 - 500\text{cm}^{-1}$, RMS $= 0.05$, $\chi^2_{d.o.f} = 0.08$), with the exception being the RB1 and RB2 zones: the main issue here appeared to have been in the spectral contrast, as the main features were present in the modelled spectrum but appeared slightly offset, by $\sim 8.6\text{cm}^{-1}$.

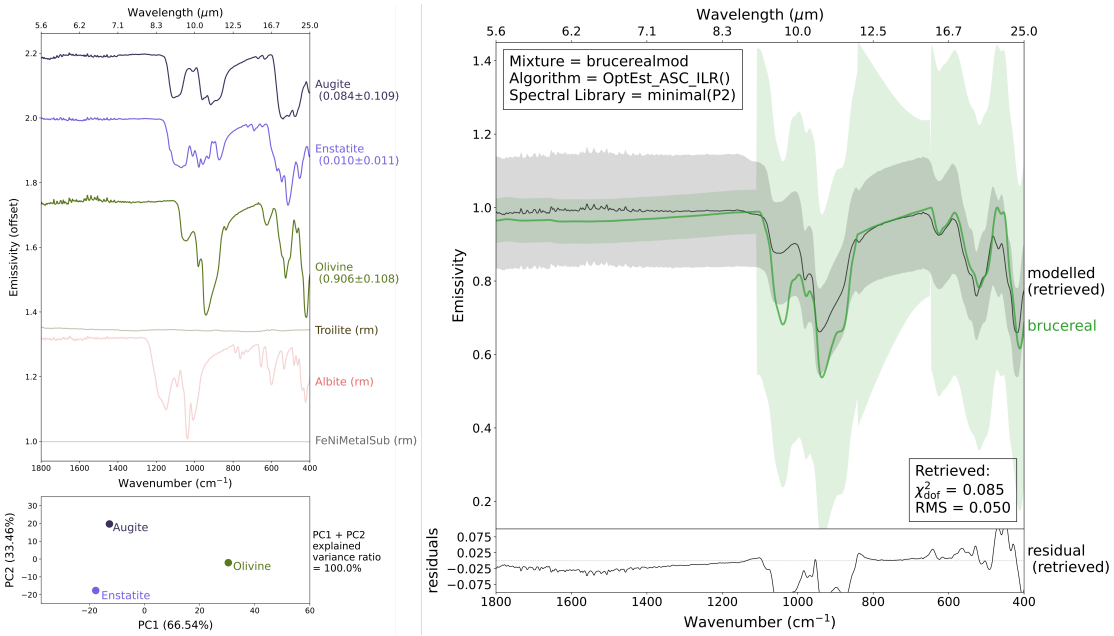


Figure 7.24: *brucerealmodminP2* `OptEst_ASC_ILR()` unmixing reduced spectral library with model fit.

***P3* (Figure 7.25, Table B.81)**:

The *brucerealmodminP3* unmixing retrieved the correct abundances exactly, with very high precisions ($< 0.1\%$) and accuracies (within 0.005σ; Table B.81). Therefore, the modelled spectrum here was essentially what the coarse version of *brucemath* would be expected to look like; with the caveat that the coarse end-members used in the *minimal* spectral library may not have had the exact composition as those originating from the Blind Test suite, in the original Bruce *minimal* spectral library (Figure 7.17).

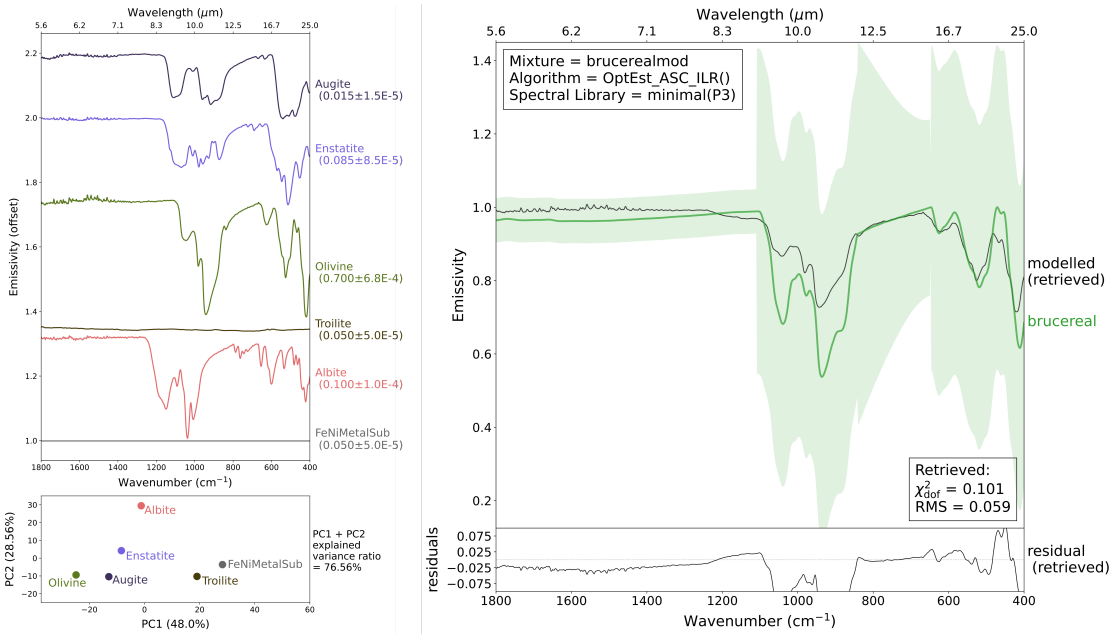


Figure 7.25: *brucerealmodminP3* `OptEst_ASC_ILR()` unmixing reduced spectral library with model fit.

P4 (Figure A.43, Table B.82):

Lastly, the *brucerealmodminP4* `OptEst_ASC_ILR()` unmixing retained all endmembers, retrieving abundances very accurate to their priors (within 0.4σ) and less accurate to the true abundances ($|1.2| - |21|\sigma$), yet giving a fit visually similar to that for *P3* (Figures A.43 for *P4* and 7.25 for *P3*), with RMS = 0.07 and $\chi^2_{d.o.f} = 0.11$ (Table B.82).

Overall, the *brucerealmodminP1→P4* `OptEst_ASC_ILR()` unmixings again showed that tighter priors could act to decrease correlation, where the scale was seemingly even smaller on the whole for coarse compared to fine spectra. However, the large similarities between retrieved values and their priors for the *P3* and *P4* unmixings indicated a higher influence from the priors here than for *brucerealminP3,P4* `OptEst_ASC_ILR()` unmixings (Section 6.1.1.2).

7.3.5.2 *brucerealmodexpP1→P4*

The `OptEst_ASC_ILR()` *brucerealmodexpP1→P4* unmixings displayed a mix of endmember selections, with none of them being identical. For the *brucerealmodexpP4*

`OptEst_ASC_ILR()` unmixing, all the correct end-members were kept and the incorrect ones discarded; with the exception of retaining calcite, which had the lowest retrieved abundance and very large uncertainty ($0.0019 \pm 0.0085(447\%)$; Table B.86). This could suggest that it was easier for `OptEst_ASC_ILR()` to select end-members (compared to `WLS_ASC_ILR()`), but this was still dependant on the nature of the priors. However, with the *P4* version of priors being considered the most realistic (Table 4.4), this showed encouraging potential for the coarsification approach.

A higher reliance on the priors with coarsification was again implied from these *brucerealmodexpP1→P4* `OptEst_ASC_ILR()` unmixings; particularly with the retrieved abundance uncertainties being almost the same as their prior uncertainties for *P1* and *P3* (Tables B.83 and B.85, respectively). This also strengthened a previous observation that the uncertainty on the priors seemed to be what drove prior influence, more so than the prior abundance value itself. The greater reliance on priors here could also be indicative of an unsuitable model, as was seen with the Glenn `OptEst_ASC_ILR()` unmixings in Section 6.1.2.

Overall, based on the abundance quality metric, the *brucerealmodexpP1→P4* unmixings using `OptEst_ASC_ILR()` performed better – with values: 5.58 (*P1*), 2.25 (*P2*), 0.20 (*P3* retrieved), 0.19 (*P3* BBnorm), 2.66 (*P4* retrieved), 0.45 (*P4* BBnorm) – than those of *brucerealexpP1→P4* – values: 5.81 (*P1*), 3.15 (*P2*), 0.31 (*P3* retrieved), 0.29 (*P3* BBnorm), 1.44 (*P4*); Table 7.4 – thus suggesting an improvement with coarsification, however this was not an overwhelming improvement.

7.3.5.3 *brucerealmodextP1→P4*

Similarly to *brucerealmodexpP1→P4* (Section 7.3.5.2), no two of the unmixings with `OptEst_ASC_ILR()` for *brucerealmodextP1→P4* had the same choice of end-members. But, again, the *P4* unmixing retained all the correct end-members, and removed all the incorrect ones; with the exception of calcite (retrieved with abundance $0.0019 \pm 0.0085(447\%)$; Table B.90). Although *P4* had the best choice

of end-members, their accuracies and precisions were somewhat mixed (accuracies between $|0.09| - |23|\sigma$, and precisions between $0.83 - 447\%$; Table B.90).

These *brucerealmodextP1→P4* `OptEst_ASC_ILR()` unmixings again showed improvements on their *brucerealextP1→P4* counterparts, based on both retrieval quality metrics (Table 7.4), but there was perhaps a greater reliance on priors for the coarsified Bruce.

Overall, based on the retrieval quality metrics (Table 7.4), the `OptEst_ASC_ILR()` unmixings of *brucerealmod* seemed to perform better than the *brucereal* equivalents; however, the *brucerealmod* retrievals here were still not all correct. This may have been partly due to the current, preliminary coarsification model, which could potentially be improved with further research.

Table 7.4: Retrieval quality metrics summary table for the `OptEst_ASC_ILR()` unmixings of the real and coarsified versions of Bruce (*brucereal* and *brucerealmod*, respectively). Values in square brackets correspond to metrics derived from the blackbody renormalised abundances (BBnorm). Details on these metrics and how to interpret them are covered in Section 3.3.3, where generally the smaller/closer to zero, the better the quality.

`OptEst_ASC_ILR()`		Fit Quality [BBnorm]				Abundance Quality [BBnorm]			
		P1	*P2*	*P3*	*P4*	*P1*	*P2*	*P3*	*P4*
Real Bruce	*brucerealmin*	-15.6	-8.9	-46.4	-8.9	4.04	1.13	0.12	1.13
	brucerealexp	-33.4	-7.4	-26.8 [-33.9]	-7.6	5.81	3.15	0.31 [0.29]	1.44
	brucerealext	-21.9 [-15.5]	-3.6	-17.0 [-19.4]	-3.6 [-10.3]	1.49 [1.18]	1.33	0.73 [0.68]	66.2 [37.0]
Coarsified Bruce	*brucerealmodmin*	0.077	0.046	0.053	0.059	4.489	1.315	1.73E-06	0.558
	brucerealmodexp	0.077	0.069	0.053 [0.053]	0.064 [0.053]	5.584	2.253	0.200 [0.186]	2.661 [0.452]
	brucerealmodext	0.096 [0.088]	0.054	0.053 [0.053]	0.064 [0.053]	0.815 [0.652]	0.336	0.541 [0.506]	1.478 [0.251]

7.3.6 `MCMC()`

7.3.6.1 *brucerealmodminU→P4*

The *brucerealmodminU* `MCMC()` unmixing gave a poor fit, seen clearly by the large residuals (with a mean of ± 0.07 across the entire spectral range, reaching a maximum of ± 0.18 at 450cm^{-1}; Figure 7.26). However, although the RMS = 0.073 was

indicative of a poor fit, the $\chi^2_{d.o.f} = 0.55$ suggested a relatively good model fit to the *brucerealmod* spectrum, with a value closer to 1 than many of the other unmixings.

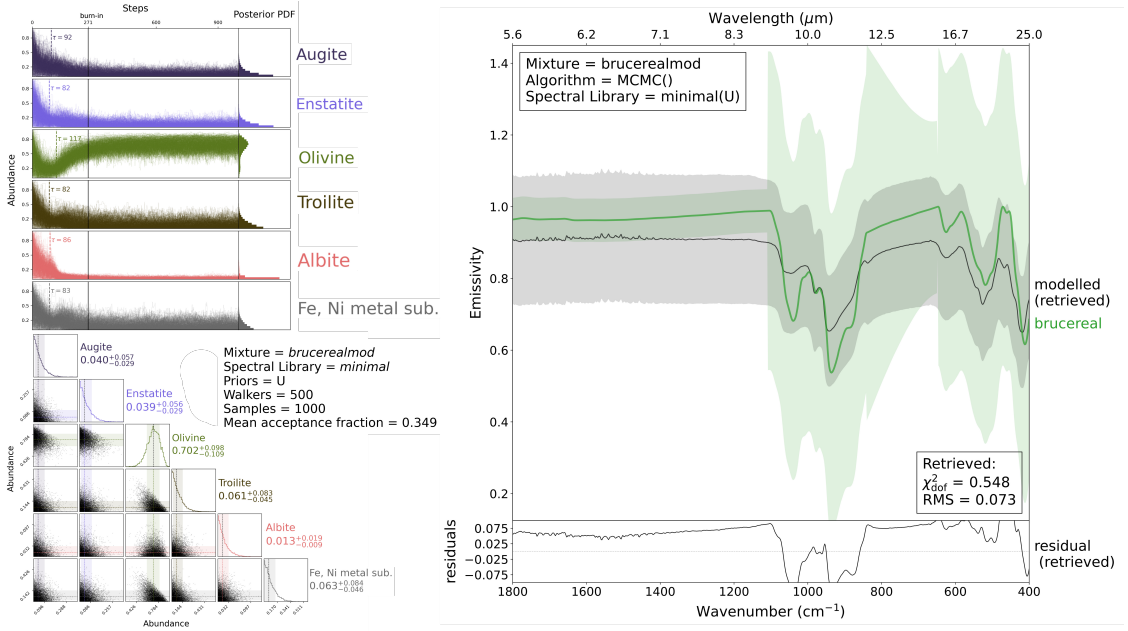


Figure 7.26: *brucerealmodminU* `MCMC()` walkers and corner plots with model fit.

A large difference between the *brucerealmodminU* and *brucerealminU* `MCMC()` unmixings was the degree of correlation – the *brucerealminU* unmixing using `MCMC()` (Section 6.2.1.2) had four highly correlated pairs (-0.74 between augite and olivine, -0.72 between enstatite and troilite, 0.73 between enstatite and FeNiMetalSub, and -0.95 between troilite and FeniMetalSub), whereas for *brucerealmodminU*, there were none (Table C.46). As these unmixings both used the Uniform distribution for the priors, which was almost equivalent to having no priors, it became clear that the weaker correlation seen for *brucerealmodminU* compared to *brucerealminU* with `MCMC()` (and as seen for *brucerealmod* compared to *brucereal* with `OptEst_ASC_ILR()`) was likely due to the coarsification process rather than an effect of the priors.

The issues of lacking the abundance sum constraint in `MCMC()` were already evident in the *brucerealmodminP1* unmixing, as the retrieved abundances were all much more accurate to their priors than to their true values (Table 7.5), and summed to > 1. However, with the *minimal* library, there was no BB end-member to

normalise out and take care of the sum to one constraint. The reduced correlation and seemingly greater reliance on priors for *brucerealmodmin* compared to its equivalent *brucerealmin* unmixings were evident again for the *P1*, *P2*, *P3* and *P4* `MCMC()` unmixings.

From the abundance quality metric, the *brucerealmodminU→P4* `MCMC()` retrieved abundances (Table 7.6) were of comparable quality to those from `WLS_ASC_ILR()` (Table 7.3) and `OptEst_ASC_ILR()` (Table 7.4), which was quite different to the *brucerealmin* main unmixings (Chapters 5 and 6), where the `MCMC()` retrieved abundances were considerably worse than their equivalents from `WLS_ASC_ILR()` and `OptEst_ASC_ILR()` (with the exception of *P3*).

All of the *brucerealmodmin* `MCMC()` unmixings had mean acceptance fractions within the acceptable range of $0.2-0.5$, and their walkers plots across *U→P4* showed convergence by or shortly after the burn-in mark, with some for *brucerealmodmin* seemingly converging closer to their priors than their *brucerealmin* equivalents.

7.3.6.2 *brucerealmodexpU→P4*

The *brucerealmodexpU→P4* unmixings with `MCMC()` were generally of similar quality to those for *brucerealexpU→P4* (Table 7.6). On the whole, the *brucerealmodexpU→P4* `MCMC()` unmixings had visually poor fits (shown by large residuals with means $\sim \pm 0.05$ across the entire spectral range; Figures A.55 to A.58 and 7.27), but due to the scale of uncertainties, the fit quality metric often indicated a good fit (Table 7.6), as the modelled spectrum was fully contained within the *brucerealmod* uncertainty envelope (e.g., Figure 7.27).

For the `MCMC()` unmixings, the retrieved abundances were generally better for *brucerealmodexp* than for *brucerealexp*; with the exception of the *P1* retrieved and BB normalised, and *P2* retrieved and BB normalised abundances, but these had very little difference (Table 7.6).

The general pattern observed in the *brucerealmodexpU→P4* `MCMC()` unmixings was that the tighter priors of *P1* and *P3* led to stronger correlation, with averages

of |0.31| for *P1* (Table C.48) and |0.45| for *P3* (Table C.50), compared to |0.10|, |0.11| and |0.12| for *U*, *P2* and *P4* (Tables C.47, C.49 and C.51, respectively), which was the opposite to the general observations from the `OptEst_ASC_ILR()` *brucerealmod* unmixings (Section 7.3.5), but more consistent with those from the main `MCMC()` unmixings of Section 6.2.1.

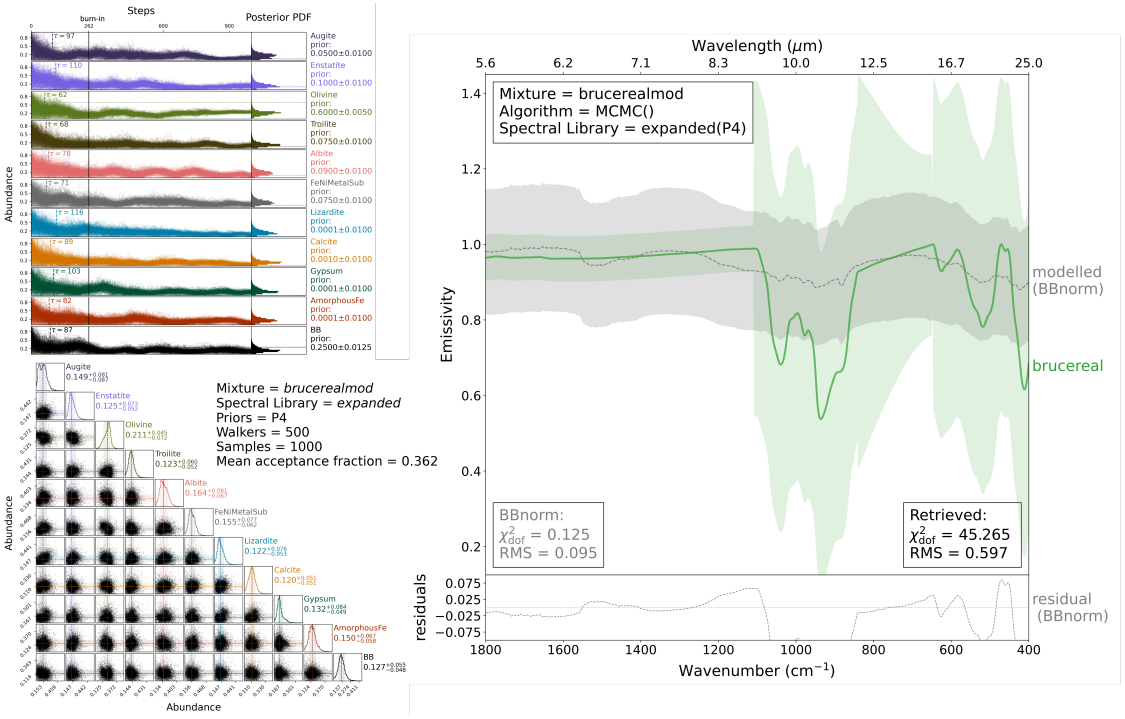


Figure 7.27: *brucerealmodexpP4* `MCMC()` walkers and corner plots with model fit.

7.3.6.3 *brucerealmodextU→P4*

The *brucerealmodextU→P4* `MCMC()` unmixings generally displayed very poor fits, where the mean of the residuals across the entire spectral range was $\sim \pm 0.06$. The residuals showed fairly similar morphologies (e.g., peaks at $\sim 1512\text{cm}^{-1}$ and $\sim 1100\text{cm}^{-1}$, troughs at $\sim 626\text{cm}^{-1}$, and reaching values of $\sim \pm 0.39$ at $\sim 936\text{cm}^{-1}$), indicating that they were struggling in the same ways in the same spectral regions (e.g., Figures A.59 to A.61 and 7.28).

Out of *brucerealmodext* and *brucerealext*, the better fits were from *brucerealmodext*, as indicated by the fit quality metric (Table 7.6); however this was largely

influenced by the scale of uncertainties via the $\chi^2_{d.o.f}$ term. The measurement uncertainty envelopes were very different between *brucereal* (mean of ±0.0045 across the entire spectral range) and *brucerealmod* (mean of ±0.24 across the entire spectral range; e.g., Figure 7.12), due to the propagation of errors through each step of the coarsification process (as outlined in Section 7.2.2). Therefore the abundance quality metric was perhaps more reliable for comparisons between the *brucereal* and *brucerealmod* unmixings.

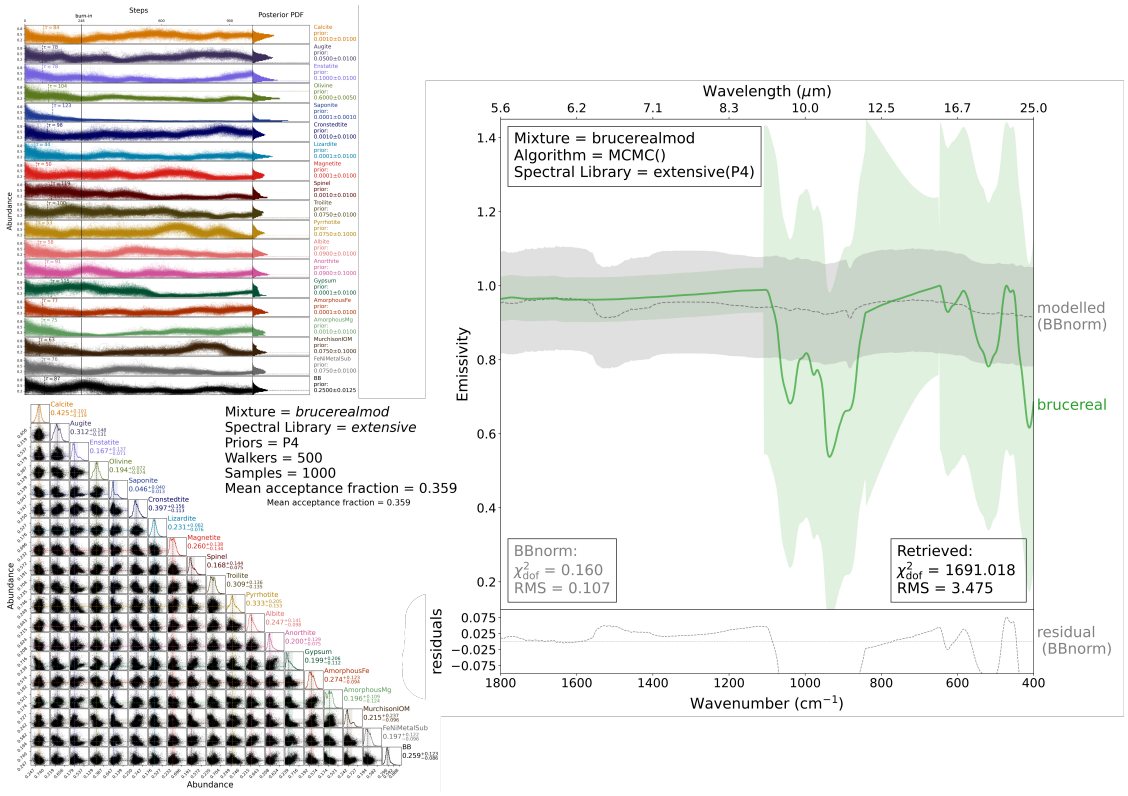


Figure 7.28: *brucerealmodextP4* `MCMC()` walkers and corner plots with model fit.

Table 7.5: *brucerealmodminP1* `MCMC()` results. The unit for accuracy, σ, represents the retrieved abundance uncertainty, and a negative value here corresponds to an overestimation, whereas a positive value shows an underestimation.

End-member	**'True' Abundance**	**Prior, P1**	**Retrieved Abundance**	**Accuracy to 'True' Abundance** σ	**Accuracy to P1 Abundance** σ
Augite	0.0150	0.3004 ± 3.00E-04 (0.10%)	0.2877 ± 3.23E-04 (0.11%)	-843.26	39.33
Enstatite	0.0850	0.0110 ± 1.10E-05 (0.10%)	0.0110 ± 1.22E-05 (0.11%)	6089.4	1.45
Olivine	0.7000	0.3872 ± 3.87E-04 (0.10%)	0.3660 ± 4.21E-04 (0.12%)	793.4	50.4
Troilite	0.0500	0.5015 ± 5.02E-04 (0.10%)	0.4657 ± 5.43E-04 (0.12%)	-766.11	65.97
Albite	0.1000	0.6452 ± 6.45E-04 (0.10%)	0.5875 ± 6.67E-04 (0.11%)	-730.47	86.57
Fe, Ni metal sub.	0.0500	0.8508 ± 8.51E-04 (0.10%)	0.7473 ± 0.0011 (0.14%)	-663.43	98.52
		RMS error	1.475		
		$\chi^2_{d.o.f}$	302.6		

Table 7.6: Retrieval quality metrics summary table for the `MCMC()` unmixings of the real and coarsified versions of Bruce (*brucereal* and *brucerealmod*, respectively). Values in square brackets correspond to metrics derived from the blackbody renormalised abundances (BBnorm). Details on these metrics and how to interpret them are covered in Section 3.3.3, where generally the smaller/closer to zero, the better the quality.

`MCMC()`		Fit Quality [BBnorm]					Abundance Quality [BBnorm]				
		U	P1	P2	P3	P4	U	P1	P2	P3	P4
Real Bruce	*brucerealmin*	-7.6200289	-13.442623	-7.6190243	-18.327448	-7.6119262	893.51	11.48	928.98	0.043	895.97
	brucerealexp	-1,957,366 [-291]	-973,197 [-259]	-573,962 [-153]	-302,930 [-196]	-630,329 [-230]	1.11 [1.35]	1.12 [1.43]	1.08 [1.19]	0.99 [1.03]	1.06 [1.20]
	brucerealext	-128613955 [-214.6]	-143390860 [-142.0]	-159392477 [-214.0]	-103247084 [-252.3]	-163659837 [-162.4]	1.17 [1.92]	0.98 [1.27]	1.14 [2.06]	1.20 [1.91]	1.01 [1.64]
Coarsified Bruce	*brucerealmodmin*	0.033	-444.8	0.040	0.053	0.056	1.244	1.946	2.245	3.06E-04	0.585
	brucerealmodexp	-91.59 [0.082]	-5625.12 [0.088]	-35.0 [0.082]	0.053 [0.053]	-26.4 [0.083]	1.015 [1.150]	1.015 [1.150]	1.096 [1.203]	0.466 [0.301]	1.024 [1.123]
	brucerealmodext	-8022.5 [0.096]	-24128.3 [0.0933]	-5756.7 [0.096]	0.053 [0.056]	-5872.9 [0.090]	1.060 [1.527]	1.700 [1.359]	1.140 [2.180]	1.297 [1.067]	1.216 [2.189]

With the `MCMC()` unmixings against the *extensive* spectral library, the abundances retrieved across *brucerealmodextU→P4* were largely of similar quality ($1.06 - 1.70$ for retrieved abundances and $1.07 - 2.19$ for BBnorm abundances; Table 7.6), leading to an inconsistency of whether these were, on the whole, better or worse than the equivalent *brucerealextU→P4* `MCMC()` unmixings ($0.98 - 1.20$ for retrieved abundances, and $1.27 - 2.06$ for BBnorm abundances; Table 7.6). The posterior pdfs for *brucerealmodextU→P4* were generally single peaked Gaussians, although appeared to have slight tails which could make them more Poisson/lognormal, and some displayed varying degrees of bimodality (e.g., calcite for *U*, olivine and albite for *P1*, olivine, cronstedtite and amorphous Mg for *P3*, and saponite, troilite, amorphous Mg and Murchison IOM for *P4*).

Overall, the `MCMC()` unmixings showed slight improvement when unmixing *brucerealmod* compared to *brucereal* (based on retrieval quality metrics in Table 7.6); however `MCMC()` generally performed poorly for both, with the consistent issue of a lack of abundance sum constraint, implying that the `MCMC()` algorithm itself has room for improvement. Although the improvements seen with the coarsified Bruce were small, with the many known weak links tied to the preliminary coarsification process, these small improvements could be indicative of potential in the coarsification technique.

7.3.7 Discussion

Across `WLS_ASC_ILR()`, `OptEst_ASC_ILR()` and `MCMC()`, there were generally slight improvements seen with the coarsified version of Bruce, although there were some cases where the original *brucereal* unmixings from Chapters 5 and 6 performed slightly better. A major success with the coarsification method was the almost exact correct end-member selection for the *P4* priors against the *expanded* and *extensive* spectral libraries within the `OptEst_ASC_ILR()` algorithm; where the end-member selection had previously been a significant downfall of `OptEst_ASC_ILR()` (see Section 6.1).

The main conclusion from these small improvements seen for *brucerealmod* compared to *brucereal* was that the coarsification method showed potential, but clearly requires more extensive studies to refine the coarsification process; which could be done via more quantitative research into how spectra change with grain size (i.e., a more thorough spectral morphology study). Additionally, these results demonstrated that the Bayesian algorithms used (`OptEst_ASC_ILR()` and `MCMC()`) also showed potential but require further development.

Overall, the `OptEst_ASC_ILR()` algorithm performed better than the `MCMC()` algorithm. However, the ability to visualise probability distributions and potential bimodality, that came with `MCMC()`, brought valuable additional information. Thus, an attempt to combine the benefits of the `OptEst_ASC_ILR()` and `MCMC()` algorithms could lead to a powerful spectral interpretation tool, and would be a compelling avenue for future research.

Chapter 8

Summary, Conclusions and Future Work

Contents

8.1 Overview: The Bigger Picture 254
8.2 Overview: This Project 256
8.3 Avenues for Future Research 259

8.1 Overview: The Bigger Picture

Asteroids may be considered as time capsules of the Solar System, carrying with them details of its birth and evolution; so studying them offers a unique opportunity to unravel the history of our planetary system. The origin of water and organics on Earth is one of science's biggest questions, and it is hypothesised that these may have been brought by asteroids (e.g., Broadley et al. 2022; Morbidelli, Chambers, et al. 2000; Trigo-Rodríguez et al. 2019), thus research into asteroid composition is particularly valuable towards this endeavour. Understanding the distribution of asteroid compositions across the Solar System is also key to deciphering the evolutionary history of planetary dynamics and migration – another big question in the field without a definitive answer (e.g., Kleine et al. 2020; Morbidelli, Walsh, et al. 2015; Walsh, Morbidelli, et al. 2012).

There are a variety of ways to determine compositional information, with spectroscopy being particularly useful in providing a link between what is measured

in the laboratory, and what is seen from remote sensing and telescopic observations. The fundamental molecular motions of relevant rock-forming compounds (e.g., SiO_2) give rise to unique features in the thermal infrared (TIR) that are diagnostic of composition, therefore TIR spectroscopy is often used in both laboratory and remote sensing investigations to probe into mineralogy.

Interpreting TIR spectra is commonly done via spectral unmixing algorithms using the linear mixing model; whereby spectra of individual components (known as end-members) sum linearly in proportion to their abundances to form the spectrum of their mixture, and their abundances then found via inverse methods. The linear mixing model has been used successfully for modal mineralogy estimates where coarse or whole rock samples are being considered (e.g., Hamilton, Christensen, et al. 1997), however, it is widely recognised to be unsuitable when fine grains begin to dominate (as is the case for the Moon and many asteroids), due to the change in scattering regime from specular to volumetric as grain size decreases.

The spectral unmixing algorithm of choice is often a linear least squares (e.g., Ramsey and Christensen 1998), which may be effective for certain scenarios where a lot of good prior knowledge is already available (e.g., for Mars; Hamilton, Christensen, et al. 1997); however this often involves a lot of implicit bias, which becomes problematic in a degenerate problem such as this. Here, the degeneracy is rooted in similarities that may be present between different end-member spectra (which are referred to as part of the inverse methods), deriving from commonality in chemical makeup. Additionally, in ensuring non-negative retrieved abundances, the Ramsey and Christensen 1998 style algorithm iteratively removes end-members giving negative solutions, however this can often lead to correct end-members being discarded, and incorrect ones retained.

It is clear that the current combination of model (linear mixing) and algorithm (linear least squares) has a number of faults, particularly in applications to fine grained samples. However, spectral unmixing via the linear mixing model is a powerful concept due to its intuitive simplicity and straightforward calculation; thus

the aim of this thesis has been to develop and investigate a selection of differing spectral unmixing algorithms in an effort to answer the question: do we need a new model, or just a new algorithm?

8.2 Overview: This Project

The algorithms developed included a weighted least squares with abundance sum constraint and iterative library reduction (`WLS_ASC_ILR()`), to represent current techniques, and therefore provide a baseline for comparison with alternative methods. The issues of implicit bias, and potentially also degeneracy, could be tackled by setting explicit, quantitative priors that can only be done by adopting a Bayesian approach. To see what effect the addition of such priors has in an otherwise similar method to the linear least squares, the optimal estimation with abundance sum constraint and iterative library reduction (`OptEst_ASC_ILR()`) algorithm was developed to form a stepping stone between current Frequentist techniques (i.e., linear least squares) and fully Bayesian methods. The final algorithm developed and tested was the popular Bayesian technique, Markov Chain Monte Carlo (`MCMC()`) for application to spectral unmixing.

The data used in the unmixing algorithm investigation mostly came from the OSIRIS-REx Blind Test suite of Donaldson Hanna et al. 2019, with a few substitute end-members required, as outlined in Table 4.1. The samples unmixed were:

- Bruce – an anhydrous simulant mixture that had the most complete knowledge available, and
- Glenn – a particulate sample of the Murchison meteorite.

For initial insight into the accuracy of the linear mixing model with these fine grained samples, 'mathematical' versions of Bruce and Glenn were created, where their end-members were summed linearly in the appropriate abundances. These mathematical mixture spectra were then compared to their 'real', measured spectra.

For abundance retrieval, three different spectral libraries were unmixed against:

- *minimal* – containing only the end-members known/believed to be in the samples,
- *expanded* – containing four randomly selected end-members, as well as a blackbody component if not already randomly selected, in addition to those in *minimal*, and
- *extensive* – containing all end-members available from the Blind Test suite (and relevant substitutes).

The motivation behind using these different spectral libraries was to demonstrate the issues of implicit bias tied into spectral library curation. Doing principal component analysis (PCA) on the different spectral libraries also provided an independent way of investigating the degree of degeneracy in the problem, due to spectral similarities across end-members. To see the effect of priors in the Bayesian algorithms, different versions of these were used in the `OptEst_ASC_ILR()` and `MCMC()` unmixings. Each of the real and mathematical versions of Bruce and Glenn were then unmixed against each of the *minimal*, *expanded* and *extensive* spectral libraries in `WLS_ASC_ILR()`, `OptEst_ASC_ILR()` and `MCMC()`, using different priors where applicable.

To evaluate the performance of each unmixing, bespoke retrieval quality metrics were devised to quantify how well the model fit the measured mixture spectrum, and how well the abundances matched the true answers. Using these as part of the overall analysis showed that **we cannot get around the limits of linear mixing by adopting a Bayesian approach with a more sophisticated algorithm, and therefore an alternative model to linear mixing for spectral interpretation is required**.

In an effort to begin laying the foundations to such an alternative model, the changes in spectral morphology with decreasing grain size were studied and attempted to be quantified. The aim of this was to identify a trend that could be used to parameterise linear mixing, such that it would contain more complete physics, based on empirical findings. From this, the 'coarsification' method was

derived, whereby the spectrum of a fine grained mixture is modified to appear as a coarse spectrum, via alterations of spectral contrast in different regions according to observations from the spectral morphology study. Some initial work has shown that this approach could have potential, but certainly needs further refinement. Future work will require more data in order to to model more quantitatively and accurately how spectral morphology evolves with grain size.

Although it is widely accepted amongst the planetary community that the linear mixing model is inappropriate for fine particulate samples, it remains the most commonly used option for compositional analysis from TIR spectra. This research essentially proved the unsuitability of linear mixing in a more quantitative way, and demonstrated just how poor the results can be (regardless of algorithm sophistication, or having appropriately sized end-members in the spectral library), thus moving forward the overall understanding and conversation surrounding TIR spectral interpretation.

Part of this has been in adding to the justification of further efforts into the development of an alternative spectral unmixing model, since it is still somewhat unfeasible to completely replace linear mixing with full radiative transfer models, due to their more intensive requirements for computational power and optical constants data. Additionally, this has perhaps brought new light to just how inaccurate linear mixing is when fine grains dominate, which in itself furthers our understanding of how fine grained end-member spectra may (or in this case, may not) combine to produce a mixture spectrum. This therefore brings into question the robustness of previously reported compositions based on linearly unmixed TIR spectra, and consequently anything that may have been based on such results (e.g., constraints on planetary migration models). Thus, moving forward, it is perhaps wise to consider past results with greater caution, and to treat them as having larger uncertainties than originally thought (particularly if using these as priors for future similar studies). Overall, the main bulk of this work has emphasised

the importance of a more complete treatment of uncertainties and wider statistical analysis when determining the quality of a result.

Experimenting with the 'coarsification' approach has also helped further our understanding of spectra, particularly in quantifying the behaviours displayed as grain size decreases, through the spectral morphology study. It has also brought forward the idea that interpreting spectra of fine grained mixtures may require multiple stages, each of which would require specialist knowledge from the analyst to ensure physical and geological context and feasibility are considered throughout. Trialling different methods and their combinations at each stage could also further our understanding of spectral interpretation as it would perhaps be easier to pinpoint the stage at which inaccuracies may be introduced and/or exacerbated.

The foundations laid by this thesis can provide a basis for future work towards more accurate TIR spectral modelling, which would be particularly useful when interpreting data from more immediate future missions with TIR spectrometers, such as Lucy (e.g., Levison 2016; see Section 1.4). Gaining a better understanding of spectra and how we can extract compositional information from them, building from the work presented in this thesis, could also aid in future mission designs and selection.

8.3 Avenues for Future Research

As well as more measurements for a range of end-members, refining the coarsification pipeline would require taking measurements of the same mixtures using fine and coarse end-members at a variety of specific size fractions. It would be particularly insightful to start with a coarse mixture, gradually grind it to finer and finer size fractions, and take measurements at frequent size intervals, to see how this compares to a mixture made with fines to begin with. The ultimate goal of more detailed spectral morphology studies would be to determine whether there is a relation which can be empirically found, that translates a fine spectrum into its coarse equivalent for a wide range of planetary surfaces, and thus be usable in linear mixing based models. Such a relation could be particularly valuable for interpreting remote sensing data

of planetary bodies we do not have samples for. Of course, to do this, it is also vital to strengthen the links between laboratory and remote sensing observations, for which returned samples are essential, and much research into which is ongoing.

A good starting point for a more extensive spectral morphology study would be to focus first on the grain size fractions expected for planetary surfaces. On Mars, the dust and drift material has been estimated to be within the $0.1 - 10\mu$m range (e.g., Christensen and Moore 1992); and for the Moon, although regolith in the $< 25\mu$m size fraction makes up $\sim 10 - 20$wt.% of the total mass (Carrier et al. 1991), reflectance spectra of mature lunar soils are dominated by signatures from this $< 25\mu$m range (Pieters et al. 1993). Meteorites have displayed a range of grain sizes, from the fine-grained rims (FGRs) that surround chondrules typically being $< 5\mu$m (e.g., Zanetta et al. 2022), to the matrix of primitive meteorites ranging between 0.103μm and 2.02μm (e.g., Vaccaro et al. 2023). In-situ measurements from Hayabusa showed Itokawa to have two main types of terrain: a rough terrain consisting of many boulders, and a smoother regolith layer; and the returned sample had grain sizes between $30 - 300\mu$m (e.g., Yoshikawa, Kawaguchi, et al. 2021). The Ryugu sample returned by Hayabusa2 contained grains from fine, submillimetre dust particles, up to the largest grains being ~ 8mm, with the most common size range being at the millimetre scale (e.g., Yada et al. 2022).

Building on the foundations laid in this thesis, additional future work should focus on the full development of a spectral interpretation tool, with the aim of being accessible and open-source, enabling the community to make desired additions and allow it to grow as needed. This would require proper software development in collaboration with the planetary science community so that it could also be highly customisable to the users' needs. Such a tool could streamline research on connections between remote sensing and returned sample measurements by returning a multitude of useful metrics, such as the retrieval quality metrics devised for this thesis. Additionally, comparing the mathematical spectrum expected from different models to what is actually observed, could be valuable additional analysis provided

by such a spectral interpretation tool. Comparisons between newly developed future models and radiative transfer and linear mixing models could also be valuable, particularly in assessing computing expense vs retrieval quality.

Such a versatile spectral interpretation tool would have the added benefits of being useful and adaptable for past, current and future asteroid missions and sample return. This would allow for consistency across interpretation of TIR spectral data from missions such as OSIRIS-REx and Lucy, allowing for clearer comparisons and conclusions surrounding their target objects.

Finally, the novel use of principal component analysis (PCA) in this thesis could be taken further. Would it be possible to unmix with principal components rather than directly with spectra? Could PCA be used as an intermediate step in composition estimates by seeing if a mixture spectrum falls in a cluster with any particular end-members in PC1-PC2 space? The additional context that can be provided by PCA may also aid in setting quantitative priors in Bayesian inference; such as ensuring that more probable end-members which may form clusters with less probable ones have their priors set appropriately.

In conclusion, the work presented in this thesis has aimed to explore spectral unmixing algorithms to determine whether improvements to these can compensate for the inaccuracies of the linear mixing model, such that we may still be able to use linear mixing, and avoid resorting to computationally intense models that require extra data not widely available. Through a detailed study I have found that an alternative model to linear mixing is necessary, and begun experimenting with ways to derive such a model, starting with investigating how spectral morphology varies with grain size. From these investigations, my work has identified a wealth of potential paths that future research may take to increase our understanding of asteroid composition; and therefore also the evolution of the Solar System and potentially even the sources of water and organics on Earth.

Bibliography

Amelin, Y., Kaltenbach, A., et al. (2010). "U–Pb chronology of the Solar System's oldest solids with variable 238U/235U". In: *Earth and Planetary Science Letters* 300.3-4, pp. 343–350.

Amelin, Y., Krot, A. N., et al. (2002). "Lead isotopic ages of chondrules and calcium-aluminum-rich inclusions". In: *Science* 297.5587, pp. 1678–1683.

Anders, E. (1971). "Meteorites and the Early Solar System". In: *Annual Review of Astronomy and Astrophysics* 9.1, pp. 1–34.

Bandfield, J. L., Christensen, P. R., and Smith, M. D. (2000). "Spectral data set factor analysis and end-member recovery: Application to analysis of Martian atmospheric particulates". In: *Journal of Geophysical Research: Planets* 105.E4, pp. 9573–9587.

Bates, H. (2020). "Understanding the formation and evolution of asteroids through analysis of carbonaceous chondrites". PhD thesis. University of Oxford.

Beckett, J., Connolly, H., and Ebel, D. (2006). "Chemical Processes in Igneous Calcium-Aluminum-rich Inclusions: A Mostly CMAS View of Melting and Crystallization". In: *Meteorites and the Early Solar System II*, p. 399.

Bishop, J. L. et al. (2019). *Remote Compositional Analysis: Techniques for Understanding Spectroscopy, Mineralogy, and Geochemistry of Planetary Surfaces*. Vol. 24. Cambridge University Press.

Broadley, M. W. et al. (2022). "Origin of life-forming volatile elements in the inner Solar System". In: *Nature* 611.7935, pp. 245–255.

Carrier, W. D., Olhoeft, G. R., and Mendell, W. (1991). "Physical properties of the lunar surface". In: *Lunar sourcebook, a user's guide to the moon*, pp. 475–594.

Cheng, A. F. (2002). "Near Earth asteroid rendezvous: mission summary". In: *Asteroids III* 1, pp. 351–366.

Christensen, P. R., Hamilton, V. E., et al. (2018). "The OSIRIS-REx Thermal Emission Spectrometer (OTES) Instrument". In: *Space Science Reviews* 214.

Christensen, P. and Moore, H. J. (1992). "The Martian surface layer". In: *Mars*. University of Arizona Press, Space Science Series, pp. 686–729.

Christensen, P. R., Bandfield, J. L., et al. (2000). "A thermal emission spectral library of rock-forming minerals". In: *Journal of Geophysical Research: Planets* 105.E4, pp. 9735–9739.

Christensen, P. R., Jakosky, B. M., et al. (2004). "The thermal emission imaging system (THEMIS) for the Mars 2001 Odyssey Mission". In: *Space Science Reviews* 110.1, pp. 85–130.

Clark, B. E. et al. (2011). "Asteroid (101955) 1999 RQ36: Spectroscopy from 0.4 to 2.4 μm and meteorite analogs". In: *Icarus* 216.2, pp. 462–475.

Conel, J. E. (1969). "Infrared emissivities of silicates: Experimental results and a cloudy atmosphere model of spectral emission from condensed particulate mediums". In: *Journal of Geophysical Research* 74.6, pp. 1614–1634.

Connelly, J. N. et al. (2012). "The absolute chronology and thermal processing of solids in the solar protoplanetary disk". In: *Science* 338.6107, pp. 651–655.

Connolly Jr., H. C. and Jones, R. H. (2016). "Chondrules: The Canonical and Noncanonical Views". In: *Journal of Geophysical Research: Planets* 121.10, pp. 1885–1899.

Davis, D. R. et al. (2002). "Collisional evolution of small-body populations". In: *Asteroids III* 545.

DeMeo, F. et al. (2015). "The compositional structure of the asteroid belt". In: *Asteroids iv* 1, p. 13.

Desch, S. et al. (2005). "Heating of chondritic materials in solar nebula shocks". In: *Chondrites and the protoplanetary disk*. Vol. 341, p. 849.

Donaldson Hanna, K. et al. (2019). "Spectral Characterization of Analog Samples in Anticipation of OSIRIS-REx's Arrival at Bennu: A Blind Test Study". In: *Icarus* 319, pp. 701–723.

Donaldson Hanna, K. et al. (2012). "Laboratory emissivity measurements of the plagioclase solid solution series under varying environmental conditions". In: *Journal of Geophysical Research: Planets* 117.E11.

Eisberg, R. and Resnick, R. (1985). *Quantum physics of atoms, molecules, solids, nuclei, and particles*.

Feely, K. C. and Christensen, P. R. (1999). "Quantitative compositional analysis using thermal emission spectroscopy: Application to igneous and metamorphic rocks". In: *Journal of Geophysical Research* 104, pp. 24195–24210.

Foreman-Mackey, D. et al. (Mar. 2013). "emcee: The MCMC Hammer". In: 125.925, p. 306. arXiv: `1202.3665 [astro-ph.IM]`.

Gavin, H. P. (2017). "The Levenberg-Marquardt method for nonlinear least squares curve-fitting problems". In.

Glotch, T. D. and Bandfield, J. L. (2006). "Determination and interpretation of surface and atmospheric Miniature Thermal Emission Spectrometer spectral end-members at the Meridiani Planum landing site". In: *Journal of Geophysical Research: Planets* 111.E12.

Glotch, T. D., Lucey, P. G., et al. (2010). "Highly silicic compositions on the Moon". In: *science* 329.5998, pp. 1510–1513.

Goodman, J. and Weare, J. (2010). "Ensemble samplers with affine invariance". In: *Communications in applied mathematics and computational science* 5.1, pp. 65–80.

Hamilton, V., Simon, A., et al. (2019). "Evidence for widespread hydrated minerals on asteroid (101955) Bennu". In: *Nature Astronomy* 3.4, pp. 332–340.

Hamilton, V. E. (2010). "Thermal infrared (vibrational) spectroscopy of Mg–Fe olivines: A review and applications to determining the composition of planetary surfaces". In: *Geochemistry* 70.1, pp. 7–33.

Hamilton, V. E., Christensen, P. R., and McSween Jr, H. Y. (1997). "Determination of Martian Meteorite Lithologies and Mineralogies Using Vibrational Spectroscopy". In: *Journal of Geophysical Research: Planets* 102.E11, pp. 25593–25603.

Hapke, B. (1993). "Theory of reflectance and emittance spectroscopy. Cambridge Univ". In: *Press, Cambridge, UK*.

Hapke, B. (1996). "A model of radiative and conductive energy transfer in planetary regoliths". In: *Journal of Geophysical Research: Planets* 101.E7, pp. 16817–16831.

Hapke, B. (2012). *Theory of reflectance and emittance spectroscopy*. Cambridge university press.

Heinz, D. and Chang, C. (2001). "Fully Constrained Least Squares Linear Spectral Mixture Analysis Method for Material Quantification in Hyperspectral Imagery". In: *IEEE Transactions on Geoscience and Remote Sensing* 39.3, pp. 529–545.

Howard, K. et al. (2015). "Classification of hydrous meteorites (CR, CM and C2 ungrouped) by phyllosilicate fraction: PSD-XRD modal mineralogy and planetesimal environments". In: *Geochimica et Cosmochimica Acta* 149, pp. 206–222.

Hulst, H. C. and van de Hulst, H. C. (1981). *Light scattering by small particles*. Courier Corporation.

Irwin, P. et al. (2008). "The NEMESIS planetary atmosphere radiative transfer and retrieval tool". In: *Journal of Quantitative Spectroscopy and Radiative Transfer* 109.6, pp. 1136–1150.

Ito, G., Arnold, J. A., and Glotch, T. D. (2017). "T-Matrix and Radiative Transfer Hybrid Models for Densely Packed Particulates at Mid-Infrared Wavelengths". In: *Journal of Geophysical Research: Planets* 122.5, pp. 822–838.

Jones, E., Oliphant, T., Peterson, P., et al. (2001). *SciPy: Open source scientific tools for Python*. URL: `http://www.scipy.org/`.

Kleine, T. et al. (2020). "The non-carbonaceous–carbonaceous meteorite dichotomy". In: *Space Science Reviews* 216, pp. 1–27.

Kokaly, R. et al. (2017). "USGS Spectral Library Version 7 Data: US Geological Survey Data Release". In: *United States Geological Survey (USGS): Reston, VA, USA*.

Kuramoto, K. et al. (2018). "Martian Moons eXploration (MMX) conceptual study update". In: *49th Annual Lunar and Planetary Science Conference*. 2083, p. 2143.

Lambert, B. (2018). *A Student's Guide to Bayesian Statistics*. Sage.

Lambert, B. (2019). *Bayesian Short Course – Lecture 1: Introduction to Inference and Bayes' Rule*. URL: `https://ben-lambert.com/bayesian-short-course/`.

Lauretta, D. S., Enos, H. L., et al. (2021). "Chapter 8 - OSIRIS-REx at Bennu: Overcoming challenges to collect a sample of the early Solar System". In: *Sample Return Missions*. Ed. by A. Longobardo. Elsevier, pp. 163–194.

Lauretta, D., Balram-Knutson, S., et al. (2017). "OSIRIS-REx: Sample Return from Asteroid (101955) Bennu". In: *Space Science Reviews* 212.1, pp. 925–984.

Lauretta, D., DellaGiustina, D., et al. (2019). "The unexpected surface of asteroid (101955) Bennu". In: *Nature* 568.7750, pp. 55–60.

Lawson, C. L. and Hanson, R. J. (1995). *Solving Least Squares Problems*. SIAM.

Lecar, M. et al. (2006). "On the location of the snow line in a protoplanetary disk". In: *The Astrophysical Journal* 640.2, p. 1115.

Levenberg, K. (1944). "A Method for the Solution of Certain Non-Linear Problems in Least Squares". In: *The Quarterly of Applied Mathematics* 2, pp. 164–168.

Levison, H. F. (2016). "Lucy: Surveying the Diversity of the Trojan Asteroids: The Fossils of Planet Formation". In: *47th Lunar and Planetary Science Conference*.

Li, S. et al. (2012). "Hybridization of partial least squares and neural network models for quantifying lunar surface minerals". In: *Icarus* 221.1, pp. 208–225.

Lyon, R. J. P. (1964). "Evaluation of Infrared Spectrophotometry for Compositional Analysis of Lunar and Planetary Soils. Part II: Rough and Powdered Surfaces". In: *NASA Contractor Report* CR-100.

Mackowski, D. W. and Mishchenko, M. I. (1996). "Calculation of the T matrix and the scattering matrix for ensembles of spheres". In: *JOSA A* 13.11, pp. 2266–2278.

Mackowski, D. W. and Mishchenko, M. I. (2011). "A multiple sphere T-matrix Fortran code for use on parallel computer clusters". In: *Journal of Quantitative Spectroscopy and Radiative Transfer* 112.13. Polarimetric Detection, Characterization, and Remote Sensing, pp. 2182–2192.

MacPherson, G. J. (2003). "Calcium-aluminum-rich inclusions in chondritic meteorites". In: *Treatise on Geochemistry* 1, p. 711.

Marquardt, D. W. (1963). "An Algorithm for Least-Squares Estimation of Nonlinear Parameters". In: *Journal of the Society for Industrial and Applied Mathematics* 11, pp. 431–441.

"Meteoritical Bulletin, No. 36-48" (June 1970). In: *Meteoritics* 5, pp. 85–109.

Morbidelli, A., Chambers, J., et al. (2000). "Source Regions and Timescales for the Delivery of Water to the Earth". In: *Meteoritics & Planetary Science* 35.6, pp. 1309–1320.

Morbidelli, A., Walsh, K. J., et al. (2015). "The Dynamical Evolution of the Asteroid Belt". In: *Asteroids IV*.

Mustard, J. F. and Hays, J. E. (1997). "Effects of hyperfine particles on reflectance spectra from 0.3 to 25 μm". In: *Icarus* 125.1, pp. 145–163.

Newville, M. et al. (Feb. 2021). *lmfit/lmfit-py 1.0.2*. Version 1.0.2. URL: `https://doi.org/10.5281/zenodo.4516651`.

Ostro, S. J. et al. (2006). "Radar imaging of binary near-Earth asteroid (66391) 1999 KW4". In: *Science* 314.5803, pp. 1276–1280.

Pan, C., Rogers, A., and Thorpe, M. (2015). "Quantitative compositional analysis of sedimentary materials using thermal emission spectroscopy: 2. Application to compacted fine-grained mineral mixtures and assessment of applicability of partial least squares methods". In: *Journal of Geophysical Research: Planets* 120.11, pp. 1984–2001.

Pedregosa, F. et al. (2011). "Scikit-learn: Machine Learning in Python". In: *Journal of Machine Learning Research* 12, pp. 2825–2830.

Petit, J.-M. C. et al. (2002). *Primordial excitation and depletion of the main belt*.

Pieters, C. M. et al. (1993). "Optical effects of space weathering: The role of the finest fraction". In: *Journal of Geophysical Research: Planets* 98.E11, pp. 20817–20824.

Press, W. H. et al. (1992). *Numerical recipes in C (The Art of Scientific Computing)*. Press Syndicate of the University of Cambridge.

Ramsey, M. S. and Christensen, P. R. (1998). "Mineral Abundance Determination: Quantitative Deconvolution of Thermal Emission Spectra". In: *Journal of Geophysical Research: Solid Earth* 103.B1, pp. 577–596.

Rivkin, A. S. and Cheng, A. F. (2023). "Planetary defense with the Double Asteroid Redirection Test (DART) mission and prospects". In: *nature communications* 14.1, p. 1003.

Rodgers, C. D. (2000). *Inverse methods for atmospheric sounding: theory and practice*. Vol. 2. World scientific.

Rogers, A. D. and Aharonson, O. (2008). "Mineralogical composition of sands in Meridiani Planum determined from Mars Exploration Rover data and comparison to orbital measurements". In: *Journal of Geophysical Research* 113.

Russell, S. S. (2007). "The formation of the Solar System". In: *Journal of the Geological Society* 164.3, pp. 481–492.

Salisbury, J. W., Walter, L. S., and Vergo, N. (1987). *Mid-Infrared (2.1-25 μm) Spectra of Minerals: First Edition*.

Shirley, K. and Glotch, T. (2019). "Particle size effects on mid-infrared spectra of lunar analog minerals in a simulated lunar environment". In: *Journal of Geophysical Research: Planets* 124.4, pp. 970–988.

Stuart, B. H. (2004). *Infrared Spectroscopy: Fundamentals and Applications*. John Wiley & Sons.

Suttle, M. et al. (2021). "The aqueous alteration of CM chondrites, a review". In: *Geochimica et Cosmochimica Acta* 299, pp. 219–256.

Tachibana, S. et al. (2014). "Hayabusa2: Scientific Importance of Samples Returned from C-type Near-Earth Asteroid (162173) 1999 JU3". In: *Geochemical Journal* 48.6, pp. 571–587.

Trigo-Rodríguez, J. M. et al. (2019). "Accretion of water in carbonaceous chondrites: Current evidence and implications for the delivery of water to early Earth". In: *Space Science Reviews* 215, pp. 1–27.

Tsuda, Y. et al. (2013). "System Design of the Hayabusa 2—Asteroid Sample Return Mission to 1999 JU3". In: *Acta Astronautica* 91, pp. 356–362.

Vaccaro, E. et al. (2023). "The grain size distribution of matrix in primitive chondrites". In: *Meteoritics & Planetary Science*.

Virtanen, P. et al. (2020). "SciPy 1.0: Fundamental Algorithms for Scientific Computing in Python". In: *Nature Methods* 17, pp. 261–272.

Walsh, K. J., Morbidelli, A., et al. (2012). "Populating the Asteroid Belt from Two Parent Source Regions due to the Migration of Giant Planets—"The Grand Tack"". In: *Meteoritics & Planetary Science* 47.12, pp. 1941–1947.

Walsh, K. J., Richardson, D. C., and Michel, P. (2008). "Rotational breakup as the origin of small binary asteroids". In: *Nature* 454.7201, pp. 188–191.

Weisberg, M. K., McCoy, T. J., Krot, A. N., et al. (2006). "Systematics and evaluation of meteorite classification". In: *Meteorites and the early solar system II* 19, pp. 19–52.

Yada, T. et al. (2022). "Preliminary analysis of the Hayabusa2 samples returned from C-type asteroid Ryugu". In: *Nature Astronomy* 6.2, pp. 214–220.

Yoshikawa, M., Fujiwara, A., and Kawaguchi, J. (2006). "Hayabusa and its Adventure Around the Tiny Asteroid Itokawa". In: *Proceedings of the International Astronomical Union* 2.14, pp. 323–324.

Yoshikawa, M., Kawaguchi, J., et al. (2021). "The Hayabusa mission". In: *Sample return missions*. Elsevier, pp. 123–146.

Zanetta, P.-M. et al. (2022). "Processes and temperatures of FGR formation in chondrites". In: *Geochimica et Cosmochimica Acta* 319, pp. 94–117.

Zolensky, M., Barrett, R., and Browning, L. (1993). "Mineralogy and composition of matrix and chondrule rims in carbonaceous chondrites". In: *Geochimica et Cosmochimica Acta* 57.13, pp. 3123–3148.

Appendices

Chapter A

Additional Figures to Accompany Chapters 5, 6 and 7

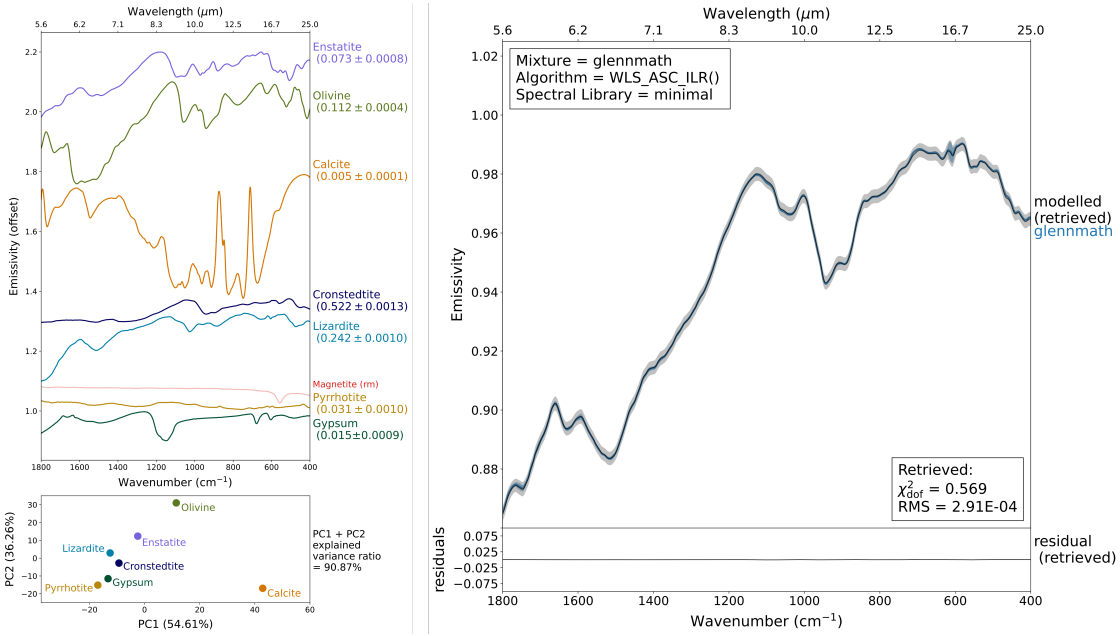


Figure A.1: *glennmathmin* `WLS_ASC_ILR()` reduced spectral library with model fit.

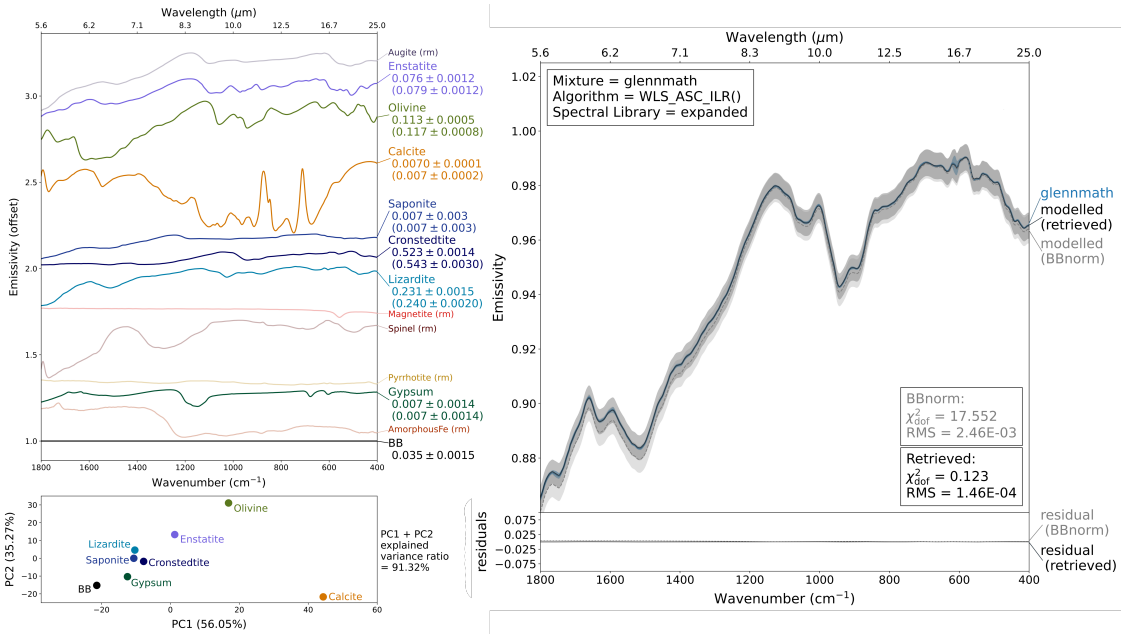


Figure A.2: *glennmathexp* `WLS_ASC_ILR()` reduced spectral library with model fit.

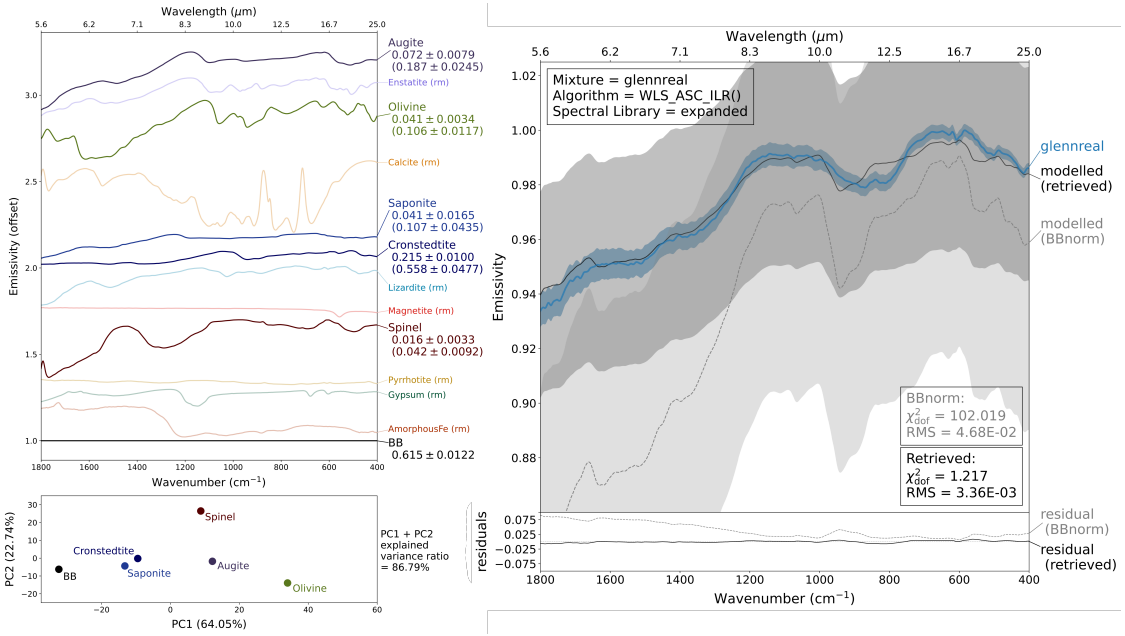


Figure A.3: *glennrealexp* `WLS_ASC_ILR()` reduced spectral library with model fit.

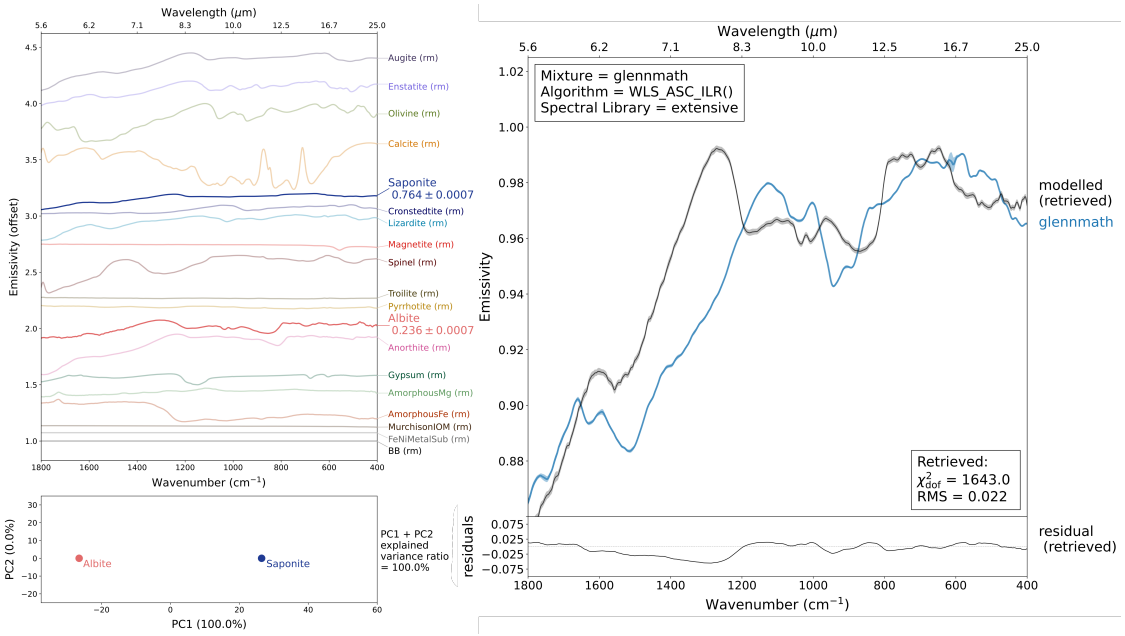


Figure A.4: *glennmathext* `WLS_ASC_ILR()` reduced spectral library with model fit.

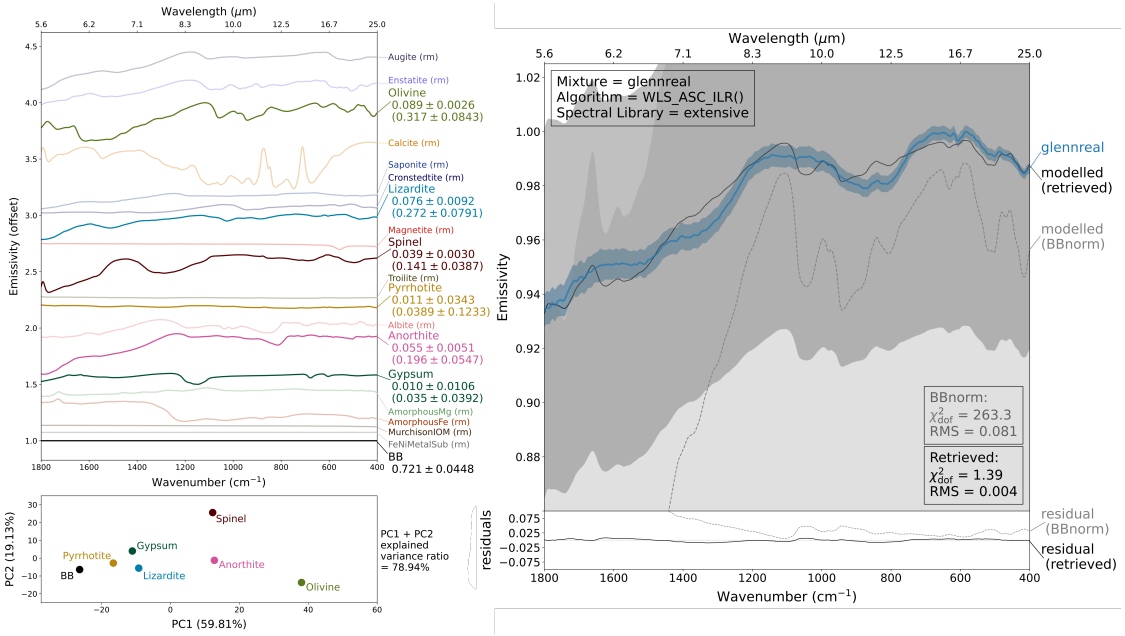


Figure A.5: *glennrealext* `WLS_ASC_ILR()` reduced spectral library with model fit.

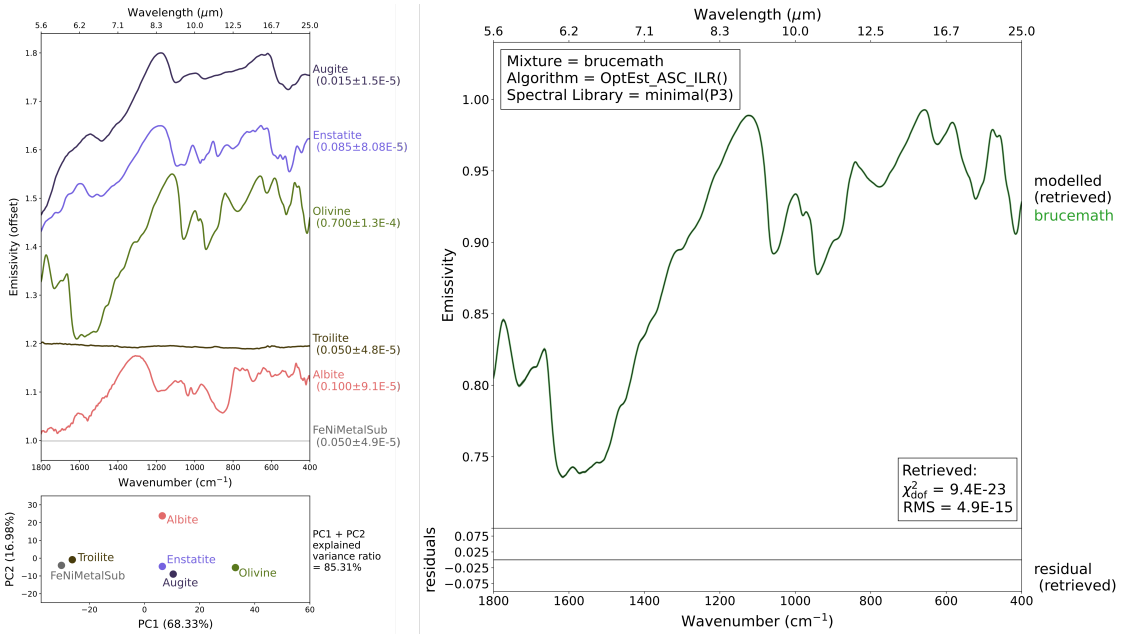


Figure A.6: *brucemathminP3* `OptEst_ASC_ILR()` reduced spectral library with model fit.

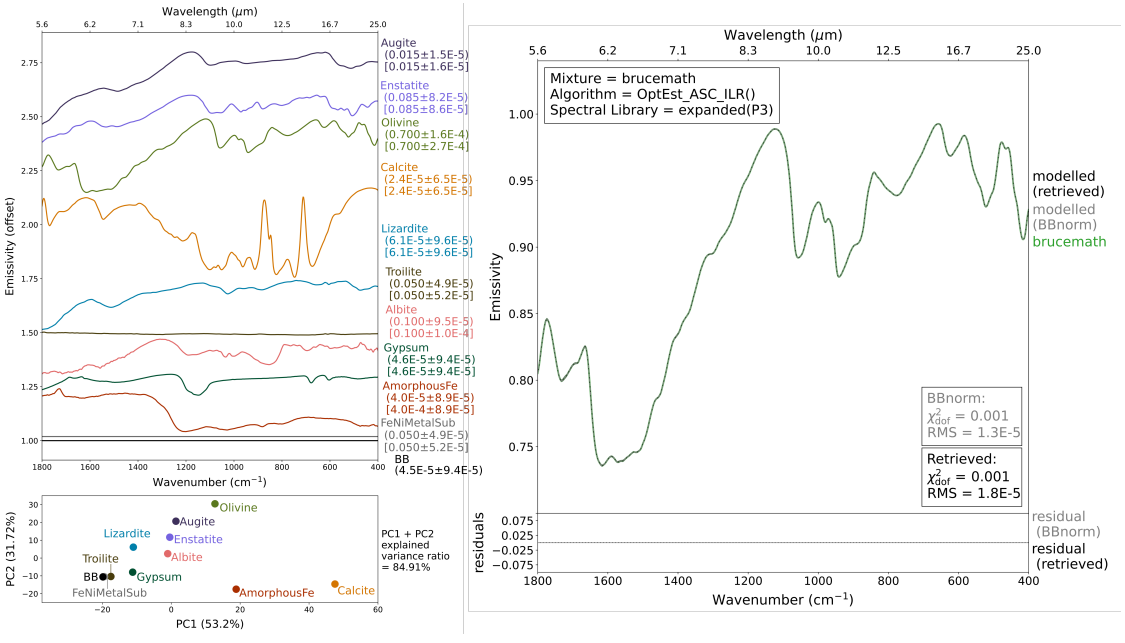


Figure A.7: *brucemathexpP3* `OptEst_ASC_ILR()` reduced spectral library with model fit.

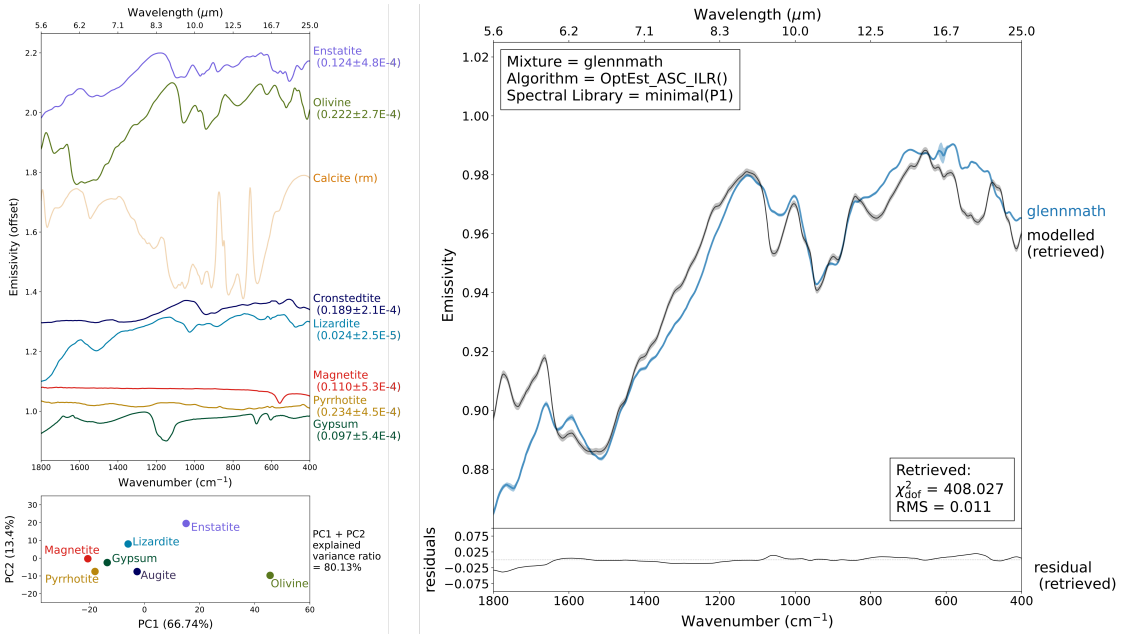


Figure A.8: *glennmathminP1* `OptEst_ASC_ILR()` reduced spectral library with model fit.

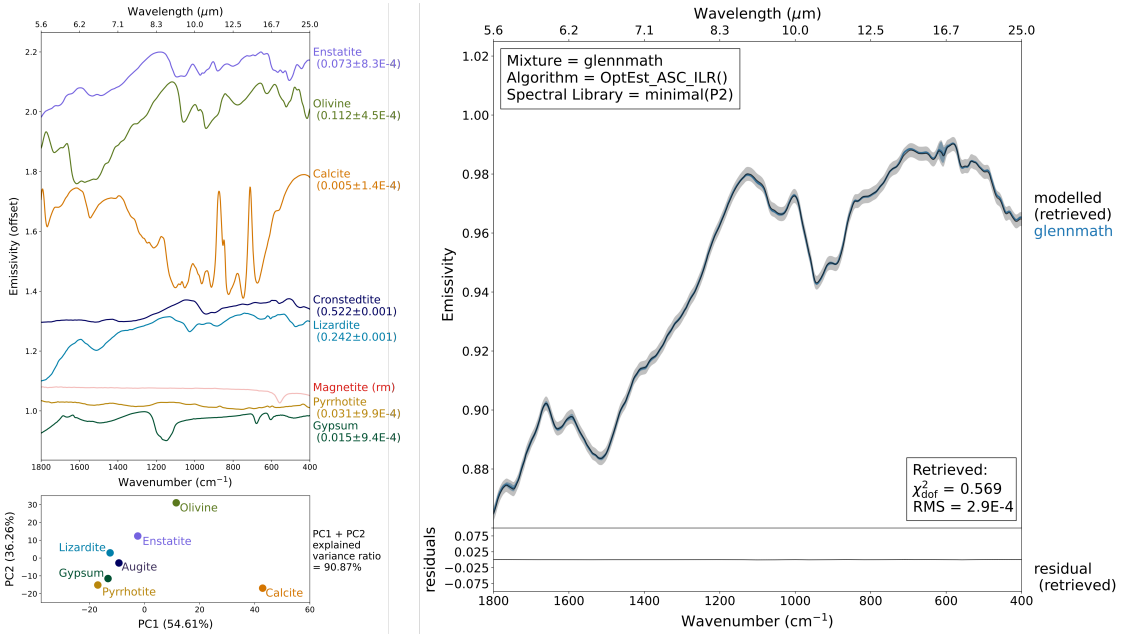


Figure A.9: *glennmathminP2* `OptEst_ASC_ILR()` reduced spectral library with model fit.

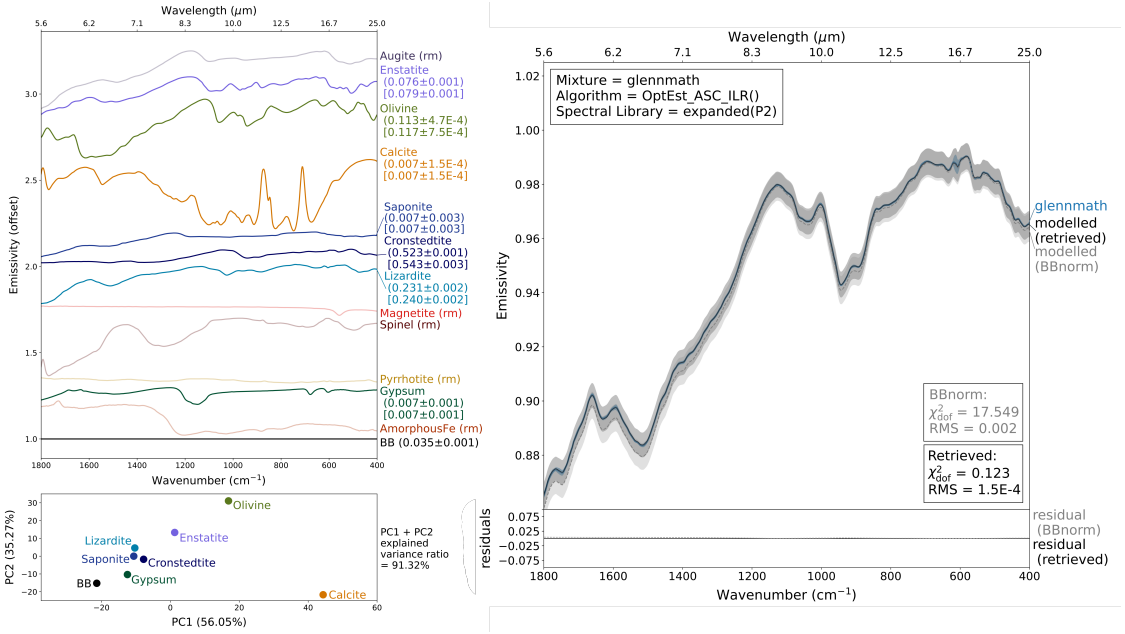


Figure A.10: *glennmathexpP2* `OptEst_ASC_ILR()` reduced spectral library with model fit.

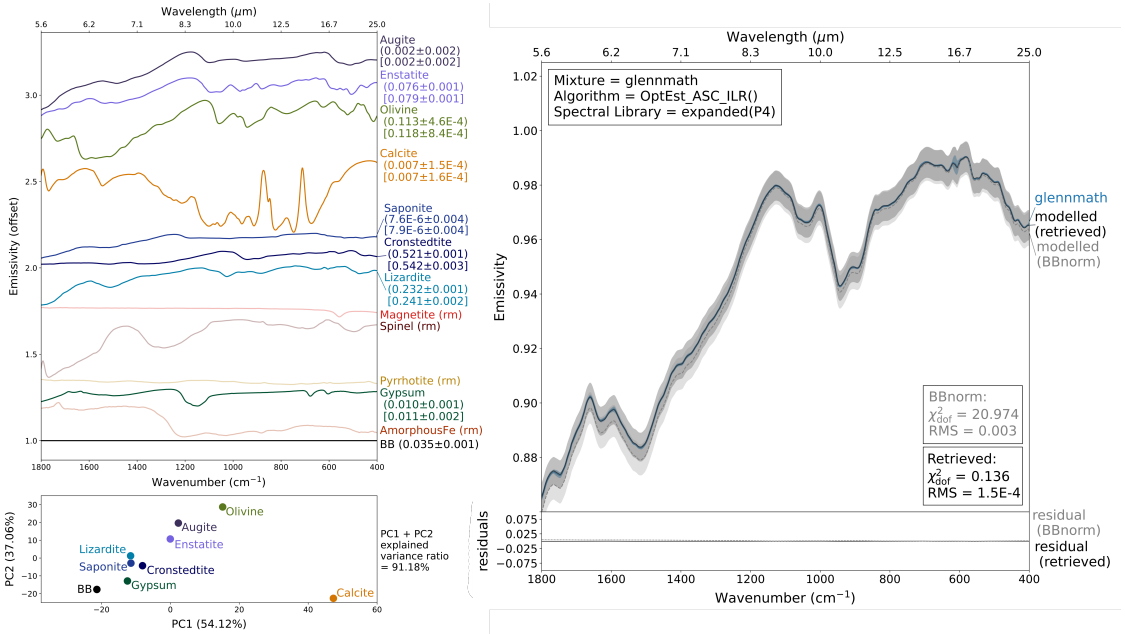


Figure A.11: *glennmathexpP4* `OptEst_ASC_ILR()` reduced spectral library with model fit.

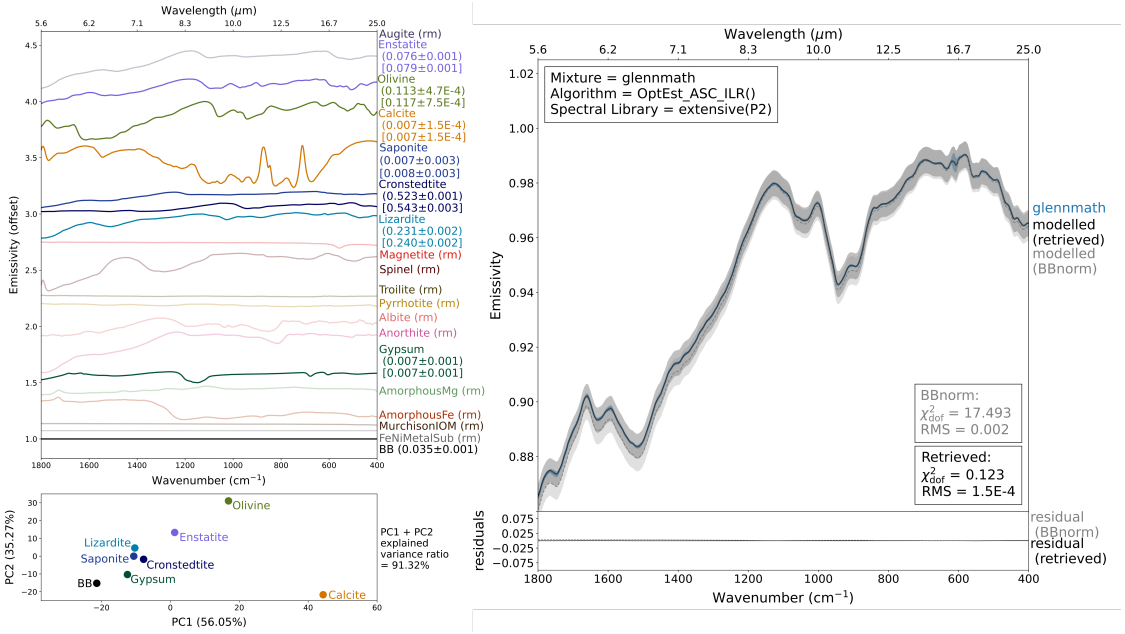


Figure A.12: *glennmathextP2* `OptEst_ASC_ILR()` reduced spectral library with model fit.

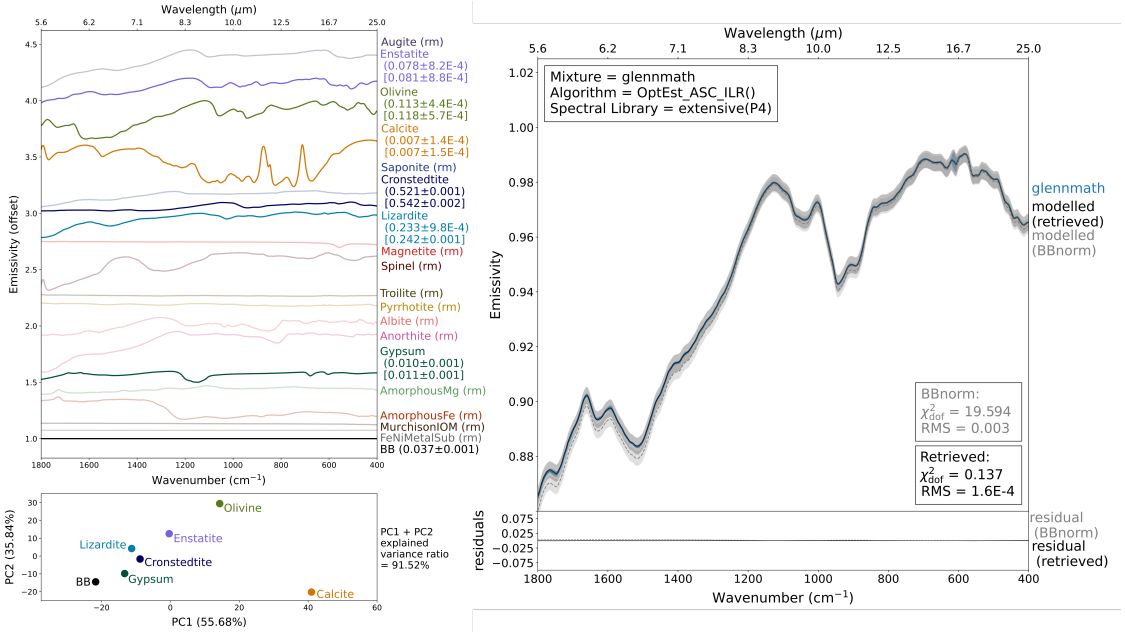


Figure A.13: *glennmathextP4* `OptEst_ASC_ILR()` reduced spectral library with model fit.

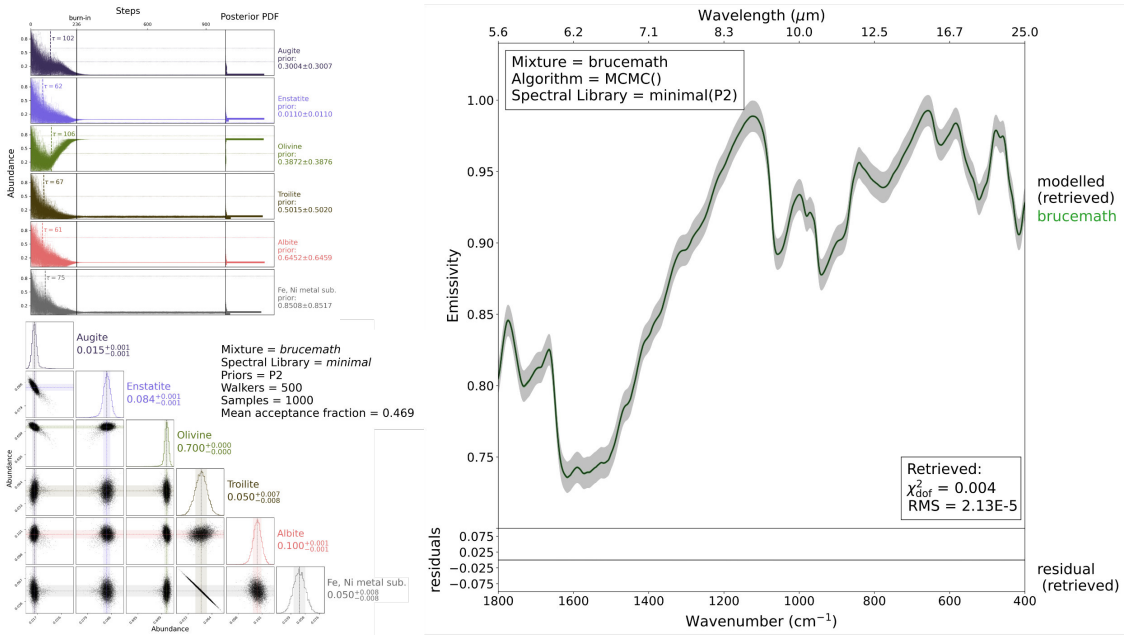


Figure A.14: *brucemathminP2* `MCMC()` walkers and corner plots with model fit.

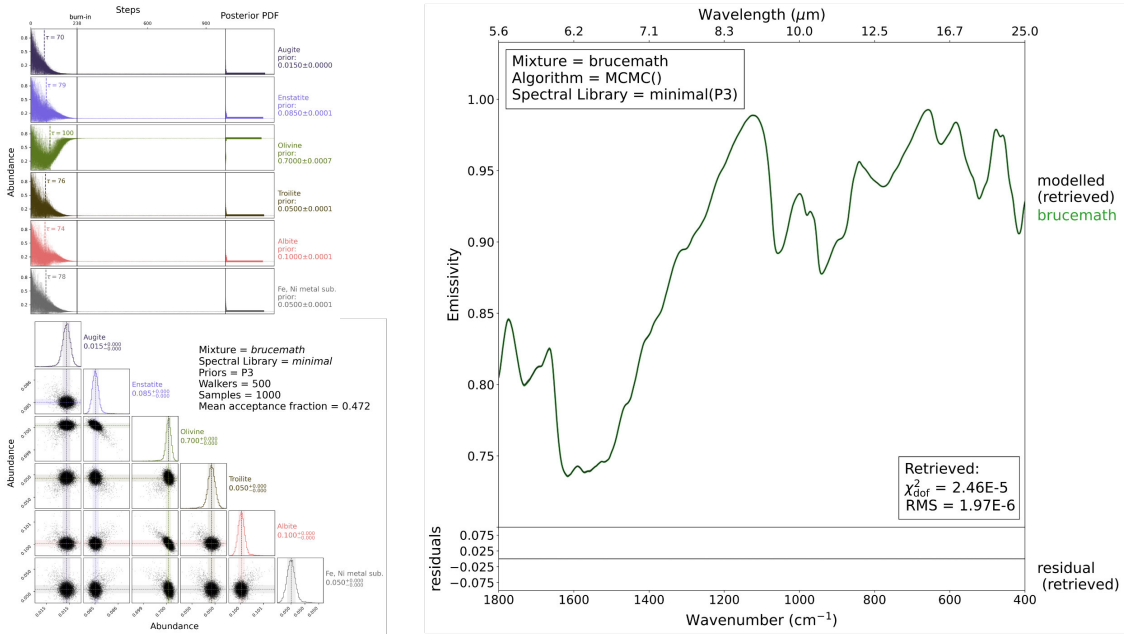


Figure A.15: *brucemathminP3* `MCMC()` walkers and corner plots with model fit.

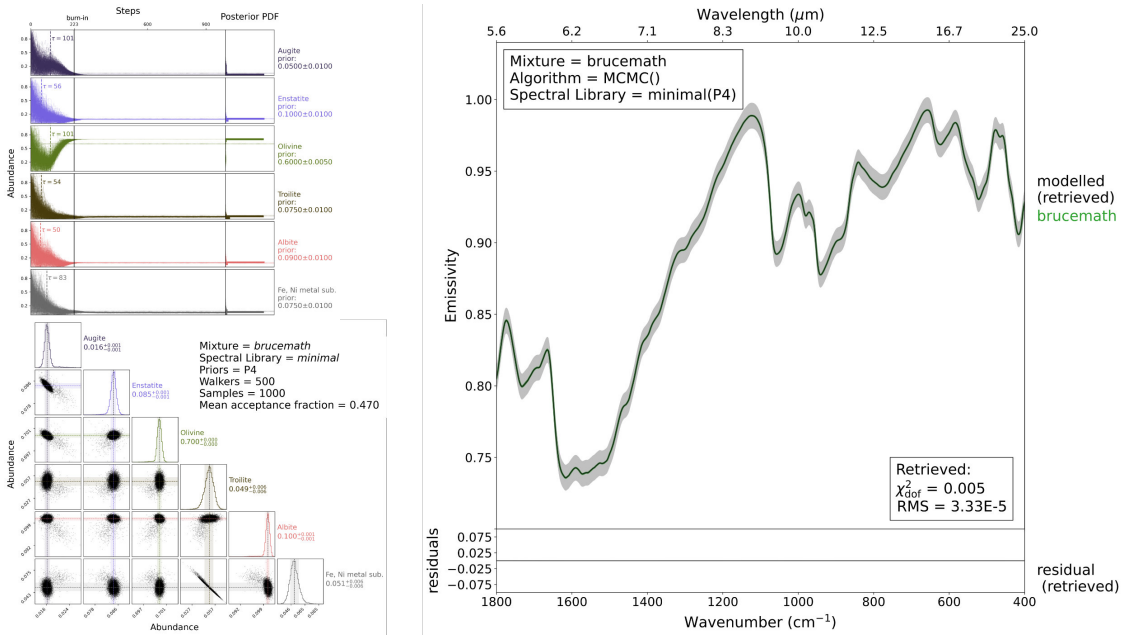


Figure A.16: *brucemathminP4* `MCMC()` walkers and corner plots with model fit.

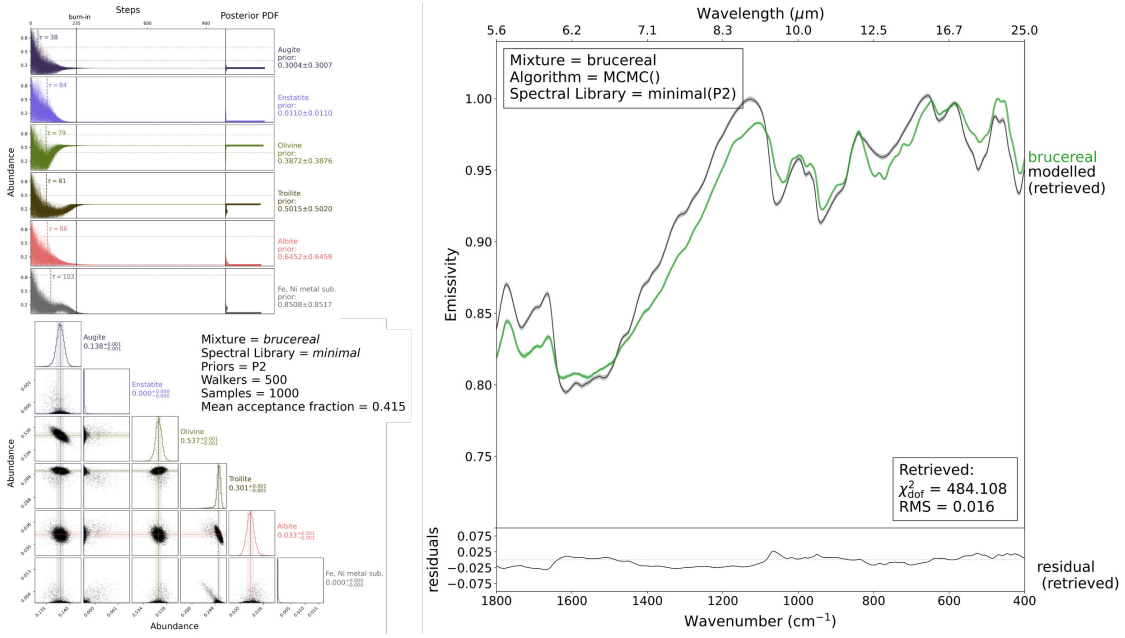


Figure A.17: *brucerealminP2* `MCMC()` walkers and corner plots with model fit.

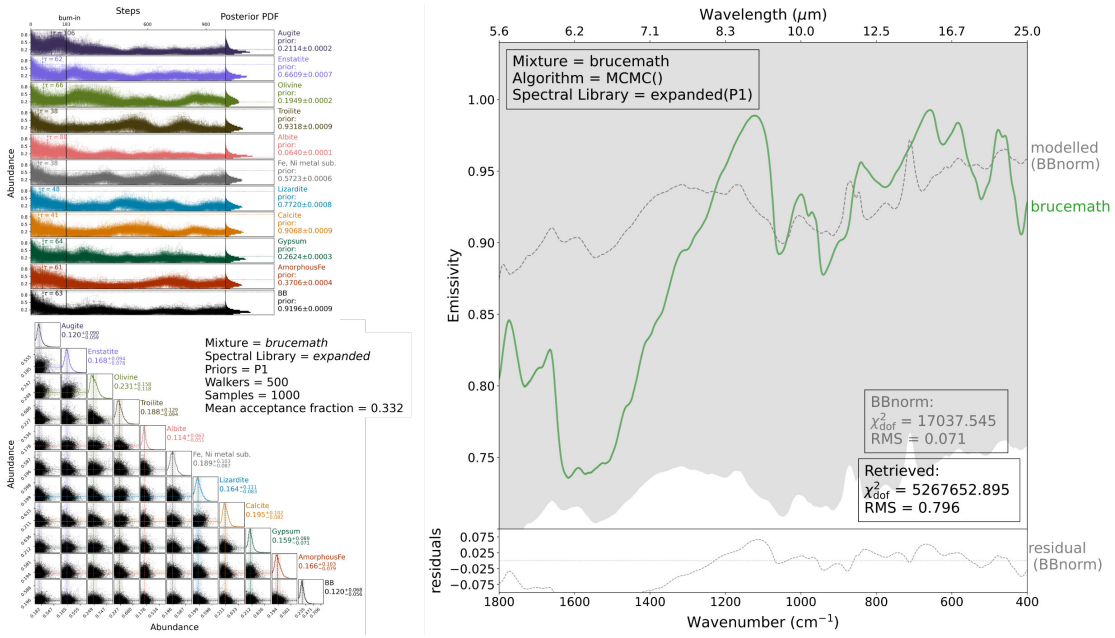


Figure A.18: *brucemathexpP1* `MCMC()` walkers and corner plots with model fit.

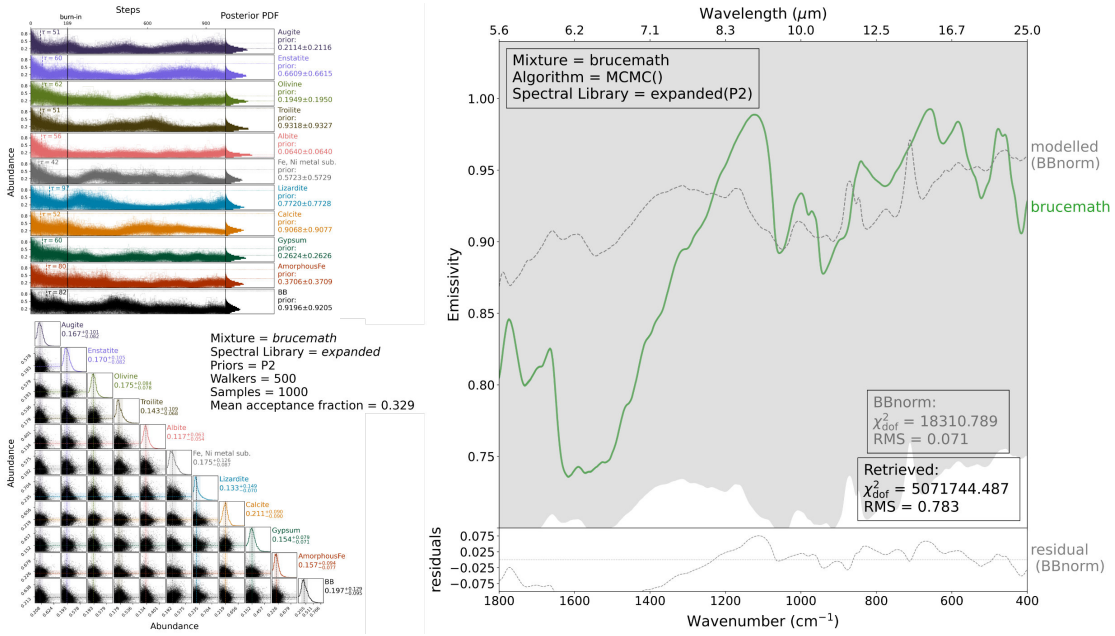


Figure A.19: *brucemathexpP2* `MCMC()` walkers and corner plots with model fit.

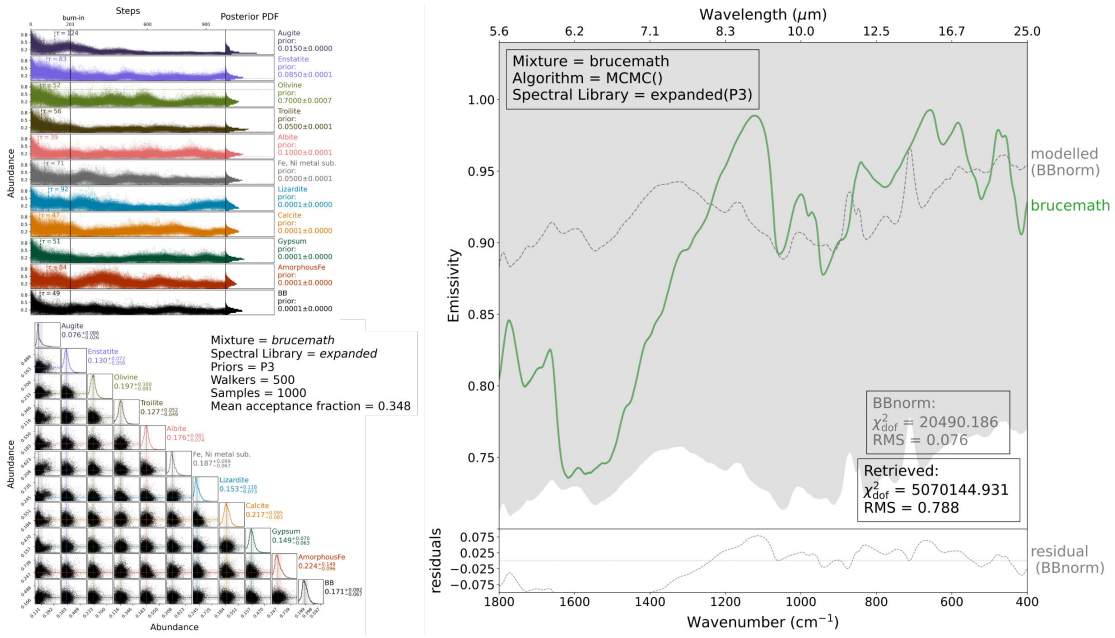


Figure A.20: *brucemathexpP3* `MCMC()` walkers and corner plots with model fit.

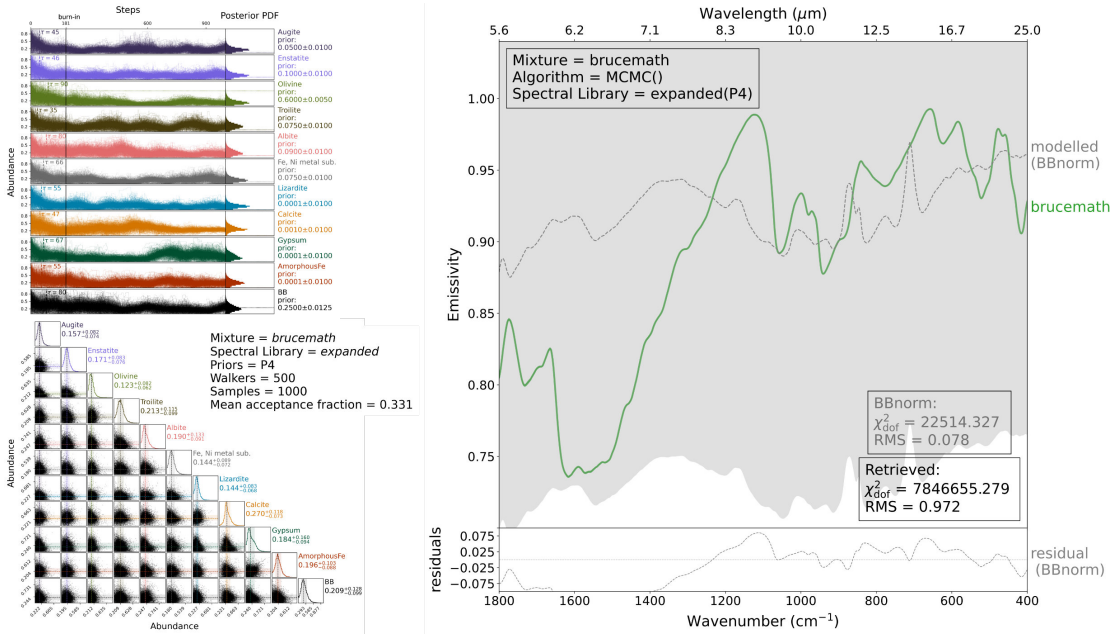


Figure A.21: *brucemathexpP4* `MCMC()` walkers and corner plots with model fit.

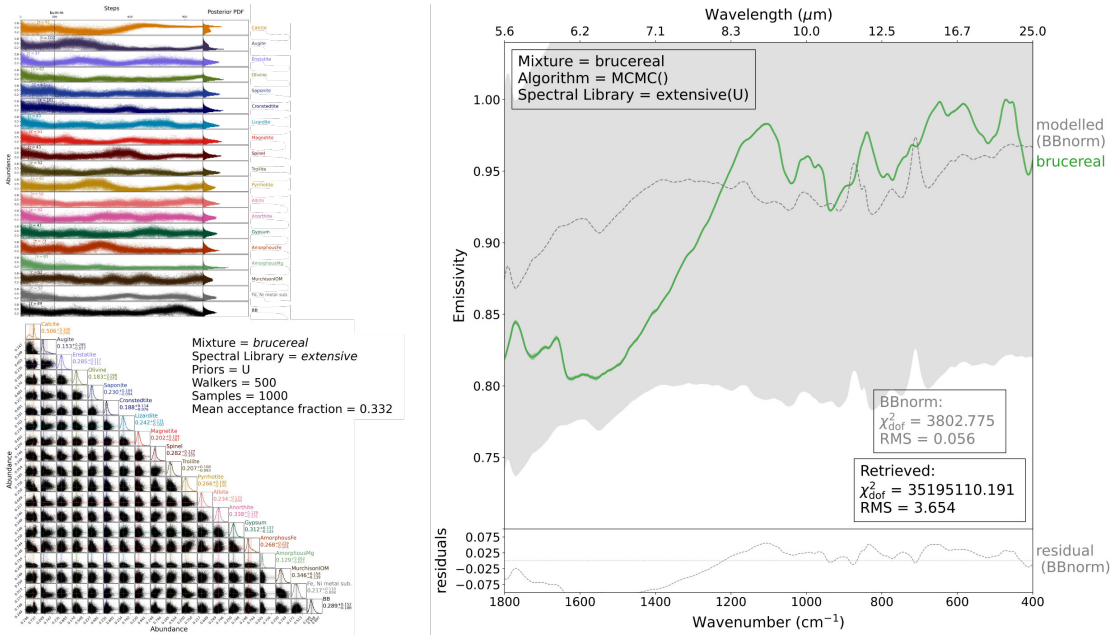


Figure A.22: *brucerealextU* `MCMC()` walkers and corner plots with model fit.

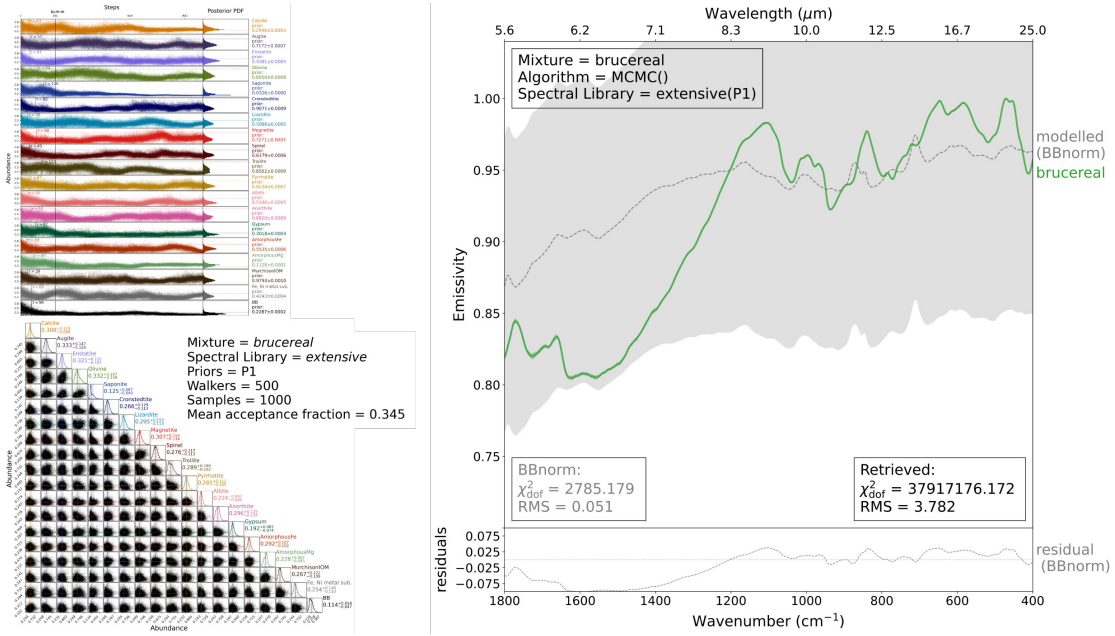


Figure A.23: *brucerealextP1* `MCMC()` walkers and corner plots with model fit.

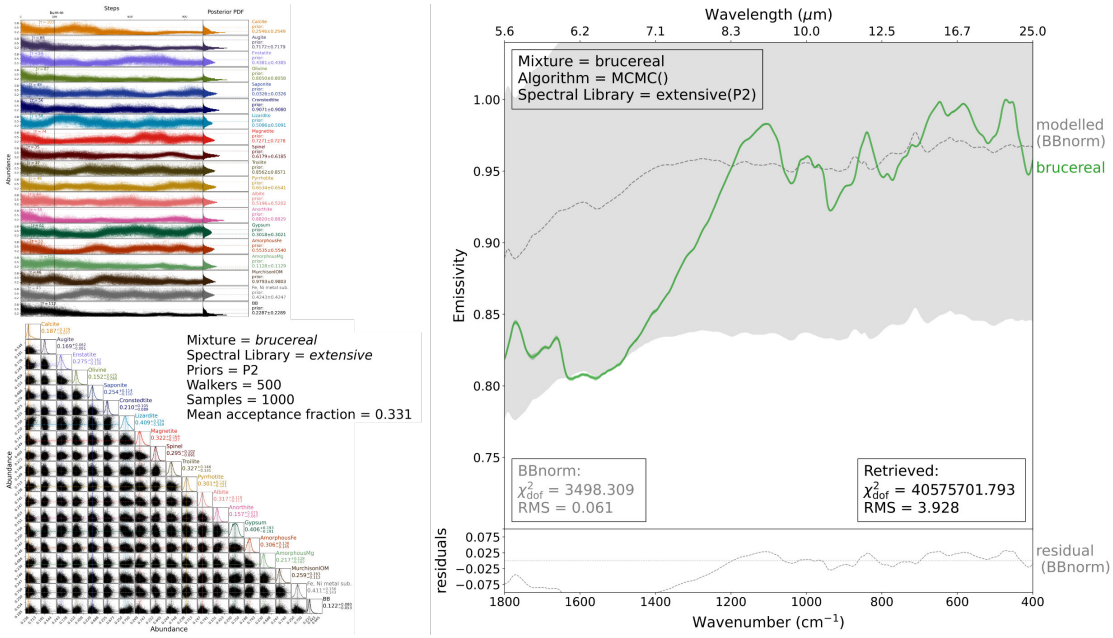


Figure A.24: *brucerealextP2* `MCMC()` walkers and corner plots with model fit.

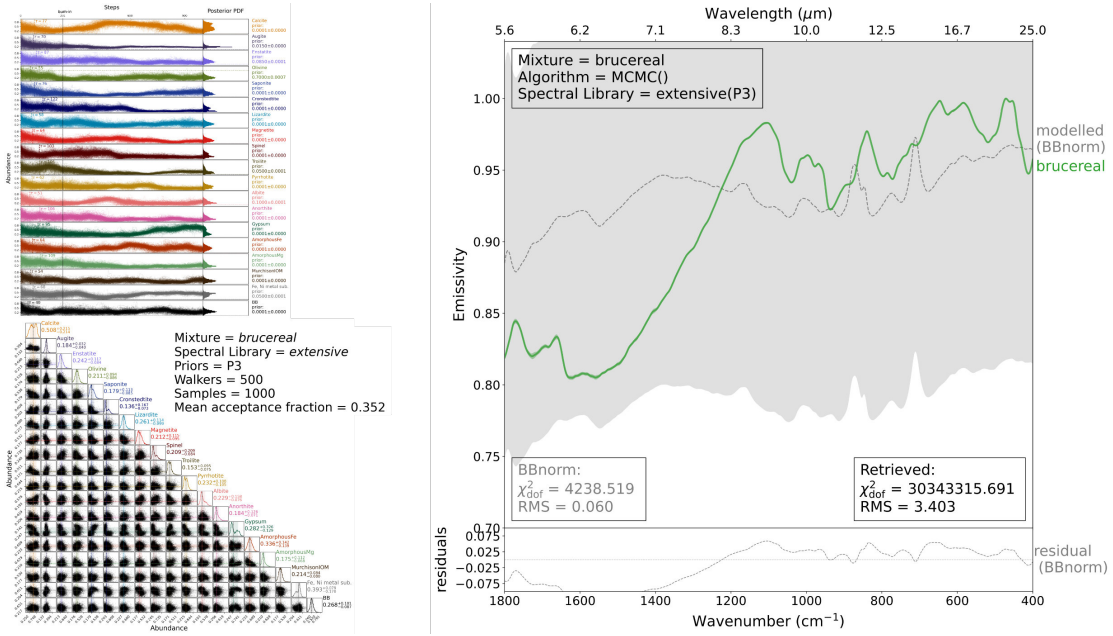


Figure A.25: *brucerealextP3* `MCMC()` walkers and corner plots with model fit.

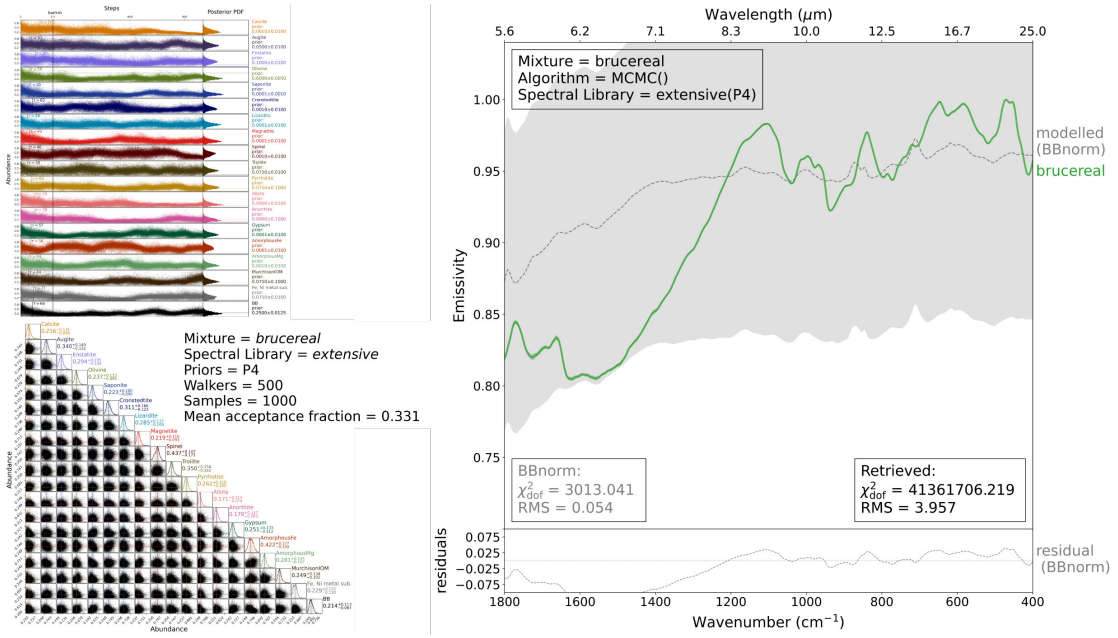


Figure A.26: *brucerealextP4* `MCMC()` walkers and corner plots with model fit.

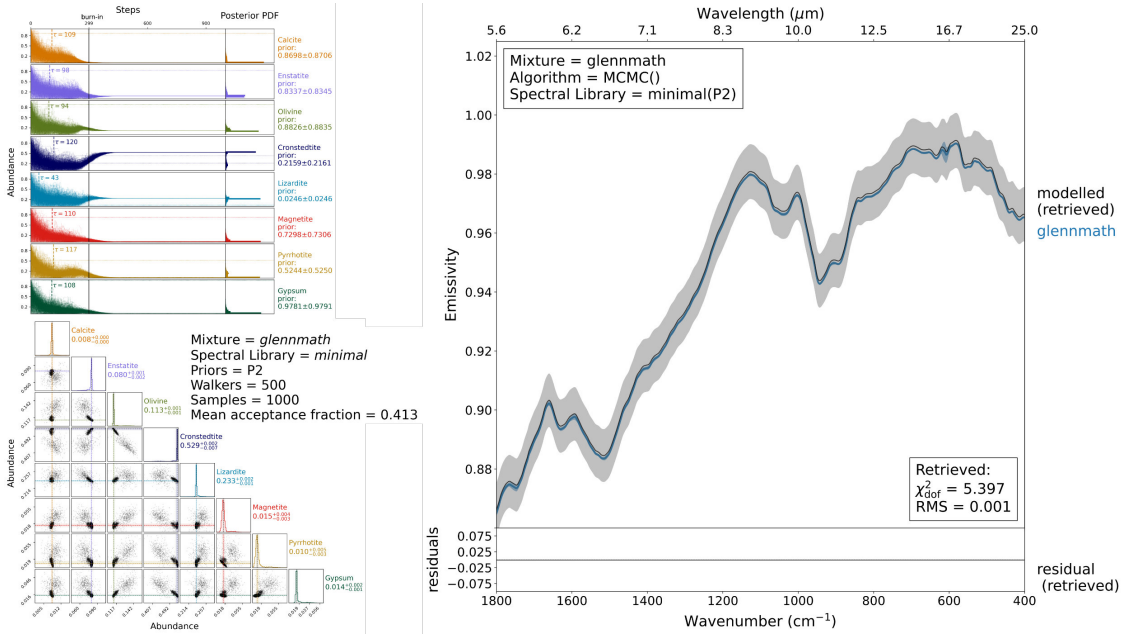


Figure A.27: *glennmathminP2* `MCMC()` walkers and corner plots with model fit.

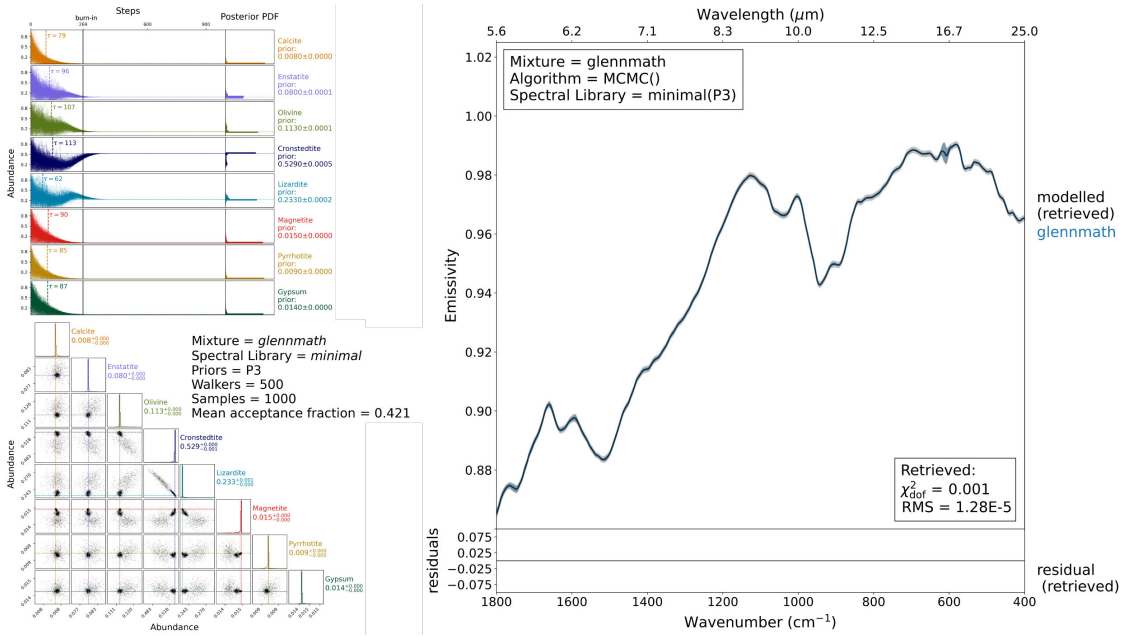


Figure A.28: *glennmathminP3* `MCMC()` walkers and corner plots with model fit.

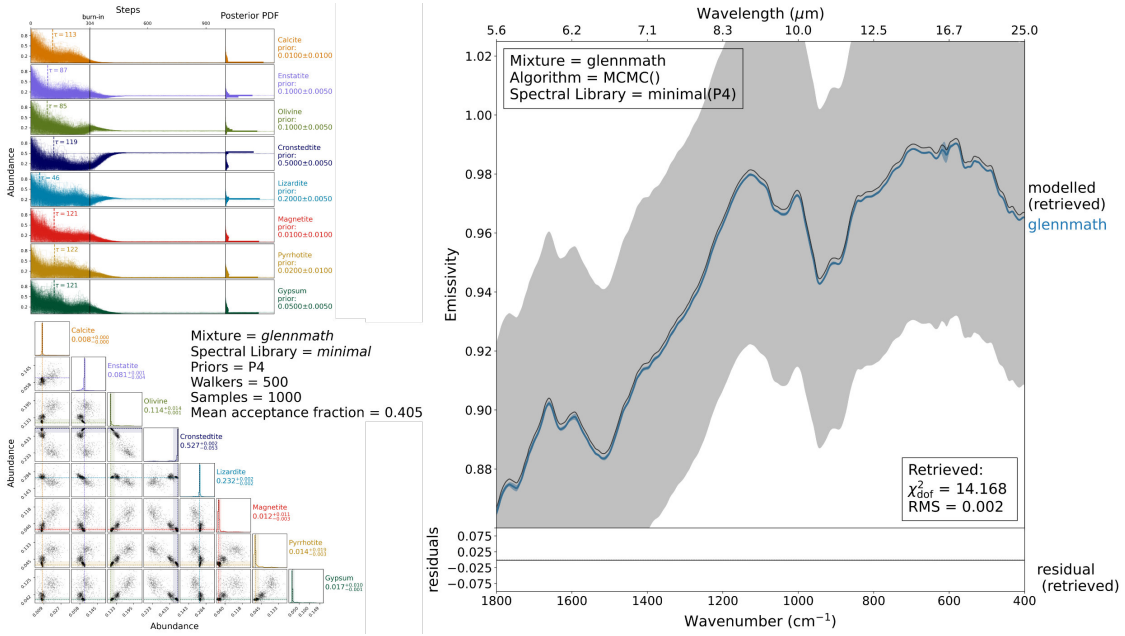


Figure A.29: *glennmathminP4* `MCMC()` walkers and corner plots with model fit.

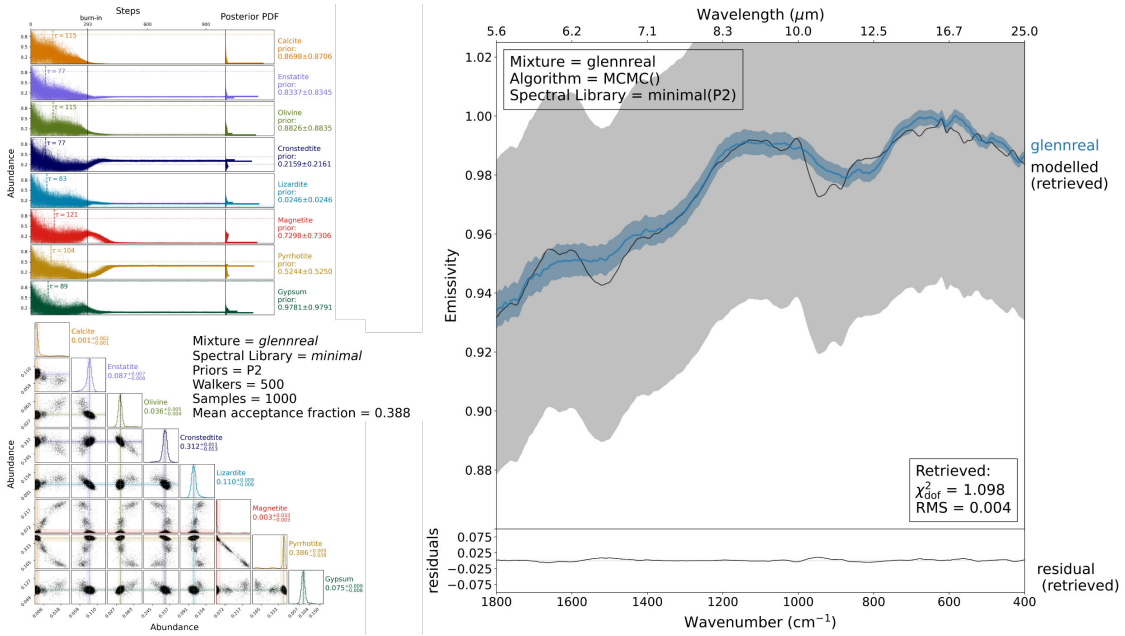


Figure A.30: *glennrealminP2* `MCMC()` walkers and corner plots with model fit.

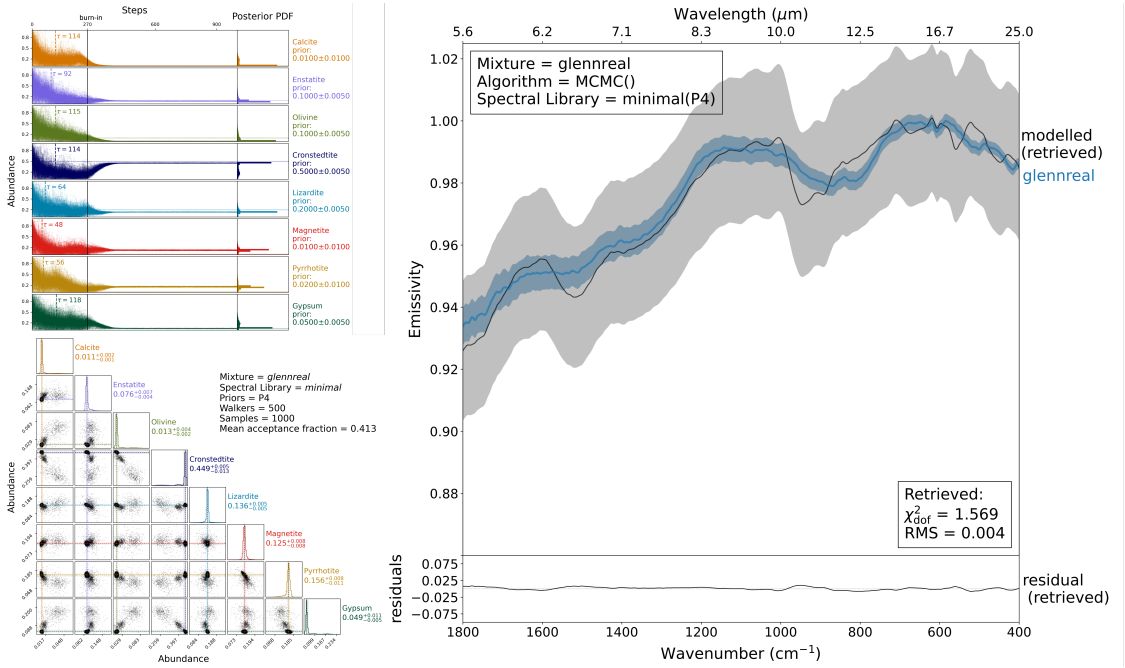


Figure A.31: *glennrealminP4* `MCMC()` walkers and corner plots with model fit.

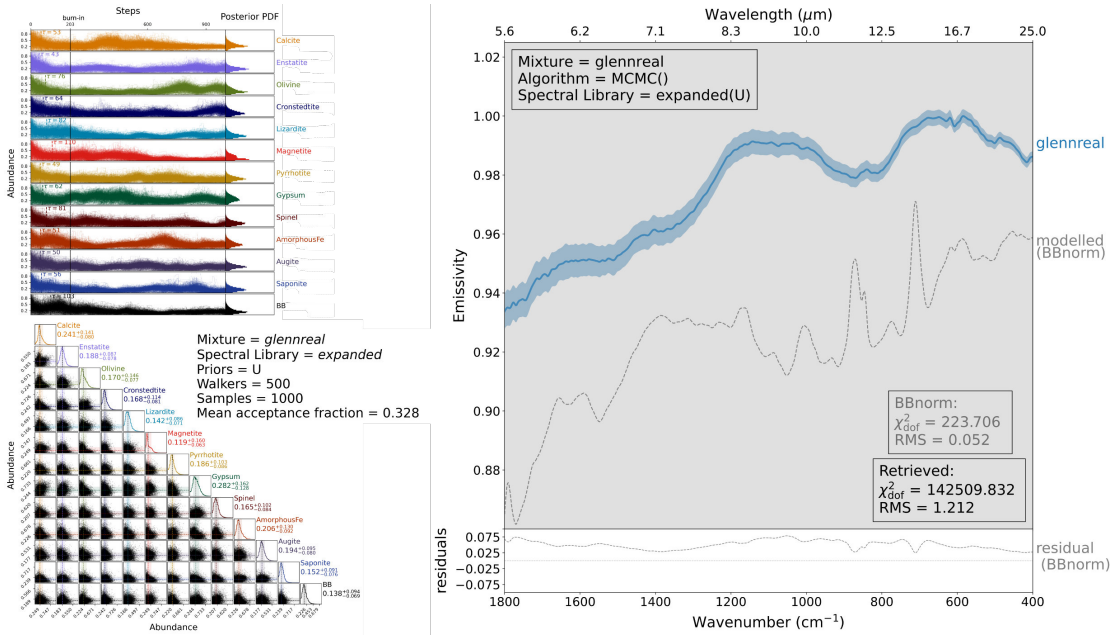


Figure A.32: *glennrealexpU* `MCMC()` walkers and corner plots with model fit.

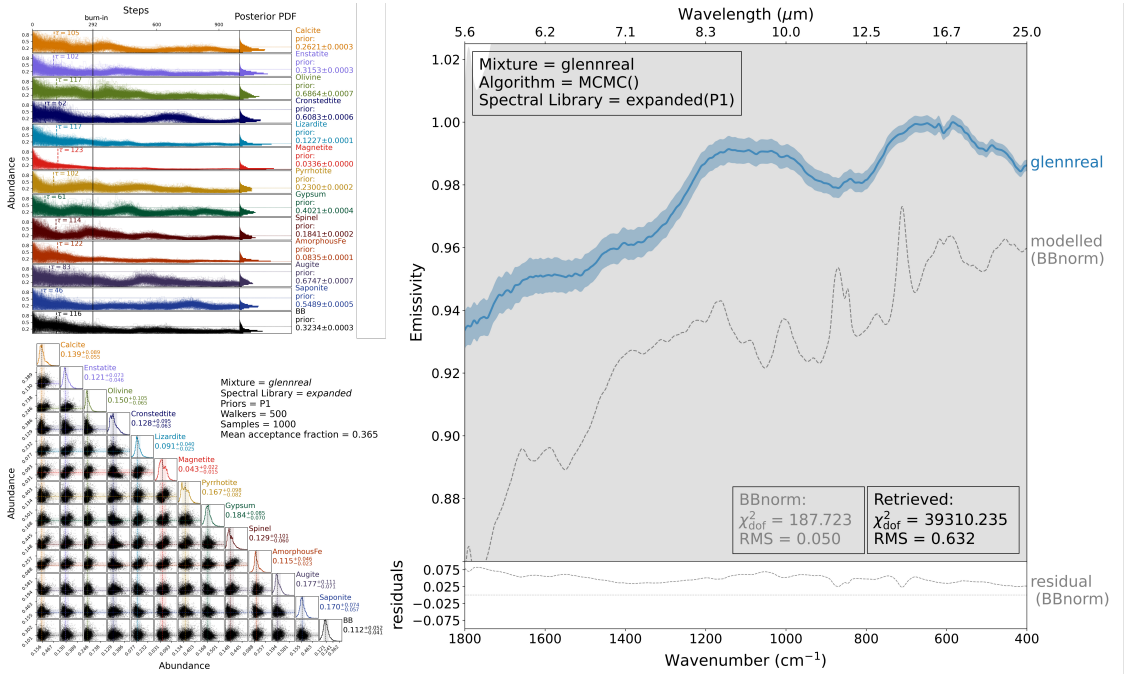


Figure A.33: *glennrealexpP1* `MCMC()` walkers and corner plots with model fit.

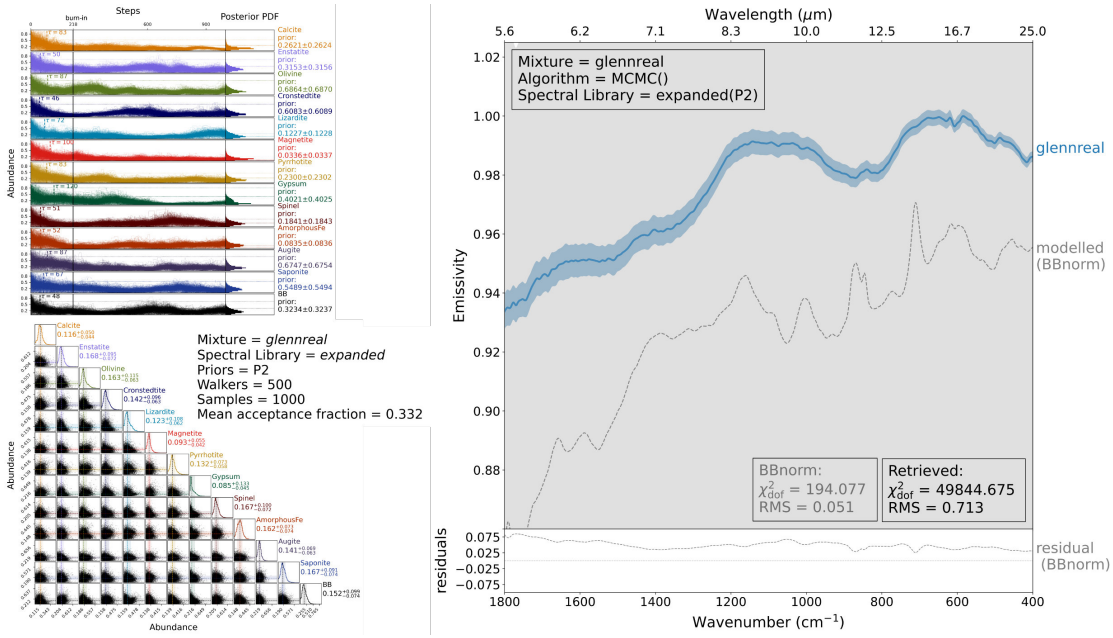


Figure A.34: *glennrealexpP2* `MCMC()` walkers and corner plots with model fit.

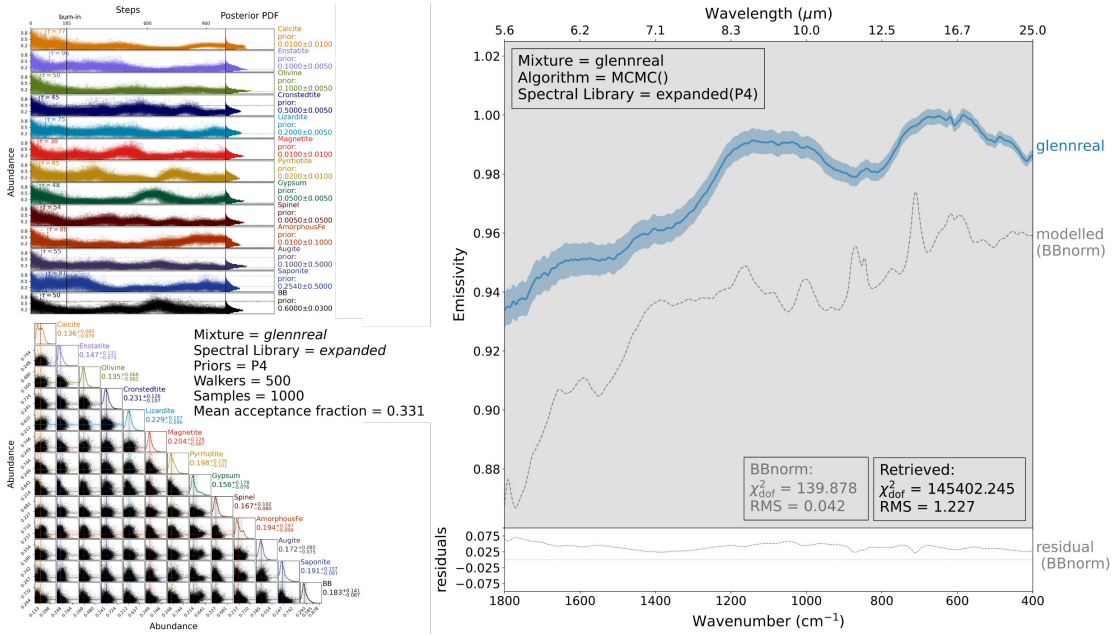


Figure A.35: *glennrealexpP4* `MCMC()` walkers and corner plots with model fit.

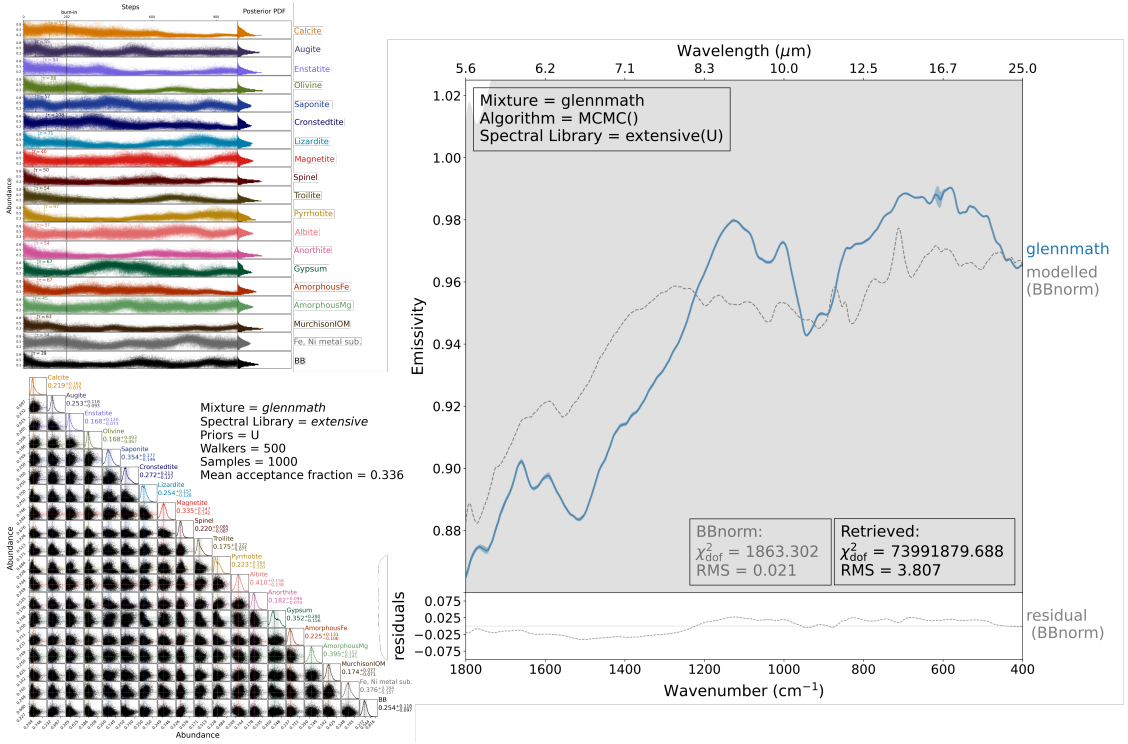


Figure A.36: *glennmathextU* `MCMC()` walkers and corner plots with model fit.

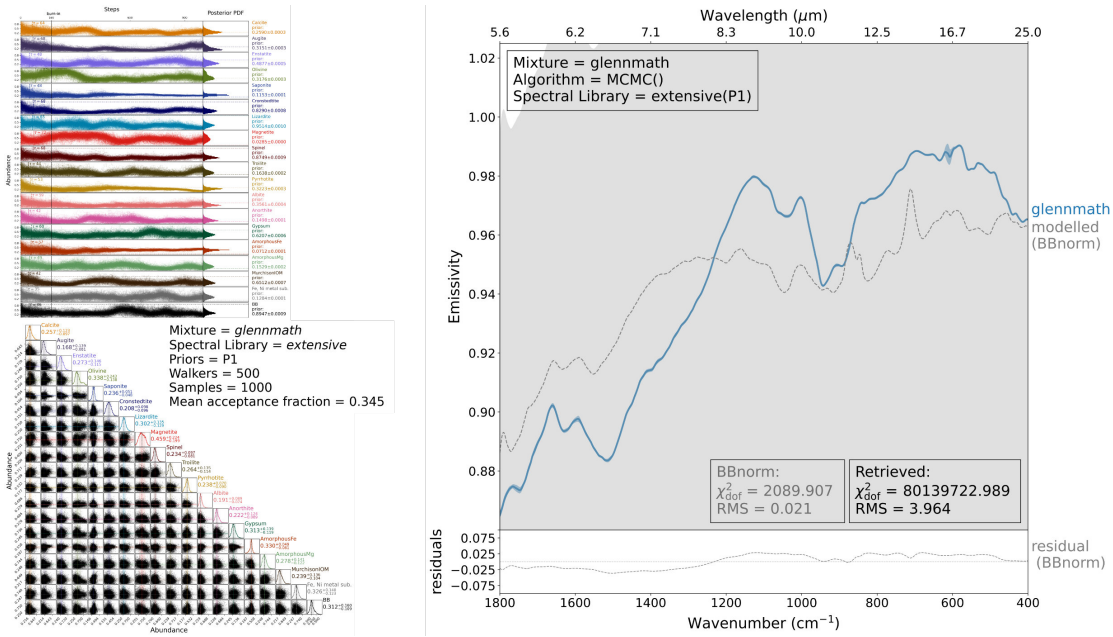


Figure A.37: *glennmathextP1* `MCMC()` walkers and corner plots with model fit.

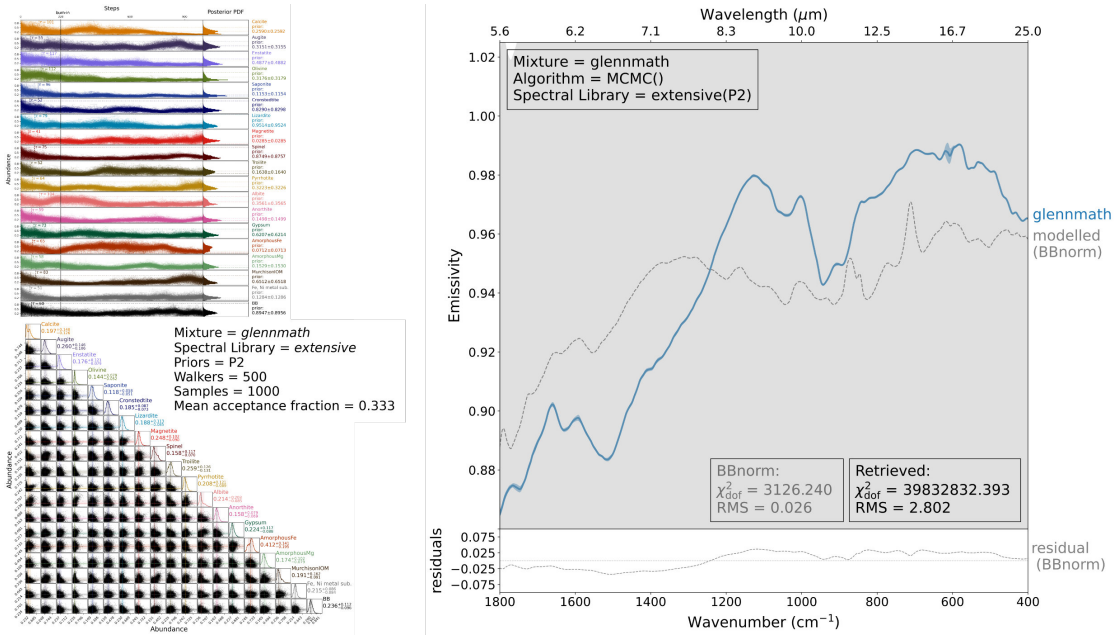


Figure A.38: *glennmathextP2* `MCMC()` walkers and corner plots with model fit.

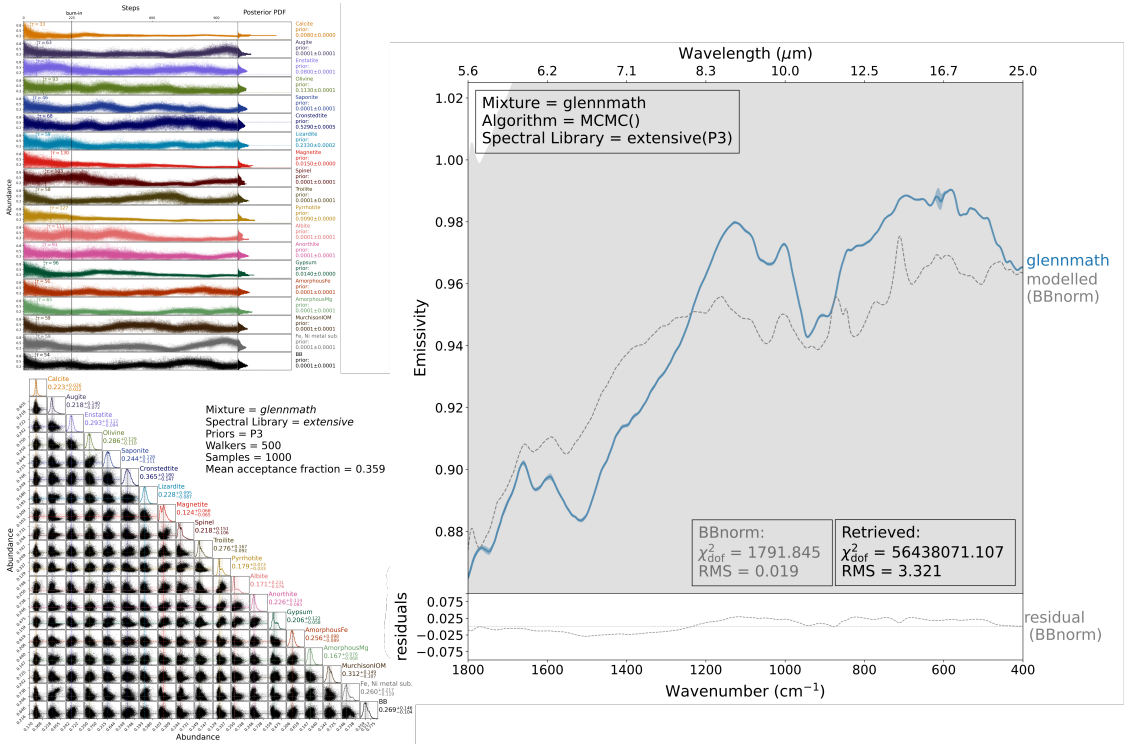


Figure A.39: *glennmathextP3* `MCMC()` walkers and corner plots with model fit.

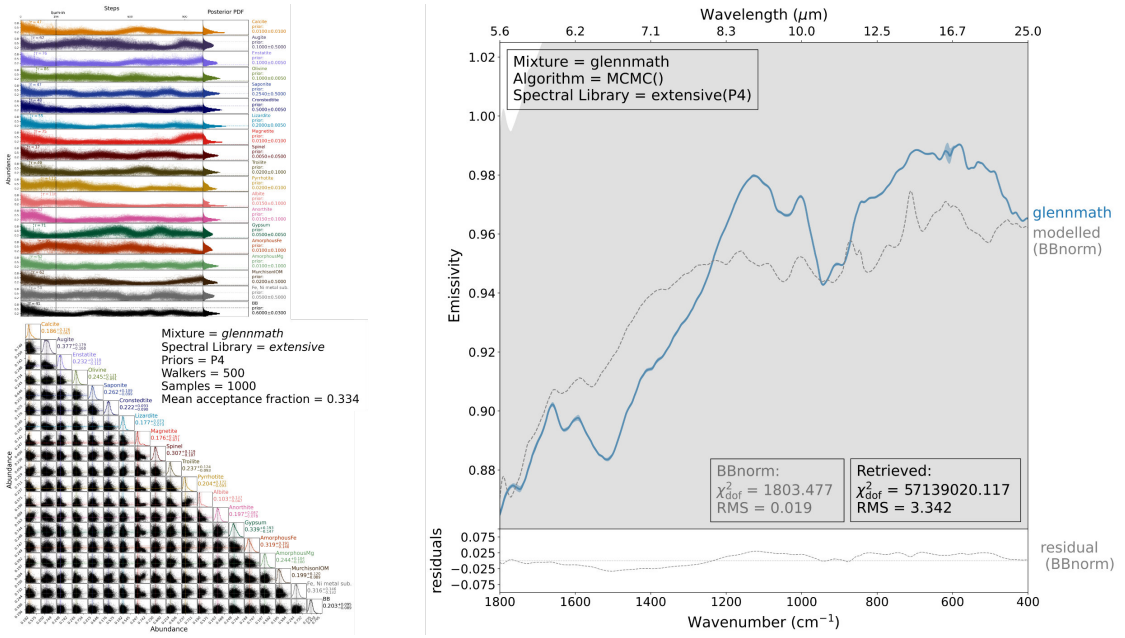


Figure A.40: *glennmathextP4* `MCMC()` walkers and corner plots with model fit.

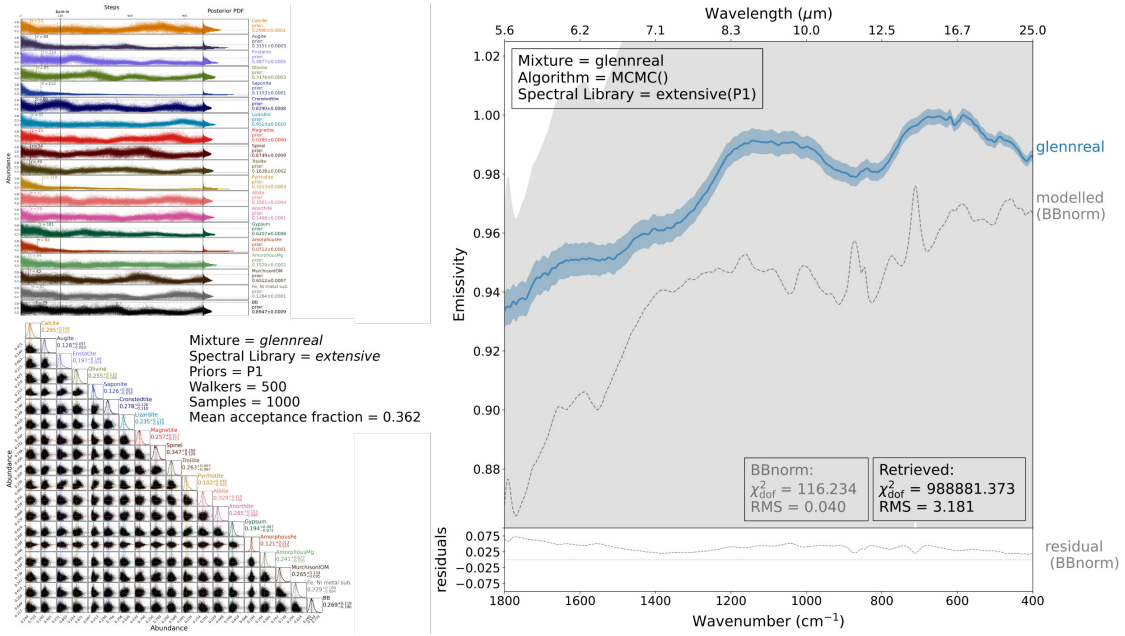


Figure A.41: *glennrealextP1* `MCMC()` walkers and corner plots with model fit.

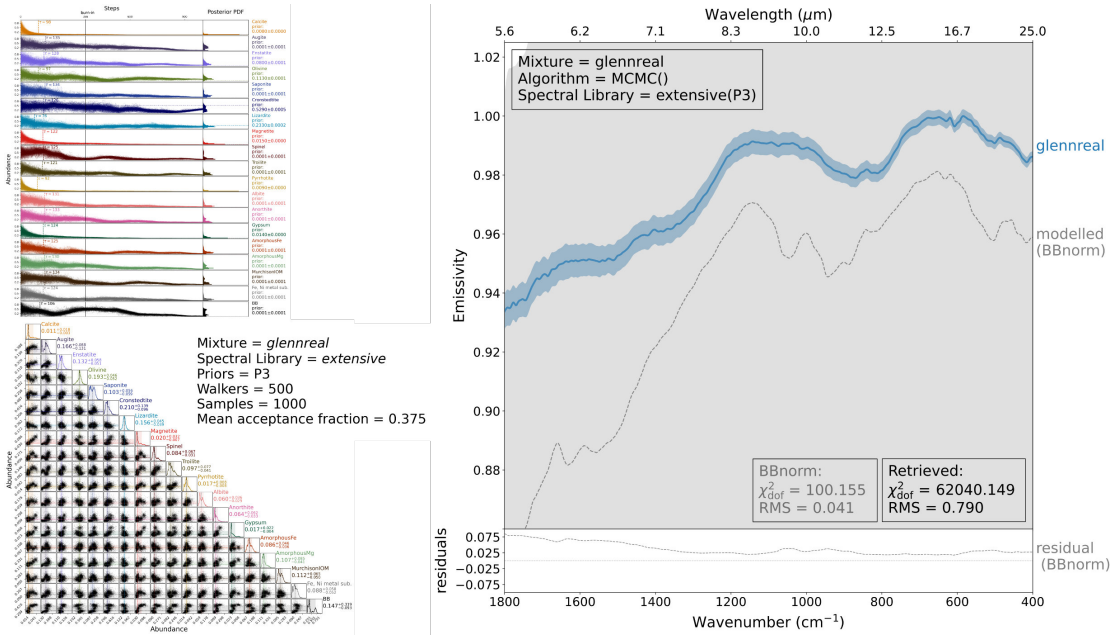


Figure A.42: *glennrealextP3* `MCMC()` walkers and corner plots with model fit.

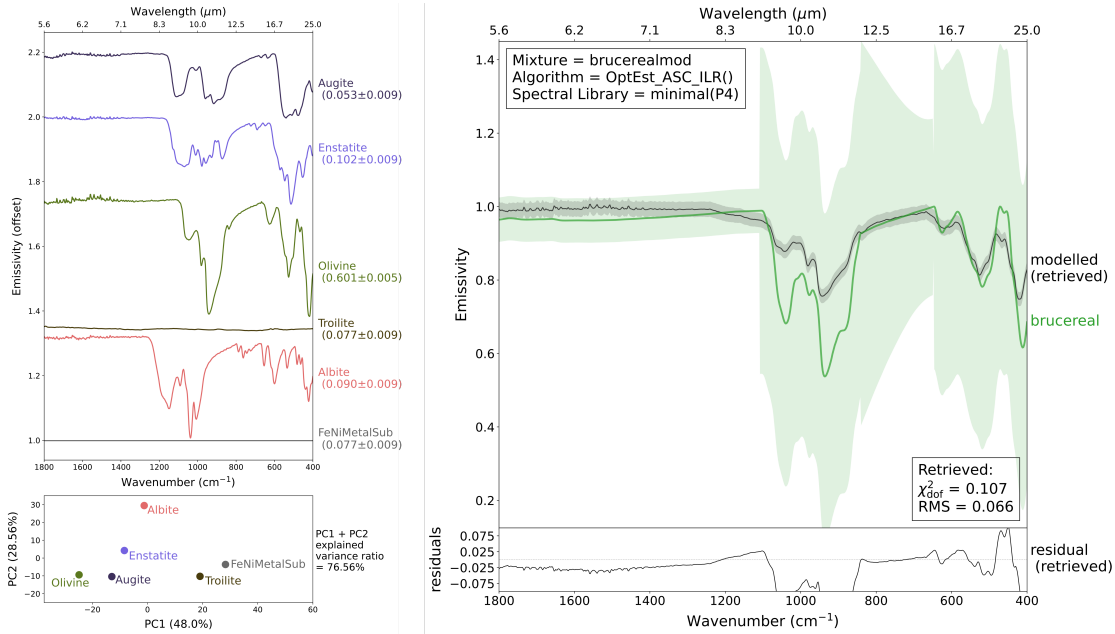


Figure A.43: *brucerealmodminP4* `OptEst_ASC_ILR()` reduced spectral library with model fit.

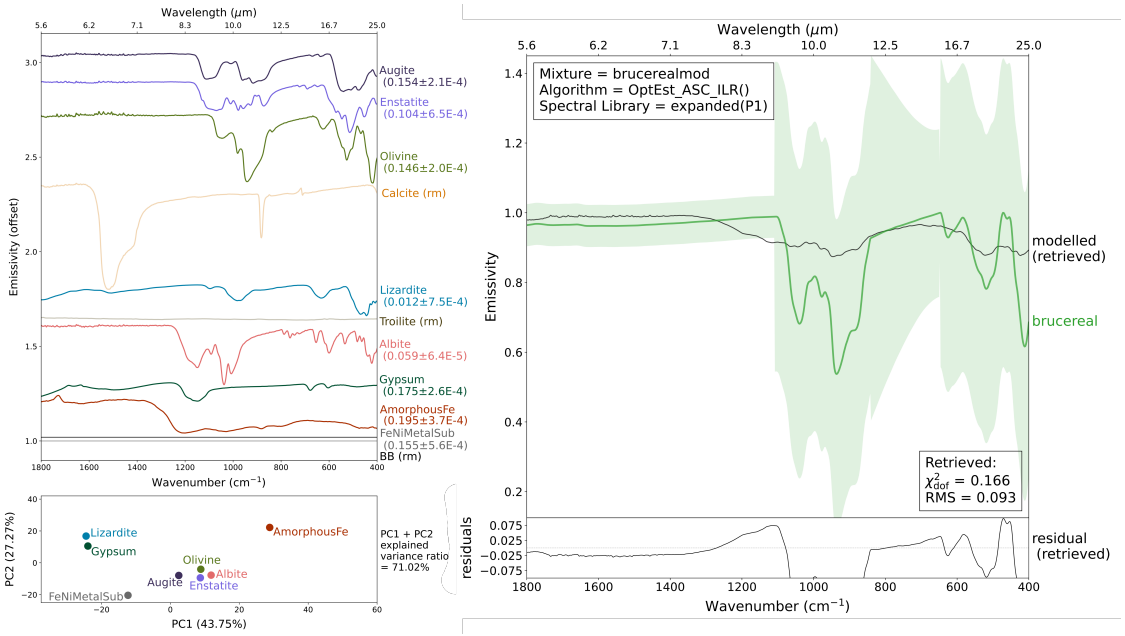


Figure A.44: *brucerealmodexpP1* `OptEst_ASC_ILR()` reduced spectral library with model fit.

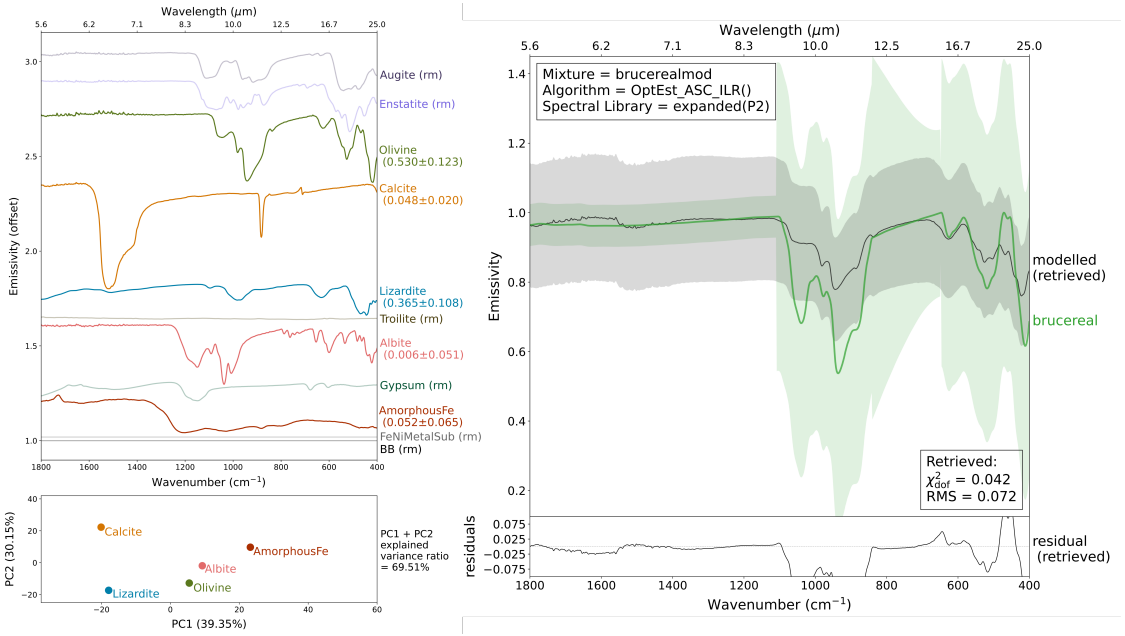


Figure A.45: *brucerealmodexpP2* `OptEst_ASC_ILR()` reduced spectral library with model fit.

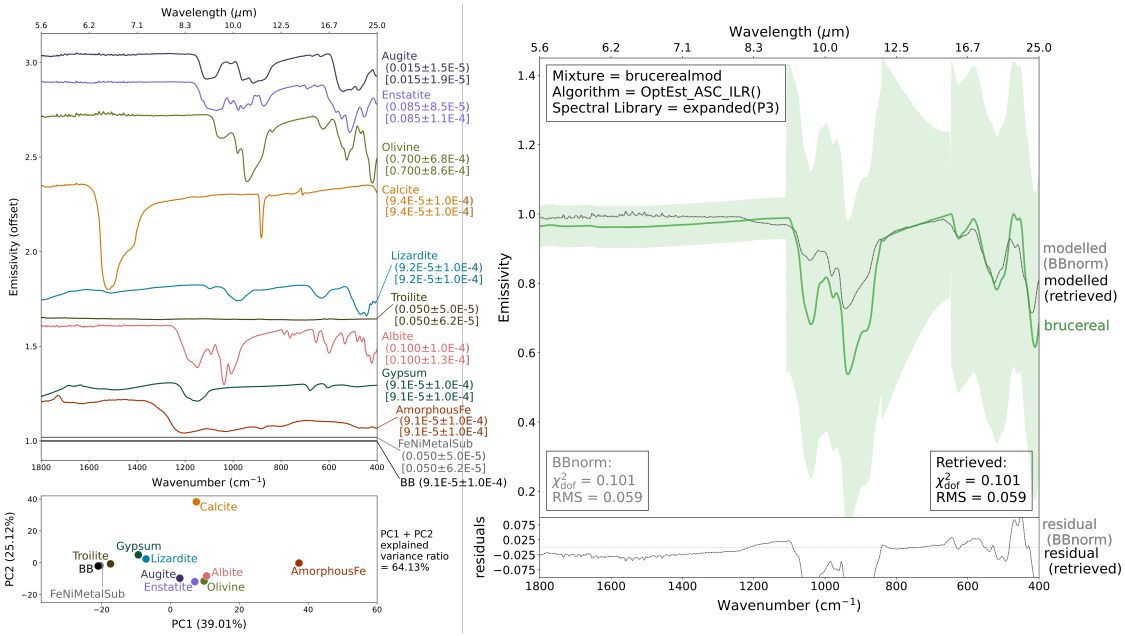


Figure A.46: *brucerealmodexpP3* `OptEst_ASC_ILR()` reduced spectral library with model fit.

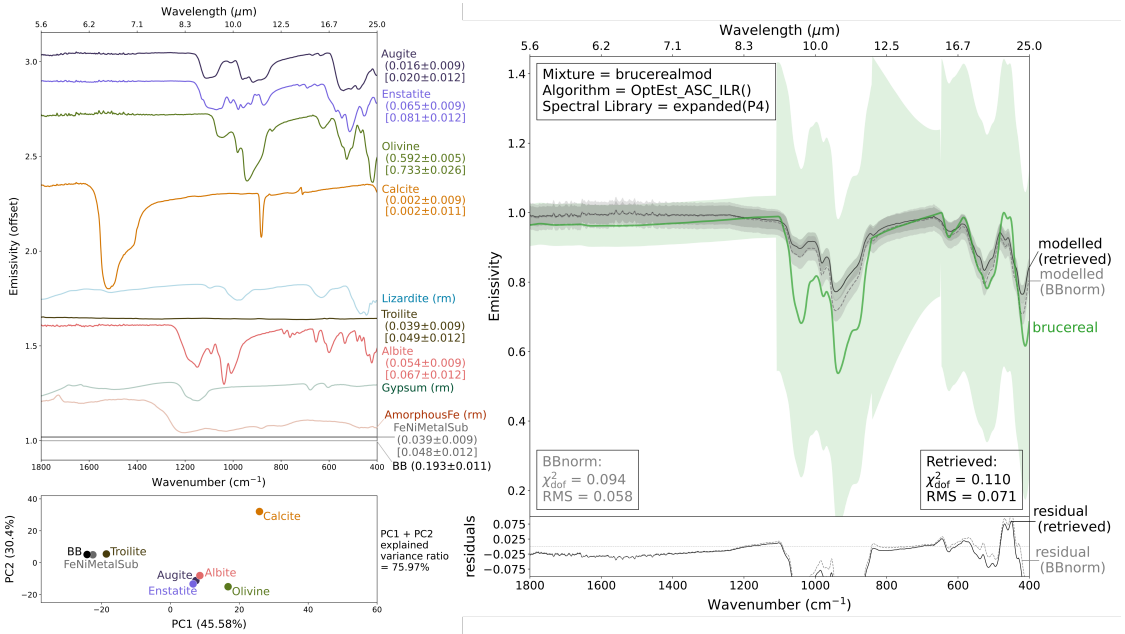


Figure A.47: *brucerealmodexpP4* `OptEst_ASC_ILR()` reduced spectral library with model fit.

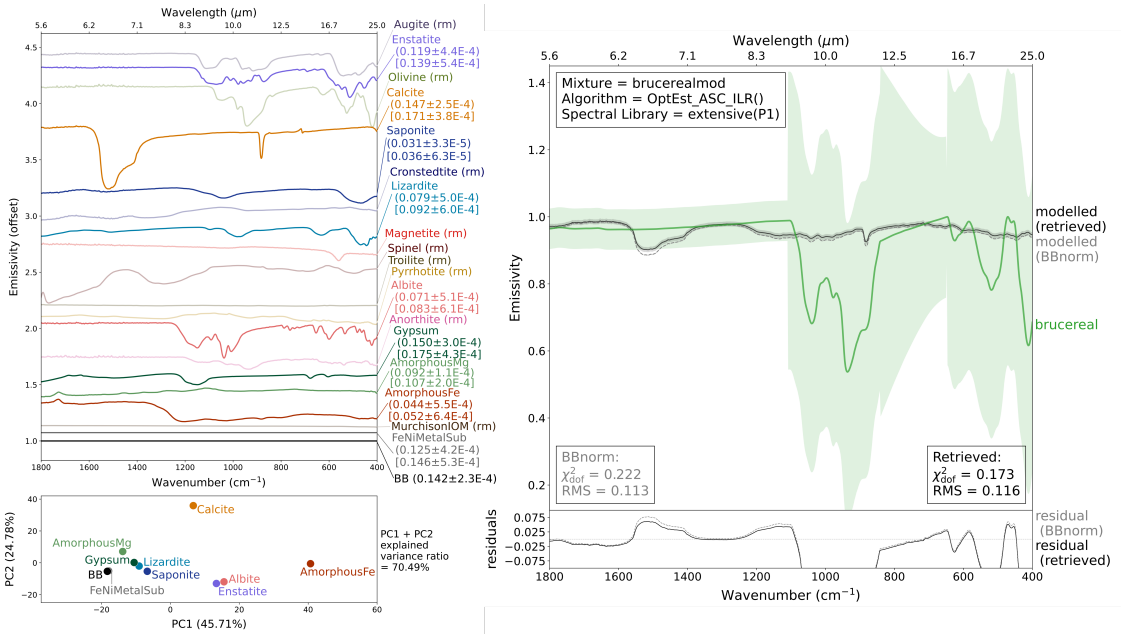


Figure A.48: *brucerealmodextP1* `OptEst_ASC_ILR()` reduced spectral library with model fit.

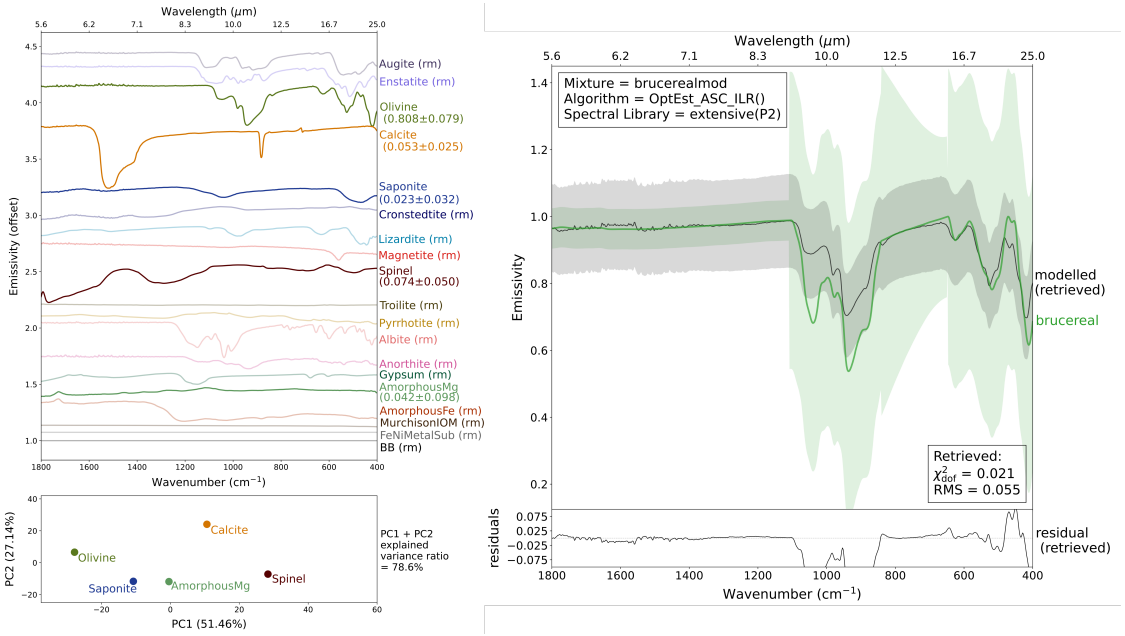


Figure A.49: *brucerealmodextP2* `OptEst_ASC_ILR()` reduced spectral library with model fit.

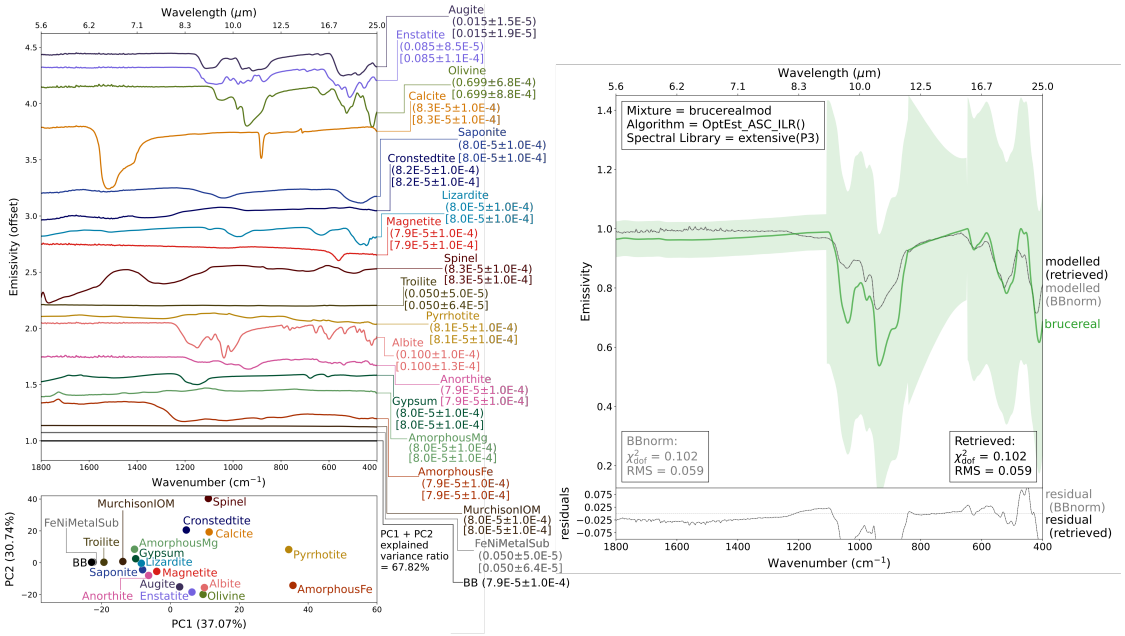


Figure A.50: *brucerealmodextP3* `OptEst_ASC_ILR()` reduced spectral library with model fit.

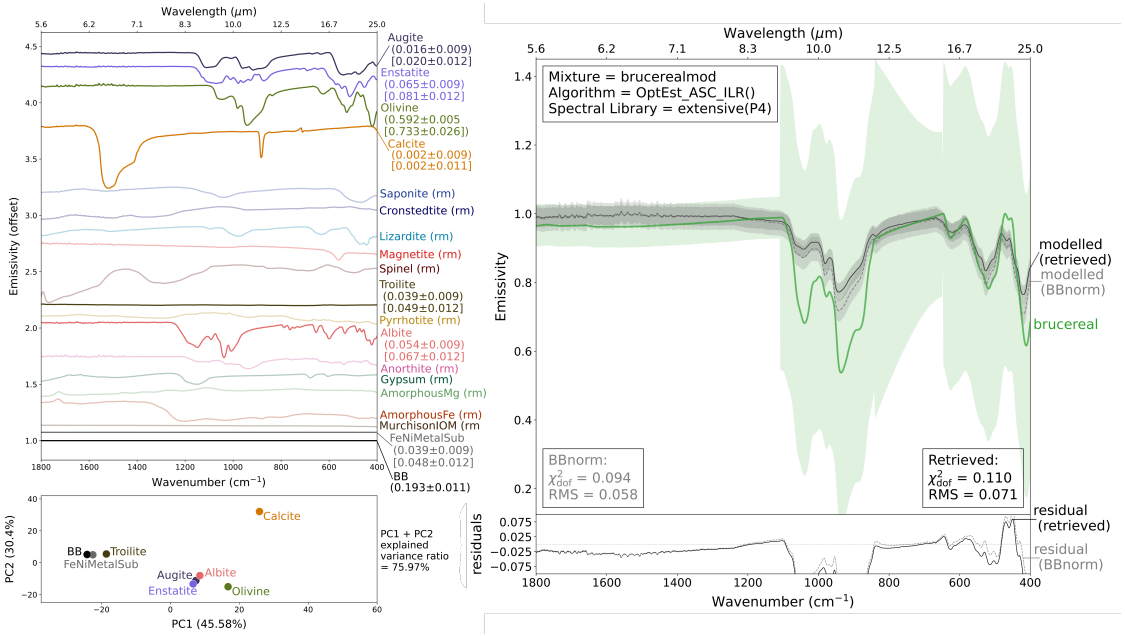


Figure A.51: *brucerealmodextP4*

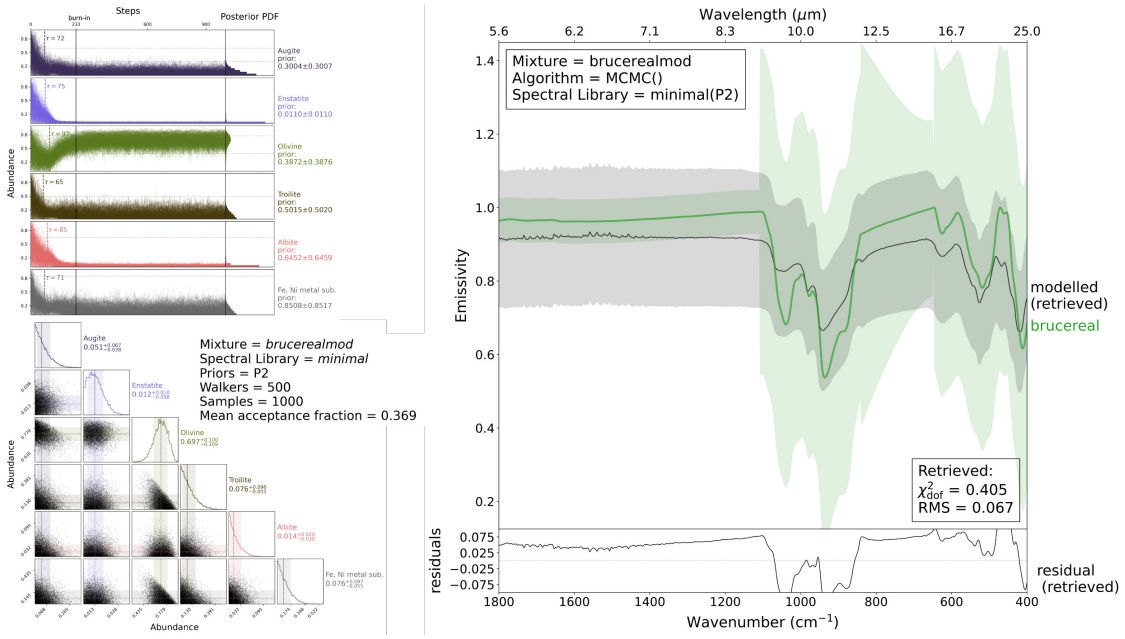


Figure A.52: *brucerealmodminP2* `MCMC()` walkers and corner plots with model fit.

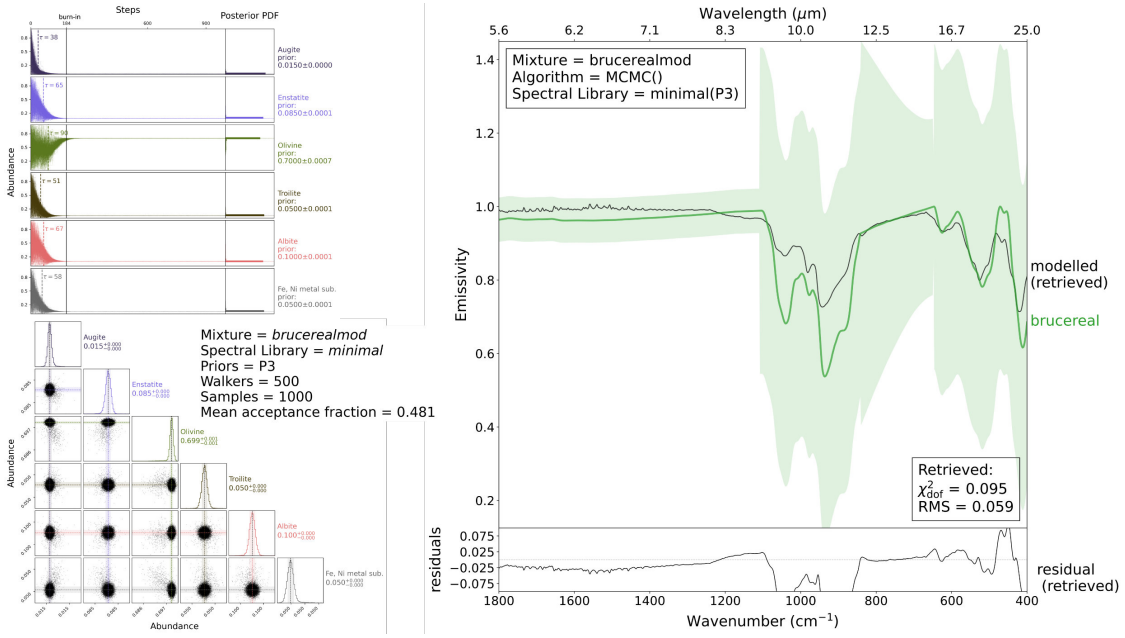


Figure A.53: *brucerealmodminP3* `MCMC()` walkers and corner plots with model fit.

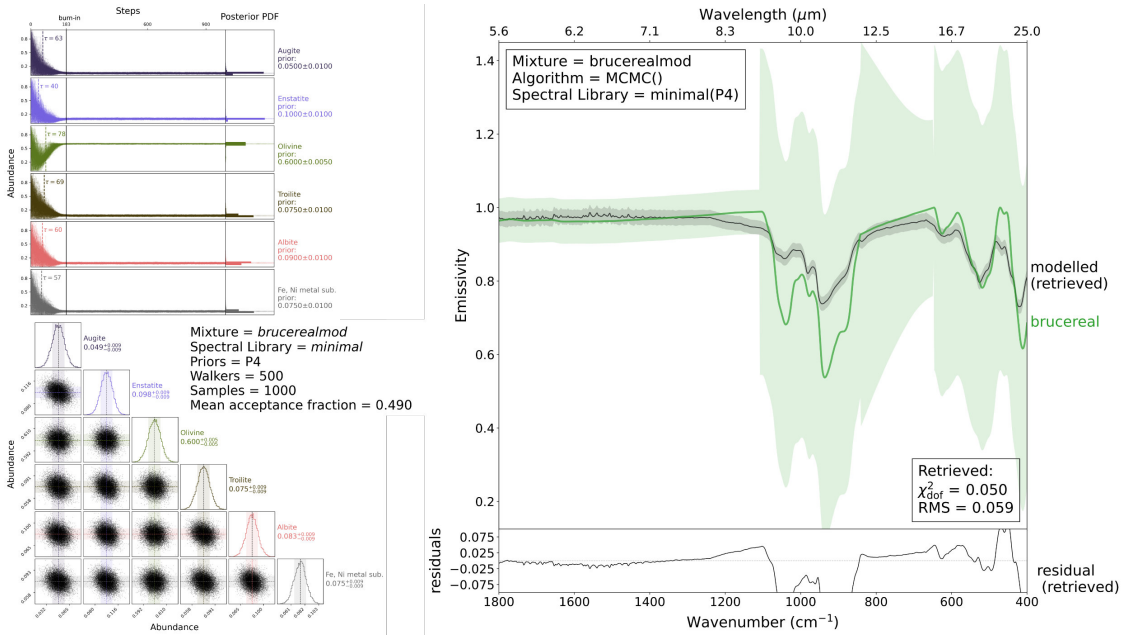


Figure A.54: *brucerealmodminP4* `MCMC()` walkers and corner plots with model fit.

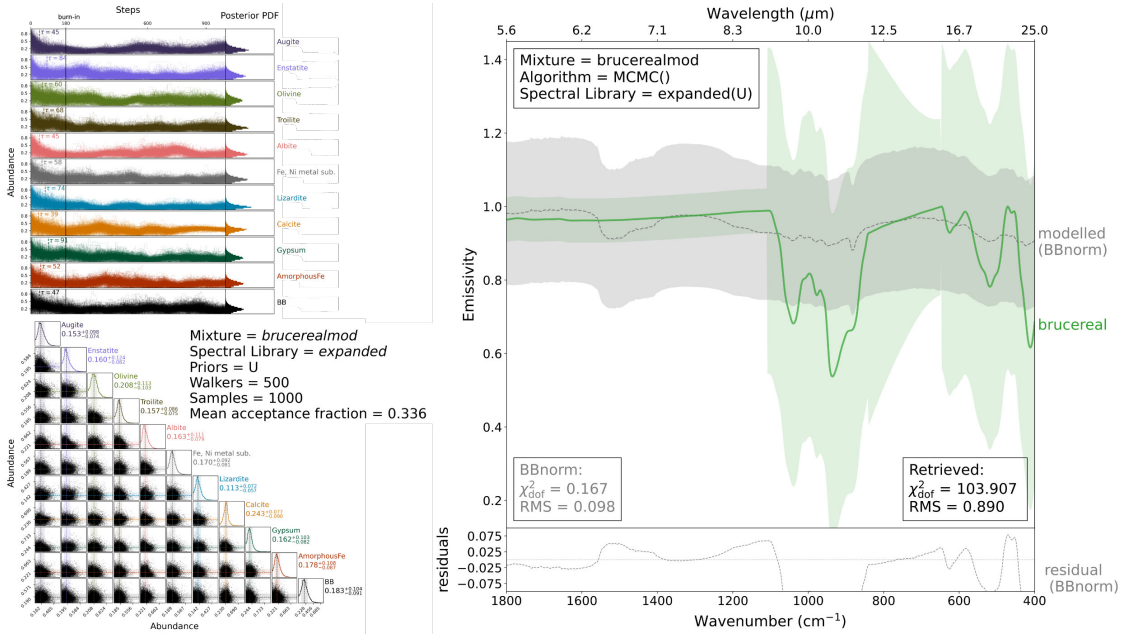


Figure A.55: *brucerealmodexpU* `MCMC()` walkers and corner plots with model fit.

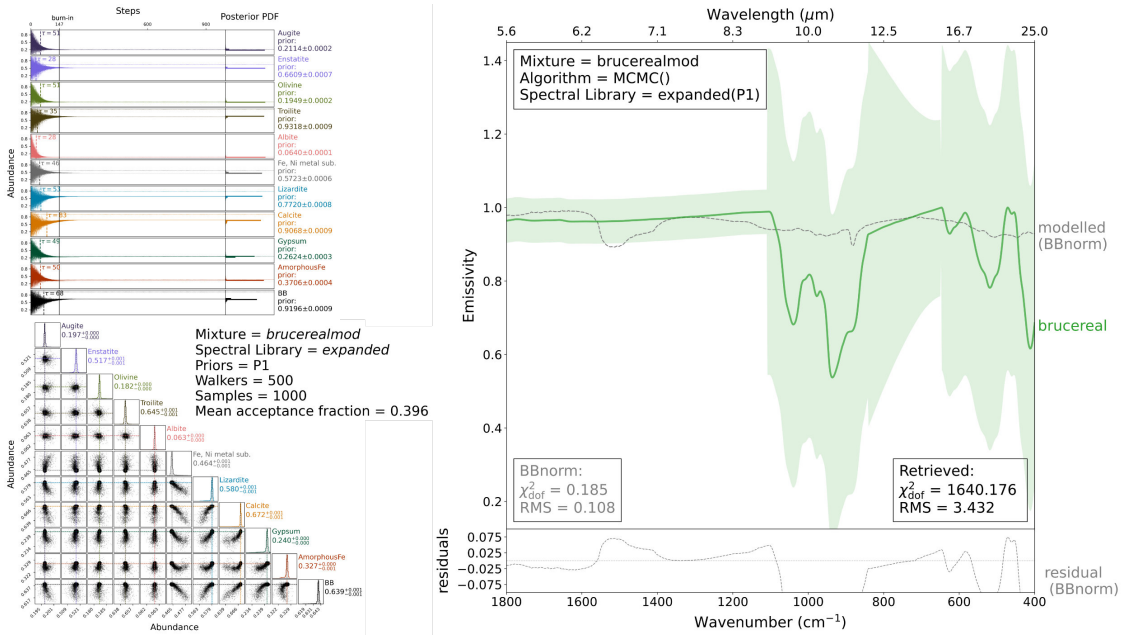


Figure A.56: *brucerealmodexpP1* `MCMC()` walkers and corner plots with model fit.

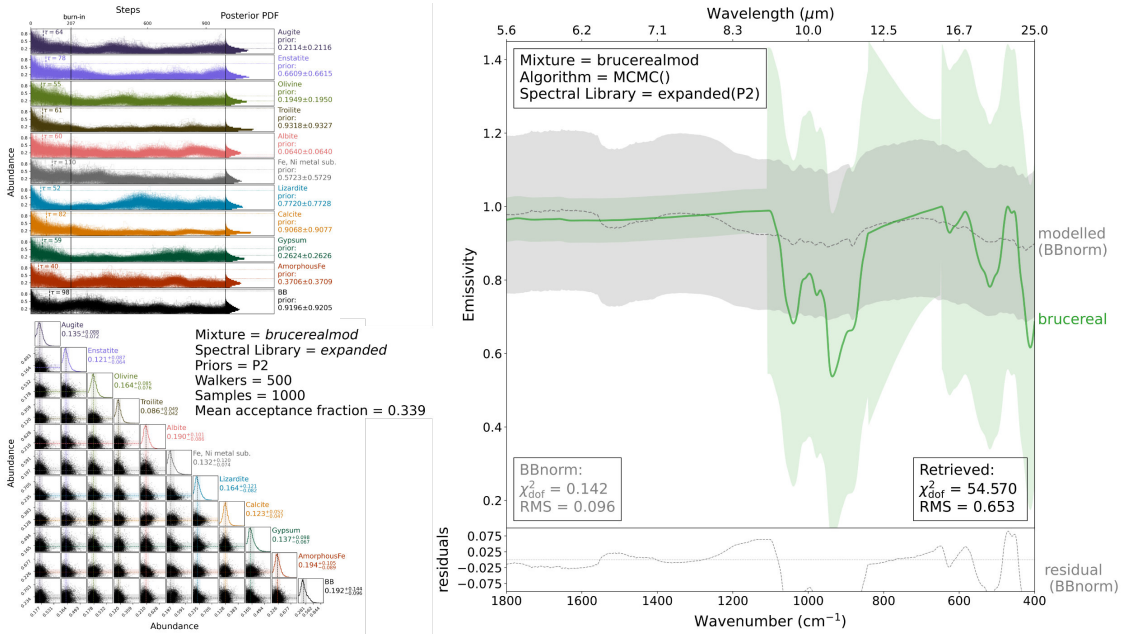


Figure A.57: *brucerealmodexpP2* `MCMC()` walkers and corner plots with model fit.

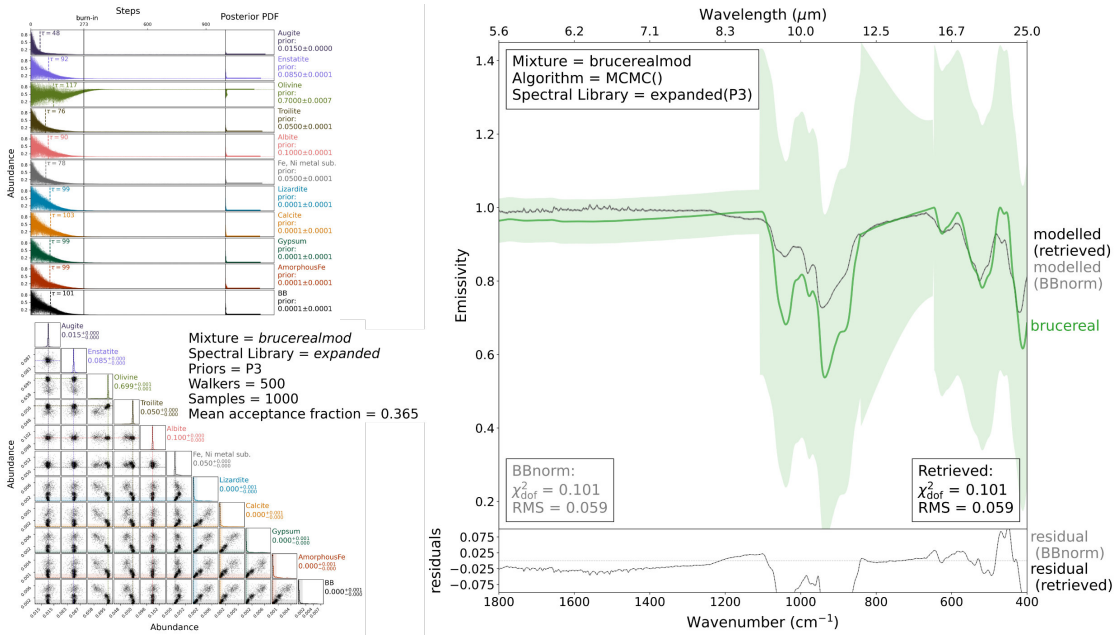


Figure A.58: *brucerealmodexpP3* `MCMC()` walkers and corner plots with model fit.

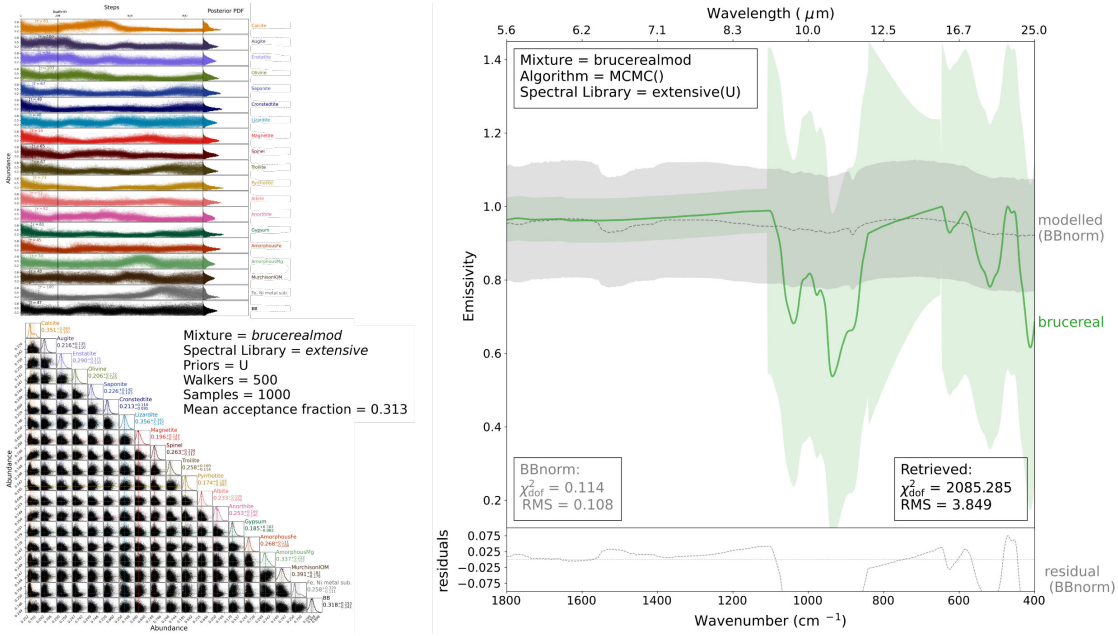


Figure A.59: *brucerealmodextU* `MCMC()` walkers and corner plots with model fit.

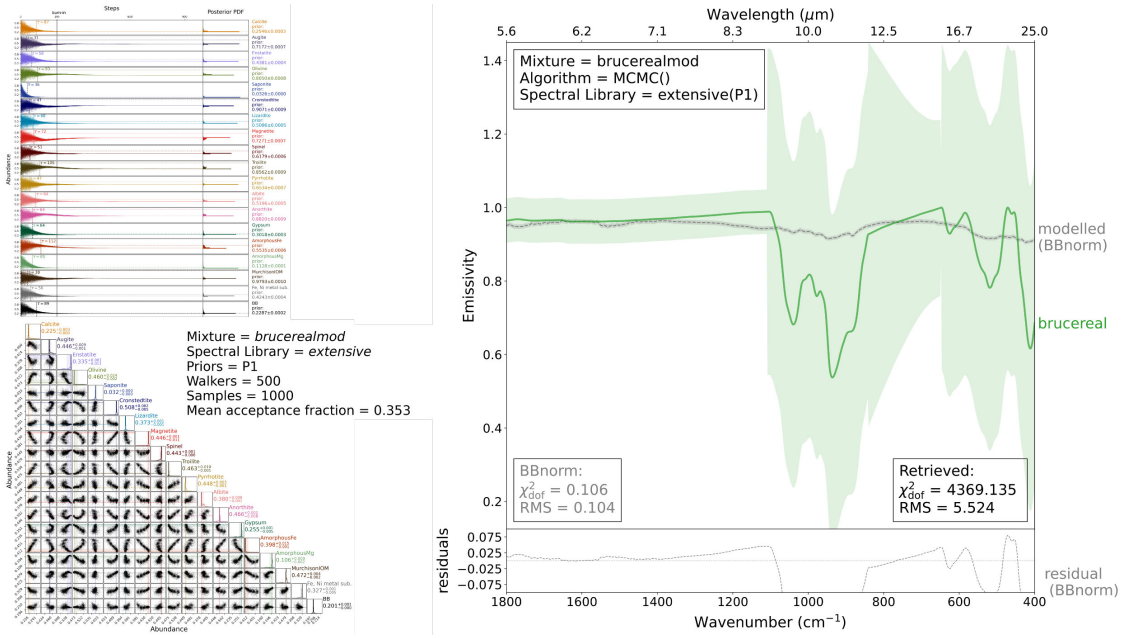


Figure A.60: *brucerealmodextP1* `MCMC()` walkers and corner plots with model fit.

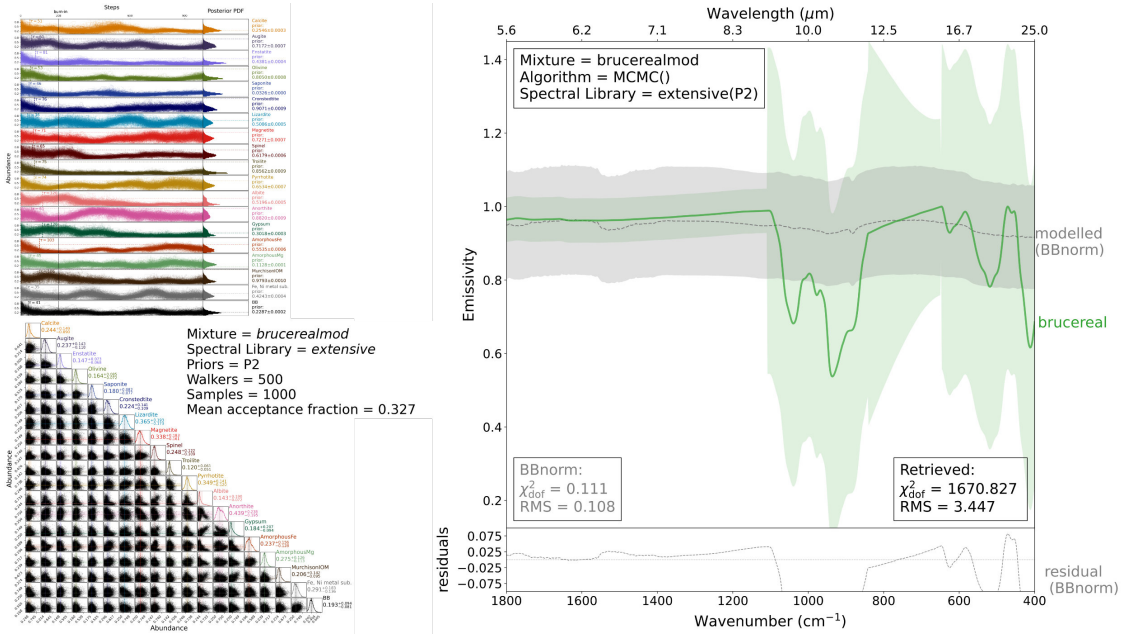


Figure A.61: *brucerealmodextP2* `MCMC()` walkers and corner plots with model fit.

Chapter B

Additional Results Tables to Accompany Chapters 5, 6 and 7

Table B.1: *brucerealexp* `WLS_ASC_ILR()` unmixing results.

End-member	**'True' Abundance**	**Retrieved Abundance**	**Uncertainty**	**Precision %**	**Accuracy σ**
Augite	0.015				
Enstatite	0.085				
Olivine	0.700	0.497	0.000495	0.10	410
Calcite		0.015	0.00017	1.11	91
Lizardite		0.250	0.00114	0.46	220
Troilite	0.050				
Albite	0.100				
Gypsum					
Amorphous Fe					
FeNiMetalSub BB	0.050	0.237	0.0.000900	0.38	209
RMS error	**0.0157**				
$\chi^2_{\mathbf{d.o.f}}$	**479.0**				

Table B.2: *brucemathext* `WLS_ASC_ILR()` unmixing results.

End-member	**'True' Abundance**	**Retrieved Abundance**	**Uncertainty**	**Precision %**	**Accuracy σ**
Augite	0.015				
Enstatite	0.085	0.795	0.00035	0.04	2006
Olivine	0.700				
Calcite					
Saponite					
Cronstedtite					
Lizardite					
Magnetite					
Spinel					
Troilite	0.050				
Pyrrhotite					
Albite	0.100	0.205	0.00035	0.17	297
Anorthite					
Gypsum					
Amorphous Mg					
Amorphous Fe					
MurchisonIOM					
FeNiMetalSub	0.050				
BB					
RMS error	**0.0560**				
$\chi^2_{\mathrm{d.o.f}}$	**13303.5**				

Table B.3: *glennrealmin* `WLS_ASC_ILR()` unmixing results.

End-member	**True' Abundance**	**Retrieved Abundance**	**Uncertainty**	**Precision %**	**Accuracy σ**
Enstatite	0.080				
Olivine	0.113				
Calcite	0.008				
Cronstedtite	0.529	0.1662	0.0078	4.67	47
Lizardite	0.233	0.3048	0.0049	1.61	-15
Magnetite	0.015				
Pyrrhotite	0.009	0.5291	0.0048	0.91	-108
Gypsum	0.014				
	RMS error	0.0066			
	$\chi^2_{d.o.f}$	4.577			

Table B.4: Results for *glennrealexp* `WLS_ASC_ILR()` unmixing.

End-member	**'True' Abundance**	**Retrieved Abundance [BBnorm]**	**Accuracy to 'True' Abundance σ [BBnorm]**
Augite	0.0000	0.0719 ± 0.0079 (10.99%) [0.1868 ± 0.0245 (13.11%)]	-9.10 [-7.63]
Enstatite	0.0800	rm	
Olivine	0.1130	0.0408 ± 0.0034 (8.38%) [0.1059 ± 0.0117 (11.01%)]	21.15 [0.60]
Calcite	0.0080	rm	
Saponite	0.0000	0.0412 ± 0.0165 (40.06%) [0.1070 ± 0.0435 (40.69%)]	-2.50 [-2.46]

Table B.4 continued from previous page

End-member	'True' Abundance	Retrieved Abundance [BBnorm]	Accuracy to 'True' Abundance σ [BBnorm]
Cronstedtite	0.5290	0.2149 ± 0.0100 (4.67%) [0.5585 ± 0.0477 (8.54%)]	31.27 [-0.62]
Lizardite	0.2330	rm	
Magnetite	0.0150	rm	
Spinel	0.0000	0.0160 ± 0.0033 (20.83%) [0.0417 ± 0.0092 (22.02%)]	-4.80 [-4.54]
Pyrrhotite	0.0090	rm	
Gypsum	0.0140	rm	
AmorphousFe	0.0000	rm	
BB	n/a	0.6153 ± 0.0122 (1.98%)	n/a
	RMS error	0.0034 [0.0468]	
	$\chi^2_{d.o.f}$	1.22 [102.0]	

Table B.5: Results for *glennmathext* `WLS_ASC_ILR()` unmixing.

End-member	'True' Abundance	Retrieved Abundance	Accuracy to 'True' Abundance σ
Augite	0.0000	rm	
Enstatite	0.0800	rm	
Olivine	0.1130	rm	
Calcite	0.0080	rm	
Saponite	0.0000	0.7641 ± 6.70E-04 (0.09%)	-1141.13

Table B.5 continued from previous page

End-member	'True' Abundance	Retrieved Abundance	Accuracy to 'True' Abundance σ
Cronstedtite	0.5290	rm	
Lizardite	0.2330	rm	
Magnetite	0.0150	rm	
Spinel	0.0000	rm	
Troilite	0.0000	rm	
Pyrrhotite	0.0090	rm	
Albite	0.0000	0.2359 ± 6.91E-04 (0.29%)	-341.57
Anorthite	0.0000	rm	
Gypsum	0.0140	rm	
AmorphousMg	0.0000	rm	
AmorphousFe	0.0000	rm	
MurchisonIOM	0.0000	rm	
FeNiMetalSub	0.0000	rm	
BB	n/a	rm	n/a
	RMS error	0.0216	
	$\chi^2_{d.o.f}$	1643.0	

Table B.6: Results for *glennrealext* `WLS_ASC_ILR()` unmixing.

End-member	'True' Abundance	Retrieved Abundance [BBnorm]	Accuracy to 'True' Abundance σ [BBnorm]
Calcite	0.0080	rm	
Augite	0.0000	rm	
Enstatite	0.0800	rm	

Table B.6 continued from previous page

End-member	'True' Abundance	Retrieved Abundance [BBnorm]	Accuracy to 'True' Abundance σ [BBnorm]
Olivine	0.1130	0.0886 ± 0.0026 (2.98%) [0.3174 ± 0.0843 (26.55%)]	9.25 [-2.43]
Saponite	0.0000	rm	
Cronstedtite	0.5290	rm	
Lizardite	0.2330	0.0761 ± 0.0092 (12.11%) [0.2725 ± 0.0791 (29.03%)]	17.04 [-0.50]
Magnetite	0.0150	rm	
Spinel	0.0000	0.0393 ± 0.0030 (7.73%) [0.1406 ± 0.0387 (27.50%)]	-12.94 [-3.64]
Troilite	0.0000	rm	
Pyrrhotite	0.0090	0.0109 ± 0.0343 (316.03%) [0.0389 ± 0.1233 (317.13%)]	-0.05 [-0.24]
Albite	0.0000	rm	
Anorthite	0.0000	0.0546 ± 0.0051 (9.28%) [0.1957 ± 0.0547 (27.97%)]	-10.77 [-3.58]
Gypsum	0.0140	0.0098 ± 0.0106 (109.01%) [0.0349 ± 0.0392 (112.16%)]	0.40 [-0.53]
AmorphousFe	0.0000	rm	
AmorphousMg	0.0000	rm	
MurchisonIOM	0.0000	rm	
FeNiMetalSub	0.0000	rm	
BB	n/a	0.7208 ± 0.0448 (6.21%)	n/a
	RMS error	0.0044 [0.0807]	

Table B.6 continued from previous page

End-member	'True' Abundance	Retrieved Abundance [BBnorm]	Accuracy to 'True' Abundance σ [BBnorm]
	$\chi^2_{d.o.f}$	1.39 [263.3]	

Table B.7: *brucemathminP3* `OptEst_ASC_ILR()` results. Accuracy calculations in relation to the 'true' abundances and prior abundances use the retrieved abundance uncertainties for σ.

End-member	'True' Abundance	Prior, P3	Retrieved Abundance	Accuracy to 'True' Abundance σ	Accuracy to P3 Abundance σ
Augite	0.015	0.0150 ± 1.50E-5 (0.10%)	0.0150 ± 1.50E-5 (0.10%)	-3.34E-10	-3.34E-10
Enstatite	0.085	0.0850 ± 8.50E-5 (0.10%)	0.0850 ± 8.08E-5 (0.10%)	9.91E-11	9.91E-11
Olivine	0.700	0.7000 ± 7.00E-4 (0.10%)	0.7000 ± 1.27E-4 (0.02%)	2.44E-10	2.44E-10
Troilite	0.050	0.0500 ± 5.00E-5 (0.10%)	0.0500 ± 4.84E-5 (0.10%)	-2.52E-10	-2.52E-10
Albite	0.100	0.1000 ± 1.00E-4 (0.10%)	0.1000 ± 9.07E-5 (0.09%)	-6.61E-11	-6.61E-11
FeNiMetalSub	0.050	0.0500 ± 5.00E-5 (0.10%)	0.0500 ± 4.85E-5 (0.10%)	-3.05E-10	-3.05E-10
		RMS	4.91E-15		
		red. Chi squ.	9.43E-23		

Table B.8: *brucemathminP4* `OptEst_ASC_ILR()` results. Accuracy calculations in relation to the 'true' abundances and prior abundances use the retrieved abundance uncertainties for σ.

End-member	**'True' Abundance**	**Prior, P4**	**Retrieved Abundance**	**Accuracy to 'True' Abundance** σ	**Accuracy to P4 Abundance** σ
Augite	0.015	0.0500 +- 0.0100 (20.0%)	0.0156 +- 0.0008 (5.11%)	-0.78	43.09
Enstatite	0.085	0.1000 +- 0.0100 (10.0%)	0.0848 +- 0.0009 (1.03%)	0.23	17.46
Olivine	0.700	0.6000 +- 0.0050 (0.8%)	0.6996 +- 0.0003 (0.04%)	1.30	-327.45
Troilite	0.050	0.0750 +-0.0100 (13.3%)	0.0507 +- 0.0052 (10.19%)	-0.14	4.70
Albite	0.100	0.0900 +- 0.0100 (11.1%)	0.1001 +- 0.0005 (0.48%)	-0.19	-21.17
FeNiMetalSub	0.050	0.0750 +- 0.0100 (13.3%)	0.0492 +- 0.0053 (10.84%)	0.16	4.85
		RMS	2.72E-05		
		red. Chi squ.	0.0025		

Table B.9: *brucerealminP1* `OptEst_ASC_ILR()` results. Accuracy calculations in relation to the 'true' abundances and prior abundances use the retrieved abundance uncertainties for σ.

End-member	**'True' Abundance**	**Prior, P1**	**Retrieved Abundance**	**Accuracy to 'True' Abundance** σ	**Accuracy to P1 Abundance** σ
Augite	0.015	0.3004 ± 0.0003 (0.1%)	0.2186 ± 0.0003 (0.12%)	-758.8	304.6
Enstatite	0.085	0.0110 ± 1.10E-5 (0.1%)	0.0109 ± 1.10E-5 (0.10%)	6734.0	13.2
Olivine	0.700	0.3782 ± 0.0004 (0.1%)	0.3382 ± 0.0003 (0.08%)	1327.9	179.9
Troilite	0.050	0.5015 ± 0.0005 (0.1%)	0.2244 ± 0.0004 (0.20%)	-390.9	621.1
Albite	0.100	0.6452 ± 0.0006 (0.1%)	0.1339 ± 0.0005 (0.35%)	-71.8	1084.3
FeNiMetalSub	0.050	0.8508 ± 0.0009 (0.1%)	0.0740 ± 0.0005 (0.74%)	-43.7	1416.1
		RMS	0.02038544		
		red. Chi squ.	764.743053		

Table B.9 continued from previous page

End-member	'True' Abundance	Prior, P1	Retrieved Abundance	Accuracy to 'True' Abundance σ	Accuracy to P1 Abundance σ

Table B.10: *brucerealminP2* `OptEst_ASC_ILR()` results. Accuracy calculations in relation to the 'true' abundances and prior abundances use the retrieved abundance uncertainties for σ.

End-member	'True' Abundance	Prior, P2	Retrieved Abundance	Accuracy to 'True' Abundance σ	Accuracy to P2 Abundance σ
Augite	0.015	0.3004 ± 0.3007 (100.1%)	0.1053 ± 0.0008 (0.75%)	-115.0	248.5
Enstatite	0.085	0.0110 ± 0.110 (100.1%)			
Olivine	0.700	0.3782 ± 0.3876 (100.1%)	0.5195 ± 0.0005 (0.10%)	339.1	-248.5
Troilite	0.050	0.5015 ± 0.5020 (100.1%)			
Albite	0.100	0.6452 ± 0.6459 (100.1%)			
FeNiMetalSub	0.050	0.8508 ± 0.8517 (100.1%)	0.3752 ± 0.0005 (0.13%)	-672.4	983.4
		RMS	0.016997148		
		red. Chi squ.	525.883445		

Table B.11: *brucerealminP3* `OptEst_ASC_ILR()` results. Accuracy calculations in relation to the 'true' abundances and prior abundances use the retrieved abundance uncertainties for σ.

End-member	'True' Abundance	Prior, P3	Retrieved Abundance	Accuracy to 'True' Abundance σ	Accuracy to P3 Abundance σ
Augite	0.015	0.0150 ± 1.50E-5 (0.10%)	0.0153 ± 1.50E-5 (0.10%)	-20.4	-20.4
Enstatite	0.085	0.0850 ± 8.50E-5 (0.10%)	0.0951 ± 0.0001 (0.09%)	-121.2	-121.2

Table B.11 continued from previous page

End-member	'True' Abundance	Prior, P3	Retrieved Abundance	Accuracy to 'True' Abundance σ	Accuracy to P3 Abundance σ
Olivine	0.700	0.7000 ± 7.00E-4 (0.10%)	0.6560 ± 0.0001 (0.02%)	303.9	303.9
Troilite	0.050	0.0500 ± 5.00E-5 (0.10%)	0.0588 ± 4.93E-5 (0.08%)	-177.6	-177.6
Albite	0.100	0.1000 ± 1.00E-4 (0.10%)	0.1156 ± 0.0001 (0.08%)	-162.6	-162.6
FeNiMetalSub	0.050	0.0500 ± 5.00E-5 (0.10%)	0.0592 ± 4.93E-5 (0.08%)	-187.3	-187.3
		RMS	0.027269773		
		red. Chi squ.	1703.380642		

Table B.12: *brucerealminP4* `OptEst_ASC_ILR()` results. Accuracy calculations in relation to the 'true' abundances and prior abundances use the retrieved abundance uncertainties for σ.

End-member	'True' Abundance	Prior, P4	Retrieved Abundance	Accuracy to 'True' Abundance σ	Accuracy to P4 Abundance σ
Augite	0.015	0.0500 ± 0.0100 (20.0%)	0.1045 ± 0.0008 (0.75%)	-114.9	-70.0
Enstatite	0.085	0.1000 ± 0.0100 (10.0%)			
Olivine	0.700	0.6000 ± 0.0050 (0.8%)	0.5203 ± 0.0005 (0.10%)	340.2	150.9
Troilite	0.050	0.0750 ±0.0100 (13.3%)			
Albite	0.100	0.0900 ± 0.0100 (11.1%)			
FeNiMetalSub	0.050	0.0750 ± 0.0100 (13.3%)	0.3752 ± 0.0005 (0.13%)	-674.5	-622.6
		RMS	0.01699614		
		red. Chi squ.	525.8875545		

Table B.13: *brucemathexpP1* `OptEst_ASC_ILR()` results. Accuracy calculations in relation to the 'true' abundances and prior abundances use the retrieved abundance uncertainties for σ.

End-member	**'True' Abundance**	**Prior, P1**	**Retrieved Abundance**	**Accuracy to 'True' Abundance** σ	**Accuracy to P1 Abundance** σ
Augite	0.015	0.2114 ± 0.0002 (0.10%)	0.2048 ± 0.0002 (0.10%)	-940.7	32.8
Enstatite	0.085	0.6609 ± 0.0007 (0.10%)	0.2305 ± 0.0004 (0.17%)	-366.3	1083.2
Olivine	0.700	0.1949 ± 0.0002 (0.10%)	0.3664 ± 0.0002 (0.04%)	2081.0	-1069.8
Calcite	0.000	0.9068 ± 0.0009 (0.10%)	0.0208 ± 0.0001 (0.43%)	-231.1	9834.7
Lizardite	0.000	0.7720 ± 0.0008 (0.10%)	0.0191 ± 0.0004 (2.26%)	-44.2	1746.7
Troilite	0.050	0.9318 ± 0.0009 (0.10%)			
Albite	0.100	0.0640 ± 0.0001 (0.10%)	0.0597 ± 0.0001 (0.11%)	634.6	67.0
Gypsum	0.000	0.2624 ± 0.0003 (0.10%)	0.0725 ± 0.0002 (0.33%)	-304.9	799.1
AmorphousFe	0.000	0.3706 ± 0.0004 (0.10%)	0.0263 ± 0.0002 (0.79%)	-126.1	1653.3
FeNiMetalSub	0.050	0.5723 ± 0.0006 (0.10%)			
BB	n/a	0.9196 ± 0.0009 (0.10%)			
		RMS	**0.0242**		
		red. Chi squ.	**2406.6**		

Table B.14: *brucemathexpP2* `OptEst_ASC_ILR()` results. Accuracy calculations in relation to the 'true' abundances and prior abundances use the retrieved abundance uncertainties for σ.

End-member	**'True' Abundance**	**Prior, P2**	**Retrieved Abundance**	**Accuracy to 'True' Abundance** σ	**Accuracy to P2 Abundance** σ
Augite	0.015	0.2114 ± 0.2116 (100.1%)	0.0150 ± 0.0008 (5.55%)	-0.005	236.0
Enstatite	0.085	0.6609 ± 0.6615 (100.1%)	0.0850 ± 0.0009 (1.03%)	0.001	655.7
Olivine	0.700	0.1949 ± 0.1958 (100.1%)	0.7000 ± 0.0003 (0.04%)	0.005	-1638.4

Table B.14 continued from previous page

End-member	'True' Abundance	Prior, P2	Retrieved Abundance	Accuracy to 'True' Abundance σ	Accuracy to P2 Abundance σ
Calcite	0.000	0.9068 ± 0.9077 (100.1%)	5.23E-7 ± 1.14E-4 (21809.10%)	-0.005	7951.4
Lizardite	0.000	0.7720 ± 0.7728 (100.1%)			
Troilite	0.050	0.9318 ± 0.9327 (100.1%)	0.0500 ± 0.0086 (17.15%)	0.001	102.8
Albite	0.100	0.0640 ± 0.0640 (100.1%)	0.100 ± 0.0005 (0.52%)	0.004	-69.0
Gypsum	0.000	0.2624 ± 0.2626 (100.1%)			
AmorphousFe	0.000	0.3706 ± 0.3709 (100.1%)			
FeNiMetalSub	0.050	0.5723 ± 0.5729 (100.1%)	0.0500 ± 0.0088 (17.58%)	-0.001	59.4
BB	n/a	0.9196 ± 0.9205 (100.1%)			
		RMS	**1.55E-07**		
		red. Chi squ.	**8.54E-08**		

Table B.15: *brucemathexpP4* `OptEst_ASC_ILR()` results. Accuracy calculations in relation to the 'true' abundances and prior abundances use the retrieved abundance uncertainties for σ.

End-member	'True' Abundance	Prior, P4	Retrieved Abundance [BBnorm]	Accuracy to 'True' Abundance σ [BBnorm value]	Accuracy to P4 Abundance σ [BBnorm value]
Augite	0.015	0.0500 ± 0.0100 (20.0%)	0.0169 ± 0.0011 (6.50%) [0.0181 ± 0.0012 (6.61%)]	-1.7 [-2.6]	30.2
Enstatite	0.085	0.1000 ± 0.0100 (10.0%)	0.0840 ± 0.0010 (1.16%) [0.0902 ± 0.0015 (1.65%)]	1.1 [-3.5]	16.5
Olivine	0.700	0.6000 ± 0.0050 (0.8%)	0.6998 ± 0.0003 (0.05%) [0.7514 ± 0.0088 (1.17%)]	0.7 [-5.8]	-313.8

Table B.15 continued from previous page

End-member	'True' Abundance	Prior, P4	Retrieved Abundance [BBnorm]	Accuracy to 'True' Abundance σ [BBnorm value]	Accuracy to P4 Abundance σ [BBnorm value]
Calcite	0.000	0.0010 ± 0.0100 (1000.0%)	0.0003 ± 0.0001 (38.88%) [0.0003 ± 0.0001 (38.90%)]	-2.6 [-2.6]	6.6
Lizardite	0.000	0.0001 ± 0.0100 (1000.0%)	rm		
Troilite	0.050	0.0750 ± 0.0100 (13.3%)	0.0300 ± 0.0060 (19.95%) [0.0322 ± 0.0064 (19.98%)]	3.4 [2.8]	7.5
Albite	0.100	0.0900 ± 0.0100 (11.1%)	0.0993 ± 0.0005 (0.54%) [0.1067 ± 0.0014 (1.29%)]	1.3 [-4.8]	-17.5
Gypsum	0.000	0.0001 ± 0.0100 (1000.0%)	rm		
AmorphousFe	0.000	0.0001 ± 0.0100 (10000.0%)	0.0011 ± 0.0006 (52.72%) [0.0012 ± 0.0006 (52.73%)]	-1.9 [-1.9]	-1.7
FeNiMetalSub	0.050	0.0750 ± 0.0100 (13.3%)	rm		
BB	n/a	0.2500 ± 0.0125 (5.0%)	0.0687 ± 0.0063 (9.22%)	n/a	28.6
		RMS	**7.45E-05** **[0.0098]**		
		red. Chi squ.	**0.024** **[361.6]**		

Table B.16: *brucerealexpP1* `OptEst_ASC_ILR()` results. Accuracy calculations in relation to the 'true' abundances and prior abundances use the retrieved abundance uncertainties for σ.

End-member	**'True' Abundance**	**Prior, P1**	**Retrieved Abundance**	**Accuracy to 'True' Abundance** σ	**Accuracy to P1 Abundance** σ
Augite	0.015	0.2114 +- 0.0002 (0.10%)	0.1750 +- 0.0002 (0.12%)	-780.7	177.2
Enstatite	0.085	0.6609 +- 0.0007 (0.10%)	0.1200 +-0.0005 (0.41%)	-71.1	1098.1
Olivine	0.700	0.1949 +- 0.0002 (0.10%)	0.2082 +- 0.0002 (0.09%)	2752.8	-74.8
Calcite	0.000	0.9068 +- 0.0009 (0.10%)	0.0190 +- 0.0002 (0.85%)	-118.1	5505.0
Lizardite	0.000	0.7720 +- 0.0008 (0.10%)	0.1510 +- 0.0005 (0.36%)	-276.8	1138.0
Troilite	0.050	0.9318 +- 0.0009 (0.10%)			
Albite	0.100	0.0640 +- 0.0001 (0.10%)	0.0586 +- 0.0001 (0.11%)	648.4	83.6
Gypsum	0.000	0.2624 +- 0.0003 (0.10%)	0.1574 +- 0.0003 (0.16%)	-624.5	416.7
AmorphousFe	0.000	0.3706 +- 0.0004 (0.10%)	0.0047 +- 0.0003 (6.18%)	-16.2	1261.9
FeNiMetalSub	0.050	0.5723 +- 0.0006 (0.10%)	0.1060 +- 0.0005 (0.44%)	-119.0	991.7
BB	n/a	0.9196 +- 0.0009 (0.10%)		n/a	
		RMS	**0.028**		
		red. Chi squ.	**1174.7**		

Table B.17: *brucerealexpP2* `OptEst_ASC_ILR()` results. Accuracy calculations in relation to the 'true' abundances and prior abundances use the retrieved abundance uncertainties for σ.

End-member	**'True' Abundance**	**Prior, P2**	**Retrieved Abundance**	**Accuracy to 'True' Abundance** σ	**Accuracy to P2 Abundance** σ
Augite	0.015	0.2114 +- 0.2116 (100.1%)	0.0163 +- 0.0011 (6.97%)	-1.1	171.9
Enstatite	0.085	0.6609 +- 0.6615 (100.1%)			
Olivine	0.700	0.1949 +- 0.1958 (100.1%)	0.4914 +- 0.0006 (0.11%)	378.2	-537.9

Table B.17 continued from previous page

End-member	'True' Abundance	Prior, P2	Retrieved Abundance	Accuracy to 'True' Abundance σ	Accuracy to P2 Abundance σ
Calcite	0.000	0.9068 +- 0.9077 (100.1%)	0.0151 +- 0.0002 (1.19%)	-84.1	4956.9
Lizardite	0.000	0.7720 +- 0.7728 (100.1%)	0.2356 +- 0.0015 (0.65%)	-153.7	350.0
Troilite	0.050	0.9318 +- 0.9327 (100.1%)			
Albite	0.100	0.0640 +- 0.0640 (100.1%)			
Gypsum	0.000	0.2624 +- 0.2626 (100.1%)			
AmorphousFe	0.000	0.3706 +- 0.3709 (100.1%)			
FeNiMetalSub	0.050	0.5723 +- 0.5729 (100.1%)	0.2415 +- 0.0009 (0.38%)	-211.4	365.0
BB	n/a	0.9196 +- 0.9205 (100.1%)			
		RMS	**0.016**		
		red. Chi squ.	**479.3**		

Table B.18: *brucerealexpP3* `OptEst_ASC_ILR()` results. Accuracy calculations in relation to the 'true' abundances and prior abundances use the retrieved abundance uncertainties for σ.

End-member	'True' Abundance	Prior, P3	Retrieved Abundance [BBnorm]	Accuracy to 'True' Abundance σ [BBnorm value]	Accuracy to P3 Abundance σ
Augite	0.015	0.0150 +- 1.50E-5 (0.10%)	0.0152 +- 1.50E-5 (0.10%) [0.0156 +- 1.62E-5 (0.10%)]	-13.0 [-37.7]	-13.0
Enstatite	0.085	0.0850 +- 8.50E-5 (0.10%)	0.0909 +- 8.34E-5 (0.09%) [0.0934 +- 9.08E-5 (0.10%)]	-70.9 [-92.5]	-70.9
Olivine	0.700	0.7000 +- 7.00E-4 (0.10%)	0.6051 +- 1.99E-4 (0.03%) [0.6217 +- 2.86E-4 (0.05%)]	477.2 [274.0]	477.2

Table B.18 continued from previous page

End-member	**'True' Abundance**	**Prior, P3**	**Retrieved Abundance [BBnorm]**	**Accuracy to 'True' Abundance σ [BBnorm value]**	**Accuracy to P3 Abundance σ**
Calcite	0.000	0.0001 +- 1.00E-4 (100.1%)	0.0196 +- 9.74E-5 (0.50%) [0.0202 +- 1.00E-4 (0.50%)]	-201.5 [-201.1]	825.5
Lizardite	0.000	0.0001 +- 1.00E-4 (100.1%)	0.0562 +- 4.95E-5 (0.09%) [0.0577 +- 5.41E-5 (0.09%)]	-124.8 [-142.6]	-124.8
Troilite	0.050	0.0500 +- 5.00E-5 (0.10%)	0.1093 +- 9.68E-5 (0.09%) [0.1123 +- 1.06E-4 (0.095)]	-96.0 [-116.2]	-1128.4
Albite	0.100	0.1000 +- 1.00E-4 (0.10%)	0.0205 +- 9.58E-5 (0.47%) [0.0211 +- 9.86E-5 (0.47%)]	-214.0 [-213.5]	-212.9
Gypsum	0.000	0.0001 +- 1.00E-4 (100.1%)	0.0566 +- 4.95E-5 (0.09%) [0.0581 +- 5.42E-5 (0.09%)]	-132.6 [-149.8]	-1141.2
AmorphousFe	0.000	0.0001 +- 1.00E-4 (100.1%)			
FeNiMetalSub	0.050	0.0500 +- 5.00E-5 (0.10%)			
BB	n/a	0.0001 +- 1.00E-4 (100.1%)	0.0267 +- 9.58E-5 (0.36%)		-277.4
		RMS	**0.022** **[0.024]**		
		red. Chi squ.	**1244.3** **[1424.1]**		

Table B.19: *brucerealexpP4* `OptEst_ASC_ILR()` results. Accuracy calculations in relation to the 'true' abundances and prior abundances use the retrieved abundance uncertainties for σ.

End-member	**'True' Abundance**	**Prior, P4**	**Retrieved Abundance**	**Accuracy to 'True' Abundance σ**	**Accuracy to P4 Abundance σ**
Augite	0.015	0.0500 +- 0.0100 (20.0%)			
Enstatite	0.085	0.1000 +- 0.0100 (10.0%)			
Olivine	0.700	0.6000 +- 0.0050 (0.8%)	0.4864 +- 0.0005 (0.10%)	436.4	232.1
Calcite	0.000	0.0010 +- 0.0100 (1000%)	0.0117 +- 0.0002 (1.46%)	-68.5	-62.6
Lizardite	0.000	0.0001 +- 0.0100 (10000%)	0.2797 +- 0.0011 (0.39%)	-256.3	-256.2
Troilite	0.050	0.0750 +- 0.0100 (13.3%)	0.2222 +- 0.0009 (0.39%)	-199.6	-170.7
Albite	0.100	0.0900 +- 0.0100 (11.1%)			
Gypsum	0.000	0.0001 +- 0.0100 (10000%)			
AmorphousFe	0.000	0.0001 +- 0.0100 (10000%)			
FeNiMetalSub	0.050	0.0750 +- 0.0100 (13.3%)			
BB	n/a	0.2500 +- 0.0125 (5.0%)			
		RMS	**0.015**		
		red. Chi squ.	**493.7**		

Table B.20: *brucemathextP1* `OptEst_ASC_ILR()` results. Accuracy calculations in relation to the 'true' abundances and prior abundances use the retrieved abundance uncertainties for σ.

End-member	**'True' Abundance**	**Prior, P1**	**Retrieved Abundance [BBnorm]**	**Accuracy to 'True' Abundance σ [BBnorm value]**	**Accuracy to P1 Abundance σ [BBnorm value]**
Augite	0.015	0.7172 +- 0.0007 (0.10%)	0.0054 +- 0.0004 (8.02%) [0.0058 +- 0.0005 (8.02%)]	22.4 [20.0]	1653.4

Table B.20 continued from previous page

End-member	'True' Abundance	Prior, P1	Retrieved Abundance [BBnorm]	Accuracy to 'True' Abundance σ [BBnorm value]	Accuracy to P1 Abundance σ [BBnorm value]
Enstatite	0.085	0.4381 +- 0.0004 (0.10%)	0.1061 +- 0.0004 (0.34%) [0.1139 +- 0.0004 (0.35%)]	-58.5 [-72.3]	920.8
Olivine	0.700	0.8050 +-0.0008 (0.10%)	0.6402 +- 0.0003 (0.04%) [0.6873 +- 0.0007 (0.10%)]	229.2 [19.2]	631.9
Calcite	0.000	0.2546 +- 0.0003 (0.10%)	0.0227 +- 0.0001 (0.39%) [0.0244 +- 0.0001 (0.40%)]	-254.8 [-248.7]	2601.4
Saponite	0.000	0.0326 +- 3.26E-5 (0.10%)	0.0301 +- 3.26E-5 (0.11%) [0.0323 +- 4.49E-5 (0.14%)]	-924.3 [-719.1]	76.5
Cronstedtite	0.000	0.9071 +- 0.0009 (0.10%)			
Lizardite	0.000	0.5086 +- 0.0005 (0.10%)			
Magnetite	0.000	0.7271 +- 0.0007 (0.10%)			
Spinel	0.000	0.6179 +- 0.0006 (0.10%)			
Troilite	0.050	0.8562 +- 0.0009 (0.10%)			
Pyrrhotite	0.000	0.6534 +- 0.0007 (0.10%)			
Albite	0.100	0.5196 +- 0.0005 (0.10%)	0.0056 +- 0.0003 (5.95%) [0.0060+-0.0004 (5.95%)]	285.8 [265.1]	1555.9
Anorthite	0.000	0.8820 +- 0.0009 (0.10%)			
Gypsum	0.000	0.3018 +- 0.0003 (0.10%)	0.0405 +- 0.0003 (0.62%) [0.0435 +- 0.0003 (0.63%)]	-160.1 [-158.6]	1033.1
AmorphousMg	0.000	0.1128 +- 0.0001 (0.10%)	0.0810 +- 0.0001 (0.14%) [0.0869 +- 0.0001 (0.16%)]	-731.6 [-616.4]	286.9
AmorphousFe	0.000	0.5535 +-0.0006 (0.10%)			
MurchisonIOM	0.000	0.9793 +- 0.0010 (0.10%)			
FeNiMetalSub	0.050	0.4243 +- 0.0004 (0.10%)			

Table B.20 continued from previous page

End-member	'True' Abundance	Prior, P1	Retrieved Abundance [BBnorm]	Accuracy to 'True' Abundance σ [BBnorm value]	Accuracy to P1 Abundance σ [BBnorm value]
BB	n/a	0.2287 +- 0.0002 (0.10%)	0.0685 +- 0.0002 (0.30%)		779.1
		RMS	**0.0093** **[0.0046]**		
		red. Chi squ.	**295.7** **[193.4]**		

Table B.21: *brucemathextP2* `OptEst_ASC_ILR()` results. Accuracy calculations in relation to the 'true' abundances and prior abundances use the retrieved abundance uncertainties for σ.

End-member	'True' Abundance	Prior, P2	Retrieved Abundance [BBnorm]	Accuracy to 'True' Abundance σ [BBnorm value]	Accuracy to P2 Abundance σ [BBnorm value]
Augite	0.015	0.7172 +- 0.7179 (100.1%)	0.0148 +- 0.0017 (11.23%) [0.0155 +- 0.0018 (11.79%)]	0.12 [-0.28]	422.5
Enstatite	0.085	0.4381 +- 0.4385 (100.1%)	0.0851 +- 0.0012 (1.44%) [0.0892 +- 0.0035 (3.87%)]	-0.07 [-1.22]	287.2
Olivine	0.700	0.8050 +- 0.8058 (100.1%)	0.7000 +- 0.0004 (0.06%) [0.7340 +- 0.0263 (3.59%)]	-0.01 [-1.29]	269.2
Calcite	0.000	0.2546 +- 0.2549 (100.1%)	1.37E-05 +- 0.0002 (1229.8%) [1.44E-5 +- 0.0002 (1229.8%)]	-0.08 [-0.08]	1511.9
Saponite	0.000	0.0326 +- 0.0326 (100.1%)	0.0005 +- 0.0035 (740.6%) [0.0005 +- 0.0036 (740.6%)]	-0.14 [-0.14]	9.2

Table B.21 continued from previous page

End-member	'True' Abundance	Prior, P2	Retrieved Abundance [BBnorm]	Accuracy to 'True' Abundance σ [BBnorm value]	Accuracy to P2 Abundance σ [BBnorm value]
Cronstedtite	0.000	0.9071 +- 0.9080 (100.1%)	0.0001 +- 0.0012 (1225.8%) [0.0001 +- 0.0013 (1225.8%)]	-0.08 [-0.08]	745.8
Lizardite	0.000	0.5086 +- 0.5091 (100.1%)			
Magnetite	0.000	0.7271 +- 0.7278 (100.1%)			
Spinel	0.000	0.6179 +- 0.6185 (100.1%)	4.52E-05 +- 0.0005 (1045.7%) [4.74E-5 +- 0.0005 (1045.7%)]	-0.10 [-0.10]	1307.3
Troilite	0.050	0.8562 +- 0.8571 (100.1%)	0.0518 +- 0.0136 (26.27%) [0.0543 +- 0.0144 (26.52%)]	-0.13 [-0.30]	59.1
Pyrrhotite	0.000	0.6534 +- 0.6541 (100.1%)			
Albite	0.100	0.5196 +- 0.5202 (1001.%)	0.1000 +- 0.0007 (0.71%) [0.1048 +- 0.0038 (3.66%)]	0.06 [-1.26]	592.8
Anorthite	0.000	0.8820 +- 0.8829 (100.1%)			
Gypsum	0.000	0.3018 +- 0.3021 (100.1%)			
AmorphousMg	0.000	0.1128 +- 0.1129 (100.1%)			
AmorphousFe	0.000	0.5535 +- 0.5540 (100.1%)			
MurchisonIOM	0.000	0.9793 +- 0.9803 (100.1%)	0.0013 +- 0.0094 (698.3%) [0.0014 +- 0.0099 (698.3%)]	-0.14 [-0.14]	104.1
FeNiMetalSub	0.050	0.4243 +- 0.4247 (100.1%)			
BB	n/a	0.2287 +- 0.2289 (100.1%)	0.0464 +- 0.0210 (45.21%)		8.7
		RMS	**3.13E-06 [0.0064]**		
		red. Chi squ.	**4.79E-05 [158.0]**		

Table B.22: *brucemathextP3* `OptEst_ASC_ILR()` results. Accuracy calculations in relation to the 'true' abundances and prior abundances use the retrieved abundance uncertainties for σ.

End-member	**'True' Abundance**	**Prior, P3**	**Retrieved Abundance [BBnorm]**	**Accuracy to 'True' Abundance σ [BBnorm value]**	**Accuracy to P3 Abundance σ [BBnorm value]**
Augite	0.015	0.0150 +- 1.50E-5 (0.10%)	0.0150 +- 1.50E-5 (0.10%) [0.0150 +- 1.63E-5 (0.11%)]	0.06 [0.05]	0.06
Enstatite	0.085	0.0850 +- 0.0001 (0.10%)	0.0850 +- 8.30E-5 (0.10%) [0.0850 +-9.05E-5 (0.11%)]	0.43 [0.38]	0.43
Olivine	0.700	0.7000 +- 0.0007 (0.10%)	0.6998 +- 1.88E-4 (0.03%) [0.6998 +- 3.52E-4 (0.05%)]	1.15 [0.59]	1.15
Calcite	0.000	0.0001 +- 0.0001 (100.1%)	2.78E-05 +- 6.56E-5 (235.84%) [2.78E-5 +- 6.56E-5 (235.84%)]	-0.42 [-0.42]	1.10
Saponite	0.000	0.0001 +- 0.0001 (100.1%)	3.11E-05 +- 9.75E-5 (313.97%) [3.11E-5 +- 9.75E-5 (313.97%)]	-0.32 [-0.32]	0.71
Cronstedtite	0.000	0.0001 +- 0.0001 (100.1%)	3.23E-05 +- 9.74E-5 (301.84%) [3.23E-5 +- 9.74E-5 (301.84%)]	-0.33 [-0.33]	0.70
Lizardite	0.000	0.0001 +- 0.0001 (100.1%)	3.52E-05 +- 9.74E-5 (276.87%) [3.52E-5 +- 9.74E-5 (276.87%)]	-0.36 [-0.36]	0.67
Magnetite	0.000	0.0001 +- 0.0001 (100.1%)	1.50E-05 +- 9.58E-5 (638.87%) [1.50E-5 +- 9.63E-5 (635.00%)]	-0.16 [-0.16]	0.89
Spinel	0.000	0.0001 +- 0.0001 (100.1%)	4.03E-05 +- 9.27E-5 (230.33%) [4.03E-5 +- 9.27E-5 (230.33%)]	-0.43 [-0.43]	0.64
Troilite	0.050	0.0500 +- 0.0001 (0.10%)	0.0500 +- 4.96E-5 (0.10%) [0.0500 +- 5.39E-5 (0.11%)]	0.43 [0.39]	0.43
Pyrrhotite	0.000	0.0001 +- 0.0001 (100.1%)	1.52E-05 +- 9.63E-5 (635.00%) [1.52E-5 +- 9.63E-5 (635.00%)]	-0.16 [-0.16]	0.88

Table B.22 continued from previous page

End-member	'True' Abundance	Prior, P3	Retrieved Abundance [BBnorm]	Accuracy to 'True' Abundance σ [BBnorm value]	Accuracy to P3 Abundance σ [BBnorm value]
Albite	0.100	0.1000 +- 0.0001 (0.10%)	0.0999 +- 9.62E-5 (0.10%) [0.0999 +- 1.05E-4 (0.11%)]	0.63 [0.56]	0.63
Anorthite	0.000	0.0001 +- 0.0001 (100.1%)	5.33E-05 +- 9.59E-5 (179.91%) [5.33E-5 +- 9.59E-5 (179.91%)]	-0.56 [-0.56]	0.49
Gypsum	0.000	0.0001 +- 0.0001 (100.1%)	1.80E-05 +- 9.62E-5 (533.06%) [1.81E-5 +- 9.62E-5 (533.06%)]	-0.19 [-0.19]	0.85
AmorphousMg	0.000	0.0001 +- 0.0001 (100.1%)	2.75E-05 +- 9.73E-5 (353.36%) [2.75E-5 +- 9.73E-5 (353.36%)]	-0.28 [-0.28]	0.75
AmorphousFe	0.000	0.0001 +- 0.0001 (100.1%)	3.08E-05 +- 9.19E-5 (298.14%) [3.08E-5 +- 9.19E-5 (298.14%)]	-0.34 [-0.34]	0.75
MurchisonIOM	0.000	0.0001 +- 0.0001 (100.1%)	1.77E-05 +- 9.65E-5 (545.94%) [1.77E-5 +- 9.65E-5 (545.94%)]	-0.18 [-0.18]	0.85
FeNiMetalSub	0.050	0.0500 +- 0.0001 (0.10%)	0.0500 +- 4.96E-5 (0.10%) [0.0500 +- 5.39E-5 (0.11%)]	0.44 [0.39]	0.44
BB	n/a	0.0001 +- 0.0001 (100.1%)	1.22E-05 +- 9.65E-5 (791.30%)		0.91
		RMS	**2.37E-05** **[2.22E-5]**		
		red. Chi squ.	**0.0021** **[0.0018]**		

Table B.23: *brucemathextP4* `OptEst_ASC_ILR()` results. Accuracy calculations in relation to the 'true' abundances and prior abundances use the retrieved abundance uncertainties for σ.

End-member	**'True' Abundance**	**Prior, P4**	**Retrieved Abundance [BBnorm]**	**Accuracy to 'True' Abundance σ [BBnorm value]**	**Accuracy to P4 Abundance σ [BBnorm value]**
Augite	0.015	0.05 +- 0.01 (20%)	0.0166 -+ 0.0011 (6.88%) [0.0179 +- 0.0013 (7.00%)]	-1.42 [-2.32]	29.21
Enstatite	0.085	0.1 +- 0.01 (10.0%)	0.0843 +- 0.0011 (1.30%) [0.0909 +- 0.0017 (1.86%)]	0.60 [-3.48]	14.26
Olivine	0.700	0.6 +- 0.005 (0.83%)	0.6997 +- 0.0004 (0.05%) [0.7540 +- 0.0100 (1.33%)]	0.77 [-5.38]	-263.53
Calcite	0.000	0.001 +- 0.01 (1000%)	0.0003 +- 0.0001 (39.57%) [0.0003 +- 0.0001 (39.59%)]	-2.53 [-2.53]	6.56
Saponite	0.000	0.0001 +- 0.001 (1000%)			
Cronstedtite	0.000	0.001 +- 0.01 (1000%)	0.0001 +- 0.0010 (765.10%) [0.0001 +- 0.0011 (765.10%)]	-0.13 [-0.13]	0.84
Lizardite	0.000	0.0001 +-0.01 (10000%)			
Magnetite	0.000	0.0001 +- 0.01 (10000%)			
Spinel	0.000	0.001 +- 0.01 (1000%)			
Troilite	0.050	0.075 +- 0.01 (13.33%)	0.0219 +- 0.0072 (32.75%) [0.0236 +- 0.0077 (32.78%)]	3.91 [3.40]	7.39
Pyrrhotite	0.000	0.075 +- 0.1 (133.33%)	0.0046 +- 0.0029 (64.01%) [0.0050 +- 0.0032 (64.02%)]	-1.56 [-1.56]	23.91
Albite	0.100	0.09 +- 0.01 (11.11%)	0.0994 +- 0.0005 (0.54%) [0.1071 +- 0.0015 (1.43%)]	1.17 [-4.61]	-17.56
Anorthite	0.000	0.09 +- 0.1 (111.11%)			
Gypsum	0.000	0.0001 +- 0.01 (10000%)			

Table B.23 continued from previous page

End-member	'True' Abundance	Prior, P4	Retrieved Abundance [BBnorm]	Accuracy to 'True' Abundance σ [BBnorm value]	Accuracy to P4 Abundance σ [BBnorm value]
AmorphousMg	0.000	0.001 +- 0.01 (1000%)			
AmorphousFe	0.000	0.0001 +- 0.01 (10000%)	0.0010 +- 0.0006 (59.36%) [0.0011 +- 0.0006 (59.38%)]	-1.68 [-1.68]	-1.51
MurchisonIOM	0.000	0.075 +- 0.1 (133.33%)			
FeNiMetalSub	0.050	0.075 +- 0.01 (13.33%)			
BB	n/a	0.25 +- 0.0125 (5.00%)	0.0720 +- 0.0066 (9.20%)		26.86
		RMS	**7.05E-05** [**0.0103**]		
		red. Chi squ.	**0.0203** [**401.6**]		

Table B.24: *brucerealextP1* `OptEst_ASC_ILR()` results. Accuracy calculations in relation to the 'true' abundances and prior abundances use the retrieved abundance uncertainties for σ.

End-member	'True' Abundance	Prior, P1	Retrieved Abundance [BBnorm]	Accuracy to 'True' Abundance σ [BBnorm value]	Accuracy to P1 Abundance σ [BBnorm value]
Augite	0.015	0.7172 +- 0.0007 (0.10%)			
Enstatite	0.085	0.4381 +- 0.0004 (0.10%)	0.0847 +- 0.0004 (0.44%) [0.0964 +- 0.0004 (0.46%)]	0.66 [-25.75]	937.86
Olivine	0.700	0.8050 +-0.0008 (0.10%)	0.3209 +- 0.0004 (0.11%) [0.3649 +- 0.0006 (0.16%)]	1043.97 [580.36]	1333.19

Table B.24 continued from previous page

End-member	**'True' Abundance**	**Prior, P1**	**Retrieved Abundance [BBnorm]**	**Accuracy to 'True' Abundance σ [BBnorm value]**	**Accuracy to P1 Abundance σ [BBnorm value]**
Calcite	0.000	0.2546 +- 0.0003 (0.10%)	0.0390 +- 0.0001 (0.35%) [0.0444 +- 0.0002 (0.37%)]	-286.81 [-273.37]	1584.62
Saponite	0.000	0.0326 +- 3.26E-5 (0.10%)	0.0306 +- 3.26E-05 (0.11%) [0.0348 +- 5.34E-05 (0.15%)]	-939.58 [-651.36]	60.92
Cronstedtite	0.000	0.9071 +- 0.0009 (0.10%)			
Lizardite	0.000	0.5086 +- 0.0005 (0.10%)	0.0837 +- 0.0004 (0.52%) [0.0952 +- 0.0005 (0.54%)]	-190.77 [-186.66]	968.50
Magnetite	0.000	0.7271 +- 0.0007 (0.10%)			
Spinel	0.000	0.6179 +- 0.0006 (0.10%)	0.0819 +- 0.0004 (0.46%) [0.0931 +- 0.0004 (0.48%)]	-215.52 [-209.64]	1410.28
Troilite	0.050	0.8562 +- 0.0009 (0.10%)			
Pyrrhotite	0.000	0.6534 +- 0.0007 (0.10%)			
Albite	0.100	0.5196 +- 0.0005 (0.10%)			
Anorthite	0.000	0.8820 +- 0.0009 (0.10%)			
Gypsum	0.000	0.3018 +- 0.0003 (0.10%)	0.0999 +- 0.0003 (0.28%) [0.1136 +- 0.0003 (0.30%)]	-358.45 [-333.20]	724.19
AmorphousMg	0.000	0.1128 +- 0.0001 (0.10%)	0.0875 +- 0.0001 (0.13%) [0.0996 +- 0.0002 (0.17%)]	-782.37 [-591.52]	225.26
AmorphousFe	0.000	0.5535 +-0.0006 (0.10%)			
MurchisonIOM	0.000	0.9793 +- 0.0010 (0.10%)			
FeNiMetalSub	0.050	0.4243 +- 0.0004 (0.10%)	0.0511 +- 0.0004 (0.71%) [0.0581 +- 0.0004 (0.71%)]	-3.09 [-19.57]	1034.63
BB	n/a	0.2287 +- 0.0002 (0.10%)	0.1206 +- 0.0002 (0.18%)		493.24

Table B.24 continued from previous page

End-member	'True' Abundance	Prior, P1	Retrieved Abundance [BBnorm]	Accuracy to 'True' Abundance σ [BBnorm value]	Accuracy to P1 Abundance σ [BBnorm value]
		RMS	**0.026 [0.019]**		
		red. Chi squ.	**845.2 [813.2]**		

Table B.25: *brucerealextP2* `OptEst_ASC_ILR()` results. Accuracy calculations in relation to the 'true' abundances and prior abundances use the retrieved abundance uncertainties for σ.

End-member	'True' Abundance	Prior, P2	Retrieved Abundance [BBnorm]	Accuracy to 'True' Abundance σ [BBnorm value]	Accuracy to P2 Abundance σ [BBnorm value]
Augite	0.015	0.7172 +- 0.7179 (100.1%)			
Enstatite	0.085	0.4381 +- 0.4385 (100.1%)			
Olivine	0.700	0.8050 +- 0.8058 (100.1%)	0.3967 +- 0.0006 (0.15%)	506.70	682.18
Calcite	0.000	0.2546 +- 0.2549 (100.1%)			
Saponite	0.000	0.0326 +- 0.0326 (100.1%)			
Cronstedtite	0.000	0.9071 +- 0.9080 (100.1%)	0.2756 +- 0.0018 (0.66%)	-151.27	346.52
Lizardite	0.000	0.5086 +- 0.5091 (100.1%)			
Magnetite	0.000	0.7271 +- 0.7278 (100.1%)			
Spinel	0.000	0.6179 +- 0.6185 (100.1%)	0.0679 +- 0.0006 (0.90%)	-110.75	897.28
Troilite	0.050	0.8562 +- 0.8571 (100.1%)			
Pyrrhotite	0.000	0.6534 +- 0.6541 (100.1%)			
Albite	0.100	0.5196 +- 0.5202 (1001.%)			

Table B.25 continued from previous page

End-member	'True' Abundance	Prior, P2	Retrieved Abundance [BBnorm]	Accuracy to 'True' Abundance σ [BBnorm value]	Accuracy to P2 Abundance σ [BBnorm value]
Anorthite	0.000	0.8820 +- 0.8829 (100.1%)	0.1296 +- 0.0007 (0.56%)	-178.14	1033.76
Gypsum	0.000	0.3018 +- 0.3021 (100.1%)			
AmorphousMg	0.000	0.1128 +- 0.1129 (100.1%)			
AmorphousFe	0.000	0.5535 +- 0.5540 (100.1%)			
MurchisonIOM	0.000	0.9793 +- 0.9803 (100.1%)			
FeNiMetalSub	0.050	0.4243 +- 0.4247 (100.1%)	0.1301 +- 0.0013 (1.03%)	-59.71	219.28
BB	n/a	0.2287 +- 0.2289 (100.1%)			
		RMS	**0.0109**		
		red. Chi squ.	**332.1**		

Table B.26: *brucerealextP3* `OptEst_ASC_ILR()` results. Accuracy calculations in relation to the 'true' abundances and prior abundances use the retrieved abundance uncertainties for σ.

End-member	'True' Abundance	Prior, P3	Retrieved Abundance [BBnorm]	Accuracy to 'True' Abundance σ [BBnorm value]	Accuracy to P3 Abundance σ [BBnorm value]
Augite	0.015	0.0150 +- 1.50E-5 (0.10%)	0.0151 +- 1.50E-05 (0.10%) [0.0154 +- 1.68E-05 (0.11%)]	-6.04 [-21.26]	-6.04
Enstatite	0.085	0.0850 +- 0.0001 (0.10%)	0.0871 +- 8.38E-05 (0.10%) [0.0887 +- 9.45E-05 (0.11%)]	-25.50 [-38.92]	-25.50
Olivine	0.700	0.7000 +- 0.0007 (0.10%)	0.5504 +- 2.59E-04 (0.05%) [0.5602 +- 3.68E-04 (0.07%)]	577.64 [380.06]	577.64

Table B.26 continued from previous page

End-member	'True' Abundance	Prior, P3	Retrieved Abundance [BBnorm]	Accuracy to 'True' Abundance σ [BBnorm value]	Accuracy to P3 Abundance σ [BBnorm value]
Calcite	0.000	0.0001 +- 0.0001 (100.1%)	0.0113 +- 9.81E-05 (0.87%) [0.0115 +- 1.00E-04 (0.87%)]	-114.88 [-114.72]	-113.86
Saponite	0.000	0.0001 +- 0.0001 (100.1%)	0.0127 +- 9.81E-05 (0.77%) [0.0129 +- 1.00E-04 (0.78%)]	-129.25 [-129.03]	-128.23
Cronstedtite	0.000	0.0001 +- 0.0001 (100.1%)	0.0125 +- 9.82E-05 (0.78%) [0.0127 +- 1.00E-04 (0.79%)]	-127.50 [-127.28]	-126.48
Lizardite	0.000	0.0001 +- 0.0001 (100.1%)	0.0128 +- 9.70E-05 (0.75%) [0.0131 +- 9.89E-05 (0.76%)]	-132.50 [-132.25]	-131.46
Magnetite	0.000	0.0001 +- 0.0001 (100.1%)	0.0109 +- 9.69E-05 (0.89%) [0.0111 +- 9.87E-05 (0.89%)]	-112.93 [-112.78]	-111.90
Spinel	0.000	0.0001 +- 0.0001 (100.1%)	0.0539 +- 4.96E-05 (0.09%) [0.0549 +- 5.64E-05 (0.10%)]	-79.17 [-86.53]	-79.17
Troilite	0.050	0.0500 +- 0.0001 (0.10%)	0.0142 +- 9.71E-05 (0.68%) [0.0145 +- 9.91E-05 (0.68%)]	-146.38 [-146.05]	-145.35
Pyrrhotite	0.000	0.0001 +- 0.0001 (100.1%)	0.1036 +- 9.76E-05 (0.09%) [0.1055 +- 1.11E-04 (0.10%)]	-37.11 [-49.37]	-37.11
Albite	0.100	0.1000 +- 0.0001 (0.10%)	0.0077 +- 9.80E-05 (1.27%) [0.0079 +- 9.98E-05 (1.27%)]	-78.80 [-78.75]	-77.78
Anorthite	0.000	0.0001 +- 0.0001 (100.1%)	0.0124 +- 9.72E-05 (0.78%) [0.0126 +- 9.90E-05 (0.78%)]	-127.74 [-127.52]	-126.71
Gypsum	0.000	0.0001 +- 0.0001 (100.1%)	0.0112 +- 9.79E-05 (0.87%) [0.0114 +- 9.97E-05 (0.88%)]	-114.35 [-114.19]	-113.33
AmorphousMg	0.000	0.0001 +- 0.0001 (100.1%)			
AmorphousFe	0.000	0.0001 +- 0.0001 (100.1%)			

Table B.26 continued from previous page

End-member	'True' Abundance	Prior, P3	Retrieved Abundance [BBnorm]	Accuracy to 'True' Abundance σ [BBnorm value]	Accuracy to P3 Abundance σ [BBnorm value]
MurchisonIOM	0.000	0.0001 +- 0.0001 (100.1%)	0.0123 +- 9.72E-05 (0.79%) [0.0126 +- 9.91E-05 (0.79%)]	-126.97 [-126.76]	-125.95
FeNiMetalSub	0.050	0.0500 +- 0.0001 (0.10%)	0.0543 +- 4.96E-05 (0.09%) [0.0552 +- 5.65E-05 (0.10%)]	-85.62 [-92.19]	-85.62
BB	n/a	0.0001 +- 0.0001 (100.1%)	0.0174 +- 9.72E-05 (0.56%)		-177.59
		RMS **red. Chi squ.**	**0.0176** **[0.0185]** **970.8** **[1050.1]**		

Table B.27: *brucerealextP4* `OptEst_ASC_ILR()` results. Accuracy calculations in relation to the 'true' abundances and prior abundances use the retrieved abundance uncertainties for σ.

End-member	'True' Abundance	Prior, P4	Retrieved Abundance [BBnorm]	Accuracy to 'True' Abundance σ [BBnorm value]	Accuracy to P4 Abundance σ [BBnorm value]
Augite	0.015	0.05 +- 0.01 (20%)			
Enstatite	0.085	0.1 +- 0.01 (10.0%)			
Olivine	0.700	0.6 +- 0.005 (0.83%)	0.4050 +- 0.0006 (0.15%) [0.4746 +- 0.0017 (0.36%)]	492.8 [130.82]	325.73
Calcite	0.000	0.001 +- 0.01 (1000%)	9.70E-05 +- 0.0002 (177.18%) [0.0001 +- 0.0002 (177.18%)]	-0.56 [-0.56]	5.26

Table B.27 continued from previous page

End-member	'True' Abundance	Prior, P4	Retrieved Abundance [BBnorm]	Accuracy to 'True' Abundance σ [BBnorm value]	Accuracy to P4 Abundance σ [BBnorm value]
Saponite	0.000	0.0001 +- 0.001 (1000%)			
Cronstedtite	0.000	0.001 +- 0.01 (1000%)	0.2504 +- 0.0018 (0.72%) [0.2935 +- 0.0023 (0.79%)]	-139.2 [-126.36]	-138.60
Lizardite	0.000	0.0001 +-0.01 (10000%)			
Magnetite	0.000	0.0001 +- 0.01 (10000%)			
Spinel	0.000	0.001 +- 0.01 (1000%)	0.0717 +- 0.0006 (0.88%) [0.0840 +- 0.0008 (0.94%)]	-113.9 [-106.58]	-112.34
Troilite	0.050	0.075 +- 0.01 (13.33%)			
Pyrrhotite	0.000	0.075 +- 0.1 (133.33%)			
Albite	0.100	0.09 +- 0.01 (11.11%)			
Anorthite	0.000	0.09 +- 0.1 (111.11%)	0.1261 +- 0.0007 (0.58%) [0.1477 +- 0.0010 (0.67%)]	-173.1 [-150.13]	-49.52
Gypsum	0.000	0.0001 +- 0.01 (10000%)			
AmorphousMg	0.000	0.001 +- 0.01 (1000%)			
AmorphousFe	0.000	0.0001 +- 0.01 (10000%)			
MurchisonIOM	0.000	0.075 +- 0.1 (133.33%)			
FeNiMetalSub	0.050	0.075 +- 0.01 (13.33%)			
BB	n/a	0.25 +- 0.0125 (5.00%)	0.1467 +- 0.0013 (0.89%)		78.70
		RMS	**0.0109** [**0.0162**]		
		red. Chi squ.	**330.3** [**638.1**]		

Table B.28: Results for *glennmathminP1* `OptEst_ASC_ILR()` unmixing.

End-member	**'True' Abundance**	**Prior, P1**	**Retrieved Abundance**	**Accuracy to 'True' Abundance** σ	**Accuracy to P1 Abundance** σ
Enstatite	0.0800	0.8337 ± 8.34E-04 (0.10%)	0.1244 ± 4.81E-04 (0.39%)	-92.35	1474.15
Olivine	0.1130	0.8826 ± 8.83E-04 (0.10%)	0.2217 ± 2.68E-04 (0.12%)	-405.65	2467.21
Calcite	0.0080	0.8698 ± 8.70E-04 (0.10%)	rm		
Cronstedtite	0.5290	0.2159 ± 2.16E-04 (0.10%)	0.1885 ± 2.10E-04 (0.11%)	1622.73	130.45
Lizardite	0.2330	0.0246 ± 2.46E-05 (0.10%)	0.0244 ± 2.46E-05 (0.10%)	8474.89	8.42
Magnetite	0.0150	0.7298 ± 7.30E-04 (0.10%)	0.1098 ± 5.30E-04 (0.48%)	-178.79	1168.88
Pyrrhotite	0.0090	0.5244 ± 5.24E-04 (0.10%)	0.2340 ± 4.52E-04 (0.19%)	-497.8	642.43
Gypsum	0.0140	0.9781 ± 0.0010 (0.10%)	0.0971 ± 5.37E-04 (0.55%)	-154.71	1640.12
		RMS error	0.0111		
		$\chi^2_{d.o.f}$	408.0		

Table B.29: Results for *glennmathminP2* `OptEst_ASC_ILR()` unmixing.

End-member	**'True' Abundance**	**Prior, P2**	**Retrieved Abundance**	**Accuracy to 'True' Abundance** σ	**Accuracy to P2 Abundance** σ
Enstatite	0.0800	0.8337 ± 0.8345 (100.10%)	0.0728 ± 8.33E-04 (1.14%)	8.59	912.93
Olivine	0.1130	0.8826 ± 0.8835 (100.10%)	0.1117 ± 4.46E-04 (0.40%)	2.86	1728.55
Calcite	0.0080	0.8698 ± 0.8706 (100.10%)	0.0054 ± 1.41E-04 (2.59%)	18.23	6137.44
Cronstedtite	0.5290	0.2159 ± 0.2161 (100.10%)	0.5220 ± 0.0013 (0.25%)	5.26	-230.15
Lizardite	0.2330	0.0246 ± 0.0246 (100.10%)	0.2419 ± 0.0010 (0.42%)	-8.66	-211.93
Magnetite	0.0150	0.7298 ± 0.7306 (100.10%)	rm		
Pyrrhotite	0.0090	0.5244 ± 0.5250 (100.10%)	0.0306 ± 0.0010 (3.24%)	-21.79	497.59

Table B.29 continued from previous page

End-member	'True' Abundance	Prior, P2	Retrieved Abundance	Accuracy to 'True' Abundance σ	Accuracy to P2 Abundance σ
Gypsum	0.0140	0.9781 ± 0.9791 (100.10%)	0.0155 ± 0.0009 (6.04%)	-1.6	1027.6
		RMS error	0.0003		
		$\chi^2_{d.o.f}$	0.569		

Table B.30: Results for *glennrealminP1* `OptEst_ASC_ILR()` unmixing.

End-member	'True' Abundance	Prior, P1	Retrieved Abundance	Accuracy to 'True' Abundance σ	Accuracy to P1 Abundance σ
Calcite	0.0080	0.8698 ± 8.70E-04 (0.10%)	0.0170 ± 5.92E-04 (3.48%)	-15.24	1440.01
Enstatite	0.0800	0.8337 ± 8.34E-04 (0.10%)	0.1444 ± 7.37E-04 (0.51%)	-87.45	935.81
Olivine	0.1130	0.8826 ± 8.83E-04 (0.10%)	0.0855 ± 7.18E-04 (0.84%)	38.36	1110.66
Cronstedtite	0.5290	0.2159 ± 2.16E-04 (0.10%)	0.1713 ± 2.14E-04 (0.13%)	1668.56	207.94
Lizardite	0.2330	0.0246 ± 2.46E-05 (0.10%)	0.0240 ± 2.46E-05 (0.10%)	8486.54	23.38
Magnetite	0.0150	0.7298 ± 7.30E-04 (0.10%)	0.2264 ± 6.60E-04 (0.29%)	-320.47	763.02
Pyrrhotite	0.0090	0.5244 ± 5.24E-04 (0.10%)	0.2651 ± 5.01E-04 (0.19%)	-511.4	517.98
Gypsum	0.0140	0.9781 ± 0.0010 (0.10%)	0.0662 ± 8.22E-04 (1.24%)	-63.55	1109.16
		RMS error	0.0173		
		$\chi^2_{d.o.f}$	32.0		

Table B.31: Results for *glennrealminP4* `OptEst_ASC_ILR()` unmixing.

End-member	**'True' Abundance**	**Prior, P4**	**Retrieved Abundance**	**Accuracy to 'True' Abundance** σ	**Accuracy to P4 Abundance** σ
Enstatite	0.0800	0.1000 ± 0.0050 (5.00%)	rm		
Olivine	0.1130	0.1000 ± 0.0050 (5.00%)	rm		
Calcite	0.0080	0.0100 ± 0.0100 (100.00%)	rm		
Cronstedtite	0.5290	0.5000 ± 0.0050 (1.00%)	0.3974 ± 0.0039 (0.98%)	33.85	26.39
Lizardite	0.2330	0.2000 ± 0.0050 (2.50%)	0.1955 ± 0.0030 (1.54%)	12.44	1.5
Magnetite	0.0150	0.0100 ± 0.0100 (100.00%)	0.1394 ± 0.0061 (4.36%)	-20.47	-21.3
Pyrrhotite	0.0090	0.0200 ± 0.0100 (50.00%)	0.2572 ± 0.0066 (2.58%)	-37.4	-35.74
Gypsum	0.0140	0.0500 ± 0.0050 (10.00%)	0.0105 ± 0.0039 (37.12%)	0.88	10.09
		RMS error	0.0076		
		$\chi^2_{d.o.f}$	6.77		

Table B.32: Results for *glennrealexpP1* `OptEst_ASC_ILR()` unmixing.

End-member	**'True' Abundance**	**Prior, P1**	**Retrieved Abundance [BBnorm]**	**Accuracy to 'True' Abundance** σ **[BBnorm]**	**Accuracy to P1 Abundance** σ **[BBnorm]**
Augite	0.0000	0.6747 ± 6.75E-04 (0.10%)	rm		
Enstatite	0.0800	0.3153 ± 3.15E-04 (0.10%)	0.1364 ± 2.96E-04 (0.22%) [0.1599 ± 3.84E-04 (0.24%)]	-190.24 [-208.23]	604.10 [404.99]
Olivine	0.1130	0.6864 ± 6.86E-04 (0.10%)	rm		
Calcite	0.0080	0.2621 ± 2.62E-04 (0.10%)	0.1105 ± 2.44E-04 (0.22%) [0.1295 ± 3.15E-04 (0.24%)]	-419.32 [-385.21]	620.72 [420.28]

Table B.32 continued from previous page

End-member	'True' Abundance	Prior, P1	Retrieved Abundance [BBnorm]	Accuracy to 'True' Abundance σ [BBnorm]	Accuracy to P1 Abundance σ [BBnorm]
Saponite	0.0000	0.5489 ± 5.49E-04 (0.10%)	0.0258 ± 4.38E-04 (1.70%) [0.0302 ± 5.15E-04 (1.70%)]	-58.78 [-58.67]	1193.55 [1007.33]
Cronstedtite	0.5290	0.6083 ± 6.08E-04 (0.10%)	rm		
Lizardite	0.2330	0.1227 ± 1.23E-04 (0.10%)	0.0967 ± 1.22E-04 (0.13%) [0.1134 ± 1.83E-04 (0.16%)]	1121.71 [651.99]	213.99 [50.75]
Magnetite	0.0150	0.0336 ± 3.36E-05 (0.10%)	0.0317 ± 3.36E-05 (0.11%) [0.0372 ± 5.47E-05 (0.15%)]	-496.79 [-405.54]	57.69 [-64.65]
Spinel	0.0000	0.1841 ± 1.84E-04 (0.10%)	0.1229 ± 1.80E-04 (0.15%) [0.1442 ± 2.57E-04 (0.18%)]	-682.97 [-560.52]	339.87 [155.32]
Pyrrhotite	0.0090	0.2300 ± 2.30E-04 (0.10%)	0.1392 ± 2.22E-04 (0.16%) [0.1632 ± 3.09E-04 (0.19%)]	-585.57 [-498.65]	408.63 [216.02]
Gypsum	0.0140	0.4021 ± 4.02E-04 (0.10%)	0.1200 ± 3.61E-04 (0.30%) [0.1407 ± 4.47E-04 (0.32%)]	-293.97 [-283.80]	782.20 [585.26]
AmorphousFe	0.0000	0.0835 ± 8.35E-05 (0.10%)	0.0697 ± 8.32E-05 (0.12%) [0.0817 ± 1.28E-04 (0.16%)]	-838.12 [-637.24]	166.01 [13.80]
BB	n/a	0.3234 ± 3.23E-04 (0.10%)	0.1473 ± 3.01E-04 (0.20%)	n/a	584.88
		RMS error	0.0395 [0.0496]		
		$\chi^2_{d.o.f}$	143.2 [214.6]		

Table B.33: Results for *glennrealexpP3* `OptEst_ASC_ILR()` unmixing.

End-member	**'True' Abundance**	**Prior, P3**	**Retrieved Abundance [BBnorm]**	**Accuracy to 'True' Abundance σ [BBnorm]**	**Accuracy to P3 Abundance σ [BBnorm]**
Augite	0.0000	1.00E-04 ± 1.00E-04 (100.10%)	rm		
Enstatite	0.0800	0.0800 ± 8.00E-05 (0.10%)	0.0797 ± 7.94E-05 (0.10%) [0.0798 ± 8.61E-05 (0.11%)]	3.81 [2.83]	3.81 [2.83]
Olivine	0.1130	0.1130 ± 1.13E-04 (0.10%)	0.1113 ± 1.11E-04 (0.10%) [0.1114 ± 1.21E-04 (0.11%)]	15.03 [13.18]	15.03 [13.18]
Calcite	0.0080	0.0080 ± 8.00E-06 (0.10%)	0.0080 ± 8.00E-06 (0.10%) [0.0080 ± 8.67E-06 (0.11%)]	1.33 [0.55]	1.33 [0.55]
Saponite	0.0000	1.00E-04 ± 1.00E-04 (100.10%)	1.64E-04 ± 9.88E-05 (60.21%) [1.64E-04 ± 9.89E-05 (60.21%)]	-1.66 [-1.66]	-0.65 [-0.65]
Cronstedtite	0.5290	0.5290 ± 5.29E-04 (0.10%)	0.5292 ± 2.81E-04 (0.05%) [0.5296 ± 3.57E-04 (0.07%)]	-0.75 [-1.68]	-0.75 [-1.68]
Lizardite	0.2330	0.2330 ± 2.33E-04 (0.10%)	0.2329 ± 2.16E-04 (0.09%) [0.2330 ± 2.37E-04 (0.10%)]	0.68 [-0.11]	0.68 [-0.11]
Magnetite	0.0150	0.0150 ± 1.50E-05 (0.10%)	0.0150 ± 1.50E-05 (0.10%) [0.0150 ± 1.63E-05 (0.11%)]	-0.73 [-1.35]	-0.73 [-1.35]
Spinel	0.0000	1.00E-04 ± 1.00E-04 (100.10%)	rm		
Pyrrhotite	0.0090	0.0090 ± 9.00E-06 (0.10%)	0.0090 ± 9.00E-06 (0.10%) [0.0090 ± 9.76E-06 (0.11%)]	-0.42 [-1.07]	-0.42 [-1.07]
Gypsum	0.0140	0.0140 ± 1.40E-05 (0.10%)	0.0140 ± 1.40E-05 (0.10%) [0.0140 ± 1.52E-05 (0.11%)]	-0.36 [-1.01]	-0.36 [-1.01]
AmorphousFe	0.0000	1.00E-04 ± 1.00E-04 (100.10%)	rm		
BB	n/a	1.00E-04 ± 1.00E-04 (100.10%)	7.36E-04 ± 9.87E-05 (13.41%)	n/a	-6.44

Table B.33 continued from previous page

End-member	'True' Abundance	Prior, P3	Retrieved Abundance [BBnorm]	Accuracy to 'True' Abundance σ [BBnorm]	Accuracy to P3 Abundance σ [BBnorm]
		RMS error	0.0375 [0.0375]		
		$\chi^2_{d.o.f}$	68.3 [68.4]		

Table B.34: Results for *glennrealexpP4* `OptEst_ASC_ILR()` unmixing.

End-member	'True' Abundance	Prior, P4	Retrieved Abundance [BBnorm]	Accuracy to 'True' Abundance σ [BBnorm]	Accuracy to P4 Abundance σ [BBnorm]
Augite	0.0000	0.1000 ± 0.5000 (500.00%)	rm		
Enstatite	0.0800	0.1000 ± 0.0050 (5.00%)	0.0280 ± 0.0032 (11.32%) [0.0493 ± 0.0056 (11.42%)]	16.44 [5.45]	22.76 [9.01]
Olivine	0.1130	0.1000 ± 0.0050 (5.00%)	rm		
Calcite	0.0080	0.0100 ± 0.0100 (100.00%)	rm		
Saponite	0.0000	0.2540 ± 0.5000 (196.85%)	rm		
Cronstedtite	0.5290	0.5000 ± 0.0050 (1.00%)	0.3995 ± 0.0040 (1.01%) [0.7046 ± 0.0125 (1.78%)]	32.19 [-13.99]	24.98 [-16.30]
Lizardite	0.2330	0.2000 ± 0.0050 (2.50%)	0.1395 ± 0.0036 (2.55%) [0.2461 ± 0.0072 (2.94%)]	26.26 [-1.81]	16.99 [-6.36]
Magnetite	0.0150	0.0100 ± 0.0100 (100.00%)	rm		
Spinel	0.0000	0.0050 ± 0.0500 (1000.00%)	rm		

Table B.34 continued from previous page

End-member	'True' Abundance	Prior, P4	Retrieved Abundance [BBnorm]	Accuracy to 'True' Abundance σ [BBnorm]	Accuracy to P4 Abundance σ [BBnorm]
Pyrrhotite	0.0090	0.0200 ± 0.0100 (50.00%)	rm		
Gypsum	0.0140	0.0500 ± 0.0050 (10.00%)	rm		
AmorphousFe	0.0000	0.0100 ± 0.1000 (1000.00%)	rm		
BB	n/a	0.6000 ± 0.0300 (5.00%)	0.4330 ± 0.0039 (0.90%)	n/a	42.73
		RMS error	0.0042 [0.0255]		
		$\chi^2_{d.o.f}$	1.71 [31.8]		

Table B.35: Results for *glennmathextP2* `OptEst_ASC_ILR()` unmixing.

End-member	'True' Abundance	Prior, P2	Retrieved Abundance [BBnorm]	Accuracy to 'True' Abundance σ [BBnorm]	Accuracy to P2 Abundance σ [BBnorm]
Augite	0.000	0.5921 ± 0.5927 (100.10%)	rm		
Enstatite	0.080	0.3011 ± 0.3014 (100.10%)	0.0763 ± 0.0011 (1.42%) [0.0790 ± 0.0012 (1.50%)]	3.44 [0.80]	207.19 [186.68]
Olivine	0.113	0.4687 ± 0.4692 (100.10%)	0.1125 ± 4.69E-04 (0.42%) [0.1166 ± 7.50E-04 (0.64%)]	0.99 [-4.85]	759.18 [469.37]
Calcite	0.008	0.6976 ± 0.6983 (100.10%)	0.0070 ± 1.45E-04 (2.07%) [0.0072 ± 1.54E-04 (2.13%)]	6.99 [4.91]	4768.58 [4475.72]
Saponite	0.000	0.0272 ± 0.0273 (100.10%)	0.0074 ± 0.0033 (44.23%) [0.0076 ± 0.0034 (44.23%)]	-2.26 [-2.26]	6.08 [5.79]

Table B.35 continued from previous page

End-member	'True' Abundance	Prior, P2	Retrieved Abundance [BBnorm]	Accuracy to 'True' Abundance σ [BBnorm]	Accuracy to P2 Abundance σ [BBnorm]
Cronstedtite	0.529	0.9895 ± 0.9905 (100.10%)	0.5235 ± 0.0014 (0.26%) [0.5426 ± 0.0030 (0.55%)]	4.06 [-4.50]	341.22 [148.47]
Lizardite	0.233	0.4050 ± 0.4054 (100.10%)	0.2314 ± 0.0015 (0.65%) [0.2398 ± 0.0020 (0.81%)]	1.09 [-3.48]	115.32 [84.58]
Magnetite	0.015	0.8932 ± 0.8941 (100.10%)	rm		
Spinel	0.000	0.7193 ± 0.7200 (100.10%)	rm		
Troilite	0.000	0.4880 ± 0.4885 (100.10%)	rm		
Pyrrhotite	0.009	0.0385 ± 0.0386 (100.10%)	rm		
Albite	0.000	0.6164 ± 0.6170 (100.10%)	rm		
Anorthite	0.000	0.9767 ± 0.9776 (100.10%)	rm		
Gypsum	0.014	0.2391 ± 0.2394 (100.10%)	0.0068 ± 0.0014 (20.08%) [0.0071 ± 0.0014 (20.08%)]	5.25 [4.89]	169.72 [163.52]
AmorphousMg	0.000	0.9921 ± 0.9931 (100.10%)	rm		
AmorphousFe	0.000	0.0353 ± 0.0353 (100.10%)	rm		
MurchisonIOM	0.000	0.7350 ± 0.7357 (100.10%)	rm		
FeNiMetalSub	0.000	0.9467 ± 0.9477 (100.10%)	rm		
BB	n/a	0.9347 ± 0.9356 (100.10%)	0.0352 ± 0.0015 (4.14%)	n/a	616.96
		RMS error	0.0001 [0.0025]		
		$\chi^2_{d.o.f}$	0.123 [17.5]		

Table B.36: Results for *glennmathextP3* `OptEst_ASC_ILR()` unmixing.

End-member	**'True' Abundance**	**Prior, P3**	**Retrieved Abundance [BBnorm]**	**Accuracy to 'True' Abundance σ [BBnorm]**	**Accuracy to P3 Abundance σ [BBnorm]**
Augite	0.0000	1.00E-04 ± 1.00E-04 (100.10%)	rm		
Enstatite	0.0800	0.0800 ± 8.00E-05 (0.10%)	0.0796 ± 7.86E-05 (0.10%) [0.0796 ± 8.68E-05 (0.11%)]	5.69 [4.45]	5.69 [4.45]
Olivine	0.1130	0.1130 ± 1.13E-04 (0.10%)	0.1113 ± 1.02E-04 (0.09%) [0.1113 ± 1.14E-04 (0.10%)]	17.18 [14.60]	17.18 [14.60]
Calcite	0.0080	0.0080 ± 8.00E-06 (0.10%)	0.0080 ± 7.98E-06 (0.10%) [0.0080 ± 8.79E-06 (0.11%)]	3.55 [2.53]	3.55 [2.53]
Saponite	0.0000	1.00E-04 ± 1.00E-04 (100.10%)	1.51E-04 ± 9.85E-05 (65.03%) [1.52E-04 ± 9.85E-05 (65.03%)]	-1.54 [-1.54]	-0.52 [-0.52]
Cronstedtite	0.5290	0.5290 ± 5.29E-04 (0.10%)	0.5269 ± 2.90E-04 (0.05%) [0.5273 ± 3.78E-04 (0.07%)]	7.29 [4.53]	7.29 [4.53]
Lizardite	0.2330	0.2330 ± 2.33E-04 (0.10%)	0.2337 ± 2.08E-04 (0.09%) [0.2339 ± 2.34E-04 (0.10%)]	-3.59 [-3.95]	-3.59 [-3.95]
Magnetite	0.0150	0.0150 ± 1.50E-05 (0.10%)	0.0150 ± 1.50E-05 (0.10%) [0.0150 ± 1.65E-05 (0.11%)]	-0.45 [-1.10]	-0.45 [-1.10]
Spinel	0.0000	1.00E-04 ± 1.00E-04 (100.10%)	rm		
Troilite	0.0000	1.00E-04 ± 1.00E-04 (100.10%)	5.72E-04 ± 9.79E-05 (17.12%) [5.72E-04 ± 9.80E-05 (17.12%)]	-5.84 [-5.84]	-4.82 [-4.82]
Pyrrhotite	0.0090	0.0090 ± 9.00E-06 (0.10%)	0.0090 ± 9.00E-06 (0.10%) [0.0090 ± 9.91E-06 (0.11%)]	-0.26 [-0.92]	-0.26 [-0.92]
Albite	0.0000	1.00E-04 ± 1.00E-04 (100.10%)	rm		
Anorthite	0.0000	1.00E-04 ± 1.00E-04 (100.10%)	rm		

Table B.36 continued from previous page

End-member	'True' Abundance	Prior, P3	Retrieved Abundance [BBnorm]	Accuracy to 'True' Abundance σ [BBnorm]	Accuracy to P3 Abundance σ [BBnorm]
Gypsum	0.0140	0.0140 ± 1.40E-05 (0.10%)	0.0140 ± 1.40E-05 (0.10%) [0.0140 ± 1.54E-05 (0.11%)]	-2E-5 [-0.69]	-2E-5 [-0.69]
AmorphousMg	0.0000	1.00E-04 ± 1.00E-04 (100.10%)	1.18E-04 ± 9.85E-05 (83.23%) [1.19E-04 ± 9.86E-05 (83.23%)]	-1.20 [-1.20]	-0.19 [-0.19]
AmorphousFe	0.0000	1.00E-04 ± 1.00E-04 (100.10%)	rm		
MurchisonIOM	0.0000	1.00E-04 ± 1.00E-04 (100.10%)	2.48E-04 ± 9.79E-05 (39.39%) [2.49E-04 ± 9.79E-05 (39.39%)]	-2.54 [-2.54]	-1.52 [-1.52]
FeNiMetalSub	0.0000	1.00E-04 ± 1.00E-04 (100.10%)	7.32E-04 ± 9.80E-05 (13.38%) [7.33E-04 ± 9.80E-05 (13.38%)]	-7.48 [-7.48]	-6.46 [-6.46]
BB	n/a	1.00E-04 ± 1.00E-04 (100.10%)	7.59E-04 ± 9.80E-05 (12.91%)	n/a	-6.72
		RMS error	0.0007 [0.0008]		
		$\chi^2_{d.o.f}$	3.08 [3.29]		

Table B.37: Results for *glennmathextP4* `OptEst_ASC_ILR()` unmixing.

End-member	'True' Abundance	Prior, P4	Retrieved Abundance [BBnorm]	Accuracy to 'True' Abundance σ [BBnorm]	Accuracy to P4 Abundance σ [BBnorm]
Augite	0.0000	0.1000 ± 0.5000 (500.00%)	rm		
Enstatite	0.0800	0.1000 ± 0.0050 (5.00%)	0.0781 ± 8.18E-04 (1.05%) [0.0811 ± 8.81E-04 (1.09%)]	2.38 [-1.23]	26.83 [21.47]

Table B.37 continued from previous page

End-member	'True' Abundance	Prior, P4	Retrieved Abundance [BBnorm]	Accuracy to 'True' Abundance σ [BBnorm]	Accuracy to P4 Abundance σ [BBnorm]
Olivine	0.1130	0.1000 ± 0.0050 (5.00%)	0.1133 ± 4.39E-04 (0.39%) [0.1177 ± 5.68E-04 (0.48%)]	-0.74 [-8.31]	-30.38 [-31.19]
Calcite	0.0080	0.0100 ± 0.0100 (100.00%)	0.0068 ± 1.39E-04 (2.05%) [0.0071 ± 1.46E-04 (2.07%)]	8.55 [6.35]	22.89 [20.02]
Saponite	0.0000	0.2540 ± 0.5000 (196.85%)	rm		
Cronstedtite	0.5290	0.5000 ± 0.0050 (1.00%)	0.5215 ± 0.0013 (0.25%) [0.5417 ± 0.0021 (0.38%)]	5.82 [-6.17]	-16.61 [-20.25]
Lizardite	0.2330	0.2000 ± 0.0050 (2.50%)	0.2328 ± 0.0010 (0.42%) [0.2418 ± 0.0012 (0.51%)]	0.20 [-7.15]	-33.41 [-33.86]
Magnetite	0.0150	0.0100 ± 0.0100 (100.00%)	rm		
Spinel	0.0000	0.0050 ± 0.0500 (1000.00%)	rm		
Troilite	0.0000	0.0200 ± 0.1000 (500.00%)	rm		
Pyrrhotite	0.0090	0.0200 ± 0.0100 (50.00%)	rm		
Albite	0.0000	0.0150 ± 0.1000 (666.67%)	rm		
Anorthite	0.0000	0.0150 ± 0.1000 (666.67%)	rm		
Gypsum	0.0140	0.0500 ± 0.0050 (10.00%)	0.0102 ± 0.0010 (9.94%) [0.0106 ± 0.0011 (9.94%)]	3.78 [3.26]	39.36 [37.50]
AmorphousMg	0.0000	0.0100 ± 0.1000 (1000.00%)	rm		
AmorphousFe	0.0000	0.0100 ± 0.1000 (1000.00%)	rm		
MurchisonIOM	0.0000	0.0200 ± 0.5000 (2500.00%)	rm		
FeNiMetalSub	0.0000	0.0500 ± 0.5000 (1000.00%)	rm		
BB	n/a	0.6000 ± 0.0300 (5.00%)	0.0374 ± 0.0013 (3.37%)	n/a	447.21
		RMS error	0.0002 [0.0026]		

Table B.37 continued from previous page

End-member	'True' Abundance	Prior, P4	Retrieved Abundance [BBnorm]	Accuracy to 'True' Abundance σ [BBnorm]	Accuracy to P4 Abundance σ [BBnorm]
		$\chi^2_{d.o.f}$	0.137 [19.6]		

Table B.38: Results for *glennrealextP3* `OptEst_ASC_ILR()` unmixing.

End-member	'True' Abundance	Prior, P3	Retrieved Abundance [BBnorm]	Accuracy to 'True' Abundance σ [BBnorm]	Accuracy to P3 Abundance σ [BBnorm]
Augite	0.0000	1.00E-04 ± 1.00E-04 (100.10%)	rm		
Enstatite	0.0800	0.0800 ± 8.00E-05 (0.10%)	0.0797 ± 7.94E-05 (0.10%) [0.0797 ± 8.83E-05 (0.11%)]	4.21 [3.17]	4.21 [3.17]
Olivine	0.1130	0.1130 ± 1.13E-04 (0.10%)	0.1113 ± 1.11E-04 (0.10%) [0.1113 ± 1.24E-04 (0.11%)]	15.56 [13.39]	15.56 [13.39]
Calcite	0.0080	0.0080 ± 8.00E-06 (0.10%)	0.0080 ± 8.00E-06 (0.10%) [0.0080 ± 8.89E-06 (0.11%)]	1.37 [0.62]	1.37 [0.62]
Saponite	0.0000	1.00E-04 ± 1.00E-04 (100.10%)	1.13E-04 ± 9.89E-05 (87.26%) [1.13E-04 ± 9.90E-05 (87.26%)]	-1.15 [-1.15]	-0.13 [-0.14]
Cronstedtite	0.5290	0.5290 ± 5.29E-04 (0.10%)	0.5278 ± 3.13E-04 (0.06%) [0.5282 ± 4.04E-04 (0.08%)]	3.83 [2.08]	3.83 [2.08]
Lizardite	0.2330	0.2330 ± 2.33E-04 (0.10%)	0.2326 ± 2.17E-04 (0.09%) [0.2327 ± 2.45E-04 (0.11%)]	1.93 [1.06]	1.93 [1.06]
Magnetite	0.0150	0.0150 ± 1.50E-05 (0.10%)	0.0150 ± 1.50E-05 (0.10%) [0.0150 ± 1.67E-04 (0.11%)]	-0.65 [-1.20]	-0.65 [-1.20]

Table B.38 continued from previous page

End-member	'True' Abundance	Prior, P3	Retrieved Abundance [BBnorm]	Accuracy to 'True' Abundance σ [BBnorm]	Accuracy to P3 Abundance σ [BBnorm]
Spinel	0.0000	1.00E-04 ± 1.00E-04 (100.10%)	rm		
Troilite	0.0000	1.00E-04 ± 1.00E-04 (100.10%)	5.99E-04 ± 9.89E-05 (16.51%) [5.99E-04 ± 9.89E-05 (16.51%)]	-6.06 [-6.06]	-5.04 [-5.05]
Pyrrhotite	0.0090	0.0090 ± 9.00E-06 (0.10%)	0.0090 ± 9.00E-06 (0.10%) [0.0090 ± 1.00E-05 (0.11%)]	-0.37 [-0.95]	-0.37 [-0.95]
Albite	0.0000	1.00E-04 ± 1.00E-04 (100.10%)	rm		
Anorthite	0.0000	1.00E-04 ± 1.00E-04 (100.10%)	rm		
Gypsum	0.0140	0.0140 ± 1.40E-05 (0.10%)	0.0140 ± 1.40E-05 (0.10%) [0.0140 ± 1.56E-05 (0.11%)]	-0.28 [-0.87]	-0.28 [-0.87]
AmorphousMg	0.0000	1.00E-04 ± 1.00E-04 (100.10%)	1.94E-04 ± 9.89E-05 (50.94%) [1.94E-04 ± 9.90E-05 (50.94%)]	-1.96 [-1.96]	-0.95 [-0.95]
AmorphousFe	0.0000	1.00E-04 ± 1.00E-04 (100.10%)	rm		
MurchisonIOM	0.0000	1.00E-04 ± 1.00E-04 (100.10%)	4.21E-04 ± 9.89E-05 (23.51%) [4.21E-04 ± 9.90E-05 (23.51%)]	-4.25 [-4.25]	-3.24 [-3.24]
Fe, Ni metal sub.	0.0000	1.00E-04 ± 1.00E-04 (100.10%)	6.70E-04 ± 9.88E-05 (14.76%) [6.70E-04 ± 9.89E-05 (14.76%)]	-6.77 [-6.77]	-5.76 [-5.76]
BB	n/a	1.00E-04 ± 1.00E-04 (100.10%)	6.84E-04 ± 9.88E-05 (14.45%)	n/a	-5.91
		RMS error	0.0374 [0.0374]		
		$\chi^2_{d.o.f}$	68.5 [68.5]		

Table B.39: Results for *glennrealextP4* `OptEst_ASC_ILR()` unmixing.

End-member	**'True' Abundance**	**Prior, P4**	**Retrieved Abundance [BBnorm]**	**Accuracy to 'True' Abundance σ [BBnorm]**	**Accuracy to P4 Abundance σ [BBnorm]**
Augite	0.0000	0.1000 ± 0.5000 (500.00%)	rm		
Enstatite	0.0800	0.1000 ± 0.0050 (5.00%)	0.0280 ± 0.0032 (11.32%) [0.0493 ± 0.0056 (11.42%)]	16.44 [5.45]	22.76 [9.01]
Olivine	0.1130	0.1000 ± 0.0050 (5.00%)	rm		
Calcite	0.0080	0.0100 ± 0.0100 (100.00%)	rm		
Saponite	0.0000	0.2540 ± 0.5000 (196.85%)	rm		
Cronstedtite	0.5290	0.5000 ± 0.0050 (1.00%)	0.3995 ± 0.0040 (1.01%) [0.7046 ± 0.0125 (1.78%)]	32.19 [-13.99]	24.98 [-16.30]
Lizardite	0.2330	0.2000 ± 0.0050 (2.50%)	0.1395 ± 0.0036 (2.55%) [0.2461 ± 0.0072 (2.94%)]	26.26 [-1.81]	16.99 [-6.36]
Magnetite	0.0150	0.0100 ± 0.0100 (100.00%)	rm		
Spinel	0.0000	0.0050 ± 0.0500 (1000.00%)	rm		
Troilite	0.0000	0.0200 ± 0.1000 (500.00%)	rm		
Pyrrhotite	0.0090	0.0200 ± 0.0100 (50.00%)	rm		
Albite	0.0000	0.0150 ± 0.1000 (666.67%)	rm		
Anorthite	0.0000	0.0150 ± 0.1000 (666.67%)	rm		
Gypsum	0.0140	0.0500 ± 0.0050 (10.00%)	rm		
AmorphousMg	0.0000	0.0100 ± 0.1000 (1000.00%)	rm		
AmorphousFe	0.0000	0.0100 ± 0.1000 (1000.00%)	rm		
MurchisonIOM	0.0000	0.0200 ± 0.5000 (2500.00%)	rm		
FeNiMetalSub	0.0000	0.0500 ± 0.5000 (1000.00%)	rm		
BB	n/a	0.6000 ± 0.0300 (5.00%)	0.4330 ± 0.0039 (0.90%)	n/a	42.73
		RMS error	0.0042 [0.0255]		

Table B.39 continued from previous page

End-member	'True' Abundance	Prior, P4	Retrieved Abundance [BBnorm]	Accuracy to 'True' Abundance σ [BBnorm]	Accuracy to P4 Abundance σ [BBnorm]
		$\chi^2_{d.o.f}$	1.71 [31.8]		

Table B.40: Results for the *brucemathminP2* `MCMC()` unmixing.

End-member	'True' Abundance	Prior, P2	Retrieved Abundance	Accuracy to 'True' Abundance σ	Accuracy to P2 Abundance σ
Augite	0.0150	0.3004 ± 0.3007 (100.10%)	0.0155 ± 0.0010 (6.17%)	-0.48	298.81
Enstatite	0.0850	0.0110 ± 0.0110 (100.10%)	0.0844 ± 0.0010 (1.17%)	0.58	-74.08
Olivine	0.7000	0.3872 ± 0.3876 (100.10%)	0.7000 ± 3.47E-04 (0.05%)	0.12	-901.95
Troilite	0.0500	0.5015 ± 0.5020 (100.10%)	0.0502 ± 0.0075 (15.04%)	-0.02	59.82
Albite	0.1000	0.6452 ± 0.6459 (100.10%)	0.1000 ± 5.36E-04 (0.54%)	-0.01	1017.94
FeNiMetalSub	0.0500	0.8508 ± 0.8517 (100.10%)	0.0500 ± 0.0078 (15.63%)	0.0004	102.45
		RMS error	2.13E-05		
		$\chi^2_{d.o.f}$	0.0042		

Table B.41: Results for the *brucemathminP4* `MCMC()` unmixing.

End-member	'True' Abundance	Prior, P4	Retrieved Abundance	Accuracy to 'True' Abundance σ	Accuracy to P4 Abundance σ
Augite	0.0150	0.0500 ± 0.0100 (20.00%)	0.0157 ± 0.0009 (5.98%)	-0.77	36.46
Enstatite	0.0850	0.1000 ± 0.0100 (10.00%)	0.0847 ± 0.0010 (1.15%)	0.3	15.71

Table B.41 continued from previous page

End-member	'True' Abundance	Prior, P4	Retrieved Abundance	Accuracy to 'True' Abundance σ	Accuracy to P4 Abundance σ
Olivine	0.7000	0.6000 ± 0.0050 (0.83%)	0.6996 ± 3.41E-04 (0.05%)	1.26	-292.15
Troilite	0.0500	0.0750 ± 0.0100 (13.33%)	0.0494 ± 0.0061 (12.25%)	0.1	4.23
Albite	0.1000	0.0900 ± 0.0100 (11.11%)	0.1000 ± 5.92E-04 (0.59%)	0.01	-16.89
FeNiMetalSub	0.0500	0.0750 ± 0.0100 (13.33%)	0.0506 ± 0.0065 (12.79%)	-0.09	3.77
		RMS error	3.33E-05		
		$\chi^2_{d.o.f}$	0.0052		

Table B.42: Results for the *brucerealminP1* `MCMC` unmixing.

End-member	'True' Abundance	Prior, P1	Retrieved Abundance	Accuracy to 'True' Abundance σ	Accuracy to P1 Abundance σ
Augite	0.0150	0.3004 ± 3.00E-04 (0.10%)	0.2257 ± 3.86E-04 (0.17%)	-546.28	193.65
Enstatite	0.0850	0.0110 ± 1.10E-05 (0.10%)	0.0109 ± 1.32E-05 (0.12%)	5598.93	10.07
Olivine	0.7000	0.3872 ± 3.87E-04 (0.10%)	0.3568 ± 3.28E-04 (0.09%)	1045.57	92.53
Troilite	0.0500	0.5015 ± 5.02E-04 (0.10%)	0.2156 ± 6.11E-04 (0.28%)	-270.89	467.84
Albite	0.1000	0.6452 ± 6.45E-04 (0.10%)	0.1793 ± 6.55E-04 (0.37%)	-120.97	711.1
Fe, Ni metal sub.	0.0500	0.8508 ± 8.51E-04 (0.10%)	0.0192 ± 8.42E-04 (4.39%)	36.64	988.21
		RMS error	0.0197		
		$\chi^2_{d.o.f}$	683.6		

Table B.43: Results for the *brucerealminP2* `MCMC()` unmixing.

End-member	**'True' Abundance**	**Prior, P2**	**Retrieved Abundance**	**Accuracy to 'True' Abundance** σ	**Accuracy to P2 Abundance** σ
Augite	0.0150	0.3004 ± 0.3007 (100.10%)	0.1376 ± 8.62E-04 (0.63%)	-142.25	188.92
Enstatite	0.0850	0.0110 ± 0.0110 (100.10%)	5.94E-06 ± 1.53E-05 (257.21%)	5559.38	719.78
Olivine	0.7000	0.3872 ± 0.3876 (100.10%)	0.5373 ± 5.82E-04 (0.11%)	279.42	-257.71
Troilite	0.0500	0.5015 ± 0.5020 (100.10%)	0.3011 ± 0.0010 (0.32%)	-257.78	205.7
Albite	0.1000	0.6452 ± 0.6459 (100.10%)	0.0328 ± 0.0010 (2.95%)	69.29	631.78
FeNiMetalSub	0.0500	0.8508 ± 0.8517 (100.10%)	1.05E-04 ± 2.67E-04 (253.66%)	187.17	3191.32
		RMS error	0.0158		
		$\chi^2_{d.o.f}$	484.1		

Table B.44: Results for the *brucemathexpU* `MCMC()` unmixing.

End-member	**'True' Abundance**	**Prior, U**	**Retrieved Abundance [BBnorm]**	**Accuracy to 'True' Abundance** σ **[BBnorm]**	**Accuracy to U Abundance** σ
Augite	0.0150	n/a	0.2290 ± 0.1218 (53.17%) [0.1159 ± 0.0656 (56.58%)]	-1.76 [-1.54]	n/a
Enstatite	0.0850	n/a	0.1812 ± 0.1165 (64.26%) [0.0918 ± 0.0616 (67.10%)]	-0.83 [-0.11]	n/a
Olivine	0.7000	n/a	0.2171 ± 0.1523 (70.14%) [0.1099 ± 0.0800 (72.75%)]	3.17 [7.38]	n/a
Calcite	0.0000	n/a	0.1571 ± 0.0842 (53.62%) [0.0795 ± 0.0453 (57.00%)]	-1.87 [-1.75]	n/a

Table B.44 continued from previous page

End-member	'True' Abundance	Prior, U	Retrieved Abundance [BBnorm]	Accuracy to 'True' Abundance σ [BBnorm]	Accuracy to U Abundance σ
Lizardite	0.0000	n/a	0.2398 ± 0.1352 (56.39%) [0.1214 ± 0.0724 (59.61%)]	-1.77 [-1.68]	n/a
Troilite	0.0500	n/a	0.1646 ± 0.0869 (52.77%) [0.0834 ± 0.0468 (56.20%)]	-1.32 [-0.71]	n/a
Albite	0.1000	n/a	0.2136 ± 0.1020 (47.77%) [0.1082 ± 0.0557 (51.53%)]	-1.11 [-0.15]	n/a
Gypsum	0.0000	n/a	0.1758 ± 0.0961 (54.66%) [0.0890 ± 0.0516 (57.98%)]	-1.83 [-1.72]	n/a
AmorphousFe	0.0000	n/a	0.2004 ± 0.0951 (47.46%) [0.1015 ± 0.0520 (51.25%)]	-2.11 [-1.95]	n/a
FeNiMetalSub	0.0500	n/a	0.1964 ± 0.1379 (70.18%) [0.0995 ± 0.0724 (72.80%)]	-1.06 [-0.68]	n/a
BB	n/a	n/a	0.1553 ± 0.0826 (53.19%)	n/a	n/a
		RMS error	1.0942 [0.0683]		
		$\chi^2_{d.o.f}$	10217490.4 [15457.9]		

Table B.45: Results for the *brucemathexpP1* `MCMC()` unmixing.

End-member	**'True' Abundance**	**Prior, P1**	**Retrieved Abundance [BBnorm]**	**Accuracy to 'True' Abundance σ [BBnorm]**	**Accuracy to P1 Abundance σ [BBnorm]**
Augite	0.0150	0.2114 ± 2.11E-04 (0.10%)	0.1203 ± 0.0897 (74.59%) [0.0710 ± 0.0549 (77.42%)]	-1.17 [-1.02]	1.02 [2.56]
Enstatite	0.0850	0.6609 ± 6.61E-04 (0.10%)	0.1679 ± 0.0941 (56.04%) [0.0991 ± 0.0592 (59.75%)]	-0.88 [-0.24]	5.24 [9.49]
Olivine	0.7000	0.1949 ± 1.95E-04 (0.10%)	0.2310 ± 0.1579 (68.35%) [0.1363 ± 0.0973 (71.42%)]	2.97 [5.79]	-0.23 [0.60]
Calcite	0.0000	0.9068 ± 0.0009 (0.10%)	0.1947 ± 0.1022 (52.50%) [0.1149 ± 0.0649 (56.45%)]	-1.90 [-1.77]	6.96 [12.21]
Lizardite	0.0000	0.7720 ± 7.72E-04 (0.10%)	0.1641 ± 0.1110 (67.66%) [0.0968 ± 0.0685 (70.77%)]	-1.48 [-1.41]	5.48 [9.86]
Troilite	0.0500	0.9318 ± 0.0009 (0.10%)	0.1881 ± 0.1288 (68.45%) [0.1110 ± 0.0794 (71.52%)]	-1.07 [-0.77]	5.78 [10.34]
Albite	0.1000	0.0640 ± 6.40E-05 (0.10%)	0.1137 ± 0.0632 (55.60%) [0.0671 ± 0.0398 (59.34%)]	-0.22 [0.83]	-0.79 [-0.08]
Gypsum	0.0000	0.2624 ± 2.62E-04 (0.10%)	0.1593 ± 0.0885 (55.57%) [0.0940 ± 0.0558 (59.32%)]	-1.80 [-1.69]	1.16 [3.02]
AmorphousFe	0.0000	0.3706 ± 3.71E-04 (0.10%)	0.1665 ± 0.1032 (61.98%) [0.0982 ± 0.0642 (65.36%)]	-1.61 [-1.53]	1.98 [4.24]
FeNiMetalSub	0.0500	0.5723 ± 5.72E-04 (0.10%)	0.1893 ± 0.1027 (54.27%) [0.1117 ± 0.0649 (58.10%)]	-1.36 [-0.95]	3.73 [7.10]
BB	n/a	0.9196 ± 0.0009 (0.10%)	0.1204 ± 0.0684 (56.81%)	n/a	11.68
		RMS error	0.7964 [0.0708]		

Table B.45 continued from previous page

End-member	'True' Abundance	Prior, P1	Retrieved Abundance [BBnorm]	Accuracy to 'True' Abundance σ [BBnorm]	Accuracy to P1 Abundance σ [BBnorm]
		$\chi^2_{d.o.f}$	5267652.9 [17037.5]		

Table B.46: Results for the *brucemathexpP2* `MCMC()` unmixing.

End-member	'True' Abundance	Prior, P2	Retrieved Abundance [BBnorm]	Accuracy to 'True' Abundance σ [BBnorm]	Accuracy to P2 Abundance σ [BBnorm]
Augite	0.0150	0.2114 ± 0.2116 (100.10%)	0.1669 ± 0.1007 (60.34%) [0.1042 ± 0.0674 (64.67%)]	-1.51 [-1.32]	0.44 [1.59]
Enstatite	0.0850	0.6609 ± 0.6615 (100.10%)	0.1696 ± 0.1052 (62.05%) [0.1059 ± 0.0701 (66.27%)]	-0.80 [-0.30]	4.67 [7.91]
Olivine	0.7000	0.1949 ± 0.1950 (100.10%)	0.1747 ± 0.0842 (48.20%) [0.1091 ± 0.0584 (53.52%)]	6.24 [10.12]	0.24 [1.47]
Calcite	0.0000	0.9068 ± 0.9077 (100.10%)	0.2115 ± 0.0904 (42.75%) [0.1320 ± 0.0642 (48.67%)]	-2.34 [-2.05]	7.69 [12.06]
Lizardite	0.0000	0.7720 ± 0.7728 (100.10%)	0.1334 ± 0.1490 (111.67%) [0.0832 ± 0.0950 (114.07%)]	-0.90 [-0.88]	4.29 [7.25]
Troilite	0.0500	0.9318 ± 0.9327 (100.10%)	0.1426 ± 0.1090 (76.40%) [0.0890 ± 0.0711 (79.86%)]	-0.85 [-0.55]	7.24 [11.86]
Albite	0.1000	0.0640 ± 0.0640 (100.10%)	0.1172 ± 0.0625 (53.37%) [0.0731 ± 0.0426 (58.22%)]	-0.27 [0.63]	-0.85 [-0.21]

Table B.46 continued from previous page

End-member	'True' Abundance	Prior, P2	Retrieved Abundance [BBnorm]	Accuracy to 'True' Abundance σ [BBnorm]	Accuracy to P2 Abundance σ [BBnorm]
Gypsum	0.0000	0.2624 ± 0.2626 (100.10%)	0.1540 ± 0.0794 (51.60%) [0.0961 ± 0.0544 (56.60%)]	-1.94 [-1.77]	1.36 [3.06]
AmorphousFe	0.0000	0.3706 ± 0.3709 (100.10%)	0.1574 ± 0.0942 (59.81%) [0.0982 ± 0.0630 (64.17%)]	-1.67 [-1.56]	2.26 [4.32]
FeNiMetalSub	0.0500	0.5723 ± 0.5729 (100.10%)	0.1750 ± 0.1259 (71.95%) [0.1092 ± 0.0826 (75.62%)]	-0.99 [-0.72]	3.16 [5.61]
BB	n/a	0.9196 ± 0.9205 (100.10%)	0.1974 ± 0.1294 (65.55%)	n/a	5.58
		RMS error	0.7834 [0.0714]		
		$\chi^2_{d.o.f}$	5071744.5 [18310.8]		

Table B.47: Results for the *brucemathexpP3* `MCMC()` unmixing.

End-member	'True' Abundance	Prior, P3	Retrieved Abundance [BBnorm]	Accuracy to 'True' Abundance σ [BBnorm]	Accuracy to P3 Abundance σ [BBnorm]
Augite	0.0150	0.0150 ± 1.50E-05 (0.10%)	0.0755 ± 0.0863 (114.32%) [0.0461 ± 0.0535 (116.03%)]	-0.70 [-0.58]	-0.70 [-0.58]
Enstatite	0.0850	0.0850 ± 8.50E-05 (0.10%)	0.1300 ± 0.0724 (55.68%) [0.0794 ± 0.0469 (59.10%)]	-0.62 [0.12]	-0.62 [0.12]
Olivine	0.7000	0.7000 ± 7.00E-04 (0.10%)	0.1975 ± 0.0996 (50.41%) [0.1207 ± 0.0654 (54.17%)]	5.05 [8.86]	5.05 [8.86]

Table B.47 continued from previous page

End-member	'True' Abundance	Prior, P3	Retrieved Abundance [BBnorm]	Accuracy to 'True' Abundance σ [BBnorm]	Accuracy to P3 Abundance σ [BBnorm]
Calcite	0.0000	1.00E-04 ± 1.00E-04 (100.10%)	0.2175 ± 0.0949 (43.65%) [0.1329 ± 0.0637 (47.95%)]	-2.29 [-2.09]	-2.29 [-2.08]
Lizardite	0.0000	1.00E-04 ± 1.00E-04 (100.10%)	0.1525 ± 0.1183 (77.58%) [0.0932 ± 0.0746 (80.08%)]	-1.29 [-1.25]	-1.29 [-1.25]
Troilite	0.0500	0.0500 ± 5.00E-05 (0.10%)	0.1268 ± 0.0516 (40.68%) [0.0775 ± 0.0351 (45.26%)]	-1.49 [-0.78]	-1.49 [-0.78]
Albite	0.1000	0.1000 ± 1.00E-04 (0.10%)	0.1763 ± 0.0805 (45.66%) [0.1077 ± 0.0536 (49.78%)]	-0.95 [-0.14]	-0.95 [-0.14]
Gypsum	0.0000	1.00E-04 ± 1.00E-04 (100.10%)	0.1492 ± 0.0702 (47.07%) [0.0911 ± 0.0466 (51.08%)]	-2.12 [-1.96]	-2.12 [-1.96]
AmorphousFe	0.0000	1.00E-04 ± 1.00E-04 (100.10%)	0.2244 ± 0.1492 (66.51%) [0.1371 ± 0.0952 (69.40%)]	-1.50 [-1.44]	-1.50 [-1.44]
FeNiMetalSub	0.0500	0.0500 ± 5.00E-05 (0.10%)	0.1868 ± 0.0994 (53.22%) [0.1142 ± 0.0648 (56.79%)]	-1.38 [-0.99]	-1.38 [-0.99]
BB	n/a	1.00E-04 ± 1.00E-04 (100.10%)	0.1708 ± 0.0821 (48.08%)	n/a	-2.08
		RMS error	0.7876 [0.0755]		
		$\chi^2_{d.o.f}$	5070144.9 [20490.2]		

Table B.48: Results for the *brucemathexpP4* `MCMC()` unmixing.

End-member	**'True' Abundance**	**Prior, P4**	**Retrieved Abundance [BBnorm]**	**Accuracy to 'True' Abundance σ [BBnorm]**	**Accuracy to P4 Abundance σ [BBnorm]**
Augite	0.0150	0.0500 ± 0.0100 (20.00%)	0.1567 ± 0.0817 (52.11%) [0.0874 ± 0.0493 (56.36%)]	-1.74 [-1.47]	-1.31 [-0.76]
Enstatite	0.0850	0.1000 ± 0.0100 (10.00%)	0.1714 ± 0.0827 (48.26%) [0.0956 ± 0.0505 (52.83%)]	-1.04 [-0.21]	-0.86 [0.09]
Olivine	0.7000	0.6000 ± 0.0050 (0.83%)	0.1232 ± 0.0816 (66.28%) [0.0687 ± 0.0479 (69.67%)]	7.07 [13.19]	5.84 [11.10]
Calcite	0.0000	0.0010 ± 0.0100 (1000.00%)	0.2701 ± 0.1177 (43.58%) [0.1507 ± 0.0732 (48.59%)]	-2.29 [-2.06]	-2.29 [-2.04]
Lizardite	0.0000	0.0001 ± 0.0100 (10000.00%)	0.1438 ± 0.0831 (57.81%) [0.0802 ± 0.0495 (61.67%)]	-1.73 [-1.62]	-1.73 [-1.62]
Troilite	0.0500	0.0750 ± 0.0100 (13.33%)	0.2129 ± 0.1149 (53.99%) [0.1187 ± 0.0690 (58.11%)]	-1.42 [-1.00]	-1.20 [-0.63]
Albite	0.1000	0.0900 ± 0.0100 (11.11%)	0.1904 ± 0.1326 (69.61%) [0.1062 ± 0.0774 (72.85%)]	-0.68 [-0.08]	-0.76 [-0.21]
Gypsum	0.0000	0.0001 ± 0.0100 (10000.00%)	0.1841 ± 0.1601 (86.99%) [0.1027 ± 0.0920 (89.60%)]	-1.15 [-1.12]	-1.15 [-1.11]
AmorphousFe	0.0000	0.0001 ± 0.0100 (10000.00%)	0.1962 ± 0.1028 (52.40%) [0.1094 ± 0.0620 (56.63%)]	-1.91 [-1.77]	-1.91 [-1.76]
FeNiMetalSub	0.0500	0.0750 ± 0.0100 (13.33%)	0.1443 ± 0.0891 (61.72%) [0.0805 ± 0.0526 (65.36%)]	-1.06 [-0.58]	-0.78 [-0.10]
BB	n/a	0.2500 ± 0.0125 (5.00%)	0.2094 ± 0.1275 (60.89%)	n/a	0.32
		RMS error	0.9725 [0.0781]		
		$\chi^2_{d.o.f}$	7846655.3 [22514.3]		

Table B.49: Results for the *brucerealexpU* `MCMC()` unmixing.

End-member	**'True' Abundance**	**Prior, U**	**Retrieved Abundance [BBnorm]**	**Accuracy to 'True' Abundance σ [BBnorm]**	**Accuracy to U Abundance σ**
Augite	0.0150	n/a	0.1988 ± 0.1148 (57.76%) [0.1090 ± 0.0665 (61.01%)]	-1.60 [-1.41]	n/a
Enstatite	0.0850	n/a	0.1802 ± 0.1036 (57.50%) [0.0988 ± 0.0600 (60.77%)]	-0.92 [-0.23]	n/a
Olivine	0.7000	n/a	0.1627 ± 0.0851 (52.29%) [0.0892 ± 0.0498 (55.86%)]	6.31 [12.26]	n/a
Calcite	0.0000	n/a	0.2624 ± 0.0835 (31.82%) [0.1439 ± 0.0538 (37.39%)]	-3.14 [-2.67]	n/a
Lizardite	0.0000	n/a	0.1257 ± 0.0830 (65.99%) [0.0689 ± 0.0475 (68.85%)]	-1.52 [-1.45]	n/a
Troilite	0.0500	n/a	0.1980 ± 0.1073 (54.19%) [0.1086 ± 0.0626 (57.64%)]	-1.38 [-0.94]	n/a
Albite	0.1000	n/a	0.1565 ± 0.0951 (60.77%) [0.0858 ± 0.0548 (63.87%)]	-0.59 [0.26]	n/a
Gypsum	0.0000	n/a	0.2002 ± 0.1144 (57.13%) [0.1098 ± 0.0663 (60.41%)]	-1.75 [-1.66]	n/a
AmorphousFe	0.0000	n/a	0.1728 ± 0.1009 (58.40%) [0.0947 ± 0.0584 (61.61%)]	-1.71 [-1.62]	n/a
FeNiMetalSub	0.0500	n/a	0.1665 ± 0.0810 (48.64%) [0.0913 ± 0.0479 (52.46%)]	-1.44 [-0.86]	n/a
BB	n/a	n/a	0.1569 ± 0.1284 (81.83%)	n/a	n/a
		RMS error	0.9235 [0.0574]		
		$\chi^2_{d.o.f}$	2119412.4 [5080.3]		

Table B.50: Results for the *brucerealexpP1* `MCMC()` unmixing.

End-member	**'True' Abundance**	**Prior, P1**	**Retrieved Abundance [BBnorm]**	**Accuracy to 'True' Abundance σ [BBnorm]**	**Accuracy to P1 Abundance σ [BBnorm]**
Augite	0.0150	0.2114 ± 2.11E-04 (0.10%)	0.1331 ± 0.0987 (74.15%) [0.0830 ± 0.0637 (76.77%)]	-1.20 [-1.07]	0.79 [2.01]
Enstatite	0.0850	0.6609 ± 6.61E-04 (0.10%)	0.1559 ± 0.0934 (59.90%) [0.0973 ± 0.0614 (63.12%)]	-0.76 [-0.20]	5.41 [9.18]
Olivine	0.7000	0.1949 ± 1.95E-04 (0.10%)	0.1561 ± 0.0703 (45.05%) [0.0974 ± 0.0480 (49.25%)]	7.73 [12.56]	0.55 [2.03]
Calcite	0.0000	0.9068 ± 0.0009 (0.10%)	0.2106 ± 0.1033 (49.05%) [0.1314 ± 0.0695 (52.94%)]	-2.04 [-1.89]	6.74 [11.15]
Lizardite	0.0000	0.7720 ± 7.72E-04 (0.10%)	0.1897 ± 0.1073 (56.60%) [0.1183 ± 0.0710 (60.00%)]	-1.77 [-1.67]	5.43 [9.21]
Troilite	0.0500	0.9318 ± 0.0009 (0.10%)	0.1591 ± 0.1099 (69.07%) [0.0993 ± 0.0713 (71.88%)]	-0.99 [-0.69]	7.03 [11.67]
Albite	0.1000	0.0640 ± 6.40E-05 (0.10%)	0.1000 ± 0.0569 (56.91%) [0.0624 ± 0.0376 (60.29%)]	-0.0006 [1.00]	-0.63 [0.04]
Gypsum	0.0000	0.2624 ± 2.62E-04 (0.10%)	0.1397 ± 0.0831 (59.46%) [0.0872 ± 0.0547 (62.71%)]	-1.68 [-1.59]	1.48 [3.20]
AmorphousFe	0.0000	0.3706 ± 3.71E-04 (0.10%)	0.1630 ± 0.0806 (49.45%) [0.1017 ± 0.0542 (53.30%)]	-2.02 [-1.88]	2.57 [4.96]
FeNiMetalSub	0.0500	0.5723 ± 5.72E-04 (0.10%)	0.1956 ± 0.1042 (53.28%) [0.1220 ± 0.0694 (56.88%)]	-1.40 [-1.04]	3.62 [6.49]
BB	n/a	0.9196 ± 0.0009 (0.10%)	0.1677 ± 0.0911 (54.33%)	n/a	8.25
		RMS error	0.7360 [0.0567]		
		$\chi^2_{d.o.f}$	1322284.1 [4566.7]		

Table B.51: Results for the *brucerealexpP2* `MCMC()` unmixing.

End-member	**'True' Abundance**	**Prior, P2**	**Retrieved Abundance [BBnorm]**	**Accuracy to 'True' Abundance σ [BBnorm]**	**Accuracy to P2 Abundance σ [BBnorm]**
Augite	0.0150	0.2114 ± 0.2116 (100.10%)	0.1539 ± 0.1064 (69.14%) [0.1023 ± 0.0742 (72.59%)]	-1.31 [-1.18]	0.54 [1.47]
Enstatite	0.0850	0.6609 ± 0.6615 (100.10%)	0.1629 ± 0.0878 (53.90%) [0.1083 ± 0.0631 (58.26%)]	-0.89 [-0.37]	5.67 [8.76]
Olivine	0.7000	0.1949 ± 0.1950 (100.10%)	0.1549 ± 0.1035 (66.82%) [0.1029 ± 0.0724 (70.38%)]	5.27 [8.25]	0.39 [1.27]
Calcite	0.0000	0.9068 ± 0.9077 (100.10%)	0.1068 ± 0.0466 (43.64%) [0.0710 ± 0.0347 (48.92%)]	-2.29 [-2.04]	17.17 [24.08]
Lizardite	0.0000	0.7720 ± 0.7728 (100.10%)	0.2037 ± 0.1161 (57.02%) [0.1353 ± 0.0828 (61.16%)]	-1.75 [-1.64]	4.89 [7.69]
Troilite	0.0500	0.9318 ± 0.9327 (100.10%)	0.1752 ± 0.0937 (53.47%) [0.1164 ± 0.0674 (57.86%)]	-1.34 [-0.99]	8.08 [12.10]
Albite	0.1000	0.0640 ± 0.0640 (100.10%)	0.1500 ± 0.0907 (60.46%) [0.0996 ± 0.0641 (64.38%)]	-0.55 [0.01]	-0.95 [-0.56]
Gypsum	0.0000	0.2624 ± 0.2626 (100.10%)	0.1242 ± 0.0892 (71.88%) [0.0825 ± 0.0620 (75.21%)]	-1.39 [-1.33]	1.55 [2.90]
AmorphousFe	0.0000	0.3706 ± 0.3709 (100.10%)	0.1468 ± 0.1423 (96.96%) [0.0975 ± 0.0970 (99.45%)]	-1.03 [-1.01]	1.57 [2.82]
FeNiMetalSub	0.0500	0.5723 ± 0.5729 (100.10%)	0.1268 ± 0.0974 (76.85%) [0.0842 ± 0.0674 (79.97%)]	-0.79 [-0.51]	4.57 [7.25]
BB	n/a	0.9196 ± 0.9205 (100.10%)	0.1326 ± 0.0733 (55.28%)	n/a	10.74
		RMS error	0.6176 [0.0496]		
		$\chi^2_{d.o.f}$	929367.7 [3088.6]		

Table B.52: Results for the *brucerealexpP3* `MCMC()` unmixing.

End-member	**'True' Abundance**	**Prior, P3**	**Retrieved Abundance [BBnorm]**	**Accuracy to 'True' Abundance σ [BBnorm]**	**Accuracy to P3 Abundance σ [BBnorm]**
Augite	0.0150	0.0150 ± 1.50E-05 (0.10%)	0.0644 ± 0.0231 (35.87%) [0.0471 ± 0.0192 (40.88%)]	-2.14 [-1.67]	-2.14 [-1.67]
Enstatite	0.0850	0.0850 ± 8.50E-05 (0.10%)	0.1151 ± 0.0805 (69.93%) [0.0841 ± 0.0610 (72.63%)]	-0.37 [0.02]	-0.37 [0.02]
Olivine	0.7000	0.7000 ± 7.00E-04 (0.10%)	0.1808 ± 0.0929 (51.39%) [0.1320 ± 0.0726 (55.01%)]	5.59 [7.82]	5.59 [7.82]
Calcite	0.0000	1.00E-04 ± 1.00E-04 (100.10%)	0.1292 ± 0.0884 (68.45%) [0.0944 ± 0.0672 (71.20%)]	-1.46 [-1.40]	-1.46 [-1.40]
Lizardite	0.0000	1.00E-04 ± 1.00E-04 (100.10%)	0.1690 ± 0.0899 (53.16%) [0.1235 ± 0.0700 (56.67%)]	-1.88 [-1.76]	-1.88 [-1.76]
Troilite	0.0500	0.0500 ± 5.00E-05 (0.10%)	0.1375 ± 0.0481 (34.97%) [0.1005 ± 0.0403 (40.09%)]	-1.82 [-1.25]	-1.82 [-1.25]
Albite	0.1000	0.1000 ± 1.00E-04 (0.10%)	0.1715 ± 0.0603 (35.18%) [0.1253 ± 0.0505 (40.27%)]	-1.19 [-0.50]	-1.19 [-0.50]
Gypsum	0.0000	1.00E-04 ± 1.00E-04 (100.10%)	0.1371 ± 0.0727 (53.03%) [0.1002 ± 0.0566 (56.54%)]	-1.89 [-1.77]	-1.88 [-1.77]
AmorphousFe	0.0000	1.00E-04 ± 1.00E-04 (100.10%)	0.1417 ± 0.0849 (59.88%) [0.1035 ± 0.0652 (63.01%)]	-1.67 [-1.59]	-1.67 [-1.59]
FeNiMetalSub	0.0500	0.0500 ± 5.00E-05 (0.10%)	0.1226 ± 0.0665 (54.25%) [0.0896 ± 0.0517 (57.69%)]	-1.09 [-0.77]	-1.09 [-0.77]
BB	n/a	1.00E-04 ± 1.00E-04 (100.10%)	0.1495 ± 0.0941 (62.93%)	n/a	-1.59
		RMS error	0.5040 [0.0526]		
		$\chi^2_{d.o.f}$	601043.6 [3724.7]		

Table B.53: Results for the *brucerealexpP4* `MCMC()` unmixing.

End-member	**'True' Abundance**	**Prior, P4**	**Retrieved Abundance [BBnorm]**	**Accuracy to 'True' Abundance σ [BBnorm]**	**Accuracy to P4 Abundance σ [BBnorm]**
Augite	0.0150	0.0500 ± 0.0100 (20.00%)	0.1699 ± 0.0803 (47.28%) [0.1093 ± 0.0567 (51.85%)]	-1.93 [-1.66]	-1.49 [-1.05]
Enstatite	0.0850	0.1000 ± 0.0100 (10.00%)	0.1137 ± 0.0673 (59.19%) [0.0732 ± 0.0460 (62.90%)]	-0.43 [0.26]	-0.20 [0.58]
Olivine	0.7000	0.6000 ± 0.0050 (0.83%)	0.1600 ± 0.0980 (61.24%) [0.1030 ± 0.0668 (64.84%)]	5.51 [8.94]	4.49 [7.44]
Calcite	0.0000	0.0010 ± 0.0100 (1000.00%)	0.1920 ± 0.0712 (37.06%) [0.1236 ± 0.0528 (42.74%)]	-2.70 [-2.34]	-2.68 [-2.32]
Lizardite	0.0000	0.0001 ± 0.0100 (10000.00%)	0.1635 ± 0.0816 (49.90%) [0.1052 ± 0.0571 (54.25%)]	-2.00 [-1.84]	-2.00 [-1.84]
Troilite	0.0500	0.0750 ± 0.0100 (13.33%)	0.1493 ± 0.1248 (83.57%) [0.0961 ± 0.0828 (86.24%)]	-0.80 [-0.56]	-0.60 [-0.25]
Albite	0.1000	0.0900 ± 0.0100 (11.11%)	0.1680 ± 0.0868 (51.66%) [0.1081 ± 0.0604 (55.88%)]	-0.78 [-0.13]	-0.90 [-0.30]
Gypsum	0.0000	0.0001 ± 0.0100 (10000.00%)	0.1530 ± 0.0994 (64.95%) [0.0984 ± 0.0673 (68.35%)]	-1.54 [-1.46]	-1.54 [-1.46]
AmorphousFe	0.0000	0.0001 ± 0.0100 (10000.00%)	0.1433 ± 0.0789 (55.04%) [0.0922 ± 0.0544 (59.01%)]	-1.82 [-1.69]	-1.82 [-1.69]
FeNiMetalSub	0.0500	0.0750 ± 0.0100 (13.33%)	0.1414 ± 0.0911 (64.48%) [0.0910 ± 0.0618 (67.90%)]	-1.00 [-0.66]	-0.73 [-0.26]
BB	n/a	0.2500 ± 0.0125 (5.00%)	0.1170 ± 0.1217 (103.99%)	n/a	1.09
		RMS error	0.6374 [0.0537]		
		$\chi^2_{d.o.f}$	988868.3 [4282.6]		

Table B.54: Results for the *brucemathextU* `MCMC()` unmixing.

End-member	**'True' Abundance**	**Prior, U**	**Retrieved Abundance [BBnorm]**	**Accuracy to 'True' Abundance σ [BBnorm]**	**Accuracy to U Abundance σ**
Augite	0.0150	n/a	0.3570 ± 0.1859 (52.07%) [0.0721 ± 0.0388 (53.84%)]	-1.84 [-1.47]	n/a
Enstatite	0.0850	n/a	0.2342 ± 0.1448 (61.84%) [0.0473 ± 0.0299 (63.33%)]	-1.03 [1.26]	n/a
Olivine	0.7000	n/a	0.1636 ± 0.0682 (41.66%) [0.0330 ± 0.0145 (43.85%)]	7.87 [46.04]	n/a
Calcite	0.0000	n/a	0.1929 ± 0.0899 (46.57%) [0.0390 ± 0.0189 (48.54%)]	-2.15 [-2.06]	n/a
Saponite	0.0000	n/a	0.2779 ± 0.2444 (87.95%) [0.0561 ± 0.0500 (89.01%)]	-1.14 [-1.12]	n/a
Cronstedtite	0.0000	n/a	0.3286 ± 0.1784 (54.27%) [0.0664 ± 0.0371 (55.97%)]	-1.84 [-1.79]	n/a
Lizardite	0.0000	n/a	0.2116 ± 0.1071 (50.61%) [0.0427 ± 0.0224 (52.43%)]	-1.98 [-1.91]	n/a
Magnetite	0.0000	n/a	0.2842 ± 0.1189 (41.84%) [0.0574 ± 0.0253 (44.02%)]	-2.39 [-2.27]	n/a
Spinel	0.0000	n/a	0.3166 ± 0.1485 (46.91%) [0.0639 ± 0.0312 (48.87%)]	-2.13 [-2.05]	n/a
Troilite	0.0500	n/a	0.1894 ± 0.1067 (56.32%) [0.0382 ± 0.0222 (57.96%)]	-1.31 [0.53]	n/a
Pyrrhotite	0.0000	n/a	0.2981 ± 0.1360 (45.64%) [0.0602 ± 0.0287 (47.65%)]	-2.19 [-2.10]	n/a

Table B.54 continued from previous page

End-member	'True' Abundance	Prior, U	Retrieved Abundance [BBnorm]	Accuracy to 'True' Abundance σ [BBnorm]	Accuracy to U Abundance σ
Albite	0.1000	n/a	0.3008 ± 0.1843 (61.26%) [0.0607 ± 0.0381 (62.78%)]	-1.09 [1.03]	n/a
Anorthite	0.0000	n/a	0.2968 ± 0.1366 (46.02%) [0.0599 ± 0.0288 (48.01%)]	-2.17 [-2.08]	n/a
Gypsum	0.0000	n/a	0.3418 ± 0.1598 (46.75%) [0.0690 ± 0.0336 (48.71%)]	-2.14 [-2.05]	n/a
AmorphousMg	0.0000	n/a	0.2370 ± 0.1634 (68.93%) [0.0479 ± 0.0336 (70.28%)]	-1.45 [-1.42]	n/a
AmorphousFe	0.0000	n/a	0.4110 ± 0.2096 (51.01%) [0.0830 ± 0.0438 (52.81%)]	-1.96 [-1.89]	n/a
MurchisonIOM	0.0000	n/a	0.1803 ± 0.0835 (46.31%) [0.0364 ± 0.0176 (48.29%)]	-2.16 [-2.07]	n/a
FeNiMetalSub	0.0500	n/a	0.3305 ± 0.1677 (50.76%) [0.0667 ± 0.0351 (52.57%)]	-1.67 [-0.48]	n/a
BB	n/a	n/a	0.3548 ± 0.1387 (39.10%)	n/a	n/a
		RMS error	4.1268 [0.0788]		
		$\chi^2_{d.o.f}$	151819732.7 [21308.3]		

Table B.55: Results for the *brucerealextU* `MCMC()` unmixing.

End-member	'True' Abundance	Prior, U	Retrieved Abundance [BBnorm]	Accuracy to 'True' Abundance σ [BBnorm]	Accuracy to U Abundance σ
Calcite	0.0000	n/a	0.5058 ± 0.2958 (58.48%) [0.1102 ± 0.0667 (60.51%)]	-1.71 [-1.65]	n/a
Augite	0.0150	n/a	0.1527 ± 0.2951 (193.30%) [0.0333 ± 0.0645 (193.92%)]	-0.47 [-0.28]	n/a
Enstatite	0.0850	n/a	0.2852 ± 0.1175 (41.19%) [0.0622 ± 0.0274 (44.02%)]	-1.70 [0.83]	n/a
Olivine	0.7000	n/a	0.1831 ± 0.0980 (53.52%) [0.0399 ± 0.0222 (55.72%)]	5.28 [29.69]	n/a
Saponite	0.0000	n/a	0.2298 ± 0.1043 (45.39%) [0.0501 ± 0.0240 (47.97%)]	-2.20 [-2.08]	n/a
Cronstedtite	0.0000	n/a	0.1876 ± 0.1137 (60.57%) [0.0409 ± 0.0256 (62.53%)]	-1.65 [-1.60]	n/a
Lizardite	0.0000	n/a	0.2416 ± 0.1306 (54.07%) [0.0527 ± 0.0296 (56.25%)]	-1.85 [-1.78]	n/a
Magnetite	0.0000	n/a	0.2020 ± 0.1041 (51.53%) [0.0440 ± 0.0237 (53.81%)]	-1.94 [-1.86]	n/a
Spinel	0.0000	n/a	0.2820 ± 0.1270 (45.02%) [0.0615 ± 0.0293 (47.62%)]	-2.22 [-2.10]	n/a
Troilite	0.0500	n/a	0.2071 ± 0.1079 (52.10%) [0.0451 ± 0.0245 (54.37%)]	-1.46 [0.20]	n/a
Pyrrhotite	0.0000	n/a	0.2656 ± 0.1903 (71.64%) [0.0579 ± 0.0424 (73.30%)]	-1.40 [-1.36]	n/a

Table B.55 continued from previous page

End-member	'True' Abundance	Prior, U	Retrieved Abundance [BBnorm]	Accuracy to 'True' Abundance σ [BBnorm]	Accuracy to U Abundance σ
Albite	0.1000	n/a	0.2343 ± 0.1329 (56.74%) [0.0511 ± 0.0300 (58.83%)]	-1.01 [1.63]	n/a
Anorthite	0.0000	n/a	0.3383 ± 0.1310 (38.74%) [0.0737 ± 0.0308 (41.73%)]	-2.58 [-2.40]	n/a
Gypsum	0.0000	n/a	0.3120 ± 0.1367 (43.82%) [0.0680 ± 0.0316 (46.49%)]	-2.28 [-2.15]	n/a
AmorphousFe	0.0000	n/a	0.2681 ± 0.2285 (85.23%) [0.0584 ± 0.0506 (86.63%)]	-1.17 [-1.15]	n/a
AmorphousMg	0.0000	n/a	0.1295 ± 0.0619 (47.80%) [0.0282 ± 0.0142 (50.26%)]	-2.09 [-1.99]	n/a
MurchisonIOM	0.0000	n/a	0.3457 ± 0.1581 (45.72%) [0.0754 ± 0.0364 (48.28%)]	-2.19 [-2.07]	n/a
FeNiMetalSub	0.0500	n/a	0.2175 ± 0.1103 (50.70%) [0.0474 ± 0.0251 (53.02%)]	-1.52 [0.10]	n/a
BB	n/a	n/a	0.2889 ± 0.1524 (52.77%)	n/a	n/a
		RMS error	3.6543 [0.0564]		
		$\chi^2_{d.o.f}$	35195110.2 [3802.8]		

Table B.56: Results for the *brucerealextP1* `MCMC()` unmixing.

End-member	**'True' Abundance**	**Prior, P1**	**Retrieved Abundance [BBnorm]**	**Accuracy to 'True' Abundance σ [BBnorm]**	**Accuracy to P1 Abundance σ [BBnorm]**
Augite	0.0150	0.7172 ± 7.17E-04 (0.10%)	0.3331 ± 0.1474 (44.24%) [0.0681 ± 0.0311 (45.72%)]	-2.16 [-1.71]	2.61 [20.84]
Enstatite	0.0850	0.4381 ± 4.38E-04 (0.10%)	0.3209 ± 0.1099 (34.23%) [0.0656 ± 0.0237 (36.13%)]	-2.15 [0.82]	1.07 [15.71]
Olivine	0.7000	0.8050 ± 8.05E-04 (0.10%)	0.3319 ± 0.1972 (59.42%) [0.0679 ± 0.0411 (60.53%)]	1.87 [15.39]	2.40 [17.95]
Calcite	0.0000	0.2546 ± 2.55E-04 (0.10%)	0.3076 ± 0.1187 (38.58%) [0.0629 ± 0.0253 (40.27%)]	-2.59 [-2.48]	-0.45 [7.57]
Saponite	0.0000	0.0326 ± 3.26E-05 (0.10%)	0.1253 ± 0.0868 (69.32%) [0.0256 ± 0.0180 (70.28%)]	-1.44 [-1.42]	-1.07 [0.39]
Cronstedtite	0.0000	0.9071 ± 0.0009 (0.10%)	0.2657 ± 0.1289 (48.53%) [0.0543 ± 0.0271 (49.88%)]	-2.06 [-2.00]	4.97 [31.47]
Lizardite	0.0000	0.5086 ± 5.09E-04 (0.10%)	0.2946 ± 0.1528 (51.88%) [0.0602 ± 0.0320 (53.15%)]	-1.93 [-1.88]	1.40 [14.01]
Magnetite	0.0000	0.7271 ± 7.27E-04 (0.10%)	0.3074 ± 0.1558 (50.68%) [0.0629 ± 0.0327 (51.98%)]	-1.97 [-1.92]	2.69 [20.33]
Spinel	0.0000	0.6179 ± 6.18E-04 (0.10%)	0.2763 ± 0.1173 (42.46%) [0.0565 ± 0.0249 (44.00%)]	-2.36 [-2.27]	2.91 [22.59]
Troilite	0.0500	0.8562 ± 8.56E-04 (0.10%)	0.2892 ± 0.1893 (65.46%) [0.0591 ± 0.0393 (66.47%)]	-1.26 [-0.23]	3.00 [20.28]
Pyrrhotite	0.0000	0.6534 ± 6.53E-04 (0.10%)	0.2854 ± 0.1123 (39.36%) [0.0584 ± 0.0239 (41.02%)]	-2.54 [-2.44]	3.28 [24.86]

Table B.56 continued from previous page

End-member	'True' Abundance	Prior, P1	Retrieved Abundance [BBnorm]	Accuracy to 'True' Abundance σ [BBnorm]	Accuracy to P1 Abundance σ [BBnorm]
Albite	0.1000	0.5196 ± 5.20E-04 (0.10%)	0.2236 ± 0.0970 (43.36%) [0.0457 ± 0.0205 (44.88%)]	-1.27 [2.64]	3.05 [23.10]
Anorthite	0.0000	0.8820 ± 8.82E-04 (0.10%)	0.2962 ± 0.1338 (45.16%) [0.0606 ± 0.0282 (46.62%)]	-2.21 [-2.15]	4.38 [29.09]
Gypsum	0.0000	0.3018 ± 3.02E-04 (0.10%)	0.1923 ± 0.0845 (43.95%) [0.0393 ± 0.0179 (45.44%)]	-2.28 [-2.20]	1.30 [14.69]
AmorphousMg	0.0000	0.1128 ± 1.13E-04 (0.10%)	0.2282 ± 0.0929 (40.71%) [0.0467 ± 0.0197 (42.31%)]	-2.46 [-2.36]	-1.24 [3.35]
AmorphousFe	0.0000	0.5535 ± 5.53E-04 (0.10%)	0.2923 ± 0.1072 (36.69%) [0.0598 ± 0.0230 (38.46%)]	-2.73 [-2.60]	2.44 [21.48]
MurchisonIOM	0.0000	0.9793 ± 0.0010 (0.10%)	0.2669 ± 0.1221 (45.74%) [0.0546 ± 0.0257 (47.17%)]	-2.19 [-2.12]	5.84 [35.92]
FeNiMetalSub	0.0500	0.4243 ± 4.24E-04 (0.10%)	0.2536 ± 0.1487 (58.62%) [0.0519 ± 0.0310 (59.74%)]	-1.37 [-0.06]	1.15 [12.02]
BB	n/a	0.2287 ± 2.29E-04 (0.10%)	0.1142 ± 0.0576 (50.46%)	n/a	1.99
		RMS error	3.7817 [0.0510]		
		$\chi^2_{d.o.f}$	37917176.2 [2785.2]		

Table B.57: Results for the *brucerealextP2* `MCMC()` unmixing.

End-member	**'True' Abundance**	**Prior, P2**	**Retrieved Abundance [BBnorm]**	**Accuracy to 'True' Abundance σ [BBnorm]**	**Accuracy to P2 Abundance σ [BBnorm]**
Augite	0.0150	0.7172 ± 0.7179 (100.10%)	0.1692 ± 0.0617 (36.47%) [0.0340 ± 0.0131 (38.51%)]	-2.50 [-1.45]	8.88 [52.17]
Enstatite	0.0850	0.4381 ± 0.4385 (100.10%)	0.2749 ± 0.1616 (58.80%) [0.0552 ± 0.0332 (60.08%)]	-1.17 [0.90]	1.01 [11.53]
Olivine	0.7000	0.8050 ± 0.8058 (100.10%)	0.1519 ± 0.0751 (49.41%) [0.0305 ± 0.0156 (50.93%)]	7.30 [43.05]	8.70 [49.81]
Calcite	0.0000	0.2546 ± 0.2549 (100.10%)	0.1870 ± 0.1789 (95.63%) [0.0376 ± 0.0362 (96.42%)]	-1.05 [-1.04]	0.38 [5.99]
Saponite	0.0000	0.0326 ± 0.0326 (100.10%)	0.2542 ± 0.1141 (44.89%) [0.0511 ± 0.0238 (46.56%)]	-2.23 [-2.15]	-1.94 [-0.78]
Cronstedtite	0.0000	0.9071 ± 0.9080 (100.10%)	0.2105 ± 0.1052 (49.96%) [0.0423 ± 0.0218 (51.46%)]	-2.00 [-1.94]	6.62 [39.72]
Lizardite	0.0000	0.5086 ± 0.5091 (100.10%)	0.4094 ± 0.2344 (57.25%) [0.0823 ± 0.0482 (58.57%)]	-1.75 [-1.71]	0.42 [8.85]
Magnetite	0.0000	0.7271 ± 0.7278 (100.10%)	0.3220 ± 0.1640 (50.93%) [0.0647 ± 0.0339 (52.41%)]	-1.96 [-1.91]	2.47 [19.53]
Spinel	0.0000	0.6179 ± 0.6185 (100.10%)	0.2952 ± 0.1018 (34.49%) [0.0593 ± 0.0217 (36.63%)]	-2.90 [-2.73]	3.17 [25.70]
Troilite	0.0500	0.8562 ± 0.8571 (100.10%)	0.3268 ± 0.1461 (44.70%) [0.0657 ± 0.0305 (46.38%)]	-1.89 [-0.51]	3.62 [25.95]
Pyrrhotite	0.0000	0.6534 ± 0.6541 (100.10%)	0.3008 ± 0.1215 (40.40%) [0.0605 ± 0.0255 (42.25%)]	-2.48 [-2.37]	2.90 [23.22]

Table B.57 continued from previous page

End-member	'True' Abundance	Prior, P2	Retrieved Abundance [BBnorm]	Accuracy to 'True' Abundance σ [BBnorm]	Accuracy to P2 Abundance σ [BBnorm]
Albite	0.1000	0.5196 ± 0.5202 (100.10%)	0.3169 ± 0.1179 (37.20%) [0.0637 ± 0.0250 (39.19%)]	-1.84 [1.45]	1.72 [18.26]
Anorthite	0.0000	0.8820 ± 0.8829 (100.10%)	0.1573 ± 0.0752 (47.83%) [0.0316 ± 0.0156 (49.40%)]	-2.09 [-2.02]	9.64 [54.48]
Gypsum	0.0000	0.3018 ± 0.3021 (100.10%)	0.4063 ± 0.1928 (47.46%) [0.0817 ± 0.0400 (49.04%)]	-2.11 [-2.04]	-0.54 [5.50]
AmorphousMg	0.0000	0.1128 ± 0.1129 (100.10%)	0.2173 ± 0.1283 (59.05%) [0.0437 ± 0.0263 (60.33%)]	-1.69 [-1.66]	-0.81 [2.62]
AmorphousFe	0.0000	0.5535 ± 0.5540 (100.10%)	0.3062 ± 0.1454 (47.49%) [0.0615 ± 0.0302 (49.07%)]	-2.11 [-2.04]	1.70 [16.29]
MurchisonIOM	0.0000	0.9793 ± 0.9803 (100.10%)	0.2588 ± 0.1627 (62.87%) [0.0520 ± 0.0333 (64.07%)]	-1.59 [-1.56]	4.43 [27.83]
FeNiMetalSub	0.0500	0.4243 ± 0.4247 (100.10%)	0.4111 ± 0.1564 (38.04%) [0.0826 ± 0.0330 (40.00%)]	-2.31 [-0.99]	0.08 [10.34]
BB	n/a	0.2287 ± 0.2289 (100.10%)	0.1221 ± 0.0800 (65.52%)	n/a	1.33
		RMS error	3.9283 [0.0612]		
		$\chi^2_{d.o.f}$	40575701.8 [3498.3]		

Table B.58: Results for the *brucerealextP3* `MCMC()` unmixing.

End-member	**'True' Abundance**	**Prior, P3**	**Retrieved Abundance [BBnorm]**	**Accuracy to 'True' Abundance σ [BBnorm]**	**Accuracy to P3 Abundance σ [BBnorm]**
Augite	0.0150	0.0150 ± 1.50E-05 (0.10%)	0.1837 ± 0.0402 (21.88%) [0.0423 ± 0.0113 (26.66%)]	-4.20 [-2.42]	-4.20 [-2.42]
Enstatite	0.0850	0.0850 ± 8.50E-05 (0.10%)	0.2422 ± 0.1166 (48.15%) [0.0558 ± 0.0282 (50.50%)]	-1.35 [1.04]	-1.35 [1.04]
Olivine	0.7000	0.7000 ± 7.00E-04 (0.10%)	0.2114 ± 0.0938 (44.39%) [0.0487 ± 0.0229 (46.93%)]	5.21 [28.50]	5.21 [28.50]
Calcite	0.0000	1.00E-04 ± 1.00E-07 (0.10%)	0.5081 ± 0.2152 (42.35%) [0.1171 ± 0.0527 (45.00%)]	-2.36 [-2.22]	-2.36 [-2.22]
Saponite	0.0000	1.00E-04 ± 1.00E-07 (0.10%)	0.1789 ± 0.1131 (63.20%) [0.0412 ± 0.0268 (65.01%)]	-1.58 [-1.54]	-1.58 [-1.53]
Cronstedtite	0.0000	1.00E-04 ± 1.00E-07 (0.10%)	0.1364 ± 0.1666 (122.13%) [0.0314 ± 0.0387 (123.07%)]	-0.82 [-0.81]	-0.82 [-0.81]
Lizardite	0.0000	1.00E-04 ± 1.00E-07 (0.10%)	0.2608 ± 0.1136 (43.58%) [0.0601 ± 0.0277 (46.17%)]	-2.29 [-2.17]	-2.29 [-2.16]
Magnetite	0.0000	1.00E-04 ± 1.00E-07 (0.10%)	0.2125 ± 0.1149 (54.08%) [0.0489 ± 0.0275 (56.18%)]	-1.85 [-1.78]	-1.85 [-1.78]
Spinel	0.0000	1.00E-04 ± 1.00E-07 (0.10%)	0.2087 ± 0.2091 (100.18%) [0.0481 ± 0.0487 (101.33%)]	-1.00 [-0.99]	-1.00 [-0.98]
Troilite	0.0500	0.0500 ± 5.00E-05 (0.10%)	0.1533 ± 0.0949 (61.88%) [0.0353 ± 0.0225 (63.72%)]	-1.09 [0.65]	-1.09 [0.65]
Pyrrhotite	0.0000	1.00E-04 ± 1.00E-07 (0.10%)	0.2318 ± 0.1081 (46.63%) [0.0534 ± 0.0262 (49.06%)]	-2.14 [-2.04]	-2.14 [-2.03]

Table B.58 continued from previous page

End-member	'True' Abundance	Prior, P3	Retrieved Abundance [BBnorm]	Accuracy to 'True' Abundance σ [BBnorm]	Accuracy to P3 Abundance σ [BBnorm]
Albite	0.1000	0.1000 ± 1.00E-04 (0.10%)	0.2290 ± 0.1577 (68.89%) [0.0527 ± 0.0372 (70.55%)]	-0.82 [1.27]	-0.82 [1.27]
Anorthite	0.0000	1.00E-04 ± 1.00E-07 (0.10%)	0.1844 ± 0.1256 (68.09%) [0.0425 ± 0.0296 (69.77%)]	-1.47 [-1.43]	-1.47 [-1.43]
Gypsum	0.0000	1.00E-04 ± 1.00E-07 (0.10%)	0.2816 ± 0.3259 (115.74%) [0.0649 ± 0.0757 (116.74%)]	-0.86 [-0.86]	-0.86 [-0.86]
AmorphousMg	0.0000	1.00E-04 ± 1.00E-07 (0.10%)	0.1747 ± 0.1116 (63.88%) [0.0402 ± 0.0264 (65.67%)]	-1.57 [-1.52]	-1.56 [-1.52]
AmorphousFe	0.0000	1.00E-04 ± 1.00E-07 (0.10%)	0.3364 ± 0.1424 (42.32%) [0.0775 ± 0.0349 (44.98%)]	-2.36 [-2.22]	-2.36 [-2.22]
MurchisonIOM	0.0000	1.00E-04 ± 1.00E-07 (0.10%)	0.2140 ± 0.0836 (39.06%) [0.0493 ± 0.0207 (41.93%)]	-2.56 [-2.39]	-2.56 [-2.38]
FeNiMetalSub	0.0500	0.0500 ± 5.00E-05 (0.10%)	0.3931 ± 0.1696 (43.14%) [0.0906 ± 0.0414 (45.75%)]	-2.02 [-0.98]	-2.02 [-0.98]
BB	n/a	1.00E-04 ± 1.00E-07 (0.10%)	0.2677 ± 0.1010 (37.74%)	n/a	-2.65
		RMS error	3.4026 [0.0595]		
		$\chi^2_{d.o.f}$	30343315.7 [4238.5]		

Table B.59: Results for the *brucerealextP4* `MCMC()` unmixing.

End-member	'True' Abundance	Prior, P4	Retrieved Abundance [BBnorm]	Accuracy to 'True' Abundance σ [BBnorm]	Accuracy to P4 Abundance σ [BBnorm]
Augite	0.0150	0.0500 ± 0.0100 (20.00%)	0.3403 ± 0.1494 (43.89%) [0.0687 ± 0.0312 (45.51%)]	-2.18 [-1.72]	-1.94 [-0.60]
Enstatite	0.0850	0.1000 ± 0.0100 (10.00%)	0.2937 ± 0.1354 (46.10%) [0.0593 ± 0.0282 (47.64%)]	-1.54 [0.91]	-1.43 [1.44]
Olivine	0.7000	0.6000 ± 0.0050 (0.83%)	0.2367 ± 0.1147 (48.44%) [0.0478 ± 0.0238 (49.91%)]	4.04 [27.36]	3.17 [23.16]
Calcite	0.0000	0.0010 ± 0.0100 (1000.00%)	0.2161 ± 0.1315 (60.85%) [0.0436 ± 0.0270 (62.03%)]	-1.64 [-1.61]	-1.64 [-1.58]
Saponite	0.0000	0.0001 ± 0.0010 (1000.00%)	0.2228 ± 0.1003 (45.02%) [0.0450 ± 0.0210 (46.59%)]	-2.22 [-2.15]	-2.22 [-2.14]
Cronstedtite	0.0000	0.0010 ± 0.0100 (1000.00%)	0.3112 ± 0.1659 (53.32%) [0.0628 ± 0.0343 (54.66%)]	-1.88 [-1.83]	-1.87 [-1.80]
Lizardite	0.0000	0.0001 ± 0.0100 (10000.00%)	0.2845 ± 0.1168 (41.06%) [0.0574 ± 0.0246 (42.78%)]	-2.44 [-2.34]	-2.43 [-2.33]
Magnetite	0.0000	0.0001 ± 0.0100 (10000.00%)	0.2190 ± 0.1184 (54.08%) [0.0442 ± 0.0245 (55.39%)]	-1.85 [-1.81]	-1.85 [-1.80]
Spinel	0.0000	0.0010 ± 0.0100 (1000.00%)	0.4368 ± 0.1735 (39.71%) [0.0881 ± 0.0366 (41.49%)]	-2.52 [-2.41]	-2.51 [-2.38]
Troilite	0.0500	0.0750 ± 0.0100 (13.33%)	0.3503 ± 0.1497 (42.74%) [0.0707 ± 0.0314 (44.40%)]	-2.01 [-0.66]	-1.84 [0.14]
Pyrrhotite	0.0000	0.0750 ± 0.1000 (133.33%)	0.2622 ± 0.1163 (44.37%) [0.0529 ± 0.0243 (45.97%)]	-2.25 [-2.18]	-1.61 [0.91]

Table B.59 continued from previous page

End-member	'True' Abundance	Prior, P4	Retrieved Abundance [BBnorm]	Accuracy to 'True' Abundance σ [BBnorm]	Accuracy to P4 Abundance σ [BBnorm]
Albite	0.1000	0.0900 ± 0.0100 (11.11%)	0.1706 ± 0.1138 (66.71%) [0.0344 ± 0.0233 (67.79%)]	-0.62 [2.81]	-0.71 [2.38]
Anorthite	0.0000	0.0900 ± 0.1000 (111.11%)	0.1794 ± 0.1173 (65.38%) [0.0362 ± 0.0241 (66.48%)]	-1.53 [-1.50]	-0.76 [2.24]
Gypsum	0.0000	0.0001 ± 0.0100 (10000.00%)	0.2514 ± 0.1326 (52.75%) [0.0507 ± 0.0274 (54.10%)]	-1.90 [-1.85]	-1.90 [-1.84]
AmorphousMg	0.0000	0.0010 ± 0.0100 (1000.00%)	0.2805 ± 0.1340 (47.78%) [0.0566 ± 0.0279 (49.27%)]	-2.09 [-2.03]	-2.09 [-1.99]
AmorphousFe	0.0000	0.0001 ± 0.0100 (10000.00%)	0.4221 ± 0.1766 (41.84%) [0.0852 ± 0.0371 (43.53%)]	-2.39 [-2.30]	-2.39 [-2.29]
MurchisonIOM	0.0000	0.0750 ± 0.1000 (133.33%)	0.2491 ± 0.1342 (53.90%) [0.0503 ± 0.0278 (55.22%)]	-1.86 [-1.81]	-1.30 [0.89]
FeNiMetalSub	0.0500	0.0750 ± 0.0100 (13.33%)	0.2289 ± 0.1218 (53.21%) [0.0462 ± 0.0252 (54.55%)]	-1.47 [0.15]	-1.26 [1.14]
BB	n/a	0.2500 ± 0.0125 (5.00%)	0.2138 ± 0.1132 (52.95%)	n/a	0.32
		RMS error	3.9568 [0.0539]		
		$\chi^2_{d.o.f}$	41361706.2 [3013.0]		

Table B.60: Results for the *glennrealminU* `MCMC()` unmixing.

End-member	**'True' Abundance**	**Prior, U**	**Retrieved Abundance**	**Accuracy to 'True' Abundance** σ	**Accuracy to U Abundance** σ
Enstatite	0.0800	n/a	0.0842 ± 0.0065 (7.69%)	-0.66	n/a
Olivine	0.1130	n/a	0.0362 ± 0.0042 (11.62%)	18.28	n/a
Calcite	0.0080	n/a	0.0013 ± 0.0013 (99.64%)	5.37	n/a
Cronstedtite	0.5290	n/a	0.3057 ± 0.0122 (3.99%)	18.29	n/a
Lizardite	0.2330	n/a	0.1165 ± 0.0078 (6.67%)	15.01	n/a
Magnetite	0.0150	n/a	0.0033 ± 0.0074 (228.38%)	1.58	n/a
Pyrrhotite	0.0090	n/a	0.3895 ± 0.0113 (2.90%)	-33.68	n/a
Gypsum	0.0140	n/a	0.0732 ± 0.0082 (11.21%)	-7.22	n/a
		RMS error	0.0039		
		$\chi^2_{d.o.f}$	1.35		

Table B.61: Results for the *glennrealminP2* `MCMC()` unmixing.

End-member	**'True' Abundance**	**Prior, P2**	**Retrieved Abundance**	**Accuracy to 'True' Abundance** σ	**Accuracy to P2 Abundance** σ
Enstatite	0.0800	0.8337 ± 0.8345 (100.10%)	0.0871 ± 0.0081 (9.32%)	-0.87	92
Olivine	0.1130	0.8826 ± 0.8835 (100.10%)	0.0359 ± 0.0048 (13.30%)	16.12	177.1
Calcite	0.0080	0.8698 ± 0.8706 (100.10%)	0.0014 ± 0.0021 (153.26%)	3.19	417.05
Cronstedtite	0.5290	0.2159 ± 0.2161 (100.10%)	0.3119 ± 0.0132 (4.23%)	16.47	-7.29
Lizardite	0.2330	0.0246 ± 0.0246 (100.10%)	0.1099 ± 0.0090 (8.16%)	13.73	-9.51
Magnetite	0.0150	0.7298 ± 0.7306 (100.10%)	0.0034 ± 0.0327 (949.14%)	0.35	22.19
Pyrrhotite	0.0090	0.5244 ± 0.5250 (100.10%)	0.3859 ± 0.0378 (9.80%)	-9.96	3.66

Table B.61 continued from previous page

End-member	'True' Abundance	Prior, P2	Retrieved Abundance	Accuracy to 'True' Abundance σ	Accuracy to P2 Abundance σ
Gypsum	0.0140	0.9781 ± 0.9791 (100.10%)	0.0753 ± 0.0094 (12.43%)	-6.55	96.45
		RMS error	0.0036		
		$\chi^2_{d.o.f}$	1.10		

Table B.62: Results for the *glennmathexpU* `MCMC()` unmixing.

End-member	'True' Abundance	Prior, U	Retrieved Abundance [BBnorm]	Accuracy to 'True' Abundance σ [BBnorm]	Accuracy to U Abundance σ
Augite	0.0000	n/a	0.2216 ± 0.1135 (51.22%) [0.0902 ± 0.0488 (54.14%)]	-1.95 [-1.85]	n/a
Enstatite	0.0800	n/a	0.1600 ± 0.0923 (57.69%) [0.0651 ± 0.0393 (60.29%)]	-0.87 [0.38]	n/a
Olivine	0.1130	n/a	0.2622 ± 0.1364 (52.03%) [0.1067 ± 0.0586 (54.91%)]	-1.09 [0.11]	n/a
Calcite	0.0080	n/a	0.1968 ± 0.0788 (40.03%) [0.0801 ± 0.0350 (43.70%)]	-2.40 [-2.06]	n/a
Saponite	0.0000	n/a	0.2307 ± 0.1289 (55.88%) [0.0939 ± 0.0550 (58.56%)]	-1.79 [-1.71]	n/a
Cronstedtite	0.5290	n/a	0.1801 ± 0.1011 (56.14%) [0.0733 ± 0.0431 (58.81%)]	3.45 [10.57]	n/a
Lizardite	0.2330	n/a	0.1684 ± 0.1065 (63.21%) [0.0685 ± 0.0450 (65.60%)]	0.61 [3.66]	n/a

Table B.62 continued from previous page

End-member	'True' Abundance	Prior, U	Retrieved Abundance [BBnorm]	Accuracy to 'True' Abundance σ [BBnorm]	Accuracy to U Abundance σ
Magnetite	0.0150	n/a	0.2593 ± 0.1614 (62.25%) [0.1055 ± 0.0682 (64.67%)]	-1.51 [-1.33]	n/a
Spinel	0.0000	n/a	0.2272 ± 0.1229 (54.08%) [0.0925 ± 0.0526 (56.85%)]	-1.85 [-1.76]	n/a
Pyrrhotite	0.0090	n/a	0.1466 ± 0.0917 (62.55%) [0.0596 ± 0.0387 (64.96%)]	-1.50 [-1.31]	n/a
Gypsum	0.0140	n/a	0.1558 ± 0.1030 (66.09%) [0.0634 ± 0.0433 (68.38%)]	-1.38 [-1.14]	n/a
AmorphousFe	0.0000	n/a	0.2486 ± 0.0969 (38.99%) [0.1012 ± 0.0432 (42.75%)]	-2.56 [-2.34]	n/a
BB	n/a	n/a	0.2230 ± 0.1258 (56.41%)	n/a	n/a
		RMS error	1.5548 [0.0260]		
		$\chi^2_{d.o.f}$	12237713.3 [3959.1]		

Table B.63: Results for the *glennmathexpP1* `MCMC()` unmixing.

End-member	'True' Abundance	Prior, P1	Retrieved Abundance [BBnorm]	Accuracy to 'True' Abundance σ [BBnorm]	Accuracy to P1 Abundance σ [BBnorm]
Augite	0.0000	0.6747 ± 6.75E-04 (0.10%)	0.2206 ± 0.1283 (58.17%) [0.0731 ± 0.0441 (60.37%)]	-1.72 [-1.66]	3.54 [13.64]
Enstatite	0.0800	0.3153 ± 3.15E-04 (0.10%)	0.3007 ± 0.1529 (50.83%) [0.0996 ± 0.0531 (53.33%)]	-1.44 [-0.37]	0.10 [4.06]

Table B.63 continued from previous page

End-member	'True' Abundance	Prior, P1	Retrieved Abundance [BBnorm]	Accuracy to 'True' Abundance σ [BBnorm]	Accuracy to P1 Abundance σ [BBnorm]
Olivine	0.1130	0.6864 ± 6.86E-04 (0.10%)	0.2161 ± 0.1432 (66.27%) [0.0716 ± 0.0488 (68.20%)]	-0.72 [0.85]	3.28 [12.59]
Calcite	0.0080	0.2621 ± 2.62E-04 (0.10%)	0.2131 ± 0.1445 (67.79%) [0.0706 ± 0.0492 (69.69%)]	-1.42 [-1.27]	0.34 [3.89]
Saponite	0.0000	0.5489 ± 5.49E-04 (0.10%)	0.2983 ± 0.1227 (41.14%) [0.0988 ± 0.0437 (44.19%)]	-2.43 [-2.26]	2.04 [10.30]
Cronstedtite	0.5290	0.6083 ± 6.08E-04 (0.10%)	0.2234 ± 0.1241 (55.53%) [0.0740 ± 0.0428 (57.83%)]	2.46 [10.63]	3.10 [12.48]
Lizardite	0.2330	0.1227 ± 1.23E-04 (0.10%)	0.2354 ± 0.1103 (46.87%) [0.0780 ± 0.0387 (49.57%)]	-0.02 [4.01]	-1.02 [1.16]
Magnetite	0.0150	0.0336 ± 3.36E-05 (0.10%)	0.2672 ± 0.0603 (22.57%) [0.0885 ± 0.0246 (27.75%)]	-4.18 [-2.99]	-3.87 [-2.23]
Spinel	0.0000	0.1841 ± 1.84E-04 (0.10%)	0.3262 ± 0.1323 (40.55%) [0.1081 ± 0.0472 (43.64%)]	-2.47 [-2.29]	-1.07 [1.61]
Pyrrhotite	0.0090	0.2300 ± 2.30E-04 (0.10%)	0.2551 ± 0.1121 (43.96%) [0.0845 ± 0.0396 (46.83%)]	-2.19 [-1.91]	-0.22 [3.68]
Gypsum	0.0140	0.4021 ± 4.02E-04 (0.10%)	0.2427 ± 0.2001 (82.47%) [0.0804 ± 0.0676 (84.03%)]	-1.14 [-0.98]	0.80 [4.76]
AmorphousFe	0.0000	0.0835 ± 8.35E-05 (0.10%)	0.2195 ± 0.0842 (38.37%) [0.0727 ± 0.0303 (41.63%)]	-2.61 [-2.40]	-1.61 [0.36]
BB	n/a	0.3234 ± 3.23E-04 (0.10%)	0.2465 ± 0.1274 (51.69%)	n/a	0.60
		RMS error	2.1141 [0.0222]		
		$\chi^2_{d.o.f}$	22685898.6 [2791.8]		

Table B.64: Results for the *glennmathexpP2* `MCMC()` unmixing.

End-member	**'True' Abundance**	**Prior, P2**	**Retrieved Abundance [BBnorm]**	**Accuracy to 'True' Abundance σ [BBnorm]**	**Accuracy to P2 Abundance σ [BBnorm]**
Augite	0.0000	0.6747 ± 0.6754 (100.10%)	0.1886 ± 0.1557 (82.57%) [0.0983 ± 0.0835 (84.95%)]	-1.21 [-1.18]	3.12 [6.91]
Enstatite	0.0800	0.3153 ± 0.3156 (100.10%)	0.1530 ± 0.0863 (56.39%) [0.0797 ± 0.0477 (59.82%)]	-0.85 [0.01]	1.88 [4.94]
Olivine	0.1130	0.6864 ± 0.6870 (100.10%)	0.1376 ± 0.0731 (53.12%) [0.0717 ± 0.0407 (56.75%)]	-0.34 [1.01]	7.50 [15.10]
Calcite	0.0080	0.2621 ± 0.2624 (100.10%)	0.1491 ± 0.0623 (41.82%) [0.0777 ± 0.0360 (46.34%)]	-2.26 [-1.94]	1.81 [5.12]
Saponite	0.0000	0.5489 ± 0.5494 (100.10%)	0.1918 ± 0.0946 (49.30%) [0.0999 ± 0.0532 (53.19%)]	-2.03 [-1.88]	3.78 [8.45]
Cronstedtite	0.5290	0.6083 ± 0.6089 (100.10%)	0.1298 ± 0.0894 (68.83%) [0.0677 ± 0.0485 (71.67%)]	4.47 [9.51]	5.35 [11.15]
Lizardite	0.2330	0.1227 ± 0.1228 (100.10%)	0.2158 ± 0.1290 (59.79%) [0.1124 ± 0.0709 (63.04%)]	0.13 [1.70]	-0.72 [0.14]
Magnetite	0.0150	0.0336 ± 0.0337 (100.10%)	0.1834 ± 0.1235 (67.32%) [0.0956 ± 0.0671 (70.22%)]	-1.36 [-1.20]	-1.21 [-0.92]
Spinel	0.0000	0.1841 ± 0.1843 (100.10%)	0.1296 ± 0.0725 (55.95%) [0.0675 ± 0.0401 (59.41%)]	-1.79 [-1.68]	0.75 [2.91]
Pyrrhotite	0.0090	0.2300 ± 0.2302 (100.10%)	0.1475 ± 0.1282 (86.90%) [0.0768 ± 0.0685 (89.16%)]	-1.08 [-0.99]	0.64 [2.24]
Gypsum	0.0140	0.4021 ± 0.4025 (100.10%)	0.1390 ± 0.0835 (60.03%) [0.0724 ± 0.0458 (63.27%)]	-1.50 [-1.28]	3.15 [7.19]

Table B.64 continued from previous page

End-member	'True' Abundance	Prior, P2	Retrieved Abundance [BBnorm]	Accuracy to 'True' Abundance σ [BBnorm]	Accuracy to P2 Abundance σ [BBnorm]
AmorphousFe	0.0000	0.0835 ± 0.0836 (100.10%)	0.1540 ± 0.1097 (71.24%) [0.0803 ± 0.0594 (73.98%)]	-1.40 [-1.35]	-0.64 [0.05]
BB	n/a	0.3234 ± 0.3237 (100.10%)	0.1925 ± 0.0906 (47.08%)	n/a	1.44
		RMS error	1.0356 [0.0230]		
		$\chi^2_{d.o.f}$	5405667.1 [3014.6]		

Table B.65: Results for the *glennmathexpP3* `MCMC()` unmixing.

End-member	'True' Abundance	Prior, P3	Retrieved Abundance [BBnorm]	Accuracy to 'True' Abundance σ [BBnorm]	Accuracy to P3 Abundance σ [BBnorm]
Augite	0.0000	1.00E-04 ± 1.00E-04 (100.10%)	0.2454 ± 0.0998 (40.66%) [0.1227 ± 0.0548 (44.67%)]	-2.46 [-2.24]	-2.46 [-2.24]
Enstatite	0.0800	0.0800 ± 8.00E-05 (0.10%)	0.1327 ± 0.0881 (66.45%) [0.0663 ± 0.0458 (68.98%)]	-0.60 [0.30]	-0.60 [0.30]
Olivine	0.1130	0.1130 ± 1.13E-04 (0.10%)	0.2157 ± 0.1178 (54.63%) [0.1079 ± 0.0622 (57.68%)]	-0.87 [0.08]	-0.87 [0.08]
Calcite	0.0080	0.0080 ± 8.00E-06 (0.10%)	0.0569 ± 0.0459 (80.69%) [0.0285 ± 0.0236 (82.78%)]	-1.07 [-0.87]	-1.07 [-0.87]
Saponite	0.0000	1.00E-04 ± 1.00E-04 (100.10%)	0.2161 ± 0.1133 (52.40%) [0.1081 ± 0.0601 (55.58%)]	-1.91 [-1.80]	-1.91 [-1.80]
Cronstedtite	0.5290	0.5290 ± 5.29E-04 (0.10%)	0.1772 ± 0.1565 (88.36%) [0.0886 ± 0.0800 (90.28%)]	2.25 [5.51]	2.25 [5.51]

Table B.65 continued from previous page

End-member	'True' Abundance	Prior, P3	Retrieved Abundance [BBnorm]	Accuracy to 'True' Abundance σ [BBnorm]	Accuracy to P3 Abundance σ [BBnorm]
Lizardite	0.2330	0.2330 ± 2.33E-04 (0.10%)	0.2174 ± 0.0971 (44.64%) [0.1087 ± 0.0525 (48.33%)]	0.16 [2.37]	0.16 [2.37]
Magnetite	0.0150	0.0150 ± 1.50E-05 (0.10%)	0.1245 ± 0.0783 (62.88%) [0.0622 ± 0.0408 (65.55%)]	-1.40 [-1.16]	-1.40 [-1.16]
Spinel	0.0000	1.00E-04 ± 1.00E-04 (100.10%)	0.2082 ± 0.1178 (56.57%) [0.1041 ± 0.0620 (59.53%)]	-1.77 [-1.68]	-1.77 [-1.68]
Pyrrhotite	0.0090	0.0090 ± 9.00E-06 (0.10%)	0.1029 ± 0.0468 (45.47%) [0.0515 ± 0.0253 (49.09%)]	-2.01 [-1.68]	-2.01 [-1.68]
Gypsum	0.0140	0.0140 ± 1.40E-05 (0.10%)	0.0915 ± 0.0510 (55.72%) [0.0457 ± 0.0269 (58.71%)]	-1.52 [-1.18]	-1.52 [-1.18]
AmorphousFe	0.0000	1.00E-04 ± 1.00E-04 (100.10%)	0.2112 ± 0.0940 (44.52%) [0.1056 ± 0.0509 (48.21%)]	-2.25 [-2.07]	-2.25 [-2.07]
BB	n/a	1.00E-04 ± 1.00E-04 (100.10%)	0.1535 ± 0.1072 (69.84%)	n/a	-1.43
		RMS error	1.0674 [0.0194]		
		$\chi^2_{d.o.f}$	5800881.1 [2106.4]		

Table B.66: Results for the *glennmathexpP4* `MCMC()` unmixing.

End-member	'True' Abundance	Prior, P4	Retrieved Abundance [BBnorm]	Accuracy to 'True' Abundance σ [BBnorm]	Accuracy to P4 Abundance σ [BBnorm]
Augite	0.0000	0.1000 ± 0.5000 (500.00%)	0.2197 ± 0.1432 (65.20%) [0.0836 ± 0.0567 (67.88%)]	-1.53 [-1.47]	-0.84 [0.29]
Enstatite	0.0800	0.1000 ± 0.0050 (5.00%)	0.1910 ± 0.0995 (52.09%) [0.0727 ± 0.0403 (55.41%)]	-1.12 [0.18]	-0.91 [0.68]
Olivine	0.1130	0.1000 ± 0.0050 (5.00%)	0.1636 ± 0.1030 (62.97%) [0.0622 ± 0.0409 (65.75%)]	-0.49 [1.24]	-0.62 [0.92]
Calcite	0.0080	0.0100 ± 0.0100 (100.00%)	0.3340 ± 0.2019 (60.46%) [0.1271 ± 0.0805 (63.34%)]	-1.61 [-1.48]	-1.60 [-1.45]
Saponite	0.0000	0.2540 ± 0.5000 (196.85%)	0.1629 ± 0.1455 (89.33%) [0.0620 ± 0.0566 (91.30%)]	-1.12 [-1.10]	0.63 [3.39]
Cronstedtite	0.5290	0.5000 ± 0.0050 (1.00%)	0.1814 ± 0.1099 (60.59%) [0.0690 ± 0.0438 (63.47%)]	3.16 [10.50]	2.90 [9.84]
Lizardite	0.2330	0.2000 ± 0.0050 (2.50%)	0.2450 ± 0.1067 (43.55%) [0.0932 ± 0.0442 (47.47%)]	-0.11 [3.16]	-0.42 [2.41]
Magnetite	0.0150	0.0100 ± 0.0100 (100.00%)	0.2326 ± 0.1295 (55.66%) [0.0885 ± 0.0520 (58.78%)]	-1.68 [-1.41]	-1.72 [-1.51]
Spinel	0.0000	0.0050 ± 0.0500 (1000.00%)	0.3203 ± 0.1647 (51.43%) [0.1219 ± 0.0668 (54.79%)]	-1.94 [-1.83]	-1.91 [-1.75]
Pyrrhotite	0.0090	0.0200 ± 0.0100 (50.00%)	0.1803 ± 0.0997 (55.29%) [0.0686 ± 0.0401 (58.43%)]	-1.72 [-1.49]	-1.61 [-1.21]
Gypsum	0.0140	0.0500 ± 0.0050 (10.00%)	0.1841 ± 0.1207 (65.59%) [0.0700 ± 0.0478 (68.26%)]	-1.41 [-1.17]	-1.11 [-0.42]

Table B.66 continued from previous page

End-member	'True' Abundance	Prior, P4	Retrieved Abundance [BBnorm]	Accuracy to 'True' Abundance σ [BBnorm]	Accuracy to P4 Abundance σ [BBnorm]
AmorphousFe	0.0000	0.0100 ± 0.1000 (1000.00%)	0.2135 ± 0.1143 (53.52%) [0.0812 ± 0.0461 (56.76%)]	-1.87 [-1.76]	-1.78 [-1.54]
BB	n/a	0.6000 ± 0.0300 (5.00%)	0.2093 ± 0.1392 (66.51%)	n/a	2.81
		RMS error	1.6902 [0.0328]		
		$\chi^2_{d.o.f}$	14472017.1 [6017.9]		

Table B.67: Results for the *glennrealexpU* `MCMC()` unmixing.

End-member	'True' Abundance	Prior, U	Retrieved Abundance [BBnorm]	Accuracy to 'True' Abundance σ [BBnorm]	Accuracy to U Abundance σ
Augite	0.0000	n/a	0.1945 ± 0.0945 (48.62%) [0.0878 ± 0.0461 (52.52%)]	-2.06 [-1.90]	n/a
Enstatite	0.0800	n/a	0.1883 ± 0.0871 (46.28%) [0.0850 ± 0.0428 (50.36%)]	-1.24 [-0.12]	n/a
Olivine	0.1130	n/a	0.1700 ± 0.1457 (85.70%) [0.0767 ± 0.0675 (87.97%)]	-0.39 [0.54]	n/a
Calcite	0.0080	n/a	0.2413 ± 0.1413 (58.56%) [0.1090 ± 0.0674 (61.84%)]	-1.65 [-1.50]	n/a
Saponite	0.0000	n/a	0.1515 ± 0.0913 (60.21%) [0.0684 ± 0.0434 (63.41%)]	-1.66 [-1.58]	n/a
Cronstedtite	0.5290	n/a	0.1679 ± 0.1137 (67.74%) [0.0758 ± 0.0535 (70.59%)]	3.18 [8.47]	n/a

Table B.67 continued from previous page

End-member	**'True' Abundance**	**Prior, U**	**Retrieved Abundance [BBnorm]**	**Accuracy to 'True' Abundance σ [BBnorm]**	**Accuracy to U Abundance σ**
Lizardite	0.2330	n/a	0.1423 ± 0.0858 (60.25%) [0.0643 ± 0.0408 (63.44%)]	1.06 [4.14]	n/a
Magnetite	0.0150	n/a	0.1191 ± 0.1598 (134.22%) [0.0538 ± 0.0730 (135.68%)]	-0.65 [-0.53]	n/a
Spinel	0.0000	n/a	0.1653 ± 0.1018 (61.59%) [0.0746 ± 0.0483 (64.71%)]	-1.62 [-1.55]	n/a
Pyrrhotite	0.0090	n/a	0.1859 ± 0.1031 (55.48%) [0.0839 ± 0.0495 (58.93%)]	-1.72 [-1.52]	n/a
Gypsum	0.0140	n/a	0.2824 ± 0.1624 (57.51%) [0.1275 ± 0.0776 (60.84%)]	-1.65 [-1.46]	n/a
AmorphousFe	0.0000	n/a	0.2062 ± 0.1299 (62.97%) [0.0931 ± 0.0615 (66.03%)]	-1.59 [-1.51]	n/a
BB	n/a	n/a	0.1382 ± 0.0937 (67.80%)	n/a	n/a
		RMS error	1.2119 [0.0522]		
		$\chi^2_{d.o.f}$	142509.8 [223.7]		

Table B.68: Results for the *glennrealexpP1* `MCMC()` unmixing.

End-member	**'True' Abundance**	**Prior, P1**	**Retrieved Abundance [BBnorm]**	**Accuracy to 'True' Abundance σ [BBnorm]**	**Accuracy to P1 Abundance σ [BBnorm]**
Augite	0.0000	0.6747 ± 6.75E-04 (0.10%)	0.1775 ± 0.1114 (62.78%) [0.1100 ± 0.0720 (65.40%)]	-1.59 [-1.53]	4.46 [7.85]
Enstatite	0.0800	0.3153 ± 3.15E-04 (0.10%)	0.1208 ± 0.0734 (60.77%) [0.0749 ± 0.0476 (63.48%)]	-0.56 [0.11]	2.65 [5.05]
Olivine	0.1130	0.6864 ± 6.86E-04 (0.10%)	0.1500 ± 0.1048 (69.84%) [0.0930 ± 0.0672 (72.21%)]	-0.35 [0.30]	5.12 [8.83]
Calcite	0.0080	0.2621 ± 2.62E-04 (0.10%)	0.1386 ± 0.0888 (64.11%) [0.0859 ± 0.0573 (66.68%)]	-1.47 [-1.36]	1.39 [3.08]
Saponite	0.0000	0.5489 ± 5.49E-04 (0.10%)	0.1703 ± 0.0741 (43.49%) [0.1056 ± 0.0498 (47.21%)]	-2.30 [-2.12]	5.11 [8.90]
Cronstedtite	0.5290	0.6083 ± 6.08E-04 (0.10%)	0.1278 ± 0.0947 (74.10%) [0.0792 ± 0.0605 (76.34%)]	4.24 [7.44]	5.08 [8.75]
Lizardite	0.2330	0.1227 ± 1.23E-04 (0.10%)	0.0907 ± 0.0396 (43.67%) [0.0562 ± 0.0266 (47.36%)]	3.59 [6.64]	0.81 [2.50]
Magnetite	0.0150	0.0336 ± 3.36E-05 (0.10%)	0.0433 ± 0.0220 (50.79%) [0.0268 ± 0.0145 (54.00%)]	-1.29 [-0.82]	-0.44 [0.47]
Spinel	0.0000	0.1841 ± 1.84E-04 (0.10%)	0.1287 ± 0.1014 (78.79%) [0.0798 ± 0.0645 (80.90%)]	-1.27 [-1.24]	0.55 [1.62]
Pyrrhotite	0.0090	0.2300 ± 2.30E-04 (0.10%)	0.1667 ± 0.0978 (58.69%) [0.1034 ± 0.0636 (61.49%)]	-1.61 [-1.48]	0.65 [1.99]
Gypsum	0.0140	0.4021 ± 4.02E-04 (0.10%)	0.1840 ± 0.0846 (45.97%) [0.1141 ± 0.0565 (49.50%)]	-2.01 [-1.77]	2.58 [5.10]

Table B.68 continued from previous page

End-member	'True' Abundance	Prior, P1	Retrieved Abundance [BBnorm]	Accuracy to 'True' Abundance σ [BBnorm]	Accuracy to P1 Abundance σ [BBnorm]
AmorphousFe	0.0000	0.0835 ± 8.35E-05 (0.10%)	0.1147 ± 0.0456 (39.72%) [0.0711 ± 0.0311 (43.76%)]	-2.52 [-2.29]	-0.68 [0.40]
BB	n/a	0.3234 ± 3.23E-04 (0.10%)	0.1120 ± 0.0516 (46.07%)	n/a	4.10
		RMS error	0.6319 [0.0504]		
		$\chi^2_{d.o.f}$	39310.2 [187.7]		

Table B.69: Results for the *glennrealexpP2* `MCMC()` unmixing.

End-member	'True' Abundance	Prior, P2	Retrieved Abundance [BBnorm]	Accuracy to 'True' Abundance σ [BBnorm]	Accuracy to P2 Abundance σ [BBnorm]
Augite	0.0000	0.6747 ± 0.6754 (100.10%)	0.1414 ± 0.0691 (48.89%) [0.0852 ± 0.0453 (53.15%)]	-2.05 [-1.88]	7.71 [13.02]
Enstatite	0.0800	0.3153 ± 0.3156 (100.10%)	0.1685 ± 0.0946 (56.14%) [0.1015 ± 0.0608 (59.88%)]	-0.94 [-0.35]	1.55 [3.52]
Olivine	0.1130	0.6864 ± 0.6870 (100.10%)	0.1630 ± 0.1146 (70.31%) [0.0982 ± 0.0720 (73.33%)]	-0.44 [0.21]	4.57 [8.17]
Calcite	0.0080	0.2621 ± 0.2624 (100.10%)	0.1165 ± 0.0505 (43.35%) [0.0702 ± 0.0338 (48.10%)]	-2.15 [-1.84]	2.88 [5.69]
Saponite	0.0000	0.5489 ± 0.5494 (100.10%)	0.1666 ± 0.0910 (54.65%) [0.1004 ± 0.0587 (58.49%)]	-1.83 [-1.71]	4.20 [7.64]
Cronstedtite	0.5290	0.6083 ± 0.6089 (100.10%)	0.1422 ± 0.0961 (67.59%) [0.0857 ± 0.0606 (70.73%)]	4.02 [7.31]	4.85 [8.62]

Table B.69 continued from previous page

End-member	'True' Abundance	Prior, P2	Retrieved Abundance [BBnorm]	Accuracy to 'True' Abundance σ [BBnorm]	Accuracy to P2 Abundance σ [BBnorm]
Lizardite	0.2330	0.1227 ± 0.1228 (100.10%)	0.1230 ± 0.1075 (87.39%) [0.0741 ± 0.0666 (89.85%)]	1.02 [2.38]	-0.00 [0.73]
Magnetite	0.0150	0.0336 ± 0.0337 (100.10%)	0.0925 ± 0.0551 (59.59%) [0.0558 ± 0.0352 (63.13%)]	-1.41 [-1.16]	-1.07 [-0.63]
Spinel	0.0000	0.1841 ± 0.1843 (100.10%)	0.1666 ± 0.0998 (59.87%) [0.1004 ± 0.0637 (63.39%)]	-1.67 [-1.58]	0.18 [1.31]
Pyrrhotite	0.0090	0.2300 ± 0.2302 (100.10%)	0.1322 ± 0.0727 (54.99%) [0.0797 ± 0.0469 (58.80%)]	-1.69 [-1.51]	1.34 [3.21]
Gypsum	0.0140	0.4021 ± 0.4025 (100.10%)	0.0849 ± 0.1328 (156.53%) [0.0511 ± 0.0808 (157.91%)]	-0.53 [-0.46]	2.39 [4.35]
AmorphousFe	0.0000	0.0835 ± 0.0836 (100.10%)	0.1620 ± 0.0738 (45.54%) [0.0976 ± 0.0489 (50.08%)]	-2.20 [-2.00]	-1.06 [-0.29]
BB	n/a	0.3234 ± 0.3237 (100.10%)	0.1518 ± 0.0993 (65.45%)	n/a	1.73
		RMS error	0.7131 [0.0513]		
		$\chi^2_{d.o.f}$	49844.7 [194.1]		

Table B.70: Results for the *glennrealexpP3* `MCMC()` unmixing.

End-member	'True' Abundance	Prior, P3	Retrieved Abundance [BBnorm]	Accuracy to 'True' Abundance σ [BBnorm]	Accuracy to P3 Abundance σ [BBnorm]
Augite	0.0000	1.00E-04 ± 1.00E-04 (100.10%)	0.0010 ± 0.0147 (1528.52%) [0.0009 ± 0.0144 (1528.55%)]	-0.07 [-0.07]	-0.06 [-0.06]
Enstatite	0.0800	0.0800 ± 8.00E-05 (0.10%)	0.0803 ± 0.0007 (0.85%) [0.0786 ± 0.0081 (10.34%)]	-0.49 [0.17]	-0.49 [0.17]
Olivine	0.1130	0.1130 ± 1.13E-04 (0.10%)	0.1130 ± 0.0171 (15.10%) [0.1106 ± 0.0202 (18.28%)]	0.002 [0.12]	0.00 [0.12]
Calcite	0.0080	0.0080 ± 8.00E-06 (0.10%)	0.0080 ± 1.85E-04 (2.31%) [0.0078 ± 8.28E-04 (10.56%)]	-0.01 [0.20]	-0.01 [0.20]
Saponite	0.0000	1.00E-04 ± 1.00E-04 (100.10%)	0.0008 ± 0.0234 (2916.14%) [0.0008 ± 0.0230 (2916.15%)]	-0.03 [-0.03]	-0.03 [-0.03]
Cronstedtite	0.5290	0.5290 ± 5.29E-04 (0.10%)	0.5434 ± 0.0588 (10.82%) [0.5320 ± 0.0795 (14.94%)]	-0.24 [-0.04]	-0.24 [-0.04]
Lizardite	0.2330	0.2330 ± 2.33E-04 (0.10%)	0.2348 ± 0.0607 (25.84%) [0.2299 ± 0.0639 (27.82%)]	-0.03 [0.05]	-0.03 [0.05]
Magnetite	0.0150	0.0150 ± 1.50E-05 (0.10%)	0.0150 ± 0.0013 (8.81%) [0.0147 ± 0.0020 (13.56%)]	-0.03 [0.14]	-0.03 [0.14]
Spinel	0.0000	1.00E-04 ± 1.00E-04 (100.10%)	0.0007 ± 0.0317 (4407.30%) [0.0007 ± 0.0310 (4407.31%)]	-0.02 [-0.02]	-0.02 [-0.02]
Pyrrhotite	0.0090	0.0090 ± 9.00E-06 (0.10%)	0.0090 ± 0.0007 (7.77%) [0.0088 ± 0.0011 (12.91%)]	-0.01 [0.16]	-0.01 [0.16]
Gypsum	0.0140	0.0140 ± 1.40E-05 (0.10%)	0.0140 ± 0.0010 (7.11%) [0.0137 ± 0.0017 (12.52%)]	-0.04 [0.15]	-0.04 [0.15]

Table B.70 continued from previous page

End-member	'True' Abundance	Prior, P3	Retrieved Abundance [BBnorm]	Accuracy to 'True' Abundance σ [BBnorm]	Accuracy to P3 Abundance σ [BBnorm]
AmorphousFe	0.0000	1.00E-04 ± 1.00E-04 (100.10%)	0.0014 ± 0.0190 (1367.74%) [0.0014 ± 0.0186 (1367.78%)]	-0.07 [-0.07]	-0.07 [-0.07]
BB	n/a	1.00E-04 ± 1.00E-04 (100.10%)	0.0012 ± 0.0276 (2289.38%)	n/a	-0.04
		RMS error	0.0228 [0.0375]		
		$\chi^2_{d.o.f}$	23.0 [68.8]		

Table B.71: Results for the *glennrealexpP4* `MCMC()` unmixing.

End-member	'True' Abundance	Prior, P4	Retrieved Abundance [BBnorm]	Accuracy to 'True' Abundance σ [BBnorm]	Accuracy to P4 Abundance σ [BBnorm]
Augite	0.0000	0.1000 ± 0.5000 (500.00%)	0.1716 ± 0.0846 (49.31%) [0.0795 ± 0.0433 (54.48%)]	-2.03 [-1.84]	-0.85 [0.47]
Enstatite	0.0800	0.1000 ± 0.0050 (5.00%)	0.1467 ± 0.1305 (88.97%) [0.0680 ± 0.0625 (91.93%)]	-0.51 [0.19]	-0.36 [0.51]
Olivine	0.1130	0.1000 ± 0.0050 (5.00%)	0.1348 ± 0.0680 (50.41%) [0.0624 ± 0.0346 (55.48%)]	-0.32 [1.46]	-0.51 [1.08]
Calcite	0.0080	0.0100 ± 0.0100 (100.00%)	0.1358 ± 0.0839 (61.78%) [0.0629 ± 0.0415 (65.98%)]	-1.52 [-1.32]	-1.50 [-1.27]
Saponite	0.0000	0.2540 ± 0.5000 (196.85%)	0.1905 ± 0.1571 (82.43%) [0.0882 ± 0.0756 (85.62%)]	-1.21 [-1.17]	0.40 [2.19]
Cronstedtite	0.5290	0.5000 ± 0.0050 (1.00%)	0.2309 ± 0.1261 (54.62%) [0.1069 ± 0.0634 (59.33%)]	2.36 [6.65]	2.13 [6.20]

Table B.71 continued from previous page

End-member	**'True' Abundance**	**Prior, P4**	**Retrieved Abundance [BBnorm]**	**Accuracy to 'True' Abundance σ [BBnorm]**	**Accuracy to P4 Abundance σ [BBnorm]**
Lizardite	0.2330	0.2000 ± 0.0050 (2.50%)	0.2287 ± 0.1068 (46.69%) [0.1059 ± 0.0552 (52.12%)]	0.04 [2.30]	-0.27 [1.71]
Magnetite	0.0150	0.0100 ± 0.0100 (100.00%)	0.2044 ± 0.1264 (61.80%) [0.0947 ± 0.0625 (66.00%)]	-1.50 [-1.28]	-1.54 [-1.36]
Spinel	0.0000	0.0050 ± 0.0500 (1000.00%)	0.1668 ± 0.1018 (61.04%) [0.0772 ± 0.0504 (65.29%)]	-1.64 [-1.53]	-1.59 [-1.43]
Pyrrhotite	0.0090	0.0200 ± 0.0100 (50.00%)	0.1980 ± 0.1593 (80.46%) [0.0917 ± 0.0768 (83.73%)]	-1.19 [-1.08]	-1.12 [-0.93]
Gypsum	0.0140	0.0500 ± 0.0050 (10.00%)	0.1565 ± 0.1778 (113.61%) [0.0725 ± 0.0840 (115.95%)]	-0.80 [-0.70]	-0.60 [-0.27]
AmorphousFe	0.0000	0.0100 ± 0.1000 (1000.00%)	0.1945 ± 0.1973 (101.47%) [0.0901 ± 0.0937 (104.08%)]	-0.99 [-0.96]	-0.93 [-0.85]
BB	n/a	0.6000 ± 0.0300 (5.00%)	0.1828 ± 0.1415 (77.39%)	n/a	2.95
		RMS error	1.2266 [0.0419]		
		$\chi^2_{d.o.f}$	145402.2 [139.9]		

Table B.72: Results for the *glennmathextU* `MCMC()` unmixing.

End-member	**'True' Abundance**	**Prior, U**	**Retrieved Abundance [BBnorm]**	**Accuracy to 'True' Abundance σ [BBnorm]**	**Accuracy to U Abundance σ**
Augite	0.0000	n/a	0.2529 ± 0.1184 (46.81%) [0.0532 ± 0.0260 (48.91%)]	-2.14 [-2.04]	n/a
Enstatite	0.0800	n/a	0.1682 ± 0.1197 (71.19%) [0.0354 ± 0.0257 (72.59%)]	-0.74 [1.74]	n/a
Olivine	0.1130	n/a	0.1679 ± 0.0928 (55.28%) [0.0353 ± 0.0202 (57.07%)]	-0.59 [3.85]	n/a
Calcite	0.0080	n/a	0.2189 ± 0.1635 (74.69%) [0.0460 ± 0.0350 (76.02%)]	-1.29 [-1.09]	n/a
Saponite	0.0000	n/a	0.3539 ± 0.1770 (50.01%) [0.0744 ± 0.0387 (51.99%)]	-2.00 [-1.92]	n/a
Cronstedtite	0.5290	n/a	0.2717 ± 0.2129 (78.38%) [0.0571 ± 0.0455 (79.65%)]	1.21 [10.37]	n/a
Lizardite	0.2330	n/a	0.2537 ± 0.1570 (61.87%) [0.0534 ± 0.0339 (63.48%)]	-0.13 [5.30]	n/a
Magnetite	0.0150	n/a	0.3352 ± 0.1474 (43.97%) [0.0705 ± 0.0326 (46.21%)]	-2.17 [-1.70]	n/a
Spinel	0.0000	n/a	0.2201 ± 0.0872 (39.64%) [0.0463 ± 0.0195 (42.11%)]	-2.52 [-2.37]	n/a
Troilite	0.0000	n/a	0.1749 ± 0.1216 (69.52%) [0.0368 ± 0.0261 (70.96%)]	-1.44 [-1.41]	n/a
Pyrrhotite	0.0090	n/a	0.2227 ± 0.1640 (73.65%) [0.0468 ± 0.0351 (75.00%)]	-1.30 [-1.08]	n/a

Table B.72 continued from previous page

End-member	**'True' Abundance**	**Prior, U**	**Retrieved Abundance [BBnorm]**	**Accuracy to 'True' Abundance σ [BBnorm]**	**Accuracy to U Abundance σ**
Albite	0.0000	n/a	0.4096 ± 0.1575 (38.46%) [0.0862 ± 0.0353 (41.00%)]	-2.60 [-2.44]	n/a
Anorthite	0.0000	n/a	0.1824 ± 0.0961 (52.70%) [0.0384 ± 0.0209 (54.58%)]	-1.90 [-1.83]	n/a
Gypsum	0.0140	n/a	0.3519 ± 0.2796 (79.46%) [0.0740 ± 0.0598 (80.72%)]	-1.21 [-1.00]	n/a
AmorphousMg	0.0000	n/a	0.3949 ± 0.1516 (38.40%) [0.0831 ± 0.0340 (40.94%)]	-2.60 [-2.44]	n/a
AmorphousFe	0.0000	n/a	0.2249 ± 0.1314 (58.42%) [0.0473 ± 0.0284 (60.13%)]	-1.71 [-1.66]	n/a
MurchisonIOM	0.0000	n/a	0.1745 ± 0.0771 (44.20%) [0.0367 ± 0.0170 (46.42%)]	-2.26 [-2.15]	n/a
FeNiMetalSub	0.0000	n/a	0.3755 ± 0.1841 (49.03%) [0.0790 ± 0.0403 (51.04%)]	-2.04 [-1.96]	n/a
BB	n/a	n/a	0.2536 ± 0.1180 (46.54%)	n/a	n/a
		RMS error	3.8071 [0.0211]		
		$\chi^2_{d.o.f}$	73991879.7 [1863.3]		

Table B.73: Results for the *glennmathextP1* `MCMC()` unmixing.

End-member	**'True' Abundance**	**Prior, P1**	**Retrieved Abundance [BBnorm]**	**Accuracy to 'True' Abundance σ [BBnorm]**	**Accuracy to P1 Abundance σ [BBnorm]**
Augite	0.0000	0.5921 ± 5.92E-04 (0.10%)	0.1683 ± 0.1388 (82.47%) [0.0345 ± 0.0288 (83.46%)]	-1.21 [-1.20]	3.05 [19.34]
Enstatite	0.0800	0.3011 ± 3.01E-04 (0.10%)	0.2728 ± 0.1459 (53.46%) [0.0560 ± 0.0308 (54.97%)]	-1.32 [0.78]	0.19 [7.97]
Olivine	0.1130	0.4687 ± 4.69E-04 (0.10%)	0.3377 ± 0.2434 (72.06%) [0.0693 ± 0.0507 (73.19%)]	-0.92 [0.86]	0.54 [7.88]
Calcite	0.0080	0.6976 ± 6.98E-04 (0.10%)	0.2566 ± 0.1228 (47.87%) [0.0526 ± 0.0261 (49.55%)]	-2.02 [-1.71]	3.59 [24.73]
Saponite	0.0000	0.0272 ± 2.72E-05 (0.10%)	0.2361 ± 0.0506 (21.43%) [0.0484 ± 0.0121 (24.96%)]	-4.67 [-4.01]	-4.13 [-1.75]
Cronstedtite	0.5290	0.9895 ± 0.0010 (0.10%)	0.2081 ± 0.0982 (47.18%) [0.0427 ± 0.0209 (48.89%)]	3.27 [23.29]	7.96 [45.35]
Lizardite	0.2330	0.4050 ± 4.05E-04 (0.10%)	0.3023 ± 0.1345 (44.50%) [0.0620 ± 0.0287 (46.30%)]	-0.52 [5.95]	0.76 [11.94]
Magnetite	0.0150	0.8932 ± 8.93E-04 (0.10%)	0.4587 ± 0.2237 (48.77%) [0.0941 ± 0.0475 (50.42%)]	-1.98 [-1.67]	1.94 [16.84]
Spinel	0.0000	0.7193 ± 7.19E-04 (0.10%)	0.2337 ± 0.0968 (41.44%) [0.0479 ± 0.0208 (43.37%)]	-2.41 [-2.31]	5.01 [32.28]
Troilite	0.0000	0.4880 ± 4.88E-04 (0.10%)	0.2635 ± 0.1354 (51.36%) [0.0541 ± 0.0286 (52.93%)]	-1.95 [-1.89]	1.66 [15.16]
Pyrrhotite	0.0090	0.0385 ± 3.85E-05 (0.10%)	0.2380 ± 0.0900 (37.80%) [0.0488 ± 0.0195 (39.91%)]	-2.55 [-2.04]	-2.22 [-0.53]

Table B.73 continued from previous page

End-member	'True' Abundance	Prior, P1	Retrieved Abundance [BBnorm]	Accuracy to 'True' Abundance σ [BBnorm]	Accuracy to P1 Abundance σ [BBnorm]
Albite	0.0000	0.6164 ± 6.16E-04 (0.10%)	0.1912 ± 0.0887 (46.37%) [0.0392 ± 0.0189 (48.11%)]	-2.16 [-2.08]	4.80 [30.59]
Anorthite	0.0000	0.9767 ± 0.0010 (0.10%)	0.2217 ± 0.1242 (56.00%) [0.0455 ± 0.0261 (57.45%)]	-1.79 [-1.74]	6.08 [35.64]
Gypsum	0.0140	0.2391 ± 2.39E-04 (0.10%)	0.3129 ± 0.1388 (44.37%) [0.0642 ± 0.0296 (46.18%)]	-2.15 [-1.69]	-0.53 [5.90]
AmorphousMg	0.0000	0.9921 ± 0.0010 (0.10%)	0.2777 ± 0.1409 (50.74%) [0.0570 ± 0.0298 (52.33%)]	-1.97 [-1.91]	5.07 [31.36]
AmorphousFe	0.0000	0.0353 ± 3.53E-05 (0.10%)	0.3303 ± 0.0807 (24.45%) [0.0678 ± 0.0187 (27.59%)]	-4.09 [-3.62]	-3.65 [-1.74]
MurchisonIOM	0.0000	0.7350 ± 7.35E-04 (0.10%)	0.2388 ± 0.1356 (56.79%) [0.0490 ± 0.0285 (58.22%)]	-1.76 [-1.72]	3.66 [24.05]
FeNiMetalSub	0.0000	0.9467 ± 0.0009 (0.10%)	0.3256 ± 0.1396 (42.87%) [0.0668 ± 0.0299 (44.74%)]	-2.33 [-2.24]	4.45 [29.45]
BB	n/a	0.9347 ± 0.0009 (0.10%)	0.3119 ± 0.1599 (51.27%)	n/a	3.9
		RMS error	3.9639 [0.0214]		
		$\chi^2_{d.o.f}$	80139723.0 [2089.9]		

Table B.74: Results for the *glennmathextP2* `MCMC()` unmixing.

End-member	**'True' Abundance**	**Prior, P2**	**Retrieved Abundance [BBnorm]**	**Accuracy to 'True' Abundance σ [BBnorm]**	**Accuracy to P2 Abundance σ [BBnorm]**
Augite	0.0000	0.5921 ± 0.5927 (100.10%)	0.2603 ± 0.1458 (56.02%) [0.0698 ± 0.0405 (57.98%)]	-1.79 [-1.72]	2.27 [12.90]
Enstatite	0.0800	0.3011 ± 0.3014 (100.10%)	0.1756 ± 0.1212 (69.00%) [0.0471 ± 0.0332 (70.60%)]	-0.79 [0.99]	1.04 [7.64]
Olivine	0.1130	0.4687 ± 0.4692 (100.10%)	0.1441 ± 0.0789 (54.74%) [0.0386 ± 0.0219 (56.74%)]	-0.39 [3.39]	4.12 [19.62]
Calcite	0.0080	0.6976 ± 0.6983 (100.10%)	0.1971 ± 0.1399 (70.98%) [0.0529 ± 0.0383 (72.54%)]	-1.35 [-1.17]	3.58 [16.81]
Saponite	0.0000	0.0272 ± 0.0273 (100.10%)	0.1182 ± 0.0582 (49.21%) [0.0317 ± 0.0163 (51.43%)]	-2.03 [-1.94]	-1.56 [-0.27]
Cronstedtite	0.5290	0.9895 ± 0.9905 (100.10%)	0.1845 ± 0.0869 (47.09%) [0.0495 ± 0.0244 (49.40%)]	3.96 [19.61]	9.26 [38.45]
Lizardite	0.2330	0.4050 ± 0.4054 (100.10%)	0.1882 ± 0.1134 (60.23%) [0.0505 ± 0.0313 (62.06%)]	0.40 [5.83]	1.91 [11.32]
Magnetite	0.0150	0.8932 ± 0.8941 (100.10%)	0.2475 ± 0.1020 (41.21%) [0.0664 ± 0.0291 (43.84%)]	-2.28 [-1.77]	6.33 [28.41]
Spinel	0.0000	0.7193 ± 0.7200 (100.10%)	0.1581 ± 0.1169 (73.96%) [0.0424 ± 0.0320 (75.45%)]	-1.35 [-1.33]	4.80 [21.16]
Troilite	0.0000	0.4880 ± 0.4885 (100.10%)	0.2592 ± 0.1312 (50.63%) [0.0695 ± 0.0367 (52.79%)]	-1.97 [-1.89]	1.74 [11.41]
Pyrrhotite	0.0090	0.0385 ± 0.0386 (100.10%)	0.2083 ± 0.1207 (57.96%) [0.0559 ± 0.0334 (59.85%)]	-1.65 [-1.40]	-1.41 [-0.52]

Table B.74 continued from previous page

End-member	'True' Abundance	Prior, P2	Retrieved Abundance [BBnorm]	Accuracy to 'True' Abundance σ [BBnorm]	Accuracy to P2 Abundance σ [BBnorm]
Albite	0.0000	0.6164 ± 0.6170 (100.10%)	0.2137 ± 0.2035 (95.21%) [0.0573 ± 0.0552 (96.38%)]	-1.05 [-1.04]	1.98 [10.12]
Anorthite	0.0000	0.9767 ± 0.9776 (100.10%)	0.1578 ± 0.0793 (50.29%) [0.0423 ± 0.0222 (52.46%)]	-1.99 [-1.91]	10.32 [42.10]
Gypsum	0.0140	0.2391 ± 0.2394 (100.10%)	0.2241 ± 0.1168 (52.10%) [0.0601 ± 0.0326 (54.20%)]	-1.80 [-1.42]	0.13 [5.50]
AmorphousMg	0.0000	0.9921 ± 0.9931 (100.10%)	0.1739 ± 0.1024 (58.90%) [0.0466 ± 0.0283 (60.76%)]	-1.70 [-1.65]	7.99 [33.36]
AmorphousFe	0.0000	0.0353 ± 0.0353 (100.10%)	0.4119 ± 0.1955 (47.46%) [0.1105 ± 0.0550 (49.75%)]	-2.11 [-2.01]	-1.93 [-1.37]
MurchisonIOM	0.0000	0.7350 ± 0.7357 (100.10%)	0.1911 ± 0.1622 (84.88%) [0.0512 ± 0.0442 (86.19%)]	-1.18 [-1.16]	3.35 [15.48]
FeNiMetalSub	0.0000	0.9467 ± 0.9477 (100.10%)	0.2153 ± 0.0864 (40.13%) [0.0577 ± 0.0247 (42.82%)]	-2.49 [-2.34]	8.46 [35.95]
BB	n/a	0.9347 ± 0.9356 (100.10%)	0.2364 ± 0.1122 (47.46%)	n/a	6.22
		RMS error	2.8021 [0.0258]		
		$\chi^2_{d.o.f}$	39832832.4 [3126.2]		

Table B.75: Results for the *glennrealextU* `MCMC()` unmixing.

End-member	'True' Abundance	Prior, U	Retrieved Abundance [BBnorm]	Accuracy to 'True' Abundance σ [BBnorm]	Accuracy to U Abundance σ
Augite	0.0000	n/a	0.3059 ± 0.1451 (47.44%) [0.0670 ± 0.0330 (49.29%)]	-2.11 [-2.03]	n/a
Enstatite	0.0800	n/a	0.1703 ± 0.0877 (51.50%) [0.0373 ± 0.0199 (53.20%)]	-1.03 [2.15]	n/a
Olivine	0.1130	n/a	0.2062 ± 0.0867 (42.03%) [0.0452 ± 0.0199 (44.10%)]	-1.08 [3.40]	n/a
Calcite	0.0080	n/a	0.3955 ± 0.1738 (43.94%) [0.0866 ± 0.0398 (45.93%)]	-2.23 [-1.98]	n/a
Saponite	0.0000	n/a	0.2354 ± 0.1450 (61.60%) [0.0516 ± 0.0325 (63.03%)]	-1.62 [-1.59]	n/a
Cronstedtite	0.5290	n/a	0.1736 ± 0.1015 (58.46%) [0.0380 ± 0.0228 (59.97%)]	3.50 [21.53]	n/a
Lizardite	0.2330	n/a	0.2024 ± 0.1175 (58.07%) [0.0443 ± 0.0264 (59.59%)]	0.26 [7.14]	n/a
Magnetite	0.0150	n/a	0.3419 ± 0.1620 (47.38%) [0.0749 ± 0.0369 (49.22%)]	-2.02 [-1.62]	n/a
Spinel	0.0000	n/a	0.1641 ± 0.1060 (64.62%) [0.0359 ± 0.0237 (65.99%)]	-1.55 [-1.52]	n/a
Troilite	0.0000	n/a	0.1054 ± 0.0694 (65.78%) [0.0231 ± 0.0155 (67.12%)]	-1.52 [-1.49]	n/a
Pyrrhotite	0.0090	n/a	0.2830 ± 0.1514 (53.50%) [0.0620 ± 0.0342 (55.15%)]	-1.81 [-1.55]	n/a

Table B.75 continued from previous page

End-member	'True' Abundance	Prior, U	Retrieved Abundance [BBnorm]	Accuracy to 'True' Abundance σ [BBnorm]	Accuracy to U Abundance σ
Albite	0.0000	n/a	0.2287 ± 0.1376 (60.16%) [0.0501 ± 0.0309 (61.63%)]	-1.66 [-1.62]	n/a
Anorthite	0.0000	n/a	0.2447 ± 0.1009 (41.24%) [0.0536 ± 0.0232 (43.36%)]	-2.42 [-2.31]	n/a
Gypsum	0.0140	n/a	0.3583 ± 0.1756 (49.02%) [0.0785 ± 0.0399 (50.81%)]	-1.96 [-1.62]	n/a
AmorphousMg	0.0000	n/a	0.3097 ± 0.1394 (45.03%) [0.0678 ± 0.0319 (46.97%)]	-2.22 [-2.13]	n/a
AmorphousFe	0.0000	n/a	0.2221 ± 0.2259 (101.71%) [0.0486 ± 0.0499 (102.59%)]	-0.98 [-0.97]	n/a
MurchisonIOM	0.0000	n/a	0.2918 ± 0.1313 (45.00%) [0.0639 ± 0.0300 (46.94%)]	-2.22 [-2.13]	n/a
FeNiMetalSub	0.0000	n/a	0.3260 ± 0.1510 (46.34%) [0.0714 ± 0.0344 (48.22%)]	-2.16 [-2.07]	n/a
BB	n/a	n/a	0.2267 ± 0.1117 (49.27%)	n/a	n/a
		RMS error	3.5409 [0.0378]		
		$\chi^2_{d.o.f}$	1216339.1 [124.2]		

Table B.76: Results for the *glennrealextP1* `MCMC()` unmixing.

End-member	**'True' Abundance**	**Prior, P1**	**Retrieved Abundance [BBnorm]**	**Accuracy to 'True' Abundance σ [BBnorm]**	**Accuracy to P1 Abundance σ [BBnorm]**
Augite	0.0000	0.5921 ± 5.92E-04 (0.10%)	0.1279 ± 0.0567 (44.35%) [0.0309 ± 0.0142 (45.93%)]	-2.25 [-2.18]	8.18 [39.60]
Enstatite	0.0800	0.3011 ± 3.01E-04 (0.10%)	0.1967 ± 0.1480 (75.20%) [0.0475 ± 0.0361 (76.15%)]	-0.79 [0.90]	0.71 [7.02]
Olivine	0.1130	0.4687 ± 4.69E-04 (0.10%)	0.2547 ± 0.1331 (52.27%) [0.0614 ± 0.0329 (53.62%)]	-1.06 [1.56]	1.61 [12.36]
Calcite	0.0080	0.6976 ± 6.98E-04 (0.10%)	0.2946 ± 0.1440 (48.90%) [0.0711 ± 0.0358 (50.35%)]	-1.99 [-1.76]	2.80 [17.51]
Saponite	0.0000	0.0272 ± 2.72E-05 (0.10%)	0.1260 ± 0.0248 (19.71%) [0.0304 ± 0.0070 (23.05%)]	-5.07 [-4.34]	-3.98 [-0.45]
Cronstedtite	0.5290	0.9895 ± 0.0010 (0.10%)	0.2778 ± 0.1264 (45.49%) [0.0670 ± 0.0315 (47.03%)]	1.99 [14.66]	5.63 [29.26]
Lizardite	0.2330	0.4050 ± 4.05E-04 (0.10%)	0.2347 ± 0.1181 (50.33%) [0.0566 ± 0.0293 (51.73%)]	-0.01 [6.02]	1.44 [11.89]
Magnetite	0.0150	0.8932 ± 8.93E-04 (0.10%)	0.2571 ± 0.1166 (45.34%) [0.0620 ± 0.0291 (46.89%)]	-2.08 [-1.62]	5.46 [28.58]
Spinel	0.0000	0.7193 ± 7.19E-04 (0.10%)	0.3469 ± 0.1495 (43.11%) [0.0837 ± 0.0374 (44.74%)]	-2.32 [-2.24]	2.49 [16.98]
Troilite	0.0000	0.4880 ± 4.88E-04 (0.10%)	0.2628 ± 0.0975 (37.09%) [0.0634 ± 0.0247 (38.97%)]	-2.70 [-2.57]	2.31 [17.18]
Pyrrhotite	0.0090	0.0385 ± 3.85E-05 (0.10%)	0.1020 ± 0.0478 (46.86%) [0.0246 ± 0.0119 (48.36%)]	-1.95 [-1.31]	-1.33 [1.17]

Table B.76 continued from previous page

End-member	'True' Abundance	Prior, P1	Retrieved Abundance [BBnorm]	Accuracy to 'True' Abundance σ [BBnorm]	Accuracy to P1 Abundance σ [BBnorm]
Albite	0.0000	0.6164 ± 6.16E-04 (0.10%)	0.3292 ± 0.1188 (36.10%) [0.0794 ± 0.0302 (38.03%)]	-2.77 [-2.63]	2.42 [17.78]
Anorthite	0.0000	0.9767 ± 0.0010 (0.10%)	0.2853 ± 0.1029 (36.07%) [0.0688 ± 0.0262 (38.01%)]	-2.77 [-2.63]	6.72 [34.70]
Gypsum	0.0140	0.2391 ± 2.39E-04 (0.10%)	0.1938 ± 0.0970 (50.06%) [0.0467 ± 0.0241 (51.47%)]	-1.85 [-1.36]	0.47 [8.00]
AmorphousMg	0.0000	0.9921 ± 0.0010 (0.10%)	0.2411 ± 0.0794 (32.94%) [0.0582 ± 0.0204 (35.04%)]	-3.04 [-2.85]	9.46 [45.82]
AmorphousFe	0.0000	0.0353 ± 3.53E-05 (0.10%)	0.1213 ± 0.0151 (12.47%) [0.0293 ± 0.0051 (17.28%)]	-8.02 [-5.79]	-5.69 [1.19]
MurchisonIOM	0.0000	0.7350 ± 7.35E-04 (0.10%)	0.2646 ± 0.1536 (58.07%) [0.0638 ± 0.0378 (59.29%)]	-1.72 [-1.69]	3.06 [17.74]
FeNiMetalSub	0.0000	0.9467 ± 0.0009 (0.10%)	0.2289 ± 0.1088 (47.54%) [0.0552 ± 0.0271 (49.02%)]	-2.10 [-2.04]	6.60 [32.93]
BB	n/a	0.9347 ± 0.0009 (0.10%)	0.2691 ± 0.1184 (43.98%)	n/a	5.62
		RMS error	3.1811 [0.0399]		
		$\chi^2_{d.o.f}$	988881.4 [116.2]		

Table B.77: Results for the *brucerealmodmin* `WLS_ASC_ILR()` unmixing.

End-member	**'True' Abundance**	**Retrieved Abundance**	**Accuracy to 'True' Abundance** σ
Augite	0.0150	0.0079 ± 0.1222 (1548.57%)	0.06
Enstatite	0.0850	rm	
Olivine	0.7000	0.9921 ± 0.1217 (12.27%)	-2.4
Troilite	0.0500	rm	
Albite	0.1000	rm	
FeNiMetalSub	0.0500	rm	
	RMS error	0.0480	
	$\chi^2_{d.o.f}$	0.084	

Table B.78: Results for the *brucerealmodexp* `WLS_ASC_ILR()` unmixing.

End-member	**'True' Abundance**	**Retrieved Abundance**	**Accuracy to 'True' Abundance** σ
Augite	0.0150	rm	
Enstatite	0.0850	rm	
Olivine	0.7000	0.9231 ± 0.0167 (1.81%)	-13.37
Calcite	0.0000	0.0769 ± 0.0189 (24.63%)	-4.06
Lizardite	0.0000	rm	
Troilite	0.0500	rm	
Albite	0.1000	rm	
Gypsum	0.0000	rm	
AmorphousFe	0.0000	rm	
FeNiMetalSub	0.0500	rm	
BB	0.0000	rm	
	RMS error	0.0485	
	$\chi^2_{d.o.f}$	0.045	

Table B.79: Results for the *brucerealmodext* `WLS_ASC_ILR()` unmixing.

End-member	**'True' Abundance**	**Retrieved Abundance**	**Accuracy to 'True' Abundance** σ
Augite	0.0150	rm	
Enstatite	0.0850	0.3565 ± 0.1349 (37.84%)	-2.01
Olivine	0.7000	rm	
Calcite	0.0000	rm	
Saponite	0.0000	rm	
Cronstedtite	0.0000	rm	
Lizardite	0.0000	0.1407 ± 0.2601 (184.84%)	-0.54
Magnetite	0.0000	rm	
Spinel	0.0000	rm	
Troilite	0.0500	rm	
Pyrrhotite	0.0000	rm	
Albite	0.1000	rm	
Anorthite	0.0000	rm	
Gypsum	0.0000	rm	
AmorphousMg	0.0000	0.4851 ± 0.2320 (47.82%)	-2.09
AmorphousFe	0.0000	0.0177 ± 0.0603 (341.08%)	-0.29
MurchisonIOM	0.0000	rm	
Fe, Ni metal sub.	0.0500	rm	
BB	0.0000	rm	
	RMS error	0.1083	
	$\chi^2_{d.o.f}$	0.070	

Table B.80: Results for the *brucerealmodminP1* `OptEst_ASC_ILR()` unmixing.

End-member	**'True' Abundance**	**Prior, P1**	**Retrieved Abundance**	**Accuracy to 'True' Abundance** σ	**Accuracy to P1 Abundance** σ
Augite	0.0150	0.3004 ± 3.00E-04 (0.10%)	0.2066 ± 2.99E-04 (0.14%)	-640.23	313.37
Enstatite	0.0850	0.0110 ± 1.10E-05 (0.10%)	0.0109 ± 1.10E-05 (0.10%)	6731.58	11.44
Olivine	0.7000	0.3872 ± 3.87E-04 (0.10%)	0.2314 ± 3.85E-04 (0.17%)	1217.8	404.92
Troilite	0.0500	0.5015 ± 5.02E-04 (0.10%)	0.2401 ± 4.96E-04 (0.21%)	-383.11	526.82
Albite	0.1000	0.6452 ± 6.45E-04 (0.10%)	0.2125 ± 6.34E-04 (0.30%)	-177.34	682.02
Fe, Ni metal sub.	0.0500	0.8508 ± 8.51E-04 (0.10%)	0.0985 ± 8.24E-04 (0.84%)	-58.8	912.48
		RMS error	0.0915		
		$\chi^2_{d.o.f}$	0.157		

Table B.81: Results for the *brucerealmodminP3* `OptEst_ASC_ILR()` unmixing.

End-member	**'True' Abundance**	**Prior, P3**	**Retrieved Abundance**	**Accuracy to 'True' Abundance** σ	**Accuracy to P3 Abundance** σ
Augite	0.0150	0.0150 ± 1.50E-05 (0.10%)	0.0150 ± 1.50E-05 (0.10%)	0.0002	0.0002
Enstatite	0.0850	0.0850 ± 8.50E-05 (0.10%)	0.0850 ± 8.50E-05 (0.10%)	0.0019	0.0019
Olivine	0.7000	0.7000 ± 7.00E-04 (0.10%)	0.7000 ± 6.84E-04 (0.10%)	-0.0011	-0.0011
Troilite	0.0500	0.0500 ± 5.00E-05 (0.10%)	0.0500 ± 5.00E-05 (0.10%)	0.0010	0.0010
Albite	0.1000	0.1000 ± 1.00E-04 (0.10%)	0.1000 ± 1.00E-04 (0.10%)	0.0048	0.0048
Fe, Ni metal sub.	0.0500	0.0500 ± 5.00E-05 (0.10%)	0.0500 ± 5.00E-05 (0.10%)	0.0013	0.0013
		RMS error	0.0593		
		$\chi^2_{d.o.f}$	0.101		

Table B.82: Results for the *brucerealmodminP4* `OptEst_ASC_ILR()` unmixing.

End-member	**'True' Abundance**	**Prior, P4**	**Retrieved Abundance**	**Accuracy to 'True' Abundance** σ	**Accuracy to P4 Abundance** σ
Augite	0.0150	0.0500 ± 0.0100 (20.00%)	0.0528 ± 0.0090 (17.05%)	-4.2	-0.32
Enstatite	0.0850	0.1000 ± 0.0100 (10.00%)	0.1021 ± 0.0090 (8.82%)	-1.9	-0.23
Olivine	0.7000	0.6000 ± 0.0050 (0.83%)	0.6012 ± 0.0049 (0.81%)	20.25	-0.25
Troilite	0.0500	0.0750 ± 0.0100 (13.33%)	0.0773 ± 0.0090 (11.62%)	-3.04	-0.25
Albite	0.1000	0.0900 ± 0.0100 (11.11%)	0.0898 ± 0.0089 (9.95%)	1.14	0.02
Fe, Ni metal sub.	0.0500	0.0750 ± 0.0100 (13.33%)	0.0768 ± 0.0090 (11.69%)	-2.98	-0.2
		RMS error	0.0656		
		$\chi^2_{d.o.f}$	0.107		

Table B.83: Results for the *brucerealmodexpP1* `OptEst_ASC_ILR()` unmixing.

End-member	**'True' Abundance**	**Prior, P1**	**Retrieved Abundance**	**Accuracy to 'True' Abundance** σ	**Accuracy to P1 Abundance** σ
Augite	0.0150	0.2114 ± 2.11E-04 (0.10%)	0.1544 ± 2.11E-04 (0.14%)	-660.67	270.08
Enstatite	0.0850	0.6609 ± 6.61E-04 (0.10%)	0.1039 ± 6.49E-04 (0.62%)	-29.07	858.46
Olivine	0.7000	0.1949 ± 1.95E-04 (0.10%)	0.1464 ± 1.95E-04 (0.13%)	2845.41	248.88
Calcite	0.0000	0.9068 ± 0.0009 (0.10%)	rm		
Lizardite	0.0000	0.7720 ± 7.72E-04 (0.10%)	0.0120 ± 7.53E-04 (6.30%)	-15.87	1008.79
Troilite	0.0500	0.9318 ± 0.0009 (0.10%)	rm		
Albite	0.1000	0.0640 ± 6.40E-05 (0.10%)	0.0588 ± 6.40E-05 (0.11%)	644.78	81.61
Gypsum	0.0000	0.2624 ± 2.62E-04 (0.10%)	0.1746 ± 2.62E-04 (0.15%)	-667.22	335.49
AmorphousFe	0.0000	0.3706 ± 3.71E-04 (0.10%)	0.1954 ± 3.69E-04 (0.19%)	-530.14	475.14

Fe, Ni metal sub.	0.0500	0.5723 ± 5.72E-04 (0.10%)	0.1546 ± 5.64E-04 (0.37%)	-185.32	740.16
BB	0.0000	0.9196 ± 0.0009 (0.10%)	rm		
		RMS error	0.0926		
		$\chi^2_{d.o.f}$	0.166		

Table B.84: Results for the *brucerealmodexpP2* `OptEst_ASC_ILR()` unmixing.

End-member	**'True' Abundance**	**Prior, P2**	**Retrieved Abundance**	**Accuracy to 'True' Abundance** σ	**Accuracy to P2 Abundance** σ
Augite	0.0150	0.2114 ± 0.2116 (100.10%)	rm		
Enstatite	0.0850	0.6609 ± 0.6615 (100.10%)	rm		
Olivine	0.7000	0.1949 ± 0.1950 (100.10%)	0.5297 ± 0.1226 (23.14%)	1.39	-2.73
Calcite	0.0000	0.9068 ± 0.9077 (100.10%)	0.0482 ± 0.0197 (40.94%)	-2.44	43.51
Lizardite	0.0000	0.7720 ± 0.7728 (100.10%)	0.3646 ± 0.1081 (29.65%)	-3.37	3.77
Troilite	0.0500	0.9318 ± 0.9327 (100.10%)	rm		
Albite	0.1000	0.0640 ± 0.0640 (100.10%)	0.0055 ± 0.0513 (925.66%)	1.84	1.14
Gypsum	0.0000	0.2624 ± 0.2626 (100.10%)	rm		
AmorphousFe	0.0000	0.3706 ± 0.3709 (100.10%)	0.0520 ± 0.0653 (125.57%)	-0.8	4.88
FeNiMetalSub	0.0500	0.5723 ± 0.5729 (100.10%)	rm		
BB	n/a	0.9196 ± 0.9205 (100.10%)	rm	n/a	
		RMS error	0.0723		
		$\chi^2_{d.o.f}$	0.042		

Table B.85: Results for the *brucerealmodexpP3* `OptEst_ASC_ILR()` unmixing.

End-member	**'True' Abundance**	**Prior, P3**	**Retrieved Abundance [BBnorm]**	**Accuracy to 'True' Abundance σ [BBnorm]**	**Accuracy to P3 Abundance σ [BBnorm]**
Augite	0.0150	0.0150 ± 1.50E-05 (0.10%)	0.0150 ± 1.50E-05 (0.10%) [0.0150 ± 1.87E-05 (0.12%)]	0.01 [-0.06]	0.01 [-0.06]
Enstatite	0.0850	0.0850 ± 8.50E-05 (0.10%)	0.0850 ± 8.50E-05 (0.10%) [0.0850 ± 1.06E-04 (0.12%)]	0.08 [-0.01]	0.08 [-0.01]
Olivine	0.7000	0.7000 ± 7.00E-04 (0.10%)	0.6996 ± 6.84E-04 (0.10%) [0.6996 ± 8.59E-04 (0.12%)]	0.64 [0.44]	0.64 [0.44]
Calcite	0.0000	1.00E-04 ± 1.00E-04 (100.10%)	9.44E-05 ± 1.00E-04 (106.04%) [9.44E-05 ± 1.00E-04 (106.04%)]	-0.94 [-0.94]	0.06 [0.06]
Lizardite	0.0000	1.00E-04 ± 1.00E-04 (100.10%)	9.15E-05 ± 1.00E-04 (109.41%) [9.15E-05 ± 1.00E-04 (109.41%)]	-0.91 [-0.91]	0.09 [0.09]
Troilite	0.0500	0.0500 ± 5.00E-05 (0.10%)	0.0500 ± 5.00E-05 (0.10%) [0.0500 ± 6.23E-05 (0.12%)]	0.05 [-0.04]	0.05 [-0.04]
Albite	0.1000	0.1000 ± 1.00E-04 (0.10%)	0.1000 ± 1.00E-04 (0.10%) [0.1000 ± 1.25E-04 (0.12%)]	0.09 [0.00]	0.09 [0.00]
Gypsum	0.0000	1.00E-04 ± 1.00E-04 (100.10%)	9.12E-05 ± 1.00E-04 (109.71%) [9.12E-05 ± 1.00E-04 (109.71%)]	-0.91 [-0.91]	0.09 [0.09]
AmorphousFe	0.0000	1.00E-04 ± 1.00E-04 (100.10%)	9.09E-05 ± 1.00E-04 (110.09%) [9.09E-05 ± 1.00E-04 (110.09%)]	-0.91 [-0.91]	0.09 [0.09]
FeNiMetalSub	0.0500	0.0500 ± 5.00E-05 (0.10%)	0.0500 ± 5.00E-05 (0.10%) [0.0500 ± 6.23E-05 (0.12%)]	0.05 [-0.04]	0.05 [-0.04]
BB	n/a	1.00E-04 ± 1.00E-04 (100.10%)	9.08E-05 ± 1.00E-04 (110.25%)	n/a	0.09
		RMS error	0.0593 [0.0593]		

$\chi^2_{d.o.f}$	0.1013 [0.1011]

Table B.86: Results for the *brucerealmodexpP4* `OptEst_ASC_ILR()` unmixing.

End-member	**'True' Abundance**	**Prior, P4**	**Retrieved Abundance [BBnorm]**	**Accuracy to 'True' Abundance σ [BBnorm]**	**Accuracy to P4 Abundance σ [BBnorm]**
Augite	0.0150	0.0500 ± 0.0100 (20.00%)	0.0158 ± 0.0093 (58.75%) [0.0196 ± 0.0115 (58.85%)]	-0.09 [-0.40]	3.67 [2.63]
Enstatite	0.0850	0.1000 ± 0.0100 (10.00%)	0.0651 ± 0.0093 (14.29%) [0.0806 ± 0.0118 (14.70%)]	2.14 [0.37]	3.76 [1.64]
Olivine	0.7000	0.6000 ± 0.0050 (0.83%)	0.5918 ± 0.0049 (0.83%) [0.7333 ± 0.0260 (3.54%)]	22.02 [-1.28]	1.66 [-5.13]
Calcite	0.0000	0.0010 ± 0.0100 (1000.00%)	0.0019 ± 0.0085 (447.15%) [0.0024 ± 0.0105 (447.17%)]	-0.22 [-0.22]	-0.11 [-0.13]
Lizardite	0.0000	0.0001 ± 0.0100 (10000.00%)	rm		
Troilite	0.0500	0.0750 ± 0.0100 (13.33%)	0.0393 ± 0.0093 (23.66%) [0.0487 ± 0.0116 (23.91%)]	1.15 [0.11]	3.84 [2.26]
Albite	0.1000	0.0900 ± 0.0100 (11.11%)	0.0544 ± 0.0092 (16.89%) [0.0674 ± 0.0116 (17.24%)]	4.97 [2.81]	3.88 [1.95]
Gypsum	0.0000	0.0001 ± 0.0100 (10000.00%)	rm		
AmorphousFe	0.0000	0.0001 ± 0.0100 (10000.00%)	rm		
FeNiMetalSub	0.0500	0.0750 ± 0.0100 (13.33%)	0.0387 ± 0.0093 (24.00%) [0.0480 ± 0.0116 (24.25%)]	1.21 [0.17]	3.90 [2.32]
BB	n/a	0.2500 ± 0.0125 (5.00%)	0.1930 ± 0.0111 (5.74%)	n/a	5.14

RMS error	0.0714 [0.0580]
$\chi^2_{d.o.f}$	0.110 [0.094]

Table B.87: Results for the *brucerealmodextP1* `OptEst_ASC_ILR()` unmixing.

End-member	**'True' Abundance**	**Prior, P1**	**Retrieved Abundance [BBnorm]**	**Accuracy to 'True' Abundance σ [BBnorm]**	**Accuracy to P1 Abundance σ [BBnorm]**
Augite	0.0150	0.7172 ± 7.17E-04 (0.10%)	rm		
Enstatite	0.0850	0.4381 ± 4.38E-04 (0.10%)	0.1192 ± 4.35E-04 (0.36%) [0.1389 ± 5.43E-04 (0.39%)]	-78.67 [-99.28]	733.90 [551.39]
Olivine	0.7000	0.8050 ± 8.05E-04 (0.10%)	rm		
Calcite	0.0000	0.2546 ± 2.55E-04 (0.10%)	0.1469 ± 2.54E-04 (0.17%) [0.1711 ± 3.81E-04 (0.22%)]	-578.06 [-448.63]	424.08 [218.85]
Saponite	0.0000	0.0326 ± 3.26E-05 (0.10%)	0.0308 ± 3.26E-05 (0.11%) [0.0359 ± 6.32E-05 (0.18%)]	-945.90 [-568.55]	54.15 [-52.69]
Cronstedtite	0.0000	0.9071 ± 0.0009 (0.10%)	rm		
Lizardite	0.0000	0.5086 ± 5.09E-04 (0.10%)	0.0788 ± 5.03E-04 (0.64%) [0.0918 ± 6.00E-04 (0.65%)]	-156.51 [-152.85]	854.21 [694.29]
Magnetite	0.0000	0.7271 ± 7.27E-04 (0.10%)	rm		
Spinel	0.0000	0.6179 ± 6.18E-04 (0.10%)	rm		
Troilite	0.0500	0.8562 ± 8.56E-04 (0.10%)	rm		
Pyrrhotite	0.0000	0.6534 ± 6.53E-04 (0.10%)	rm		
Albite	0.1000	0.5196 ± 5.20E-04 (0.10%)	0.0709 ± 5.14E-04 (0.72%) [0.0827 ± 6.10E-04 (0.74%)]	56.56 [28.44]	873.12 [716.39]

Table B.87 continued from previous page

End-member	'True' Abundance	Prior, P1	Retrieved Abundance [BBnorm]	Accuracy to 'True' Abundance σ [BBnorm]	Accuracy to P1 Abundance σ [BBnorm]
Anorthite	0.0000	0.8820 ± 8.82E-04 (0.10%)	rm		
Gypsum	0.0000	0.3018 ± 3.02E-04 (0.10%)	0.1504 ± 3.01E-04 (0.20%) [0.1753 ± 4.28E-04 (0.24%)]	-500.27 [-409.22]	503.40 [295.37]
AmorphousMg	0.0000	0.1128 ± 1.13E-04 (0.10%)	0.0916 ± 1.13E-04 (0.12%) [0.1068 ± 1.99E-04 (0.19%)]	-813.04 [-535.39]	187.46 [30.02]
AmorphousFe	0.0000	0.5535 ± 5.53E-04 (0.10%)	0.0444 ± 5.47E-04 (1.23%) [0.0518 ± 6.41E-04 (1.24%)]	-81.24 [-80.72]	930.93 [782.32]
MurchisonIOM	0.0000	0.9793 ± 0.0010 (0.10%)	rm		
FeNiMetalSub	0.0500	0.4243 ± 4.24E-04 (0.10%)	0.1251 ± 4.21E-04 (0.34%) [0.1458 ± 5.32E-04 (0.36%)]	-178.50 [-180.24]	710.57 [523.78]
BB	n/a	0.2287 ± 2.29E-04 (0.10%)	0.1418 ± 2.28E-04 (0.16%)	n/a	380.9
		RMS error	0.1161 [0.1133]		
		$\chi^2_{d.o.f}$	0.173 [0.222]		

Table B.88: Results for the *brucerealmodextP2* `OptEst_ASC_ILR()` unmixing.

End-member	'True' Abundance	Prior, P2	Retrieved Abundance	Accuracy to 'True' Abundance σ	Accuracy to P2 Abundance σ
Augite	0.0150	0.7172 ± 0.7179 (100.10%)	rm		
Enstatite	0.0850	0.4381 ± 0.4385 (100.10%)	rm		
Olivine	0.7000	0.8050 ± 0.8058 (100.10%)	0.8080 ± 0.0787 (9.74%)	-1.37	-0.04
Calcite	0.0000	0.2546 ± 0.2549 (100.10%)	0.0529 ± 0.0255 (48.14%)	-2.08	7.92

Table B.88 continued from previous page

End-member	'True' Abundance	Prior, P2	Retrieved Abundance	Accuracy to 'True' Abundance σ	Accuracy to P2 Abundance σ
Saponite	0.0000	0.0326 ± 0.0326 (100.10%)	0.0232 ± 0.0322 (138.49%)	-0.72	0.29
Cronstedtite	0.0000	0.9071 ± 0.9080 (100.10%)	rm		
Lizardite	0.0000	0.5086 ± 0.5091 (100.10%)	rm		
Magnetite	0.0000	0.7271 ± 0.7278 (100.10%)	rm		
Spinel	0.0000	0.6179 ± 0.6185 (100.10%)	0.0739 ± 0.0501 (67.79%)	-1.48	10.85
Troilite	0.0500	0.8562 ± 0.8571 (100.10%)	rm		
Pyrrhotite	0.0000	0.6534 ± 0.6541 (100.10%)	rm		
Albite	0.1000	0.5196 ± 0.5202 (100.10%)	rm		
Anorthite	0.0000	0.8820 ± 0.8829 (100.10%)	rm		
Gypsum	0.0000	0.3018 ± 0.3021 (100.10%)	rm		
AmorphousMg	0.0000	0.1128 ± 0.1129 (100.10%)	0.0419 ± 0.0981 (234.09%)	-0.43	0.72
AmorphousFe	0.0000	0.5535 ± 0.5540 (100.10%)	rm		
MurchisonIOM	0.0000	0.9793 ± 0.9803 (100.10%)	rm		
FeNiMetalSub	0.0500	0.4243 ± 0.4247 (100.10%)	rm		
BB	n/a	0.2287 ± 0.2289 (100.10%)	rm	n/a	
		RMS error	0.0550		
		$\chi^2_{d.o.f}$	0.021		

Table B.89: Results for the *brucerealmodextP3* `OptEst_ASC_ILR()` unmixing.

End-member	**'True' Abundance**	**Prior, P3**	**Retrieved Abundance [BBnorm]**	**Accuracy to 'True' Abundance σ [BBnorm]**	**Accuracy to P3 Abundance σ [BBnorm]**
Augite	0.0150	0.0150 ± 1.50E-05 (0.10%)	0.0150 ± 1.50E-05 (0.10%) [0.0150 ± 1.92E-05 (0.13%)]	0.03 [-0.04]	0.03 [-0.04]
Enstatite	0.0850	0.0850 ± 8.50E-05 (0.10%)	0.0850 ± 8.50E-05 (0.10%) [0.0850 ± 1.09E-04 (0.13%)]	0.18 [0.08]	0.18 [0.08]
Olivine	0.7000	0.7000 ± 7.00E-04 (0.10%)	0.6990 ± 6.84E-04 (0.10%) [0.6991 ± 8.81E-04 (0.13%)]	1.46 [1.07]	1.46 [1.07]
Calcite	0.0000	1.00E-04 ± 1.00E-04 (100.10%)	8.29E-05 ± 1.00E-04 (120.71%) [8.29E-05 ± 1.00E-04 (120.71%)]	-0.83 [-0.83]	0.17 [0.17]
Saponite	0.0000	1.00E-04 ± 1.00E-04 (100.10%)	7.97E-05 ± 1.00E-04 (125.47%) [7.98E-05 ± 1.00E-04 (125.47%)]	-0.80 [-0.80]	0.20 [0.20]
Cronstedtite	0.0000	1.00E-04 ± 1.00E-04 (100.10%)	8.15E-05 ± 1.00E-04 (122.83%) [8.15E-05 ± 1.00E-04 (122.83%)]	-0.81 [-0.81]	0.19 [0.19]
Lizardite	0.0000	1.00E-04 ± 1.00E-04 (100.10%)	8.00E-05 ± 1.00E-04 (125.09%) [8.00E-05 ± 1.00E-04 (125.09%)]	-0.80 [-0.80]	0.20 [0.20]
Magnetite	0.0000	1.00E-04 ± 1.00E-04 (100.10%)	7.94E-05 ± 1.00E-04 (126.00%) [7.94E-05 ± 1.00E-04 (126.00%)]	-0.79 [-0.79]	0.21 [0.21]
Spinel	0.0000	1.00E-04 ± 1.00E-04 (100.10%)	8.25E-05 ± 1.00E-04 (121.24%) [8.25E-05 ± 1.00E-04 (121.24%)]	-0.82 [-0.82]	0.17 [0.17]
Troilite	0.0500	0.0500 ± 5.00E-05 (0.10%)	0.0500 ± 5.00E-05 (0.10%) [0.0500 ± 6.39E-05 (0.13%)]	0.10 [0.02]	0.10 [0.02]
Pyrrhotite	0.0000	1.00E-04 ± 1.00E-04 (100.10%)	8.13E-05 ± 1.00E-04 (123.13%) [8.13E-05 ± 1.00E-04 (123.13%)]	-0.81 [-0.81]	0.19 [0.19]

Table B.89 continued from previous page

End-member	'True' Abundance	Prior, P3	Retrieved Abundance [BBnorm]	Accuracy to 'True' Abundance σ [BBnorm]	Accuracy to P3 Abundance σ [BBnorm]
Albite	0.1000	0.1000 ± 1.00E-04 (0.10%)	0.1000 ± 1.00E-04 (0.10%) [0.1000 ± 1.28E-04 (0.13%)]	0.21 [0.10]	0.21 [0.10]
Anorthite	0.0000	1.00E-04 ± 1.00E-04 (100.10%)	7.93E-05 ± 1.00E-04 (126.15%) [7.93E-05 ± 1.00E-04 (126.15%)]	-0.79 [-0.79]	0.21 [0.21]
Gypsum	0.0000	1.00E-04 ± 1.00E-04 (100.10%)	7.97E-05 ± 1.00E-04 (125.48%) [7.97E-05 ± 1.00E-04 (125.48%)]	-0.80 [-0.80]	0.20 [0.20]
AmorphousMg	0.0000	1.00E-04 ± 1.00E-04 (100.10%)	8.03E-05 ± 1.00E-04 (124.55%) [8.03E-05 ± 1.00E-04 (124.55%)]	-0.80 [-0.80]	0.20 [0.20]
AmorphousFe	0.0000	1.00E-04 ± 1.00E-04 (100.10%)	7.94E-05 ± 1.00E-04 (125.98%) [7.94E-05 ± 1.00E-04 (125.98%)]	-0.79 [-0.79]	0.21 [0.21]
MurchisonIOM	0.0000	1.00E-04 ± 1.00E-04 (100.10%)	7.96E-05 ± 1.00E-04 (125.77%) [7.96E-05 ± 1.00E-04 (125.77%)]	-0.80 [-0.80]	0.20 [0.20]
FeNiMetalSub	0.0500	0.0500 ± 5.00E-05 (0.10%)	0.0500 ± 5.00E-05 (0.10%) [0.0500 ± 6.39E-05 (0.13%)]	0.10 [0.02]	0.10 [0.02]
BB	n/a	1.00E-04 ± 1.00E-04 (100.10%)	7.93E-05 ± 1.00E-04 (126.19%)	n/a	0.21
		RMS error	0.05938 [0.05937]		
		$\chi^2_{d.o.f}$	0.1023 [0.1022]		

Table B.90: Results for the *brucerealmodextP4* `OptEst_ASC_ILR()` unmixing.

End-member	**'True' Abundance**	**Prior, P4**	**Retrieved Abundance [BBnorm]**	**Accuracy to 'True' Abundance σ [BBnorm]**	**Accuracy to P4 Abundance σ [BBnorm]**
Augite	0.0150	0.0500 ± 0.0100 (20.00%)	0.0158 ± 0.0093 (58.75%) [0.0196 ± 0.0115 (58.85%)]	-0.09 [-0.40]	3.67 [2.63]
Enstatite	0.0850	0.1000 ± 0.0100 (10.00%)	0.0651 ± 0.0093 (14.29%) [0.0806 ± 0.0118 (14.70%)]	2.14 [0.37]	3.76 [1.64]
Olivine	0.7000	0.6000 ± 0.0050 (0.83%)	0.5918 ± 0.0049 (0.83%) [0.7333 ± 0.0260 (3.54%)]	22.02 [-1.28]	1.66 [-5.13]
Calcite	0.0000	0.0010 ± 0.0100 (1000.00%)	0.0019 ± 0.0085 (447.15%) [0.0024 ± 0.0105 (447.17%)]	-0.22 [-0.22]	-0.11 [-0.13]
Saponite	0.0000	0.0001 ± 0.0010 (1000.00%)	rm		
Cronstedtite	0.0000	0.0010 ± 0.0100 (1000.00%)	rm		
Lizardite	0.0000	0.0001 ± 0.0100 (10000.00%)	rm		
Magnetite	0.0000	0.0001 ± 0.0100 (10000.00%)	rm		
Spinel	0.0000	0.0010 ± 0.0100 (1000.00%)	rm		
Troilite	0.0500	0.0750 ± 0.0100 (13.33%)	0.0393 ± 0.0093 (23.66%) [0.0487 ± 0.0116 (23.91%)]	1.15 [0.11]	3.84 [2.26]
Pyrrhotite	0.0000	0.0750 ± 0.1000 (133.33%)	rm		
Albite	0.1000	0.0900 ± 0.0100 (11.11%)	0.0544 ± 0.0092 (16.89%) [0.0674 ± 0.0116 (17.24%)]	4.97 [2.81]	3.88 [1.95]
Anorthite	0.0000	0.0900 ± 0.1000 (111.11%)	rm		
Gypsum	0.0000	0.0001 ± 0.0100 (10000.00%)	rm		
AmorphousMg	0.0000	0.0010 ± 0.0100 (1000.00%)	rm		
AmorphousFe	0.0000	0.0001 ± 0.0100 (10000.00%)	rm		
MurchisonIOM	0.0000	0.0750 ± 0.1000 (133.33%)	rm		

Fe, Ni metal sub.	0.0500	0.0750 ± 0.0100 (13.33%)	0.0387 ± 0.0093 (24.00%) [0.0480 ± 0.0116 (24.25%)]	1.21 [0.17]	3.90 [2.32]
BB	n/a	0.2500 ± 0.0125 (5.00%)	0.1930 ± 0.0111 (5.74%)	n/a	5.14
		RMS error	0.0714 [0.0580]		
		$\chi^2_{d.o.f}$	0.110 [0.094]		

Chapter C

Additional Correlation Matrices to Accompany Chapters 5, 6 and 7

Key: Au=augite; En=enstatite; Ol=olivine; Ca=calcite; Sa=saponite; Cr=cronstedtite; Li=lizardite; Ma=magnetite; Sp=spinel; Tr=troilite; Py=pyrrhotite; Al=albite; An=anorthite; Gy=gypsum; AmMg=amorphous Mg; AmFe=amorphous Fe; IOM=MurchisonIOM; FeNi=FeNiMetalSub

Table C.1: *brucerealexp* `WLS_ASC_ILR()` unmixing correlation matrix.

	Ol	**FeNi**	**Li**	**Ca**
Olivine (Ol)	1.000	0.388	**-0.714**	-0.027
FeNiMetalSub (FeNi)	0.388	1.000	**-0.914**	-0.382
Lizardite (Li)	**-0.714**	**-0.914**	1.000	0.195
Calcite (Ca)	-0.027	-0.382	0.195	1.000

Table C.2: Correlation matrix for retrieved abundances from the *brucemathminP3* `OptEst_ASC_ILR()` unmixing.

brucemathminP3	Au	En	Ol	Tr	Al	FeNi
Augite (Au)	1	-0.015	-0.093	-0.009	-0.016	-0.0091
Enstatite (En)	-0.015	1	-0.513	-0.068	-0.117	-0.06842
Olivine (Ol)	-0.093	-0.513	1	-0.263	-0.572	-0.2664
Troilite (Tr)	-0.009	-0.068	-0.263	1	-0.103	-0.06507
Albite (Al)	-0.016	-0.117	-0.572	-0.103	1	-0.10245
FeNiMetalSub (FeNi)	-0.009	-0.068	-0.266	-0.065	-0.102	1

Table C.3: Correlation matrix for the *brucerealminP1* `OptEst_ASC_ILR()` unmixing.

brucerealminP1	Au	En	Ol	Tr	Al	FeNi
Augite (Au)	1.0000	-0.0063	-0.2864	-0.0605	-0.1456	-0.1641
Enstatite (En)	-0.0063	1.0000	-0.0066	-0.0027	-0.0049	-0.0069
Olivine (Ol)	-0.2864	-0.0066	1.0000	-0.0313	-0.2457	-0.0981
Troilite (Tr)	-0.0605	-0.0027	-0.0313	1.0000	-0.1960	**-0.6059**
Albite (Al)	-0.1456	-0.0049	-0.2457	-0.1960	1.0000	-0.4765
FeNiMetalSub (FeNi)	-0.1641	-0.0069	-0.0981	**-0.6059**	-0.4765	1.0000

Table C.4: Correlation matrix for the *brucerealminP2* `OptEst_ASC_ILR()` unmixing.

brucerealminP2	Au	Ol	FeNi
Augite (Au)	1.0000	**-0.7669**	**-0.7593**
Olivine (Ol)	**-0.7669**	1.0000	0.1659
FeNiMetalSub (FeNi)	**-0.7593**	0.1659	1.0000

Table C.5: Correlation matrix for the *brucerealminP3* `OptEst_ASC_ILR()` unmixing.

brucerealminP3	Au	En	Ol	Tr	Al	FeNi
Augite (Au)	1.0000	-0.0070	-0.0936	-0.0044	-0.0076	-0.0044
Enstatite (En)	-0.0070	1.0000	-0.5296	-0.0312	-0.0531	-0.0312
Olivine (Ol)	-0.0936	-0.5296	1.0000	-0.3076	**-0.6164**	-0.3100
Troilite (Tr)	-0.0044	-0.0312	-0.3076	1.0000	-0.0435	-0.0273
Albite (Al)	-0.0076	-0.0531	**-0.6164**	-0.0435	1.0000	-0.0434
FeNiMetalSub (FeNi)	-0.0044	-0.0312	-0.3100	-0.0273	-0.0434	1.0000

Table C.6: Correlation matrix for retrieved abundances from the *brucerealminP4* `OptEst_ASC_ILR()` unmixing.

brucerealminP4	Au	Ol	FeNi
Augite (Au)	1	**0.764**	**0.759**
Olivine (Ol)	**0.764**	1	0.162
FeNiMetalSub (FeNi)	**0.759**	0.162	1

Table C.7: Correlation matrix for the *glennmathminP1* `OptEst_ASC_ILR()` unmixing.

glennmathminP1	En	Ol	Cr	Li	Ma	Py	Gy
Enstatite (En)	1.0000	**-0.6926**	-0.0068	-0.0179	-0.2466	-0.0449	-0.2561
Olivine (Ol)	**-0.6926**	1.0000	-0.1879	-0.0190	0.1776	-0.0125	0.0438
Cronstedtite (Cr)	-0.0068	-0.1879	1.0000	-0.0036	-0.0787	-0.0767	-0.1505
Lizardite (Li)	-0.0179	-0.0190	-0.0036	1.0000	-0.0031	-0.0032	-0.0143
Magnetite (Ma)	-0.2466	0.1776	-0.0787	-0.0031	1.0000	-0.4465	-0.4581
Pyrrhotite (Py)	-0.0449	-0.0125	-0.0767	-0.0032	-0.4465	1.0000	-0.3302
Gypsum (Gy)	-0.2561	0.0438	-0.1505	-0.0143	-0.4581	-0.3302	1.0000

Table C.8: Correlation matrix for the *glennmathminP2* `OptEst_ASC_ILR()` unmixing.

glennmathminP2	Ca	En	Ol	Cr	Li	Py	Gy
Calcite (Ca)	1.0000	0.2552	-0.1126	0.0618	0.0180	-0.1393	-0.2522
Enstatite (En)	0.2552	1.0000	-0.5021	0.4192	**-0.6104**	-0.3634	-0.2032
Olivine (Ol)	-0.1126	-0.5021	1.0000	**-0.6288**	-0.0226	0.4726	0.4083
Cronstedtite (Cr)	0.0618	0.4192	**-0.6288**	1.0000	-0.4686	**-0.6332**	-0.3083
Lizardite (Li)	0.0180	**-0.6104**	-0.0226	-0.4686	1.0000	0.2497	-0.1685
Pyrrhotite (Py)	-0.1393	-0.3634	0.4726	**-0.6332**	0.2497	1.0000	-0.3316
Gypsum (Gy)	-0.2522	-0.2032	0.4083	-0.3083	-0.1685	-0.3316	1.0000

Table C.9: Correlation matrix for retrieved abundances from the *glennmathminP3* `OptEst_ASC_ILR()` unmixing.

glennmathminP3	Ca	En	Ol	Cr	Li	Ma	Py	Gy
Calcite (Ca)	1.0000	0.0013	0.0074	-0.0332	-0.0003	-0.0005	-0.0005	-0.0009
Enstatite (En)	0.0013	1.0000	-0.0484	-0.2402	-0.0867	-0.0038	-0.0019	-0.0032
Olivine (Ol)	0.0074	-0.0484	1.0000	-0.2969	-0.1213	0.0038	0.0019	0.0025
Cronstedtite (Cr)	-0.0332	-0.2402	-0.2969	1.0000	**-0.8404**	-0.0593	-0.0358	-0.0535
Lizardite (Li)	-0.0003	-0.0867	-0.1213	**-0.8404**	1.0000	-0.0101	-0.0057	-0.0101
Magnetite (Ma)	-0.0005	-0.0038	0.0038	-0.0593	-0.0101	1.0000	-0.0008	-0.0011
Pyrrhotite (Py)	-0.0005	-0.0019	0.0019	-0.0358	-0.0057	-0.0008	1.0000	-0.0006
Gypsum (Gy)	-0.0009	-0.0032	0.0025	-0.0535	-0.0101	-0.0011	-0.0006	1.0000

Table C.10: Correlation matrix for the *glennmathminP4* `OptEst_ASC_ILR()` unmixing.

glennmathminP4	Ca	En	Ol	Cr	Li	Py	Gy
Calcite (Ca)	1.0000	0.2524	-0.1047	0.0542	0.0226	-0.1393	-0.2472
Enstatite (En)	0.2524	1.0000	-0.4904	0.3932	-0.5952	-0.3466	-0.1965

Table C.10 continued from previous page

glennmathminP4	Ca	En	Ol	Cr	Li	Py	Gy
Olivine (Ol)	-0.1047	-0.4904	1.0000	**-0.6132**	-0.0489	0.4608	0.3960
Cronstedtite (Cr)	0.0542	0.3932	**-0.6132**	1.0000	-0.4491	**-0.6211**	-0.2989
Lizardite (Li)	0.0226	-0.5952	-0.0489	-0.4491	1.0000	0.2243	-0.1771
Pyrrhotite (Py)	-0.1393	-0.3466	0.4608	**-0.6211**	0.2243	1.0000	-0.3470
Gypsym (Gy)	-0.2472	-0.1965	0.3960	-0.2989	-0.1771	-0.3470	1.0000

Table C.11: Correlation matrix for the *glennrealminP1* `OptEst_ASC_ILR()` unmixing.

glennrealminP1	Ca	En	Ol	Cr	Li	Ma	Py	Gy
Calcite (Ca)	1.0000	-0.1024	-0.0862	-0.0395	-0.0035	-0.1417	-0.1187	-0.2483
Enstatite (En)	-0.1024	1.0000	-0.2944	-0.0552	-0.0070	-0.2081	-0.1368	-0.2909
Olivine (Ol)	-0.0862	-0.2944	1.0000	-0.0631	-0.0078	-0.1783	-0.1248	-0.2667
Cronstedtite (Cr)	-0.0395	-0.0552	-0.0631	1.0000	-0.0016	-0.0513	-0.0346	-0.0717
Lizardite (Li)	-0.0035	-0.0070	-0.0078	-0.0016	1.0000	-0.0056	-0.0037	-0.0080
Magnetite (Ma)	-0.1417	-0.2081	-0.1783	-0.0513	-0.0056	1.0000	-0.1458	-0.2900
Pyrrhotite (Py)	-0.1187	-0.1368	-0.1248	-0.0346	-0.0037	-0.1458	1.0000	-0.1918
Gypsum (Gy)	-0.2483	-0.2909	-0.2667	-0.0717	-0.0080	-0.2900	-0.1918	1.0000

Table C.12: Correlation matrix for the *glennrealminP2* `OptEst_ASC_ILR()` unmixing.

glennrealminP2	Cr	Li	Py
Cronstedtite (Cr)	1.0000	**-0.7838**	**-0.7892**
Lizardite (Li)	**-0.7838**	1.0000	0.2376
Pyrrhotite (Py)	**-0.7892**	0.2376	1.0000

Table C.13: Correlation matrix for retrieved abundances from the *glennrealminP3* `OptEst_ASC_ILR()` unmixing.

glennrealminP3	Ca	En	Ol	Cr	Li	Ma	Py	Gy
Calcite (Ca)	1.0000	-0.0014	-0.0019	-0.0200	-0.0046	-0.0003	-0.0002	-0.0003
Enstatite (En)	-0.0014	1.0000	-0.0234	-0.2281	-0.0546	-0.0032	-0.0019	-0.0030
Olivine (Ol)	-0.0019	-0.0234	1.0000	-0.3141	-0.0751	-0.0043	-0.0026	-0.0040
Cronstedtite (Cr)	-0.0200	-0.2281	-0.3141	1.0000	**-0.7399**	-0.0445	-0.0267	-0.0411
Lizardite (Li)	-0.0046	-0.0546	-0.0751	**-0.7399**	1.0000	-0.0104	-0.0063	-0.0097
Magnetite (Ma)	-0.0003	-0.0032	-0.0043	-0.0445	-0.0104	1.0000	-0.0004	-0.0006
Pyrrhotite (Py)	-0.0002	-0.0019	-0.0026	-0.0267	-0.0063	-0.0004	1.0000	-0.0004
Gypsum (Gy)	-0.0003	-0.0030	-0.0040	-0.0411	-0.0097	-0.0006	-0.0004	1.0000

Table C.14: Correlation matrix for the *glennrealminP4* `OptEst_ASC_ILR()` unmixing.

glennrealminP4	Cr	Li	Ma	Py	Gy
Cronstedtite (Cr)	1.0000	-0.4804	-0.0176	-0.2646	-0.1364
Lizardite (Li)	-0.4804	1.0000	-0.0403	-0.0195	-0.1997
Magnetite (Ma)	-0.0176	-0.0403	1.0000	**-0.7694**	-0.2007
Pyrrhotite (Py)	-0.2646	-0.0195	**-0.7694**	1.0000	-0.2310
Gypsum (Gy)	-0.1364	-0.1997	-0.2007	-0.2310	1.0000

Table C.15: Correlation matrix for retrieved abundances from the *glennmathexpP2* `OptEst_ASC_ILR()` unmixing.

glennmathexpP2	Ca	En	Ol	Cr	Li	Gy	Sa	BB
Calcite (Ca)	1.0000	0.0035	-0.1499	0.0559	-0.1693	-0.3467	0.2639	-0.1794
Enstatite (En)	0.0035	1.0000	-0.1905	0.2329	0.1608	0.3644	**-0.6344**	0.0354
Olivine (Ol)	-0.1499	-0.1905	1.0000	**-0.6447**	0.1889	0.3788	-0.2943	0.5453
Cronstedtite (Cr)	0.0559	0.2329	**-0.6447**	1.0000	-0.4050	-0.1954	0.1546	**-0.6366**
Lizardite (Li)	-0.1693	0.1608	0.1889	-0.4050	1.0000	0.3957	**-0.7418**	0.4656
Gypsum (Gy)	-0.3467	0.3644	0.3788	-0.1954	0.3957	1.0000	**-0.6572**	-0.0377
Saponite (Sa)	0.2639	**-0.6344**	-0.2943	0.1546	**-0.7418**	**-0.6572**	1.0000	-0.4693
BB	-0.1794	0.0354	0.5453	**-0.6366**	0.4656	-0.0377	-0.4693	1.0000

Table C.16: Correlation matrix for retrieved abundances from the *glennmathexpP4* `OptEst_ASC_ILR()` unmixing.

glennmathexpP4	Ca	En	Ol	Cr	Li	Gy	Au	Sa	BB
Calcite (Ca)	1.0000	-0.0782	-0.1144	-0.0184	-0.1549	-0.2260	0.1491	0.1233	-0.0404
Enstatite (En)	-0.0782	1.0000	-0.2394	0.4047	0.1312	-0.0211	-0.5948	-0.0915	-0.3509
Olivine (Ol)	-0.1144	-0.2394	1.0000	**-0.6276**	0.1552	0.3879	0.1453	-0.3141	0.5005
Cronstedtite (Cr)	-0.0184	0.4047	**-0.6276**	1.0000	-0.3413	-0.3216	-0.3910	0.3163	**-0.6882**
Lizardite (Li)	-0.1549	0.1312	0.1552	-0.3413	1.0000	0.3180	-0.0172	-0.5949	0.3328
Gypsum (Gy)	-0.2260	-0.0211	0.3879	-0.3216	0.3180	1.0000	0.4550	**-0.7233**	0.2450
Augite (Au)	0.1491	-0.5948	0.1453	-0.3910	-0.0172	0.4550	1.0000	-0.5562	**0.6341**
Saponite (Sa)	0.1233	-0.0915	-0.3141	0.3163	-0.5949	**-0.7233**	-0.5562	1.0000	**-0.6533**
BB	-0.0404	-0.3509	0.5005	**-0.6882**	0.3328	0.2450	**0.6341**	**-0.6533**	1.0000

Table C.17: Correlation matrix for retrieved abundances from the *glennrealexpP1* `OptEst_ASC_ILR()` unmixing.

glennrealexpP1	Ca	En	Li	Ma	Py	Gy	Sp	AmFe	Sa	BB
Calcite (Ca)	1.0000	-0.0771	-0.0309	-0.0090	-0.0673	-0.1253	-0.0425	-0.0230	-0.1749	-0.0980
Enstatite (En)	-0.0771	1.0000	-0.0495	-0.0130	-0.0917	-0.1714	-0.0730	-0.0273	-0.2711	-0.1363
Lizardite (Li)	-0.0309	-0.0495	1.0000	-0.0050	-0.0350	-0.0657	-0.0282	-0.0106	-0.1032	-0.0521
Magnetite (Ma)	-0.0090	-0.0130	-0.0050	1.0000	-0.0100	-0.0184	-0.0072	-0.0032	-0.0278	-0.0147
Pyrrhotite (Py)	-0.0673	-0.0917	-0.0350	-0.0100	1.0000	-0.1295	-0.0509	-0.0227	-0.1960	-0.1040
Gypsum (Gy)	-0.1253	-0.1714	-0.0657	-0.0184	-0.1295	1.0000	-0.0959	-0.0418	-0.3663	-0.1918
Spinel (Sp)	-0.0425	-0.0730	-0.0282	-0.0072	-0.0509	-0.0959	1.0000	-0.0147	-0.1523	-0.0759
Amorphous Fe (AmFe)	-0.0230	-0.0273	-0.0106	-0.0032	-0.0227	-0.0418	-0.0147	1.0000	-0.0604	-0.0334
Saponite (Sa)	-0.1749	-0.2711	-0.1032	-0.0278	-0.1960	-0.3663	-0.1523	-0.0604	1.0000	-0.2908
BB	-0.0980	-0.1363	-0.0521	-0.0147	-0.1040	-0.1918	-0.0759	-0.0334	-0.2908	1.0000

Table C.18: Correlation matrix for retrieved abundances from the *glennrealexpP3* `OptEst_ASC_ILR()` unmixing.

glennrealexpP3	Ca	En	Ol	Cr	Li	Ma	Py	Gy	Sa	BB
Calcite (Ca)	1.0000	-0.0013	-0.0017	-0.0175	-0.0043	-0.0003	-0.0002	-0.0003	-0.0018	-0.0019
Enstatite (En)	-0.0013	1.0000	-0.0221	-0.1998	-0.0514	-0.0031	-0.0018	-0.0028	-0.0207	-0.0210
Olivine (Ol)	-0.0017	-0.0221	1.0000	-0.2752	-0.0708	-0.0041	-0.0025	-0.0038	-0.0282	-0.0282
Cronstedtite (Cr)	-0.0175	-0.1998	-0.2752	1.0000	**-0.6454**	-0.0390	-0.0234	-0.0360	-0.2598	-0.2676
Lizardite (Li)	-0.0043	-0.0514	-0.0708	**-0.6454**	1.0000	-0.0098	-0.0059	-0.0091	-0.0664	-0.0676
Magnetite (Ma)	-0.0003	-0.0031	-0.0041	-0.0390	-0.0098	1.0000	-0.0004	-0.0006	-0.0040	-0.0042
Pyrrhotite (Py)	-0.0002	-0.0018	-0.0025	-0.0234	-0.0059	-0.0004	1.0000	-0.0003	-0.0024	-0.0025
Gypsum (Gy)	-0.0003	-0.0028	-0.0038	-0.0360	-0.0091	-0.0006	-0.0003	1.0000	-0.0037	-0.0038
Saponite (Sa)	-0.0018	-0.0207	-0.0282	-0.2598	-0.0664	-0.0040	-0.0024	-0.0037	1.0000	-0.0274
BB	-0.0019	-0.0210	-0.0282	-0.2676	-0.0676	-0.0042	-0.0025	-0.0038	-0.0274	1.0000

Table C.19: Correlation matrix for the *glennrealextP3* `OptEst_ASC_ILR()` unmixing.

glennrealextP3	Ca	En	Ol	Sa	Cr	Li	Ma	Tr	Py	Gy	AmMg	IOM	FeNi	BB
Calcite (Ca)	1.000	-0.001	-0.002	-0.002	-0.014	-0.004	0.000	-0.002	0.000	0.000	-0.002	-0.002	-0.002	-0.002
Enstatite (En)	-0.001	1.000	-0.020	-0.019	-0.162	-0.046	-0.003	-0.019	-0.002	-0.003	-0.018	-0.019	-0.019	-0.019
Olivine (Ol)	-0.002	-0.020	1.000	-0.025	-0.223	-0.064	-0.004	-0.025	-0.002	-0.003	-0.025	-0.025	-0.025	-0.025
Saponite (Sa)	-0.002	-0.019	-0.025	1.000	-0.210	-0.060	-0.004	-0.024	-0.002	-0.003	-0.024	-0.024	-0.025	-0.025
Cronstedtite (Cr)	-0.014	-0.162	-0.223	-0.210	1.000	-0.519	-0.032	-0.215	-0.019	-0.029	-0.210	-0.212	-0.216	-0.216
Lizardite (Li)	-0.004	-0.046	-0.064	-0.060	-0.519	1.000	-0.009	-0.060	-0.005	-0.008	-0.059	-0.059	-0.060	-0.060
Magnetite (Ma)	0.000	-0.003	-0.004	-0.004	-0.032	-0.009	1.000	-0.004	0.000	-0.001	-0.004	-0.004	-0.004	-0.004
Troilite (Tr)	-0.002	-0.019	-0.025	-0.024	-0.215	-0.060	-0.004	1.000	-0.002	-0.003	-0.025	-0.025	-0.025	-0.025
Pyrrhotite (Py)	0.000	-0.002	-0.002	-0.002	-0.019	-0.005	0.000	-0.002	1.000	0.000	-0.002	-0.002	-0.002	-0.002
Gypsum (Gy)	0.000	-0.003	-0.003	-0.003	-0.029	-0.008	-0.001	-0.003	0.000	1.000	-0.003	-0.003	-0.003	-0.003
Amorphous Mg (AmMg)	-0.002	-0.018	-0.025	-0.024	-0.210	-0.059	-0.004	-0.025	-0.002	-0.003	1.000	-0.024	-0.025	-0.025
MurchisonIOM (IOM)	-0.002	-0.019	-0.025	-0.024	-0.212	-0.059	-0.004	-0.025	-0.002	-0.003	-0.024	1.000	-0.025	-0.025
FeNiMetalSub (FeNi)	-0.002	-0.019	-0.025	-0.025	-0.216	-0.060	-0.004	-0.025	-0.002	-0.003	-0.025	-0.025	1.000	-0.026
BB	-0.002	-0.019	-0.025	-0.025	-0.216	-0.060	-0.004	-0.025	-0.002	-0.003	-0.025	-0.025	-0.026	1.000

Table C.20: Correlation matrix for the *brucemathextU* `MCMC()` unmixing.

	Ca	Au	En	Ol	Sa	Cr	Li	Ma	Sp	Tr	Py	Al	An	Gy	AmFe	AmMg	IOM	FeNi	BB
Ca	1.00	-0.01	0.32	-0.16	0.11	-0.17	-0.11	-0.08	0.12	-0.10	-0.10	0.07	-0.12	-0.02	0.01	0.20	-0.11	-0.14	-0.33
Au	-0.01	1.00	-0.29	-0.21	-0.37	0.22	-0.06	-0.01	0.22	-0.41	0.15	-0.22	-0.05	-0.05	0.18	-0.19	0.10	-0.28	-0.01
En	0.32	-0.29	1.00	-0.11	0.30	-0.26	-0.09	-0.16	-0.22	0.08	-0.23	0.13	-0.30	-0.07	0.08	0.27	-0.19	0.04	-0.22
Ol	-0.16	-0.21	-0.11	1.00	0.08	-0.15	-0.04	-0.04	-0.38	0.16	-0.05	-0.08	0.07	-0.02	0.01	0.01	-0.01	0.30	0.08
Sa	0.11	-0.37	0.30	0.08	1.00	-0.46	-0.02	-0.11	-0.35	0.22	-0.11	0.18	-0.37	0.06	-0.26	0.14	-0.19	0.12	-0.07

Table C.20 continued from previous page

	Ca	Au	En	Ol	Sa	Cr	Li	Ma	Sp	Tr	Py	Al	An	Gy	AmFe	AmMg	IOM	FeNi	BB
Cr	-0.17	0.22	-0.26	-0.15	-0.46	1.00	-0.09	-0.12	0.31	-0.15	0.10	-0.28	0.33	-0.17	-0.02	-0.24	-0.02	-0.17	0.08
Li	-0.11	-0.06	-0.09	-0.04	-0.02	-0.09	1.00	0.02	-0.05	0.09	0.08	-0.08	-0.07	-0.16	-0.21	-0.21	0.10	0.13	0.11
Ma	-0.08	-0.01	-0.16	-0.04	-0.11	-0.12	0.02	1.00	-0.15	-0.03	0.02	0.07	0.10	0.07	-0.17	-0.23	0.08	-0.13	0.07
Sp	0.12	0.22	-0.22	-0.38	-0.35	0.31	-0.05	-0.15	1.00	-0.24	0.16	-0.27	0.31	-0.08	-0.01	-0.10	0.01	-0.31	-0.13
Tr	-0.10	-0.41	0.08	0.16	0.22	-0.15	0.09	-0.03	-0.24	1.00	-0.20	-0.03	0.04	-0.14	-0.26	0.11	-0.15	0.27	0.05
Py	-0.10	0.15	-0.23	-0.05	-0.11	0.10	0.08	0.02	0.16	-0.20	1.00	-0.25	0.21	-0.14	-0.05	-0.37	-0.04	-0.12	-0.07
Al	0.07	-0.22	0.13	-0.08	0.18	-0.28	-0.08	0.07	-0.27	-0.03	-0.25	1.00	-0.45	0.05	0.14	0.17	-0.17	0.02	-0.18
An	-0.12	-0.05	-0.30	0.07	-0.37	0.33	-0.07	0.10	0.31	0.04	0.21	-0.45	1.00	-0.15	-0.12	-0.37	0.20	-0.05	0.06
Gy	-0.02	-0.05	-0.07	-0.02	0.06	-0.17	-0.16	0.07	-0.08	-0.14	-0.14	0.05	-0.15	1.00	-0.09	0.08	0.31	-0.31	-0.19
AmFe	0.01	0.18	0.08	0.01	-0.26	-0.02	-0.21	-0.17	-0.01	-0.26	-0.05	0.14	-0.12	-0.09	1.00	0.22	-0.12	-0.22	-0.36
AmMg	0.20	-0.19	0.27	0.01	0.14	-0.24	-0.21	-0.23	-0.10	0.11	-0.37	0.17	-0.37	0.08	0.22	1.00	-0.22	-0.12	-0.26
IOM	-0.11	0.10	-0.19	-0.01	-0.19	-0.02	0.10	0.08	0.01	-0.15	-0.04	-0.17	0.20	0.31	-0.12	-0.22	1.00	-0.21	0.09
FeNi	-0.14	-0.28	0.04	0.30	0.12	-0.17	0.13	-0.13	-0.31	0.27	-0.12	0.02	-0.05	-0.31	-0.22	-0.12	-0.21	1.00	0.24
BB	-0.33	-0.01	-0.22	0.08	-0.07	0.08	0.11	0.07	-0.13	0.05	-0.07	-0.18	0.06	-0.19	-0.36	-0.26	0.09	0.24	1.00

Table C.21: Correlation matrix for the *brucemathextP1* `MCMC()` unmixing.

	Ca	Au	En	Ol	Sa	Cr	Li	Ma	Sp	Tr	Py	Al	An	Gy	AmFe	AmMg	IOM	FeNi	BB
Ca	1.00	0.00	0.18	-0.41	-0.44	0.00	0.12	0.30	-0.27	0.21	-0.35	-0.29	0.39	0.13	-0.54	0.33	-0.19	0.18	-0.18
Au	0.00	1.00	-0.18	-0.27	0.48	-0.19	0.01	0.04	-0.13	-0.39	0.13	-0.15	-0.17	-0.30	0.11	-0.02	0.10	-0.29	0.04
En	0.18	-0.18	1.00	-0.09	-0.40	-0.03	-0.10	0.12	-0.24	0.21	-0.12	0.02	0.06	0.25	-0.30	0.12	-0.04	0.23	-0.25
Ol	-0.41	-0.27	-0.09	1.00	0.05	0.13	-0.09	-0.31	0.17	0.00	0.02	0.06	-0.31	0.06	0.13	-0.19	0.25	0.01	-0.02
Sa	-0.44	0.48	-0.40	0.05	1.00	-0.07	0.07	-0.22	0.18	-0.48	0.32	0.05	-0.47	-0.58	**0.63**	-0.30	0.11	-0.59	0.26
Cr	0.00	-0.19	-0.03	0.13	-0.07	1.00	-0.25	-0.13	-0.04	0.34	-0.36	-0.22	-0.13	-0.07	-0.06	0.00	0.00	0.13	-0.08
Li	0.12	0.01	-0.10	-0.09	0.07	-0.25	1.00	-0.09	-0.17	-0.18	-0.18	-0.16	0.16	-0.15	0.06	0.03	0.11	-0.08	-0.25
Ma	0.30	0.04	0.12	-0.31	-0.22	-0.13	-0.09	1.00	-0.21	0.02	0.04	0.11	0.27	-0.01	-0.30	0.07	-0.28	0.05	-0.25

Table C.21 continued from previous page

	Ca	Au	En	Ol	Sa	Cr	Li	Ma	Sp	Tr	Py	Al	An	Gy	AmFe	AmMg	IOM	FeNi	BB
Sp	-0.27	-0.13	-0.24	0.17	0.18	-0.04	-0.17	-0.21	1.00	-0.07	0.13	0.13	-0.38	-0.02	0.43	-0.23	-0.04	-0.25	0.15
Tr	0.21	-0.39	0.21	0.00	-0.48	0.34	-0.18	0.02	-0.07	1.00	-0.33	-0.23	0.10	0.30	-0.46	0.16	-0.26	0.42	-0.24
Py	-0.35	0.13	-0.12	0.02	0.32	-0.36	-0.18	0.04	0.13	-0.33	1.00	0.31	-0.12	-0.16	0.19	-0.23	-0.01	-0.39	0.11
Al	-0.29	-0.15	0.02	0.06	0.05	-0.22	-0.16	0.11	0.13	-0.23	0.31	1.00	-0.17	-0.11	0.07	-0.19	-0.07	-0.11	-0.02
An	0.39	-0.17	0.06	-0.31	-0.47	-0.13	0.16	0.27	-0.38	0.10	-0.12	-0.17	1.00	0.17	-0.45	0.03	-0.21	0.23	-0.10
Gy	0.13	-0.30	0.25	0.06	-0.58	-0.07	-0.15	-0.01	-0.02	0.30	-0.16	-0.11	0.17	1.00	-0.40	0.19	-0.06	0.35	-0.11
AmFe	-0.54	0.11	-0.30	0.13	**0.63**	-0.06	0.06	-0.30	0.43	-0.46	0.19	0.07	-0.45	-0.40	1.00	-0.42	0.21	-0.54	0.26
AmMg	0.33	-0.02	0.12	-0.19	-0.30	0.00	0.03	0.07	-0.23	0.16	-0.23	-0.19	0.03	0.19	-0.42	1.00	-0.14	0.10	-0.05
IOM	-0.19	0.10	-0.04	0.25	0.11	0.00	0.11	-0.28	-0.04	-0.26	-0.01	-0.07	-0.21	-0.06	0.21	-0.14	1.00	-0.19	-0.10
FeNi	0.18	-0.29	0.23	0.01	-0.59	0.13	-0.08	0.05	-0.25	0.42	-0.39	-0.11	0.23	0.35	-0.54	0.10	-0.19	1.00	-0.31
BB	-0.18	0.04	-0.25	-0.02	0.26	-0.08	-0.25	-0.25	0.15	-0.24	0.11	-0.02	-0.10	-0.11	0.26	-0.05	-0.10	-0.31	1.00

Table C.22: Correlation matrix for retrieved abundances from the *glennrealminP3* `MCMC()` unmixing. Strong correlations ($> |0.6|$) are indicated in bold.

glennrealminP3	Ca	En	Ol	Cr	Li	Ma	Py	Gy
Calcite (Ca)	1.000	**-0.670**	**0.864**	**-0.874**	**0.847**	**0.617**	-0.269	0.303
Enstatite (En)	**-0.670**	1.000	**-0.702**	**0.686**	**-0.703**	-0.523	0.300	-0.161
Olivine (Ol)	**0.864**	**-0.702**	1.000	**-0.943**	**0.881**	**0.667**	-0.337	0.311
Cronstedtite (Cr)	**-0.874**	**0.686**	**-0.943**	1.000	**-0.967**	**-0.658**	0.322	-0.334
Lizardite (Li)	**0.847**	**-0.703**	**0.881**	**-0.967**	1.000	**0.632**	-0.330	0.355
Magnetite (Ma)	**0.617**	-0.523	**0.667**	**-0.658**	**0.632**	1.000	-0.154	0.253
Pyrrhotite (Py)	-0.269	0.300	-0.337	0.322	-0.330	-0.154	1.000	0.005
Gypsum (Gy)	0.303	-0.161	0.311	-0.334	0.355	0.253	0.005	1.000

Table C.23: Correlation matrix for the *glennmathexpU* `MCMC()` unmixing.

	Ca	En	Ol	Cr	Li	Ma	Py	Gy	Sp	AmFe	Au	Sa	BB
Ca	1.000	0.123	-0.028	-0.008	0.020	-0.219	-0.140	0.231	0.156	-0.107	-0.131	-0.065	-0.237
En	0.123	1.000	-0.268	0.180	-0.004	-0.265	-0.208	0.184	-0.003	0.010	-0.208	-0.058	-0.055
Ol	-0.028	-0.268	1.000	-0.321	-0.086	0.064	0.072	-0.273	-0.184	-0.082	0.012	-0.174	0.030
Cr	-0.008	0.180	-0.321	1.000	0.134	-0.323	-0.074	0.176	0.102	-0.132	-0.183	-0.012	-0.052
Li	0.020	-0.004	-0.086	0.134	1.000	-0.183	-0.080	0.088	-0.081	-0.091	-0.236	0.099	-0.220
Ma	-0.219	-0.265	0.064	-0.323	-0.183	1.000	-0.041	-0.281	-0.199	-0.073	0.052	-0.154	-0.063
Py	-0.140	-0.208	0.072	-0.074	-0.080	-0.041	1.000	-0.052	0.098	-0.060	0.002	-0.058	-0.228
Gy	0.231	0.184	-0.273	0.176	0.088	-0.281	-0.052	1.000	0.044	-0.106	-0.167	-0.116	-0.114
Sp	0.156	-0.003	-0.184	0.102	-0.081	-0.199	0.098	0.044	1.000	-0.057	-0.152	-0.083	-0.116
AmFe	-0.107	0.010	-0.082	-0.132	-0.091	-0.073	-0.060	-0.106	-0.057	1.000	-0.013	-0.045	-0.015
Au	-0.131	-0.208	0.012	-0.183	-0.236	0.052	0.002	-0.167	-0.152	-0.013	1.000	-0.265	0.005
Sa	-0.065	-0.058	-0.174	-0.012	0.099	-0.154	-0.058	-0.116	-0.083	-0.045	-0.265	1.000	-0.163
BB	-0.237	-0.055	0.030	-0.052	-0.220	-0.063	-0.228	-0.114	-0.116	-0.015	0.005	-0.163	1.000

Table C.24: Correlation matrix for the *glennmathexpP1* `MCMC()` unmixing.

	Ca	En	Ol	Cr	Li	Ma	Py	Gy	Sp	AmFe	Au	Sa	BB
Ca	1.000	-0.185	-0.326	-0.150	0.106	0.153	-0.063	0.250	-0.221	-0.044	-0.212	0.012	0.017
En	-0.185	1.000	-0.056	-0.047	0.003	0.003	-0.123	-0.299	0.052	-0.213	-0.218	-0.139	-0.024
Ol	-0.326	-0.056	1.000	0.107	-0.226	-0.299	-0.110	-0.220	0.019	0.007	0.152	-0.242	-0.045
Cr	-0.150	-0.047	0.107	1.000	-0.289	-0.149	-0.118	-0.204	-0.210	-0.163	0.156	-0.054	0.022
Li	0.106	0.003	-0.226	-0.289	1.000	0.141	-0.063	-0.048	0.039	0.001	-0.158	-0.116	-0.123
Ma	0.153	0.003	-0.299	-0.149	0.141	1.000	0.085	-0.037	0.051	-0.044	-0.175	0.037	-0.187
Py	-0.063	-0.123	-0.110	-0.118	-0.063	0.085	1.000	-0.141	0.023	-0.016	-0.050	-0.121	-0.165
Gy	0.250	-0.299	-0.220	-0.204	-0.048	-0.037	-0.141	1.000	-0.254	0.123	-0.179	0.019	-0.106
Sp	-0.221	0.052	0.019	-0.210	0.039	0.051	0.023	-0.254	1.000	-0.079	-0.163	-0.176	-0.150

Table C.24 continued from previous page

	Ca	En	Ol	Cr	Li	Ma	Py	Gy	Sp	AmFe	Au	Sa	BB
AmFe	-0.044	-0.213	0.007	-0.163	0.001	-0.044	-0.016	0.123	-0.079	1.000	-0.013	-0.018	-0.227
Au	-0.212	-0.218	0.152	0.156	-0.158	-0.175	-0.050	-0.179	-0.163	-0.013	1.000	-0.139	-0.066
Sa	0.012	-0.139	-0.242	-0.054	-0.116	0.037	-0.121	0.019	-0.176	-0.018	-0.139	1.000	-0.072
BB	0.017	-0.024	-0.045	0.022	-0.123	-0.187	-0.165	-0.106	-0.150	-0.227	-0.066	-0.072	1.000

Table C.25: Correlation matrix for the *glennmathexpP2* `MCMC()` unmixing.

	Ca	En	Ol	Cr	Li	Ma	Py	Gy	Sp	AmFe	Au	Sa	BB
Ca	1.000	-0.031	0.031	-0.023	-0.165	0.076	0.086	-0.041	0.113	-0.244	-0.142	-0.100	0.039
En	-0.031	1.000	-0.108	-0.183	-0.278	-0.272	-0.054	0.041	-0.047	0.071	-0.021	-0.089	0.079
Ol	0.031	-0.108	1.000	0.027	0.067	0.053	-0.107	-0.129	-0.088	-0.024	-0.162	-0.032	-0.141
Cr	-0.023	-0.183	0.027	1.000	0.121	0.070	-0.206	-0.191	-0.110	-0.081	0.005	0.014	-0.165
Li	-0.165	-0.278	0.067	0.121	1.000	0.158	-0.323	-0.270	-0.091	-0.021	-0.053	-0.144	-0.191
Ma	0.076	-0.272	0.053	0.070	0.158	1.000	-0.114	-0.072	0.036	-0.242	-0.274	0.068	-0.234
Py	0.086	-0.054	-0.107	-0.206	-0.323	-0.114	1.000	0.232	-0.012	-0.373	-0.263	-0.117	0.113
Gy	-0.041	0.041	-0.129	-0.191	-0.270	-0.072	0.232	1.000	0.039	-0.210	-0.240	-0.065	-0.031
Sp	0.113	-0.047	-0.088	-0.110	-0.091	0.036	-0.012	0.039	1.000	0.049	-0.250	0.039	-0.130
AmFe	-0.244	0.071	-0.024	-0.081	-0.021	-0.242	-0.373	-0.210	0.049	1.000	0.277	-0.050	-0.153
Au	-0.142	-0.021	-0.162	0.005	-0.053	-0.274	-0.263	-0.240	-0.250	0.277	1.000	-0.243	-0.211
Sa	-0.100	-0.089	-0.032	0.014	-0.144	0.068	-0.117	-0.065	0.039	-0.050	-0.243	1.000	-0.076
BB	0.039	0.079	-0.141	-0.165	-0.191	-0.234	0.113	-0.031	-0.130	-0.153	-0.211	-0.076	1.000

Table C.26: Correlation matrix for the *glennmathexpP3* `MCMC()` unmixing.

	Ca	En	Ol	Cr	Li	Ma	Py	Gy	Sp	AmFe	Au	Sa	BB
Ca	1.000	0.492	0.031	-0.361	0.153	0.287	0.549	0.541	0.377	0.212	-0.083	0.107	0.478

Table C.26 continued from previous page

	Ca	En	Ol	Cr	Li	Ma	Py	Gy	Sp	AmFe	Au	Sa	BB
En	0.492	1.000	0.009	-0.314	-0.029	0.224	0.400	0.391	0.325	0.011	-0.115	0.038	0.277
Ol	0.031	0.009	1.000	-0.310	-0.110	0.275	0.155	0.030	-0.054	-0.055	-0.284	0.146	-0.051
Cr	-0.361	-0.314	-0.310	1.000	-0.148	-0.450	-0.416	-0.333	-0.300	-0.192	-0.012	-0.358	-0.335
Li	0.153	-0.029	-0.110	-0.148	1.000	0.022	0.134	0.011	0.078	-0.023	-0.150	-0.042	-0.047
Ma	0.287	0.224	0.275	-0.450	0.022	1.000	0.425	0.310	0.264	-0.003	-0.349	0.160	0.225
Py	0.549	0.400	0.155	-0.416	0.134	0.425	1.000	0.458	0.398	0.008	-0.181	0.182	0.336
Gy	0.541	0.391	0.030	-0.333	0.011	0.310	0.458	1.000	0.519	-0.014	-0.157	0.082	0.384
Sp	0.377	0.325	-0.054	-0.300	0.078	0.264	0.398	0.519	1.000	-0.106	-0.194	-0.052	0.262
AmFe	0.212	0.011	-0.055	-0.192	-0.023	-0.003	0.008	-0.014	-0.106	1.000	0.002	-0.065	0.052
Au	-0.083	-0.115	-0.284	-0.012	-0.150	-0.349	-0.181	-0.157	-0.194	0.002	1.000	-0.263	-0.162
Sa	0.107	0.038	0.146	-0.358	-0.042	0.160	0.182	0.082	-0.052	-0.065	-0.263	1.000	0.034
BB	0.478	0.277	-0.051	-0.335	-0.047	0.225	0.336	0.384	0.262	0.052	-0.162	0.034	1.000

Table C.27: Correlation matrix for the *glennmathexpP4* `MCMC()` unmixing.

	Ca	En	Ol	Cr	Li	Ma	Py	Gy	Sp	AmFe	Au	Sa	BB
Ca	1.000	-0.189	0.277	-0.397	0.030	-0.152	-0.077	-0.171	0.204	-0.113	-0.323	-0.225	-0.090
En	-0.189	1.000	-0.063	0.121	-0.072	-0.184	-0.013	-0.019	-0.244	0.026	0.016	0.094	-0.149
Ol	0.277	-0.063	1.000	-0.107	-0.100	0.068	-0.181	-0.272	-0.091	0.044	-0.244	-0.237	0.054
Cr	-0.397	0.121	-0.107	1.000	-0.225	-0.087	0.114	0.013	-0.260	-0.037	0.270	0.155	-0.232
Li	0.030	-0.072	-0.100	-0.225	1.000	-0.156	-0.164	0.022	0.031	-0.198	-0.217	-0.039	-0.038
Ma	-0.152	-0.184	0.068	-0.087	-0.156	1.000	-0.125	-0.130	-0.263	-0.214	0.068	-0.115	0.244
Py	-0.077	-0.013	-0.181	0.114	-0.164	-0.125	1.000	-0.192	-0.108	-0.098	0.100	-0.023	0.002
Gy	-0.171	-0.019	-0.272	0.013	0.022	-0.130	-0.192	1.000	0.087	-0.060	-0.114	-0.025	-0.241
Sp	0.204	-0.244	-0.091	-0.260	0.031	-0.263	-0.108	0.087	1.000	0.018	-0.381	-0.349	-0.115
AmFe	-0.113	0.026	0.044	-0.037	-0.198	-0.214	-0.098	-0.060	0.018	1.000	-0.043	-0.054	-0.215

Table C.27 continued from previous page

	Ca	En	Ol	Cr	Li	Ma	Py	Gy	Sp	AmFe	Au	Sa	BB
Au	-0.323	0.016	-0.244	0.270	-0.217	0.068	0.100	-0.114	-0.381	-0.043	1.000	0.232	-0.091
Sa	-0.225	0.094	-0.237	0.155	-0.039	-0.115	-0.023	-0.025	-0.349	-0.054	0.232	1.000	-0.181
BB	-0.090	-0.149	0.054	-0.232	-0.038	0.244	0.002	-0.241	-0.115	-0.215	-0.091	-0.181	1.000

Table C.28: Correlation matrix for the *glennrealexpU* `MCMC()` unmixing.

	Ca	En	Ol	Cr	Li	Ma	Py	Gy	Sp	AmFe	Au	Sa	BB
Ca	1.000	-0.038	-0.301	-0.294	-0.146	0.180	-0.129	0.195	-0.044	-0.163	-0.037	-0.141	-0.090
En	-0.038	1.000	-0.077	-0.108	-0.058	-0.092	-0.147	0.160	0.043	-0.316	-0.243	-0.019	-0.008
Ol	-0.301	-0.077	1.000	0.055	0.073	-0.368	-0.138	-0.353	-0.144	0.059	-0.188	-0.027	-0.067
Cr	-0.294	-0.108	0.055	1.000	0.003	-0.208	-0.014	-0.123	-0.252	-0.060	-0.075	-0.034	-0.028
Li	-0.146	-0.058	0.073	0.003	1.000	-0.046	-0.109	-0.032	-0.021	-0.191	-0.007	-0.054	0.098
Ma	0.180	-0.092	-0.368	-0.208	-0.046	1.000	-0.059	0.215	0.139	-0.166	0.022	-0.237	0.214
Py	-0.129	-0.147	-0.138	-0.014	-0.109	-0.059	1.000	-0.222	-0.013	0.092	0.011	-0.032	-0.200
Gy	0.195	0.160	-0.353	-0.123	-0.032	0.215	-0.222	1.000	0.062	-0.385	-0.105	-0.288	0.039
Sp	-0.044	0.043	-0.144	-0.252	-0.021	0.139	-0.013	0.062	1.000	-0.108	-0.133	-0.130	0.190
AmFe	-0.163	-0.316	0.059	-0.060	-0.191	-0.166	0.092	-0.385	-0.108	1.000	0.013	0.123	-0.164
Au	-0.037	-0.243	-0.188	-0.075	-0.007	0.022	0.011	-0.105	-0.133	0.013	1.000	0.048	-0.104
Sa	-0.141	-0.019	-0.027	-0.034	-0.054	-0.237	-0.032	-0.288	-0.130	0.123	0.048	1.000	-0.133
BB	-0.090	-0.008	-0.067	-0.028	0.098	0.214	-0.200	0.039	0.190	-0.164	-0.104	-0.133	1.000

Table C.29: Correlation matrix for the *glennrealexpP1* `MCMC()` unmixing.

	Ca	En	Ol	Cr	Li	Ma	Py	Gy	Sp	AmFe	Au	Sa	BB
Ca	1.000	0.126	0.263	-0.084	0.258	0.249	0.052	0.162	0.373	0.435	-0.093	-0.017	0.020
En	0.126	1.000	0.270	-0.067	0.361	0.493	0.243	0.183	0.288	0.319	-0.046	-0.146	0.048

Table C.29 continued from previous page

	Ca	En	Ol	Cr	Li	Ma	Py	Gy	Sp	AmFe	Au	Sa	BB
Ol	0.263	0.270	1.000	-0.095	0.206	0.384	0.331	0.111	0.335	0.314	0.041	-0.149	0.126
Cr	-0.084	-0.067	-0.095	1.000	-0.093	-0.221	0.148	-0.199	0.046	-0.044	0.187	0.078	0.055
Li	0.258	0.361	0.206	-0.093	1.000	0.358	0.210	0.177	0.312	0.386	-0.056	-0.193	0.041
Ma	0.249	0.493	0.384	-0.221	0.358	1.000	0.429	0.177	0.544	0.429	0.189	-0.296	0.117
Py	0.052	0.243	0.331	0.148	0.210	0.429	1.000	0.038	0.432	0.313	0.305	-0.134	0.272
Gy	0.162	0.183	0.111	-0.199	0.177	0.177	0.038	1.000	0.002	0.093	-0.205	-0.072	-0.204
Sp	0.373	0.288	0.335	0.046	0.312	0.544	0.432	0.002	1.000	0.562	0.299	-0.205	0.254
AmFe	0.435	0.319	0.314	-0.044	0.386	0.429	0.313	0.093	0.562	1.000	0.160	-0.142	0.205
Au	-0.093	-0.046	0.041	0.187	-0.056	0.189	0.305	-0.205	0.299	0.160	1.000	-0.168	0.154
Sa	-0.017	-0.146	-0.149	0.078	-0.193	-0.296	-0.134	-0.072	-0.205	-0.142	-0.168	1.000	-0.095
BB	0.020	0.048	0.126	0.055	0.041	0.117	0.272	-0.204	0.254	0.205	0.154	-0.095	1.000

Table C.30: Correlation matrix for the *glennrealexpP2* `MCMC()` unmixing.

	Ca	En	Ol	Cr	Li	Ma	Py	Gy	Sp	AmFe	Au	Sa	BB
Ca	1.000	-0.168	0.053	-0.002	0.005	0.019	0.132	0.110	-0.057	-0.177	-0.038	-0.074	-0.210
En	-0.168	1.000	-0.141	0.121	-0.335	-0.052	-0.154	-0.044	-0.021	-0.091	-0.314	-0.144	0.112
Ol	0.053	-0.141	1.000	-0.193	-0.091	0.198	0.085	0.208	-0.229	-0.205	-0.088	-0.011	-0.244
Cr	-0.002	0.121	-0.193	1.000	-0.264	-0.180	-0.142	-0.004	-0.160	0.081	-0.231	-0.288	0.023
Li	0.005	-0.335	-0.091	-0.264	1.000	-0.165	0.064	-0.061	-0.148	0.082	0.040	-0.083	-0.075
Ma	0.019	-0.052	0.198	-0.180	-0.165	1.000	-0.019	0.209	-0.245	-0.120	0.118	0.004	-0.151
Py	0.132	-0.154	0.085	-0.142	0.064	-0.019	1.000	-0.073	-0.066	-0.253	0.039	0.041	-0.314
Gy	0.110	-0.044	0.208	-0.004	-0.061	0.209	-0.073	1.000	-0.373	-0.169	-0.069	-0.136	-0.275
Sp	-0.057	-0.021	-0.229	-0.160	-0.148	-0.245	-0.066	-0.373	1.000	-0.032	-0.065	-0.021	0.062
AmFe	-0.177	-0.091	-0.205	0.081	0.082	-0.120	-0.253	-0.169	-0.032	1.000	-0.072	-0.129	-0.107
Au	-0.038	-0.314	-0.088	-0.231	0.040	0.118	0.039	-0.069	-0.065	-0.072	1.000	0.099	-0.115

Table C.30 continued from previous page

	Ca	En	Ol	Cr	Li	Ma	Py	Gy	Sp	AmFe	Au	Sa	BB
Sa	-0.074	-0.144	-0.011	-0.288	-0.083	0.004	0.041	-0.136	-0.021	-0.129	0.099	1.000	-0.151
BB	-0.210	0.112	-0.244	0.023	-0.075	-0.151	-0.314	-0.275	0.062	-0.107	-0.115	-0.151	1.000

Table C.31: Correlation matrix for the *glennrealexpP3* `MCMC()` unmixing.

	Ca	En	Ol	Cr	Li	Ma	Py	Gy	Sp	AmFe	Au	Sa	BB
Ca	1.000	**0.619**	0.541	**-0.735**	-0.569	**0.640**	**0.778**	**0.709**	**0.807**	**0.785**	**0.804**	**0.762**	**0.779**
En	**0.619**	1.000	0.407	**-0.612**	-0.382	0.461	**0.645**	0.579	0.595	**0.613**	**0.665**	**0.611**	0.574
Ol	0.541	0.407	1.000	**-0.789**	**-0.781**	**0.633**	0.591	0.559	**0.770**	**0.724**	**0.675**	**0.759**	**0.770**
Cr	**-0.735**	**-0.612**	**-0.789**	1.000	**0.760**	**-0.730**	**-0.756**	**-0.738**	**-0.933**	**-0.902**	**-0.874**	**-0.918**	**-0.909**
Li	-0.569	-0.382	**-0.781**	**0.760**	1.000	**-0.669**	**-0.692**	-0.581	**-0.826**	**-0.773**	**-0.756**	**-0.839**	**-0.864**
Ma	**0.640**	0.461	**0.633**	**-0.730**	**-0.669**	1.000	**0.675**	**0.651**	**0.767**	**0.735**	**0.753**	**0.739**	**0.747**
Py	**0.778**	**0.645**	0.591	**-0.756**	**-0.692**	**0.675**	1.000	**0.692**	**0.829**	**0.787**	**0.827**	**0.810**	**0.811**
Gy	**0.709**	0.579	0.559	**-0.738**	-0.581	**0.651**	**0.692**	1.000	**0.753**	**0.805**	**0.791**	**0.733**	**0.760**
Sp	**0.807**	0.595	**0.770**	**-0.933**	**-0.826**	**0.767**	**0.829**	**0.753**	1.000	**0.920**	**0.902**	**0.924**	**0.930**
AmFe	**0.785**	**0.613**	**0.724**	**-0.902**	**-0.773**	**0.735**	**0.787**	**0.805**	**0.920**	1.000	**0.877**	**0.879**	**0.878**
Au	**0.804**	**0.665**	**0.675**	**-0.874**	**-0.756**	**0.753**	**0.827**	**0.791**	**0.902**	**0.877**	1.000	**0.875**	**0.871**
Sa	**0.762**	**0.611**	**0.759**	**-0.918**	**-0.839**	**0.739**	**0.810**	**0.733**	**0.924**	**0.879**	**0.875**	1.000	**0.909**
BB	**0.779**	0.574	**0.770**	**-0.909**	**-0.864**	**0.747**	**0.811**	**0.760**	**0.930**	**0.878**	**0.871**	**0.909**	1.000

Table C.32: Correlation matrix for the *glennrealexpP4* `MCMC()` unmixing.

	Ca	En	Ol	Cr	Li	Ma	Py	Gy	Sp	AmFe	Au	Sa	BB
Ca	1.000	0.220	0.073	-0.225	0.259	0.223	-0.219	-0.397	-0.011	0.106	-0.149	0.024	-0.256
En	0.220	1.000	-0.110	-0.143	0.092	-0.031	0.091	-0.382	0.058	-0.166	-0.022	0.218	-0.345
Ol	0.073	-0.110	1.000	-0.029	-0.157	0.136	-0.025	-0.068	-0.176	0.091	-0.250	-0.120	-0.063

Table C.32 continued from previous page

	Ca	En	Ol	Cr	Li	Ma	Py	Gy	Sp	AmFe	Au	Sa	BB
Cr	-0.225	-0.143	-0.029	1.000	-0.042	0.007	-0.141	0.014	0.014	-0.259	-0.018	-0.227	-0.062
Li	0.259	0.092	-0.157	-0.042	1.000	0.042	-0.042	-0.255	0.093	-0.199	-0.161	-0.085	-0.239
Ma	0.223	-0.031	0.136	0.007	0.042	1.000	-0.173	-0.245	0.004	-0.231	-0.196	-0.134	-0.180
Py	-0.219	0.091	-0.025	-0.141	-0.042	-0.173	1.000	-0.350	-0.088	-0.051	-0.098	0.154	-0.216
Gy	-0.397	-0.382	-0.068	0.014	-0.255	-0.245	-0.350	1.000	-0.066	-0.029	0.136	-0.213	0.389
Sp	-0.011	0.058	-0.176	0.014	0.093	0.004	-0.088	-0.066	1.000	-0.261	-0.068	-0.276	-0.021
AmFe	0.106	-0.166	0.091	-0.259	-0.199	-0.231	-0.051	-0.029	-0.261	1.000	-0.134	0.010	-0.106
Au	-0.149	-0.022	-0.250	-0.018	-0.161	-0.196	-0.098	0.136	-0.068	-0.134	1.000	0.047	0.067
Sa	0.024	0.218	-0.120	-0.227	-0.085	-0.134	0.154	-0.213	-0.276	0.010	0.047	1.000	-0.341
BB	-0.256	-0.345	-0.063	-0.062	-0.239	-0.180	-0.216	0.389	-0.021	-0.106	0.067	-0.341	1.000

Table C.33: Correlation matrix for the *glennmathextU* `MCMC()` unmixing.

	Ca	Au	En	Ol	Sa	Cr	Li	Ma	Sp	Tr	Py	Al	An	Gy	AmFe	AmMg	IOM	FeNi	BB
Ca	1.00	0.10	0.26	0.23	0.14	0.39	-0.31	-0.03	-0.23	-0.14	-0.46	-0.34	-0.25	0.25	0.24	-0.13	-0.18	-0.22	-0.10
Au	0.10	1.00	-0.19	0.04	-0.16	0.00	-0.08	0.11	-0.19	-0.18	-0.11	-0.25	-0.14	-0.02	0.14	0.07	-0.20	-0.05	0.21
En	0.26	-0.19	1.00	0.11	0.19	0.17	-0.07	0.03	-0.03	-0.22	-0.13	-0.08	-0.24	-0.04	-0.01	-0.02	0.03	-0.25	-0.19
Ol	0.23	0.04	0.11	1.00	0.16	0.16	0.05	-0.04	-0.19	0.27	-0.16	-0.10	-0.18	-0.15	0.07	-0.20	-0.07	-0.09	-0.36
Sa	0.14	-0.16	0.19	0.16	1.00	0.12	-0.23	0.11	-0.17	-0.15	-0.34	-0.25	-0.39	0.24	0.05	-0.05	0.04	-0.39	-0.20
Cr	0.39	0.00	0.17	0.16	0.12	1.00	-0.27	-0.17	-0.27	-0.09	-0.47	-0.07	-0.30	0.21	0.28	-0.23	-0.17	-0.18	-0.29
Li	-0.31	-0.08	-0.07	0.05	-0.23	-0.27	1.00	-0.28	0.18	0.24	0.40	0.11	0.06	-0.58	-0.22	-0.17	0.19	0.34	0.03
Ma	-0.03	0.11	0.03	-0.04	0.11	-0.17	-0.28	1.00	-0.16	-0.20	-0.11	-0.05	-0.03	0.10	-0.15	-0.02	-0.15	-0.28	0.08
Sp	-0.23	-0.19	-0.03	-0.19	-0.17	-0.27	0.18	-0.16	1.00	0.03	0.25	-0.01	0.14	-0.26	0.04	-0.06	-0.07	0.07	0.36
Tr	-0.14	-0.18	-0.22	0.27	-0.15	-0.09	0.24	-0.20	0.03	1.00	0.02	0.24	0.15	-0.35	-0.12	-0.14	-0.01	0.20	-0.12
Py	-0.46	-0.11	-0.13	-0.16	-0.34	-0.47	0.40	-0.11	0.25	0.02	1.00	0.13	0.40	-0.48	-0.34	0.07	0.08	0.24	0.19
Al	-0.34	-0.25	-0.08	-0.10	-0.25	-0.07	0.11	-0.05	-0.01	0.24	0.13	1.00	0.11	-0.20	-0.23	-0.22	0.13	0.24	-0.28

Table C.33 continued from previous page

	Ca	Au	En	Ol	Sa	Cr	Li	Ma	Sp	Tr	Py	Al	An	Gy	AmFe	AmMg	IOM	FeNi	BB
An	-0.25	-0.14	-0.24	-0.18	-0.39	-0.30	0.06	-0.03	0.14	0.15	0.40	0.11	1.00	-0.21	-0.07	0.09	0.02	0.13	0.03
Gy	0.25	-0.02	-0.04	-0.15	0.24	0.21	-0.58	0.10	-0.26	-0.35	-0.48	-0.20	-0.21	1.00	0.18	0.04	-0.02	-0.41	0.02
AmFe	0.24	0.14	-0.01	0.07	0.05	0.28	-0.22	-0.15	0.04	-0.12	-0.34	-0.23	-0.07	0.18	1.00	-0.13	-0.27	-0.27	-0.01
AmMg	-0.13	0.07	-0.02	-0.20	-0.05	-0.23	-0.17	-0.02	-0.06	-0.14	0.07	-0.22	0.09	0.04	-0.13	1.00	-0.02	-0.11	-0.01
IOM	-0.18	-0.20	0.03	-0.07	0.04	-0.17	0.19	-0.15	-0.07	-0.01	0.08	0.13	0.02	-0.02	-0.27	-0.02	1.00	0.06	-0.17
FeNi	-0.22	-0.05	-0.25	-0.09	-0.39	-0.18	0.34	-0.28	0.07	0.20	0.24	0.24	0.13	-0.41	-0.27	-0.11	0.06	1.00	-0.09
BB	-0.10	0.21	-0.19	-0.36	-0.20	-0.29	0.03	0.08	0.36	-0.12	0.19	-0.28	0.03	0.02	-0.01	-0.01	-0.17	-0.09	1.00

Table C.34: Correlation matrix for the *glennmathextP1* `MCMC()` unmixing.

	Ca	Au	En	Ol	Sa	Cr	Li	Ma	Sp	Tr	Py	Al	An	Gy	AmFe	AmMg	IOM	FeNi	BB
Ca	1.00	-0.11	-0.03	0.13	-0.34	-0.33	-0.04	0.24	0.08	0.21	-0.20	-0.16	-0.04	-0.26	-0.07	0.01	-0.08	0.04	-0.22
Au	-0.11	1.00	-0.03	0.13	-0.23	0.24	-0.14	-0.28	0.19	0.08	-0.38	0.26	-0.15	-0.13	0.17	-0.06	0.04	-0.15	-0.22
En	-0.03	-0.03	1.00	-0.16	-0.22	0.21	-0.09	-0.22	-0.28	-0.22	0.09	-0.05	0.01	0.11	0.21	-0.25	0.01	0.09	-0.17
Ol	0.13	0.13	-0.16	1.00	-0.27	-0.23	0.15	0.27	0.17	0.08	-0.36	0.12	-0.48	-0.20	-0.30	-0.01	-0.40	-0.07	-0.16
Sa	-0.34	-0.23	-0.22	-0.27	1.00	0.08	-0.01	-0.07	-0.02	-0.13	0.21	-0.11	0.15	0.25	0.02	-0.03	0.17	-0.12	0.21
Cr	-0.33	0.24	0.21	-0.23	0.08	1.00	-0.12	-0.46	0.04	0.08	0.01	0.19	-0.04	0.19	0.28	-0.08	-0.15	-0.20	-0.11
Li	-0.04	-0.14	-0.09	0.15	-0.01	-0.12	1.00	0.20	-0.16	-0.26	0.03	-0.12	-0.16	-0.12	-0.20	-0.03	-0.09	-0.04	-0.11
Ma	0.24	-0.28	-0.22	0.27	-0.07	-0.46	0.20	1.00	0.09	-0.06	-0.11	-0.22	-0.14	-0.23	-0.42	-0.11	-0.03	0.05	-0.27
Sp	0.08	0.19	-0.28	0.17	-0.02	0.04	-0.16	0.09	1.00	0.14	-0.19	0.06	-0.04	-0.08	-0.02	-0.25	-0.15	-0.12	-0.14
Tr	0.21	0.08	-0.22	0.08	-0.13	0.08	-0.26	-0.06	0.14	1.00	-0.13	-0.01	-0.10	-0.21	-0.06	0.09	-0.26	-0.08	-0.11
Py	-0.20	-0.38	0.09	-0.36	0.21	0.01	0.03	-0.11	-0.19	-0.13	1.00	-0.15	0.24	0.06	0.04	0.08	0.07	-0.04	0.17
Al	-0.16	0.26	-0.05	0.12	-0.11	0.19	-0.12	-0.22	0.06	-0.01	-0.15	1.00	-0.22	0.08	0.13	-0.05	-0.13	-0.21	0.03
An	-0.04	-0.15	0.01	-0.48	0.15	-0.04	-0.16	-0.14	-0.04	-0.10	0.24	-0.22	1.00	-0.04	0.10	-0.04	0.32	-0.16	0.22
Gy	-0.26	-0.13	0.11	-0.20	0.25	0.19	-0.12	-0.23	-0.08	-0.21	0.06	0.08	-0.04	1.00	0.16	-0.22	-0.18	0.02	-0.02
AmFe	-0.07	0.17	0.21	-0.30	0.02	0.28	-0.20	-0.42	-0.02	-0.06	0.04	0.13	0.10	0.16	1.00	-0.24	0.02	-0.13	0.05

Table C.34 continued from previous page

	Ca	Au	En	Ol	Sa	Cr	Li	Ma	Sp	Tr	Py	Al	An	Gy	AmFe	AmMg	IOM	FeNi	BB
AmMg	0.01	-0.06	-0.25	-0.01	-0.03	-0.08	-0.03	-0.11	-0.25	0.09	0.08	-0.05	-0.04	-0.22	-0.24	1.00	0.14	-0.23	0.17
IOM	-0.08	0.04	0.01	-0.40	0.17	-0.15	-0.09	-0.03	-0.15	-0.26	0.07	-0.13	0.32	-0.18	0.02	0.14	1.00	-0.02	-0.10
FeNi	0.04	-0.15	0.09	-0.07	-0.12	-0.20	-0.04	0.05	-0.12	-0.08	-0.04	-0.21	-0.16	0.02	-0.13	-0.23	-0.02	1.00	-0.10
BB	-0.22	-0.22	-0.17	-0.16	0.21	-0.11	-0.11	-0.27	-0.14	-0.11	0.17	0.03	0.22	-0.02	0.05	0.17	-0.10	-0.10	1.00

Table C.35: Correlation matrix for the *glennmathextP2* `MCMC()` unmixing.

	Ca	Au	En	Ol	Sa	Cr	Li	Ma	Sp	Tr	Py	Al	An	Gy	AmFe	AmMg	IOM	FeNi	BB
Ca	1.00	-0.26	0.35	0.22	0.06	-0.03	0.18	-0.25	-0.45	-0.17	0.04	0.36	-0.19	0.14	0.30	-0.06	-0.52	-0.21	-0.39
Au	-0.26	1.00	-0.22	-0.11	0.07	-0.07	-0.35	-0.12	0.22	0.08	-0.11	-0.16	-0.18	0.05	-0.11	-0.25	0.23	-0.12	0.13
En	0.35	-0.22	1.00	0.17	0.07	0.15	0.18	-0.28	-0.36	-0.18	-0.07	0.26	-0.16	0.18	0.22	-0.08	-0.44	-0.21	-0.15
Ol	0.22	-0.11	0.17	1.00	0.00	-0.18	0.08	-0.12	-0.16	-0.40	0.22	0.51	-0.16	0.16	-0.05	-0.08	-0.22	-0.14	-0.24
Sa	0.06	0.07	0.07	0.00	1.00	-0.23	-0.04	0.03	-0.17	-0.02	-0.05	0.13	-0.23	-0.06	0.04	0.04	-0.19	0.03	0.01
Cr	-0.03	-0.07	0.15	-0.18	-0.23	1.00	-0.07	-0.01	-0.05	-0.01	-0.18	-0.18	0.16	-0.08	-0.05	0.09	-0.04	-0.02	0.06
Li	0.18	-0.35	0.18	0.08	-0.04	-0.07	1.00	0.12	-0.36	-0.05	0.08	0.09	-0.18	0.16	0.14	-0.17	-0.26	-0.14	-0.34
Ma	-0.25	-0.12	-0.28	-0.12	0.03	-0.01	0.12	1.00	0.05	0.23	-0.15	-0.16	0.03	-0.13	-0.25	0.14	0.10	0.00	-0.27
Sp	-0.45	0.22	-0.36	-0.16	-0.17	-0.05	-0.36	0.05	1.00	-0.03	0.17	-0.23	0.06	-0.24	-0.43	0.06	0.54	0.03	0.29
Tr	-0.17	0.08	-0.18	-0.40	-0.02	-0.01	-0.05	0.23	-0.03	1.00	-0.40	-0.44	0.05	-0.35	0.01	-0.03	0.04	0.04	0.15
Py	0.04	-0.11	-0.07	0.22	-0.05	-0.18	0.08	-0.15	0.17	-0.40	1.00	0.17	-0.12	0.15	-0.28	-0.20	0.06	-0.08	-0.14
Al	0.36	-0.16	0.26	0.51	0.13	-0.18	0.09	-0.16	-0.23	-0.44	0.17	1.00	-0.22	0.37	-0.07	-0.02	-0.35	-0.25	-0.34
An	-0.19	-0.18	-0.16	-0.16	-0.23	0.16	-0.18	0.03	0.06	0.05	-0.12	-0.22	1.00	-0.20	-0.10	0.26	0.00	0.23	0.21
Gy	0.14	0.05	0.18	0.16	-0.06	-0.08	0.16	-0.13	-0.24	-0.35	0.15	0.37	-0.20	1.00	0.12	-0.24	-0.35	-0.27	-0.33
AmFe	0.30	-0.11	0.22	-0.05	0.04	-0.05	0.14	-0.25	-0.43	0.01	-0.28	-0.07	-0.10	0.12	1.00	-0.19	-0.50	-0.05	-0.14
AmMg	-0.06	-0.25	-0.08	-0.08	0.04	0.09	-0.17	0.14	0.06	-0.03	-0.20	-0.02	0.26	-0.24	-0.19	1.00	0.09	-0.04	0.08
IOM	-0.52	0.23	-0.44	-0.22	-0.19	-0.04	-0.26	0.10	0.54	0.04	0.06	-0.35	0.00	-0.35	-0.50	0.09	1.00	0.16	0.33
FeNi	-0.21	-0.12	-0.21	-0.14	0.03	-0.02	-0.14	0.00	0.03	0.04	-0.08	-0.25	0.23	-0.27	-0.05	-0.04	0.16	1.00	0.02

Table C.35 continued from previous page

	Ca	Au	En	Ol	Sa	Cr	Li	Ma	Sp	Tr	Py	Al	An	Gy	AmFe	AmMg	IOM	FeNi	BB
BB	-0.39	0.13	-0.15	-0.24	0.01	0.06	-0.34	-0.27	0.29	0.15	-0.14	-0.34	0.21	-0.33	-0.14	0.08	0.33	0.02	1.00

Table C.36: Correlation matrix for the *glennmathextP3* `MCMC()` unmixing.

	Ca	Au	En	Ol	Sa	Cr	Li	Ma	Sp	Tr	Py	Al	An	Gy	AmFe	AmMg	IOM	FeNi	BB
Ca	1.00	-0.09	-0.01	0.10	0.16	0.00	-0.20	0.14	0.22	-0.19	0.11	0.21	-0.03	0.13	0.07	0.00	-0.10	-0.19	-0.14
Au	-0.09	1.00	-0.16	-0.40	-0.37	-0.09	0.17	-0.36	0.10	-0.28	-0.18	-0.18	-0.09	-0.31	-0.05	0.12	-0.24	**0.62**	-0.10
En	-0.01	-0.16	1.00	-0.24	-0.14	0.17	0.05	-0.16	-0.09	-0.08	-0.20	-0.33	-0.18	-0.40	0.27	0.12	-0.03	-0.13	0.35
Ol	0.10	-0.40	-0.24	1.00	0.43	-0.24	-0.17	0.38	0.05	0.01	0.28	0.39	0.10	0.32	-0.37	-0.21	0.12	-0.33	-0.30
Sa	0.16	-0.37	-0.14	0.43	1.00	-0.12	-0.25	0.47	-0.10	0.13	0.24	0.15	0.13	0.35	-0.22	-0.22	-0.10	-0.43	-0.15
Cr	0.00	-0.09	0.17	-0.24	-0.12	1.00	0.00	-0.20	-0.35	0.22	-0.42	-0.41	-0.29	-0.33	0.06	0.09	-0.03	-0.18	0.18
Li	-0.20	0.17	0.05	-0.17	-0.25	0.00	1.00	-0.27	0.00	0.22	-0.25	-0.24	-0.30	-0.38	0.01	0.22	-0.33	0.16	0.00
Ma	0.14	-0.36	-0.16	0.38	0.47	-0.20	-0.27	1.00	0.26	0.05	0.55	0.43	0.39	0.48	-0.28	-0.27	-0.05	-0.54	-0.22
Sp	0.22	0.10	-0.09	0.05	-0.10	-0.35	0.00	0.26	1.00	-0.39	0.44	0.30	0.16	0.17	-0.10	0.06	-0.24	0.00	-0.28
Tr	-0.19	-0.28	-0.08	0.01	0.13	0.22	0.22	0.05	-0.39	1.00	-0.28	-0.28	-0.18	0.00	-0.16	-0.19	0.10	-0.35	0.09
Py	0.11	-0.18	-0.20	0.28	0.24	-0.42	-0.25	0.55	0.44	-0.28	1.00	**0.63**	0.45	0.57	-0.24	-0.19	-0.07	-0.25	-0.31
Al	0.21	-0.18	-0.33	0.39	0.15	-0.41	-0.24	0.43	0.30	-0.28	**0.63**	1.00	0.34	0.59	-0.33	-0.27	-0.01	-0.24	-0.35
An	-0.03	-0.09	-0.18	0.10	0.13	-0.29	-0.30	0.39	0.16	-0.18	0.45	0.34	1.00	0.38	-0.05	-0.13	-0.06	-0.20	-0.35
Gy	0.13	-0.31	-0.40	0.32	0.35	-0.33	-0.38	0.48	0.17	0.00	0.57	0.59	0.38	1.00	-0.40	-0.29	0.16	-0.32	-0.38
AmFe	0.07	-0.05	0.27	-0.37	-0.22	0.06	0.01	-0.28	-0.10	-0.16	-0.24	-0.33	-0.05	-0.40	1.00	0.26	-0.09	0.15	0.27
AmMg	0.00	0.12	0.12	-0.21	-0.22	0.09	0.22	-0.27	0.06	-0.19	-0.19	-0.27	-0.13	-0.29	0.26	1.00	-0.29	0.12	0.10
IOM	-0.10	-0.24	-0.03	0.12	-0.10	-0.03	-0.33	-0.05	-0.24	0.10	-0.07	-0.01	-0.06	0.16	-0.09	-0.29	1.00	-0.11	-0.04
FeNi	-0.19	**0.62**	-0.13	-0.33	-0.43	-0.18	0.16	-0.54	0.00	-0.35	-0.25	-0.24	-0.20	-0.32	0.15	0.12	-0.11	1.00	-0.08
BB	-0.14	-0.10	0.35	-0.30	-0.15	0.18	0.00	-0.22	-0.28	0.09	-0.31	-0.35	-0.35	-0.38	0.27	0.10	-0.04	-0.08	1.00

Table C.37: Correlation matrix for the *glennmathextP4* `MCMC()` unmixing.

	Ca	Au	En	Ol	Sa	Cr	Li	Ma	Sp	Tr	Py	Al	An	Gy	AmFe	AmMg	IOM	FeNi	BB
Ca	1.00	-0.24	0.22	-0.12	0.06	-0.11	0.18	-0.23	-0.07	0.26	-0.28	-0.20	0.34	0.01	0.00	0.16	-0.35	-0.14	0.02
Au	-0.24	1.00	-0.38	0.11	-0.25	0.12	-0.35	0.05	-0.16	-0.15	0.18	0.31	-0.38	-0.17	0.09	-0.45	0.20	0.02	0.01
En	0.22	-0.38	1.00	-0.22	0.09	-0.12	0.15	0.25	-0.10	0.03	-0.32	-0.30	0.30	-0.14	-0.25	0.28	0.04	-0.28	0.07
Ol	-0.12	0.11	-0.22	1.00	-0.07	0.00	-0.09	-0.17	-0.19	-0.17	0.29	0.22	-0.32	-0.20	0.20	-0.10	0.02	0.06	-0.08
Sa	0.06	-0.25	0.09	-0.07	1.00	-0.23	0.15	-0.25	0.26	-0.18	0.07	0.04	0.00	-0.09	0.10	0.05	-0.22	-0.07	-0.05
Cr	-0.11	0.12	-0.12	0.00	-0.23	1.00	-0.14	0.18	-0.19	0.05	-0.10	-0.11	-0.07	0.15	-0.13	-0.08	0.13	-0.20	-0.22
Li	0.18	-0.35	0.15	-0.09	0.15	-0.14	1.00	0.02	0.05	0.22	-0.18	-0.17	0.12	-0.04	-0.05	0.14	-0.09	-0.24	-0.08
Ma	-0.23	0.05	0.25	-0.17	-0.25	0.18	0.02	1.00	-0.24	-0.10	-0.27	-0.15	-0.04	-0.07	-0.45	0.17	0.43	-0.21	-0.17
Sp	-0.07	-0.16	-0.10	-0.19	0.26	-0.19	0.05	-0.24	1.00	-0.08	-0.01	-0.01	-0.06	-0.01	0.03	-0.01	-0.06	0.00	-0.02
Tr	0.26	-0.15	0.03	-0.17	-0.18	0.05	0.22	-0.10	-0.08	1.00	-0.40	-0.29	0.18	0.11	0.00	0.11	-0.39	-0.21	0.15
Py	-0.28	0.18	-0.32	0.29	0.07	-0.10	-0.18	-0.27	-0.01	-0.40	1.00	0.58	-0.30	-0.28	0.26	-0.25	0.03	0.28	-0.21
Al	-0.20	0.31	-0.30	0.22	0.04	-0.11	-0.17	-0.15	-0.01	-0.29	0.58	1.00	-0.38	-0.42	0.33	-0.26	0.12	0.24	-0.24
An	0.34	-0.38	0.30	-0.32	0.00	-0.07	0.12	-0.04	-0.06	0.18	-0.30	-0.38	1.00	0.10	0.02	0.21	-0.19	-0.29	0.11
Gy	0.01	-0.17	-0.14	-0.20	-0.09	0.15	-0.04	-0.07	-0.01	0.11	-0.28	-0.42	0.10	1.00	-0.24	-0.01	-0.21	0.00	-0.15
AmFe	0.00	0.09	-0.25	0.20	0.10	-0.13	-0.05	-0.45	0.03	0.00	0.26	0.33	0.02	-0.24	1.00	-0.27	-0.26	-0.08	-0.09
AmMg	0.16	-0.45	0.28	-0.10	0.05	-0.08	0.14	0.17	-0.01	0.11	-0.25	-0.26	0.21	-0.01	-0.27	1.00	-0.07	-0.23	-0.07
IOM	-0.35	0.20	0.04	0.02	-0.22	0.13	-0.09	0.43	-0.06	-0.39	0.03	0.12	-0.19	-0.21	-0.26	-0.07	1.00	-0.09	-0.10
FeNi	-0.14	0.02	-0.28	0.06	-0.07	-0.20	-0.24	-0.21	0.00	-0.21	0.28	0.24	-0.29	0.00	-0.08	-0.23	-0.09	1.00	0.11
BB	0.02	0.01	0.07	-0.08	-0.05	-0.22	-0.08	-0.17	-0.02	0.15	-0.21	-0.24	0.11	-0.15	-0.09	-0.07	-0.10	0.11	1.00

Table C.38: Correlation matrix for the *glennrealextU* `MCMC()` unmixing.

	Ca	Au	En	Ol	Sa	Cr	Li	Ma	Sp	Tr	Py	Al	An	Gy	AmFe	AmMg	IOM	FeNi	BB
Ca	1.00	0.07	0.01	0.02	-0.21	0.11	-0.23	0.10	0.01	-0.12	-0.17	-0.29	0.11	-0.02	-0.30	-0.06	-0.08	0.13	-0.06
Au	0.07	1.00	-0.33	-0.09	0.10	0.20	-0.10	-0.31	-0.11	-0.22	-0.14	-0.11	-0.31	-0.11	0.42	-0.03	-0.15	0.03	-0.36
En	0.01	-0.33	1.00	0.03	-0.05	-0.10	0.00	0.15	0.03	0.03	0.13	0.19	0.02	-0.04	-0.17	-0.17	0.04	-0.12	0.07

Table C.38 continued from previous page

	Ca	Au	En	Ol	Sa	Cr	Li	Ma	Sp	Tr	Py	Al	An	Gy	AmFe	AmMg	IOM	FeNi	BB
Ol	0.02	-0.09	0.03	1.00	-0.26	-0.16	0.01	-0.01	0.11	0.16	0.02	0.10	-0.06	-0.22	-0.05	-0.02	-0.06	0.09	-0.05
Sa	-0.21	0.10	-0.05	-0.26	1.00	0.26	0.02	-0.34	-0.22	-0.15	0.01	-0.06	-0.12	-0.07	0.15	0.07	-0.04	-0.22	-0.24
Cr	0.11	0.20	-0.10	-0.16	0.26	1.00	-0.22	-0.19	-0.19	-0.41	0.07	-0.41	0.00	0.10	-0.12	-0.09	-0.14	0.05	-0.10
Li	-0.23	-0.10	0.00	0.01	0.02	-0.22	1.00	0.00	-0.19	0.19	-0.18	0.04	-0.09	-0.17	0.25	0.08	-0.03	-0.38	0.12
Ma	0.10	-0.31	0.15	-0.01	-0.34	-0.19	0.00	1.00	0.12	0.03	-0.12	0.06	0.05	-0.08	-0.31	-0.21	0.08	0.09	0.10
Sp	0.01	-0.11	0.03	0.11	-0.22	-0.19	-0.19	0.12	1.00	0.13	-0.06	-0.07	-0.07	0.03	-0.15	0.00	0.03	-0.05	0.12
Tr	-0.12	-0.22	0.03	0.16	-0.15	-0.41	0.19	0.03	0.13	1.00	-0.01	0.22	0.18	-0.19	0.02	0.12	-0.13	-0.08	0.03
Py	-0.17	-0.14	0.13	0.02	0.01	0.07	-0.18	-0.12	-0.06	-0.01	1.00	0.13	0.08	-0.17	-0.25	0.11	-0.25	0.02	-0.06
Al	-0.29	-0.11	0.19	0.10	-0.06	-0.41	0.04	0.06	-0.07	0.22	0.13	1.00	-0.05	-0.22	0.26	-0.08	-0.04	-0.25	-0.08
An	0.11	-0.31	0.02	-0.06	-0.12	0.00	-0.09	0.05	-0.07	0.18	0.08	-0.05	1.00	-0.09	-0.09	-0.14	-0.12	0.13	-0.08
Gy	-0.02	-0.11	-0.04	-0.22	-0.07	0.10	-0.17	-0.08	0.03	-0.19	-0.17	-0.22	-0.09	1.00	-0.07	-0.13	0.05	-0.03	0.00
AmFe	-0.30	0.42	-0.17	-0.05	0.15	-0.12	0.25	-0.31	-0.15	0.02	-0.25	0.26	-0.09	-0.07	1.00	-0.19	-0.20	-0.36	-0.18
AmMg	-0.06	-0.03	-0.17	-0.02	0.07	-0.09	0.08	-0.21	0.00	0.12	0.11	-0.08	-0.14	-0.13	-0.19	1.00	-0.09	-0.18	-0.02
IOM	-0.08	-0.15	0.04	-0.06	-0.04	-0.14	-0.03	0.08	0.03	-0.13	-0.25	-0.04	-0.12	0.05	-0.20	-0.09	1.00	-0.04	0.03
FeNi	0.13	0.03	-0.12	0.09	-0.22	0.05	-0.38	0.09	-0.05	-0.08	0.02	-0.25	0.13	-0.03	-0.36	-0.18	-0.04	1.00	0.06
BB	-0.06	-0.36	0.07	-0.05	-0.24	-0.10	0.12	0.10	0.12	0.03	-0.06	-0.08	-0.08	0.00	-0.18	-0.02	0.03	0.06	1.00

Table C.39: Correlation matrix for the *glennrealextP1* `MCMC()` unmixing.

	Ca	Au	En	Ol	Sa	Cr	Li	Ma	Sp	Tr	Py	Al	An	Gy	AmFe	AmMg	IOM	FeNi	BB
Ca	1.00	-0.22	-0.14	-0.28	-0.32	-0.15	-0.08	0.30	-0.10	-0.24	-0.30	-0.01	0.06	-0.14	0.04	0.00	-0.02	-0.10	-0.20
Au	-0.22	1.00	0.13	0.14	0.27	-0.01	-0.10	-0.18	0.05	0.35	0.25	-0.15	-0.17	0.11	-0.05	-0.10	-0.10	0.04	-0.03
En	-0.14	0.13	1.00	0.34	0.46	0.10	-0.25	-0.13	-0.10	-0.06	0.56	-0.11	-0.05	0.26	-0.07	-0.03	-0.07	-0.10	0.16
Ol	-0.28	0.14	0.34	1.00	0.36	-0.03	-0.22	-0.20	0.03	0.10	0.40	-0.12	-0.14	0.18	-0.14	-0.17	0.05	-0.16	0.08
Sa	-0.32	0.27	0.46	0.36	1.00	0.26	-0.29	-0.23	0.09	0.12	**0.66**	-0.06	-0.17	0.18	0.02	-0.08	0.10	-0.17	0.31
Cr	-0.15	-0.01	0.10	-0.03	0.26	1.00	0.04	-0.11	-0.24	-0.14	0.18	0.07	-0.03	0.00	0.09	-0.19	-0.17	0.11	0.07

Table C.39 continued from previous page

	Ca	Au	En	Ol	Sa	Cr	Li	Ma	Sp	Tr	Py	Al	An	Gy	AmFe	AmMg	IOM	FeNi	BB
Li	-0.08	-0.10	-0.25	-0.22	-0.29	0.04	1.00	-0.01	-0.37	0.03	-0.28	0.17	0.19	-0.36	0.09	-0.09	-0.38	0.35	-0.28
Ma	0.30	-0.18	-0.13	-0.20	-0.23	-0.11	-0.01	1.00	-0.33	-0.29	-0.26	0.04	-0.03	-0.21	0.09	-0.05	0.13	0.04	-0.28
Sp	-0.10	0.05	-0.10	0.03	0.09	-0.24	-0.37	-0.33	1.00	0.23	0.09	-0.20	-0.24	0.18	-0.09	0.14	0.18	-0.31	0.03
Tr	-0.24	0.35	-0.06	0.10	0.12	-0.14	0.03	-0.29	0.23	1.00	0.09	-0.38	-0.27	0.07	-0.15	0.12	-0.09	-0.12	-0.01
Py	-0.30	0.25	0.56	0.40	**0.66**	0.18	-0.28	-0.26	0.09	0.09	1.00	-0.27	-0.12	0.44	-0.12	0.00	-0.06	-0.04	0.28
Al	-0.01	-0.15	-0.11	-0.12	-0.06	0.07	0.17	0.04	-0.20	-0.38	-0.27	1.00	0.11	-0.18	0.15	-0.26	-0.08	0.02	-0.23
An	0.06	-0.17	-0.05	-0.14	-0.17	-0.03	0.19	-0.03	-0.24	-0.27	-0.12	0.11	1.00	-0.18	0.15	-0.26	-0.17	0.17	-0.15
Gy	-0.14	0.11	0.26	0.18	0.18	0.00	-0.36	-0.21	0.18	0.07	0.44	-0.18	-0.18	1.00	-0.13	0.02	-0.01	-0.23	0.19
AmFe	0.04	-0.05	-0.07	-0.14	0.02	0.09	0.09	0.09	-0.09	-0.15	-0.12	0.15	0.15	-0.13	1.00	-0.11	-0.01	0.09	-0.02
AmMg	0.00	-0.10	-0.03	-0.17	-0.08	-0.19	-0.09	-0.05	0.14	0.12	0.00	-0.26	-0.26	0.02	-0.11	1.00	0.02	-0.22	0.16
IOM	-0.02	-0.10	-0.07	0.05	0.10	-0.17	-0.38	0.13	0.18	-0.09	-0.06	-0.08	-0.17	-0.01	-0.01	0.02	1.00	-0.42	-0.01
FeNi	-0.10	0.04	-0.10	-0.16	-0.17	0.11	0.35	0.04	-0.31	-0.12	-0.04	0.02	0.17	-0.23	0.09	-0.22	-0.42	1.00	-0.22
BB	-0.20	-0.03	0.16	0.08	0.31	0.07	-0.28	-0.28	0.03	-0.01	0.28	-0.23	-0.15	0.19	-0.02	0.16	-0.01	-0.22	1.00

Table C.40: Correlation matrix for the *glennrealextP3* `MCMC()` unmixing.

	Ca	Au	En	Ol	Sa	Cr	Li	Ma	Sp	Tr	Py	Al	An	Gy	AmFe	AmMg	IOM	FeNi	BB
Ca	1.00	**0.65**	**0.65**	-0.21	0.44	**0.64**	-0.31	**0.89**	0.45	**0.65**	0.53	0.44	**0.68**	**0.80**	0.03	**0.76**	0.16	0.41	**0.82**
Au	**0.65**	1.00	0.60	-0.17	**0.67**	0.54	-0.05	**0.68**	0.39	0.41	**0.69**	0.58	0.60	0.58	0.39	**0.61**	0.49	**0.69**	**0.79**
En	**0.65**	0.60	1.00	-0.18	0.54	0.34	-0.12	**0.69**	0.33	0.42	0.53	0.41	0.47	0.59	0.14	**0.64**	0.21	0.46	**0.66**
Ol	-0.21	-0.17	-0.18	1.00	-0.20	-0.22	-0.03	-0.17	-0.56	-0.33	-0.24	-0.20	0.13	0.00	0.22	-0.05	0.33	-0.28	-0.28
Sa	0.44	**0.67**	0.54	-0.20	1.00	0.35	0.07	0.52	0.37	0.28	**0.61**	0.55	0.43	0.43	0.40	0.45	0.26	**0.61**	**0.68**
Cr	**0.64**	0.54	0.34	-0.22	0.35	1.00	-0.29	**0.64**	0.22	0.36	0.37	0.42	0.52	**0.68**	0.06	0.53	0.25	0.34	**0.61**
Li	-0.31	-0.05	-0.12	-0.03	0.07	-0.29	1.00	-0.28	-0.17	-0.38	-0.03	-0.09	-0.15	-0.30	0.18	-0.15	0.08	-0.03	-0.17
Ma	**0.89**	**0.68**	**0.69**	-0.17	0.52	**0.64**	-0.28	1.00	0.42	**0.65**	0.57	0.44	**0.71**	**0.83**	0.08	**0.77**	0.26	0.44	**0.86**
Sp	0.45	0.39	0.33	-0.56	0.37	0.22	-0.17	0.42	1.00	**0.62**	0.53	0.29	0.10	0.23	-0.12	0.33	-0.27	0.44	0.59

Table C.40 continued from previous page

	Ca	Au	En	Ol	Sa	Cr	Li	Ma	Sp	Tr	Py	Al	An	Gy	AmFe	AmMg	IOM	FeNi	BB
Tr	**0.65**	0.41	0.42	-0.33	0.28	0.36	-0.38	**0.65**	**0.62**	1.00	0.49	0.29	0.32	0.47	-0.14	0.51	-0.20	0.29	**0.67**
Py	0.53	**0.69**	0.53	-0.24	**0.61**	0.37	-0.03	0.57	0.53	0.49	1.00	0.48	0.37	0.41	0.21	0.52	0.23	**0.62**	**0.69**
Al	0.44	0.58	0.41	-0.20	0.55	0.42	-0.09	0.44	0.29	0.29	0.48	1.00	0.43	0.36	0.31	0.37	0.31	**0.61**	**0.61**
An	**0.68**	0.60	0.47	0.13	0.43	0.52	-0.15	**0.71**	0.10	0.32	0.37	0.43	1.00	**0.80**	0.35	**0.64**	0.50	0.37	**0.64**
Gy	**0.80**	0.58	0.59	0.00	0.43	**0.68**	-0.30	**0.83**	0.23	0.47	0.41	0.36	**0.80**	1.00	0.19	**0.73**	0.36	0.41	**0.73**
AmFe	0.03	0.39	0.14	0.22	0.40	0.06	0.18	0.08	-0.12	-0.14	0.21	0.31	0.35	0.19	1.00	0.08	0.44	0.30	0.21
AmMg	**0.76**	**0.61**	**0.64**	-0.05	0.45	0.53	-0.15	**0.77**	0.33	0.51	0.52	0.37	**0.64**	**0.73**	0.08	1.00	0.31	0.45	**0.72**
IOM	0.16	0.49	0.21	0.33	0.26	0.25	0.08	0.26	-0.27	-0.20	0.23	0.31	0.50	0.36	0.44	0.31	1.00	0.23	0.20
FeNi	0.41	**0.69**	0.46	-0.28	**0.61**	0.34	-0.03	0.44	0.44	0.29	**0.62**	**0.61**	0.37	0.41	0.30	0.45	0.23	1.00	**0.67**
BB	**0.82**	**0.79**	**0.66**	-0.28	**0.68**	**0.61**	-0.17	**0.86**	0.59	**0.67**	**0.69**	**0.61**	**0.64**	**0.73**	0.21	**0.72**	0.20	**0.67**	1.00

Table C.41: brucerealmodminP1 OptEst corrSx

brucerealmodminP1	Au	En	Ol	Tr	Al	FeNi
Augite (Au)	1.0000	-0.0003	-0.0097	-0.0126	-0.0159	-0.0220
Enstatite (En)	-0.0003	1.0000	-0.0004	-0.0005	-0.0006	-0.0008
Olivine (Ol)	-0.0097	-0.0004	1.0000	-0.0164	-0.0207	-0.0285
Troilite (Tr)	-0.0126	-0.0005	-0.0164	1.0000	-0.0271	-0.0373
Albite (Al)	-0.0159	-0.0006	-0.0207	-0.0271	1.0000	-0.0470
FeNiMetalSub (FeNi)	-0.0220	-0.0008	-0.0285	-0.0373	-0.0470	1.0000

Table C.42: Correlation matrix for the *brucerealmodexpP1* `OptEst_ASC_ILR()` unmixing.

brucerealmodexpP1	Au	En	Ol	Al	FeNi	Li	Gy	AmFe
Augite (Au)	1.000	-0.012	-0.003	-0.001	-0.010	-0.014	-0.004	-0.006
Enstatite (En)	-0.012	1.000	-0.011	-0.003	-0.033	-0.043	-0.014	-0.020

Table C.42 continued from previous page

brucerealmodexpP1	Au	En	Ol	Al	FeNi	Li	Gy	AmFe
Olivine (Ol)	-0.003	-0.011	1.000	-0.001	-0.009	-0.013	-0.004	-0.006
Albite (Al)	-0.001	-0.003	-0.001	1.000	-0.003	-0.004	-0.001	-0.002
FeNiMetalSub (FeNi)	-0.010	-0.033	-0.009	-0.003	1.000	-0.038	-0.012	-0.017
Lizardite (Li)	-0.014	-0.043	-0.013	-0.004	-0.038	1.000	-0.016	-0.023
Gypsum (Gy)	-0.004	-0.014	-0.004	-0.001	-0.012	-0.016	1.000	-0.008
Amorphous Fe (AmFe)	-0.006	-0.020	-0.006	-0.002	-0.017	-0.023	-0.008	1.000

Table C.43: Correlation matrix for the *brucerealmodexpP2* `OptEst_ASC_ILR()` unmixing.

brucerealmodexpP2	Ol	Al	Li	Ca	AmFe
Olivine (Ol)	1.000	0.037	**-0.903**	-0.003	-0.455
Albite (Al)	0.037	1.000	-0.120	-0.034	**-0.662**
Lizardite (Li)	**-0.903**	-0.120	1.000	-0.216	0.229
Calcite (Ca)	-0.003	-0.034	-0.216	1.000	0.127
Amorphous (AmFe)	-0.455	**-0.662**	0.229	0.127	1.000

Table C.44: Correlation matrix for the *brucerealmodexpP3* `OptEst_ASC_ILR()` unmixing.

brucerealmodexpP3	Au	En	Ol	Tr	Al	FeNi	Li	Ca	Gy	AmFe	BB
Augite (Au)	1.0000	-0.0001	-0.0010	-0.0001	-0.0001	-0.0001	-0.0001	-0.0001	-0.0001	-0.0001	-0.0001
Enstatite (En)	-0.0001	1.0000	-0.0055	-0.0004	-0.0008	-0.0004	-0.0008	-0.0007	-0.0008	-0.0007	-0.0008
Olivine (Ol)	-0.0010	-0.0055	1.0000	-0.0033	-0.0064	-0.0033	-0.0064	-0.0056	-0.0063	-0.0062	-0.0066
Troilite (Tr)	-0.0001	-0.0004	-0.0033	1.0000	-0.0004	-0.0002	-0.0004	-0.0004	-0.0004	-0.0004	-0.0005
Albite (Al)	-0.0001	-0.0008	-0.0064	-0.0004	1.0000	-0.0004	-0.0009	-0.0008	-0.0009	-0.0009	-0.0009
FeNiMetalSub (FeNi)	-0.0001	-0.0004	-0.0033	-0.0002	-0.0004	1.0000	-0.0004	-0.0004	-0.0004	-0.0004	-0.0005
Lizardite (Li)	-0.0001	-0.0008	-0.0064	-0.0004	-0.0009	-0.0004	1.0000	-0.0008	-0.0009	-0.0009	-0.0009

Table C.44 continued from previous page

brucerealmodexpP3	Au	En	Ol	Tr	Al	FeNi	Li	Ca	Gy	AmFe	BB
Calcite (Ca)	-0.0001	-0.0007	-0.0056	-0.0004	-0.0008	-0.0004	-0.0008	1.0000	-0.0008	-0.0008	-0.0008
Gypsum (Gy)	-0.0001	-0.0008	-0.0063	-0.0004	-0.0009	-0.0004	-0.0009	-0.0008	1.0000	-0.0008	-0.0009
Amorphous Fe (AmFe)	-0.0001	-0.0007	-0.0062	-0.0004	-0.0009	-0.0004	-0.0009	-0.0008	-0.0008	1.0000	-0.0009
BB	-0.0001	-0.0008	-0.0066	-0.0005	-0.0009	-0.0005	-0.0009	-0.0008	-0.0009	-0.0009	1.0000

Table C.45: Correlation matrix for the *brucerealmodexpP4* `OptEst_ASC_ILR()` unmixing.

brucerealmodexpP4	Au	En	Ol	Tr	Al	FeNi	Ca	BB
Augite (Au)	1.000	-0.156	-0.073	-0.152	-0.152	-0.153	-0.113	-0.201
Enstatite (En)	-0.156	1.000	-0.073	-0.153	-0.154	-0.154	-0.112	-0.201
Olivine (Ol)	-0.073	-0.073	1.000	-0.073	-0.070	-0.074	-0.054	-0.097
Troilite (Tr)	-0.152	-0.153	-0.073	1.000	-0.149	-0.157	-0.122	-0.206
Albite (Al)	-0.152	-0.154	-0.070	-0.149	1.000	-0.149	-0.093	-0.196
FeNiMetalSub (FeNi)	-0.153	-0.154	-0.074	-0.157	-0.149	1.000	-0.121	-0.207
Calcite (Ca)	-0.113	-0.112	-0.054	-0.122	-0.093	-0.121	1.000	-0.159
BB	-0.201	-0.201	-0.097	-0.206	-0.196	-0.207	-0.159	1.000

Table C.46: Correlation matrix for the *brucerealmodminU* `MCMC()` unmixing.

brucerealmodminU	Au	En	Ol	Tr	Al	FeNi
Augite (Au)	1.0000	-0.1409	-0.3070	-0.0627	-0.0487	-0.0503
Enstatite (En)	-0.1409	1.0000	-0.3093	-0.0446	-0.0566	-0.0590
Olivine (Ol)	-0.3070	-0.3093	1.0000	-0.5199	-0.0745	-0.5171
Troilite (Tr)	-0.0627	-0.0446	-0.5199	1.0000	-0.0179	-0.1637
Albite (Al)	-0.0487	-0.0566	-0.0745	-0.0179	1.0000	-0.0250
FeNiMetalSub (FeNi)	-0.0503	-0.0590	-0.5171	-0.1637	-0.0250	1.0000

Table C.47: Correlation matrix for the *brucerealmodexpU* `MCMC()` unmixing.

brucerealmodexpU	Au	En	Ol	Tr	Al	FeNi	Li	Ca	Gy	AmFe	BB
Augite (Au)	1.000	-0.232	-0.109	-0.066	-0.030	-0.157	-0.008	-0.096	-0.219	-0.174	-0.038
Enstatite (En)	-0.232	1.000	-0.021	-0.068	-0.295	-0.020	0.094	-0.059	0.132	-0.037	-0.225
Olivine (Ol)	-0.109	-0.021	1.000	-0.152	-0.111	-0.165	-0.060	-0.096	-0.016	-0.166	-0.096
Troilite (Tr)	-0.066	-0.068	-0.152	1.000	-0.223	-0.045	-0.107	0.018	-0.080	-0.011	-0.120
Albite (Al)	-0.030	-0.295	-0.111	-0.223	1.000	-0.098	-0.052	-0.141	-0.152	-0.186	-0.006
FeNiMetalSub (FeNi)	-0.157	-0.020	-0.165	-0.045	-0.098	1.000	-0.011	-0.074	-0.020	-0.020	-0.179
Lizardite (Li)	-0.008	0.094	-0.060	-0.107	-0.052	-0.011	1.000	-0.204	0.008	-0.060	-0.120
Calcite (Ca)	-0.096	-0.059	-0.096	0.018	-0.141	-0.074	-0.204	1.000	-0.195	-0.020	-0.081
Gypsum (Gy)	-0.219	0.132	-0.016	-0.080	-0.152	-0.020	0.008	-0.195	1.000	-0.019	-0.146
AmorphousFe (AmFe)	-0.174	-0.037	-0.166	-0.011	-0.186	-0.020	-0.060	-0.020	-0.019	1.000	-0.207
BB	-0.038	-0.225	-0.096	-0.120	-0.006	-0.179	-0.120	-0.081	-0.146	-0.207	1.000

Table C.48: Correlation matrix for the *brucerealmodexpP1* `MCMC()` unmixing.

brucerealmodexpP1	Au	En	Ol	Tr	Al	FeNi	Li	Ca	Gy	AmFe	BB
Augite (Au)	1.000	-0.075	0.154	-0.127	-0.110	0.583	-0.575	**-0.657**	-0.392	-0.142	**-0.663**
Enstatite (En)	-0.075	1.000	0.061	-0.037	0.029	-0.180	0.157	0.151	0.230	0.165	0.088
Olivine (Ol)	0.154	0.061	1.000	-0.131	-0.163	-0.026	0.029	-0.053	0.092	0.201	-0.026
Troilite (Tr)	-0.127	-0.037	-0.131	1.000	-0.033	0.032	-0.042	0.032	-0.064	-0.131	-0.024
Albite (Al)	-0.110	0.029	-0.163	-0.033	1.000	-0.171	0.151	0.156	0.085	0.073	0.129
FeNiMetalSub (FeNi)	0.583	-0.180	-0.026	0.032	-0.171	1.000	**-0.840**	**-0.906**	**-0.770**	-0.488	**-0.884**
Lizardite (Li)	-0.575	0.157	0.029	-0.042	0.151	**-0.840**	1.000	**0.853**	**0.733**	0.520	**0.828**
Calcite (Ca)	**-0.657**	0.151	-0.053	0.032	0.156	**-0.906**	**0.853**	1.000	**0.737**	0.429	**0.908**

Table C.48 continued from previous page

brucerealmodexpU	Au	En	Ol	Tr	Al	FeNi	Li	Ca	Gy	AmFe	BB
Gypsum (Gy)	-0.392	0.230	0.092	-0.064	0.085	**-0.770**	**0.733**	**0.737**	1.000	**0.641**	**0.723**
AmorphousFe (AmFe)	-0.142	0.165	0.201	-0.131	0.073	-0.488	0.520	0.429	**0.641**	1.000	0.396
BB	**-0.663**	0.088	-0.026	-0.024	0.129	**-0.884**	**0.828**	**0.908**	**0.723**	0.396	1.000

Table C.49: Correlation matrix for the *brucerealmodexpP2* `MCMC()` unmixing.

brucerealmodexpP2	Au	En	Ol	Tr	Al	FeNi	Li	Ca	Gy	AmFe	BB
Augite (Au)	1.000	-0.125	-0.046	-0.081	-0.091	-0.050	-0.202	-0.055	-0.070	-0.133	-0.033
Enstatite (En)	-0.125	1.000	-0.106	0.014	-0.068	-0.023	-0.181	0.039	-0.049	-0.202	0.047
Olivine (Ol)	-0.046	-0.106	1.000	-0.073	-0.192	-0.107	-0.111	-0.099	-0.179	0.023	-0.121
Troilite (Tr)	-0.081	0.014	-0.073	1.000	0.017	-0.146	-0.089	0.037	0.040	-0.107	-0.128
Albite (Al)	-0.091	-0.068	-0.192	0.017	1.000	-0.089	-0.160	0.253	-0.089	-0.311	-0.101
FeNiMetalSub (FeNi)	-0.050	-0.023	-0.107	-0.146	-0.089	1.000	-0.219	-0.009	-0.219	-0.105	0.118
Lizardite (Li)	-0.202	-0.181	-0.111	-0.089	-0.160	-0.219	1.000	-0.127	-0.033	-0.051	-0.271
Calcite (Ca)	-0.055	0.039	-0.099	0.037	0.253	-0.009	-0.127	1.000	-0.109	-0.141	-0.075
Gypsum (Gy)	-0.070	-0.049	-0.179	0.040	-0.089	-0.219	-0.033	-0.109	1.000	-0.050	-0.323
AmorphousFe (AmFe)	-0.133	-0.202	0.023	-0.107	-0.311	-0.105	-0.051	-0.141	-0.050	1.000	-0.105
BB	-0.033	0.047	-0.121	-0.128	-0.101	0.118	-0.271	-0.075	-0.323	-0.105	1.000

Table C.50: Correlation matrix for the *brucerealmodexpP3* `MCMC()` unmixing.

brucerealmodexpP3	Au	En	Ol	Tr	Al	FeNi	Li	Ca	Gy	AmFe	BB
Augite (Au)	1.000	0.100	-0.231	-0.116	0.140	-0.135	0.175	0.215	0.190	0.155	0.170
Enstatite (En)	0.100	1.000	-0.412	-0.223	0.127	0.046	0.368	0.401	0.383	0.390	0.363
Olivine (Ol)	-0.231	-0.412	1.000	**0.725**	-0.114	-0.124	**-0.857**	**-0.914**	**-0.903**	**-0.887**	**-0.879**
Troilite (Tr)	-0.116	-0.223	**0.725**	1.000	-0.063	-0.213	**-0.722**	**-0.690**	**-0.739**	**-0.694**	**-0.736**

Table C.50 continued from previous page

brucerealmodexpP3	Au	En	Ol	Tr	Al	FeNi	Li	Ca	Gy	AmFe	BB
Albite (Al)	0.140	0.127	-0.114	-0.063	1.000	-0.047	0.129	0.135	0.112	0.101	0.136
FeNiMetalSub (FeNi)	-0.135	0.046	-0.124	-0.213	-0.047	1.000	0.305	0.227	0.261	0.289	0.307
Lizardite (Li)	0.175	0.368	**-0.857**	**-0.722**	0.129	0.305	1.000	**0.895**	**0.922**	**0.887**	**0.916**
Calcite (Ca)	0.215	0.401	**-0.914**	**-0.690**	0.135	0.227	**0.895**	1.000	**0.928**	**0.887**	**0.907**
Gypsum (Gy)	0.190	0.383	**-0.903**	**-0.739**	0.112	0.261	**0.922**	**0.928**	1.000	**0.909**	**0.935**
AmorphousFe (AmFe)	0.155	0.390	**-0.887**	**-0.694**	0.101	0.289	**0.887**	**0.887**	**0.909**	1.000	**0.907**
BB	0.170	0.363	**-0.879**	**-0.736**	0.136	0.307	**0.916**	**0.907**	**0.935**	**0.907**	1.000

Table C.51: Correlation matrix for the *brucerealmodexpP4* `MCMC()` unmixing.

brucerealmodexpP4	Au	En	Ol	Tr	Al	FeNi	Li	Ca	Gy	AmFe	BB
Augite (Au)	1.000	0.151	-0.292	0.038	0.222	0.202	0.382	0.170	0.190	-0.022	-0.132
Enstatite (En)	0.151	1.000	-0.288	0.112	0.042	0.014	0.242	-0.085	0.104	0.133	-0.022
Olivine (Ol)	-0.292	-0.288	1.000	0.003	-0.208	-0.386	-0.292	-0.173	-0.070	-0.157	-0.164
Troilite (Tr)	0.038	0.112	0.003	1.000	0.008	-0.144	0.054	0.102	0.022	0.045	-0.121
Albite (Al)	0.222	0.042	-0.208	0.008	1.000	0.047	0.107	0.134	0.019	-0.132	-0.087
FeNiMetalSub (FeNi)	0.202	0.014	-0.386	-0.144	0.047	1.000	0.124	0.115	0.008	0.042	-0.044
Lizardite (Li)	0.382	0.242	-0.292	0.054	0.107	0.124	1.000	0.170	0.290	0.074	0.016
Calcite (Ca)	0.170	-0.085	-0.173	0.102	0.134	0.115	0.170	1.000	0.178	-0.012	-0.063
Gypsum (Gy)	0.190	0.104	-0.070	0.022	0.019	0.008	0.290	0.178	1.000	-0.028	-0.031
AmorphousFe (AmFe)	-0.022	0.133	-0.157	0.045	-0.132	0.042	0.074	-0.012	-0.028	1.000	-0.018
BB	-0.132	-0.022	-0.164	-0.121	-0.087	-0.044	0.016	-0.063	-0.031	-0.018	1.000